Mapping the Big Island of Deformation around N=20 and 28

Ian Murray

université PARIS-SACLAY

NNT: 2018SACLS196

Thèse de doctorat

Mapping the *Big Island of Deformation* around N=20, 28

Thèse de doctorat de l'Université Paris-Saclay
préparée à l'Université Paris-Sud

École doctorale n°576 PHENIICS
Particules, Hadrons, Énergie, Noyau,
Instrumentation, Imagerie, Cosmos et Simulation

Spécialité de doctorat: Structure et réactions nucléaires

Thèse présentée et soutenue à Orsay, le 6 juillet 2018, par

Ian MURRAY

Composition du Jury :

Tiina SUOMIJARVI Professeure, IPN, Université Paris-Sud	Président
Stéphane GRÉVY Directeur de Recherche, CENBG, Université de Bordeaux	Rapporteur
Silvia LENZI Professeure, Università degli Studi di Padova	Rapporteur
Alain GILLIBERT Chargé de Recherche, IRFU CEA-Saclay	Examinateur
Riccardo RAABE Professeur, Institute for Nuclear and Radiation Physics, KU Leuven	Examinateur
Marion MACCORMICK Chargée de Recherche, IPN, Université Paris-Sud	Directrice de thèse

Acknowledgements

I would like to thank my supervisor Dr. Marion McCormick for providing the opportunity to perform this research at both IPN and RIKEN as part of the RIKEN International Program Associate program. I also thank Dr. Michiharu Wada and Dr. Sarah Naomi for their participation in the arrangement of the funding, and the funding institutes of the Université Paris Saclay doctoral school PHENIICS and RIKEN.

I am grateful to Dr. Michiharu Wada and the members of the SLOWRI group, Dr. Yuta Ito, Dr. Sota Kimura, Dr. Jun Young Moon, Dr. Marco Rosenbusch, and Dr. Peter Schury, for introducing the state-of-the-art MR-ToF technique and for providing the numerous experiences to gain practical knowledge on low-energy ion manipulation.

Furthermore, I would like to express my sincere appreciation and gratitude to the members of the Radioactive Isotope Physics Laboratory and the SUNFLOWER collaboration. I would like to thank Dr. Pieter Doornenbal who provided scientific guidance on in-beam gamma-ray spectroscopy and RIBF detectors, of which was crucial for the realization of this thesis. Many thanks to Dr. Frank Browne, Dr. Sidong Chen, Dr. Liliana Cortés, Wilmar Rodriguez, Dr. David Steppenback, Dr. Ryo Taniuchi, Victor Vaquero, and Dr. Kathrin Wimmer for the scientific interaction and the lively experiences both in and out of the lab.

I also acknowledge Dr. Daniel Bazin, Dr. Heather Crawford and Dr. Paul Fallon for providing the opportunity to analyze the excellent experimental data of the exotic isotopes of this thesis. In addition, I would like to thank Dr. Naofumi Tsunoda, Dr. Yutaka Utsuno, Dr. Jeff Tostevin and Dr. Ikuko Hamamoto for their theoretical calculations.

Special thanks to Dr. Freddy Flavigny, Dr. David Verney and others of the NESTER group at IPN for many valuable scientific discussions.

I am grateful to the rapporteurs and jury members for their comments and participation in my thesis defence.

I also thank my fellow IPN students, Anastasia Georgiadou, Clément Delafosse, Liqiang Qi and Jana Crkovska for their friendship and guidance in the French thesis process.

And lastly, no words are enough to express my gratitude to my family and Hirotaka Ihara for their words of encouragement and moral support.

Contents

1 Physics Introduction **1**
1.1 Nuclear models . . . 2
1.1.1 Liquid-drop model . . . 2
1.1.2 Nuclear shell model . . . 4
1.1.3 Shell gap evolution . . . 7
1.1.3.1 The monopole interaction . . . 7
1.1.3.2 Higher multipoles . . . 9
1.1.4 Collective and Nilsson model . . . 10
1.1.5 *Island of inversion* at $N = 20$ . . . 11
1.1.6 Quenching of $N = 28$ . . . 14
1.2 Direct nuclear reactions . . . 16
1.2.1 Nucleon knockout reactions . . . 18
1.2.2 Eikonal and sudden approximations . . . 19
1.2.2.1 Two-nucleon knockout reactions . . . 20
1.2.3 Reduction factor . . . 20
1.3 In-beam γ-ray spectroscopy . . . 20
1.3.1 Common features of γ-ray spectroscopy . . . 21
1.3.2 Emission of γ-rays at relativistic velocities . . . 22
1.3.3 Reconstructed energy resolution . . . 25
1.3.4 General properties of electromagnetic decay processes . . . 25
1.3.4.1 Transition probabilities . . . 25
1.3.4.2 Selection rules . . . 27
1.4 In-flight radioactive ion-beam production . . . 27
1.4.1 Projectile-fragmentation . . . 28

2 Experimental Setup **31**
2.1 The Radioactive Ion Beam Factory at the RIKEN Nishina Center for Accelerator-Based Science . . . 31
2.2 BigRIPS . . . 32
2.2.1 Momentum-loss achromats for in-flight production separation 33
2.3 ZeroDegree . . . 35
2.3.1 $ToF - B\rho - \Delta E$ method . . . 36
2.3.1.1 Twofold $B\rho$ method . . . 37
2.4 BigRIPS and ZeroDegree beamline detectors . . . 37
2.4.1 Parallel plate avalanche counters - PPAC . . . 38
2.4.2 Time-of-flight plastic scintillator detectors . . . 40
2.4.3 Ionization chambers . . . 41
2.4.4 RIBF DAQ . . . 42
2.5 DALI2 detector array . . . 42
2.5.1 Atomic background and shielding . . . 43
2.5.2 DALI2 DAQ . . . 45

3 Data Analysis **49**
3.1 Particle identification in BigRIPS and ZeroDegree 49
3.1.1 Event-by-event focal plane trajectories 49
3.1.2 A/Q and Z reconstruction 52
3.1.2.1 Experiment NP1312-RIBF03 53
3.1.2.2 Experiment NP906-RIBF02 53
3.1.2.3 Mass-over-charge resolution 56
3.1.3 Removal of spurious and background events 56
3.1.3.1 Photomultiplier noise rejection 57
3.1.3.2 Plastic scintillator gates 57
3.1.3.3 Fiducial cuts 57
3.1.4 Species selection 58
3.1.4.1 Species selection for experiment NP1312-RIBF03 . . . 59
3.1.4.2 Species selection for experiment NP906-RIBF02 59
3.1.5 Secondary reaction target 59
3.2 Beam velocities for γ-ray reconstruction 62
3.2.1 Additional considerations 65
3.3 Inclusive cross section measurement procedure 66
3.3.1 Correction for momentum acceptances 67
3.3.2 Correction for inefficiencies 68
3.3.3 Exclusive cross section measurement procedure 68
3.4 DALI2 70
3.4.1 Energy calibration 70
3.4.1.1 Calibration uncertainty 71
3.4.2 CFD thresholds 72
3.4.3 Time alignment 72
3.4.4 DALI GEANT4 simulations 74
Comparison between experimental and simulated DALI efficiency 75
Beam velocity uncertainty 76

4 Results **79**
4.1 ^{32}Ne 79
4.1.1 ^{34}Mg(^{9}Be,X)^{32}Ne 79
4.1.1.1 Reaction summary and inclusive cross section 79
4.1.1.2 γ-ray analysis 79
Fit summary 82
4.1.2 ^{33}Na(^{9}Be,X)^{32}Ne 84
4.1.2.1 Reaction summary and inclusive cross section 84
4.1.2.2 γ-ray analysis 84
Fit summary 84
4.1.3 Summary 84
4.1.3.1 2_1^+ lifetime uncertainty 85
4.1.3.2 Beam velocity uncertainty 87
4.2 ^{39}Al 88
4.2.1 ^{39}Al(C/C_2H_4,γ)^{39}Al 88
4.2.1.1 γ-ray analysis 88
4.2.2 ^{40}Al(C/C_2H_4,X)^{39}Al 90
4.2.2.1 Reaction summary and inclusive cross section 90
4.2.2.2 γ-ray analysis 90
Fit summary 97

γ-γ coincidence . . . 98
Summary . . . 107
4.3 ^{40}Al . . . 110
4.3.1 ^{40}Al(C/C_2H_4,γ)^{40}Al . . . 110
4.3.1.1 γ-ray analysis . . . 110
4.3.2 ^{41}Si(C/C_2H_4,X)^{40}Al and ^{41}Al(C/C_2H_4,X)^{40}Al . . . 112
4.3.2.1 Reaction summary and inclusive cross section . . . 112
4.3.2.2 γ-ray analysis . . . 112
Fit summary . . . 119
γ-γ coincidence . . . 121
Summary . . . 123
4.4 ^{41}Al . . . 125
4.4.1 ^{41}Al(C/C_2H_4,γ)^{41}Al . . . 125
4.4.1.1 γ-ray analysis . . . 125
4.4.2 ^{42}Si(C/C_2H_4,X)^{41}Al . . . 129
4.4.2.1 Reaction summary and inclusive cross section . . . 129
4.4.2.2 γ-ray analysis . . . 129
Fit summary . . . 134
γ-γ coincidence . . . 134
Summary . . . 140
4.5 Other cross sections . . . 142
4.5.1 ^{42}Al(C/C_2H_4,X)^{41}Al . . . 142
4.5.1.1 Reaction summary and inclusive cross section . . . 142
4.5.2 ^{43}Si(C/C_2H_4,X)^{42}Al . . . 142
4.5.2.1 Reaction summary and inclusive cross section . . . 142

5 Discussion and Interpretation **143**
5.1 ^{32}Ne . . . 143
5.1.1 Systematic trends around $N = 20$ . . . 143
5.1.2 $4_1^+ \rightarrow 2_1^+$ transition . . . 144
5.1.3 Cross sections . . . 146
5.1.3.1 Two-proton knockout cross section . . . 147
5.1.3.2 One-proton knockout cross section interpretation . . . 148
5.1.3.3 Exclusive cross sections . . . 150
5.2 $^{(39-41)}_{13}$Al . . . 153
5.2.1 Systematic trends around $N = 28$ . . . 153
5.2.2 $^{39}_{13}$Al . . . 154
5.2.3 $^{40}_{13}$Al . . . 157
5.2.4 $^{41}_{13}$Al . . . 158
5.2.5 Odd-even Al systematic trends and discussion . . . 160
5.2.5.1 Deformed basis . . . 162
5.2.5.2 Observation of $^{42}_{13}$Al . . . 167
5.2.6 Cross sections . . . 167
5.2.6.1 Proton-induced quasi-free knockout reactions . . . 167
5.2.6.2 Summary of nucleon knockout cross section results . . . 169
5.2.7 Nuclear halos . . . 170

6 Conclusion **171**

A Spectroscopic factors **173**

B The upgrade of DALI2 to DALI2+ **177**

C Single crystal GAGG(Ce) scintillator study **187**

D Article **197**

E Résumé en français **207**
E.1 Introduction 207
E.2 Dispositif expérimental 208
E.3 Résultats et interprétation 209
E.4 $^{32}_{12}$Ne 209
E.5 $^{(39-41)}_{13}$Al 210
E.6 Conclusion 211

Bibliography **213**

List of Figures

1.1 Semi-empirical LDM binding energy as a function of mass number (A) and atomic number (Z) . . . 3
1.2 Illustration of the nucleon-nucleon potential for a spin-singlet state. . . 4
1.3 Phenomenological Wood-Saxon nuclear mean field potential and energy eigenvalues . . . 5
1.4 Difference in LDM binding energy and experimental and extrapolated binding energies . . . 6
1.5 Schematic view of the interaction between spin orbit partners . . . 9
1.6 Schematic view of a deformed nucleus and defining the quantities J, K, L, S, Ω, and Λ in the discussion of the Nilsson model . . . 11
1.7 First outline of the island of inversion . . . 12
1.8 Effective single particle energies for isotones of $N = 20$ as a function of Z . . . 12
1.9 Schematic level schemes around $N = 20$ . . . 13
1.10 Two neutron separation energies illustrating the canonical magic numbers . . . 14
1.11 Schematic level schemes around $N = 28$ . . . 15
1.12 Illustration of peripheral direct knockout reactions . . . 18
1.13 Schematic view of in-flight γ-ray emission . . . 21
1.14 ^{88}Y γ source measured within the DALI2 detector array illustrating general features of γ-ray energy spectra. . . . 22
1.15 Kinematic uncertainties for in-beam γ-rays. . . . 23
1.16 Example of propagation of uncertainties in in-beam γ-ray detection . . . 24
1.17 Primary production cross sections of fragmentation products of the thesis experiments . . . 29

2.1 Overview of the RIBF facility . . . 32
2.2 Schematic overview of the RIBF accelerators . . . 32
2.3 Overview of the BigRIPS separator and ZeroDegree spectrometer . . . 34
2.4 Illustration of the operating principal of a momentum-loss achromat . 35
2.5 Schematic views of RIKEN PPACs . . . 38
2.6 Identification of PPAC $\delta - ray$ events . . . 39
2.7 Side view of tilted-electrode gas ionisation chamber . . . 42
2.8 3D rendering of the DALI2 detector array . . . 43
2.9 Simulated atomic processes . . . 46
2.10 Transmittance of 1 mm Pb lead and Pb mass attenuation coefficient as a function of energy . . . 47
2.11 Schematic of the DALI2 DAQ system . . . 47

3.1 Illustration of T_{sum} gate for F5 PPAC - 1A . . . 50
3.2 Schematic and scaled view of F7 focal plane detectors (PPACS, ion chamber and plastic scintillator) and a sketch of a particle trajectory reconstruction with double PPACs . . . 50

3.3 Number of PPAC signals for various focal planes 51
3.4 Efficiency of particle trajectory reconstruction 52
3.5 A/Q correction 53
3.6 **NP1312-RIBF03**: BigRIPS separator and ZeroDegree spectrometer PID plots 54
3.7 **NP906-RIBF02**: BigRIPS separator and ZeroDegree spectrometer PID plots 55
3.8 **NP906-RIBF02**: Illustration of two methods of charge determination . 56
3.9 **NP1213-RIBF03**: Illustration removal of events with corresponding beam-line plastic scintillator PMT noise. 58
3.10 Background removal for F3 and F7 plastic scintillators 59
3.11 BigRIPS ToF and $F5X$ fiducial cuts 60
3.12 Illustration of BigRIPS ToF_{F3F7} versus $F5X$ 61
3.13 **NP1312-RIBF03**: PID plots with elliptical gates for species selection. . 62
3.14 **NP906-RIBF02**: PID plots with square and elliptical gates for species selection. 63
3.15 Projected ion position at the front of the secondary target 64
3.16 Illustration of velocity before target determination 64
3.17 Example of stopping power as a function of kinetic energy 65
3.18 Example of experimental BigRIPS and ZeroDegree and GEANT4 simulated velocities 66
3.19 Example of the selection of trajectories within full separator and spectrometer acceptance. 69
3.20 Energy resolution and fit energy deviation for all DALI detectors of NP1312-RIBF03. 70
3.21 Fitted energy resolution functions for DALI detectors. 71
3.22 Experimental and GEANT4 simulated ^{137}Cs γ source 73
3.23 DALI time offset corrected for beam-ion ToF (F3F7) 74
3.24 Selection of events in DALI time 75
3.25 Typical DALI response functions 76
3.26 Simulated influence of beam energy deviation on DALI γ-ray Doppler reconstruction for realistic experimental conditions 77

4.1 ^{34}Mg(^{9}Be,X)^{32}Ne Doppler reconstructed γ-ray energy spectrum 80
4.2 Global best fit predictions and experimental first 2_1^+ state lifetimes for Si, Mg, and Ne neutron-rich isotopes 81
4.3 Fit of ^{34}Mg(^{9}Be,X)^{32}Ne doppler reconstructed γ-ray energy spectrum . 82
4.4 Summary of fit results of ^{34}Mg(^{9}Be,X)^{32}Ne. 83
4.5 ^{33}Na(^{9}Be,X)^{32}Ne Doppler reconstructed γ-ray energy spectrum 85
4.6 Fit of ^{33}Na(^{9}Be,X)^{32}Ne doppler reconstructed γ-ray energy spectrum . 85
4.7 Summary of fit results of ^{33}Na(^{9}Be,X)^{32}Ne. 86
4.8 ^{39}Al inelastic scattering doppler reconstructed γ-ray energy spectrum . 88
4.9 Fit of doppler reconstructed ^{39}Al(C/C_2H_4,γ)^{39}Al 89
4.10 Summary of fit results of ^{39}Al inelastic scattering 89
4.11 ^{40}Al(C/C_2H_4,X)^{39}Al Doppler reconstructed γ-ray energy spectrum . . 91
4.12 Fitting 3, 4, 5 peaks of ^{40}Al(C/C_2H_4,X)^{39}Al doppler reconstructed γ-ray energy spectrum 92
4.13 Fitting 6, and 7 peaks of ^{40}Al(C/C_2H_4,X)^{39}Al doppler reconstructed γ-ray energy spectrum 93
4.14 Fitting 5, 6, 7 peaks of ^{40}Al(C/C_2H_4,X)^{39}Al doppler reconstructed γ-ray energy spectrum 94

4.15 415 keV candidate peak . . . 95
4.16 Fitting 7 peaks of ^{40}Al(C/C_2H_4,X)^{39}Al doppler reconstructed γ-ray energy spectrum with four fixed centroid energies . . . 96
4.17 Summary of fit results of ^{40}Al(C/C_2H_4,X)^{39}Al . . . 97
4.18 ^{40}Al(C/C_2H_4,X)^{39}Al γ-γ matrix . . . 98
4.19 Selections for ^{40}Al(C/C_2H_4,X)^{39}Al coincidence analysis and background coincidences, with add-back . . . 99
4.20 ^{40}Al(C/C_2H_4,X)^{39}Al selection A . . . 100
4.21 ^{40}Al(C/C_2H_4,X)^{39}Al selection B . . . 101
4.22 ^{40}Al(C/C_2H_4,X)^{39}Al selection C . . . 102
4.23 ^{40}Al(C/C_2H_4,X)^{39}Al selection D . . . 103
4.24 ^{40}Al(C/C_2H_4,X)^{39}Al selection E . . . 104
4.25 ^{40}Al(C/C_2H_4,X)^{39}Al selection F . . . 105
4.26 ^{40}Al(C/C_2H_4,X)^{39}Al selection G . . . 106
4.27 Experimental transitions and tentative level scheme of ^{39}Al . . . 109
4.28 Inelastic scattering of ^{40}Al doppler reconstructed γ-ray energy spectrum 110
4.29 Inelastic scattering of ^{40}Al with forward DALI detectors . . . 111
4.30 Summary of fit results of ^{40}Al inelastic scattering with forward DALI detectors . . . 111
4.31 ^{41}Si/^{41}Al(C/C_2H_4,X)^{40}Al Doppler reconstructed γ-ray energy spectra 114
4.32 Fitting 2, 3, 4 peaks of ^{41}Al(C/C_2H_4,X)^{40}Al doppler reconstructed γ-ray energy spectrum . . . 115
4.33 Fitting 4, 5, 6 peaks of ^{41}Al(C/C_2H_4,X)^{40}Al doppler reconstructed γ-ray energy spectrum . . . 116
4.34 Fitting 3, 4, 5 peaks of ^{41}Si(C/C_2H_4,X)^{40}Al doppler reconstructed γ-ray energy spectrum . . . 117
4.35 Fitting high energy peak of ^{41}Si(C/C_2H_4,X)^{40}Al doppler reconstructed γ-ray energy spectrum . . . 118
4.36 Summary of fit results of ^{41}Si(C/C_2H_4,X)^{40}Al . . . 119
4.37 Summary of fit results of ^{41}Al(C/C_2H_4,X)^{40}Al . . . 119
4.38 ^{41}Si/^{41}Al(C/C_2H_4,X)^{40}Al γ-γ matrix with and without add-back . . . 120
4.39 Selections for ^{41}Si/^{41}Al(C/C_2H_4,X)^{40}Al coincidence analysis . . . 120
4.40 ^{41}Si/^{41}Al(C/C_2H_4,X)^{40}Al section A and B . . . 121
4.41 ^{41}Si/^{41}Al(C/C_2H_4,X)^{40}Al section C and D . . . 122
4.42 Experimental transitions and tentative level scheme of ^{40}Al . . . 123
4.43 Inelastic scattering of ^{41}Al doppler reconstructed γ-ray energy spectrum 125
4.44 Fit of doppler reconstructed ^{41}Al(C/C_2H_4,γ)^{41}Al . . . 126
4.45 Summary of fit results of ^{41}Al inelastic scattering . . . 126
4.46 Inelastic ^{41}Al scattering $\gamma - \gamma$ coincidence spectrum . . . 127
4.47 Inelastic scattering of ^{41}Al with forward DALI detectors . . . 127
4.48 Summary of fit results of ^{41}Al inelastic scattering with forward DALI detectors . . . 128
4.49 ^{42}Si(C/C_2H_4,X)^{41}Al Doppler reconstructed γ-ray energy spectrum with add-back . . . 130
4.50 Fitting 3, 4, 5 peaks of ^{42}Si(C/C_2H_4,X)^{41}Al doppler reconstructed γ-ray energy spectrum . . . 131
4.51 Fitting 3, 4, 5 peaks of ^{42}Si(C/C_2H_4,X)^{41}Al doppler reconstructed γ-ray energy spectrum . . . 132
4.52 ^{42}Si(C/C_2H_4,X)^{41}Al Doppler recontructed with forward angle detectors 133
4.53 Summary of fit results of ^{42}Si(C/C_2H_4,X)^{41}Al . . . 134
4.54 ^{42}Si(C/C_2H_4,X)^{41}Al γ-γ matrix . . . 135

4.55 Selectons for ^{42}Si(C/C_2H_4,X)^{41}Al coincidence analysis 135
4.56 ^{42}Si(C/C_2H_4,X)^{41}Al background coicidence γ-ray energy spectrum . . 135
4.57 ^{42}Si(C/C_2H_4,X)^{41}Al selection A 136
4.58 ^{42}Si(C/C_2H_4,X)^{41}Al selection B 137
4.59 ^{42}Si(C/C_2H_4,X)^{41}Al selection C 138
4.60 ^{42}Si(C/C_2H_4,X)^{41}Al selection D 139
4.61 Experimental transitions and tentative level scheme of ^{41}Al 141

5.1 Trends of experimental $R_{4/2}$ values and first excited states of Si, Mg and Ne 145
5.2 Tentative experimental and predicted level scheme of ^{32}Ne 146
5.3 Inclusive cross sections and suppression factors of two-proton knock-out to ^{32}Ne 149
5.4 Visualization of the $^{34}_{12}$Mg ground state to $^{32}_{10}$Ne ground state TNA from shell model calculations with SDPF-M and EEdf1 interactions 149
5.5 Systematic trend of reduction factors as a function of nucleon separation energy asymmetry 150
5.6 Experimental exclusive cross sections and theoretical predictions for one- and two-proton knockout to ^{32}Ne and ^{30}Ne 151
5.7 Systematic trends of level schemes of $_{17}$Cl, $_{15}$P, $_{13}$Al and core nucleus $E(2_1^+)$ energies 154
5.8 Evolution of the $E(1/2_1^+) - E(3/2_1^+)$ energy differences for odd-mass $_{19}$K, $_{17}$Cl and $_{15}$P 155
5.9 Experimental transitions, tentative and predicted levels of $^{39}_{13}$Al 156
5.10 Experimental transitions, tentative and predicted levels of $^{40}_{13}$Al 157
5.11 Experimental transitions, tentative and predicted levels of $^{41}_{13}$Al 158
5.12 Experimental (left side of each isotope) and predicted (right side of each isotope) level scheme of odd-even neutron-rich aluminium 160
5.13 Hartree-Fock-Bogoliubov calculated energy surfaces of $^{(34,36,38,40)}_{12}$Mg, $^{(35,37,39,41)}_{13}$Al, $^{(36,38,40,42)}_{14}$Si 162
5.14 One-particle energies for protons of the $^{40}_{12}$Mg $\otimes\, \pi$ system as a function of axially symmetric quadrupole deformation with the Woods-Saxon potential 163
5.15 Rotational bands of $^{(25,27,29)}_{13}$Al and experimental tentative levels of $(39,41)_{13}$Al 164
5.16 Level energies of ground state rotational bands of $^{38}_{12}$Mg ($K^\pi = 0^+$) and $^{(39,41)}_{13}$Al ($K^\pi = 5/2^+$) and fit 165
5.17 Experimental and predicted $E(2_1^+)$ and $E(7/2_1^+)$ energies of $_{12}$Mg and $_{13}$Al 168
5.18 Inclusive cross sections on C_2H_4, C and H 169

B.1 Render of DALI2+ half section. 177
B.2 Render of DALI2+ and the MINOS liquid target. Half slice view. 179
B.3 Two of eight new different positioning plates. 180

E.1 Dispositif expérimental 208

List of Tables

2.1 Overview of general properties of the accelerators at the RIKEN Nishina Center for Accelerator-Based Science . . . 33
2.2 Main properties of BigRIPS and ZeroDegree spectrometers . . . 35
2.3 Typical properties of Sodium Iodide scintillation material . . . 44

3.1 Reconstructed A/Q resolution for selected beam species. . . . 57
3.2 Summary of reaction targets of NP906-RIBF02 and NP1312-RIBF03 experiments . . . 60
3.3 Fit deviation before/during/after NP1312-RIBF03 with γ-ray calibration sources. . . . 72
3.4 Fit deviation before NP906-RIBF02 with γ-ray calibration sources. . . . 72
3.5 Summary of full energy peak efficiency with γ sources and GEANT4 simulation . . . 76

4.1 Summary of ^{34}Mg(^{9}Be,X)^{32}Ne and inclusive cross section . . . 79
4.2 ^{34}Mg(^{9}Be,X)^{32}Ne γ-ray reconstruction settings . . . 79
4.3 Summary of ^{33}Na(^{9}Be,X)^{32}Ne and inclusive cross section . . . 84
4.4 ^{33}Na(^{9}Be,X)^{32}Ne γ-ray reconstruction settings . . . 84
4.5 ^{32}Ne fit results with statistical and systematic uncertainties . . . 85
4.6 One-proton knockout . . . 85
4.7 Two-proton knockout . . . 85
4.8 Fitted experimental peaks of one- and two-proton knockout reaction to $^{32}_{10}$Ne for selected 2^+_1 lifetimes for events with maximum $m_\gamma \leq 3$. Observed γ-rays of each transition. Statistical uncertainty provided by fit. . . . 86
4.9 Fitted experimental peaks of one- and two-proton knockout reaction to $^{32}_{10}$Ne to determine change in fitted energy and observed γ-rays of each transition, as a function of Doppler reconstruction velocity deviation, for events with maximum $m_\gamma \leq 3$. Statistical uncertainty provided by fit. . . . 87
4.10 ^{39}Al(C/C_2H_4,X)^{39}Al γ-ray reconstruction settings . . . 88
4.11 Summary of ^{40}Al(C/C_2H_4,X)^{39}Al and cross section . . . 90
4.12 ^{40}Al(C/C_2H_4,X)^{39}Al γ-ray reconstruction settings . . . 90
4.13 ^{39}Al fit results . . . 97
4.14 ^{39}Al fit results with six transitions . . . 97
4.15 ^{39}Al fit results with four fixed transition energies (764, 800, 883, 995) . . . 97
4.16 ^{40}Al(C/C_2H_4,X)^{39}Al selection A results . . . 100
4.17 ^{40}Al(C/C_2H_4,X)^{39}Al selection B results . . . 101
4.18 ^{40}Al(C/C_2H_4,X)^{39}Al selection C results . . . 102
4.19 ^{40}Al(C/C_2H_4,X)^{39}Al selection D results . . . 103
4.20 ^{40}Al(C/C_2H_4,X)^{39}Al selection E results . . . 104
4.21 ^{40}Al(C/C_2H_4,X)^{39}Al selection F results . . . 105
4.22 ^{40}Al(C/C_2H_4,X)^{39}Al selection G results . . . 106

4.23 ^{39}Al experimental transitions and coincidences . . . 108
4.24 ^{40}Al(C/C_2H_4,X)^{40}Al γ-ray reconstruction settings . . . 110
4.25 Summary of ^{41}Si(C/C_2H_4,X)^{40}Al and cross section . . . 112
4.26 Summary of ^{41}Al(C/C_2H_4,X)^{40}Al and cross section . . . 112
4.27 ^{41}Si(C/C_2H_4,X)^{40}Al γ-ray reconstruction settings . . . 112
4.28 ^{41}Al(C/C_2H_4,X)^{40}Al γ-ray reconstruction settings . . . 113
4.29 ^{40}Al fit results . . . 119
4.30 ^{41}Al(C/C_2H_4,X)^{40}Al . . . 119
4.31 ^{41}Si(C/C_2H_4,X)^{40}Al . . . 119
4.32 ^{40}Al transitions and coincidences . . . 124
4.33 ^{41}Al(C/C_2H_4,X)^{41}Al γ-ray reconstruction settings . . . 125
4.34 Summary of ^{42}Si(C/C_2H_4,X)^{41}Al and cross section . . . 129
4.35 ^{42}Si(C/C_2H_4,X)^{41}Al γ-ray reconstruction settings . . . 129
4.36 ^{42}Si(C/C_2H_4,X)^{41}Al fit results . . . 134
4.37 ^{42}Si(C/C_2H_4,X)^{41}Al selection A results . . . 136
4.38 ^{42}Si(C/C_2H_4,X)^{41}Al selection B results . . . 137
4.39 ^{42}Si(C/C_2H_4,X)^{41}Al selection C results . . . 138
4.40 ^{42}Si(C/C_2H_4,X)^{41}Al selection D results . . . 139
4.41 ^{41}Al transitions and coincidences . . . 141
4.42 Summary of ^{42}Al(C/C_2H_4,X)^{42}Al and cross section . . . 142
4.43 Summary of ^{43}Si(C/C_2H_4,X)^{42}Al and cross section . . . 142

5.1 ^{32,34}Mg and ^{30,32}Ne ground state neutron 0p-0h, 2p-2h and 4p-4h probabilties (%) calculated with the SDPF-M and EEDf1 interactions. . . . 144
5.2 One- and two-proton knockout cross sections for ^{9}Be(^{33}Na,^{32}Ne)X and ^{9}Be(^{34}Mg,^{32}Ne)X reactions . . . 152

A.1 $^{42}_{14}$Si/$^{41}_{13}$Al C^2S calculated with the SDPF-MU interaction . . . 173
A.2 Spectroscopic factor C^2S between $^{40}_{12}$Mg $\otimes$ sd proton and $^{41}_{13}$Al calculated with the SDPF-MU interaction . . . 174
A.3 Spectroscopic factor C^2S between $^{38}_{12}$Mg $\otimes$ sd proton and $^{39}_{13}$Al calculated with the SDPF-MU interaction . . . 175

List of Abbreviations

LDM	**L**iquid **d**rop **m**odel
SM	**S**hell **m**odel
NN	**N**ucleon-**n**ucleon (interaction)
SO	**S**pin-**orbit** (coupling)
SPE	**S**ingle **p**article **e**nergy
ESPE	**E**ffective **s**ingle **p**article **e**nergy
MCSM	**M**onte **c**arlo **s**hell **m**odel
IoI	**I**sland **o**f **i**nversion
CM	**C**entre-of-**m**ass
FEP	**F**ull **e**nergy **p**eak
PF	**P**rojectile **f**ragmentation
RI	**R**adioactive **i**sotope
PMT	**P**hoto **m**ultiplier **t**ube
PPAC	**P**arallel **p**late **a**valanche **c**ounter
IC	**I**on **c**hamber
ToF	**T**ime **o**f **f**light
F1, F2, F3...	**F**ocal plane 1, 2, 3... (BigRIPS/ ZeroDegree)
STQ	**S**uperconducting **t**riplet **q**uadrupole (BigRIPS/ ZeroDegree)
D1, D2, D3...	**D**ipole 1, 2, 3... (BigRIPS/ ZeroDegree)
DALI	**D**etector **a**rray for **l**ow **i**ntensity radiation
DAQ	**D**ata **a**c**q**uisition
QDC	charge**(q)**-to-**d**igital-**c**onverter
ADC	**A**nalog-to-**d**igital-**c**onverter
TDC	**T**ime-to-**d**igital-**c**onverter
CFD	**C**onstant-**f**raction **d**iscriminator

Chapter 1

Physics Introduction

The study of collective systems in nature, and their reduction to their fundamental parts has provided victories to scientific research. Such as the understanding of chemical molecules from their underlying atomic physics, or the interpretation of complete biological systems from the structure of a DNA molecule: the base pair ordering. However, the belief that all systems can be broken down into fundamental laws, a theory of everything [1, 2], has been contested by some scholars, such as P. W. Anderson [3, 4].

Anderson, in his philosophical essay, *More is Different* [3], argues that such collective systems precipitate *emergent* properties, which may be difficult or even impossible to deduce from microscopic laws. To the extreme of infinite systems, Anderson claims that the *emergent* principals take over the behaviour of the system. Furthermore, the experimental evidence of symmetry-breaking in nature provides additional arguments for this non-reductionism view.

Nuclear physics therefore is an *emergent phenomenon*. The discovery of the nucleus by Rutherford [5] could not have been predicted, even if a set of fundamental principals could have been known. A more recent example is the paradigm shift associated with the discovery of non-spherical and collective nuclear shapes of a rugby ball (axially symmetric prolate) or a pancake (axially symmetric oblate)[1] [7] even if a dipole moment does not exist. Nuclear physics can also be described as an experimental type of science. Certainly, both theoretical interpretation of experimental observations and theoretical predictions offer guides for experimental exploration and a deepening of understanding of the field.

The nature of the atomic nucleus as a quantum many-body system leads to the *emergence* of microscopic properties. One such property, the observation of so-called *magic numbers* $(8, 20, 28, 50...)$ of nucleons (section 1.1.2) has permitted the development of the independent-particle shell model of the nucleus. This thesis explores the evolution of this understanding of the nuclear system, through study of asymmetrical neutron to proton ratio isotopes. The modification of the filling of proton or neutron orbits has been demonstrated to emphasize components of the forces between nucleons, manifesting in the dissolution of the canonical *magic numbers* and precipitation of new numbers (section 1.1.3).

Exotic neutron-rich isotopes of neon ($^{32}_{10}$Ne) and aluminium ($^{(39-41)}_{13}$Al) are investigated in two experiments to better understand this evolution around two regions of the nuclear landscape with drastic changes of *magic numbers* at neutron numbers $N = 20, 28$. These areas correspond to the so-called *island of inversion* (section 1.1.5) and neutron-rich isotones near $N = 28$ close to the neutron drip-line, and both areas may collectively be described as a large area of deformation [8].

[1] and most recently, pear-shaped [6].

The experimental technique of in-beam γ-ray spectroscopy (section 1.3) is employed to interrogate excited nuclear structures of $^{32}_{10}$Ne and $^{(39-41)}_{13}$Al produced through direct nucleon knockout reactions (section 1.2). Furthermore, the measured inclusive and exclusive knockout reaction cross sections provides additional structural information, and contributes to systematic trends (section 1.2.3).

The modern production methods of radioactive ions (section 1.4) at the RIKEN world-class facility (section 2.1) allowed for realization of the experiments. The detector array at RIKEN, DALI2 (section 2.5), was employed to observe the unknown characteristic signatures of these exotic isotopes, through the measurement of emitted γ-rays.

1.1 Nuclear models

Since the birth of nuclear physics, various models have grown through great theoretical efforts to interpret and predict experimentally observed phenomena. Three famlies of nuclear models, the macroscopic semi-empirical liquid drop model (LDM), the microscopic shell model and the collective model incorporating aspects of both, provide frameworks to interpret the experimental observations of neutron-rich neon and aluminum.

1.1.1 Liquid-drop model

The liquid-drop model (LDM) was proposed in 1935 by von Weizsäcker [9] and tuned by Bethe [10]. It played a significant role in the advancement of nuclear theory and applied nuclear fields. Describing the nucleus as a Fermi fluid, the LDM reproduces the binding energy for many isotopes, chiefly the general trends of binding energy against atomic number and mass number. The LDM binding energy is built on basis components of nuclear volume, surface area of the nucleus, internal proton Coulomb repulsion, neutron to proton ratio, and a correction for even or odd numbers of neutrons and protons. The first three terms relate to a model of a Fermi liquid and latter two from basic properties of the nuclear interaction. The LDM binding energy, dependant on both mass number A (number of protons Z and neutrons N) and proton number can commonly be formulated[2] as,

$$\begin{aligned}\text{Binding energy}(A,Z) =& a_{volume}A - a_{surface}A^{2/3} - a_{Coulomb}\frac{Z(Z-1)}{\sqrt[3]{A}} \\ & - a_{asymmetry}\frac{(A-2Z)^2}{A} + \delta_{pairing}\end{aligned} \tag{1.1}$$

where the pairing term can take the formula of,

$$\delta_{pairing} = \begin{cases} a_{pairing}A^{-1/2} & \text{if } Z \text{ and } N \text{ are even} \\ 0 & \text{if } Z \text{ and } N \text{ are even-odd or odd-even} \\ -a_{pairing}A^{-1/2} & \text{if } Z \text{ and } N \text{ are odd} \end{cases}$$

A plot of the binding energy as a function Z and N is presented in Fig. 1.1.

[2]The coefficients belonging to the semi-empirical mass formula are often evaluated with latest evaluated atomic masses, and the formula can also be extended to include additional terms [11, 12, 13, 14, 15, 16].

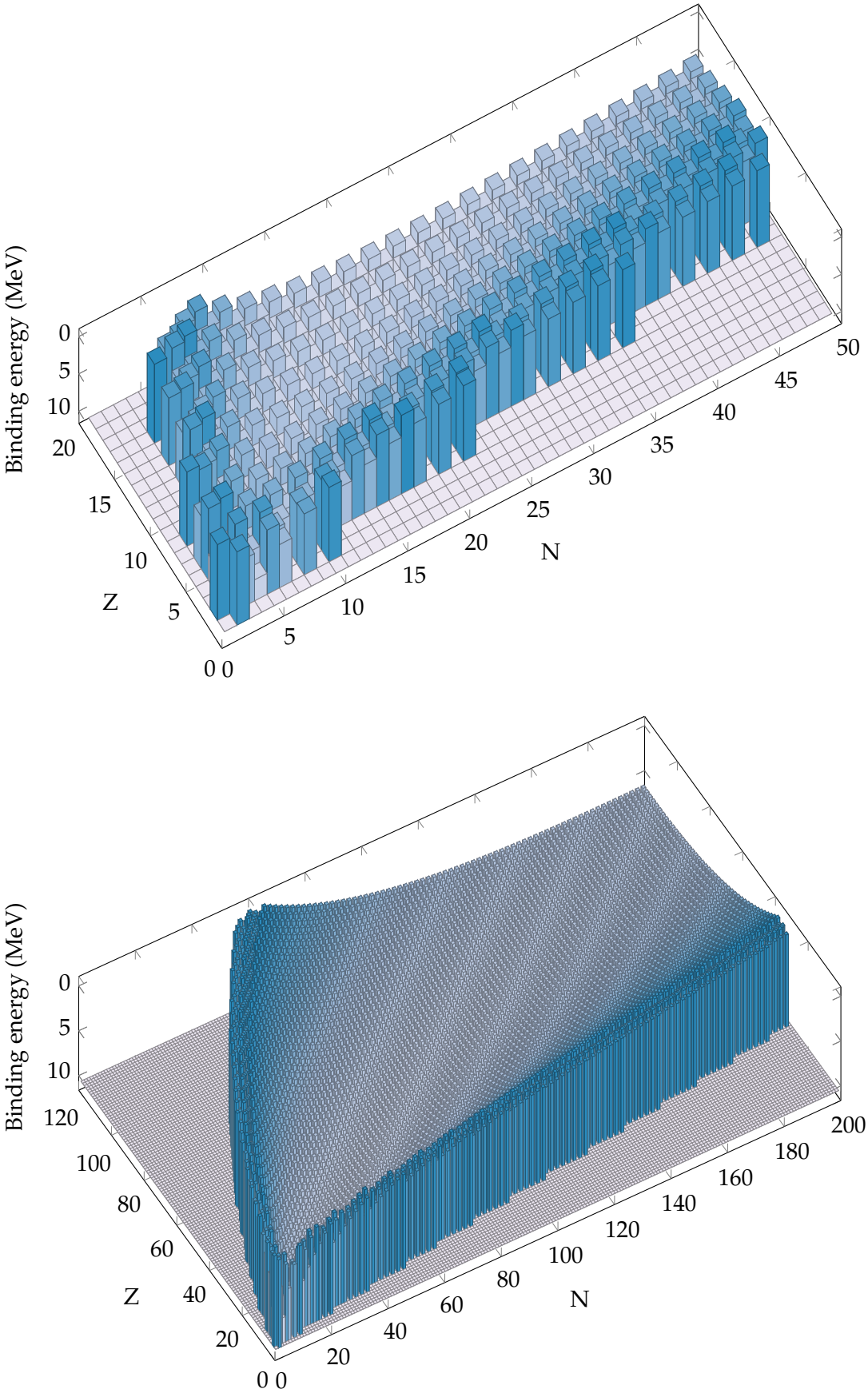

FIGURE 1.1: Semi-empirical LDM binding energy as a function of mass number (A) and atomic number (Z), coefficients from [15]

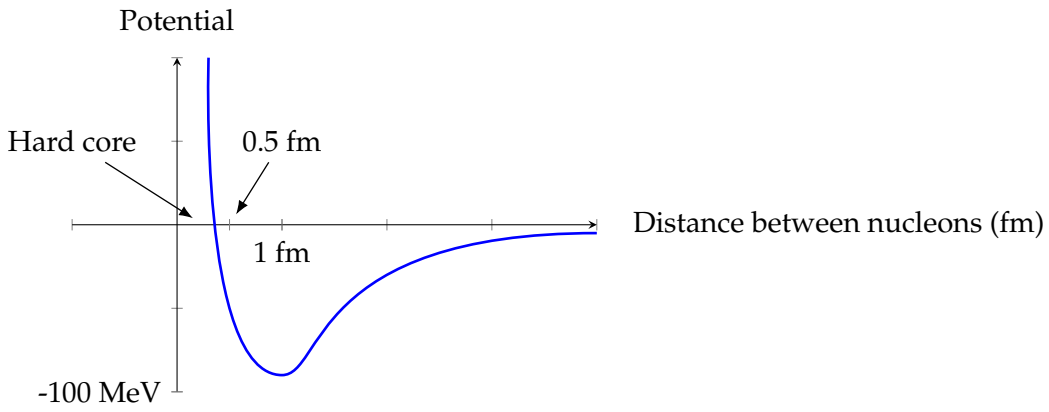

FIGURE 1.2: Illustration of the nucleon-nucleon potential for a spin-singlet state.

1.1.2 Nuclear shell model

To build a many-body system to describe a nuclear system, requires elements of nucleons (protons and neutrons) and nucleon-nucleon interactions: the nuclear force. A nucleon-nucleon interaction can be understood in terms of a potential between two nucleons as function of distance, and is generally comprised of two characteristics. At short distances the potential is repulsive and at an intermediate distance ($\approx$1 fm) an attractive part. For the case of two nucleons with coupled spin $S = 0$, relative orbital angular momentum $L = 0$, and isospin $T = 1$ (also known as a spin-singlet), the potential is schematically drawn in Fig. 1.2. The result of these main features is both saturation in density of nucleons and a common distance between nucleons. Aside from this central potential, spin-orbit, spin-spin, and tensor parts are contained in the nucleon-nucleon interaction, as detailed later.

To overcome difficulties in utilizing a multi-featured nucleon-nucleon interaction in calculations, a mean field potential can instead describe the averaged central potential felt by a nucleon within a nucleus[3]. The short range of the interaction on the order of $\approx$1 fm and the fact the density within a nucleus is nearly constant, leads to a flat mean field potential away from nuclear surface. The nuclear mean field potential is illustrated in Fig. 1.3. Near the surface, the fewer surrounding nucleons leads to a reduction in binding energy and a more shallow potential.

With the form of the mean potential known, it is possible to solve the single-particle motion or alternatively, the eigenstates and eigenvalues (single-particle energies SPE). These correspond to single-particle orbitals. In the case of a spherical potential, good quantum numbers of the eigenstates are orbital angular momentum ℓ, total angular momentum j and the number of nodes of the radial wave-function n. Furthermore, the different states of j_z, the component of j in a chosen axis, are degenerate in energy. These $2J + 1$ magnetic substates for each j orbit have the same single-particle energy.

It is possible to construct the mean field potential by basis functions of the harmonic oscillator potential[4] or Woods-Saxon potential.

[3]The remainder of the potential, not described by the mean field, becomes part of a residual potential.

[4]In the case of the harmonic oscillator, the potential takes the form: $V_{HO} = \frac{m\omega^2 r^2}{2}$, where the mass of the nucleon is m, ω is a chosen oscillator frequency and chosen to reproduce the bottom of the mean field nuclear potential, and r is the distance from the nucleus centre.

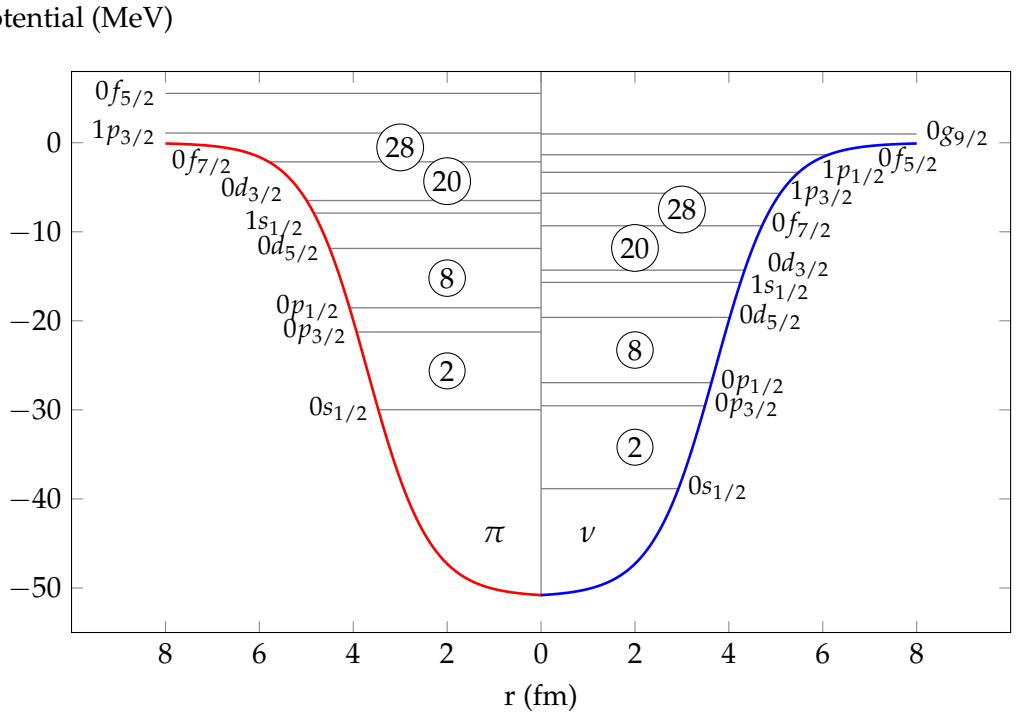

FIGURE 1.3: Plot of the phenomenological Wood-Saxon nuclear mean field potential for ^{40}Ca with the eigenvalues (single particle energies) drawn. The major shells are shown.
$v_{W.S.}(r) = \frac{-V_0}{1+e^{(r-R)/a}}$, with the usual parametrization:
$R = 1.27A^{1/3}$ fm (nuclear radius), $a = 0.67$ fm (surface diffuseness), $V_0 = (51 \pm 33(N-Z)/A)$ MeV (+ for proton / − for neutron). The SPE values are taken from [20] and were evaluated with the aforementioned Wood-Saxon potential.

Fifteen years after W. Elasasser's introduction of *special numbers* [17] in 1934, Mayer, Haxel, Suess and Jensen in mid-twentieth century [18, 19] included an additional term, spin-orbit (SO) coupling: a potential with a functional form of orbital angular momentum and $\vec{\ell}$ and nucleon spin $\vec{s}$. The consequence of such a perturbation, is the splitting of j states. The upper j state is lowered in energy ($\ell + 1/2$) and the lower j state is raised in energy ($\ell - 1/2$).

The grouping of the orbital energies first emerges with a harmonic oscillator potential. The large spacing is called a shell gap and the filling of orbitals, starting from the lowest energy, up to a shell forms a closed shell. Alternatively, an open shell is an incomplete filling up to a shell gap. The numbers referring to the number of nucleons up to a shell are commonly referred to as *magic numbers*. The first *magic numbers* produced with a harmonic oscillator potential include 2, 8 and 20 and also appear with a spin-orbit coupling perturbation, as the splitting of the orbitals is not great enough to produce a new shell. However, a new *magic number* arises at 28, with the significant lowering of the $0f_{7/2}$ orbital ($\ell = 2$), as the lowering is nearly proportional to ℓ. Additional *magic numbers* precipitate at 50, 82 and 126 while other harmonic oscillator shells disappear. To illustrate the spacing of the energy eigenvalues, a simple calculation with the phenomenological Wood-Saxon nuclear mean field potential for stable ^{40}Ca is presented in Fig. 1.3. The *magic numbers* of 8, 20, and 28 are clearly visible, and marked in the figure.

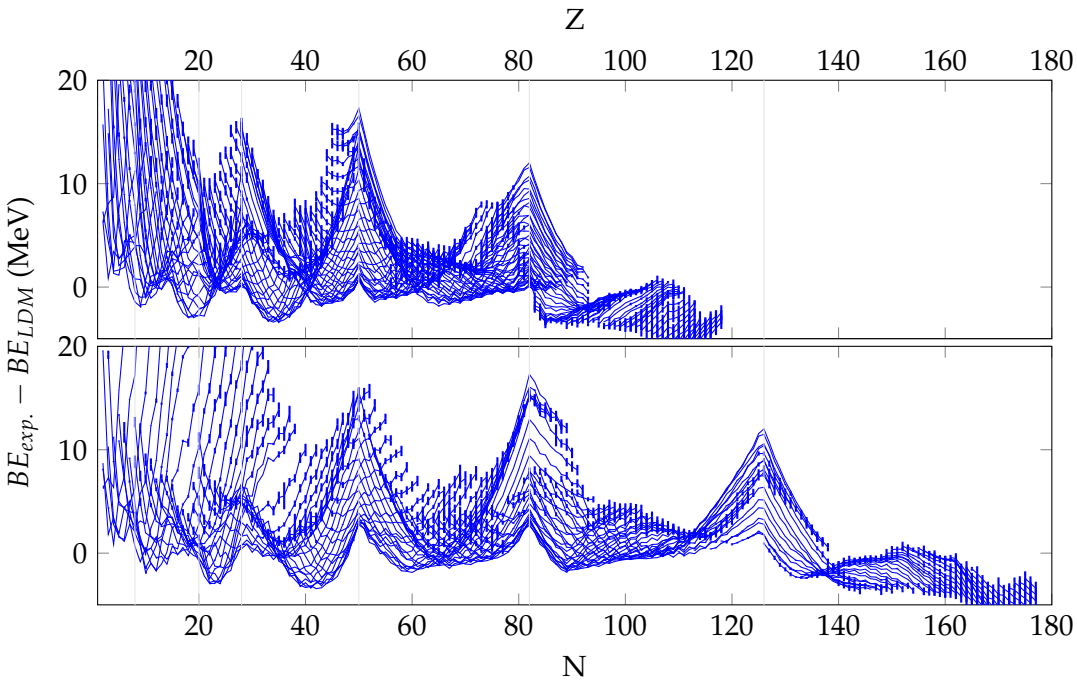

FIGURE 1.4: Difference in LDM binding energy and experimental and extrapolated binding energies as a function of atomic number (Z) and neutron number (N). Experimental and extrapolated binding energies extracted from the 2016 atomic mass evaluation [27] data tables. Overlaid are vertical grey lines at the canonical *magic numbers* of 8, 20, 28, 50, 82, 126.

Signatures of the shell structure of nuclei have been found in a number of experimentally accessible observables. Such as the neutron separation energy, the minimal energy required to remove a single neutron. Neutrons occupying an orbital above a shell gap requires less energy for removal than a neutron from a filled orbital below a shell gap. The trend of the separation energy displays kink at *magic numbers*. Another observable is first excited nuclear states energies, for the special case of even-even nuclei[5]. These state energies (E_2^+) reach a maxima at the magic numbers. In addition, the reduced transition probabilities ($B(E2)$) for even-even nuclei are found to higher. Lastly, if the difference is made between the binding energies of the macroscopic LDM model (section: 1.1.1 and equation 1.1) and experimental and extrapolated binding energies, the fine structure of the shell gaps is revealed (Fig. 1.4).

However, these and other phenomena are not universal across the complete chart of nuclides: a direct result of an evolution of nuclear shell structure. In nuclear systems with unbalanced neutron and proton numbers, regions far from stable isotopes, it has been found the canonical *magic numbers* disappear (N=8, 20, 28...) and new ones precipitate in neutron-rich nuclei (N=16, 32, 34...) [21]. The first clues to these phenomena have come through experimental evidence, through the signatures described in the previous section, such as atomic mass trends [22], nuclear radii, 2_1^+ excitation energies [23, 24, 25, 26].

[5]Even number of protons and an even number of neutrons

1.1.3 Shell gap evolution

It was suggested as early as 1954 by J. P. Elliott [28] that the previously described spin-orbit coupling term:

> .. may not be a real force in the nucleus, but rather that it is a "caricature" of a more complicated force. It has been suggest this may be a tensor force or a two-body spin orbit force.

This was deduced by the observation that the fitted SO potential increased with mass number and increased as particular shells are filled. Several years later, L. Talmi and I. Unna considered how the occupation of orbitals can lead to a change in configuration [29],

> It is often assumed that the order of single nucleon levels is the same for neighbouring odd nuclei. This, however, is not always the case if the residual (effective) two-body interactions are taken into account. The detailed consideration of these interactions leads sometimes to interesting "competition" between orbits. For example, the order of filling of neutron shells may depend on the proton configuration.

Starting from these initial theoretical explorations, and through confirmation with experimental observables, universal mechanisms are now understood as driving forces behind nuclear structure evolution. Two- and three-body[6] interactions, part of the residual interaction, are the basis of these mechanisms [21]. The so-called monopole interaction is one such example.

1.1.3.1 The monopole interaction

The potential between two nucleons can be generally regarded as depending on the distance r, spin $\vec{\sigma}$ and isospin $\vec{\mathbf{t}}$,

$$V_{1,2} = V(\vec{\mathbf{r_1}}, \vec{\sigma_1}, \vec{\mathbf{t_1}}; \vec{\mathbf{r_2}}, \vec{\sigma_2}, \vec{\mathbf{t_2}}) \tag{1.2}$$

This interaction can be divided into central and non-central parts. The non-central part of the interaction consists of the two-body spin-orbit part[7] and tensor part[8]. The central potential, and it's specific multipoles play an important role in the variation of shell structure [33, 34]. The nucleon-nucleon central potential is one which only depends on distances. It is possible to decompose this potential into multipoles,

$$V_{1,2}\left(|\vec{\mathbf{r_1}} - \vec{\mathbf{r_2}}|\right) = \sum_k v_k(r_1, r_2) P_k\left(\cos\theta_{12}\right) \tag{1.3}$$

where $v_k(r_1, r_2)$ are coefficients and $P_k\left(\cos\theta_{12}\right)$ are Legendre polynomials of the angle $\theta_{12} = \sphericalangle(\vec{r_1}, \vec{r_2})$. The different multipole orders play different roles, but one of most important to understand shell gap evolution is the monopole and quadrupole parts.

[6] Although not touched upon in this introduction, three-body interactions are a topic of current investigations [30, 31, 32].

[7] $V_{1,2}^{LS} = (V^{LS,\,is}(r) + V^{LS,\,iv}(r)\vec{\mathbf{t_1}} \cdot \vec{\mathbf{t_2}})\vec{\mathbf{L}} \cdot \vec{\mathbf{S}}$, where $V^{LS,\,is}$ and $V^{LS,\,iv}$ are the iso-scaler and iso-vector parts, $\vec{\mathbf{L}}$ is the relative angular momentum of the two nucleons and $\vec{\mathbf{S}} = \frac{1}{2}(\vec{\sigma_1} + \vec{\sigma_2})$ is the total spin.

[8] $V_{1,2}^{tensor} = (V^{tensor,\,is}(r) + V^{tensor,\,iv}(r)\vec{\mathbf{t_1}} \cdot \vec{\mathbf{t_2}})(\frac{3}{r^2}(r \cdot \vec{\sigma_1})(r \cdot \vec{\sigma_1}) - \vec{\sigma_1} \cdot \vec{\sigma_2})$, where $V^{tensor,\,is}$ and $V^{tensor,\,iv}$ are the iso-scaler and iso-vector parts, respectively.

The monopole of the central potential is the average interaction over all directions between two nucleons (j and k, with j and j' angular momentum), and can be expressed as,

$$V_{j_i,j'_k}^{monopole} = \frac{\sum_J (2J+1) \left\langle j_i, j'_k, J \middle| V \middle| j_i, j'_k, J \right\rangle}{\sum_J (2J+1)} \tag{1.4}$$

An effect of this monopole term is the spacing of the single-particle energies (SPE) and the effective single-particle energies (ESPE) [35, 36], although it is not the only contributor. Similar to SPE, the ESPE includes the bare separation energy for a level, with the addition of the monopole interaction with all other levels. These ESPE therefore determine the excitation energies of individual nucleons, and the resulting shell gaps. The ESPE can also be understood as the nucleon separation energy. It is the change in ESPE by means of the monopole interaction, as function of changing the number of neutron and protons, which strongly drives nuclear shell gap evolution.

The center-of-mass energy of a configuration, evaluated with the monopole interaction, and across a configuration specified by occupation numbers $\{n_j\}$, can be written as,

$$E(\{n_j\}) = \sum_j \varepsilon_j n_j + \sum_j \frac{1}{2} n_j (n_j - 1) V_{j,j}^{monopole} + \sum_{j \neq j'} n_j n_{j'} V_{j,j'}^{monopole} \tag{1.5}$$

where ε_j is the SPE of orbit j. The previous definition of the ESPE leads to,

$$\bar{\varepsilon}_i = \frac{\partial E(\{n_i\})}{\partial n_i} \approx \varepsilon_i + \sum_j V_{i,j}^{monopole} n_i \tag{1.6}$$

Here it becomes clear how the nuclear orbits can change as a function of occupation of an orbital j, the so-called monopole drift. This monopole drift from the central nucleon-nucleon interaction is a key driver for the global trends of ESPEs [37]. The shell gap $\bar{\varepsilon}_i - \bar{\varepsilon}_{i'}$ though does not have to follow the linearity of equation 1.6, as the sign of the of the difference between $V_{i,j}^{monopole}$ and $V_{i',j}^{monopole}$ can vary as a function of j.

A major achievement into this understanding of shell evolution by monopole terms was achieved by Otsuka et al. [38, 39, 40, 41], where the monopole effect of the tensor force was considered. The tensor force, a part of the residual interaction (section 1.1.2), is the consequence of ρ and π meson exchanges of the nucleon-nucleon interaction. The significance of the monopole part of the tensor force, between neutrons and protons, is it's influence by the orbitals' total angular momenta. More specifically, through the definition of $j_>$ or $j_<$, spin-orbit coupling partners. Where,

$$j_> = \ell + s \tag{1.7}$$

$$j_< = \ell - s \tag{1.8}$$

In the case of neutron-proton interactions between opposite orbitals (i.e. $j_>$ and $j'_<$ or $j_<$ or $j'_>$), the monopole part of the tensor acts in a different way than between matched orbitals. It also disappears for full orbitals, thereby acting only on valence orbits. The interaction between opposite orbitals is attractive, resulting in ESPE which are more bound (lowered). Between matched orbitals (i.e. $j_>$ and $j'_>$ or $j_<$ or $j'_<$), the interaction is repulsive and the ESPE are less bound (raised). This is depicted schematically in Fig. 1.5 from one of the pioneering paper by Otsuka et

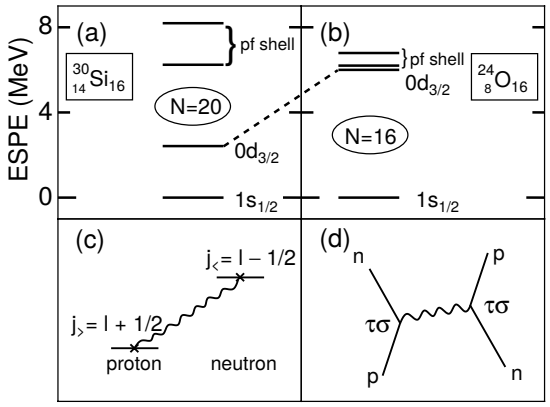

FIGURE 1.5: Graphic from Otsuka et al. (2001) [38]. The neutron ESPE are provided in (a) and (b) for ^{30}Si and ^{24}O, respectively. This change in ESPE is driven by the interaction between proton $\pi 0d_{5/2}$ and neutron $\nu 0d_{3/2}$. (c) Shows the schematic view of the interaction between spin orbit partners. (d) The meson exchange process of the interaction.

al. (2001). Generally speaking, changing the occupation of one of the spin-orbit coupling partners will induce a development of splitting of ESPEs, the result of which is an additional source of the evolution of the nuclear shell gaps. However, ESPE energies cannot be measured directly as they are uncorrelated energies, while the nucleus is correlated a system [42]. An example of the evolution of ESPE, calculated by a recently developed effective interaction [43], as function of nucleon (proton) filling is presented in Fig. 1.8. Lastly, it is important to note that the strength of the interaction is strongest for the same number of nodes n, where the wavefunction overlap is maximum, and the highest j orbitals.

1.1.3.2 Higher multipoles

As mentioned previously, the higher order multipole terms of the nucleon-nucleon interaction play important roles in nuclear structure. They can describe correlations between nucleons, resulting in particle-hole excitations, such as those across shell gaps, and deformation. It is through the monopole interaction shifting or splitting of spin-orbit partners, to reduce the shell gaps, which increases the correlation energy of configurations with particle-holes across shell gaps. When this correlation is greater than the energy to create these configurations, they become so-called *intruder states*, and take over the ground state configuration. Accordingly, there is a connection between the monopole term of the nucleon-nucleon iteration and higher multipoles to produce nuclear observables and the evolution of these across the nuclear landscape.

Within the shell mode, the intruder configuration energy can be formulated as [44],

$$E_{intruder} = 2(\varepsilon_j - \varepsilon_{j'}) - \Delta E^{pair}_{\nu\nu} + \Delta E^{monopole}_{\pi\nu} + \Delta E^{quadrupole}_{\pi\nu} \tag{1.9}$$

for the case of cross neutron (ν) shell intruders. Where ε_j and $\varepsilon_{j'}$ are the upper and lower single-particle energies, respectively. $\Delta E^{pair}_{\nu\nu}$ is the loss in pairing energy from the creation of a neutron particle-hole pair (at j and j' orbitals), with π and ν representing protons and neutrons. $\Delta E^{monopole}_{\pi\nu}$ is a monopole energy correction due to the change of orbital filling, due to a change in total proton-neutron interaction.

Lastly, $\Delta E_{\pi\nu}^{quadrupole}$ is the change in quadrupole-quadrupole interaction, often with a parabolic trend with a maximum between shells [44]. Figure 5 of [8] provides a clear picture of the energy gap between 0p-0h and 2p-2h states, with the takeover the ground state illustrated when the gap falls below zero.

1.1.4 Collective and Nilsson model

The reconciliation of the shell model with the liquid-drop model (LDM) provides the benefit of pairing the general features of nuclear structure described by the single-particle spherical shell model with the treatment of the nuclear surface like a drop. This unification of a collective model by Rainwater [45] explains rotational and vibration degrees of freedom of the nucleus and the framework was expanded by A. Bohr and B. Mottelson [46, 7].

For example, the excitation energies of a axially symmetric quadrupole rotor for even-even nuclei can be described as [47],

$$E(J) = \frac{\hbar}{2\mathcal{I}} J(J+1) \tag{1.10}$$

where J is the state angular momentum (spin), for which symmetries allow even J and positive parity. And $\mathcal{I}$ is the moment of inertia. A consequence of this simple model is the predicted energy level ratio E_{4^+}/E_{2^+} levels is 3.33. Equation 1.10 can be more generally written as a power series expansion[9] of $J(J+1)$ for small values of J[10].

The deformed shell model, the so-called Nilsson model [48], can describe behaviour of spherical shell model states in a deformed nuclear potential. For an axially symmetric nuclear system, the model can explain single-particle energies as function of deformation, with broken degeneracy $(2j+1)$ of spherical single particle states with increasing deformation [47].

Under deformation, new good quantum numbers Ω, Λ in the intrinsic frame emerge to describe the projection of orbital angular momentum (L) and projection of spin (S) onto the symmetry axis, respectively. The projected total angular momentum (J) is K, which is further related by $K = \Omega + \Lambda$. The variables are illustrated in Figure 1.6. The deformed orbits (Nilsson levels) are therefore described by the common formalism $K^{\pi}[Nn_z\Lambda]$, where N is the major harmonic oscillator number and n_z is the z-component of of N. Each deformed orbit can only be ascribed at most two nucleons.

Nuclear deformation can be quantified in different ways, however, nuclei can commonly be classified by the quadrupole deformation parameter. A negative parameter represents a prolate shape (rugby ball-like) and a positive value represents a oblate shape (pancake-like). A zero quadrupole deformation describes a spherical shape. The Nilsson level energies are commonly displayed as a function of quadrupole deformation to describe a valence orbital for a given nuclear quadrupole deformation.

The projected total angular momentum K is a constant of the rotational motion of deformed nuclei, therefore is fixed for a rotational band and known as a bandhead. For odd-A $K \neq 0$ [47]. The spin sequence for a rotational band often takes the form of $K, K+1, K+2$..... Additional rotational energy is required for coupling a particle and rotor, and is formulated for any K as [47],

[9] $E(J) = AJ(J+1) + BJ^2(J+1)^2 + ...$

[10] An important consequence is the moment of inertia does not have to be assumed to be a constant of spin.

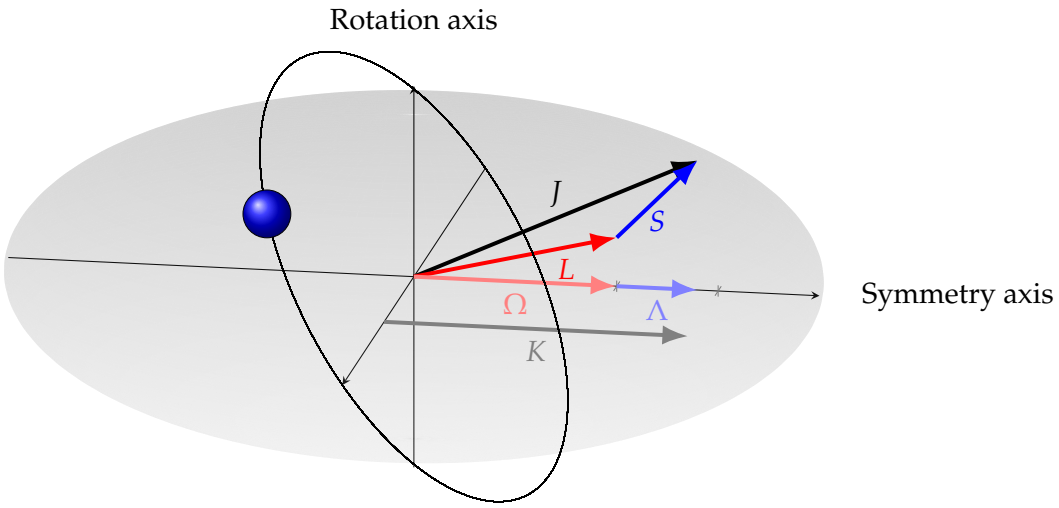

FIGURE 1.6: Schematic view of a deformed nucleus and defining the quantities J, K, L, S, Ω, and Λ in the discussion of the Nilsson model

$$\Delta E_{rot} = (-1)^{J+K} A_{2K} \frac{(J+K)!}{(J-K)!} \tag{1.11}$$

$$A_{2K} = \langle K | h_{2K} | \bar{K} \rangle \tag{1.12}$$

where A_{2K} is the Coriolis interaction strength, describing the coupling between the valence particle and the core nucleus [47]. The matrix elements contain the intrinsic rotational Hamiltonian $h_{2K} = -\frac{\hbar}{2\mathcal{I}} j_{\pm}$ where $j_{\pm}$ are the ladder operators of single-particle angular momenta [47].

In addition to a power expansion of $J(J+1)$, A_{2K} can also be expanded for better reproducibility[11] to observed rotational bands. For the special case of $K = 1/2$, which can be described by equation 1.13, the Coriolis contribution can yield strong energy straggling (or reversal) of the rotational levels due to the alternating sign [47].

$$E(J,K) = \frac{\hbar}{2\mathcal{I}} [J(J+1) + a(-1)^{J+1/2}(J+1/2)] \tag{1.13}$$

where the coefficient a is the commonly defined Coriolis decoupling parameter.

The described formalism for particle coupling to a rotor can be portrayed by two limits [47]. The strong coupling and decoupled limit. For the former, the Coriolis coupling is weak in relationship to the deformed single-particle energies and is commonly applied for large deformations. The latter involves a strong Coriolis coupling for which the total angular momentum and single-particle angular momentum are parallel.

1.1.5 *Island of inversion* at $N = 20$

About twenty years after the work of J. P. Elliott and L. Talmi and I. Unna, a large body of evidence from nuclear physics experiments established the clear disapearance of the N=20 *magic number* and the onset of collectively for very neutron-rich nuclei. The first signature of the breakdown of the N=20 major shell closure was

[11] Alternately, $J(J+1) - K^2$ can be replaced in such an expansion.

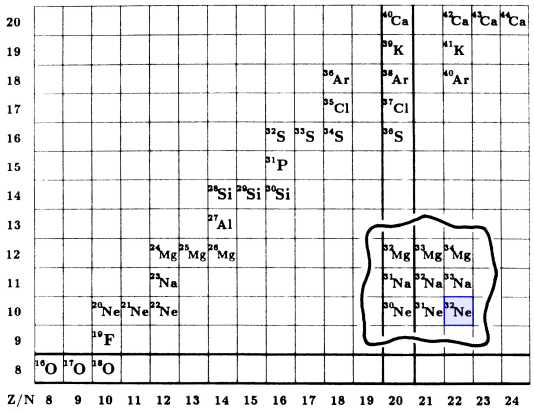

FIGURE 1.7: Graphic from E. K. Warburton et al. pioneering paper first outlining the island of inversion [49]. Blue highlighted isotope is the study of this thesis.

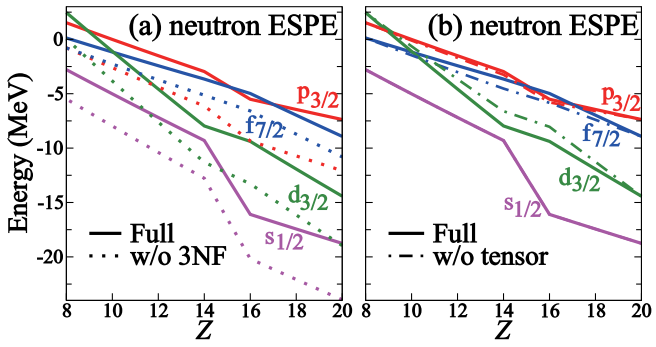

FIGURE 1.8: Effective single particle energies (ESPE) for isotones of $N = 20$ as a function of Z (under with normal filling). The dotted and dashed lines show the effect of removing the 3N force and tensor force, respectively. Figure from [43] and ESPEs calculated from a recently developed effective interaction derived from extended Kuo-Krenciglowa (EKK) theory.

the observation of excessive binding energy for sodium isotopes. It was discovered $^{31-32}$Na were more bound than predicted [50]. Following this study, an atomic mass measurement of $^{31-32}$Mg [51] displayed the same phenomena. The observation of a low lying first excited 2^+ state [52, 53] and the Coulomb excitation of ^{32}Mg [54, 55] provided additional evidence. The two-neutron separation energy, deduced from the most recent atomic mass evaluation is presented in 1.10 and shows the clear erosion of $N = 20$ below ^{32}Si.

This dramatic and sudden change in structure for Z $\leq$ 12 and N $\geq$ 20 was termed the *island of inversion* (IoI) [49] (Fig. 1.7) and interpreted as due to the introduction of intruder configurations, neutron multiparticle-multihole excitations, in the ground state. The neutrons are promoted across the $N = 20$ gap from *sd* to *pf* orbitals [56] as a consequence of an increase in quadruple correlations and reduction of the shell gap. The driving force of the evolution of orbitals is understood as being a decrease of the spin-isospin dependent attractive monopole interaction [38] from the tensor force as a function of increasing proton/neutron asymmetry [39]. As protons are removed from the $\pi 0d_{5/2}$ orbital, the neutron $\nu 0d_{3/2}$ orbital is less bound and approaches up to (or above) $\nu 0f_{7/2}$ and $\nu 0p_{3/2}$ levels, quenching the $N = 20$ shell gap. Calculated ESPEs are presented in Fig. 1.8 to illustrate the evolving orbitals,

particularly the rapid rise of $\nu 0d_{3/2}$ at $Z \leq 12$. The $N = 20$ shell gap, represented as the distance between green ($\nu 0d_{3/2}$) and blue lines ($\nu 0f_{7/2}$) contracts swiftly and disappears. Also evident is the appearance of a gap forming between $\nu 1s_{1/2}$ and $\nu 0d_{3/2}$, the emergence of the $N = 16$ shell gap [57, 58, 59]. A schematic view of the orbits involved are presented in Fig. 1.9.

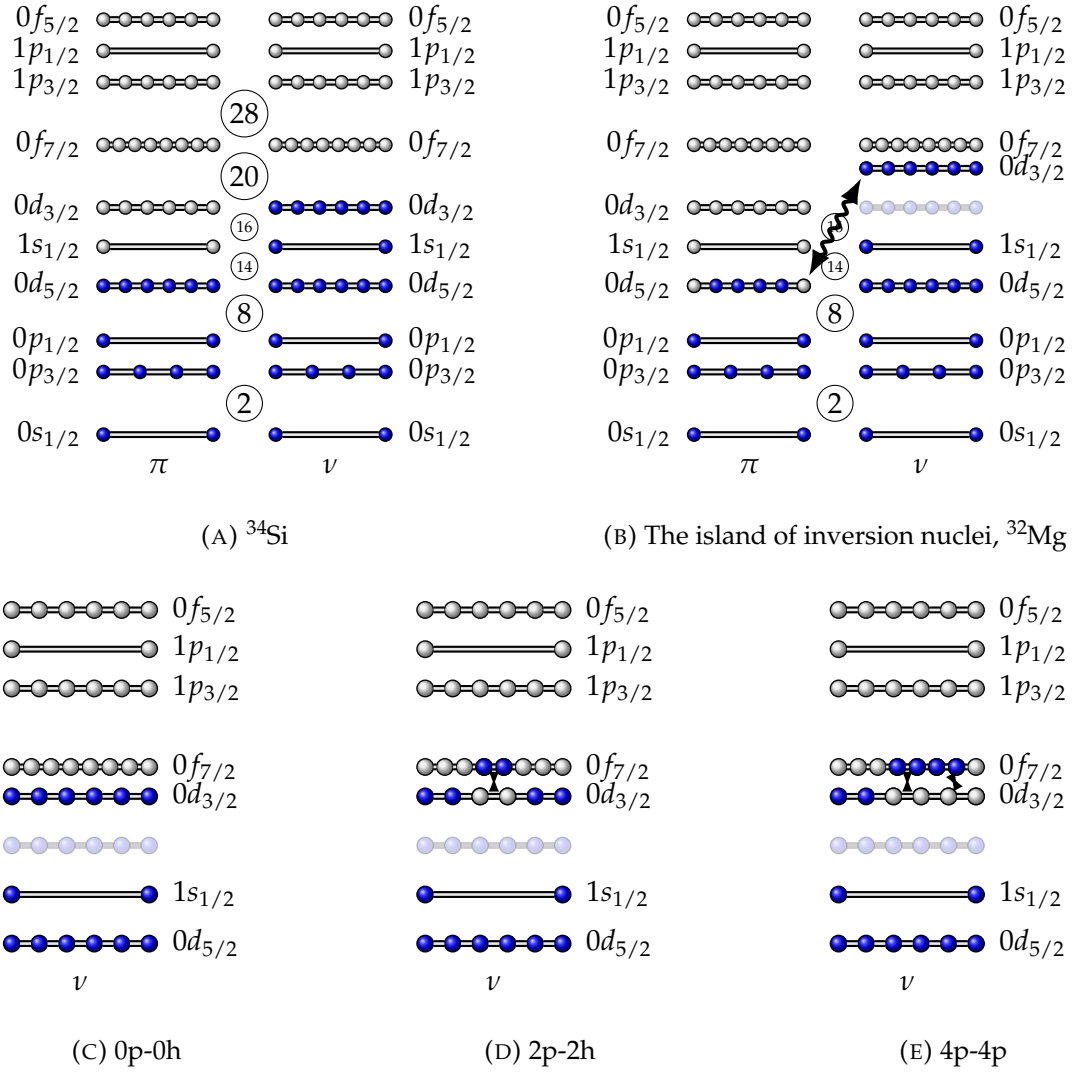

(A) ^{34}Si (B) The island of inversion nuclei, ^{32}Mg

(C) 0p-0h (D) 2p-2h (E) 4p-4p

FIGURE 1.9: Schematic level schemes, effect of the monopole part of the tensor force between spin-orbit partners $j_> \Leftrightarrow j'_<$, and mulit-particle-hole states, for the island of inversion around $N = 20$

Originally, the IoI was predicted to exist between $10 \leq Z \leq 12$ and $20 \leq N \leq 22$ [49]. However, through great experimental effort it has been revealed to be a soft transition. The borders of the *island of inversion* are not entirely delineated on the exotic south-east side, driving theoretical and experimental progress. With many studies focused on magnesium and sodium isotopes, the latter known up to $N = 24$ [60], the IoI has been barely reached for Ne ($Z = 10$) isotopes.

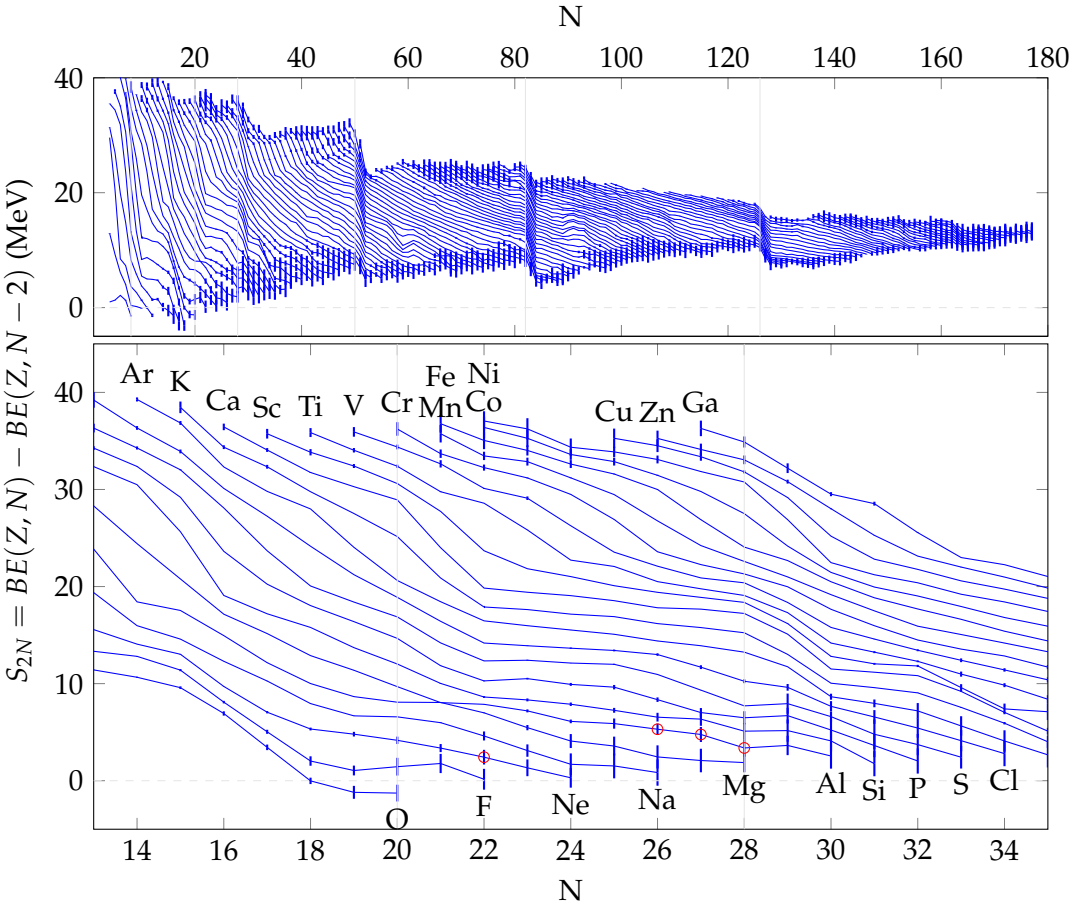

FIGURE 1.10: Two neutron separation energy as a function of neutron number (N). Experimental and extrapolated binding energies extracted from the 2016 atomic mass evaluation [27] data tables. Overlaid are vertical grey lines at the canonical *magic numbers* of 8, 20, 28, 50, 82, 126.

1.1.6 Quenching of $N = 28$

The shell gap at nucleon number 28 is the first[12] major gap created by the spin-orbit (SO) coupling mechanism (section: 1.1.2). It is formed through the separation the $0f_{7/2}$ and $0p_{3/2}$ orbitals of the same parity. Also contributing to this shell gap is neutron-neutron interactions, which can be seen in the evolution of the shell gap between ^{40}Ca and ^{48}Ca. The gap increases on the order of 3 MeV[13] through the addition of eight neutrons in the $\nu 0f_{7/2}$ orbit. The neutron-neutron monopole terms $V^{nn}_{0f_{7/2}f_{0f_{7/2}}}$ and $V^{nn}_{0f_{7/2}p_{0p_{3/2}}}$ which are opposite may be the contributors, with the former attractive and latter repulsive.

This widening can be formulated as,

$$\bar{\varepsilon}_{\nu 0f_{7/2}} - \bar{\varepsilon}_{\nu 0p_{3/2}} = n_{\nu 0f_{7/2}}(V^{nn}_{f_{7/2}p_{3/2}}) - (n_{\nu 0f_{7/2}} - 1)V^{nn}_{f_{7/2}f_{f_{7/2}}} \tag{1.14}$$

where $n_{\nu 0f_{7/2}}$ is the number of neutrons added to the $\nu 0f_{7/2}$ orbital. See previous equation 1.6 for details. This effect is cannot be reproduced by two-body interactions alone and requires the introduction of three-body (3N) forces [31].

[12] other first subshells being 6 and 14

[13] as observed in transfer reactions on ^{40}Ca [61] and ^{48}Ca [62].

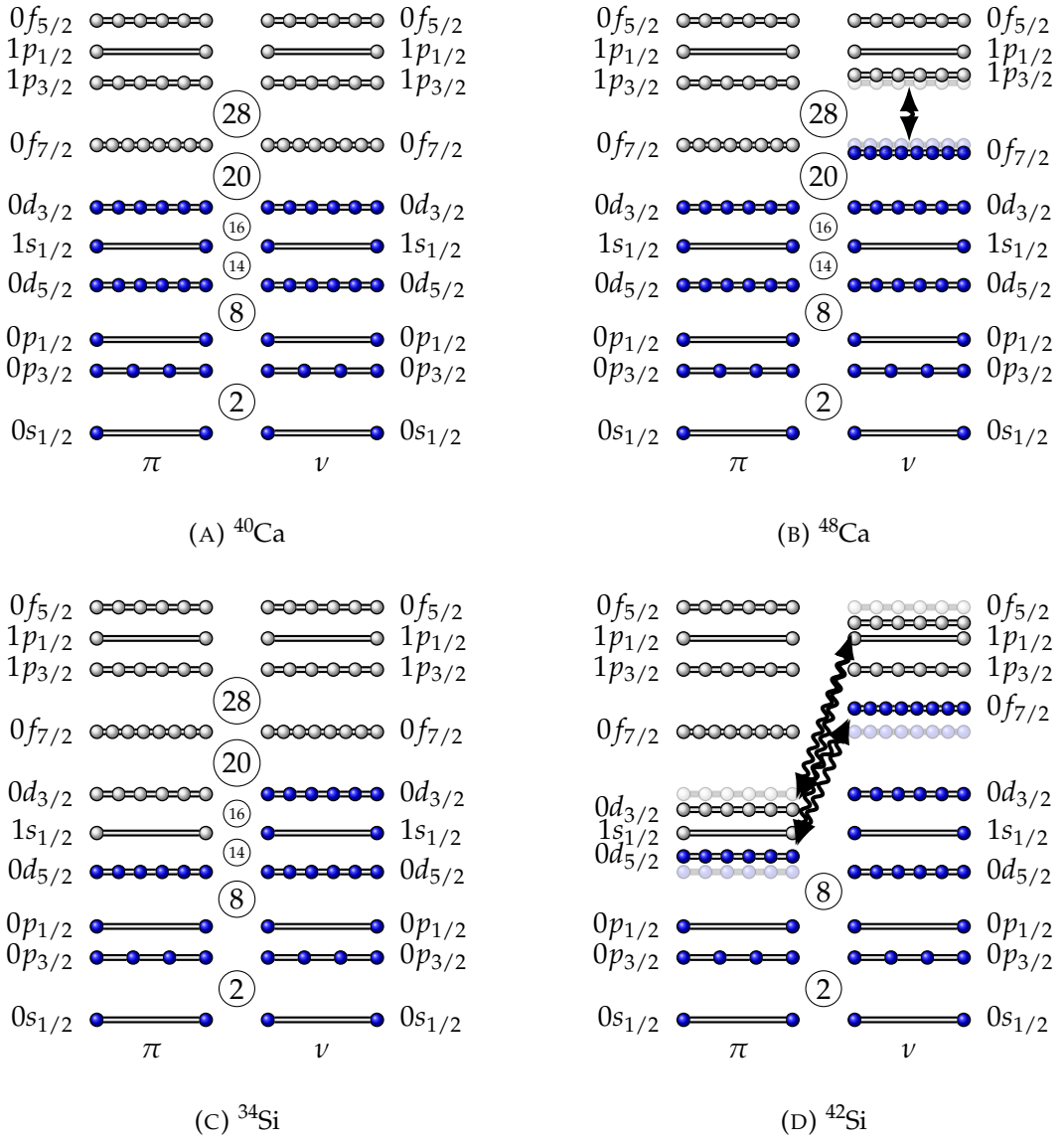

(A) ^{40}Ca (B) ^{48}Ca

(C) ^{34}Si (D) ^{42}Si

FIGURE 1.11: Schematic level schemes, effect of the monopole part of the tensor force between spin-orbit partners $j_> \Leftrightarrow j'_<$, i.e. $\pi 0d_{3/2} \Leftrightarrow \nu 1f_{5/2}$ and $\pi 0d_{3/2} \Leftrightarrow \nu 0f_{7/2}$ as protons are removed from $\pi 0d_{3/2}$ orbits moving from ^{48}Ca to ^{42}Si, reducing the $N = 28$ gap. Conversely, the neutron induced tensor between $\nu 0f_{7/2} \Leftrightarrow \pi 0d_{3/2}$ and $\nu 0f_{7/2} \Leftrightarrow \pi 0d_{5/2}$ reduces $\pi 0d$ splitting, thereby $Z = 14, 16$ proton subshells.

The neutron $N = 28$ gap, like $N = 20$, doesn't hold across the complete nuclear landscape. Below doubly-magic ($Z = 20$) ^{48}Ca, this shell closure is progressively eroded, with strong indications of collectivity or deformation seen in ^{46}Ar [63], ^{44}S [64, 65] and ^{42}Si [26, 78] observed experimentally. This transition occurs quickly, with only two protons removed to reach ^{46}Ar .

The opposite is true for the case of the $N = 20$, discussed previously (section: 1.1.5), and formed by orbitals of opposite parity, which has been found to be particularly robust. An example is the low reduced transition probabilities, $B(E2; 0^+_1 \rightarrow 2^+_1)$, of $^{32-38}$Si measured by Coulomb excitation [66]. These values, compatible with a $N = 20$ shell closure, proves the survival of the shell gap even under the removal

of six protons from ^{40}Ca. The reasons for this effect may be due to the opposite parity hampering 2^+ excitations, and proton subshells at $Z = 14, 16$ of considerable strength (2.5 MeV and 4.3 MeV from transfer reactions [67, 68]).

Along $N = 28$ isotones, removing protons to reach ^{40}Mg results in removal from $\pi 0d_{3/2}$ and $\pi 1s_{1/2}$, and finally $\pi 0d_{5/2}$ orbitals. As seen in the previous cases, this change in nucleon filling results in the modification of neutron orbitals through changing nucleon-nucleon interaction (proton-neutron). The tensor component of the monopole interaction between $\pi 0d_{3/2}$ proton orbital and $\nu 0f_{7/2}$ and $\nu 0f_{5/2}$ neutron orbitals, is attractive and repulsive, respectively [39, 69]. Therefore, with the removal of $\pi 0d_{3/2}$ protons, the decreased spiting of SO $\nu 0f_{5/2}$ and $\nu 0f_{7/2}$ occurs, with the former more bound (lowered) and the latter less bound (raised). This is depicted schematically in Fig. 1.11. The magnitude follows the tensor sum rule [38],

$$(2j_> + 1)V^{tensor}_{j>j'} + (2j_< + 1)V^{tensor}_{j<j'} = 0 \tag{1.15}$$

which for this case is,

$$(2\frac{7}{2} + 1)V^{tensor}_{d_{3/2}f_{7/2}} + (2\frac{5}{2} + 1)V^{tensor}_{d_{3/2}f_{5/2}} = 8V^{tensor}_{d_{3/2}f_{7/2}} + 6V^{tensor}_{d_{3/2}f_{5/2}} = 0 \tag{1.16}$$

The consequence is the reduction of $N = 28$ (between $\nu 0p_{3/2}$ and $\nu 0f_{7/2}$). Conversely, moving along isotopes, such as Si to ^{42}Si (increases the filling of neutron $\nu 0f_{7/2}$) results in the tensor component of the monopole interaction from neutron $\nu 0f_{7/2}$ orbit to reduce the splitting of $\pi 0d$ orbits. The ensuing decrease of the proton subshell or subshells ($Z = 14, 16$) and neutron shell $N = 28$ results in greater quadrupole correlations for neutron and protons. The role of proton excitations in Si (and Mg) remains a topic of investigation [70] as it has been argued that $N = 28$ shell gap solely can result in experimental spectroscopic properties. The size of the $Z = 14$ proton subshell may hinder proton correlations and excitation from $\pi 0d_{5/2}$ orbit.

For both protons and neutrons, the $\Delta j = 2$ difference between occupied and valence orbitals will favour cross-shell quadrupole excitations, as discussed part of SU(3) symmetries by Elliott [71, 72]. Furthermore, it is possible to understand the driver of deformation as part of the Jahn-Teller effect, due to the close degeneracy of $\nu 0f_{7/2}$ and $\nu 0p_{3/2}$ orbitals [73].

In summary, moving along $N = 28$ isotones (starting from ^{48}Ca and removing protons) gives rise to significant evolution of ESPE and the reduction of $N = 28$. The consequence of which is an increase in collective behaviour. The transition from spherical ^{48}Ca, to noncollective oblate ^{46}Ar, to two rotor coexisting ^{44}S, to oblate ^{42}Si and prolate ^{40}Mg is supported by mean-field calculations [74, 75, 76]. Reaching the most exotic and asymmetric isotopes around $N = 28$ and studying their properties will help develop understanding of the nuclear force, such as the proton-neutron interaction. An open question remains on the structures of and around ^{42}Si [77, 78] and ^{40}Mg [79]. The latter was first identified one decade ago with three events [80].

1.2 Direct nuclear reactions

Direct nuclear reactions are employed as a mechanism to produce the radioisotopes $^{32}_{10}$Ne and $^{(39-41)}_{13}$Al. The reactions additionally probe a minimal number of degrees of freedom of the nuclear system, making direct reactions particularly well suited for interrogating the single-particle structure of nuclei. The wavelength of an incident

particle (in the frame of a nucleus) decreases and localized portions of a nucleus can be *probed*. In the case of peripheral reactions, only a few nucleons on the nuclear surface participate.

A large volume of studies measuring inclusive and exclusive direct reaction cross sections across the chart of nuclides has permitted the examination of trends to reveal new physics and has been necessary for the advancement of fundamental nuclear physics [81].

There are two classes of direct reactions [82]. The first are processes where transferred energy results in only collective excitations of the target nucleus. And the second produces modification of the nuclear composition. These include mechanisms of pickup and stripping reactions, involving addition or the removal of nucleons. These encompass so-called transfer reactions and knockout reactions, the latter only involving the stripping process. Transfer reactions are highly selective reactions which probe the single-particle elements of the nuclear wave function and have been applied to many studies to gain terrific insight into single-particle evolution [83].

The information of the overlap between nuclear states is encapsulated in the so-called spectroscopic factor. If a single nucleon is removed from a nucleus in state I of A nucleons, the final state spin be written as I_c with $A-1$ nucleons. The wave function overlap between the initial and final states is [84],

$$\left\langle \vec{r}, \Psi_f^{A-1} \middle| \Psi_i^A \right\rangle = \sum_j c_j^{if} \psi_j(\vec{r}) \tag{1.17}$$

The overlap additionally posses angular momentum j between $|I - I_c| \leq j \leq I + I_c$ and is an expansion of single-particle states ψ_j. With the normalization of single-particle states to unity, the squared norm of constant is the spectroscopic factor, $\left|c_j^{if}\right|^2 = S_j^{if}$. The average occupancy of a orbital is the sum of spectroscopic factors. In isospin formalism, where the intial and final isospins are provided, a square of the isospin coupling coefficent is additionally included as part of the spectroscopic factor C^2S.

A link to the partial cross section for removal of the nucleon in a direct reaction, between initial state i and final state f, is achieved through the sum of spectroscopic factors multiplied by the single-particle cross sections. This can be formulated as [84],

$$\sigma_{th}^{if} = \sum_j^{if} S_j^{if} \sigma_{sp}(n\ell j) \tag{1.18}$$

The single-particle cross sections σ_{sp} are commonly calculated using the distorted wave Born approximation (DWBA) [85].

Another important reaction to note are proton-knockout reactions with electron inelastic scattering, $(e, e'p)$ [86, 87]. Such reactions are found to provide the *absolute* spectroscopic factors and are important for determining a precise orbital occupation. Across many studies the spectrocscopic factors determined with this technique are lower than those calculated with the shell model with effective interactions, by a factor $0.5 - 0.65$ [88]. This common suppression is currently regarded as originating from a missing component of nuclear correlations in shell model calculations. In the case of short-range nuclear correlations, the hard repulsion of the nuclear force at short distances is equivalent to high momenta $500\,\mathrm{MeV}\,{c_0}^{-1}$ and is not included in complete shell model calculations, where truncation is performed. The result of this

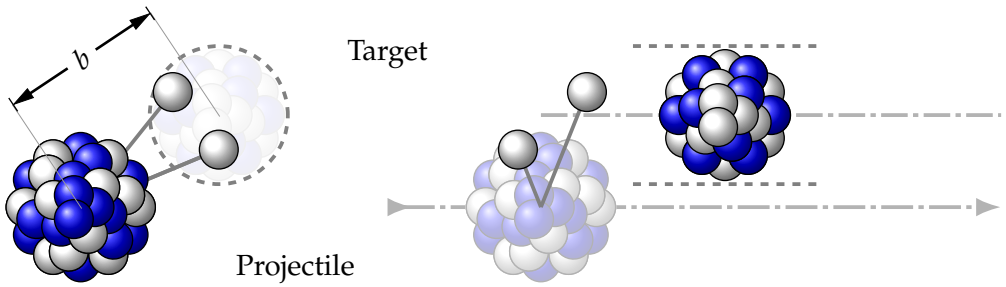

(A) Schematic view. The dotted eclipse is the cylindrical overlap of the target nucleus.

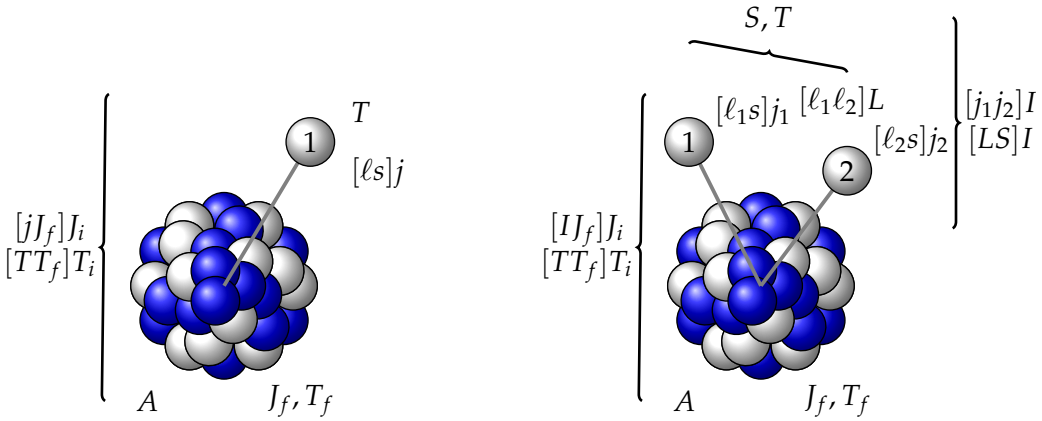

(B) One nucleon knockout

(C) Two nucleon knockout

FIGURE 1.12: Illustration of peripheral direct knockout reactions. In (B) and (C) the quantum mechanical couplings associated with the nuclear system are noted. In two-nucleon knockout reactions (C), the knockout particles are additionally correlated unlike (B). Figure (B) inspired from Fig. 1 of [89].

missing component is an increase in occupation single-particle states in shell model results [84].

1.2.1 Nucleon knockout reactions

Nucleon knockout reactions with fast beams, and particularly fast radioactive beams (see section 1.4), have provided since the 1980s a tool to study properties across a large extension of elements and isotopes. Inverse kinematics, employed in the experiments of this thesis, is commonly employed, as ion-beams of exotic radioisotopes may not be available as macroscopic targets. Inverse kinematics offers additionally kinematic advantages for specific reactions.

The reaction mechanics can be described through the *sudden approximation* or adiabatic approximation, when a target of light mass is used with a fast heavier beam. As the collision time is short, relative motion of the residue-removed system can be considered as fixed during the reaction.

The relation between the momentum of the knocked out nucleon and the momentum of the initial and final states of the projectile and residue is,

$$\vec{k_{k.o.}} = \left(\frac{A-1}{A}\right)\vec{k_A} - \vec{k_{A-1}} \tag{1.19}$$

If the final state of the residue is known through an exclusive measurement of the in-flight decay of state, such as through the observation of γ-rays, the cross section as a function of residue momentum can be reconstructed. This distribution can be described as longitudinal or transverse to the beam direction. In the case of a narrow transverse momentum, the corresponding spatial distribution is wide and has identified the phenomena of halo nuclear systems [90, 91]. If the distribution shape is compared with theoretical calculations, the final state angular-momentum can be assigned. This is analogous to the analysis of transfer reaction angular distributions. The partial cross section to a state can also be used to produce an experimental spectroscopic factor.

A semi-classical framework can be applied in the case of high beam energy reactions. In the case of light mass targets, such as beryllium ($A = 9$) or carbon ($A = 12$), stripping (inelastic breakup) and diffraction (elastic breakup) reaction processes compete. Stripping occurs when the target and the knock out nucleon interact, resulting in an excitation of the target. Stripping is the dominate process for most reactions, except in the case of halo nuclei [84]. In contrast with a stripping process, diffraction occurs when a two-body model can describe the interaction with the target. The target and residues are elastically scattered. In heavy targets, with higher atomic number, a third process will contribute involving the Coulomb interaction called Coulomb breakup. The complete single-particle cross section is the combination of all processes

$$\sigma_{sp} = \sigma_{stripping} + \sigma_{diffraction} + \sigma_{Coulomb} \tag{1.20}$$

Light targets are often employed to suppress the Coulomb breakup cross section. Furthermore, light targets are advantageous in that nuclear excitation mechanisms do not play a significant role in the reaction process. This permits good spatial localization of the reaction on the nuclear surface of the projectile.

1.2.2 Eikonal and sudden approximations

Common approximations used in modern theoretical reaction framework are eikonal and sudden approximations. In the *sudden (adiabatic) approximation*, the relative motion of the residue and knockout nucleon are assumed to be *frozen in time* during the collision (of the order of 1×10^{-23} s).

The eikonal approximation (forward scattering) describes that for two colliding bodies, the wavefunction is unchanged in space, except for the vanishing portion within a cylinder of the overlap with an effective absorption radius (Illustrated in Fig. 1.12). The eikonal approximation can also take the form of the spectator-core approximation, where the core (reaction residue) is assumed to not participate in dynamic excitation during the reaction. The many-body (projectile, residue, knockout nucleon and target) system is therefore approximated as a effective three body system. This is possible with the assumption the residue is elastically scattered off the target in the reaction and moves close to the projectile beam velocity[14].

The resulting stripping cross section is,

$$\sigma_{stripping} = \frac{1}{2j+1} \int d\vec{b} \sum_{m} \langle \psi_{jm} | \left(1 - |S_n|^2\right) |S_c|^2 | \psi_{jm} \rangle \tag{1.21}$$

[14] Although this does not completely conserve total energy and consider the real relative motion of knockout nucleon and reaction residue, at intermediate beam energies with a light target the approximation can be made.

where S_n and S_c are the elastic S-matrices of the systems of reaction residue and target, and removed nucleon and target, respectively. The $|\psi_{jm}\rangle$ is the nucleon and residue relative wave function. The expectation values are summed across all m substrates and integrated across impact parameter b.

The diffraction process cross section is,

$$\sigma_{diffraction} = \frac{1}{2j+1} \sum_{\sigma,m} \int d\vec{k} \int d\vec{b} \sum_{m} | \langle \psi_{\vec{k}\sigma} | (1 - S_n S_c) | \psi_{jm} \rangle |^2 \tag{1.22}$$

where the continuum relative-motion of the nucleon and residue is integrated and substates summed and for which the $\psi_{\vec{k}}$ continuum breakup wave functions are eigenstates of the initial Hamiltonian.

1.2.2.1 Two-nucleon knockout reactions

The two-nucleon knockout mechanism is also proposed as a direct reaction [92] and can be treated under the simillar theoretical reaction framework, as described in [89, 93]. It is important to distinguish the difference between two and one nucleon knockout reactions in that the nuclear structure (input as spectroscopic factors) and dynamical cross section can no longer be factorized like equation 1.18. They are, in a sense, mixed. The cross section is formed from a coherent sum of contributions of nuclear wave-functions, from two-nucleon amplitudes (TNA). Figure 1.12 sketches the two-nucleon knockout angular momentum and isospin couplings of this reaction.

1.2.3 Reduction factor

Through the comparison of theoretical (σ_{fi}^{th}) to experimental (σ_{fi}^{exp}) inclusive cross sections a reduction factor R_s is observed. This reduction factor in stable nuclei approaches the suppression as seen by electron inelastic scattering $(e, e'p)$ detailed in earlier and may be understood by the same origin of missing short-range nuclear correlations. However, experimental and theoretical efforts continue to investigate sources of the cross section suppression.

$$R_s = \sigma_{fi}^{th} / \sigma_{fi}^{exp} \tag{1.23}$$

In knockout reactions from very loosely bound systems the determined R_s approaches unity, and conversely for bound systems falls towards zero. A significant body of experimental work has established a robust trend for one-nucleon knockout reactions as a function of proton neutron separation-energy asymmetry $\Delta S = S_p - S_n$, where S_p is proton separation energy, and S_n is neutron separation energy [94].

1.3 In-beam γ-ray spectroscopy

In nuclear reactions of fast ion-beams with targets, such as nucleon knockout reactions (section 1.2.1), the reaction often has an appreciable probability to populate nuclear excited states of the reaction residue. The de-excitation of states can be observed while the emitter is still in motion, which can still exist as part of a well-defined ion-beam. The term *in-beam*, as part of in-beam γ-ray spectroscopy, is reference to this motion.

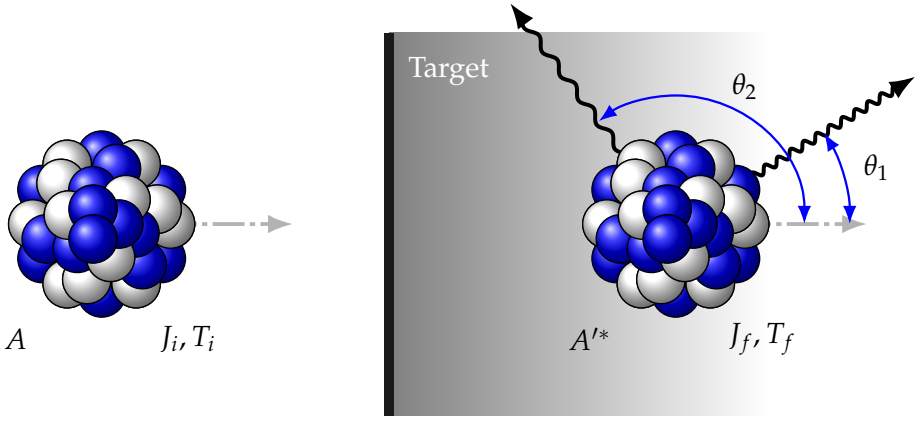

FIGURE 1.13: Schematic view of in-flight γ-ray emission following a reaction in a target at relativistic velocities. Emission in forward angles will have the laboratory energy boosted to a higher energy than the CM value, and backward will have lower energy. (See equation equation 1.24). i.e. $E_{\theta_1} > E_{\theta_2}$ for a given CM energy.

In-beam γ-ray spectroscopy is a powerful technique and is applied at numerous experimental facilities [95] for investigation of nuclear properties. In combination with a specific nuclear reaction, such as, nucleon knockout, transfer, nuclear fusion, or Coulomb, permits additional observables. A few examples include, excited state energies, transition probabilities, exclusive and differential cross-sections, deformation lengths and parameters, state lifetimes and exclusive parallel momentum distributions.

In-beam γ-ray spectroscopy is employed as a tool for the study of the isotopes of this thesis. The energies and intensities γ-rays emitted during transitions of the quantum mechanical rearrangement of the nucleus are measured. In addition, coincidences between observed transitions facilitates building of detailed level schemes.

1.3.1 Common features of γ-ray spectroscopy

An archetypal energy spectrum of a γ-ray sensitive detector is presented in Fig. 1.14a for illustration of common features present in most spectra. These include, the photopeaks, Compton edge, backscatter peak, Compton continuum, and background components.

The photopeaks are full energy peaks, wherein the complete energy signature is captured by the detector. An important consideration for a detector's performance is this peak width, for which the detector energy resolution contributes. The energy resolution for detectors varies considerably between detector types and subtypes. For some of the highest resolution detectors, solid state high purity germanium (HPGe) detectors, typical energy resolutions are 0.2% (1.33 MeV). Detectors based on inorganic and organic scintillators often posses energy resolutions one to two orders of magnitude lower energy resolution [96, 97]. Another important feature to distinguish detectors is the full energy peak (FEP) efficiency. The mechanisms of γ-ray interaction with matter have a strong dependence on material properties. An introduction into the performance characteristics (energy resolution) of the sodium iodine thallium doped (NaI(Tl)) detectors used in this thesis is presented in section 2.5.

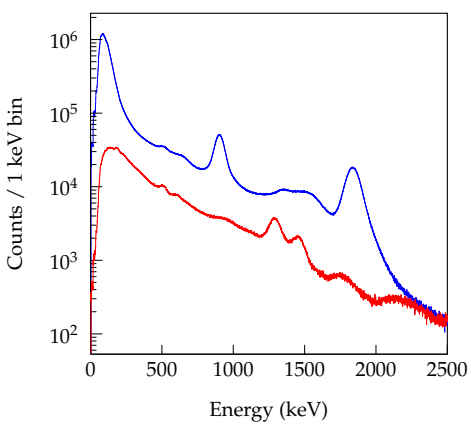

(A) Energy spectrum of ^{88}Y (blue) and environmental background (red)

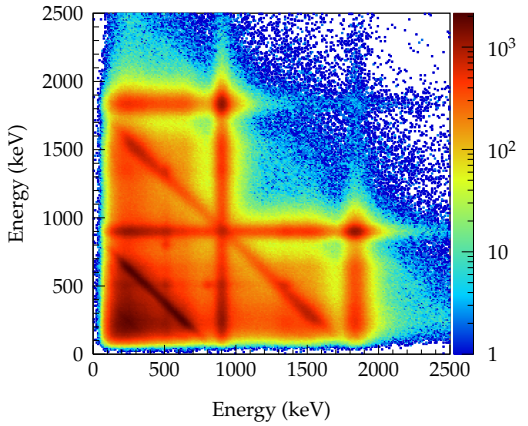

(B) Gamma gamma coincidence matrix. The coincident symmetric peaks present at 1836 keV/898 keV provide an indication of the cascade of transitions. The anti-correlated lines illustrate the Compton edge scattering and re-absorption between array detectors

FIGURE 1.14: ^{88}Y γ source measured within the DALI2 detector array illustrating general features of γ-ray energy spectra.

The Compton edge is a direct display of the Compton mechanism of interaction of gamma radiation with matter where a proportion of the energy of the γ-ray is transferred to an electron and both are scattered. When the scattering angle is maximum ($\theta = 180$), a maximum energy is transferred. The maximum energy transferred within the absorber corresponds to the Compton edge energy. Further, if the scattering occurs at a large angle in in a surrounding material, the corresponding scattered γ-ray can be detected as the backscatter peak. The Compton continuum, extending from zero the Compton edge represents the inelastic scattering within all intermediate angles to zero within the detector.

The process of photoelectric absorption can lead to the production of fluorescent x-rays[15]. If these x-rays have a chance to exit the detector, the complete energy absorbed into the detector is less by the x-ray energy and results in an x-ray escape peak. Although not present in the energy spectrum (Fig. 1.14a), in principal, an iodine escape peak exists at an energy below the full-energy peak and differing by the K_α X-ray of about 28.5 keV.

The surrounding material around detectors additionally contributes to observed energy spectra. In the case of lead, which is present within DALI2, photon interactions can result in characteristic 70 keV to 85 keV emissions. Lastly, in the specific case of high energy β particle emitting sources, interaction with matter results in Bremsstrahlung radiation and superimposes over the Compton continuum background at low energy.

1.3.2 Emission of γ-rays at relativistic velocities

The emission of electromagnetic radiation at an appreciable fraction of the speed of light results in a shift in energy observed in the laboratory frame. Such is the case

[15] often K x-ray lines

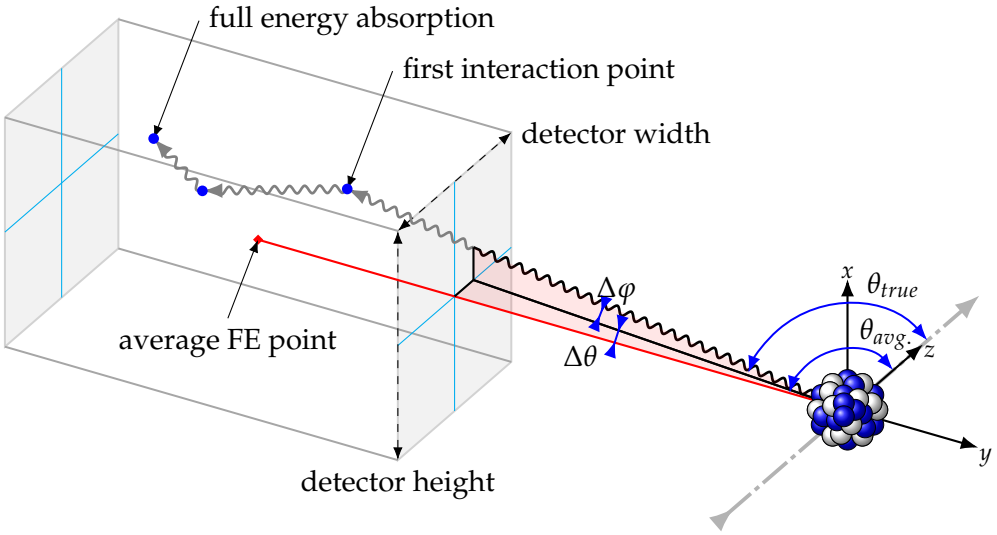

(A) $\Delta\theta$ uncertainty in due to finite γ detector opening angles.

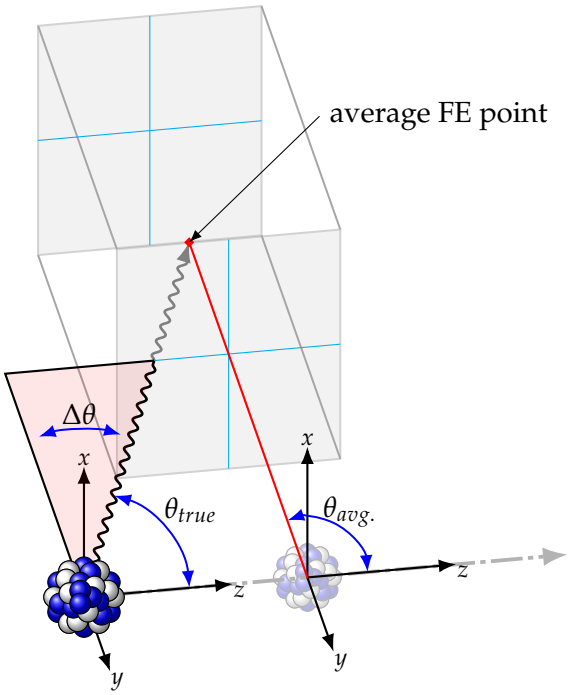

(B) $\Delta\theta$ as a result of position uncertainty.

FIGURE 1.15: Kinematic uncertainties for in-beam γ-rays.

for relativistic nuclei emitting γ-rays from the transition between excited states or to the ground state. The strength of the Doppler shift in energy depends on both the velocity and the angle between the velocity vector and observer through the equation,

$$\frac{E_\gamma}{E_{\gamma_0}} = \frac{\sqrt{1-\beta^2}}{1-\beta\cos\theta} \tag{1.24}$$

where E_γ and E_{γ_0} are the γ-ray energies in the observational frame of reference (the laboratory frame) and the frame of reference moving with the emitter (rest frame). This energy difference is related through θ, the angle between the emitter

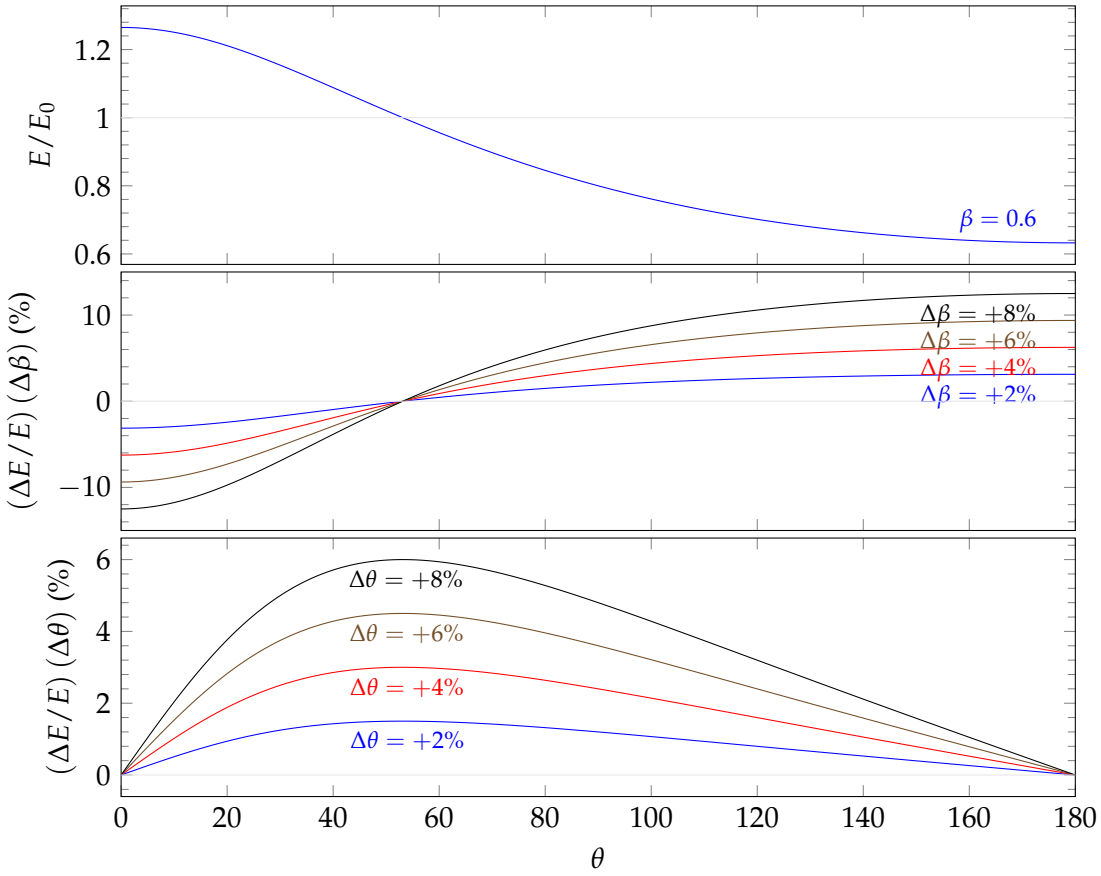

FIGURE 1.16: (Top) Doppler effect for velocity $\beta = 0.6$ as a function of observation angle. (Middle) Shift in observed energy as a function of velocity shift (symmetric). (Bottom) Shift in observed energy as function of observer opening angle shift (symmetric).

velocity vector and the observer at rest. For the application of Doppler correction for in-beam detector arrays, the observer is the γ detector and the angle is often specified relative to the reaction target. The midpoint of the detector, or more accurately, the (simulated) average full energy (FE) γ-ray interaction position, is used to calculate θ. β is velocity as expressed as a fraction of the speed of light and is related to the kinetic energy KE and rest mass m_0 through,

$$\beta = \sqrt{1 - \frac{m_0^2 c_0^4}{\left(KE + m_0 c_0^2\right)^2}} \tag{1.25}$$

The uncertainty of both velocity and observation angle translates to uncertainty in γ-ray energy. The relationship between velocity uncertainty and a broadening of the γ-ray energy is called Doppler broadening. This occurs as the velocity of each ion in an ion-beam, independent of the target properties, can often not be precisely defined. The uncertainty is,

$$\frac{\Delta E}{E} = \frac{\beta - \cos\theta}{\left(1 - \beta^2\right)\left(1 - \beta\cos\theta\right)}\Delta\beta \tag{1.26}$$

Additionally, the relationship between an uncertainty in observation angle manifests as detectors possess a finite volume, they represent a finite opening angle from

the γ source. This is a result of the position/trajectory insensitivity of most γ-ray detectors. The uncertainty relationship is,

$$\frac{\Delta E}{E} = \frac{\beta \sin\theta}{(1 - \beta\cos\theta)}\Delta\theta \tag{1.27}$$

Lastly, involving a macroscopic reaction target results in additional Doppler broadening and further observation angle uncertainty. As fast ions transverse through a reaction target, energy loss is inevitable due to the nature of the passage of charged particles in matter. As the precise position of emission cannot be truly known, an uncertainty develops for the both velocity (due to the continuous energy loss) and angle between detector and emission point. The magnitude of the contribution of Doppler broadening is related to the total energy loss, which itself is a function of target thickness and stopping power. And the uncertainty in angle is related to the target length. Further complicating the relationship is the stochastic nature of the decay of excited states. In the case of an appreciable state lifetime, an uncertainty in emission point will result, and the average decay position may move from the mid-point[16] of the target to behind the target. This additionally contributes to the uncertainty in velocity and observation angle.

These uncertainties are taken into account in the analysis of an in-beam spectroscopic experiments and depend on the particular experimental setup and conditions.

1.3.3 Reconstructed energy resolution

The attainable energy resolution can be decomposed into components of inherent detector resolution and Doppler reconstruction resolution. The latter is a consequence of the previous uncertainties in kinematics, velocity β and angle θ (equations 1.26 1.27). The combined kinematic uncertainty is,

$$\left(\frac{\Delta E_\gamma}{E_\gamma}\right)^2_{kin.} = \left(\frac{\beta\sin\theta}{1-\beta\cos\theta}\right)^2(\Delta\theta)^2 + \left(\frac{\beta - \cos\theta}{(1-\beta^2)(1-\beta\cos\theta)}\right)^2(\Delta\beta)^2 \tag{1.28}$$

and the total uncertainty is,

$$\left(\frac{\Delta E_\gamma}{E_\gamma}\right)^2_{total.} = \left(\frac{\Delta E_\gamma}{E_\gamma}\right)^2_{kin.} + \left(\frac{\Delta E_\gamma}{E_\gamma}\right)^2_{detector} \tag{1.29}$$

1.3.4 General properties of electromagnetic decay processes

The electromagnetic decay process observed in in-flight γ-ray spectroscopy can be described by the following rules and relationships.

1.3.4.1 Transition probabilities

The transition probability (T_{fi}) per unit time from an initial (i) nuclear state to a final (f) state is related to the lifetime as $\tau = 1/T_{fi}$ and to the half-life as,

$$t_{1/2} = \frac{\ln 2}{T_{if}} \tag{1.30}$$

[16]The average decay position is at the mid-length of the target if the reaction cross section does not appreciably change as function of kinetic energy.

In the more general case of more than one final state possibility, as transition probabilities are additive, making the state half-life,

$$\frac{1}{t_{1/2}} = \sum_f \frac{1}{t_{1/2}^{(f)}} \tag{1.31}$$

where $t_{1/2}^{(f)}$ is the partial half-life of the state to f. Gamma transitions are mediated by the multipole components of the radiation field of electric or magnetic type. The transition probability, as calculated through the golden rule of time-dependent perturbation theory can be written as[17] [20],

$$T_{fi}^{(\sigma L)} = \frac{2}{\epsilon_0 \hbar} \frac{L+1}{L[(2L+1)!!]^2} \left(\frac{e_\gamma}{\hbar c_0}\right)^{2L+1} B\left(\sigma L; \zeta_i J_i \to \zeta_f J_f\right) \tag{1.32}$$

where L is the photon angular momentum, J_i and J_f are the initial and final spins of the nuclear states, E_γ is the photon energy, σ is an index for electric (E) or magnetic (M) and B is the reduced transition probability which is

$$B\left(\sigma L; \zeta_i J_i \to \zeta_f J_f\right) \equiv \frac{1}{2J_i+1} \left|(\zeta_i J_i \| \boldsymbol{\mathcal{M}}_{\sigma L} \| \zeta_f J_f)\right|^2 \tag{1.33}$$

where $\boldsymbol{\mathcal{M}}_{\sigma L}$ is the multipole operator and $(\zeta_i J_i \| \boldsymbol{\mathcal{M}}_{\sigma L} \| \zeta_f J_f)$ is the reduced matrix element. The electric and magnetic transition probabilities can be reduced[18] to,

$$T_{fi}^{EL} = 5.498 \times 10^{22} \frac{L+1}{L[(2L+1)!!]^2} \left(\frac{E_\gamma[\text{MeV}]}{197.33}\right)^{2L+1} B(EL)[e^2\text{fm}^{2L}]\,1/\text{s} \tag{1.34}$$

$$T_{fi}^{ML} = 6.080 \times 10^{20} \frac{L+1}{L[(2L+1)!!]^2} \left(\frac{E_\gamma[\text{MeV}]}{197.33}\right)^{2L+1} B(ML)[(\mu_N/c_0)^2\text{fm}^{2L-2}]\,1/\text{s} \tag{1.35}$$

A reduced transition probability (equation 1.33) can reveal the characteristic of transition as either single-particle or collective in nature. Collective states involves, generally speaking, several particles. Therefore, the transition probability is large. By comparing theoretical transition probabilities (calculated assuming single-particle transitions) to experimentally deduced values, the extent of state collectively can be understood. The theoretical single-particle transitions are formulated as the Weisskopf estimates,

$$B\left(EL; \zeta_i J_i \to \zeta_f J_f\right) = \frac{1}{4\pi} \left(\frac{3}{L+3}\right) (1.2A^{1/3})^{2L}\, e^2(\text{fm})^{2L} \tag{1.36}$$

$$B\left(ML; \zeta_i J_i \to \zeta_f J_f\right) = \frac{10}{\pi} \left(\frac{3}{L+3}\right) (1.2A^{1/3})^{2L-2}\, \mu_N^2(\text{fm})^{2L-2} \tag{1.37}$$

$$\tag{1.38}$$

The ratio between experimental and Weisskopf estimates (equation 1.36) is defined by Weisskopf units (W.u.). The quantity $B(E2)$, can be shown to be related to the nuclear deformation parameter β. With the assumption of uniform charge density,

[17] with an average over substates and summing final substates

[18] note: $\frac{1}{4\pi\epsilon_0}\frac{e^2}{\hbar c_0} = \alpha = \frac{1}{137.04}$ and $\hbar c_0 = 197.33\,\text{MeV fm}$

$$\beta = \frac{4\pi}{3ZR_0^2}(B(E2)/e^2)^{1/2} \tag{1.39}$$

where there nuclear radius R_0 is typically defined as $1.2A^{1/3}$.

This relationship between a nuclear state lifetime and matrix elements of the decay can be generalized for all decays. Firstly, the lifetime (τ) of a nuclear state is related to it's width (Γ)[19], with the relationship $\Gamma\tau = \hbar$. Secondly, the width is related to the matrix element between initial and final states describing the mode of decay,

$$\Gamma \propto \left\langle \Psi_f \middle| \hat{\mathbf{O}}_{decay} \middle| \Psi_i \right\rangle \tag{1.40}$$

These matrix elements, including the previously introduced $B\left(\sigma L; \zeta_i J_i \rightarrow \zeta_f J_f\right)$ are basic experimental quantities and not model dependant.

1.3.4.2 Selection rules

Through the form of the electric and magnetic tensor operators it can be shown that no $E0$ or $M0$ ($L = 0$) transitions are possible through γ emission[20].

The angular momentum carried by the emitted photon in a nuclear transition must satisfy angular momentum conservation, namely,

$$\left|J_i - J_f\right| \leq L \leq J_i + J_f \quad \text{for} \quad (L \neq 0) \tag{1.41}$$

Also, the parity selection rule limits the choice in electric/magnetic multipole between state initial parity π_i and π_f,

$$\pi_i \pi_f = \begin{cases} (-1)^L, & \text{for } EL \\ (-1)^{L-1}, & \text{for } ML \end{cases} \tag{1.42}$$

1.4 In-flight radioactive ion-beam production

The production techniques to produce radioactive isotopes often can be described by one of two complementary approaches: isotope separator on-line (ISOL) or in-flight [98, 99]. Details of the ISOL method, including scientific highlights can be found in the recent review article [100]. The experiments as part of this thesis were undertaken employing in-flight techniques, both in production and separation.

The in-flight production scheme involves ion-beams at intermediate to high energies collisions with a macroscopic target (typically on the order of, or greater than $100\,\mathrm{MeV\,u^{-1}}$), resulting in mainly reaction mechanisms of projectile fragmentation (PF) or in-flight fission.

Heavy-ion induced projectile fragmentation or in-flight fission, as means to produce radioactive beams, offers several advantages. Firstly, a large range of radioactive isotopes are emitted in a narrow forward cone, close to the primary-beam kinetic energy. Such a kinetic feature of the reaction, in addition to the suitability of thick production targets, offers highly efficient production of useful products [101].

[19] For more than one decay mode, the total width is the sum of partial widths, $\Gamma_{total} = \sum_j \Gamma_j$

[20] $E0$ is possible through internal conversion, resulting in the decay with the emission of an atomic electron.

The independence on chemical properties allows access to the complete range of elements. Furthermore, short transit times does not typically induce a lower limit on the half-life of unstable isotopes.

1.4.1 Projectile-fragmentation

The first experiments at the Lawrence Berkeley Laboratory [102, 103, 104] fifty years ago pioneered the projectile-fragmentation mechanism for radioactive beam production. Projectile-fragmentation involves peripheral interactions[21] between a projectile and target nucleus. In this mechanism, nucleons are removed from the projectile, resulting in a lighter fragmentation product or residue and a recoil. The energetic reaction often leaves the fragmentation product in an excited state which promptly decays to the ground state [105, 106]. The repulsive Coulomb interaction with the target nucleus combined with the recoil momentum from direct nucleon removal and de-excitation produce a velocity cone leaving the target. Full utilization of the PF products requires an in-flight separator to efficiently collect products, and will be explained in 2.2.1.

Goldhaber showed that the breakup process of projectile-fragmentation is related to the Fermi momentum of the removed nucleons [107]. The parallel momentum of the PF products is modified by,

$$\sigma_{\parallel} = \sigma_0 \sqrt{\frac{A_f(A_b - A_f}{A_b - 1}} \quad \text{MeV}\, {c_0}^{-1} \tag{1.43}$$

where σ_0 is the fraction of mean Fermi momentum of the removed nucleons and often described well by 85 MeV ${c_0}^{-2}$ to 100 MeV ${c_0}^{-2}$, A_f and A_b are the mass of the fragment and beam, respectively.

The production cross section for a particular PF product is largest when close in mass. The cross section decreases exponentially with decreasing mass number and along isotopic chains the distribution is close to a Gaussian. The maximum cross section for along isotopes is close to stability. This is presented in Fig. 1.17. The PF fragments of the thesis experiments are highlighted.

The choice of a target for fragmentation reactions is a balance of nuclear cross section and managing changes in beam properties, such as in energy loss and scattering. Light atomic mass materials are advantageous for production targets, as the proportion of nuclear reactions is higher for a constant path length within a material [108]. This is a consequence of fewer atomic electrons for the same number of target atoms. Target materials of Be and C (graphite) are often employed by current in-flight beam production facilities. These targets can withstand high head loads associated with the deposition of energy from the primary ion-beam.

Great effort has been applied to predict the distribution of fragment velocities and cross sections as function of mass and charge. Generally, models of microscopic nucleon-nucleon scattering [111, 112, 113, 114, 115] and macroscopic [116, 117, 118, 119] so-called participant-spectator or abrasion-ablation models have been shown to be successful predicting power.

Lastly, it should be noted that empirical parametrization of fragmentation cross sections have been produced and examples of modern parametrizations include EPAX [120, 109] and FRACS [110]. They may provide less insight into the underlying mechanisms of fragmentation, however, they have strong predictive properties. FRACS, with it's so-called *brute-force factor* for neutron-rich fragments, shows good

[21] where the strong force is dominating

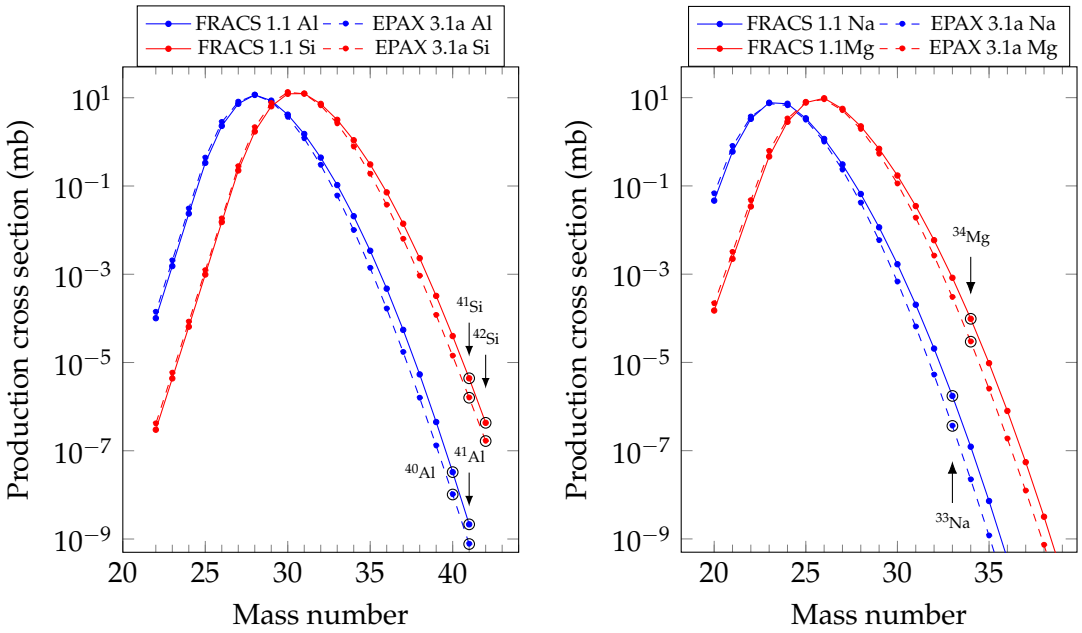

(A) PF product isotopic chains of experiment NP1312-RIBF03

(B) PF product isotopic chains of experiment NP906-RIBF02

FIGURE 1.17: Primary production cross sections of fragmentation products of the thesis experiments NP1312-RIBF03 and NP906-RIBF02. $^{48}Ca^{+20}$ ion-beam at 345 MeV u^{-1} on a Be target. Calculated with LISE++ with EPAX 3.1a [109] and FRACS 1.1 [110] parametrizations.

agreement with experimental data with very neutron-rich fragments from light, medium-mass, and heavy projectiles [110]. The predicted cross sections by both the latest EPAX and new FRACS empirical parametrizations are presented in 1.17 for the reactions of $^{48}Ca^{+20}(^{9}Be,X)X$ at energies corresponding to the fragmentation reactions used in the experiments of this thesis.

Chapter 2

Experimental Setup

This chapter applies commonly to both experiments. The two experiments investigating neutron-rich $^{32}_{10}$Ne (experiment number NP0906-RIBF02) and $^{(39-41)}_{13}$Al (experiment number NP1312-RIBF03) as part of this thesis work utilize the same experimental setup, spectrometers, beamline detectors and the DALI2 detector array at the RIKEN Nishina Center for Accelerator-based science Radioactive Ion Beam Factory (RIBF) in Wako, Saitama, Japan. Firstly, an overview of the facility is provided, including the accelerator system which provides the high intensity fast primary beams, radioactive isotope (RI) beam production method, BigRIPS separator and forward spectrometer ZeroDegree. The beamline particle detectors are then described to grant an understanding of their operational principal and performance. Finally, the heart of the experiment, the DALI2 detector array surrounding the secondary reaction target is introduced, including it's data acquisition setup.

2.1 The Radioactive Ion Beam Factory at the RIKEN Nishina Center for Accelerator-Based Science

The heavy-ion accelerator complex at the Institute of Physical and Chemical Research (RIKEN[1]) Nishina Center for Accelerator-based science integrates a K540-MeV ring cyclotron (RRC) and injectors of either a variable-frequency Wideroë linac (RIKEN Heavy-ion Linac or RILAC) or a K70-MeV AVF cyclotron (AVF)[2] [101]. Post-acceleration of RRC beams is accomplished at the RIBF facility. This is accomplished with a cascade of additional cyclotrons. The K930-MeV intermediate-stage ring cyclotron (IRC), K570-MeV fixed frequency ring cyclotron, and K2500-MeV superconducting ring cyclotron (SRC). This post-acceleration is a necessity to achieve efficient RI beam production with mechanisms of projectile fragmentation of heavy ions, up to uranium, and in-flight fission. The series of cyclotrons at the RIBF can provide beams up to 440 MeV u^{-1} for light elements (A < 40) and 350 MeV u^{-1} in the case of heavier elements up to uranium ($Z = 92$) [121]. A figure showing the schematic configuration of the linked accelerators is presented in Fig. 2.1.

The exact configuration of the heavy-ion system accelerator mode depends on the mass and charge of the species to the accelerated. In total, three modes of operation are available, as shown in Fig. 2.1. In the special case of acceleration of ^{48}Ca, the variable energy mode is used, wherein RILAC, RRC, and IRC are coupled for injection to the SRC. The ^{48}Ca beam energy in the thesis experiments, provided by the SRC, was 345 MeV u^{-1}. As mentioned earlier, this high energy allows for efficient production of radioisotopes by projectile fragmentation reactions, but also permits

[1] Rikagaku Kenkyusho

[2] For ions lighter than copper, or a mass-to-charge ratio of less than 4, the azimuthally varying field (AVF) cyclotron is used as the injector to the K540

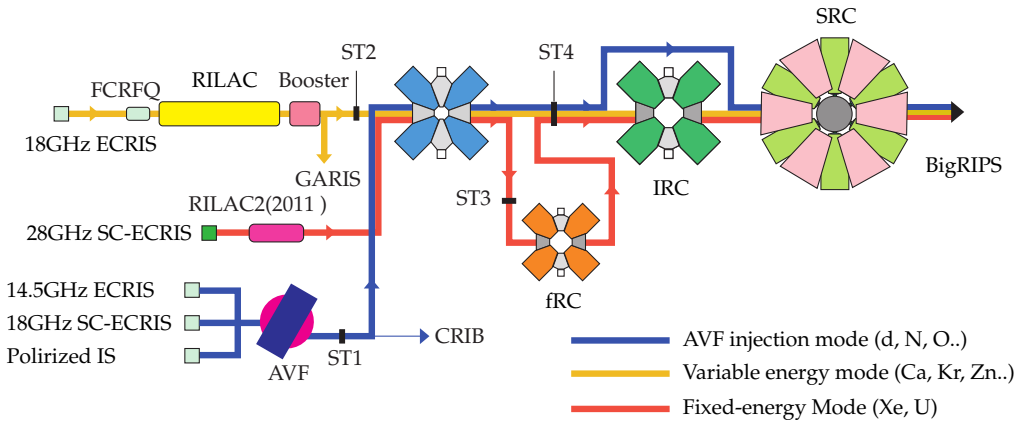

FIGURE 2.1: Overview of the RIBF facility. Image taken from [121].

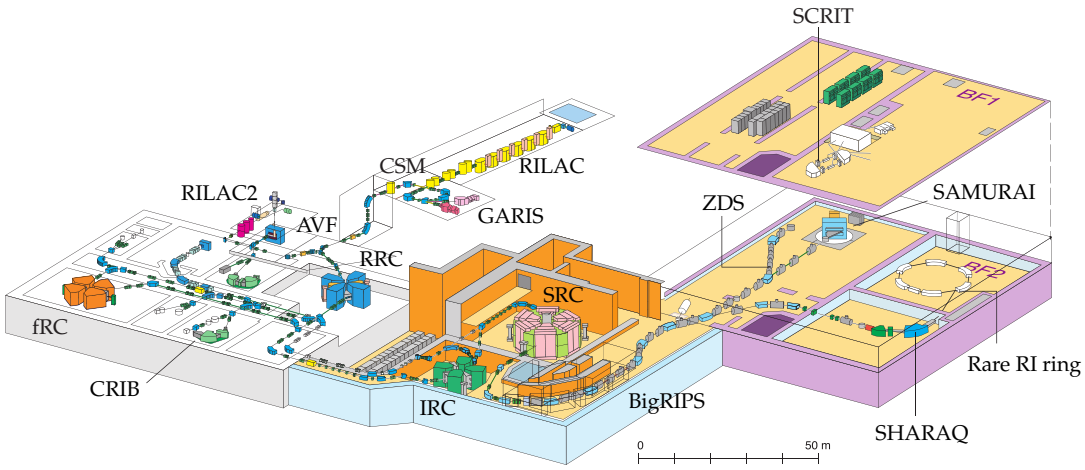

FIGURE 2.2: Schematic overview of the accelerators as part of the RIBF heavy-ion system. Image taken from [121].

the employment of thick secondary reaction targets (section 3.1.5) to achieve high luminosity experiments.

2.2 BigRIPS

The projectile-fragment separator (RIPS) at the RIKEN Accelerator Research Facility (RARF) generates high intensity light-ion RI beams at energies of 135 MeV u^{-1} and 1×10^{12} particles s^{-1} [101]. In a similar fashion, heavy-ion RI beams with larger magnetic rigidity are produced by projectile fragmentation at RIBF with the next generation BigRIPS separator [122]. BigRIPS features a tandem (or two-stage) fragment separator scheme. This permits both an event-by-event mode of tagging RI beam species [122] as well as purification by momentum and charge-state. The latter is particularly important as radioactive ion beams generated by fragmentation or in-flight fission reactions contain a mixture of various radioactive isotopes (beam cocktail.) The large acceptance of the BigRIPS ion optics permits an efficient capture of reaction products at 6% momentum acceptance, making good use of each primary ion from the accelerators. The horizontal and vertical angular acceptance is ± 40 and ± 50 mrad, respectively.

	RILAC	AVF	RRC	fRC	IRC	SRC
K-value		70 MeV	540 MeV	570 MeV	980 MeV	2500 MeV
Injector	ECR	ECR	RILAC K70 AVF	RRC	fRC, RRC	IRC, RRC
RF range	17–45 MHz	12–24 MHz	18–45 MHz	54.75 MHz	18–42 MHz	18–42 MHz
Max. flux density	-	1.7 T	1.67 T	1.68 T	1.9 T	3.8 T
Max. energy	0.7–4.0 MeV u^{-1}	3.8–14.5 MeV u^{-1}	135 MeV u^{-1}			345–440 MeV u^{-1}
Velocity gain	-	-	4	2.1	1.5	1.5
Sector magnets	-	4	4	4	4	6
Diameter	40 m length	4 m	12.6 m	10.8 m	14.0 m	18.4 m
Height		2.8 m	6.0 m			7.7 m
Total weight		110 t	2100 t	1500 t	2800 t	8300 t

TABLE 2.1: Overview of general properties of the accelerators at the RIKEN Nishina Center for Accelerator-Based Science

The first stage of BigRIPS, configured as a two-bend achromatic separator, starts from the production target to the the second focal plane (F2). The production target consists of a rotating wheel of thick beryllium, with an optimized thickness depending on the beam energy and reaction. For the experiments of this work, the Be target was 15 mm thick or 2775 mg cm^{-2}. The components of this portion of the separator include four superconducting triplet quadrupoles (STQ) and two room temperature dipoles. Sextupoles are incorporated in a number of the STQs to provide higher order corrections to achieve higher resolution. The primary purpose of the first stage is to both produce and separate RI beams. The so-called momentum-loss achromat technique [123, 124] is implemented and is achieved by the employment of wedge-shaped energy degrader at F1 for beam separation. As the first stage cannot produce isotopically pure beams, the second stage of BigRIPS permits identification of beam species. The second stage is configured as a four-bend achromatic separator and starts at F3 and continues to F7. It comprises of ten superconducting quadrupole triplets and four room temperature dipoles. Particle detectors within the beamline of the second stage permit identification of particles by the properties of atomic charge[3], mass-over-charge and momentum. The complete length from the production target to end of BigRIPS separator is 78.2 m. An overview of BigRIPS is presented in Fig. 2.3, including the labelling of the focal planes and the placement of critical beamline detectors.

2.2.1 Momentum-loss achromats for in-flight production separation

For separation of beam ions by species, two conditions needed to be bet. Namely, a resolution independent of velocity and an element to separate by mass number and atomic number. This can be achieved by so-called momentum-loss achromats and such devices have been implemented by numerous faculties over the past few decades. The application of an achromatic system results in the position of a particle at the end of the system is independent of it's initial momentum. The main elements of a momentum-loss achromat are a bending dispersive dipole, an energy loss degrader and a second bending dispersive dipole. This method is known as the $B\rho - \Delta E - B\rho$ method [126]. The first bending dipole provides separation by momentum-over-charge (also known as magnetic rigidity[4]) of the individual secondary beam species as well as from the primary beam. Given that the secondary

[3] in the case of fully stripped beam-ions: the identification by atomic number.

[4] $B\rho$, where B is the magnetic flux density, and ρ is gyroradius of a charged particle in the field B.

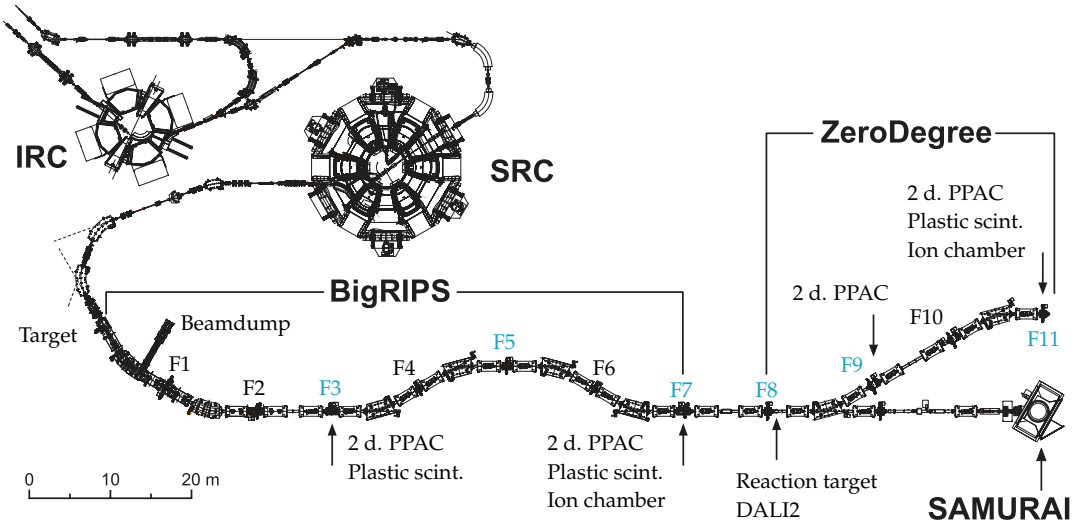

FIGURE 2.3: Overview of the IRC, SRC accelerators and the BigRIPS separator and ZeroDegree spectrometer. Image from [125] and modified. The focal planes with detectors are highlighted in blue.

species posses a similar velocity, the separation is nearly equivalent to mass-over-charge. At high beam energies, beam ions are assumed to be fully stripped. Mass-over-charge is not sufficiently exclusive, ions can posses the same ratio. The addition of an energy degrader, notably at the dispersive focal plane to preserve achromatism, results in energy losses approximately proportional to $\propto Z^2/v^2$ as seen by the Bethe equation for moderately relativistic charged heavy particles,

$$-\left\langle \frac{dE}{dx} \right\rangle = \frac{KZ^2_{particle}Z_{absorber}}{A_{absorber}\beta^2}\left[\frac{1}{2}\ln\frac{2m_ec^2\beta^2\gamma^2W_{max}}{I^2} - \beta^2 - \frac{\delta(\beta\gamma)}{2}\right] \quad \text{MeV g}^{-1}\,\text{cm}^2 \tag{2.1}$$

where K is a constant[5], Z atomic number, A mass number, I mean excitation energy (eV), m_e electron mass[6], W_{max} maximum energy transfer to an electron in a collision (MeV), and $\delta(\beta\gamma)$ density effect correction to ionization energy loss.

The momentum loss is approximately proportional to $\propto Z/v$. To a good approximation, the similar initial velocities of the beam ions, due to the production fragmentation production mechanism, results in a momentum loss proportional to $\propto Z$. Therefore, the addition of a second dispersive bend produces a separation of the new magnetic rigidities or momentum-over-charge. The degrader can be considered as a non-Liouvillean optical element, meaning phase-space density is atypically not conserved, a violation of Liouville's theorem. The optimal shape of the degrader is discussed in [108].

The use of multiple stages of degraders is advantageous as during the passage of ions, secondary reactions within a degrader can produce parasitic contaminants and additional degraders can further purify the beam cocktail. The implementation of multiple stages can furthermore enhance the selectively of the separation [124, 127].

The additional optional second degrader at F5 accomplishes this. The wedge-shaped degraders were 5 mm of aluminum at F1 and F5 for experiments NP1312-RIBF03 and NP906-RIBF02.

[5] 0.307 075 MeV mol^{-1} cm^2
[6] 0.510 998 946 1(31) MeV

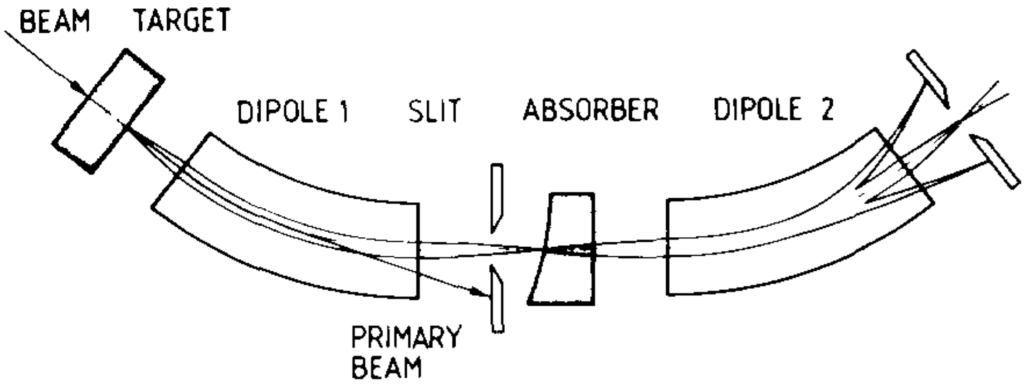

FIGURE 2.4: Illustration of the operating principal of a momentum-loss achromat from one of the first publications of this technique relevant to RI-beam separation by K.-H. Schmidt et al. (1986) [124].

TABLE 2.2: Main properties of BigRIPS and ZeroDegree spectrometers [125]

	BigRIPS	ZeroDegree
Momentum acceptance	±3%	±3%[1]
Horizontal acceptance	±40 mrad	±45 mrad[1]
Vertical acceptance	±50 mrad	±30 mrad[1]
Max. $B\rho$	9.5 T m[2]& 8.8 T m[3]	8.1 T m[1]
A/Q resolution[1]	1260[2]& 3420[3]	1240[1]
# STQ / # dipoles	12(14)/6	6/2
Length	78.2 m	36.5 m

[1] In the case of Large Acceptance Achromatic ion-optical mode.
[2] First stage.
[3] Second stage.

2.3 ZeroDegree

Following the BigRIPS separator (section 2.2) at the RIKEN RIBF, is the forward spectrometer ZeroDegree fixed at 0°. ZeroDegree can be utilized to identify and analyze reaction residues from the BigRIPS RI beams with a reaction target. The spectrometer is setup in a configuration of a two-bend achromat, consisting of six STQs and two dipoles. Similar to BigRIPS, sextupoles are incorporated in the STQs to provide higher order corrections of chromatic and geometrical aberrations. The secondary reaction target is placed between BigRIPS and ZeroDegree at F8. Like BigRIPS, surrounding the spectrometer focus locations are focal plane chambers containing beamline detectors to permit the $TOF - B\rho - \Delta E$ method with trajectory reconstruction for beam ion identification in an event-by-event mode. The focal planes of F9 and F10 are momentum dispersive. The ZeroDegree spectrometer can be operated in various ion-optical modes. The so-called Large Acceptance Achromatic mode, used in these experiments, features the F11 focal plane as achromatic and allows for the largest momentum acceptance of ±3%. Three other modes are configurable, including a Dispersive mode, which can permit F11 focal plane as momentum dispersive. Lastly, ZeroDegree can additionally deliver RI beams to the SAMURAI spectrometer [128]. A schematic overview of ZeroDegree is shown in Fig. 2.3.

2.3.1 $ToF - B\rho - \Delta E$ method

The particle identification scheme employed in the BigRIPS separator and the ZeroDegree spectrometer is called the $ToF - B\rho - \Delta E$ method, where the time-of-flight (ToF), magnetic rigidity ($B\rho$) and the energy loss (ΔE) of beam ions grants a deduction of the mass-to-charge ratio (A/Q), and atomic number (Z). The ToF of ions is measured between plastic scintillators (section 2.4.2) between F3 & F7 and F7 & F11. The magnetic rigidity calculated from the set and measured dipole magnetic fields in combination with ion trajectory reconstructions at focal planes, such as F3, F5, F7, F8, F9, and F11, commonly using PPAC detectors (section 2.4.1). The energy loss can be measured with Multi-sampling ionization chambers (MUSIC) (section 2.4.3) The relationship between mass-over-charge, velocity, and magnetic rigidity is,

$$\frac{A}{Q} = \frac{B\rho}{\gamma\beta m_u} \tag{2.2}$$

where m_u is the unified atomic mass (931.494 32 MeV $c_0{}^{-2}$). The velocity, β, as fraction of the speed of light, can be determined through the distance along the central trajectory through the spectrometer,

$$\beta = \frac{v}{c_0} = \frac{d_{central\ trajectory}/ToF}{c_0} \tag{2.3}$$

The magnetic field (rigidity) can be directly measured, through field measurements within the separator and spectrometer dipole magnets. High accuracy and precise Nuclear Magnetic Resonance (NMR) probes are employed for this purpose. However, in this case the magnetic rigidity applies only to central trajectories. For non-central beam trajectories, the position and angle at focal planes, in combination with optical transfer matrices, permits calculation of the relative magnetic rigidity and by extension a non-central A/Q calculation. The magnetic rigidity with respect to the central magnetic rigidity is,

$$B\rho = B\rho_0\,(1+\delta) \tag{2.4}$$

where δ is the relative difference in rigidity from the central magnetic rigidity $B\rho_0$. The relation between the complete phase space variables at two different planes along the separator and spectrometer beamline is described by the optical transfer matrix, in first order,

$$\begin{pmatrix} X' \\ A' \\ Y' \\ B' \\ \delta \end{pmatrix} = \begin{pmatrix} (x|x) & (x|a) & (x|y) & (x|b) & (x|\delta) \\ (a|x) & (a|a) & (a|y) & (a|b) & (a|\delta) \\ (y|x) & (y|a) & (y|y) & (y|b) & (y|\delta) \\ (b|x) & (b|a) & (b|y) & (b|b) & (b|\delta) \\ (\delta|x) & (\delta|a) & (\delta|y) & (\delta|b) & (\delta|\delta) \end{pmatrix} \begin{pmatrix} X \\ A \\ Y \\ B \\ \delta \end{pmatrix} \tag{2.5}$$

where X, A, Y, B, are the horizontal and vertical coordinates and angles, with the prime indicating the difference between planes. The transfer coefficients, e.g. $(x|x)$, describe the relationship between phase space variables. Often high orders are necessary to fully describe the relationship. Also, transfer matrix formalism can be understood as a Taylor (MacLaurin) power series[7]. In the special case between an achromatic and dispersive focal plane with certain symmetries (such as midplane symmetry), such as between F5 and F7, specific coefficients cancel[8]. Furthermore,

[7] A more complete description can be found in [129] and references within.

[8] For a completely achromatic system, $(x|\delta)$ and $(a|\delta)$ are zero.

the matrix and submatrices of x and y coordinates must have a determinate of unity to preserve particle energy [9]. The transfer matrix becomes,[10]

$$\begin{pmatrix} F7X \\ F7A \\ F7Y \\ F7B \\ \delta \end{pmatrix} = \begin{pmatrix} (x|x) & (x|a) & 0 & 0 & (x|\delta) \\ (a|x) & (a|a) & 0 & 0 & (a|\delta) \\ 0 & 0 & (y|y) & (y|b) & 0 \\ 0 & 0 & (b|y) & (b|b) & 0 \\ 0 & 0 & 0 & 0 & 1 \end{pmatrix} \begin{pmatrix} F5X \\ F5A \\ F5Y \\ F5B \\ \delta \end{pmatrix} \tag{2.6}$$

Solving for the relative magnetic rigidity in equation 2.6 reveals,

$$\delta = \frac{(a|a)F7X - (x|a)F7A - F5X}{(a|a)(x|\delta) - (x|a)(a|\delta)} \tag{2.7}$$

Therefore, the relative magnetic rigidity (2.4) can be substituted to equation (2.7) and the A/Q can be solved (2.2). The transfer coefficients between the various BigRIPS separator and ZeroDegree spectrometer used for A/Q determination are calculated from COSY INFINITY, an ion optical simulation program utilizing the differential algebra (DA) method [130].

2.3.1.1 Twofold $B\rho$ method

The inclusion of the wedge energy degrader at F5 in BigRIPS (section 2.2) leads to two ion beam velocities between the ToF detectors at F3 and F7, before and after F5. Therefore, to correctly account for energy loss for the A/Q determination, a twofold $B\rho$ determination is necessary. Firstly, the ToF_{F3F7} relation to the two beam velocities and path lengths L is,

$$ToF_{F3F7} = \frac{1}{c_0}\left(\frac{L_{F3F5}}{\beta_{F3F5}} + \frac{L_{F5F7}}{\beta_{F5F7}}\right) \tag{2.8}$$

And relation between the magnetic rigidities and velocities β, γ,

$$\frac{B\rho_{F3F5}}{B\rho_{F5F7}} = \frac{(\gamma\beta)_{F3F5}}{(\gamma\beta)_{F5F7}} \tag{2.9}$$

rearranging for either β_{F3F5} or β_{F5F7} in equation 2.8 and substituting this in 2.9 allows for a solution for the opposite β, when both $B\rho_{F3F5}$ and $B\rho_{F5F7}$ are known. With either β known, equation 2.2 can be solved for A/Q.

2.4 BigRIPS and ZeroDegree beamline detectors

To apply event-by-event identification of beam particles within the BigRIPS and ZeroDegree spectrometers, three broad classifications of detectors are utilized. These are tracking detectors (PPAC detectors, section 2.4.1), to determine an ion's position and velocity vector, energy loss detectors (ionization chambers, section 2.4.3), to determine atomic number, and time-of-flight (ToF) detectors (thin plastic scintillators, section 2.4.2), to determine beam velocity. In addition, for the particular case of absolute calibration of the separator and spectrometer, a high-purity germanium (HPGe) detector can be introduced to identify well-known isomer transitions [131].

[9] For example: $(x|x)(a|a) - (x|a)(a|x) = 1$

[10] The coefficients have an optical analogy, e.g. for x: $(x|x)$ is the magnification, $(x|a)$ is the focusing function, $(x|\delta)$ is the lateral dispersion and $(x|\delta)$ is the angular dispersion.

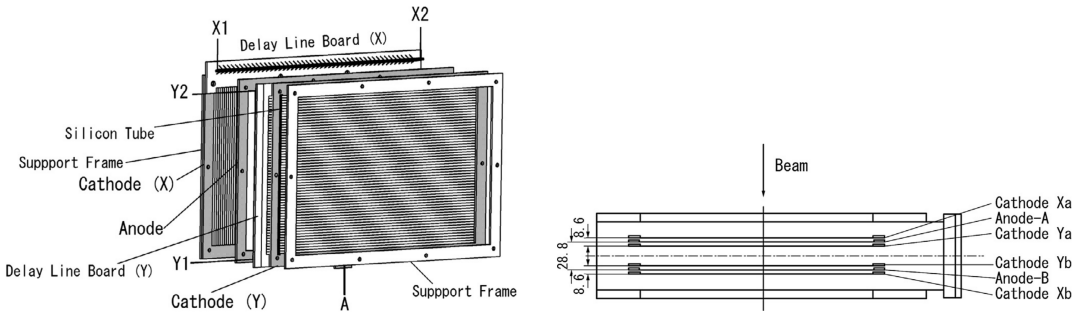

(A) Main components of a RIKEN PPAC. (B) Side view of double PPAC layers.

FIGURE 2.5: Schematic views of RIKEN PPACs for the BigRIPS and ZeroDegree separators. Images from publication [135].

2.4.1 Parallel plate avalanche counters - PPAC

Two-dimensionally sensitive Parallel Plate Avalanche Counters (PPAC) [132, 133, 134] have been intrumental in the operation of fragment separators at RIKEN since 1989 [101] and provide position and trajectory reconstruction at focal planes. This is used for both beam diagnostics, tuning and event-by-event particle identification in experiments through $B\rho$ determination as explained in section 2.3.1. The initial PPACS utilized at the RIPS separator at RIKEN [132] were based on the charge-division method for position determination, but have since been superseded by delay-line read-out PPACS. Chiefly, the pile up of signals (on the order of 3 µs) lead to limited maximum counting rates of a few thousand per second. With the delay-line read-out method, maximum rates of $1 \times 10^6\,\mathrm{s}^{-1}$ have been achieved [133].

The use of position sensitive detectors at dispersive focal planes necessitates a large sensitive area to measure a large beam momentum and phase space. The sensitive areas of the PPACS, as part of the beamline detectors of BigRIPS and ZeroDegree spectrometers, are commonly 240 mm by 100 mm and 240 mm by 150 mm [135], in the horizontal and vertical lengths. For a single PPAC, two layers are utilized to measure particles in two dimensions, horizontal and vertical. The standard PPAC assembly is comprised of two PPAC detectors, and therefore called a *double PPAC*. This structure allows for two-fold position measurements. The advantages of the double structure is to increase efficiency, reduction in event losses due to δ-rays[11] and in addition, provides a backup particle tracker. Two double PPACs reconstruct particle trajectories at focal planes of F3, F5, F7, F8, F9 and F11 (sections 2.2 and 2.3). A schematic view of a RIKEN PPAC is presented in Fig. 2.5.

The principal of operation of PPACs is the recording of energy loss in gases, often isobutene C_4H_{10} or C_3F_8, through the creation of charge (electrons and ionized gas). A strong electric field between electrode films results in the newly created electrons to initiate a Townsend discharge, producing a quantity of charge in a fast process, suitable for measurement. As the electrons are highly mobile within the gas at standard pressures, the generated charge has a characteristic fast rise and fall time.

The position is reconstructed through the pickup of the induced charge onto cathode electrode strips which are in turn connected to multitap delay lines. Due

[11] δ-rays are generated secondary electrons with sufficient energy to induce further ionization at a distance away from the primary particle. In the application of PPACs, unwanted δ-rays induce a multiple avalanche zone, resulting in an incorrect position reconstruction of the primary ion vector.

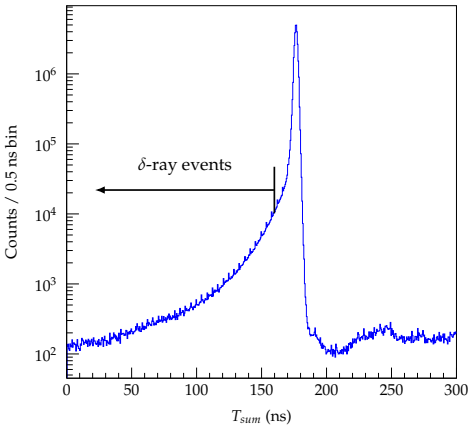

(A) Histogram of T_{sum} PPAC A - X

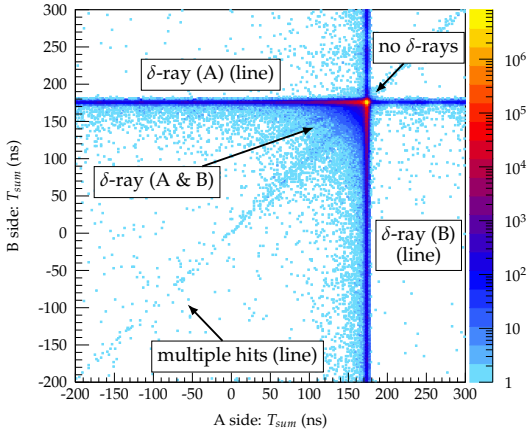

(B) T_{sum} of PPAC A and PPAC B. Identification of $\delta - ray$ events in one or both PPACs and multiple ion events.

FIGURE 2.6: PPAC of focal plane F5 from experiment NP1312-RIBF03.

to the constant characteristic impedance (50 Ω) of the delay line (resulting in a constant propagation speed of the signal), the time difference between the two ends of the delay line is proportional to the position of charge collection. The electrodes have pitch of 2 mm (equal to half width half maximum of the charge distribution) and result in time delay steps of 2 ns.

The delayed signals are measured by a time-to-digital convertor (TDC), with the start signal by the anode and stop by cathodes. The position is calculated based on the expression,

$$x = K_x \left(T_{x_1} - T_{x_2}\right)/2) + x_{offset} \tag{2.10}$$

where K_x is the propagation speed in mm ns^{-1} (on the order of 1.2 mm ns^{-1}), $T_{x_{1,2}}$ are the stop times and x_{offset} is a time offset to account for differences in signal propagation time between the ends of the delay lines and TDC. Given the fixed size of the delay line, the sum of both stop signals $T_{sum} = T_{x_1} + T_{x_2}$ is constant and independent of the position of the discharge. This is shown in Fig. 2.6a.

Other processes, such as the creation of δ-rays and particle multiple hits result in smaller T_{x_1} or T_{x_2}. This is a consequence of a widening of the avalanche region. All particles *carry* δ-rays when passing through and slowing down in matter. When the energy loss of the ion is significantly greater than the effect of the δ-ray, adjustment of the PPAC bias can prevent sensitivity to δ-rays. Such is the case with the fission products of ^{238}U + Pb. However, in the case of ^{48}Ca + Be fragments this is not possible.

The signals from the PPAC are locally amplified and an optical transmitter sends the optical signals via a100 m fibre optic cable to the DAQ area. The fast signals are preserved and received by photodiodes. The timing signals are supplied to a multihit time-to-digital convertor (TDC). A typical resolution is 0.41 mm rms for 850 V bias with C_4H_{10} gas filling at 11 Torr in the case of ^{48}Ca + Be fragments [135].

Relative to the other beamline detectors of BigRIPS and ZeroDegree, the stopping power is low as a consequence of a low effective areal density and low-Z materials. The entrance windows and electrodes of mylar[12] are in total a few tens of µm thick[13]

[12] chemical formula $(H_8C_6O_8)_n$

[13] The anode and cathode electrodes individually each 2.5 µm and 4 µm thick, respectively.

and contribute to a few mg cm^{-2}. This results in low energy losses and nuclear reactions with fast heavy ion beam interactions.

2.4.2 Time-of-flight plastic scintillator detectors

To determine the time-of-flight (ToF) between focal positions within the spectrometers, fast timing plastic scintillators are employed (Eljen Technology EJ-212 and EJ-230 with 2.4 ns and 1.5 ns decay constants, respectively [136]). The plastic scintillators during the thesis experiments were 0.2 mm to 1 mm thick. The sensitive area of the scintillators are commonly 120 mm by 100 mm.

Readout of the scintillation flash produced by the energy deposition of fast beam ions through the plastic is accomplished with (typically) two photomultiplier tubes (PMT). The PMTs are positioned on opposite edges (right and left) of the plastic to permit two-fold collection of light. Correlations between charge and timing between the two PMTs can permit rejection of spurious events, such as background noise or multiparticle events. The relationship between the difference in charge from the two PMTs (corresponding to the number of photons detected) can provide the position of interaction for fast beam-ions through the plastic sheet. The charge collected by the two PMTs can be described through,

$$Q_{left} = Q_{total} \exp\left(\frac{-L/2 + x}{\lambda}\right) \tag{2.11}$$

$$Q_{right} = Q_{total} \exp\left(\frac{-L/2 - x}{\lambda}\right) \tag{2.12}$$

$$x = \frac{\lambda}{2} \ln\left(\frac{Q_{left}}{Q_{right}}\right) \tag{2.13}$$

where $Q_{left/right}$ is charge of the left/right PMTs, Q_{total} is the total amount of charge, L is the length across the scintillator between the two PMTs, x is the position across the scintillator length, and λ is the light attenuation length in units of inverse distance. In a similar way, the time difference between the two PMTs provides another source of position reconstruction.

$$x = c_0/n \left(T_{left} - T_{right}\right) \tag{2.14}$$

where c_0 is the speed of light in a vacuum, n is the index of refraction, as the phase velocity of light in a material is $v = c_0/n$. $T_{left/right}$ is the time of the scintillation flash observed by the left/right PMTs. Combining 2.13 and 2.14,

$$c_0/n \left(T_{left} - T_{right}\right) = \frac{\lambda}{2} \ln\left(\frac{Q_{left}}{Q_{right}}\right) \tag{2.15}$$

Furthermore, the total PMT charge is roughly proportional to the energy deposited in the plastic by the ion. As the relation between deposited energy and atomic charge can be derived, the ion atomic number can be identified (see equation 2.1).

In the application of timing for event-by-event ToF, the average time of both PMT signals is used. And the time-of-flight (ToF) is calculated by the difference between this average. For the case of the time between F3 and F7 focal plane detectors, the ToF is,

$$ToF_{F3F7} = \frac{T_{F7\ left} + T_{F7\ right}}{2} - \frac{T_{F3\ left} + T_{F3\ right}}{2} + ToF_{F3F7\ offset} \tag{2.16}$$

where $ToF_{F3F7\ offset}$, an offset time must be included to take into consideration the sum of all propagation delays. The procedure to determine the offset experimentally is described in section 3.1.2. The ToF_{F7F11} is found in a similar way.

2.4.3 Ionization chambers

Evaluation of the event-by-event atomic charge can be accomplished by measurement of the energy loss of an ion. The gas ionization chamber detector is operated on this principal and can provide good energy resolution, large sensitive area, robustness to intense fast-ion beams and high rate capacity. The Bethe equation (2.1) illustrates the energy loss is proportional to the charge and velocity. The multi-sampling ionization chamber (MUSIC) concept is implemented in BigRIPS and ZeroDegree spectrometers. A specialized MUSIC detector for the application of high-rates has been developed and implemented at RIKEN as the tilted-electrode gas ionisation chamber (TEGIC) [137]. The maximum stable rate in the case of the RIKEN TEGIC has been shown to be up to 1×10^6 particles s^{-1} [137].

A schematic view of the RIKEN TEGIC is presented in Fig. 2.7. In common with a MUSIC detector, the gas volume is compartmentalized into smaller volumes (24) by 12 anode and 13 cathode electrodes. Uniquely, the electrodes are tilted to permit high beam intensity operation and a reduction of electron-ion recombination, which results in reduced charge collection efficiency. Along the particle trajectories within the gas, electrons and ions are liberated through the energy deposited. The consequence of the tilt of the electrodes ensures the electrons and positive ions move in opposite direction along the electric field lines away from the ion trajectory, with no intersecting paths. As the charge collected by the anode (electrons) occurs in a shorter time than of the cathode, only the anode signal is read out. This is a consequence of the higher mobility of electrons over ions in a gas.

The electrodes, anodes and cathodes, are made from thin aluminized mylar. The cathods are connected together and pairs of anodes are joined. This permits a reduction in outputs to only six. Each output is amplified with a charge sensitive amplifier and after a further amplification with a spectroscopy amplifier, is read by a peak-sensitive ADC. The geometric mean of the signals is proportional to the energy loss and is used to deduce the atomic charge.

The atomic charge is calculated through,

$$Z = c_3\beta\sqrt{\frac{\left(c_1\Delta E_{geo.\ mean\ raw} + c_2\right)_{MeV}}{\ln I\beta^2 - \ln 1 - \beta^2 - \beta^2}} + c_4 \tag{2.17}$$

where I is the ionization energy to produce an electron-ion pair, $\Delta E_{geo.\ mean\ raw}$ is the geometric mean of the amplified anode signals in uncalibrated channel number. The energy deposited is first calibrated to units of MeV through coefficients c_{1-2}, and the remainder of the coefficients are fit c_{3-4} to reproduce the atomic numbers. The typical filling gas used for operation is $Ar-CH_4$ in a mixture of 90%/10% with a bias on the order of 500 V. The entrance of the ion chamber is sufficiently large to capture the full phase space of the beam at F7 and F11.

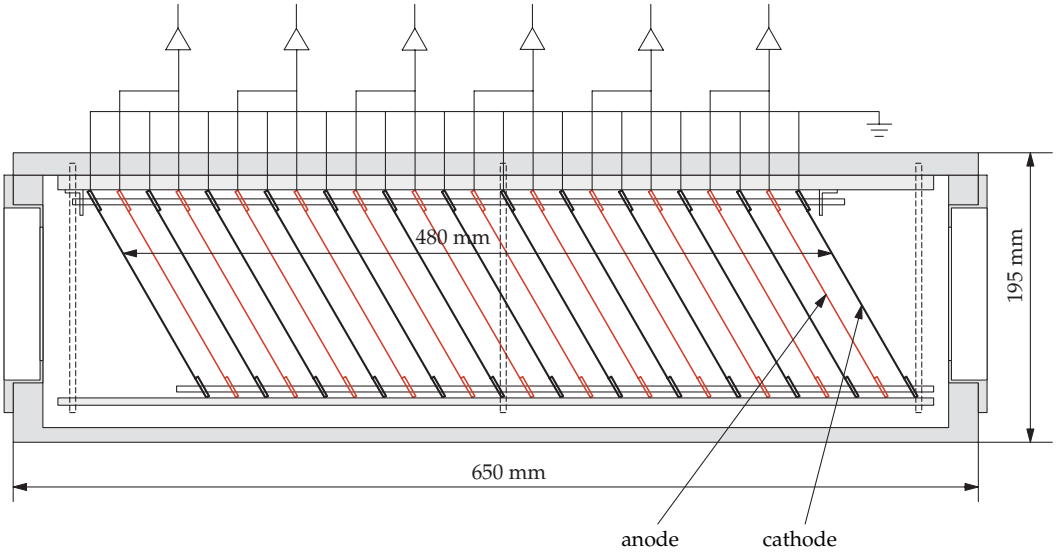

FIGURE 2.7: Side view of RIKEN developed tilted-electrode gas ionisation chamber (TEGIC) from publication [137].

2.4.4 RIBF DAQ

The data acquisition system utilized at the RIBF facility, called *RIBF DAQ*, is a scalable and versatile system implemented for all detector systems of the BigRIPS separator, ZeroDegree spectrometer and the DALI2 detector array. Its main feature is hierarchical event building during online experiments from parallel readout of distributed CAMAC[14] and VME[15] systems (which may include, for example, ADCs, TDCs QDCs, and scalers). Specific details on the structure, hardware and performance of the RIBF DAQ system can be found in [138].

It is important to note that the complete system operates under a common trigger on an event-by-event basis, which initiates the distributed front end computers (FEC) to read back the CAMAC and VME modules. The consequence of a common trigger is a common dead time, with the length of time shared between all FECs. This is accomplished through a distribution of logic busy signals. The longest readout time by an FEC as part of the system, determines the dead time of the RIBF DAQ.

2.5 DALI2 detector array

The DALI2 (Detector Array for Low Intensity radiation) in-beam detector array [139] surrounds the secondary reaction at the F8 focal plane position. Consisting of 186 thallium-doped sodium iodide (NaI(Tl)) scintillators, the array can cover a large solid angle with high granularity. The total active mass of NaI(Tl) scintillator is on the order of 560 kg. A 3D render of the array is presented in Fig. 2.8.

Three different NaI(Tl) detector types of similar size make up the detector array with either square or rectangular cuboid scintillator geometry. The sizes (and total number) of the scintillator crystals are $80 \times 40 \times 160$ mm (66), $80 \times 45 \times 160$ mm (88), and $61 \times 61 \times 120$ mm (32). The detectors are arranged on 12 layers, with 11 layers positioning the detectors transverse to the beam direction and forward layer fixing

[14] Computer-Aided Measurement And Control
[15] Versa Module Europa

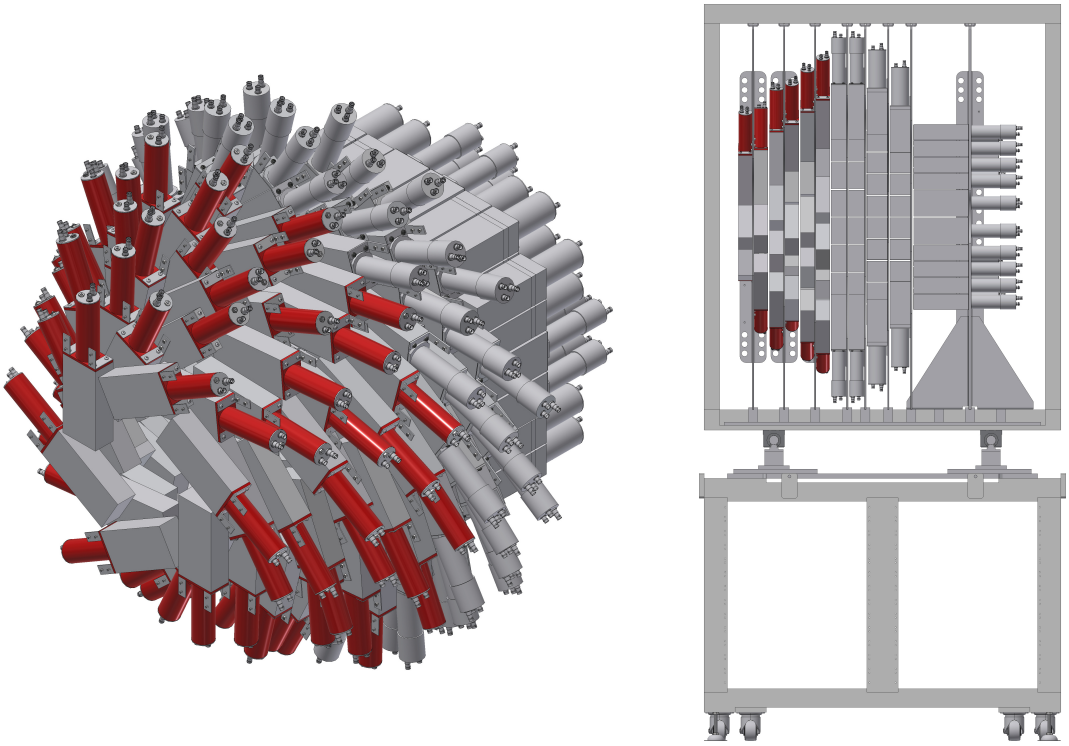

(A) Full view (B) Side

FIGURE 2.8: 3D rendering of the DALI2 detector array, comprising of 186 NaI(Tl) detectors.

the detectors parallel to the beam direction. The latter provides a longer effective length of the scintillators, resulting in a higher efficiency for high energy γ-rays[16]. The angular coverage across all detectors is 15° to 160°, depending on secondary target position. The opening angle for detectors at 60° relative the beam direction, the angular of greatest Dopper-shift at $\beta = 0.6$, is on the order of 6° (FWHM).

Inorganic thallium-doped sodium iodide (NaI(Tl)) is a well established and possibly the most extensively used scintillator for radiation detection. Its high light yield and matched emission profile to the sensitivity of bialkali photocathode PMTs, result in a moderate energy resolution for most applications. Being hygroscopic, NaI requires an airtight encapsulation for protection against moisture in ambeint air. General properties of NaI(Tl) material are summerized in table 2.3. The scinitillator's relative low cost per unit volume (and per unit mass), moderate energy resolution, high effective atomic number (Z_{eff}), and short attentuation length makes this material well suited for large arrays of in-beam γ detectors, such as the DALI2 detector array.

2.5.1 Atomic background and shielding

During the passage of heavy fast ions through the reaction target, processes other than direct nuclear reactions or Coulomb nuclear excitation can lead to the emission of high energy photons. The cross section for these atomic processes are often many orders of magnitute greater than the nuclear reaction of study. Largely, four processes contribute: radiative electron capture (REC) and primary Bremsstrahlung

[16] As demonstrated in section 1.24, at forward angles E_γ is boosted.

TABLE 2.3: Typical properties of Sodium Iodide scintillation material [140, 141]

Quantity	Value	Units
Z_{eff}[1]	50	
Density	3.67	$\mathrm{g\,cm^{-3}}$
Mean excitation energy	452	eV
Linear attenuation coeff.	0.350	$\mathrm{cm^{-1}}$ (500 keV)
Radiation length	2.59	cm
Molière radius[2]	4.1	cm
Wavelength of max. emission	415	nm
Primary decay time	250	ns
Light yield	40000	photons $\mathrm{MeV^{-1}}$

[1] [142] $\sqrt[2.94]{f_1 \times (Z_1)^2 + f_2 \times (Z_2)^2 + f_3 \times (Z_3)^2 \ldots}$, where Z_n is the atomic number of the element of the heterogeneous material, f_n is the fraction of total number of atomic electrons.

[2] $0.0265 X_0 (Z + 1.2)$, where X_0 is radiation length and Z is average atomic number

(PB) radiation, secondary Bremsstrahlung and emission of K and or L characteristic x-rays, depending on the target material [143, 144, 145]. The total cross section of these four processes is of the order of a few kb. A simulation of the atomic background is shown in Fig. 2.9e for $^{42}Si^{+14}$ on C target at 210 MeV $\mathrm{u^{-1}}$.

Radiative electron capture involves the capture of the target electrons into the (often fully stripped) projectile K and or L shells. As the x-rays are emitted in-flight, they are doppler-shifted. The cross section for this process is $\propto Z^2_{projectile} Z_{target}$. The angular distribution of the photon emissions if $\propto \sin^2\theta$, where θ is the angle between the projectile velocity vector and the emission in the laboratory frame. A simulated spectrum of the doppler shifted REC emission is presented in Fig. 2.9a and Fig. 2.9b to show the discrete x-ray lines.

Primary Bremmsstrahlung (PB) is caused by collisions of the projectile and the target electrons. The cross section is proportional to $\propto Z^2_{projectile} Z_{target}$ and the angular distribution to $\propto \sin^2\theta\,(1 - \beta\cos\theta)$. A simulated spectrum of the doppler shifted PB emission is presented in Fig. 2.9c with emission peaked at low energy.

Secondary Bremmsstrahlung (SB), similar to PB, is the result of scattering of target electrons. However the source is the highly energetic target electrons produced in PB, which re-scatter in the target or material surrounding the target to produce bremmsstrahlung radiation. The cross section is $\propto Z^2_{projectile} Z^2_{target/surrounding\ material}$. X-rays up to several hundred keV can be emitted in this process as shown in a simulation in Fig. 2.9d.

The excitation of the target atoms and the emission of K and or L characteristic x-rays can contribute significantly depending on the target. For low atomic number targets (C, Be, C_2H_4) with low energy K and L series lines [146], as well as small [147] fluorescence yields[17] makes this addition insignificant in the present experiments (NP1312-RIBF03 and NP906-RIBF02).

Lastly, it is worth nothing that the various reactions, such as knockout, secondary fragmentation, inelastic collisions, can result in a flux of protons, neutrons and other light particles, which can be boosted by the relativistic projectile velocity. These released particles can interact with the surrounding material, including the beampipe,

[17] the probablity of shell filling by radiative over non-radiative process, such as a Auger process

shield and detectors, causing both Bremmsstrahlung and nuclear reactions with prompt high energy photon emissions. Neutrons produced can furthermore cause material activation.

The intensity of the atomic background is maximum at low energy, on the order of a hundred keV and can be problematic for detector arrays. The high multiplicity of the emissions can result in pileup with detectors, which cannot be alleviated by solely an adjustment of detector thresholds. Ideally, between the reaction target (the position of γ-ray emissions from prompt decays) and the DALI detectors, little material is placed to minimize scattering and attenuation losses. However, to reduce the atomic background component, it is often necessary to apply a shield around the reaction target. Lead ($Z = 82$), due to it's high attenuation at low energy (see Fig. 2.10), is used as a sleeve over the beampipe surrounding the reaction target inside DALI2. One millimeter is chosen as a balance between shielding the atomic background flux and transmittance at higher energies, relevant to most nuclear transition energies. The transmittance of 1 mm Pb is presented in Fig. 2.10 and reveals a cutoff energy around a few hundred keV.

2.5.2 DALI2 DAQ

The electronics for the DALI2 detector array are presented in the a schematic in Fig. 2.11 [139]. The photomultipliers tubes (PMT) are biased by a CAEN multichannel power supply (model SY1527) to the order of 1 kV. The individual detector biases are set to provide a similar gain, through the observation of the photopeak of a standard γ calibration source. The output signals from PMTS are provided to a spectroscopy amplifier (CAEN model N568B) to both provide signal amplification and shaping. Amplified outputs with time constants of 3 µs are fed to a 12-bit multichannel peak sensitive analogue-to-digital convertor (ADC) (CAEN model V785) for energy measurements. The detector timing signals, provided by the fixed gain (x20) spectroscopy amplifier fast output (100 ns time constant), are provided to a constant-fraction discriminator (CFD) for signal discrimination. The constant-fraction method provides a means to reduce the time walk associated with varying signal amplitude (for the same signal shape), in contrast to threshold triggering (leading-edge).[18] The ADC requires a signal gate for acquisition.[19] This is provided by the OR trigger output logic of the CFD combined with a gate and delay generator for appropriate signal gate width and position relative to the spectroscopy amplifier shaped output signals. A common gate width is 4 µs. The OR trigger output of the CFD is also passed to the TDC for triggering. The OR logic signal is colloquially referred to as the γ trigger. The TDC has an internal time window and delay, and are set to encompass CFD logic pulses. Lastly, it is important to note that the DALI2 electronics is part of the larger RIKEN RIBF data acquisition system [138] (section 2.4.4). The data acquisition is completed system-wide, with the DALI2 DAQ operating during AND logic of both γ trigger and RIBF DAQ master trigger.

The energy threshold of the individual detector CFDs are set before an experiment to achieve an acquisition rate which balances system dead-time with the effective detection efficiency for experimental in-flight γ-rays.

[18] The constant-fraction method involves the triggering of the leading edge of a signal at *constant fraction* of its amplitude. A signal is split, with one branch attenuated and another inverted with a delay. The summed signal zero crossing point provides a the trigger time as it is independent of signal height. The CFD settings, including delay time, are chosen (often experimentally) to provide the optimum fraction point.

[19] window in time wherein, effectively, the amplified and shaped signals peaks are to be measured

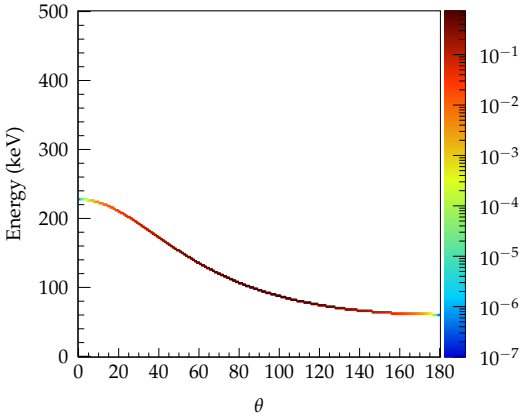

(A) REC K line (1.97 b)

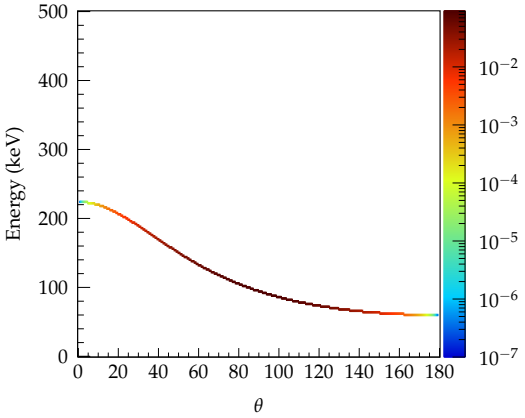

(B) REC L line (2.46×10^{-1} b)

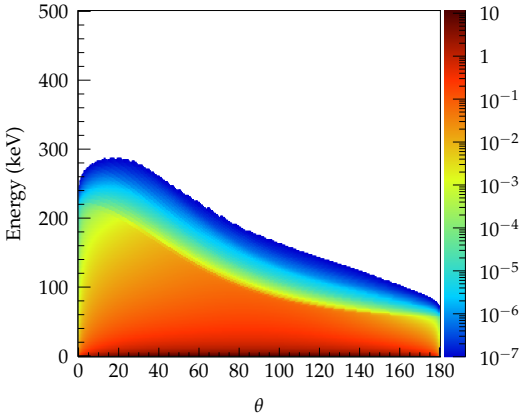

(C) PB (1.55×10^{2} b)

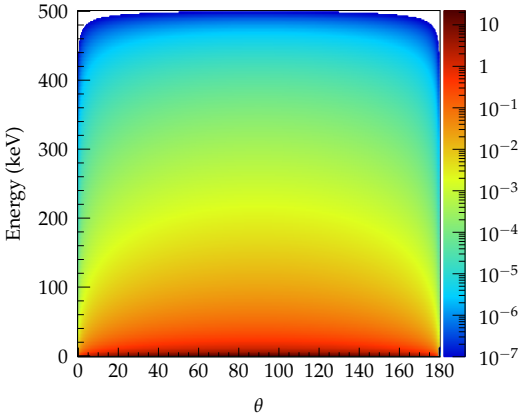

(D) SB (1.98×10^{2} b)

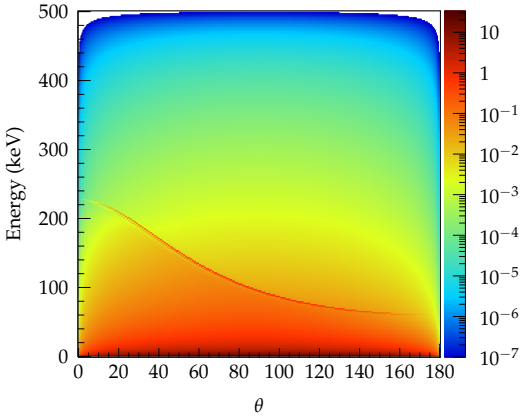

(E) Total (3.55×10^{2} b)

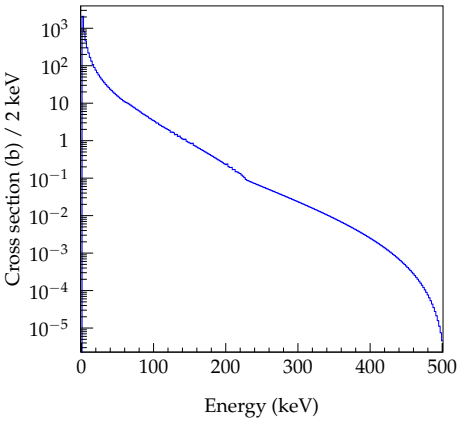

(F) Total

FIGURE 2.9: Simulation of atomic processes, with primary bremmsstrahlung, secondary bremmsstrahlung, and REC (K and L), by the ABKG program[148]. Compton profile from [149]. $^{42}Si^{+14}$ on C target at 210 MeV u^{-1}.

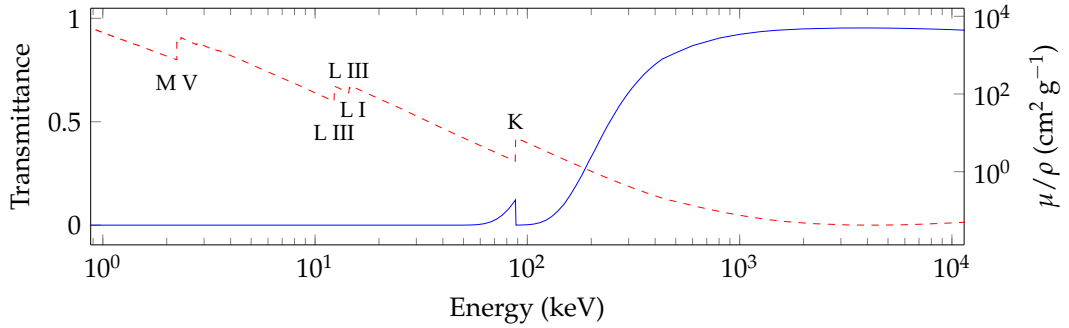

FIGURE 2.10: Transmittance of 1 mm Pb lead (solid, blue) and Pb mass attenuation coefficient μ/ρ (dashed, red) as function of energy [146]. Prominent edge energies are labelled.

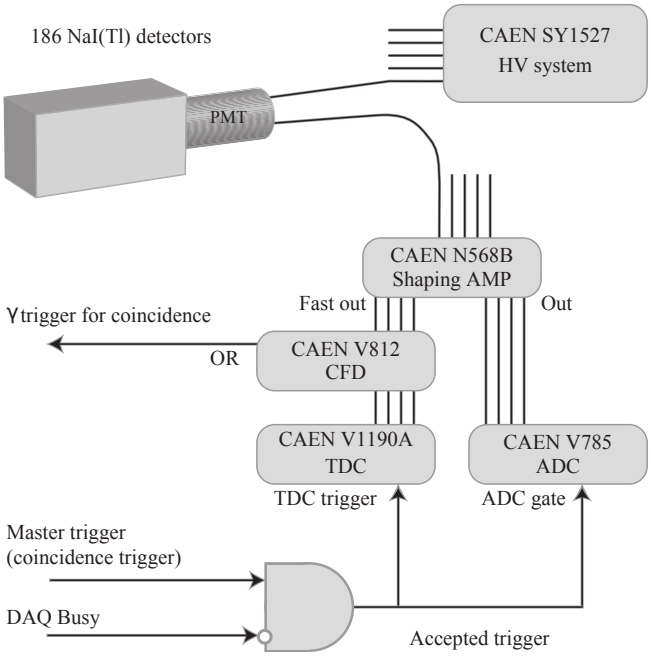

FIGURE 2.11: Schematic of the DALI2 DAQ system and components from [139]

Chapter 3

Data Analysis

The two experiments of this thesis, in-beam spectroscopy of neutron-rich $^{32}_{10}$Ne (experiment number NP906-RIBF02) and $^{(39-41)}_{13}$Al (experiment number NP1312-RIBF03) employed near identical setups and detectors. Therefore, the data analysis can be described in this chapter in a general way. The few specific cases of dissimilar analysis are identified and disclosed. This chapter begins with the in-flight separator and spectrometer and their respective detectors and concludes with the DALI2 γ-ray detector array.

3.1 Particle identification in BigRIPS and ZeroDegree

3.1.1 Event-by-event focal plane trajectories

To achieve accurate position reconstruction for A/Q determination, PPACS which record δ-rays or multiple ions must be removed in the event-by-event data. As mentioned in section 2.4.1, the physical property of a finite delay line results in a constant sum of stop signals from either delay line end, expressed as $T_{sum} = T_{x_1} + T_{x_2} =$ constant. The figures of 2.6a and 2.6b present a histogram of T_{sum} for events of an experimental run.

The rejection of unwanted events is accomplished outside of the central value of T_{sum}. The central position is determined through a fit with a skewed Gaussian function and the width of the window is a multiple of the σ of the fit Gaussian. For most PPACs, the window was 3σ. A figure of one example of this fitting procedure is displayed in Fig. 3.1. In total, 48 time windows are set for 48 individual PPAC layers.

The reconstruction of a trajectory at each focal plane is accomplished by a least squares minimization of the vector through the individual PPAC positions, as part of the tandem double PPAC system. A schematic of the F7 detectors is presented in Fig. 3.2 for illustration.

The reconstructed angle is an integral measurement for the calculation of A/Q (section 2.3.1), therefore an uncertainty in angle strongly influences the uncertainty of A/Q. In events for which only positions from one double PPAC are accepted, the uncertainty in the reconstruction angle is considerable due to the close spacing of PPAC layers. In this case, the angle is not calculated and instead is set to a mean value, which for most focal planes is zero degrees. Similarly, in events with only one individual PPAC position, the mean angle is provided for A/Q reconstruction.

A plot of the distribution of number of PPAC signals per event is shown in Fig. 3.3 for the experimental runs of NP1312-RIBF03 and the example of Si in BigRIPS and Al in ZeroDegree spectrometers, respectively.

Figure 3.3 reveals a lower PPAC efficiency for focal plane BigRIPS F3 detectors than subsequent PPACs and those in the ZeroDegree spectrometer. This may be a

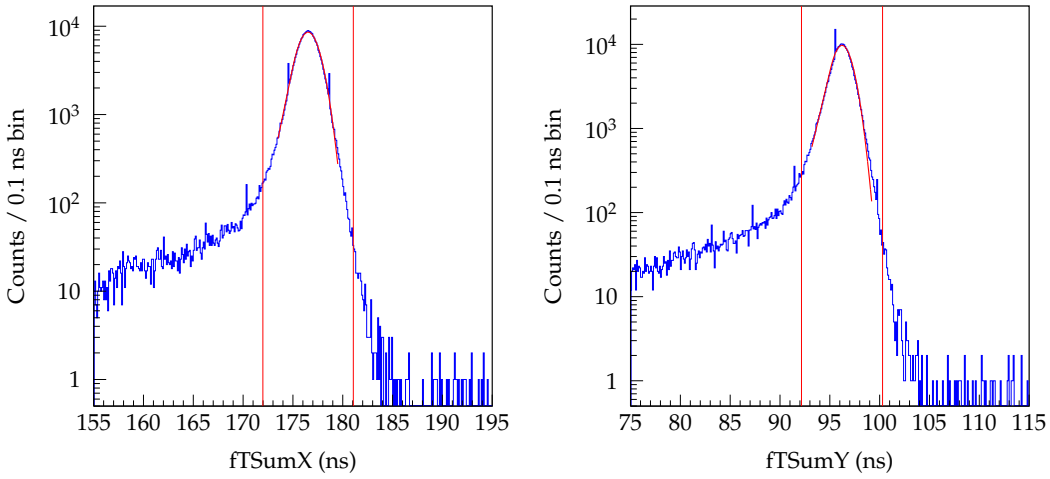

(A) PPAC A - X (B) PPAC A - Y

FIGURE 3.1: Illustration of T_{sum} gate for F5 PPAC - 1A

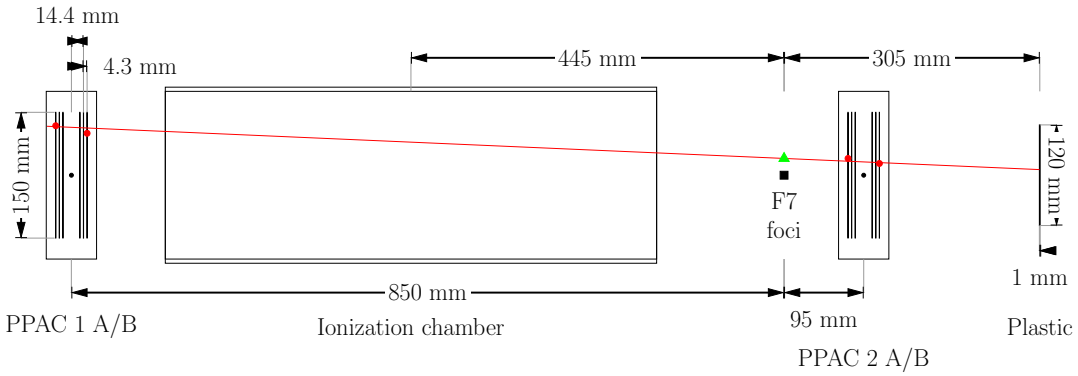

FIGURE 3.2: Schematic and scaled view of F7 focal plane detectors (PPACS, ion chamber and plastic scintillator) and a sketch of a particle trajectory reconstruction with double PPACs

consequence of higher sustained beam rate, leading to a degradation of the detector efficiency, or a lowered applied bias voltage to prevent breakdown. This consequently limits the efficiency of the BigRIPS A/Q reconstruction utilizing the twofold $B\rho$ method (described in section: 2.3.1.1). For this reason, a methodology for reconstructing A/Q based on the event-by-even number of PPAC signals per focal plane was developed and used in the analysis. The choice between the twofold $B\rho$ method (F3, F5, F7) and the singular $B\rho$ method (F5 & F7 or F5 & F8) is determined event-by-event based on if two double PPAC are measured for a focal plane.

The estimated efficiency of A/Q determination as a function of atomic number is displayed in Fig. 3.4. The estimated efficiency is relative to the number of events with ion chamber atomic charge. This estimation is justified by the prediction that the A/Q reconstruction efficiency is limited by the focal plane trajectory reconstruction efficiency[1]. The tendency of near 100% A/Q efficiency for $_{13}$Al and $_{12}$Mg beam-ions is a consequence of preparatory PPAC bias tuning. The decreasing trend with lower atomic number may be a result of the decreased energy loss and charge generation.

[1]The ToF determination and ion chamber charge efficiencies are near unity.

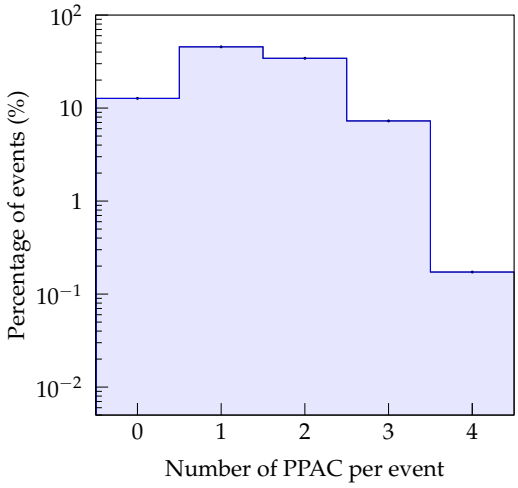

(A) F3X for Si

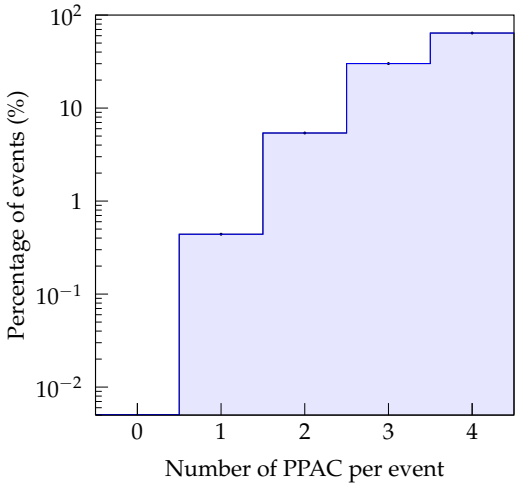

(B) F5X for Si

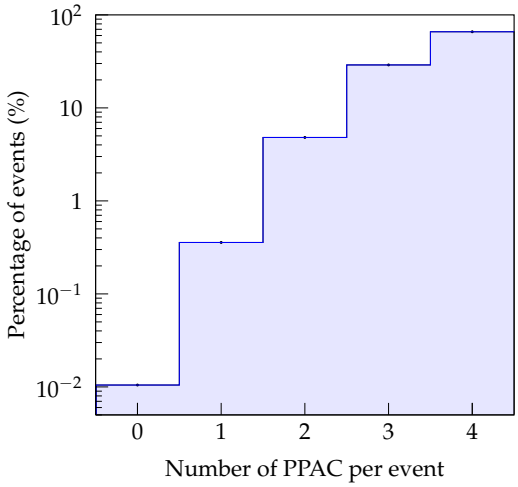

(C) F7X for Si

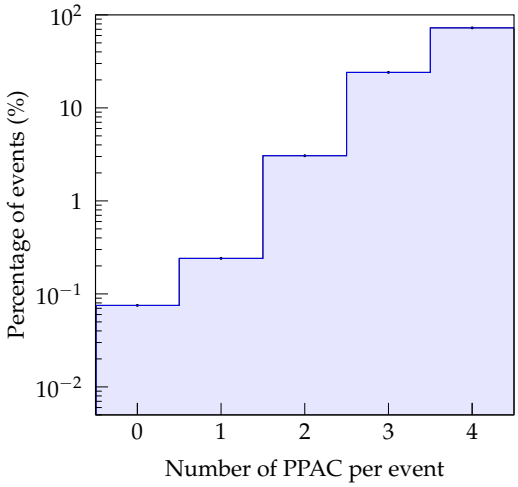

(D) F8X for Si

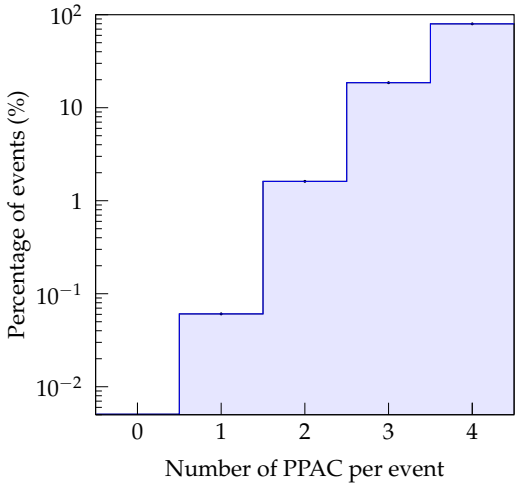

(E) F9X for Al

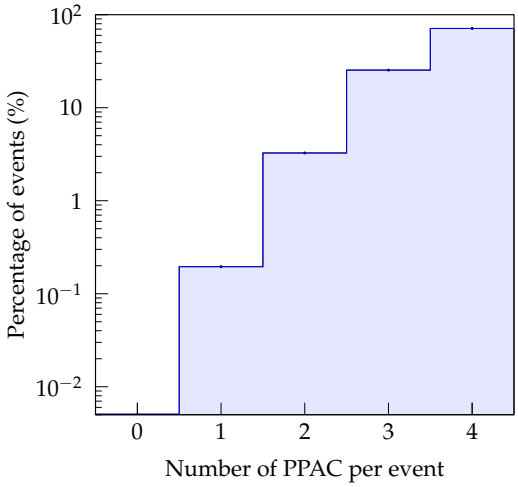

(F) F11X for Al

FIGURE 3.3: Number of PPAC signals for various focal planes. Where in this specific example, Si is defined as $13.5 < Z < 14.5$ from the calibrated F7 ion chamber and Al as $12.5 < Z < 13.5$ from the calibrated F11 ion chamber. For all experimental runs of **NP1312-RIBF03**.

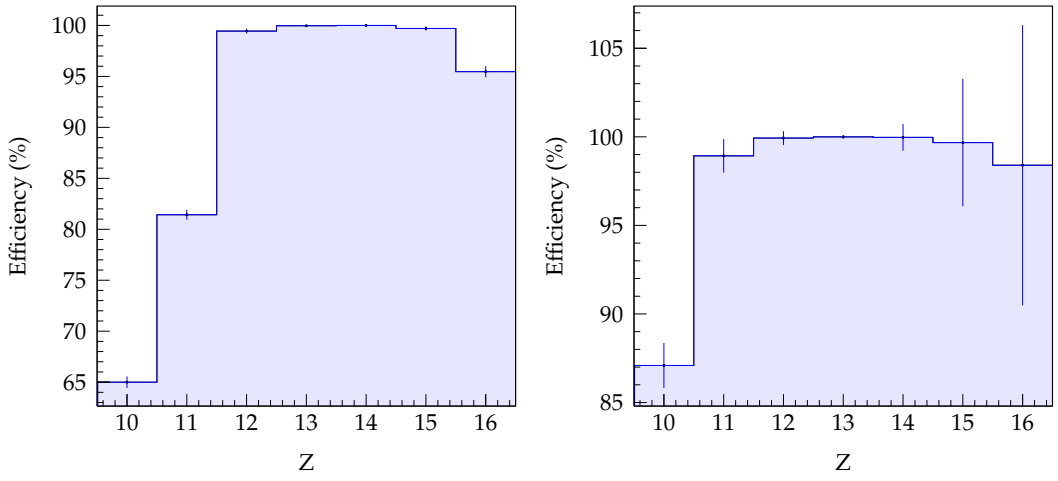

(A) BigRIPS (B) ZeroDegree

FIGURE 3.4: The ratio of number of events with reconstructed good A/Q ($1.5 < A/Q < 4$) over the number of events. This ratio provides an approximation of the efficiency of the A/Q reconstruction, which is mostly determined by the trajectory reconstruction efficiency. For all experimental runs of **NP1312-RIBF03**.

3.1.2 A/Q and Z reconstruction

The procedure explained in 2.3.1 was followed for the event-by-event reconstruction of the mass-over-charge and atomic number. The parameters for the ion chamber calibration were found to provide the correct Z. Similarly, the ToF_{offset} (equation 2.16) was adjusted to provide the correct A/Q using the $TOF - B\rho - \Delta E$ method (equation 2.2) combined with the twofold $B\rho$ method (section 2.3.1.1). Assigning the correct ToF_{offset} is important as it inherently modifies the reconstructed velocity.

As a measure to improve the selectivity for a particular reaction channel, the reconstructed A/Q resolution was improved through a set of additional corrections based on the positions and angles of the focal planes used in the event-by-event $B\rho$ determination. This has an equivalency to applying a higher order optical transport matrix, rather than the first order originally used for solving δ, the relative magnetic rigidity (equation: 2.4).

The correction coefficients were solved through a fitting procedure of selected events for a particular isotope (selected on the basis of the initial reconstructed A/Q and Z). With these isotopically pure events isolated, the relationship between the positions and angles, to the correction factor could be established (the difference between the correct A/Q and the initial reconstructed A/Q). The multidimensional fit was accomplished with the ROOT *TMultiDimFit* class[2]. Up to 5th order corrections and cross terms were permitted to be solved by the fitting function. To illustrate the effect of this procedure, the figure of 3.5 shows the relationship between the x position at the momentum dispersive plane F9 and A/Q, before and after corrections.

The A/Q as a function of Z is shown in Fig. 3.6 and 3.7 for experiments of NP1312-RIBF03 and NP906-RIBF02 to illustrate difference between the PID (particle identification) plots with and without this additional correction.

[2]ROOT version 5.35

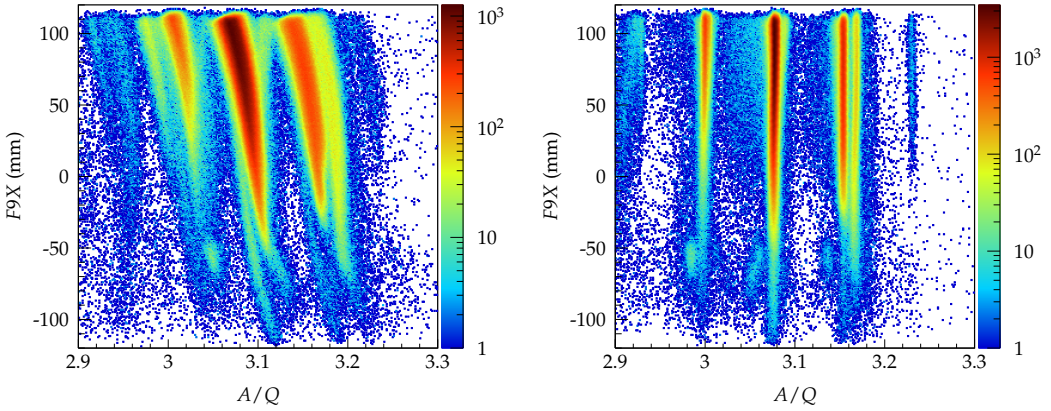

(A) Uncorrected (B) Corrected

FIGURE 3.5: Application of the A/Q correction procedure, as outlined in the text.

3.1.2.1 Experiment NP1312-RIBF03

At the beginning of the NP1312-RIBF03 experiment, it was noticed online that the counting rate between left and right PMTs of F3 plastic scintillator were different by a large margin. It was concluded this difference was a manifestation of a low CFD (constant-fraction discriminator) trigger level for one PMT, resulting in a large portion of events with only one PMT time. During a short break after 50 hours of online beam-time, the trigger level was appropriately adjusted, fixing the problem for the remaining 100 hours. The time-of-flight determination utilizes the average time between PMTs as a means to significantly increase timing resolution. Therefore, missing times would result in fewer events with a reconstructed A/Q. The analysis software was therefore modified to check event-by-event the number of PMTs with proper times and only take the average if both times were present, otherwise only one time is used. This results in two time offsets for A/Q reconstruction, and two A/Q resolutions, and double the number of selection gates, as explained in the subsequent section.

3.1.2.2 Experiment NP906-RIBF02

Evident in the PID plot of Fig. 3.7 is poor separation for atomic number across the isotopes of interest for the BigRIPS PID plot. Whether the reason for this observation is due to the experimental settings (such as bias) or the environment within the ion chamber is not clear. Nonetheless, the energy loss through F7 plastic and the readout of the scintillation flash is sufficient for charge identification as shown in 3.8. Significant spread of the event charge is illustrated in 3.8c as opposed to 3.8d. The consequence would be removal of a significant fraction of events if a window was selected around the peak of the IC reconstructed atomic number. Also, what appears to be pile-up events (with a multiple of charge) is significant with the IC reconstructed atomic number.

Fortunately, for the isotopes of interests, ^{34}Mg (A/Q : 2.83) and ^{33}Na (A/Q : 3), no beam species with similar A/Q exists in a significant fraction. Therefore, separation between species of $Z = 11, 12, 13$ by charge is unnecessary.

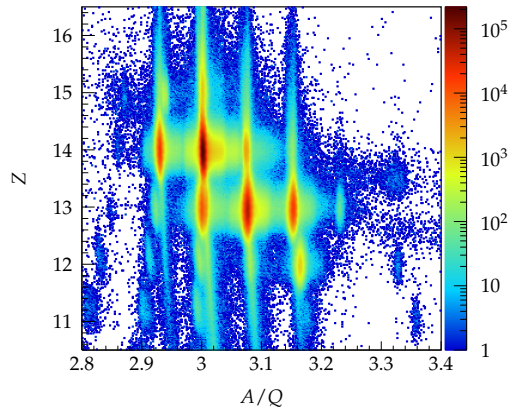

(A) BigRIPS original matrices

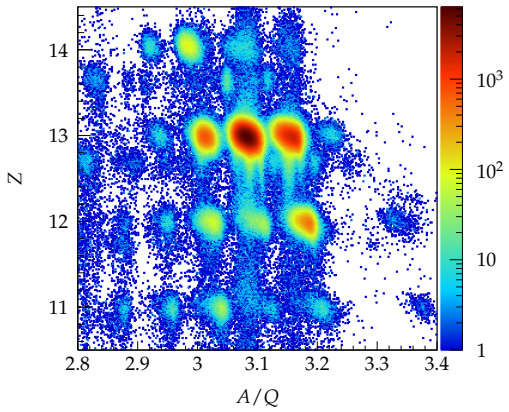

(B) ZeroDegree original matrix

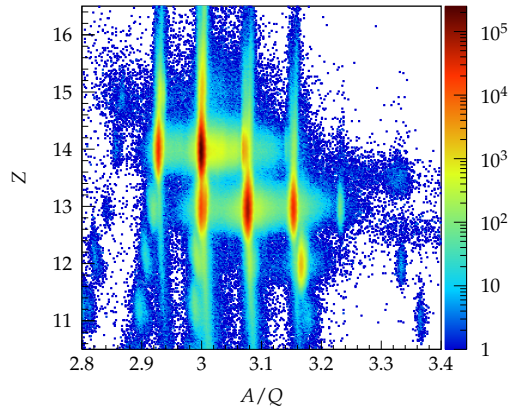

(C) BigRIPS with corrections

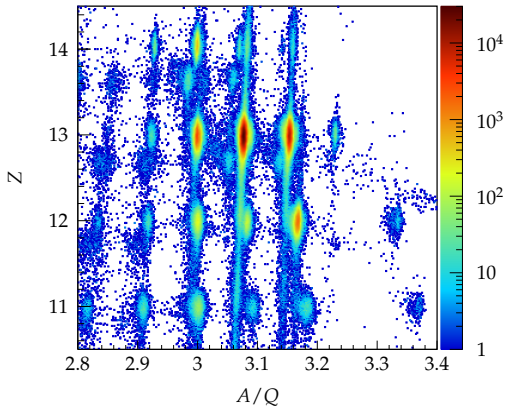

(D) ZeroDegree with corrections

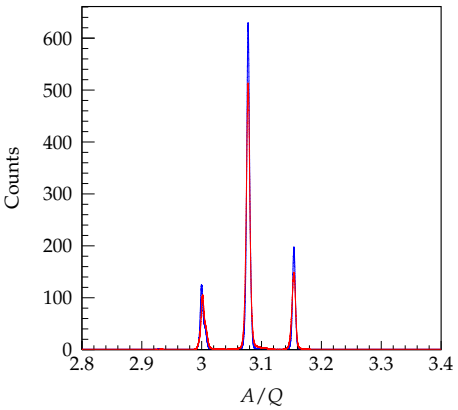

(E) BigRIPS projection across Al ($12.5 < Z < 13.5$) (red) uncorrected (blue) corrected

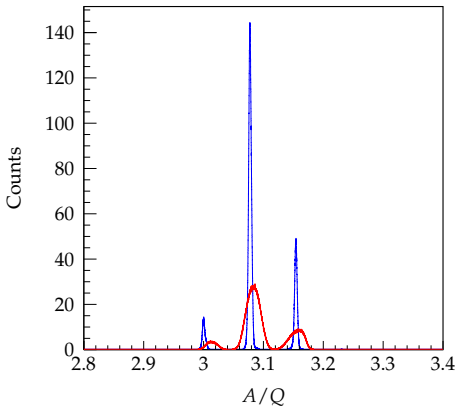

(F) ZeroDegree projection across Al ($12.5 < Z < 13.5$) (red) uncorrected (blue) corrected

FIGURE 3.6: **NP1312-RIBF03**: BigRIPS separator and ZeroDegree spectrometer PID plots generated by the $TOF - B\rho - \Delta E$ method for all experimental runs.

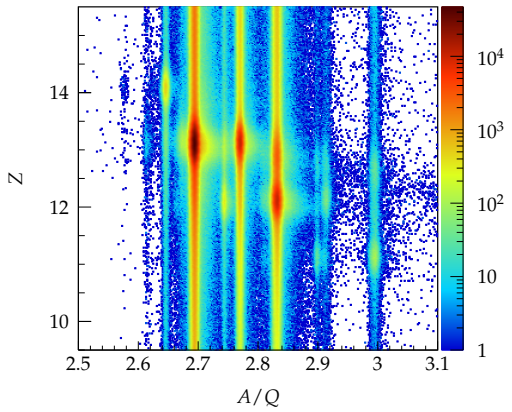

(A) BigRIPS original matrices

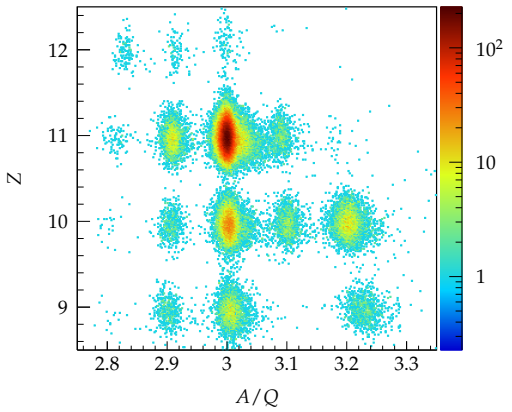

(B) ZeroDegree original matrix

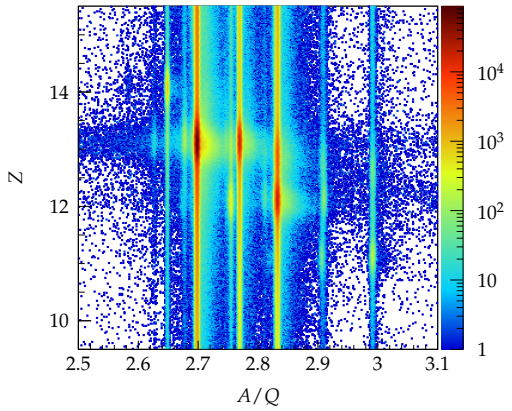

(C) BigRIPS with corrections

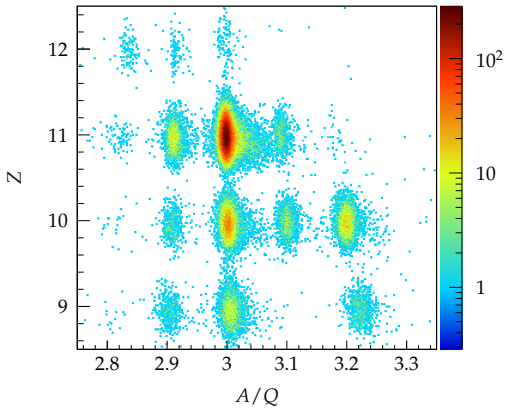

(D) ZeroDegree with corrections

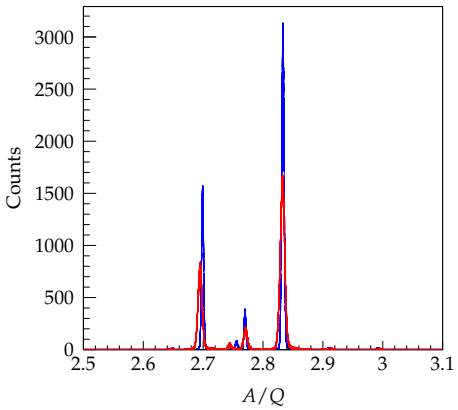

(E) BigRIPS projection
across Mg ($11.5 < Z < 12.5$)
(red) uncorrected (blue) corrected

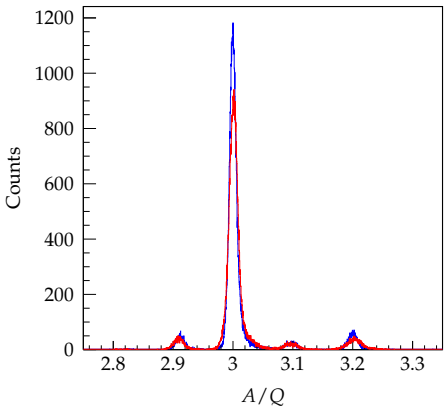

(F) ZeroDegree projection
across Ne ($9.5 < Z < 10.5$)
(red) uncorrected (blue) corrected

FIGURE 3.7: **NP906-RIBF02**: BigRIPS separator and ZeroDegree spectrometer PID plots generated by the $TOF - B\rho - \Delta E$ method for all experimental runs.

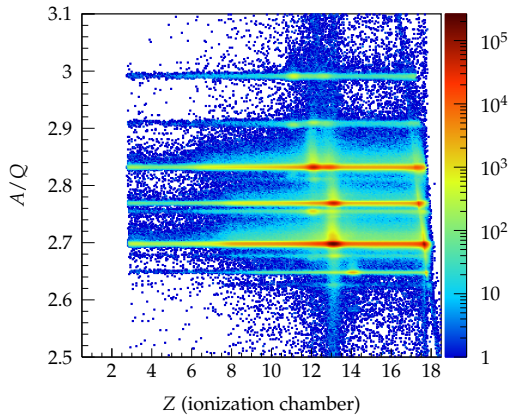

(A) BigRIPS PID

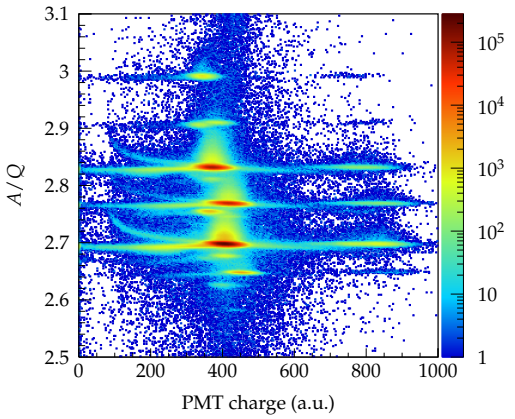

(B) BigRIPS PID with F7 PMT charge

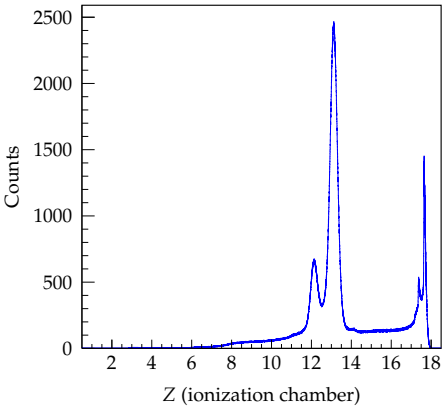

(C) Projection of 3.8a

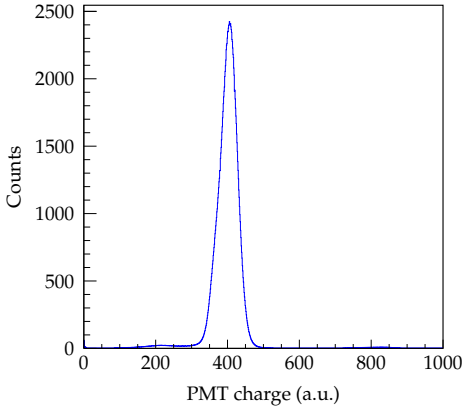

(D) Projection of 3.8b

FIGURE 3.8: **NP906-RIBF02**: Illustration of two methods of charge determination for the BigRIPS separator.

3.1.2.3 Mass-over-charge resolution

The final attained A/Q resolution for both experiments for BigRIPS and ZeroDegree are presented in table 3.1. The resolving power is completely sufficient to separate isotopes with the same calculated atomic charge. The overlap between reconstructed A/Q isotopic peaks is negligible, therefore contamination as a result of the finite A/Q resolution is not considered significant[3].

3.1.3 Removal of spurious and background events

Electromagnetic noise, nuclear reactions or elastic scatting of beam-ions with material along the separator or spectrometer, and secondary processes of charge exchanges can induce incorrectly reconstructed A/Q, ToF, and Z. In addition, beam background events comprising of light particle contamination, such as triton ions, may not be completely filtered by the magnetic dipole rigidities.

To limit these events in the reaction cross section determination, as well as γ-ray energy spectra, gates are applied to the event-by-event data experimental observables.

[3]Other sources of contamination, namely, nuclear reactions in the F7 plastic scintillator, are calculated separately for determination of inclusive and exclusive cross section sections.

TABLE 3.1: Reconstructed A/Q resolution for selected beam species.

Experiment	BigRIPS		ZeroDegree	
NP906-RIBF02	(^{34}Mg)	0.16% 0.0047 FWHM	(^{32}Ne)	0.57% 0.018 FWHM
NP1312-RIBF03	(^{41}Al)	0.14% 0.0045 FWHM	(^{41}Al)	0.14% 0.0044 FWHM

3.1.3.1 Photomultiplier noise rejection

The photomultipliers employed for detection of the scintillation flashes have an inherent dark count rate, owing to the thermionic emission of electrons as well as a non-thermal component [150, 151] from the photocathode, dynode surfaces or glass envelope. These include cosmic-ray Čerenkov radiation in glass, radioactivity in the glass, or the environment, and field emission of electrons. In addition, the CFD of the beamline photomultipliers may be triggered on noise. The readout of the signal baseline charge results in a pedestal peak. The pedestal events are removed as shown in Fig. 3.9. It was unnecessary to apply a selection cut on the F11 plastic detector for both experiments as a selection with A/Q (selecting a portion of the ToF_{F7F11}) significantly removes these events (Fig. 3.9d).

3.1.3.2 Plastic scintillator gates

As mentioned previously in section 2.4.2 and shown in equation 2.15, the proportionality of the time difference and the logarithm of fractional charge difference between left and right PMTs for the scintillator beamline detectors can be exploited for the removal of background events. An example of this removal is presented in Fig 3.10 for F3 and F7 plastic scintillators. The elliptical selection shape was determined through a bivariate Gaussian fit over the data with the elliptic major or minor axis lengths a multiple of the determined σ. All events outside of this ellipse are removed.

Furthermore, it was found that for the different beam species in the BigRIPS separator, the central position and shape of the logarithm of fractional charge difference as a function of time difference is slightly shifted. This is exploited as a weak selection of a specific species as seen later in section 3.1.4.

3.1.3.3 Fiducial cuts

Lastly, fiducial cuts on the reconstructed positions and ToF are applied to select events by reconstructed kinematics and by reconstructed positions within the physical sensitive areas of the PPACs. The formula for individual PPAC position calculations (equation 2.10) and the least square trajectory determination (section 3.1.1) makes no consideration to maximum physical sizes of the sensitive area of the PPACS.

As an example, for the PPACs at the F5 dispersive focal plane, with sensitive areas are 240 mm along the dispersive axis (x), a cut is applied $-115\,\text{mm} < x < 115\,\text{mm}$. This is shown in Fig. 3.11b.

The selection of the BigRIPS ToF is set to include all relevant beam species. To illustate this selection for experiment NP1312-RIBF03, the ToF_{F3F7} spectrum and upper and lower limits are presented in Fig. 3.11a.

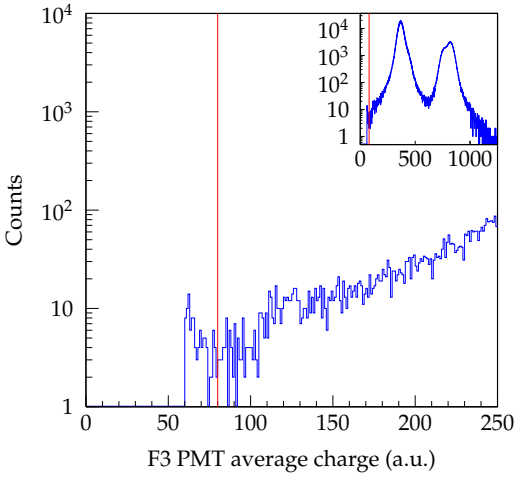

(A) F3 plastic average charge

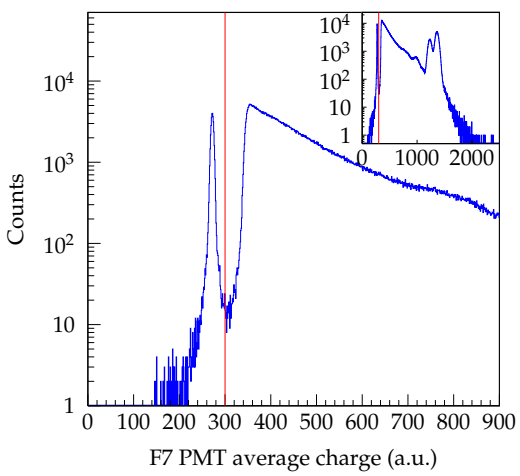

(B) F7 plastic average charge

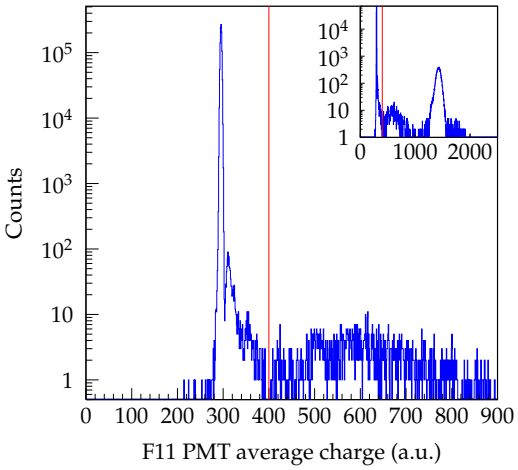

(C) F11 plastic average charge

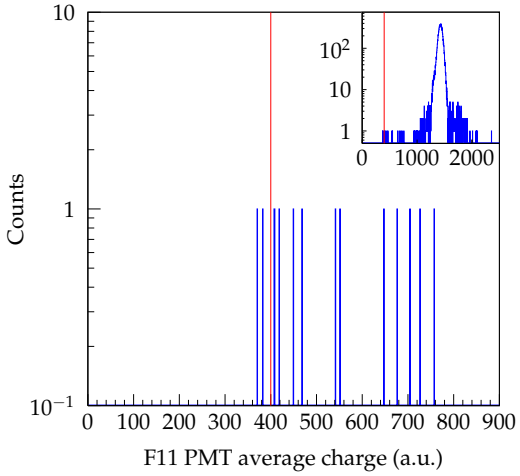

(D) 3.9c with good ZD A/Q

FIGURE 3.9: **NP1213-RIBF03**: Illustration removal of events with corresponding beam-line plastic scintillator PMT noise.

3.1.4 Species selection

To select events belonging to a specific species in the BigRIPS separator, three different selection gates are applied. They are: an elliptical selection of the F3 plastic scintillator charge fraction and time difference (section 3.1.3.2), a trapazoidal selection of ToF_{F3F7} versus dispersive plane $F5X$, and an elliptical selection of the reconstructed A/Q versus Z (or the F7 plastic charge in the case of NP906-RIBF02).

The elliptical selection shapes for the F3 plastic scintillator was chosen by a bivariate Gaussian fit over the data. As mentioned previously (section 3.1.3.2), the shift of the central provides beam-species selectivity. To show this effect, the example of experiment NP1312-RIBF03 is presented in Fig. 3.10a. Each ellipse represents a specific beam isotope.

The ToF_{F3F7} versus $F5X$ selection shape was calculated starting from a linear fit for the individual ion-beam species. From the slope and offset parameters a trapazoid cut is drawn. The selections for experiment NP1312-RIBF03 are shown in Fig. 3.12 for illustration. Furthermore, the examples of ^{41}Al (3.12b) and ^{42}Si (3.12c) are

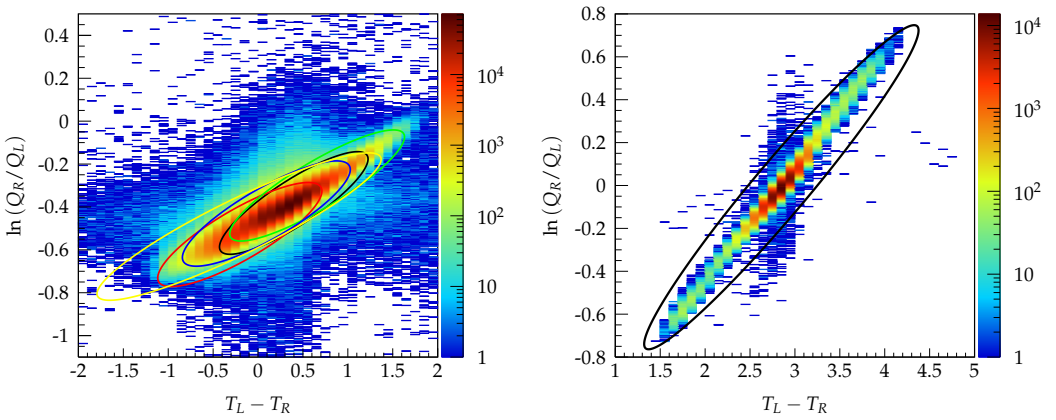

(A) F3 plastic scintillator (B) F7 plastic scintillator

FIGURE 3.10: Example of background removal for F3 and F7 plastic scintillators. For F3, different selections for the various BIgRIPS ion beam species are shown in different colours. For all experimental runs of **NP1312-RIBF03**.

presented in Fig. 3.12b and 3.12c with additional A/Q and Z selection for isolation. Moreover, Fig. 3.12b and 3.12c also indicate the selectivity of the aforementioned gates.

3.1.4.1 Species selection for experiment NP1312-RIBF03

The reconstructed A/Q and Z PID plots for BigRIPS and ZeroDegree are shown in Fig. 3.13a and 3.13b, respectively. The fiducial cuts (section 3.1.3.3) and photomultiplier noise rejection and F7 plastic scintillator fractional charge versus time difference cuts are applied. Elliptical selections are overlaid in the figure for the various species. Each ellipse is fit with a bivariate Gaussian function to determine the centroid and major and minor width. Although the ellipses may overlap in the BigRIPS PID, when selecting simultaneously a reaction residue and a ToF_{F3F7} versus $F5X$ selection, the cross-selection or contamination between different beam-ions of similar A/Q and atomic charge (for example, ^{42}Si and ^{39}Al) is not significant.

The example of one proton knockout from ^{42}Si to ^{41}Al is presented in Fig. 3.13c and 3.13d with the residue and projectile selected. These PID plots display intense peaks corresponding to elastically or inelastically scattered ions.

3.1.4.2 Species selection for experiment NP906-RIBF02

The reconstructed A/Q and Z PID plots for BigRIPS and ZeroDegree are shown in Fig. 3.14a and 3.14b. Overlaid are rectangular and elliptical gates for ^{34}Mg and ^{33}Na in BigRIPS and ^{32}Ne in ZeroDegree PID plots. The larger rectangular gates are used for tagging events for γ-ray spectroscopy and the tighter elliptical selections are used for inclusive and exclusive cross section determination.

3.1.5 Secondary reaction target

A summary of the materials and properties of the reaction targets utilized is presented in table 3.2.

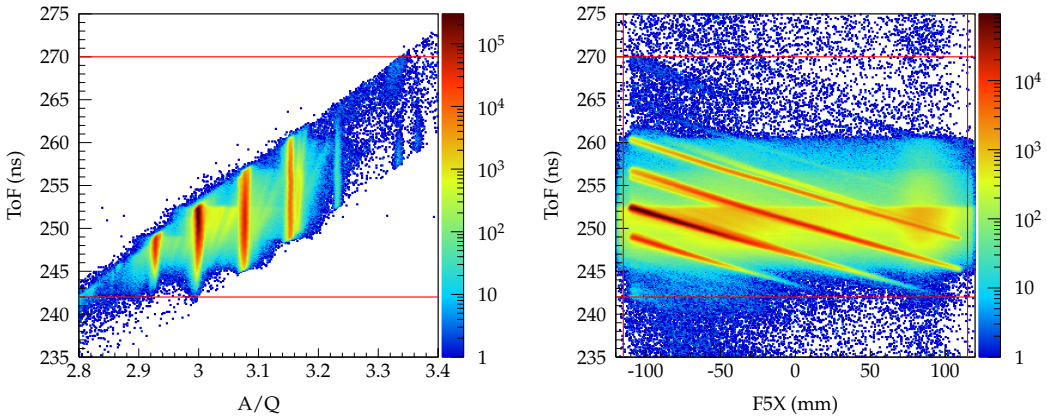

(A) ToF_{F3F7} selection (B) ToF_{F3F7} & $F5X$ selection

FIGURE 3.11: Illustration of BigRIPS ToF_{F3F7} and $F5X$ fiducial cuts. Red lines show lower and upper limits. For all experimental runs of **NP1312-RIBF03**.

TABLE 3.2: Summary of reaction targets of NP906-RIBF02 and NP1312-RIBF03 experiments

Experiment	Target material	Areal density	Diameter	Thickness
NP906-RIBF02	^{9}Be	1.032 g cm^{-1}	3.00 cm	0.56 cm
NP1312-RIBF03	C	3.795 g cm^{-1}	5.025 cm	2.17 cm
	C_2H_4	3.82 g cm^{-1}	5.12 cm	4.00 cm

It is important to consider the trajectories of particles at the secondary reaction targets. For cross section determination and γ-ray spectroscopy, only ion possessing trajectories through the volume of the reaction target are of interest. Furthermore, the average position and distribution is utilized for the GEANT4 simulation of in-flight de-excitation process and DALI.

The reconstructed position at the F8 focal plane combined with reconstructed angle (a position in phase space) permits a projection to the plane of the front face of the secondary reaction target (a rotation in phase space). The secondary reaction target is on the order of 150 mm downstream for both experiments. This position is determined precisely before an experiment through extrapolation of distances between the beam pipe (with DALI) and the F8 focal plane chamber.

A precision theodolite, calibrated with retroreflectors positioned in the experimental hall, is employed to position the secondary reaction target relative to the F8 focal plane chamber (encompassing the beamline detectors) and DALI.

The projected ion position at the front face of the secondary target is presented in Fig. 3.15 for the example of NP1312-RIBF03. A minimal shift, on the order of 0 mm to 5 mm horizontally and 0 mm to 1 mm vertically, is observed for all beam-ions for the NP1312-RIBF03 experiment. The position shift of experiment NP906-RIBF02 was less than 1 mm.

The outline of the secondary target can be identified by the shape of the beam halo, when selecting for all beam-ions which are fully accepted by ZeroDegree as shown in Fig. 3.15c. When selecting a reaction channel, this halo is not present. This is a consequence of ions which do no lose energy though the secondary target will not appear in the correct A/Q position.

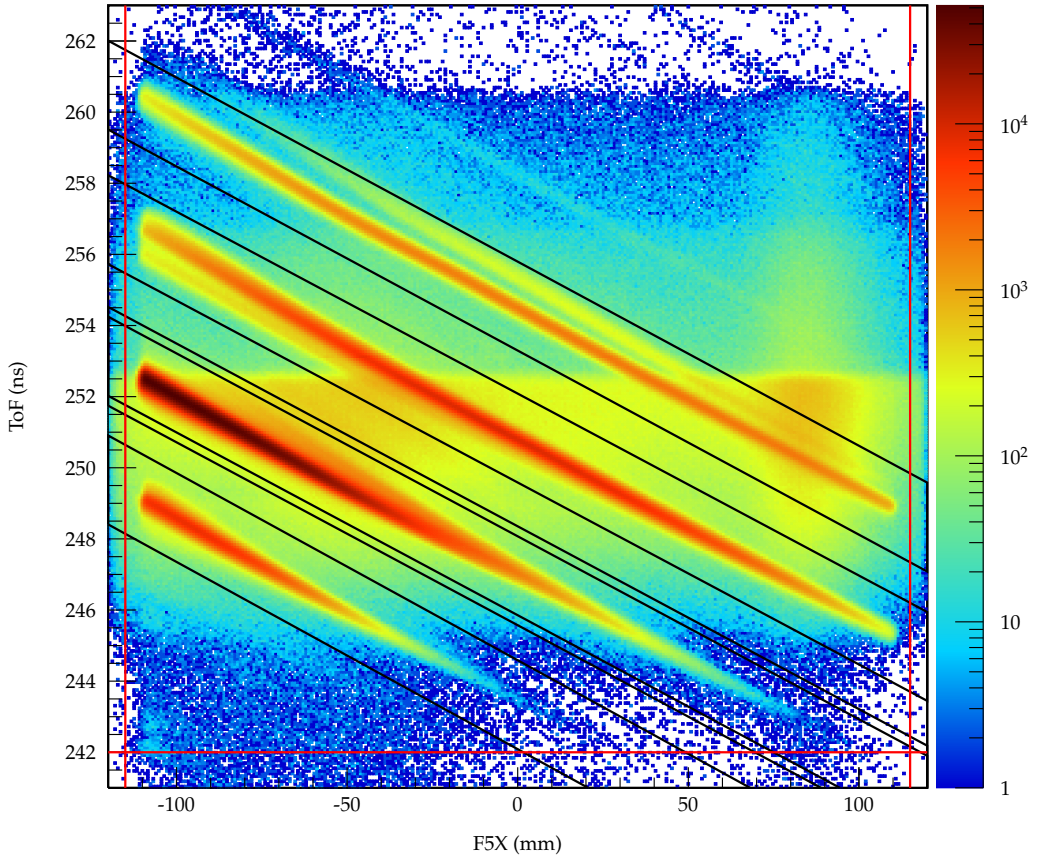

(A) All BR ion beam species cuts.

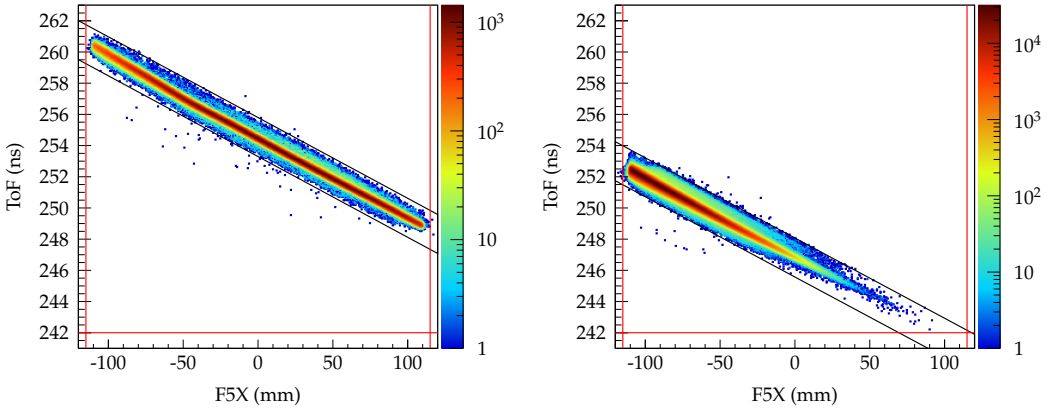

(B) ^{41}Al (C) ^{42}Si

FIGURE 3.12: Illustration of BigRIPS ToF_{F3F7} versus $F5X$ gates for the case of **NP1312-RIBF03**.

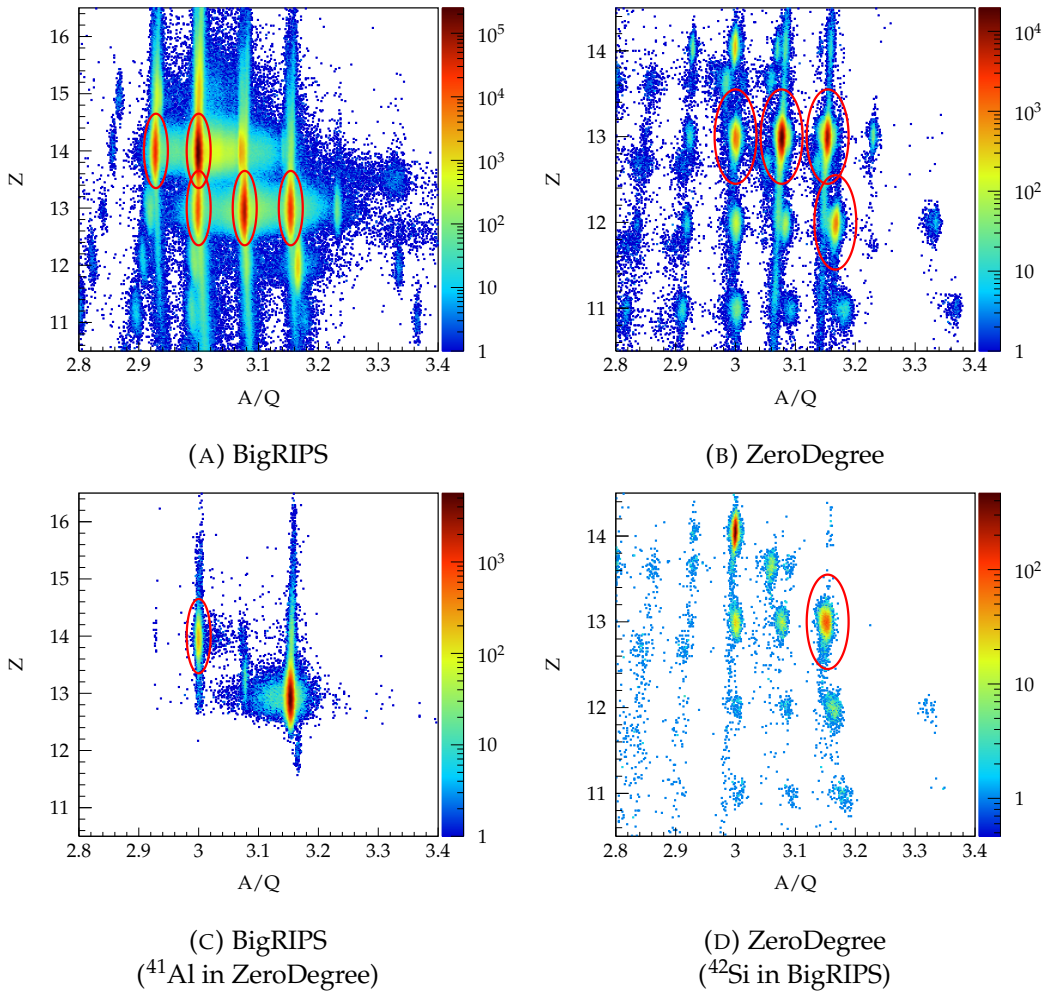

(A) BigRIPS

(B) ZeroDegree

(C) BigRIPS
(^{41}Al in ZeroDegree)

(D) ZeroDegree
(^{42}Si in BigRIPS)

FIGURE 3.13: **NP1312-RIBF03**: PID plots with elliptical gates for species selection.

3.2 Beam velocities for γ-ray reconstruction

The beam velocity, at the moment of de-excitation is a crucial input into the Doppler correction of the reconstructed γ energy (section 1.3.2). This velocity is not directly measured, however, it can be estimated through an extrapolation of velocities measured elsewhere in the separator and spectrometer. By using two experimental velocities, the systematic error and statistical uncertainty can be minimized. The statistical uncertainty can be large for the most exotic reactions.

The reconstructed velocities in BigRIPS separator and ZeroDegree spectrometer roughly correspond to the magnetic dipole regions between focal plane chambers, where the Lorentz force acts on the beam trajectory. Specifically, these areas are between focal plane chambers F5/F7 (D5 and D6) and F9/F11 (D8) (displayed in Fig. 2.3).

The BigRIPS reconstructer velocity is extrapolated to the position of the ZeroDegree recontructed velocity to compare the difference. An observed difference may be the result of choices of BigRIPS and ZeroDegree ToF_{offset}, or the extrapolation itself. Such as the theoretical energy losses in the beamline detectors or secondary target employed for the extrapolation, the energy losses are calculated by theoretical stopping powers for elemental media as function of energy, material composition and

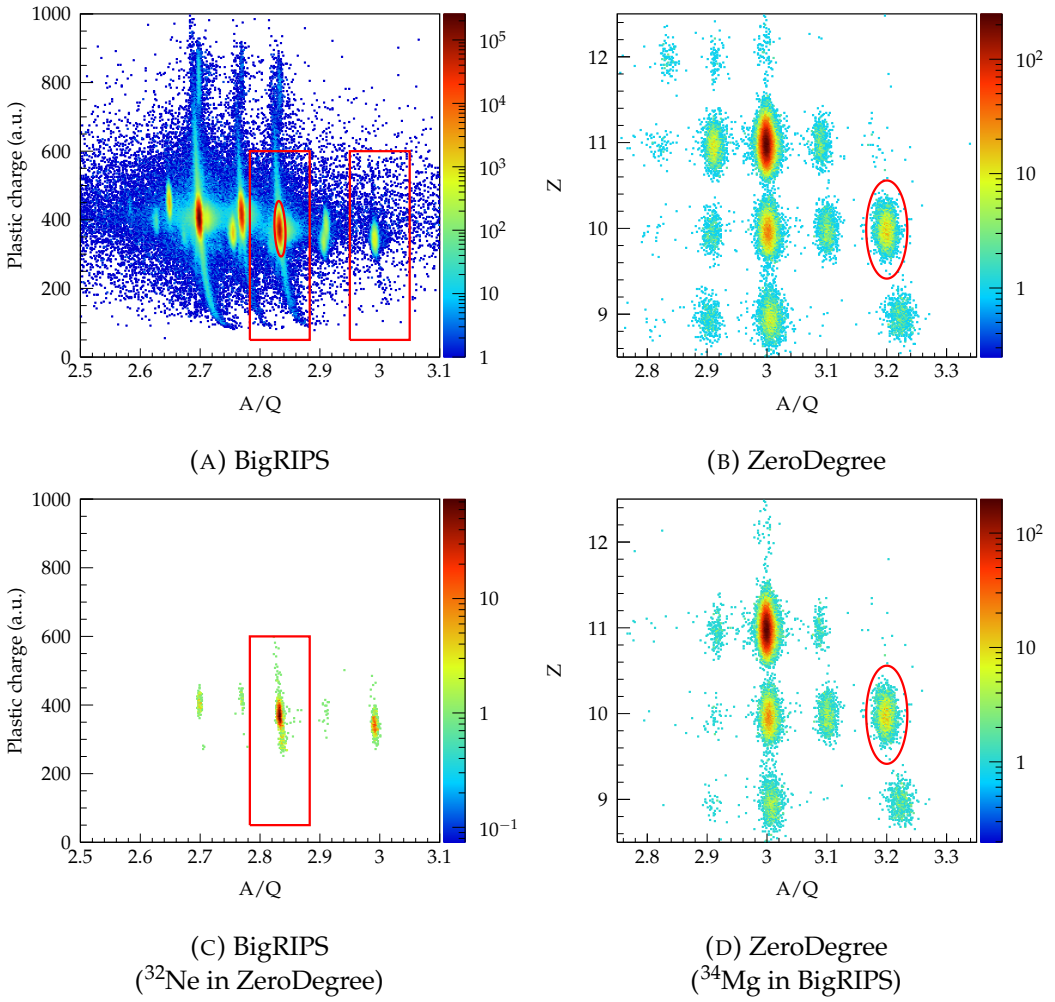

(A) BigRIPS

(B) ZeroDegree

(C) BigRIPS
(^{32}Ne in ZeroDegree)

(D) ZeroDegree
(^{34}Mg in BigRIPS)

FIGURE 3.14: **NP906-RIBF02**: PID plots with square and elliptical gates for species selection.

material density. The ATIMA (version 1.4) code provides the theoretical stopping powers for calculations used in this work. Figure 3.17 illustrates the ATIMA stopping power curve employed for experiment NP1312-RIBF03 and one proton knockout reaction from silicon to aluminum for both targets. Marks are placed the velocity change through the secondary target to show the region of kinetic energies of beam-ions.

As it is not possible to establish the nature of any observed velocity difference between the compared velocities, and the use of theoretical stopping powers is unavoidable when establishing the velocity within the target (such as at mid-point position for Doppler correction)[4], half of an observed velocity difference is added to the calculated velocity in-front of the target. This minimizes systematic uncertainty by equal weighting for BigRIPS and ZeroDegree reconstructed velocities for Doppler correction.

This methodology is depicted schematically in Fig. 3.16. The ion beam is displayed as a red arrow, and the energy losses between the two locations of velocity measurement are shown. The extrapolated velocities are grey and the velocity half difference is dotted. Also, shown in Fig. 3.18a is the experimental reconstructed velocity distributions of BigRIPS and ZeroDegree for the ^{42}Si(C_2H_4,X)^{41}Al reaction.

[4] or after mid-point if state lifetimes are not prompt

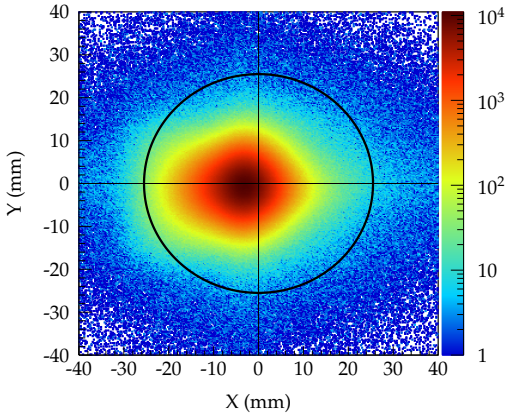

(A) All beam ions.

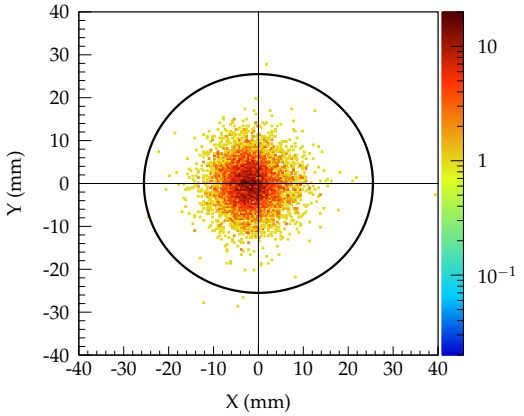

(B) ^{42}Si(C_2H_4/C,X)^{41}Al

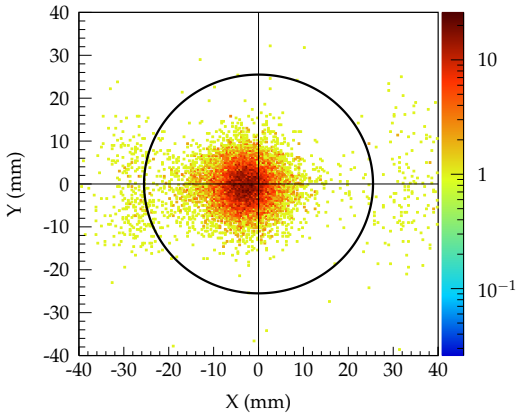

(C) All beam ions to ZeroDegree.

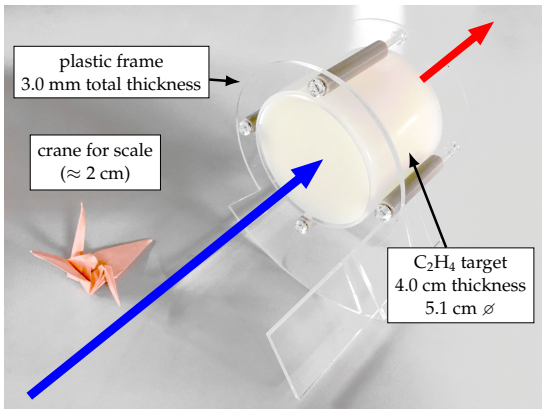

(D) Secondary reaction target

FIGURE 3.15: Projected ion position at the front of the secondary target, for the example of **NP1312-RIBF03**. For highest position accuracy, only events with three or more F8 PPAC signals are shown.

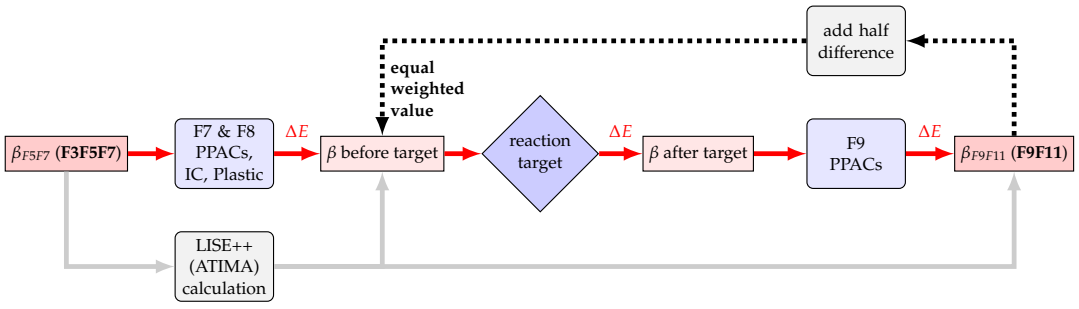

FIGURE 3.16: Illustration of velocity before target determination. The two experimentally measured velocities are β_{F5F7} (**F3F5F7**) and β_{F9F11} (**F9F11**). β_{F5F7} is extrapolated to compare to β_{F9F11}, and the half difference is added to the extrapolated $\beta_{before\ target}$ (extrapolated from β_{F5F7}).

The calculated velocity directly before the target, which is independent of the target material or areal density[5], is used for determining the velocity to any point

[5] of considerable importance in experiments using more than one target

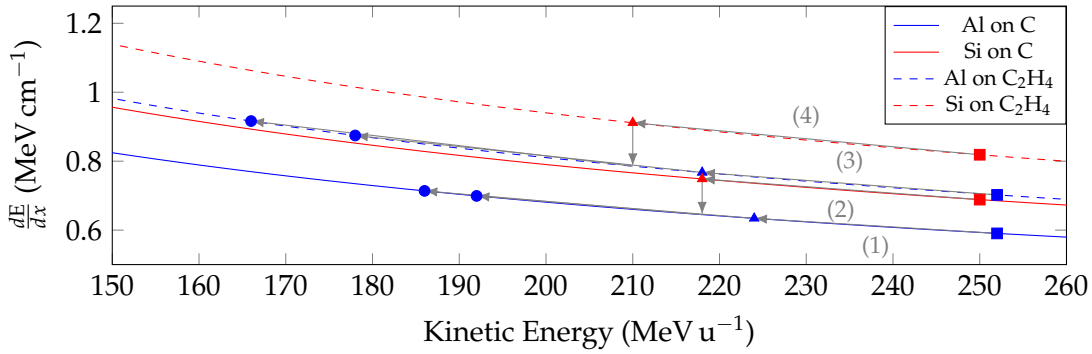

FIGURE 3.17: Fully stripped Si and Al on C (1.82 g cm^{-2}) and C_2H_4 (0.95 g cm^{-2}) stopping power as a function of kinetic energy. Calculated by GSI ATIMA version 1.4. Examples of (1) ^{41}Al(C,X)^{40}Al, (2) ^{42}Si(C,X)^{41}Al, (3) ^{41}Al(C_2H_4,X)^{40}Al, (4) ^{42}Si(C_2H_4/,X)^{41}Al. The kinetic energy directly before the target is marked by a square. The midpoint target position, the average position of reaction, is depicted by a triangle. And the kinetic energy leaving the target is marked as a circle.

within or after the target. A GEANT4 Monte Carlo code simulations the process of γ-ray emission after a reaction within the target volume. The lifetime of the simulated excited state can be included, which shifts the mean position downstream and lowers the mean velocity during γ-ray emission. For optimal Doppler correction, the mean velocity from simulation can be used. For prompt decays after a reaction within the target, the mean velocity occurs at the mid-target position.

In addition, the creation of DALI response functions for fitting employ the same velocity before the target. An example of a simulated velocity distribution is presented in Fig. 3.18b for the ^{42}Si(C_2H_4,X)^{41}Al reaction with the experimental beam velocity and distribution.

A number of assumptions are necessitated in this procedure. It is assumed all beam ions are fully stripped during their transit along the beam line, the velocity distributions can be characterized as normal distributions, and the nuclear reaction position is distributed uniformly within the length of the secondary target[6].

3.2.1 Additional considerations

In the aforementioned Monte Carlo simulation of energy loss within the target, reaction and de-excitation, two additional mechanisms from reaction kinematics are simulated. The semi-empirical Goldhuber approximation (previously introduced in equation: 1.43) and the semi-empirical formula to explain the overall velocity shift taking into account the binding energy for nucleon removal [152]. This can be formulated as,

$$\frac{v_F}{v_P} = \sqrt{1 - \frac{B_n(A_P - A_F)}{A_F E_P}} \tag{3.1}$$

[6]This assumes a constant reaction cross section as a function of energy within the energy range of the beam ions within the target. Such an approximation has a negligible influence on the mean velocity at γ-ray emission, as other uncertainties such as state lifetime have larger influence.

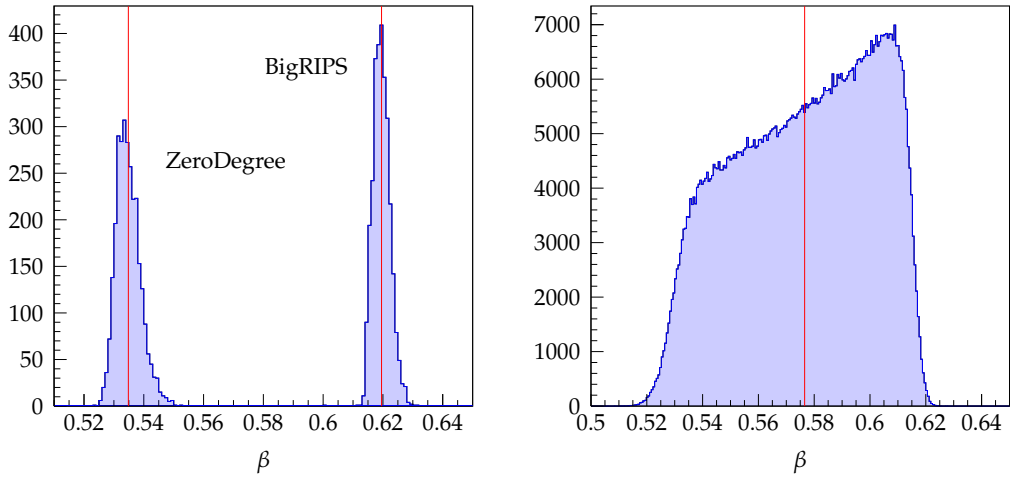

(A) Experimental velocities (B) Simulated at γ emission

FIGURE 3.18: Example of experimental BigRIPS and ZeroDegree and GEANT4 simulated γ-ray emission point velocities for ^{42}Si(C_2H_4,X)^{41}Al. Red lines indicate the position of the mean.

where v_f and v_p are the velocities of the fragment and projectile, respectively. B_n is the binding energy, and E_P is the kinetic energy of the projectile, and A_P and A_F are the mass numbers of the fragment and projectile, respectively.

3.3 Inclusive cross section measurement procedure

The calculation of inclusive cross sections to bound states from direct reactions involves the measurement (or counting) of the number of incoming projectiles and number of nuclear reactions. The latter can be quantified from the number of detected reaction residues.

With the setup of the two experiments of this work, the beam tracking detectors before and after the target permit the counting of the number of beam ions with the aid of the event-by-event data RIBF acquisition system (section 2.4.4). Depending on the trigger condition of the DAQ for a particular experiment, the number of beam-ions may need a correction factor due to the shared system dead-time.

For experiment NP906-RIBF02 (Ne), two trigger conditions of the RIBF DAQ were required. This can be ascribed to the high rate of beam-ions in BigRIPS. A trigger for each projectile ion in event-by-event mode would result in significant loss of efficiency due to the common system dead-time (section 2.4.4). This can be alleviated through triggering for only a fraction of the BigRIPS ions, while triggering on every beam-ion (mostly reaction residues) in ZeroDegree. Due to the different magnetic rigidity of ZeroDegree (set to a specific magnetic rigidity of a reaction residue), the rate of unreacted beam-ions is significantly reduced. Therefore, the efficiency for detecting all reaction residues remains close to unity, while the efficiency for unreacted projectiles is sacrificed. The is accomplished with a *downscaler*, for which the input trigger logic signal rate is dropped by a selectable magnitude. For experiment NP906-RIBF02 the BigRIPS beam trigger ($F3_{plastic\ scintillator} \otimes F7_{plastic\ scintillator}$) was reduced by a factor of 100. The recovery of the total number of projectiles for

calculation of the cross section requires multiplying by the downscale factor. In addition, the common DAQ dead-time for each trigger condition needs to be evaluated and incorporated into the cross section calculation.

In experiment NP1312-RIBF03 (Al), the trigger condition was solely the *F7* plastic beamline scintillator and the trigger rate did not appreciably reduce the live-time. No downscaler utilized and furthermore by utilizing one trigger condition, a correction for DAQ dead-time is not required for cross section calculation.

The inclusive cross section is formulated as,

$$\sigma_{incl} = \frac{N_{residues}}{N_{projectiles}} \frac{M}{d_T N_A} \frac{100\%}{T_{efficiency}(\%)} \frac{R_T}{R_T + R_{BT}} \tag{3.2}$$

where $N_{residues}$ and $N_{projectiles}$ are the numbers of ions in BigRIPS and ZeroDegree PID, M is molar mass of the target, N_A Avogadro's constant, d_T is target areal density, $T_{efficiency}$ is transmission efficiency (PID reconstruction and species selection). R_{BT} and R_T is the fractional cross section for reactions before target and in reaction target, respectively. It is not possible to discern the location of a nuclear knockout reaction between the F7 and F9 focal plane detectors as the method for particle identification applies only between F3 to F7 and F9 to F11 focal planes. Therefore, knockout reactions induced by the secondary reaction target or by beam-line detectors in this region cannot be distinguished. The largest reaction cross section of detectors in this region is the F7 plastic scintillator. For thick and high density reaction targets, the correction is minimal.

For experiment NP1312-RIBF03, $R_T = 25.8\%$ and $R_{BT} = 1.2\%$ as calculated with LISE++. An additional five percent relative uncertainty is added to these theoretical values. A 5% uncertainty is added to the target areal density.

3.3.1 Correction for momentum acceptances

In the calculation of inclusive cross section, it is necessary to correct for the limited momentum acceptance of the ZeroDegree spectrometer (section 2.3). Close to, or beyond a $\pm 3\%$ relative momentum difference from the central value results in incomplete beam-ion trajectories to the end of the spectrometer. Apertures, beam tubes and detectors block the beam-ions.

The exact transmittance spanning the phase space and momentum of the ZeroDegree is difficult to simulate or quantify accurately. Real non-Gaussian ion-beams, misaligned and off-axis elements [153] and other phenomena make a calculation or simulation difficult, especially for ion species significantly departing from the central trajectory.

Alternatively, the acceptance of ZeroDegree reaction residues can be evaluated with experimental data. It is reasonable to assume the central beam trajectories of ions within the ZeroDegree spectrometer (as measured at focal planes F9 and F11) are fully accepted. Therefore, ions at the periphery or edges of these focal planes can be removed for the purpose of inclusive cross section determination. The exact limits can be determined through observation of the ratio of projectiles over residues as a function of reconstructed positions and angles in BigRIPS. As the separator and spectrometer are dispersive in x, the $F5X$ position and $F5A$ angle are employed for this purpose.

The example of the ^{42}Si(C_2H_4,X)^{41}Al reaction is shown in Fig. 3.19, where the projectiles and reaction residues are not centred for experimental runs. The distribution in phase space at the dispersive focal plane 5 is shown in Fig. 3.19a and 3.19b, for all ^{42}Si projectiles and ^{42}Si projectiles resulting in ^{41}Al in ZeroDegree, respectively.

The ratio[7] of these two plots is presented in Fig. 3.19c. This ratio reduces towards -100 mm in F5X. The reason for a decrease is the loss of events in ZeroDegrees, with these ions at the edge of F9X, as shown in the right Fig. 3.19d. The projection of 3.19d across F5X is displayed in Fig. 3.19e which displays the characteristic fall off of a drop in efficiency. By selecting a portion of events through a selection between F5X and F5A, illustrated by the red cuts, only the phase space with full transmission is considered (Fig. 3.19f).

3.3.2 Correction for inefficiencies

An additional correction is necessary to take into consideration the efficiency of ion A/Q and Z reconstruction. Loss of reconstruction efficiency can be attributed to both beam tracking (PPACs), (ion chamber or plastic scintillator) energy loss measurement and ToF (velocity) measurement inefficiencies. The latter two are small contributors.

The efficiency is rigorously quantified through the operation of the separator and spectrometer without a reaction target, and treatment of unreacted ions as reaction residues. The difference in the number of integrated ions in the PID plots of BigRIPS and ZeroDegree is evaluated for the central beam species.

This also captures the efficiency of the applied gates and selection shape of the of the projectiles and residues in the PID diagram with predetermined ellipse or rectangular integration areas (Fig. 3.14 and 3.13).

For the experiment NP1312-RIBF03, the efficiency was determined for central ^{41}Al and near-central ^{42}Si as 95.3% and 94.8%, respectively. The statistical uncertainties are negligible. A portion of the ions near the edges of $F5X$ are discarded to avoid losses from the limited ZeroDegree momentum acceptance. Furthermore, a correction for reactions in the 1 mm F7 plastic scintillator is included. An average efficiency of 95% is used for all silicon and aluminum isotopes in the experimental NP1312-RIBF03 inclusive cross sections, with an additional 5% uncertainty. This efficiency determination is similar to the approximation of Fig. 3.4 (section 3.1.1).

Experiment NP906-RIBF02 did not have an experimental run without a reaction target, and the aforementioned procedure cannot be applied. Instead the efficiency is estimated by the same method of Fig. 3.4 (section 3.1.1). This assumes the inefficiency for energy loss determination and ToF is small relative to the inefficiency for beam tracking with PPACs. The estimated efficiency is calculated to be $98\% \pm 5\%$ for magnesium, sodium and neon.

3.3.3 Exclusive cross section measurement procedure

Exclusive cross sections to bound states is quantified through the use of DALI γ-ray sensitive spectrometer. By the buildup of a nuclear level scheme from the observables of γ-rays and their coincidences, the direct population to each excited state (and the ground state) is determined. Multiplying each of these fractional populations by the inclusive cross section provides the exclusive cross section to each bound excited state.

For incomplete nuclear level schemes with unplaced or unbalanced transitions, it is not possible to determine exclusive cross sections. For NP906-RIBF02, with only two observed transitions and a simple experimental level scheme, exclusive cross sections are calculated. Conversely, for experiment NP1312-RIBF03 the determination of exclusive cross sections is not possible.

[7] scaled by 1000

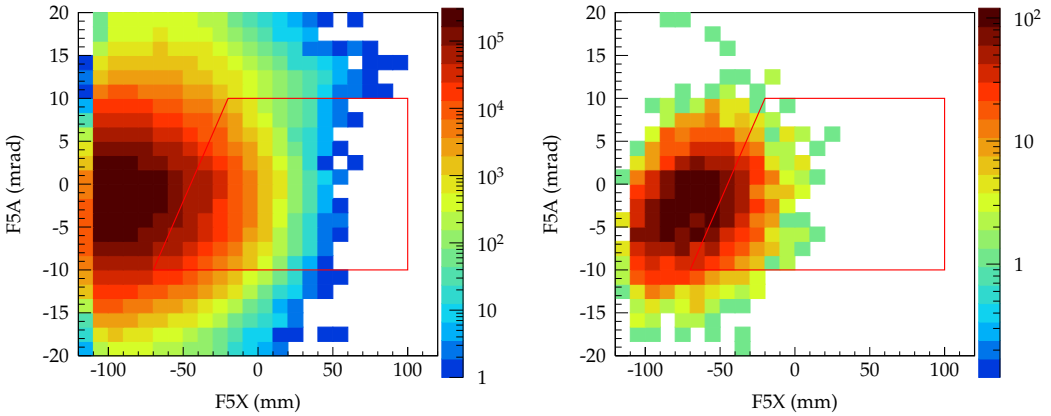

(A) ^{42}Si projectiles

(B) (A) with ^{41}Al residues in ZeroDegree

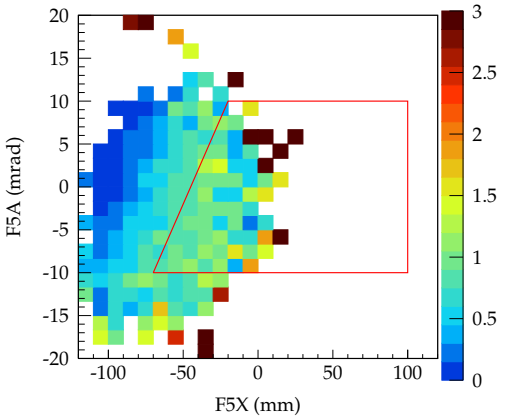

(C) Ratio of (A) over (B) $\times$1000

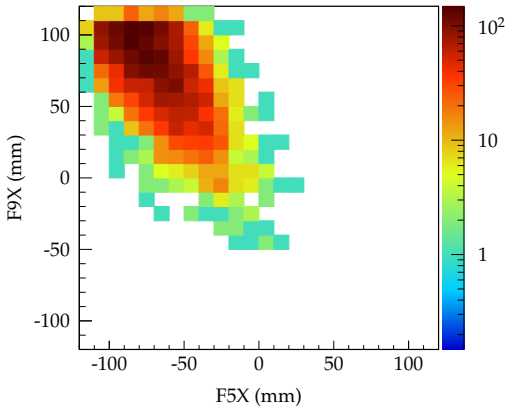

(D) Relation between F5X and F9X

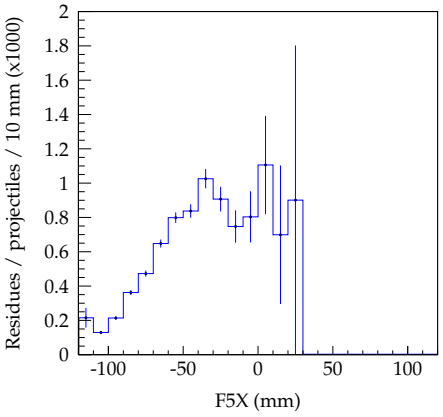

(E) Projection of (C)

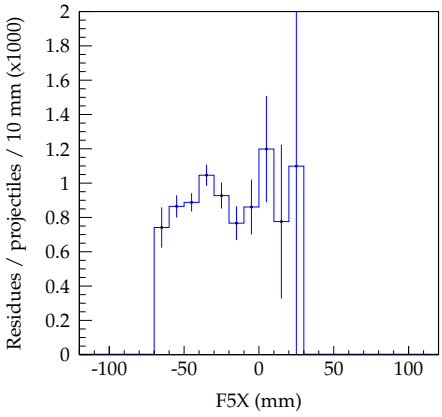

(F) Projection of (D)

FIGURE 3.19: Example of the selection of trajectories within full separator and spectrometer acceptance.

3.4 DALI2

3.4.1 Energy calibration

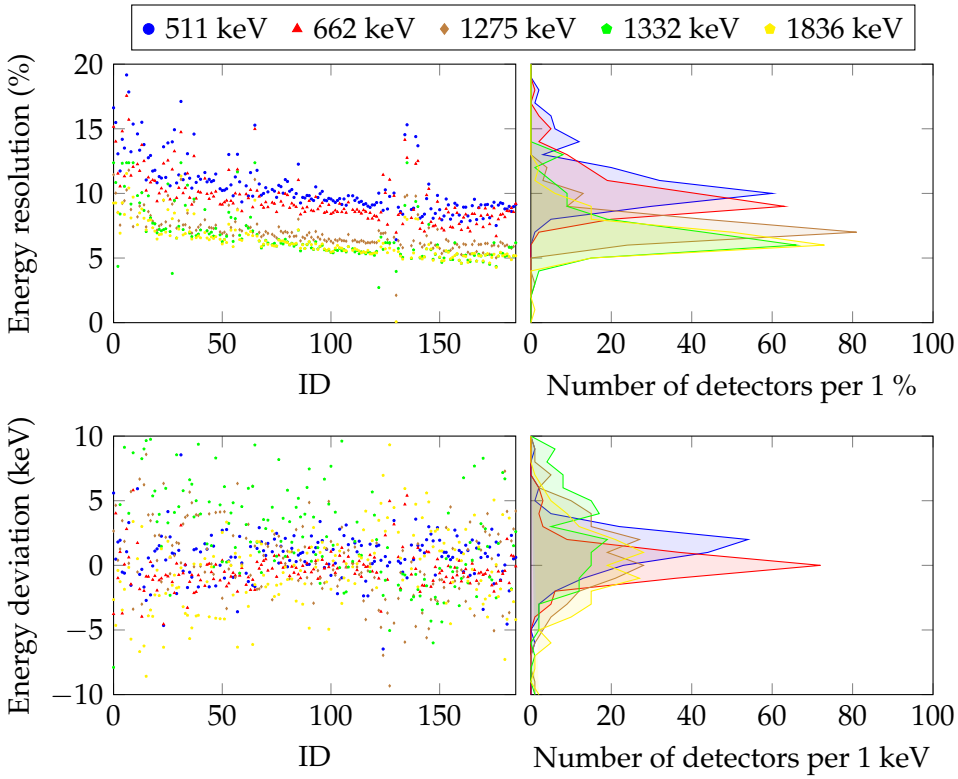

FIGURE 3.20: Energy resolution and fit energy deviation for all DALI detectors of NP1312-RIBF03.

A calibration of the DALI ADC channels for the energy dependent response of the DALI NaI scintillators to γ-rays is accomplished before and after the experiments. In the case of experiments over several days, short unplanned shutdowns permit energy calibrations between experiment runs. This allows for measurement of drifts in detector gains. The gain of a photomultiplier tube is sensitive to the magnetic field background and ambient temperature.

For calibration, γ-ray sources with sufficient intensity with only a few strong emission lines are employed. Sources are selected to cover a wide energy range. In both experiments, the radioisotopes ^{88}Y, ^{60}Co, and ^{137}Cs were utilized. Additional sources of ^{133}Ba and ^{22}Na are included in the calibration for the NP1312-RIBF03 experiment for reliable calibration at lower energy. The sources are placed at the reaction target position within the Al beampipe and Pb shield and attached to the target holder frame. In this way, the energy calibration also permits a determination of absolute detection efficiency.

For the NP0906-RIBF02 experiment, the DALI energy calibration occurred 10 hours before the first run. The photopeaks from the energy spectrum for individual detectors are fit with a Gaussian function convoluted with a background of a first order polynomial function. If during this fitting procedure, a detector's photopeak is observed to have an abnormal shape or additional features, the detector is removed in the analysis. In both experiments, several detector detectors were removed during this process. A priority is placed on the quality of the resulting DALI detector array performance over a choice of utilizing a maximum number of

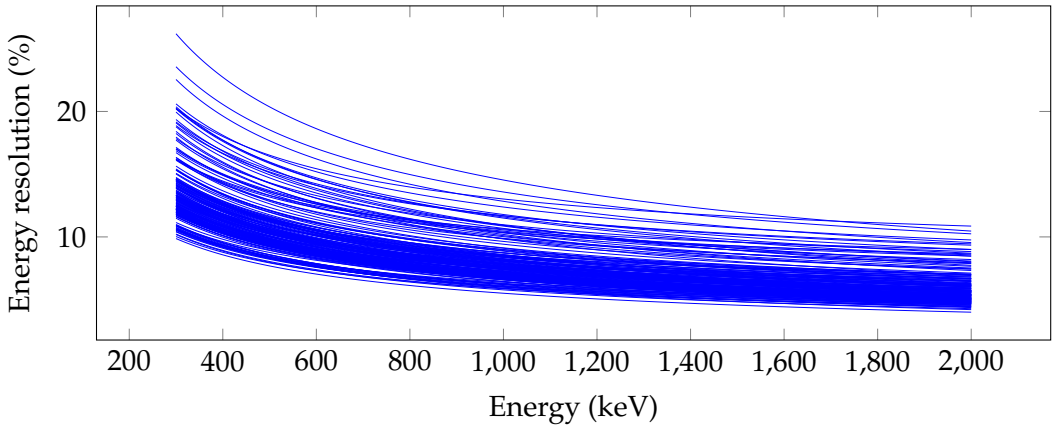

FIGURE 3.21: Fitted energy resolution functions for DALI detectors.

detectors in the analysis. Abnormal detector responses are not incorporated into the production of the DALI detector array response functions, as such, they may influence the fit of the experimental energy spectrum. 14 detectors are removed in the analysis of NP0906-RIBF02 and 9 detectors are removed from NP1312-RIBF03.

The photopeak positions as a function of ADC channel are used to linearly fit the individual PMT gains. Furthermore, the Gaussian peak widths are additionally extracted and individually fit. For the NP0906-RIBF02 experiment, the one parameter function $\sigma = a + \sqrt{\text{energy}}$ was found to best fit the data. In the NP1312-RIBF03 experiment a different two parameter function, $\text{FWHM}/\text{energy} = a/\sqrt{\text{energy}} \oplus b$, where the $\oplus$ symbol represents the quadratic sum, was utilized to fit the larger energy range of the calibration sources. The energy resolutions as a function of energy and calibration points are displayed in Fig. 3.20. And the fitted energy resolution function for all detectors is displayed in Fig. 3.21.

3.4.1.1 Calibration uncertainty

A refitting of the calibrated energy spectrum across all detectors provides a means to test the calibration. The deviation between the expected photopeak position and calibrated energy photopeaks, fit with a Gaussian function and third order polynomial, for NP0906-RIBF02 deviated between $-1.62(9)$ keV to $2.80(5)$ keV[8] for ^{88}Y, ^{60}Co, and ^{137}Cs sources, presented in table 3.4. For experiment NP1312-RIBF03, the calibrated energy photopeaks were additionally fit with DALI response functions (see section 3.4.4), in this way the Compton edge is incorporated into the fit and closely spaced photopeaks, such as with ^{60}Co are more faithfully reproduced. The resulting deviations are presented in table 3.3 and indicate a possible small shift from immediately before the start of the experiment to the first two days. A changing background magnetic field, such a slowly decay, from a change in ZeroDegree magnetic rigidity could potentially produce the observed shift. Other factors such as a change in temperature cannot be excluded. Across all spectra, the response function fits had lower deviations.

The systematic uncertainty due to the energy calibrations is 3 keV for NP0906-RIBF02 and 4 keV for NP1312-RIBF03 experiments.

[8] The $2.80(5)$ keV deviation was found for the ^{88}Y 898 keV line, which residuals over the compton continuum of the higher 1836 keV line. Poor shape of the underlying background likely contributed to the deviation.

		γ source energies and deviation (keV)							
Date	Type of fit	302.85	356.01	511	661.66	1173.23	1274.54	1332.50	1836.06
+ 6 days	gaus+pol3	2.84(1)	4.34(3)	0.75(2)	0.15(4)	2.58(4)	-0.92(4)	3.44(4)	-1.11(5)
(end)	DALI response func.	4.56(8)	3.18(2)	-0.35(1)	-0.94(4)	-0.13(4)	-0.87(4)	2.02(4)	-2.08(5)
+ 4 days	gaus+pol3			1.13(2)			1.23(5)		-1.49(6)
	DALI response func.			0.027(2)			-0.60(5)		-2.40(5)
+ 3 days	gaus+pol3			1.62(2)			2.48(7)		-3.84(7)
	DALI response func.			0.46(2)			1.60(6)		-3.72(5)
+ 2 days	gaus+pol3			1.13(2)			0.96(7)		-6.00(7)
	DALI response func.			-0.11(2)			-0.048(6)		-4.07(5)
exp.	gaus+pol3				1.66(5)	5.32(4)		6.88(5)	
start	DALI response func.				1.33(5)	2.59(4)		5.49(4)	

TABLE 3.3: Fit deviation before/during/after NP1312-RIBF03 with γ-ray calibration sources.

		γ source energies and deviation (keV)				
Date	Type of fit	661.66	898.04	1173.23	1332.50	1836.06
- 10 hours before exp.	gaus+pol1	0.41(4)	2.80(5)	-1.12(8)	-1.62(9)	-0.8(1)

TABLE 3.4: Fit deviation before NP906-RIBF02 with γ-ray calibration sources.

3.4.2 CFD thresholds

The DALI DAQ contains constant fraction discriminators (CFD) for individual detector trigger levels (section 2.5.2). Pulses from the photomultipliers at a level under the set thresholds are not processed and do not become part of the experimental data. The purpose of the individual thresholds is to balance the trigger rate of the DALI DAQ to efficiently detect the in-flight γ-rays without over sensitivity to the atomic background and to reduce the trigger rate from dark counts for individual detectors. However, this results in thresholds varying between DALI detectors.

For low energy transitions, such as in ^{40}Al, an accurate determination of the individual thresholds is necessary to faithfully reproduce the correct intensity when fitting with the generated response functions. The individual thresholds are required to be incorporated into the DALI response functions. They are individually deduced from calibration spectra before and after the experiment as well as from experimental run data, by fitting with an edge sensitive function. The thresholds additionally show no change over the course of the NP1312-RIBF03 experiment, beyond a fitting error of 1 keV. The experimental CFD thresholds and reconstructed CFD thresholds in GEANT4 simulation are compared in Fig. 3.22c and 3.22d.

In the reconstructed experimental spectrum of ^{32}Ne, the approximation of the individual thresholds as a constant is made due to the lack of low energy transitions. A threshold of 200 keV is chosen for the DALI response functions and the Doppler reconstruction of the experimental data.

3.4.3 Time alignment

The timing of DALI detector signals is measured by time-to-digital converters (TDC, section 2.5.2) relative to the trigger of the RIBF DAQ. To reduce background spurious γ-rays, which may correspond to natural background radiation or beam induced processes such as decaying short lived isomers, a time window is set for DALI detectors. This gate roughly corresponds the moment of projectile ion in the beam

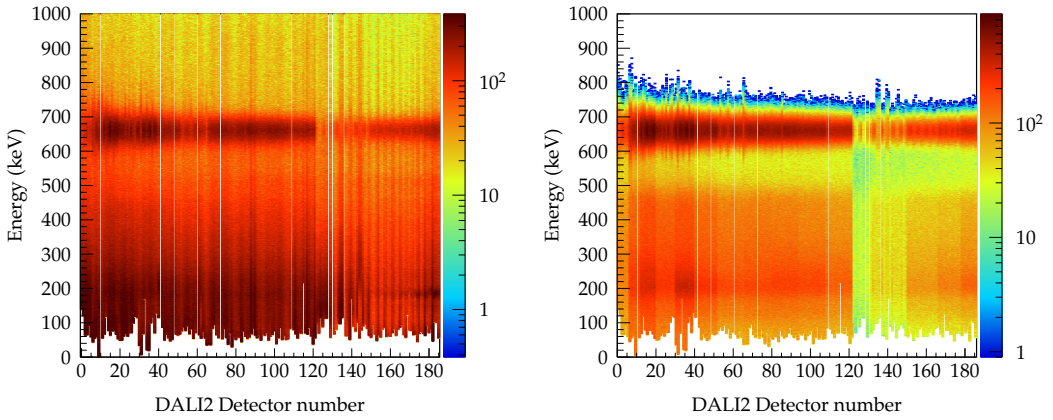

(A) Experimental ^{137}Cs source

(B) Simulated ^{137}Cs source

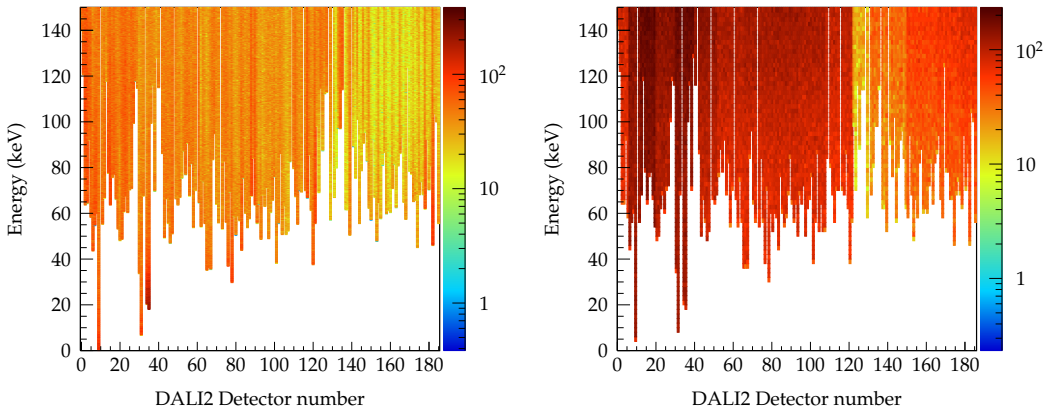

(C) Experimental CFD thresholds

(D) Simulated CFD thresholds

FIGURE 3.22: Experimental and GEANT4 simulated ^{137}Cs γ source with DALI2, with individual detector resolution and channel thresholds applied

reacting with the secondary target to capture prompt de-excitation. This requires alignment of the DALI detectors times. An offset is calculated for each detector such that the relative time difference between DALI detectors is zero. Differences in cable lengths from the PMTs to the DAQ and internal TDC offsets produce a misalignment of the individual detector timing.

The individual DALI detector offsets are determined with experimental run data. A intense reaction channel is isolated and prompt γ-rays from nuclear de-excitations and or atomic processes from the reaction target are used for time alignment. The result of a timing calibration is illustrated in Fig. 3.23. For experiment NP1312-RIBF03, beam velocity differences are additionally corrected. This manifests as the distance between DALI and the triggering F7 plastic scintillator is fixed, resulting in varying transit time to the target as a function of velocity. For the example of the ^{41}Al(C_2H_4,X)^{41}Al reaction, the timing resolution was improved from 6.9 ns to 6.6 ns with a linear correction of the DALI time as function of ToF_{F3F7}. This is shown in Fig. 3.23c and 3.23d.

The size of the DALI time window to select γ-rays for reconstruction must encompass all possible nuclear de-excitations. A limit the order of $\pm$7 ns from the peak of a fit asymmetrical Gaussian and exponential is used for the various reactions of the two experiments. An example is presented in Fig. 3.24a and 3.24b for

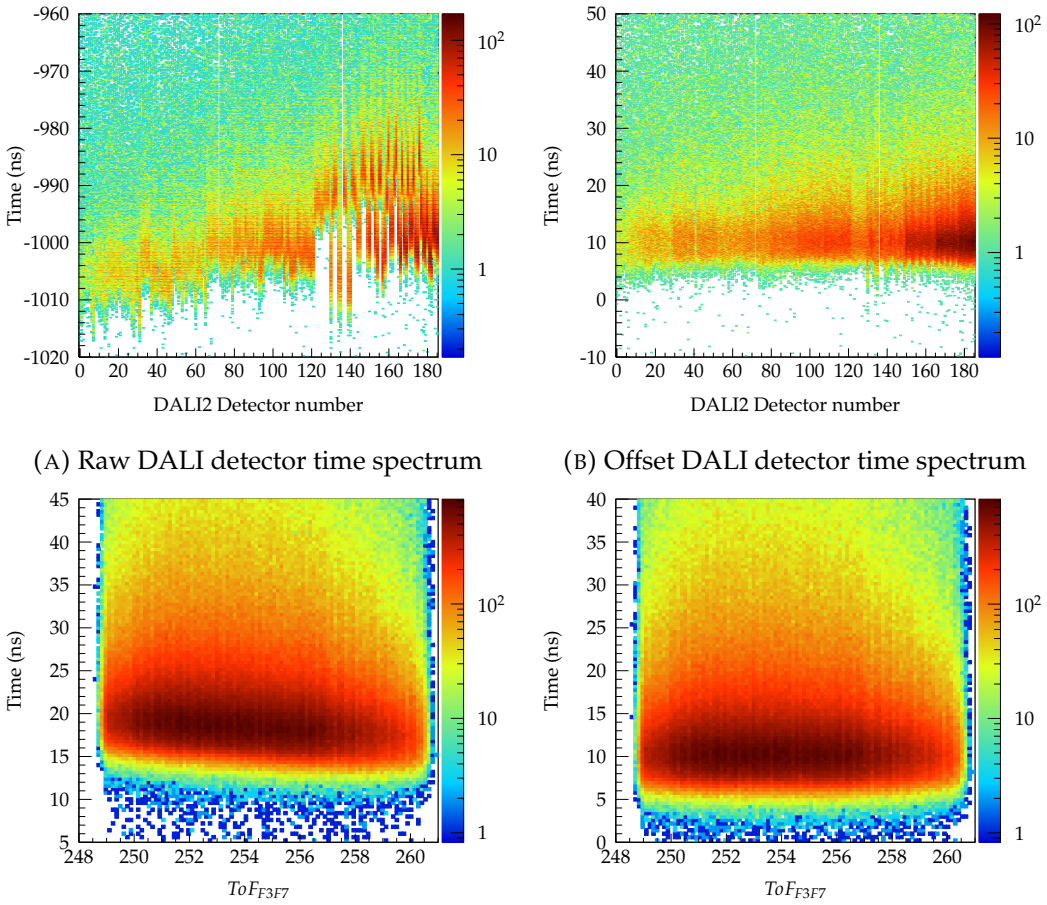

(A) Raw DALI detector time spectrum

(B) Offset DALI detector time spectrum

(C) DALI time vs. ToF_{F3F7}

(D) Corrected DALI time vs. ToF_{F3F7}

FIGURE 3.23: DALI time offset corrected for beam-ion ToF (F3F7)

the ^{42}Si(C_2H_4/C,X)^{41}Al reaction of the NP1312-RIBF03 experiment.

3.4.4 DALI GEANT4 simulations

As described previously, GEANT4 simulations of the DALI detector array response to γ-rays are used to build *response functions*. In the previous figure of 3.22, a comparison with ^{137}Cs is shown for the energy response across all 186 DALI detectors. The response functions employed in the fitting of the reconstructed experimental γ-ray energy spectra, is made by a projection across all detectors. The simulated individual detector energy response is shown in Fig. 3.22b and reproduces experimental data (Fig. 3.22a).

The simulation of in-flight emission of γ-rays with a determined velocity distribution (section 3.2) and beam position distribution allows for realistic generation of response functions for fitting experimental reconstructed DALI γ-ray energy spectra.

An example of a simulated Doppler corrected response is presented in Fig. 3.25a for 1000 keV γ-ray emissions within a C target of dimensions used in the NP1312-RIBF03 experiment . The kinematics of the knockout reaction ^{42}Si(C,X)^{41}Al, including a realistic ion beam velocity and position distribution is used. The blue curve additionally includes an add-back procedure to improve the photopeak efficiency.

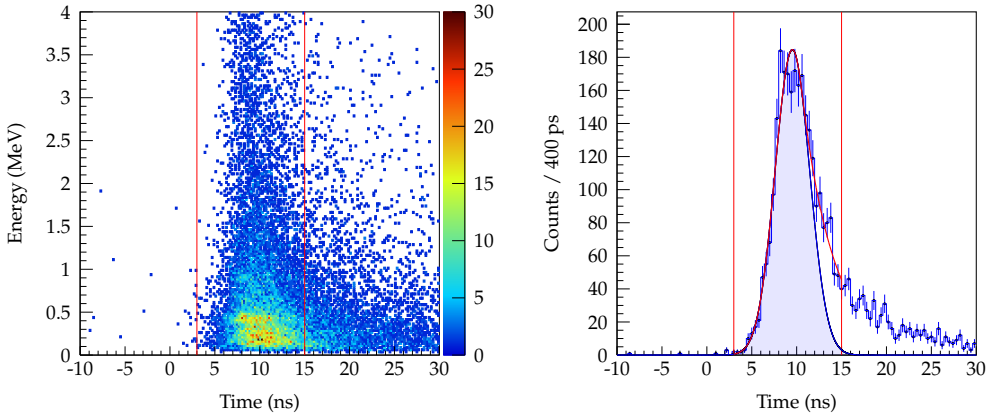

(A) DALI time vs. Energy (B) Timing of strong photopeak

FIGURE 3.24: Example of selecting γ-rays in a time window relative to the the RIBF trigger for ^{42}Si(C,X)^{41}Al reaction of NP1312-RIBF03.

The large cross section for Compton scattering (section 1.3.1) of high energy γ-rays can result in the distribution of energy across more than one detector from a single γ-ray emitted in-flight. The add-back procedure applied in the simulated and experimental reconstruction procedure, adds back the energy of detectors within a given radius. The definition of both the central position for determining the radius and Doppler correction angle for these events is the DALI detector with the largest energy detected. The balance between increasing add-back efficiency and maintaining energy resolution has resulted in a standard distance of 15 cm for add-back radius. This is equivalent to approximately one surrounding detector.

For the production of DALI response functions by GEANT4 monte carlo simulation, 10^{5-6} in-flight emissions are simulated to achieve negligible uncertainty in the overall shape.

The full energy photopeak (FEP) efficiency for realistic in-beam γ-ray emission from a knockout reaction with the DALI spectrometer is presented in 3.25b from GEANT4 simulation. The example reaction is ^{42}Si(C_2H_4,X)^{41}Al with 4 cm thick C_2H_4 at $\beta = 0.6157$ and with the standard beampipe (Al) and Pb shield of 1 mm thickness. The Pb shield contributes strongly to the reduction in FEP efficiency at low energy.

Comparison between experimental and simulated DALI efficiency For accurately determining total number of emitted γ-rays emitted in flight, the simulated DALI response functions and experimental DALI response must possess the same FEP efficiency. This is verified by comparing of experimental and simulated response to standard calibration sources previously employed for energy calibration.

The area within two standard deviations of the photopeak is integrated in the experimental energy spectrum to determine the full energy photopeak fraction. The experimental spectrum is then fit with the GEANT4 response function convoluted with the experimental background spectrum. The scaling factor of simulated response function in the fit provides the number of simulated emitted γ-rays. By taking into account the activity of the γ source at time of measurement and DAQ live-time, the relative difference can be determined. This can then be multiplied by the experimental FEP efficiency to calculate the GEANT4 simulated FEP efficiency.

The results are tabulated in 3.5. The source of deviations is not identified, but could be a consequence of a small difference in experimental and simulated detector

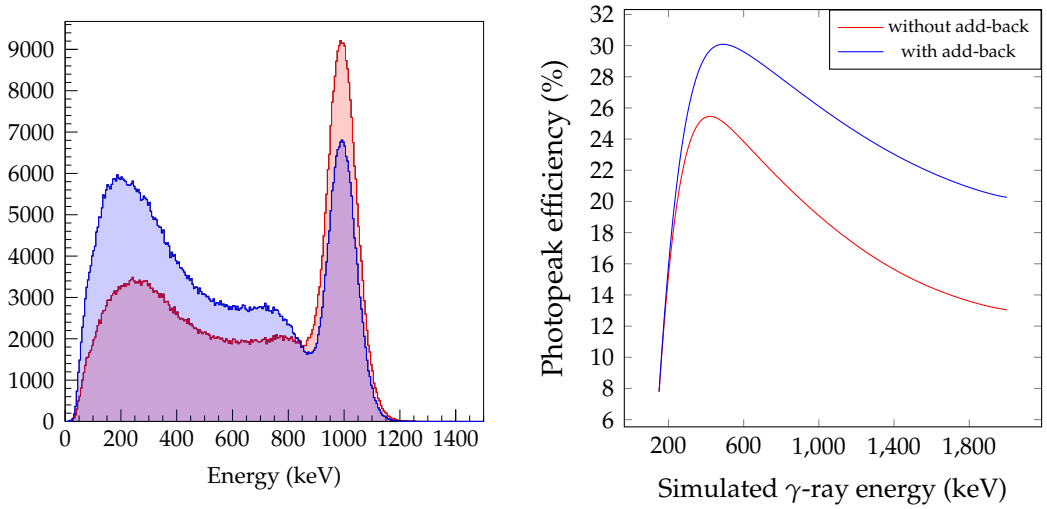

(A) Typical reconstructed DALI response functions

(B) Typical DALI photopeak efficiency

FIGURE 3.25: Examples of GEANT4 generated DALI response functions with and without add-back procedure and photopeak efficiency with the velocity distribution of the ^{42}Si(C,X)^{41}Al reaction of NP1312-RIBF03

	Energy (keV)	Exp. FEP eff. (%)	GEANT4 FEP eff. (%)	Relative diff. (%)
$^{137}_{55}$Cs	661.66	25.3 (7)	24.0 (7)	5.6 (1.0)
$^{88}_{39}$Y	1836.06	13.9 (3)	13.1 (3)	6.1 (4)
$^{60}_{27}$Co	1332.50	15.0 (5)	15.0 (4)	0.2 (6)

TABLE 3.5: Summary of full energy peak efficiency with γ sources and GEANT4 simulation

resolutions. Other sources may include deviation in the thickness or attenuation of the beampipe or shield, individual detector shielding, or γ source position. An uncertainty of 6% efficiency is added as a systematic uncertainty for exclusive cross sections.

Beam velocity uncertainty In addition, the uncertainty in ion beam velocity influences the fitting of the experimental γ-ray energy spectrum. The variation in beam velocity on the Doppler reconstruction (section 3.2) is simulated in GEANT4. A simulation is completed for representative experimental conditions, such as ^{42}Si(C_2H_4,X)^{41}Al with 4 cm thick C_2H_4 at 250 MeV u^{-1}. The photopeaks are assumed to be perturbed as an energy shift for small deviations in beam velocity[9]. The reconstruction of the γ-ray energy spectrum is completed with Doppler correction at velocities with deviations of $-4\%, -2\%, 0\%, 2\%, 4\%$ from the mid-point target energy.

The photopeaks are fit with a simple Gaussian function to extract the centroid position. The absolute difference between the Gaussian centroids are plotted in Fig. 3.26. The deviation is minimal near 600 keV, which is the consequence of the balance between the forward and background angle responses.

[9]For large deviation in beam velocity, the change in peak shape is not negligible

The difference between the velocity determination with BigRIPS and ZeroDegree, as explained in section 3.2, is on the order of 5 MeV u^{-1} for the reactions of the two experiments which corresponds to approximately a 2% difference in Fig. 3.26.

For both experiments, a constant uncertainty of 2 keV is added as a systematic uncertainty due to the reconstructed beam velocity uncertainty.

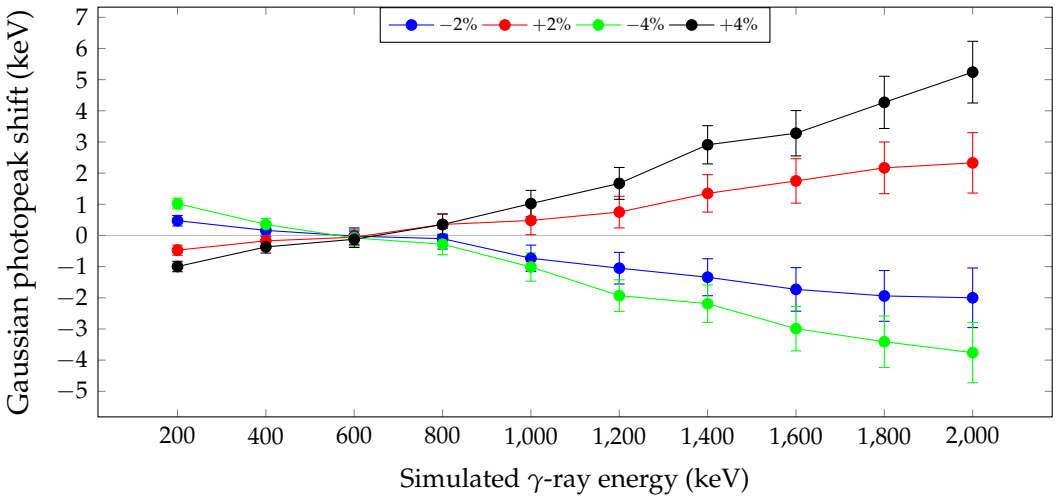

FIGURE 3.26: Simulated influence of beam energy deviation on DALI γ-ray Doppler reconstruction for realistic experimental conditions

Chapter 4

Results

This chapter details the results of this γ-ray analysis. From the parameters used in Doppler reconstruction, building histograms, and procedures and results of fitting to extract γ-ray energies and intensities, and the determination of γ-ray coincidences.

The two experiments, NP906-RIBF03 and NP1312-RIBF04 are described separately, and the individual reaction channels are treated individually. The inclusive cross sections are listed for each reaction.

4.1 ^{32}Ne

4.1.1 ^{34}Mg(^{9}Be,X)^{32}Ne

4.1.1.1 Reaction summary and inclusive cross section

TABLE 4.1: Summary of ^{34}Mg(^{9}Be,X)^{32}Ne and inclusive cross section. Livetime and downscaler corrections applied.

	within ZeroDegree full momentum acceptance		
Total reactions	Reactions	Projectiles	Inclusive cross section (mb)
2823	2823	245159399	0.144(15)

The inclusive cross section of the two-proton knockout reaction ^{34}Mg(^{9}Be,X)^{32}Ne is presented in the table above (4.1). No removal of events outside of complete ZeroDegree spectrometer momentum acceptance is necessary for this calculation, and is the only reaction analyzed with the reaction projectile and residue centred (by magnetic rigidity) in the BigRIPS separator and ZeroDegree spectrometer, respectively.

4.1.1.2 γ-ray analysis

TABLE 4.2: ^{34}Mg(^{9}Be,X)^{32}Ne γ-ray reconstruction settings

Velocity (MeV u^{-1} / β)			Beam at target (cm)			
mid-point target	before target	σ	X	fwmh	Y	fwhm
235.8 / 0.6026	242.9 / 0.6090	13	0.0	1.0	0.0	1.0

Average interaction points calculated from GEANT4 simulation of 1400 keV γ-rays.

The Doppler reconstruction of the DALI γ-ray spectra for the two-proton knockout from ^{34}Mg to ^{32}Ne was accomplished with the velocities and beam properties

presented in table 4.2. The reconstruction from mid-target position, with mid-target velocity and DALI detector angles from this position, is appropriate for prompt decays. The generation of the DALI detector positions was accomplished through the calculation of the average interaction point releasing the full energy of monochromatic 1400 keV γ-rays in-flight at the experimental velocities. This provides the optimal reconstruction of the experimental data at a peak around 1400 keV.

The event-by-event characteristic of the DALI and RIBF DAQ system permits additional classification of each event. It is profitable to classify each event by the γ-ray multiplicity (m_γ), the number of detected γ-rays by the DALI array. This is defined in two ways. The number of fired DALI detectors, those with PMT signals crossing the CFD threshold (section 2.5.2), within the specified time window for reconstruction (section 3.4.3). Or with the application of an add-back procedure (section 3.4.4), the number of Doppler corrected γ-rays. The latter will be always be less than the former in the case of more than one fired detector within a given radius (chosen as 15 cm, section 3.4.4).

The reconstructed γ-ray spectra is presented in Fig. 4.1b for all events with $m_\gamma \leq 3$ and Fig. 4.1a for events with $m_\gamma = 1$. The latter represents a smaller fraction of all events of this specific reaction channel. The generation and fitting of spectra with different maximum γ-ray multiplicities presents an additional layer of information. For example, excited states directly populated in a reaction which transition with one γ-ray to the nuclear ground state are favoured in events with lower maximum multiplicity. Furthermore, the effective peak to background in the reconstructed spectra can be optimized for fitting, with the appropriate choice in maximum multiplicity.

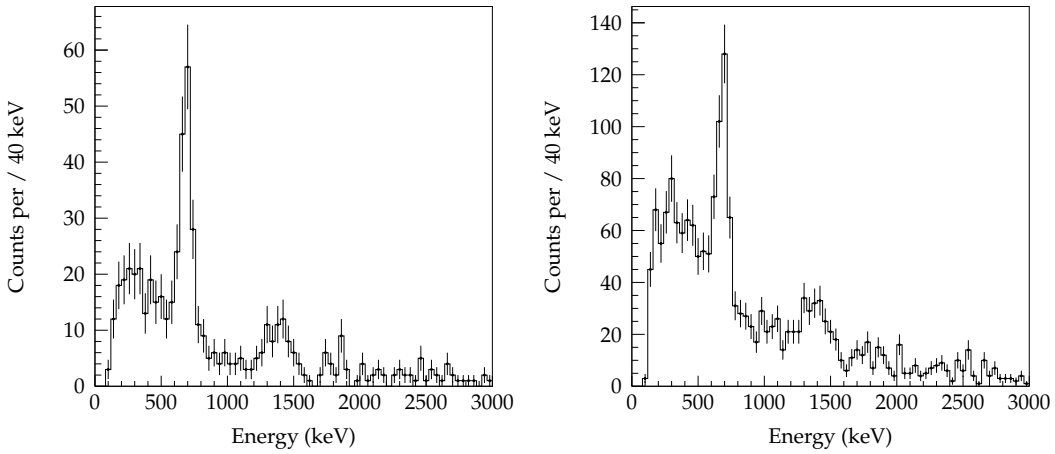

(A) $m_\gamma = 1$ (B) $m_\gamma \leq 3$

FIGURE 4.1: ^{34}Mg(^{9}Be,X)^{32}Ne Doppler reconstructed γ-ray energy spectrum with add-back

Two photopeaks are visible in Fig. 4.1b and one in 4.1a. The $2_1^+ \rightarrow 0_{g.s.}^+$ transition, previously observed at 722(9) keV [154], matches the energy of the observed lower energy photopeak.

It was previously noted that the DALI reconstruction of ^{34}Mg(^{9}Be,X)^{32}Ne reaction is accomplished for prompt decays, for excited state lifetimes sufficiently short to have limited shift on the mean decay positions from mid-target or shift in mean

velocity. In the case of ^{32}Ne, the lifetime of the 2_1^+ state cannot be assumed to sufficiently short for this approximation, and the lifetime has not been measured experimentally.

For electromagnetic decay processes, introduced in section 1.3.4, a state lifetime is related to the quantity of the reduced transition probability (equation 1.33), $B\left(\sigma L; \zeta_i J_i \rightarrow \zeta_f J_f\right)$. For decays with sufficient single-particle character, the state lifetime can be computed with Weisskopf estimates 1.36 and equations 1.32, 1.34 or 1.35. For the application of a 2_1^+ state which decays through an $E2$ transition to the ground state, the related reduced transition probability is the quantity $B(E2)$. However, as alluded to in the description of shell quenching (section 1.1.2), the divergence of $B(E2)$ values is associated with the disappearance of magic numbers. The $B(E2)$ value, in addition to the lifetime of the 2_1^+ state, is not known for ^{32}Ne.

A compilation of $B(E2)$ value and lifetimes across the nuclear landscape has permitted the establishment of global systematic trends. One global best fit [155], excluding closed-shell nuclei, was found to be,

$$\tau_\gamma = (1.59 \pm 0.28) \times 10^{14} E^{-4} Z^{-2} A^{2/3} \quad \text{ps} \tag{4.1}$$

and using equations and 1.34 and 1.39,

$$B(E2) = (2.57 \pm 0.45) \times E^{-1} Z^2 A^{-2/3} \quad \text{e}^2(\text{fm})^4 \tag{4.2}$$

$$\beta = (466 \pm 41) \times E^{-1/2} A^{-1} \tag{4.3}$$

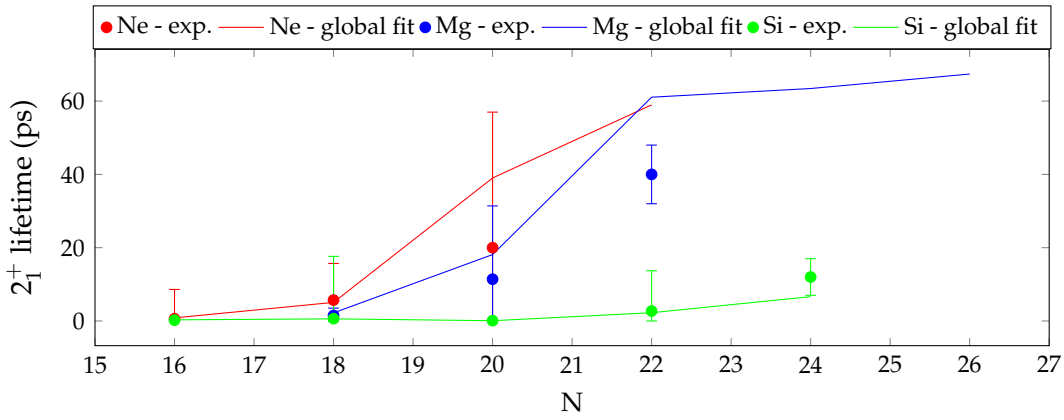

FIGURE 4.2: Global best fit predictions [155] and experimental first 2_1^+ state lifetimes for Si, Mg, and Ne neutron-rich isotopes

Observing the experimentally known lifetimes for neutron-rich Si, Mg and Ne, and comparing with extrapolated values from equation 4.1, good agreement is shown (Fig. 4.2). For the $N \geq 20$ nuclei of Mg and Ne, characterized as highly collective, the global fit uniformly overestimates the lifetime.

The lifetime of the first 2_1^+ state in ^{32}Ne is predicted to be $60(10)$ ps using the excited state energy of $722(9)$ keV [154]. This value is then utilized to generate the DALI response function for fitting the $2_1^+ \rightarrow 0_{g.s.}^+$ transition. The lifetime effect is included in the Monte Carlo DALI simulation, resulting in the shift of mean decay position and velocity. And is therefore reflected in the corresponding DALI response function.

The complete fit function thus comprises of the $2_1^+ \rightarrow 0_{g.s.}^+$ response with a simulated lifetime of 60 ps, a prompt response for the additional photopeak around

1400 keV and a double exponential background for the atomic background component (section 2.5.1). The fit of the Doppler reconstructed spectra for all events with $m_\gamma \leq 3$ is presented in Fig. 4.3 and shows a good quality fit. The reduced χ^2 is 1.71. The extended range of the fitting region to 4 MeV provides strong constraint to the double exponential background function.

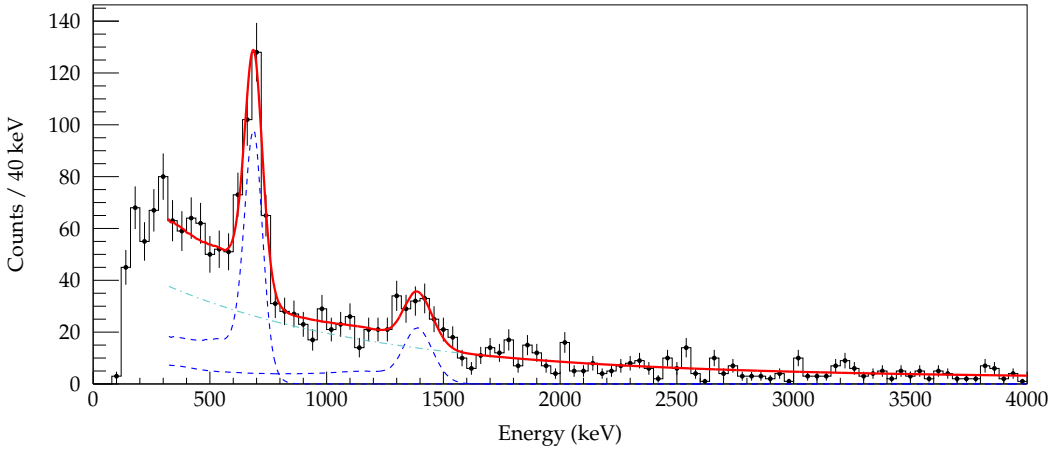

FIGURE 4.3: Fit of ^{34}Mg(^{9}Be,X)^{32}Ne doppler reconstructed γ-ray energy spectrum, $m_\gamma \leq 3$, and with add-back

Fit summary The Doppler reconstruction of the γ spectrum was completed for various m_γ and individually fit with the DALI response functions. The results of the DALI response function centroids (energy) and yield[1] are presented in the plots of Fig. 4.4. The energy centroids of the two observed transitions fluctuate between fits, however the scatter is within statistical uncertainties. With the low statistics of each histogram, the estimated centroid uncertainties by the ROOT minimizer may potentially be underestimated. This procedure of fitting multiple reconstructed spectra, with similar signal to noise ratios, provides additional confirmation of the statistical uncertainties.

The yield, as a function of maximum event multiplicity, shows an increasing trend before reaching a saturation. The strong hindrance of the 1400 keV transition at $m_\gamma = 1$ may suggest a placement as part of a cascade with another transition to the ground state. This trend is additionally observed for the one proton knockout reaction in Fig. 4.7.

[1] a product of the DALI response function scaling factor, the total number of GEANT4 simulated reactions, and the ratio of the number of bins between the experimental and response function histograms

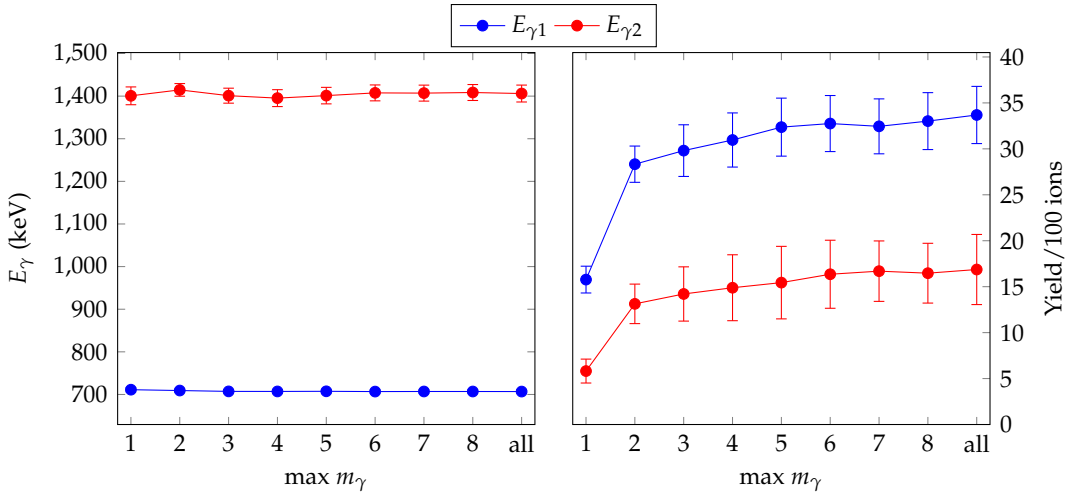

FIGURE 4.4: Summary of fit results of ^{34}Mg(^{9}Be,X)^{32}Ne.

4.1.2 ^{33}Na(^{9}Be,X)^{32}Ne

4.1.2.1 Reaction summary and inclusive cross section

TABLE 4.3: Summary of ^{33}Na(^{9}Be,X)^{32}Ne and inclusive cross section. Livetime and downscaler corrections applied.

	within ZeroDegree full momentum acceptance		
Total reactions	Reactions	Projectiles	Inclusive cross section (mb)
673	413	1225212	4.34(54)

The inclusive cross section of the one-proton knockout reaction to ^{32}Ne is presented in table 4.3. However, the reaction the projectile and the associated reaction residue did not carry the same magnetic rigidity, as such, were offset from the central trajectory in both separator and spectrometer. A culling of events to within the full momentum acceptance of ZeroDegree is required, as explained in section 3.3.1.

4.1.2.2 γ-ray analysis

TABLE 4.4: ^{33}Na(^{9}Be,X)^{32}Ne γ-ray reconstruction settings

Velocity (MeV u^{-1} / β)			Beam at target (cm)			
mid-point target	before target	σ	X	fwmh	Y	fwhm
221.2 / 0.5890	228.8 / 0.5962	6	0.0	1.0	0.0	1.0

Average interaction points calculated from GEANT4 simulation of 1400 keV γ-rays.

The Doppler reconstructed γ-ray spectra of the ^{33}Na(^{9}Be,X)^{32}Ne reaction is presented in Fig. 4.5a and 4.5b. They are comparable to the spectra to the two proton knockout reaction shown earlier, with two clear photopeaks. A greater peak to background is clear from the small component of the atomic background in the figures. A fit of the $m_\gamma \leq 3$ reconstruction is presented in Fig. 4.6.

Fit summary The results of fits of the different reconstruction of the γ-ray spectrum with varying maximum m_γ are presented in the plots of Fig. 4.7. Similar trends in the yields are observed, with the disappearance of the higher energy γ-ray for events with $m_\gamma = 1$. Moreover, the yield (per reaction residue) of the approximately 700 keV γ-ray is considerably greater than the preceding two-proton knockout reaction. This is observable as the improvement in the peak to background ratio.

4.1.3 Summary

In both knockout reactions, two γ-rays are observed. The corresponding weighted averages across fits with differing maximum event multiplicity are 708(5) keV and 1405(19) keV for the two-proton knockout and 710(5) keV and 1415(21) keV for the one-proton knockout and are comparable within statistical uncertainties.

In addition to the systematic uncertainty from the DALI2 energy calibration (section 3.4.1.1) of 3 keV, two systematic uncertainties are evaluated to consider the sensitivity of the reconstructed spectra to the lifetime of the 2_1^+ excited state and the influence of ion-beam velocity on the Doppler reconstruction.

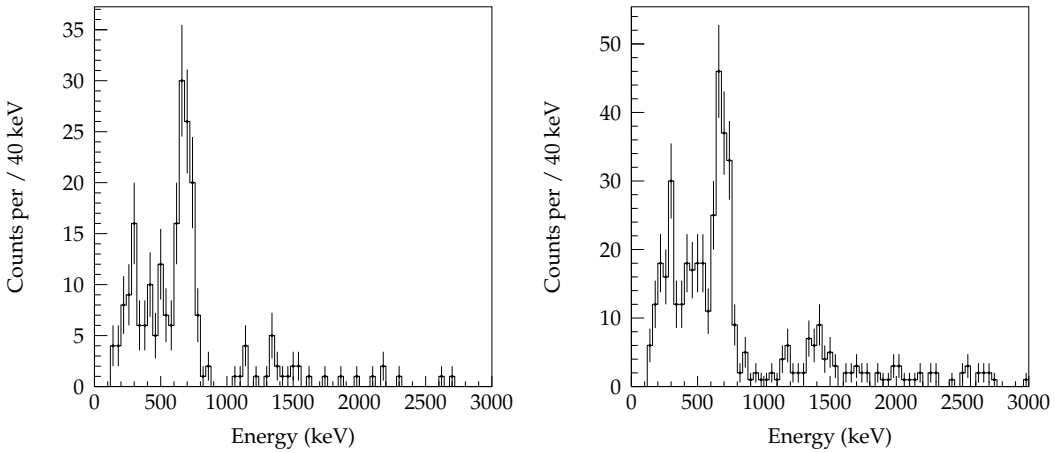

(A) $m_\gamma = 1$ (B) $m_\gamma \leq 3$

FIGURE 4.5: ^{33}Na(^{9}Be,X)^{32}Ne Doppler reconstructed γ-ray energy spectrum with add-back

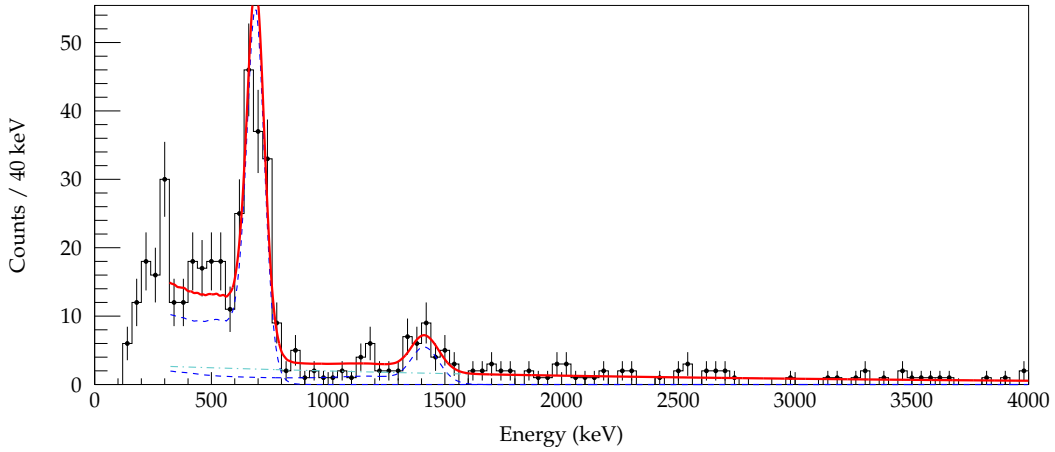

FIGURE 4.6: Fit of ^{33}Na(^{9}Be,X)^{32}Ne doppler reconstructed γ-ray energy spectrum, $m_\gamma \leq 3$, and with add-back

TABLE 4.5: ^{32}Ne fit results with statistical and systematic uncertainties

TABLE 4.6: One-proton knockout

E_γ (keV)	Yield/100 ions
$710(5)_{stat.}(12)_{syst.}$	72(7)
$1415(21)_{stat.}(4)_{syst.}$	17(5)

TABLE 4.7: Two-proton knockout

E_γ (keV)	Yield/100 ions
$708(5)_{stat.}(12)_{syst.}$	33(3)
$1405(19)_{stat.}(4)_{syst.}$	17(3)

4.1.3.1 2_1^+ lifetime uncertainty

Straying from the assumed lifetime of the 2_1^+ excited state and the associated shift in fit transition energies of the experimental spectra is evaluated. Multiple DALI response functions generated with lifetimes of 30, 90, 120 ps are incorporated into complete fit functions. The fit results are tabulated in 4.8. The insensitivity of the

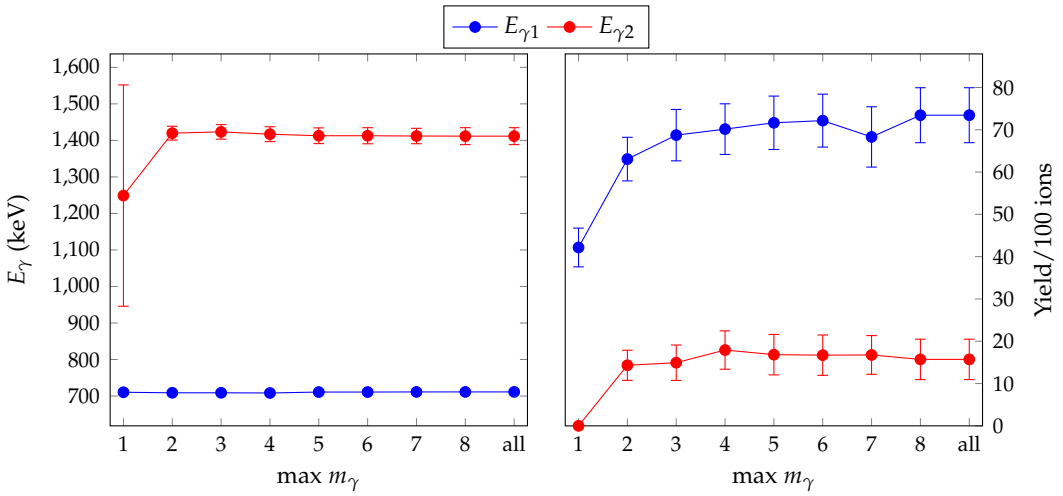

FIGURE 4.7: Summary of fit results of ^{33}Na(^{9}Be,X)^{32}Ne.

higher energy transition is noticeable by the unchanging centroid energy. This is expected, as the DALI response functions are highly bound to the shape of the photopeaks, and the modification of the shape of the complete fit function around 700 keV has little influence to the 1400 keV DALI response function position. The fit of the photopeak of around 700 keV transforms with changing lifetime.

The lifetime of the 2_1^+ between 30 ps to 120 ps can be taken as the lower and upper limits from the 60 ps predicted lifetime. Such limits were taken in the previous analysis of the 2_1^+ state in [154]. The shift is on the order of 11 keV. This shift is added as symmetric uncertainty for the centroid of the 700 keV transition. A 1 keV symmetric uncertainty is added to the 1400 keV transition.

TABLE 4.8: Fitted experimental peaks of one- and two-proton knockout reaction to $^{32}_{10}$Ne for selected 2_1^+ lifetimes for events with maximum $m_\gamma \leq 3$. Observed γ-rays of each transition. Statistical uncertainty provided by fit.

(A) One-proton knockout

Lifetime (ps)	$4_1^+ \rightarrow 2_1^+$ (keV)	Observed	$2_1^+ \rightarrow 0_{gs}^+$ (keV)	Observed
30	1423(20)	90(25)	701(5)	416(36)
60	1423(20)	90(25)	709(5)	415(37)
90	1423(22)	91(24)	716(5)	417(34)
120	1423(21)	91(25)	721(6)	420(34)

(B) Two-proton knockout

Lifetime (ps)	$4_1^+ \rightarrow 2_1^+$ (keV)	Observed	$2_1^+ \rightarrow 0_{gs}^+$ (keV)	Observed
30	1401(18)	359(69)	700(4)	741(68)
60	1401(18)	360(75)	707(4)	756(71)
90	1401(18)	362(67)	713(4)	784(71)
120	1400(18)	368(62)	718(5)	806(65)

4.1.3.2 Beam velocity uncertainty

The influence of the beam velocity on the Doppler reconstructed γ-ray spectrum is previously investigated by simulation in section 3.4.4. Experimentally, this can also be observed to confirm the simulated results. As the difference between BigRIPS and ZeroDegree methods of ion-beam velocity reconstruction has been observed to be $5\,\mathrm{MeV\,u^{-1}}$ or 2% for both the one- and two-proton knockout reaction, this deviation can be taken as a velocity uncertainty[2]. The reconstruction of the experimental γ-ray spectrum is accomplished with this velocity difference in both directions, and the refitting of the transitions can provide an estimation of the fitted energy uncertainty. The results of this procedure are displayed in table 4.9a and 4.9b.

TABLE 4.9: Fitted experimental peaks of one- and two-proton knockout reaction to $^{32}_{10}$Ne to determine change in fitted energy and observed γ-rays of each transition, as a function of Doppler reconstruction velocity deviation, for events with maximum $m_\gamma \leq 3$. Statistical uncertainty provided by fit.

(A) One-proton knockout

Velocity difference	$4_1^+ \rightarrow 2_1^+$ (keV)	Observed	$2_1^+ \rightarrow 0_{gs}^+$ (keV)	Observed
-2%	0.82(30.0)	0.76(32.0)	0.84(7.0)	2.1(23.0)
$+2\%$	0.71(32.0)	$-1.5(33.0)$	0.719(7.0)	$-3.3(25.0)$

(B) Two-proton knockout

Velocity change	$4_1^+ \rightarrow 2_1^+$ (keV)	Observed	$2_1^+ \rightarrow 0_{gs}^+$ (keV)	Observed
-2%	-0.33(25.0)	$-14(97.0)$	-1.2(6)	1.0(97.0)
$+2\%$	3.9(24.0)	$-16(96.0)$	-0.3(6)	10.6(97.0)

The uncertainty from the fits are large in comparison to the observed shifts in centroids, but the results confirm a small deviation, as seen in the previous investigation for simulating the result of a beam velocity shift (section 3.4.4) A 2 keV symmetric uncertainty is added to both transitions to account for the reconstruction of the ion-beam velocity.

[2]The statistical uncertainty for the reconstructed velocities is small in comparison to this systematic velocity difference.

4.2 ^{39}Al

4.2.1 ^{39}Al(C/C_2H_4,γ)^{39}Al

4.2.1.1 γ-ray analysis

TABLE 4.10: ^{39}Al(C/C_2H_4,X)^{39}Al γ-ray reconstruction settings

Setting		Velocity (MeV u^{-1} / β)		Beam at target (cm)			
Target	ZD $B\rho$	mid-point target	before target	X	fwmh	Y	fwhm
C	^{41}Al	232.8 / 0.5999	262.1 / 0.6252	-0.5	1.1	-0.1	1.1
C_2H_4	^{41}Al	226.5 / 0.5940					
C	^{40}Mg	243.0 / 0.6090	271.5 / 0.6328				
C_2H_4	^{40}Mg	236.9 / 0.6036					

Average interaction points calculated from GEANT4 simulation of 800 keV γ-rays.

The reconstructed γ-ray spectrum of inelastic scattering of ^{39}Al on C and C_2H_4 targets is presented in Fig. 4.8. In the spectra both targets show an intensity around 800 keV. One or two DALI response functions (generated by GEANT4 simulation) with a background consisting of a double exponential function can reproduce the spectra shape. A fit with one transition results in a centroid of 807(8) keV with χ^2/NDF of 1.281 and a two transitions fit produces centroids of 783(13) keV and 879(18) keV with a χ^2/NDF of 1.091 for all events $m_\gamma \leq 3$ (Fig. 4.12). The uncertainties are statistical. There is additional beam induced structure around 600 keV for the inelastic spectra of both targets.

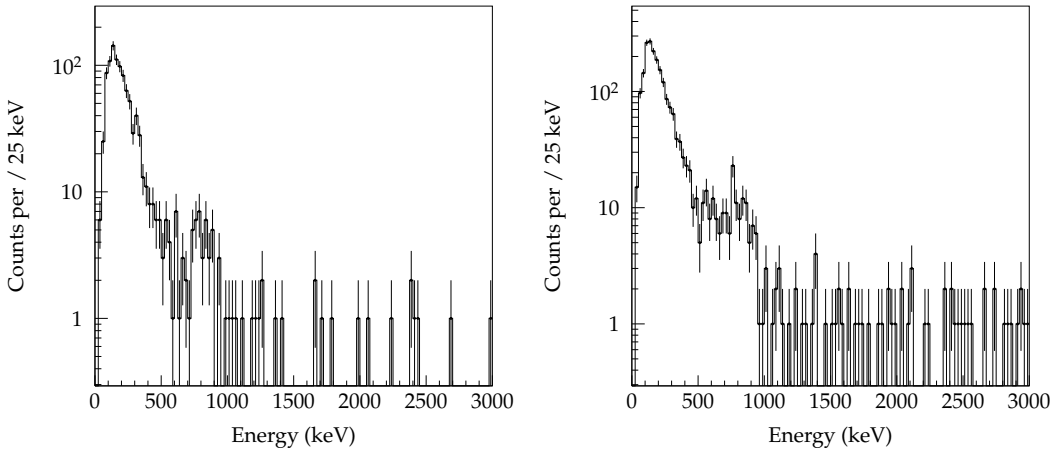

(A) C target, $m_\gamma \leq 3$ (B) C_2H_4 target, $m_\gamma \leq 3$

FIGURE 4.8: ^{39}Al inelastic scattering doppler reconstructed γ-ray energy spectrum, $m_\gamma \leq 3$, and with add-back

The influence of maximum event γ-ray multiplicity (m_γ) on the fit results, centroid and intensity is presented in graphical form in Fig. 4.10. No change in fit results is seen as a function of event maximum γ-ray multiplicity, for both fitting one or two peaks. This is consistent with a transition direct to the ground state and without significant feeding from higher laying states. Such a cascade would necessitate a low yield for selected events with γ-ray multiplicity one and an upward trend with increasing maximum γ-ray multiplicity, before reaching a saturation.

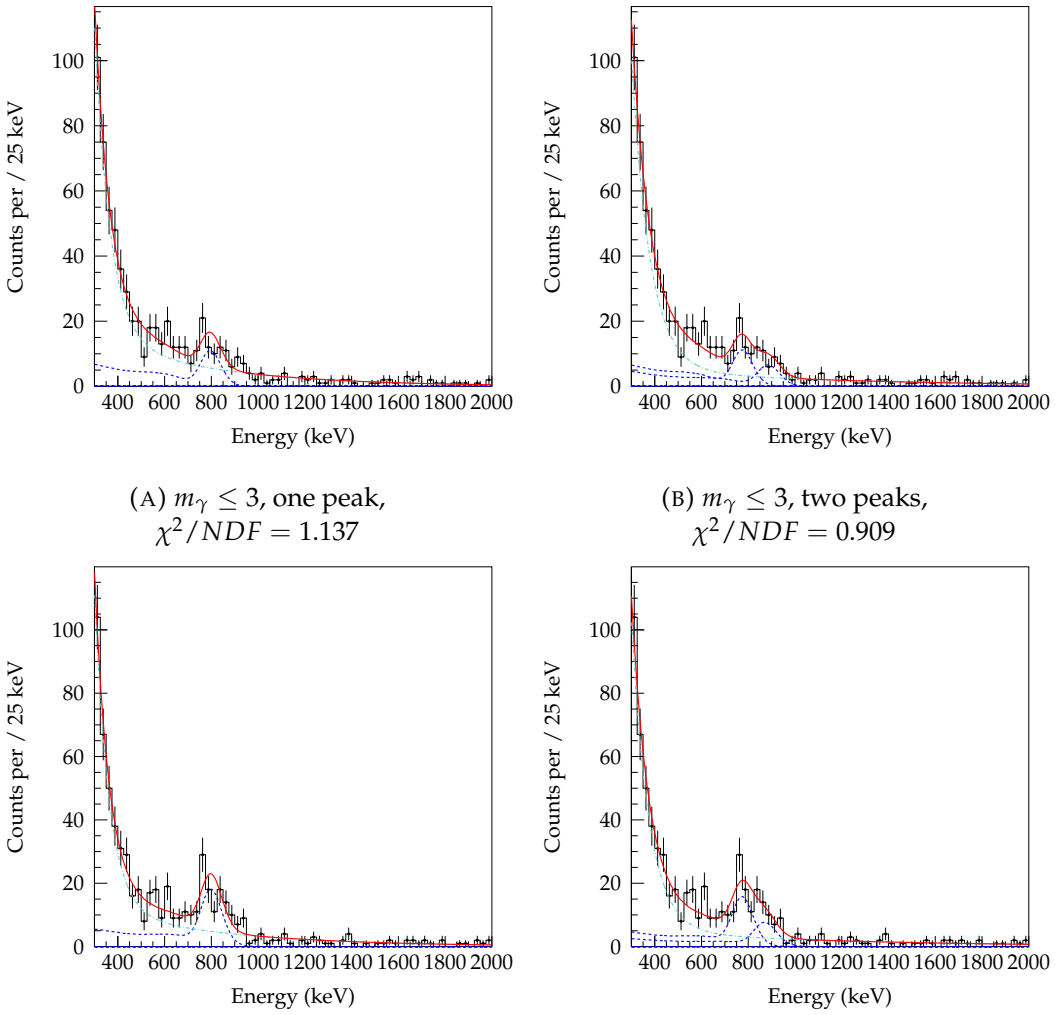

(A) $m_\gamma \leq 3$, one peak, $\chi^2/NDF = 1.137$

(B) $m_\gamma \leq 3$, two peaks, $\chi^2/NDF = 0.909$

(C) $m_\gamma \leq 3$, add-back, one peak, $\chi^2/NDF = 1.281$

(D) $m_\gamma \leq 3$, add-back, two peaks, $\chi^2/NDF = 1.091$

FIGURE 4.9: Fit of doppler reconstructed ^{39}Al(C/C_2H_4,γ)^{39}Al with add-back procedure

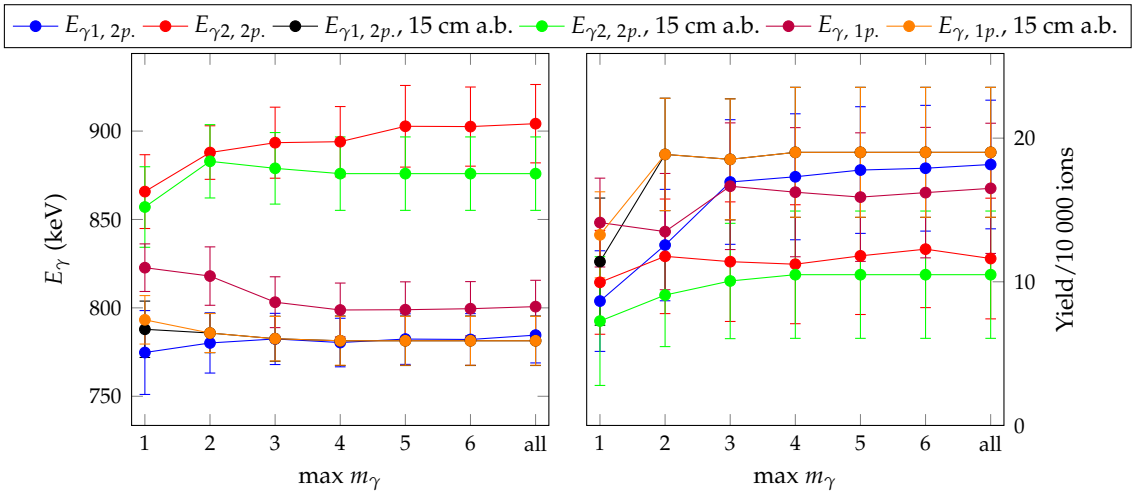

FIGURE 4.10: Summary of fit results of ^{39}Al inelastic scattering for one ($1p$) and two peak ($2p$) fitting

4.2.2 ^{40}Al(C/C_2H_4,X)^{39}Al

4.2.2.1 Reaction summary and inclusive cross section

TABLE 4.11: Summary of ^{40}Al(C/C_2H_4,X)^{39}Al and cross section

Setting			within ZeroDegree full momentum acceptance		
Target	ZD $B\rho$	Total reactions	Reactions	Projectiles	Inclusive cross section (mb)
C	^{41}Al	1070	668	52791	66.9(7.9)
C_2H_4	^{41}Al	507	337	21455	196(22)
C	^{40}Mg	686	108	8971	63.7(9.4)
C_2H_4	^{40}Mg	4246	469	36819	159.0(18)

The inclusive cross sections for both targets and ZeroDegree magnetic rigidity set to ^{41}Al and ^{40}Mg are presented in the table above (4.11). The cross sections agree within the uncertainties. It is important to note that significant removal of events by a *F5X* and *F5A* selection is necessary for experimental runs with ZeroDegree magnetic rigidity set for ^{40}Mg acceptance. This is shown by the difference between total reactions and reactions (within ZeroDegree full acceptance) in the table. For these experimental runs, the reaction residue beam of ^{39}Al is centred at the periphery of F9X and therefore at the edge of full ZeroDegree acceptance.

4.2.2.2 γ-ray analysis

TABLE 4.12: ^{40}Al(C/C_2H_4,X)^{39}Al γ-ray reconstruction settings

Setting		Velocity (MeV u^{-1} / β)		Beam at target (cm)			
Target	ZD $B\rho$	mid-point target	before target	X	fwmh	Y	fwhm
C	^{41}Al	223.2 / 0.5909	253.3 / 0.6180	-0.2	0.8	0.0	1.1
C_2H_4	^{41}Al	216.7 / 0.5846					
C	^{40}Mg	236.6 / 0.6033	265.7 / 0.6282				
C_2H_4	^{40}Mg	230.4 / 0.5976					

Average interaction points calculated from GEANT4 simulation of 800 keV γ-rays.

The gamma-ray energy spectrum from the one-neutron knockout reaction to ^{39}Al is presented in Fig. 4.11 for each of the targets, although all later fitting is completed on the sum of both. Similar features are seen in for both target γ-ray spectra. The procedure to fit the spectrum is to sequentially add photopeaks (DALI response functions) over a background of a double exponential function. The goodness of the fit is judged from the χ^2/NDF value. At the point where the addition of a peak does not convincingly improve χ^2/NDF with the scaling factor greater than $\sigma = 2.5$, no additional peaks are added. The fitting is done without *a priori* selection of peak centroids from literature (Stroberg et al. (2014) [156]).

Starting from three peaks applied to the spectrum of γ-ray $m_\gamma \leq 5$ with 15 cm add-back, up to seven peaks are tested. The reconstructed spectrum of maximum $m_\gamma \leq 5$ is found to be a good balance between signal to background and the total number of counts. The fitting range is 320 keV to 4000 keV. The sequential fitting procedure is presented in Fig. 4.12 and 4.13. The same procedure is followed for

five, six and seven peaks with $m_\gamma = 1$ (Fig. 4.14). Such a spectrum shows the best signal to background ratio and enhances some transitions, therefore may yield the identification of new transitions. A fit of these γ-ray spectrum with seven peaks, with three within the intensity around 800 keV to 950 keV may not be justified from the aforementioned procedure, with minimal improvement in χ^2/NDF. Therefore six peaks, such as shown in Fig. 4.13b and 4.14b fulfils the fitting criteria.

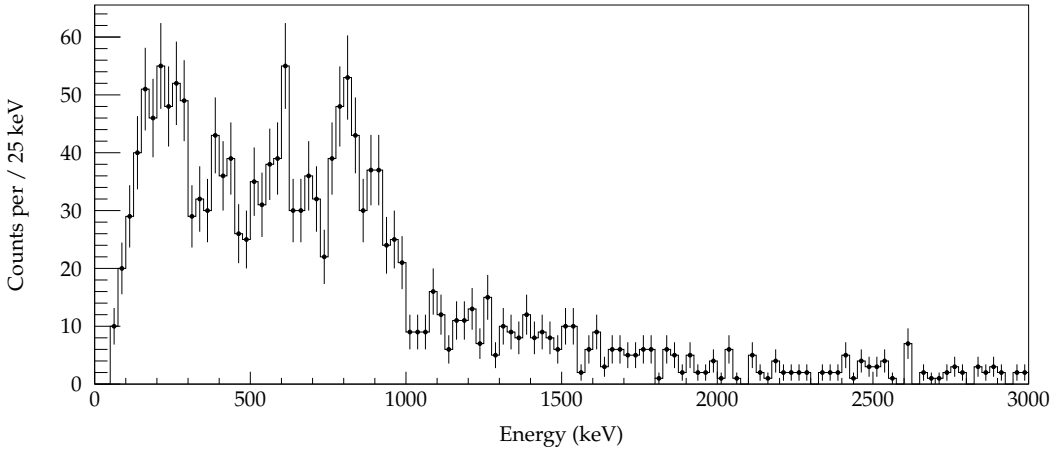

(A) C target, $m_\gamma \leq 5$

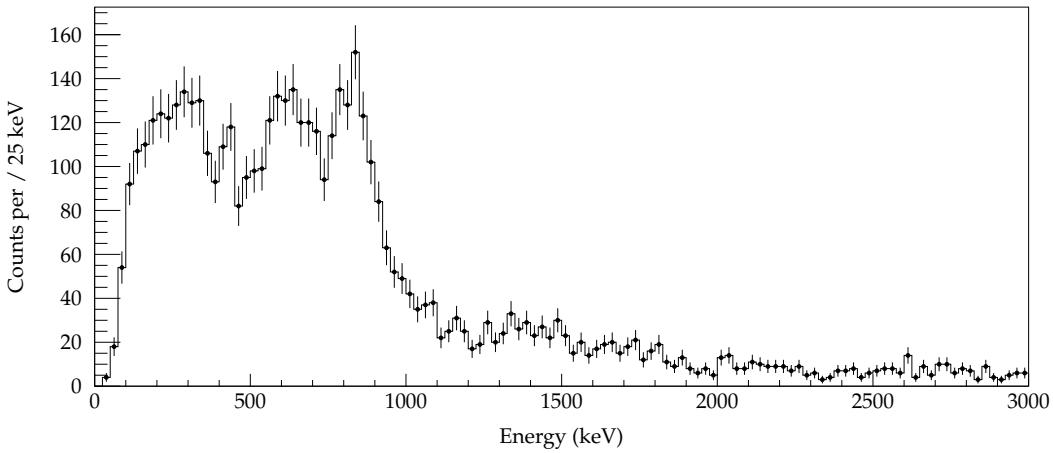

(B) C_2H_4 target, $m_\gamma \leq 5$

FIGURE 4.11: ^{40}Al(C/C_2H_4,X)^{39}Al Doppler reconstructed γ-ray energy spectrum with add-back

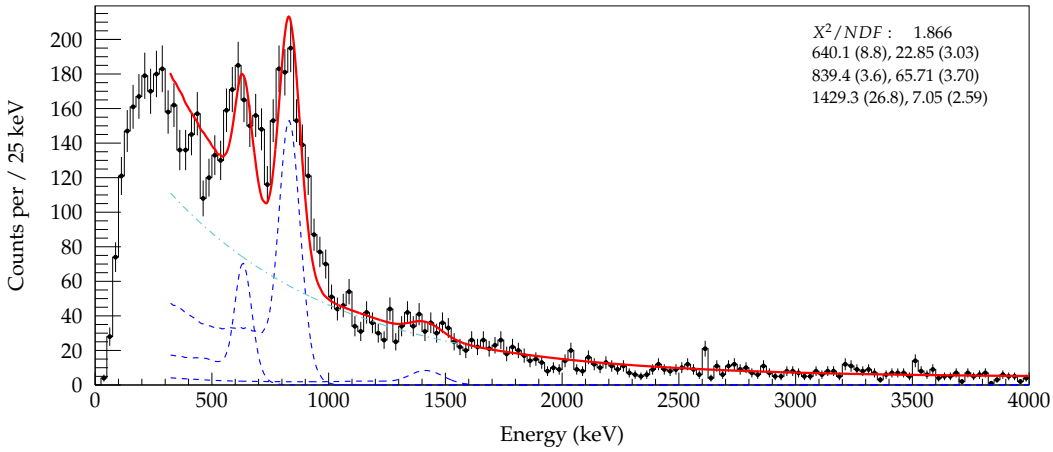

(A) 3 DALI functions, $m_\gamma \leq 5$

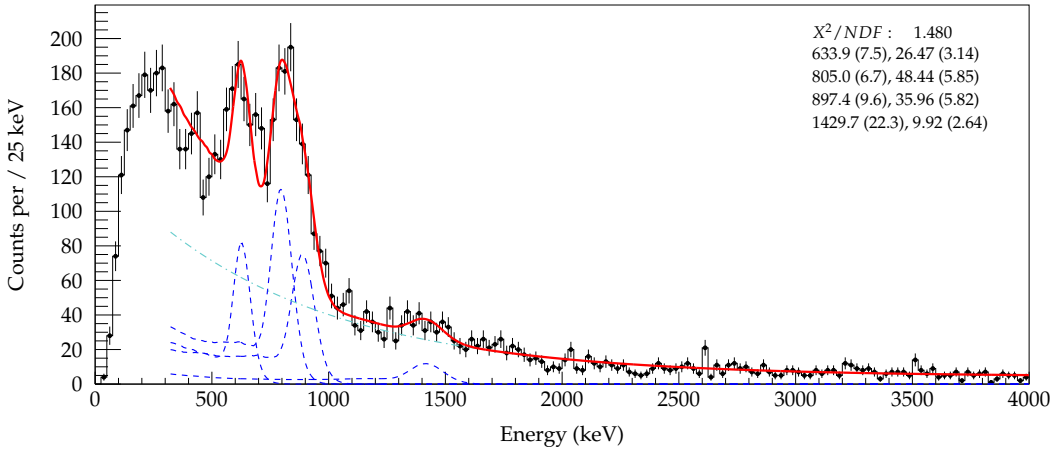

(B) 4 DALI functions, $m_\gamma \leq 5$

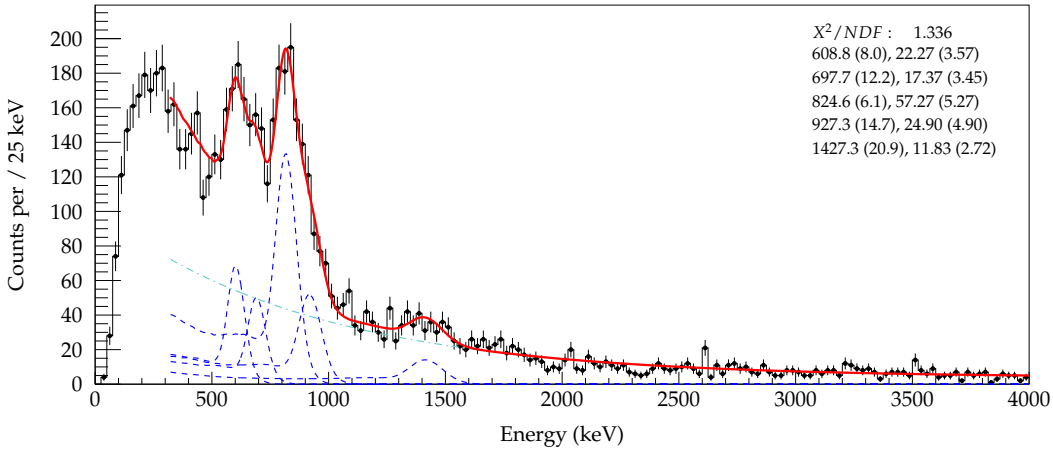

(C) 5 DALI functions, $m_\gamma \leq 5$

FIGURE 4.12: Fitting 3, 4, 5 peaks of ^{40}Al(C/C_2H_4,X)^{39}Al doppler reconstructed γ-ray energy spectrum, $m_\gamma \leq 5$, and with add-back

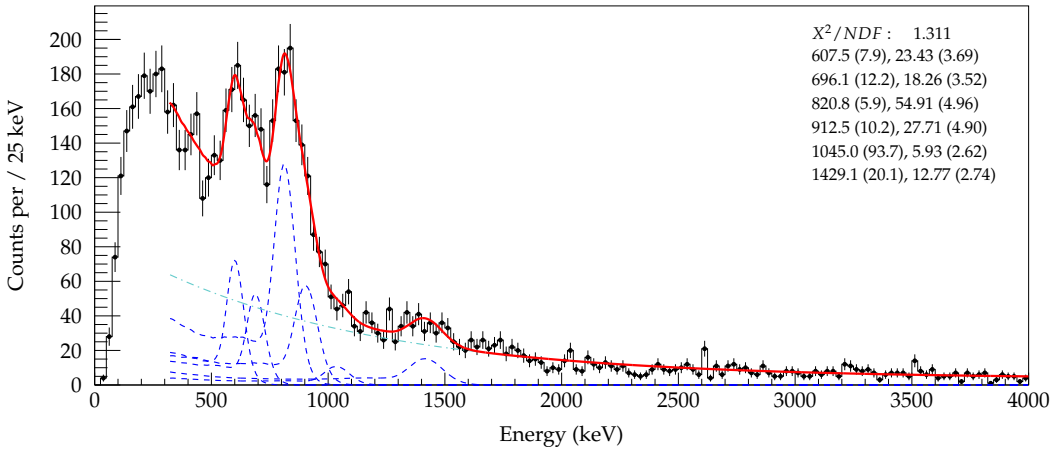

(A) 6 DALI functions, $m_\gamma \leq 5$

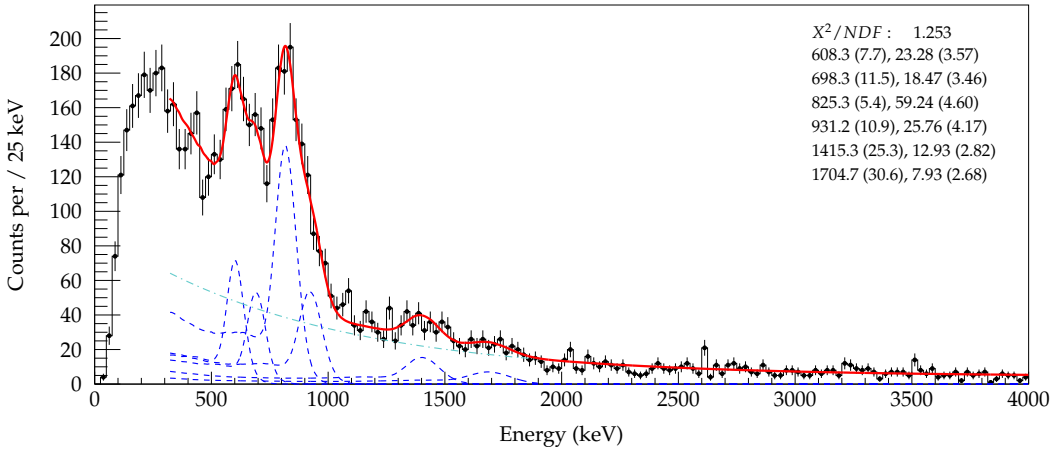

(B) 6 (alternative) DALI functions, $m_\gamma \leq 5$

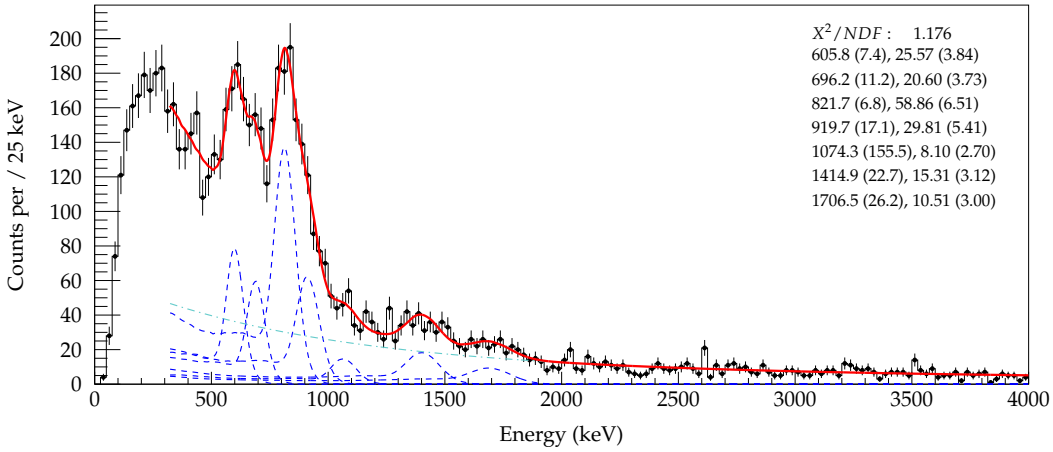

(C) 7 DALI functions, $m_\gamma \leq 5$

FIGURE 4.13: Fitting 6, and 7 peaks of ^{40}Al(C/C_2H_4,X)^{39}Al doppler reconstructed γ-ray energy spectrum, $m_\gamma \leq 5$, and with add-back

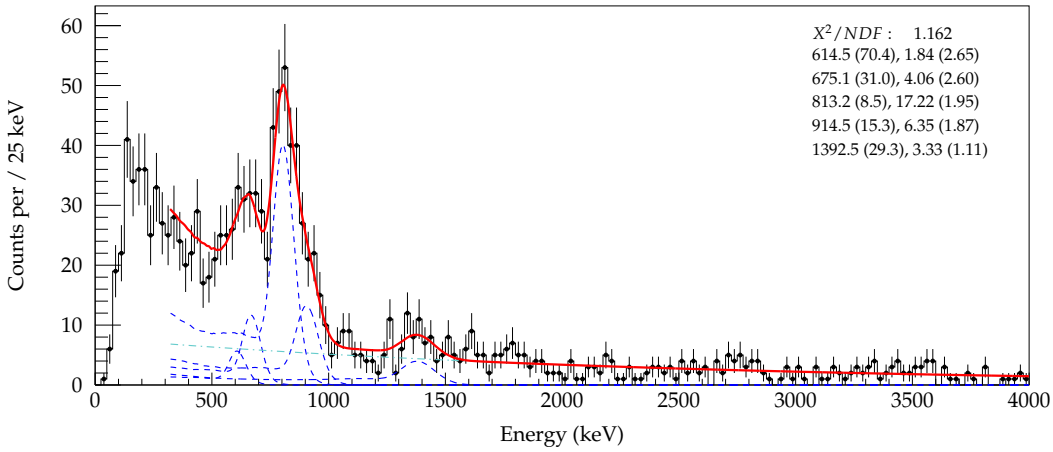

(A) 5 DALI functions, $m_\gamma = 1$

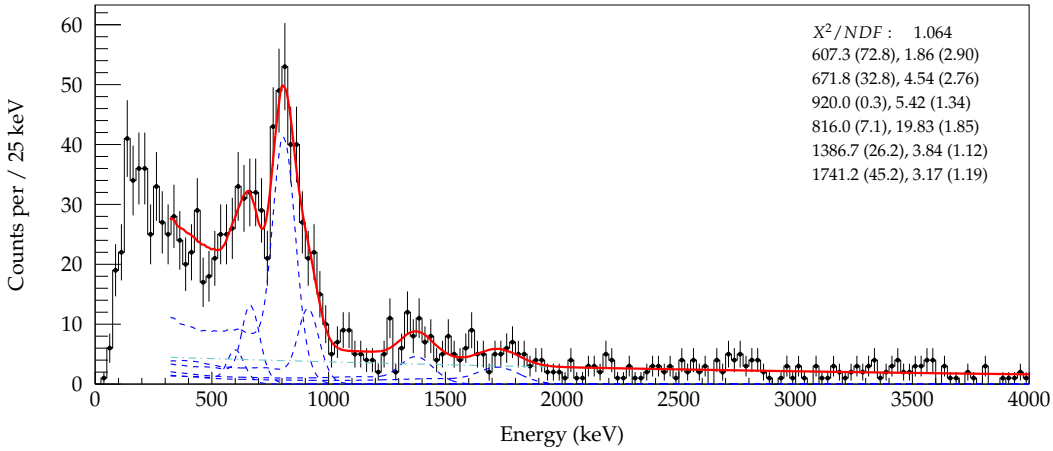

(B) 6 (alternative) DALI functions, $m_\gamma = 1$

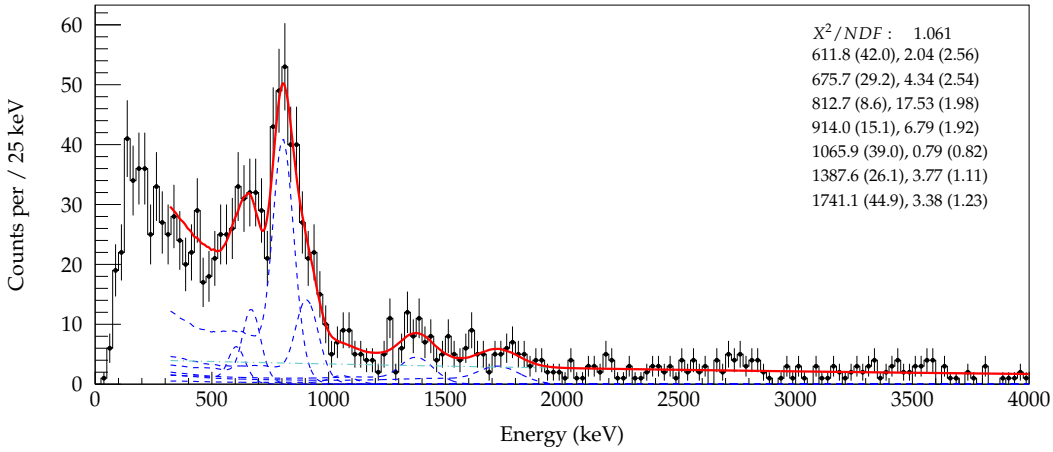

(C) 7 DALI functions, $m_\gamma = 1$

FIGURE 4.14: Fitting 5, 6, 7 peaks of ^{40}Al(C/C_2H_4,X)^{39}Al doppler reconstructed γ-ray energy spectrum, $m_\gamma \leq 5$, and with add-back

What appears to be low-energy transition at 415 keV cannot be fit with the aforementioned convoluted fit function of individual DALI response functions and a double exponential background, as shown in Fig. 4.15a. The scaling factor of the low energy DALI response functions converges to a small values or zero, with significant uncertainties. The background under these low energy peaks may be overestimated. Alternatively, fitting with a Gaussian function and a polynomial background can provide an estimation. The peak at 415 keV with a fitted Gaussian and constant background is shown in Fig. 4.15b and 4.15c. As this peak is clearly identifiable in all spectra of maximum multiplicity above one, it is considered a candidate for a transition. No uncertainty for the centroid position or yield can be produced rigorously, as such, are not assigned.

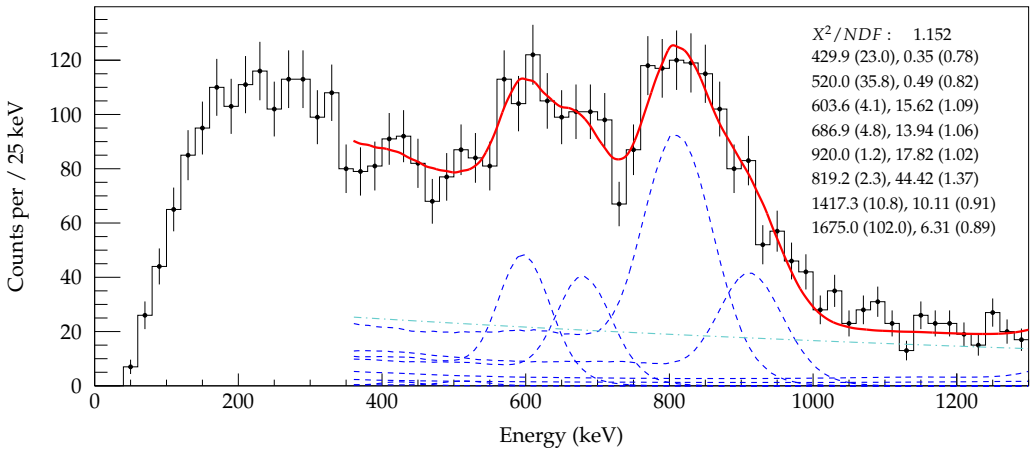

(A) Full fit, $m_\gamma \leq 3$

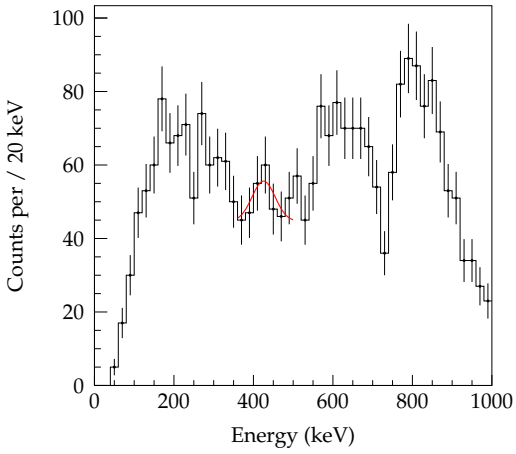

(B) Gaussian fit, $m_\gamma \leq 2$

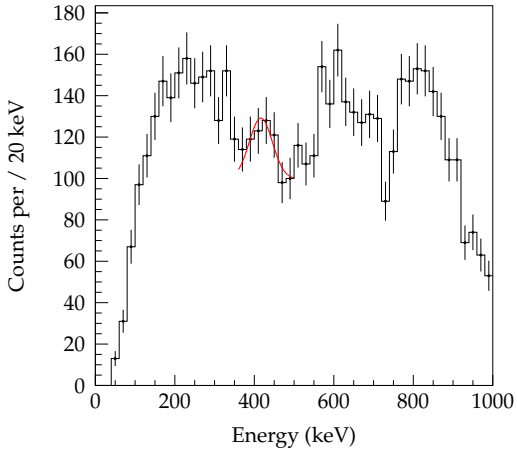

(C) Gaussian fit, all m_γ

FIGURE 4.15: 415 keV candidate peak

Lastly, a previous study employing an alternative proton knockout reaction mechanism identified 764, 800, 883 and 995 keV transitions in Stroberg et al. (2014) [156]. By using a different reaction mechanism, the population of excited states may be different. A fit with these previously identifed four peaks (764, 800, 883, 995) is presented in Fig. 4.16. Given the large overlap between peaks at 764 keV and 800 keV, the scaling of the former may be completely suppressed. The fitted energies and scaling factors presented in the top right of the figures. Lastly, the yield (γ-ray per ion) (table 4.15) for the 800 keV multiplet is similar to Stroberg et al. (2014) [156], with the highest yield for 800 keV.

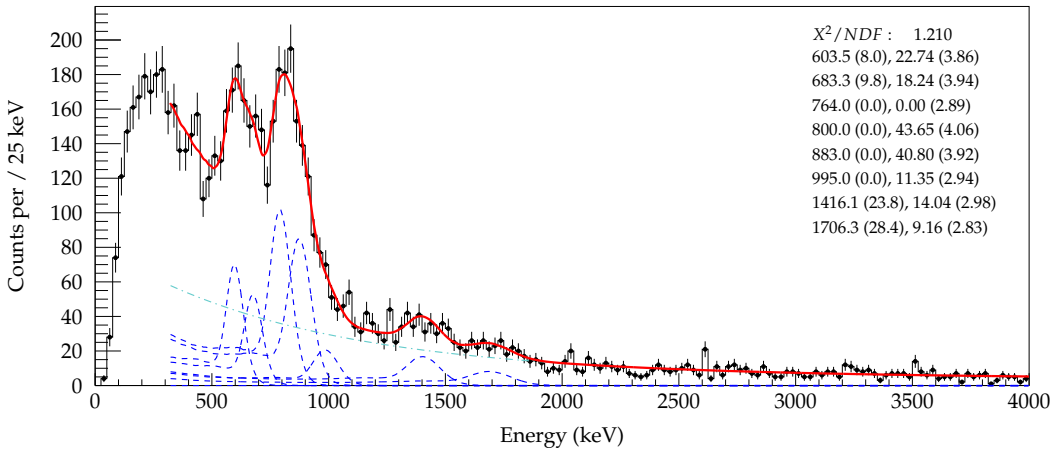

FIGURE 4.16: Fitting 7 peaks of ^{40}Al(C/C_2H_4,X)^{39}Al doppler reconstructed γ-ray energy spectrum with four fixed centroid energies, $m_\gamma \leq 5$, and with add-back

Fit summary The fit results (energies and yield) are presented in Fig. 4.17 for six transitions, such as presented previously in Fig. 4.13b and 4.14b. The general robustness of the fits is demonstrated by the minimal deviation of peak centroid.

The trend of increasing yield as a function of maximum multiplicity is similar for all transitions. The 695 (red), 1412 (purple) and 1705 (pink) transitions saturate at lower maximum multiplicity.

Table 4.14 and 4.15 present the energies and yield for the condition of fitting six transitions and for including fixed energies from Stroberg et al. (2014). As previously mentioned, the suppression of 764 keV is likely to be an artifact of the close proximity of 800 keV in the fit and the large resolution in the present experiment.

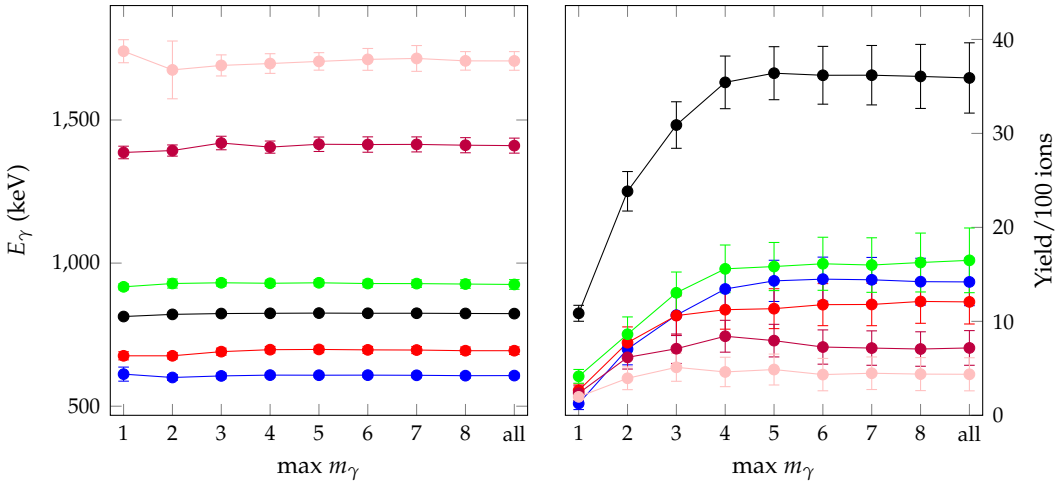

FIGURE 4.17: Summary of fit results of ^{40}Al(C/C_2H_4,X)^{39}Al with six DALI response functions.

TABLE 4.13: ^{39}Al fit results

TABLE 4.14: ^{39}Al fit results with six transitions

E_γ (keV)	Yield/100 ions
415⋆	
607(8)	14(2)
695(12)	12(2)
823(6)	36(4)
927(11)	16(3)
1412(26)	7(2)
1705(32)	4(2)

TABLE 4.15: ^{39}Al fit results with four fixed transition energies (764, 800, 883, 995)

E_γ (keV)	Yield/100 ions
415⋆	
604(8)	14(2)
683(10)	11(2)
764	0(3)
800	27(3)
883	25(2)
995	7(2)
1416(24)	9(2)
1706(28)	6(2)

γ-γ coincidence A γ-γ matrix is presented in Fig. 4.18 for the reaction. The features prematurely suggest coincidence between approximately 600 keV and 800 keV transitions.

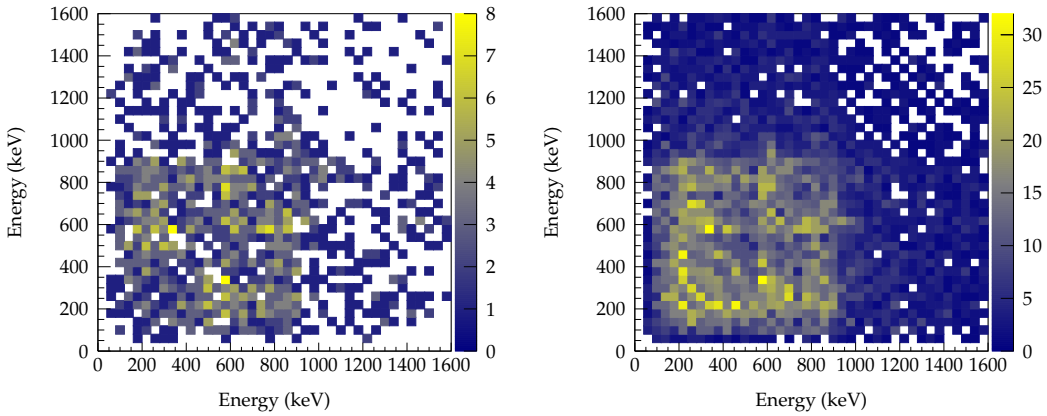

(A) $m_\gamma = 2$ (B) all m_γ

FIGURE 4.18: ^{40}Al(C/C_2H_4,X)^{39}Al γ-γ matrix

The proceeding γ-γ coincidence analysis on the following pages selects gates of the spectrum around the previously identified photopeaks, with lower and upper limits chosen to minimize the selection of auxiliary transitions. The gates are identified in Fig. 4.19a and labelled A through G. Two background regions (1 & 2) are employed for background subtraction. A significant source of uncertainty is the capture of unknown photopeaks within these background regions. Two large regions are necessitated by the very low statistics.

The evaluation of coincidences is accomplished by both qualitative and quantitative features, through fitting of the γ-γ coincidence spectrum. As to not limit transitions from multi-transition cascades, the events of all m_γ are used in the fitting. The γ-γ coincidence spectra includes a background component, owing to uncorrelated background coincidences, it is therefore necessary to the fit the spectra from the background selections. The number of true coincidences is defined as coincidence counts subtracted by background counts[3]. The ratio of the integrated double exponential background for the various gates over the integrated double exponential for the background gates provides a normalization for the uncorrelated background for each gate.

It is necessary to make a number of assumptions, ascribable to the low statistics as well as the poor energy resolution of DALI. Firstly, the energies of Stroberg et al. (2014) [156] are assumed. This reduces significantly the uncertainties associated with integrating the 800 keV multiplets. Secondly, during the fitting of the coincidence spectra, all centroids (energies) of the response functions are fixed. This is required to reduce the large parameter space for fitting with very low statistics. However, unidentified peaks within the fitting regions may induce perturbations in the calculated yields.

This procedure and assumptions necessitates a stringent criteria for identification of true γ-γ coincidences, such as greater than 2σ, particularly because it is not possible to quantify all systematic uncertainties with this procedure.

[3]where the number of counts includes consideration of DALI detection efficiency, as inherent in the GEANT4 DALI response functions

The coincidence spectra for the combined background regions are presented in Fig. 4.19b 4.19c. The all m_γ spectra is fitted with response function centroids fixed. The statistics is low and fit contains large uncertainties. Transitions for the largest intensities around 600 keV and 800 keV are predominate, as expected from uncorrelated background coincidence.

Lastly, it is important to note that the background subtracted $\gamma - \gamma$ coincidence spectra are not fitted. The GEANT4 simulated DALI response functions may not be representative of a transition in these spectra[4].

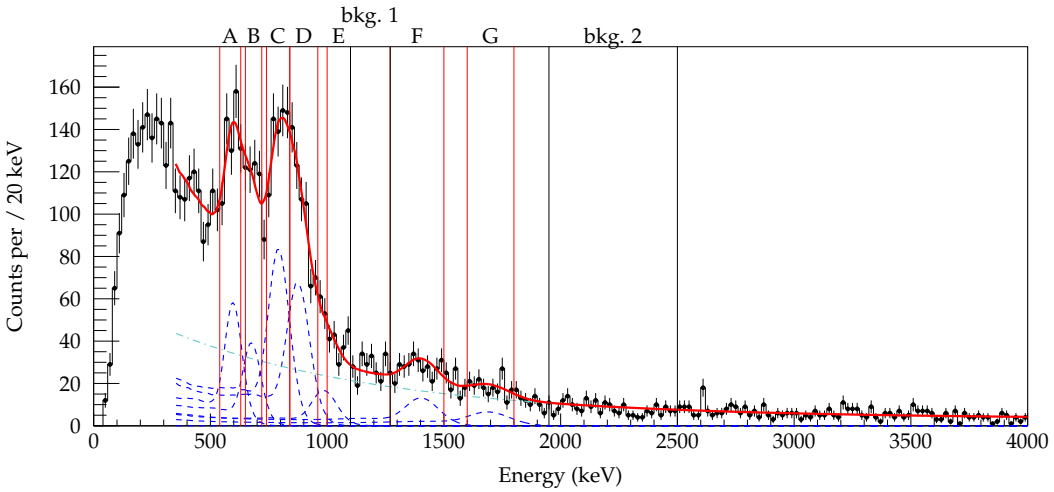

(A) Regions of selection for analysis of γ-γ coincidences, $m_\gamma \leq 5$

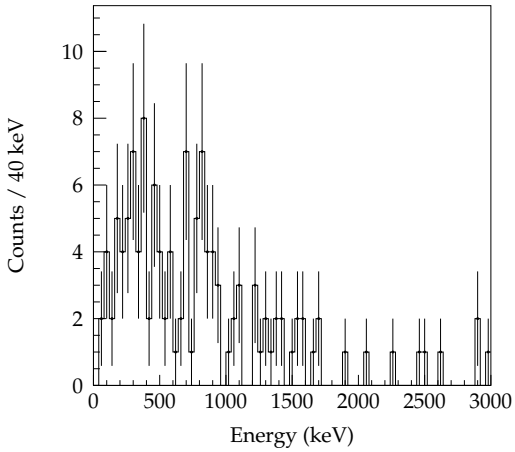

(B) Background 1 & 2, $m_\gamma = 2$

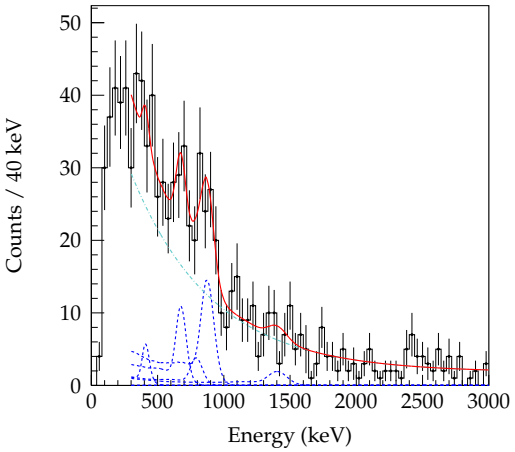

(C) Background 1 & 2, all m_γ

FIGURE 4.19: Selections for ^{40}Al(C/C_2H_4,X)^{39}Al coincidence analysis and background coincidences, with add-back

The following pages present the coincidences for the various regions (A through G), in addition to background subtracted spectra and coincidence results.

[4] As an alternative, regions of the the background subtracted $\gamma - \gamma$ coincidence spectra could be integrated or fit with another function such as a Gaussian. This would require additional consideration of detection efficiency and further sources of systematic uncertainties, for example, the choices of integration area influencing the yield.

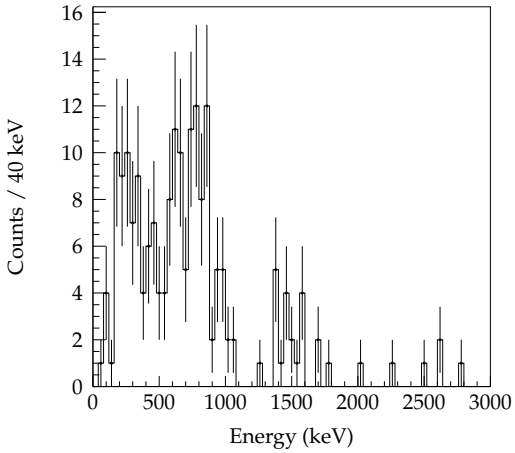

(A) $m_\gamma = 2$

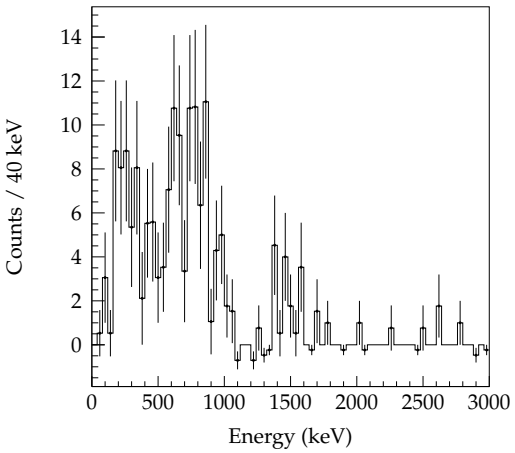

(B) $m_\gamma = 2$, background subtracted

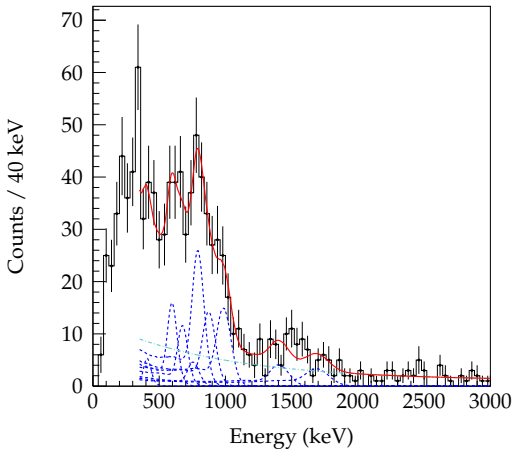

(C) all m_γ

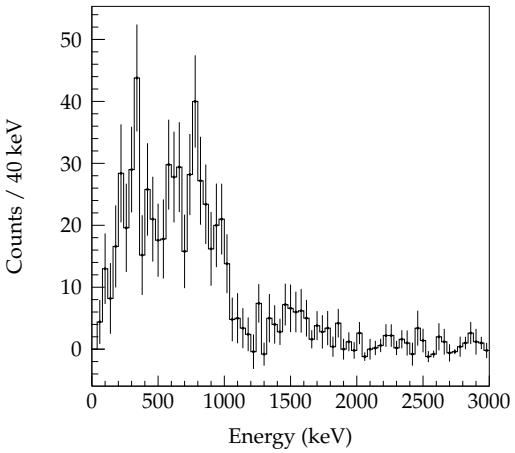

(D) all m_γ, background subtracted

FIGURE 4.20: ^{40}Al(C/C_2H_4,X)^{39}Al selection A: 540 keV to 630 keV (for 604 keV peak)

E_γ (keV)	Selected	Background	Coincidence	Coinc.-Bkg.
415 ⋆	0	13(16)	31(43)	18(46)
604(8)	198(37)	0(10)	129(56)	129(57)
683(10)	53(10)	38(17)	100(54)	62(57)
764	0(0?)	0(10)	47(184)	47(184)
800	79(6)	16(19)	278(122)	262(123)
883	66(4)	70(21)	171(65)	101(69)
995	15(4)	0(9)	206(51)	206(52)
1416(24)	15(4)	16(16)	86(42)	70(45)
1706(28)	8(3)	0(10)	93(47)	93(48)

TABLE 4.16: Number of counts for $\gamma - \gamma$ coincidence for selection A (604 keV) for all m_γ events. Significant (such as $> 2\sigma$) coincidences are highlighted in blue. The photopeak of interest is highlighted in yellow.

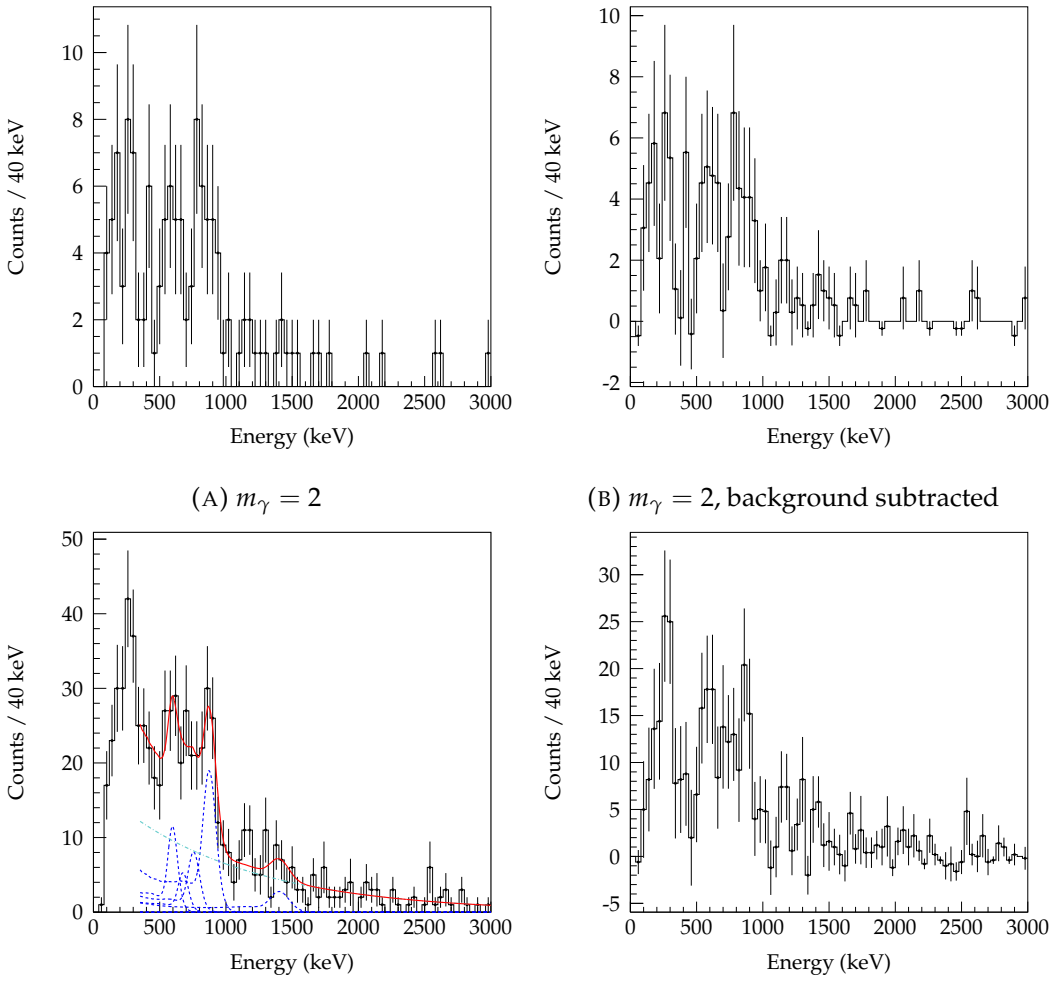

(A) $m_\gamma = 2$

(B) $m_\gamma = 2$, background subtracted

(C) all m_γ

(D) all m_γ, background subtracted

FIGURE 4.21: ^{40}Al(C/C_2H_4,X)^{39}Al selection B: 650 keV to 720 keV (for 683 keV peak)

E_γ (keV)	Selected	Background	Coincidence	Coinc.-Bkg.
415⋆	0	10(11)	0(84)	-10(85)
604(8)	25(11)	0(7)	93(38)	93(40)
683(10)	137(31)	128(26)	46(39)	19(41)
764	0(1)	0(7)	83(42)	83(42)
800	66(6)	11(13)	0(21)	-11(25)
883	52(5)	49(15)	228(44)	179(46)
995	11(3)	0(6)	0(20)	0(21)
1416(24)	10(3)	11(11)	58(35)	47(37)
1706(28)	5(2)	0(7)	0(23)	0(24)

TABLE 4.17: Number of counts for $\gamma - \gamma$ coincidence for selection B (683 keV) for all m_γ events. Significant (such as $> 2\sigma$) coincidences are highlighted in blue. The photopeak of interest is highlighted in yellow.

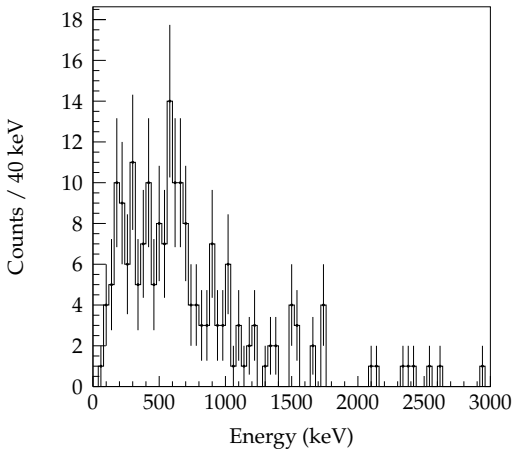

(A) $m_\gamma = 2$

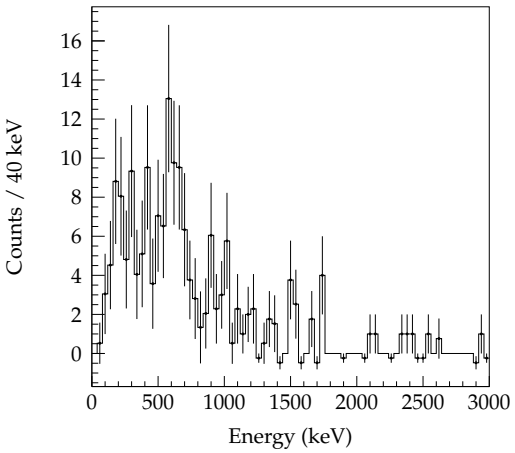

(B) $m_\gamma = 2$, background subtracted

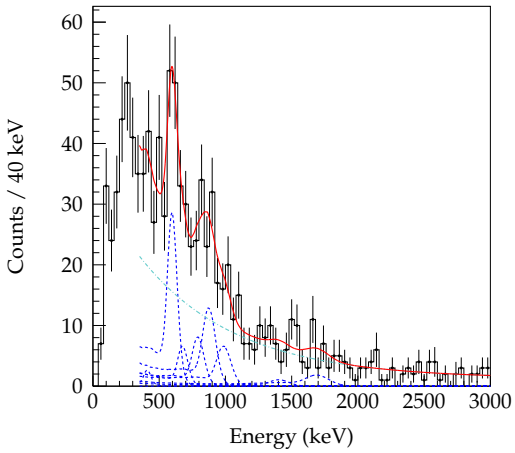

(C) all m_γ

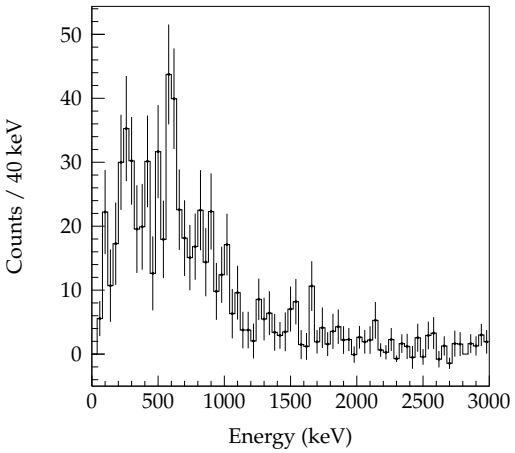

(D) all m_γ, background subtracted

FIGURE 4.22: ^{40}Al(C/C_2H_4,X)^{39}Al selection C: 740 keV to 840 keV (for 800 keV peak)

E_γ (keV)	Selected	Background	Coincidence	Coinc.-Bkg.
415⋆	0	12(14)	16(68)	3(70)
604(8)	0	0(9)	232(56)	232(56)
683(10)	16(7)	34(15)	57(45)	23(48)
764	0(1)	0(9)	0(23)	0(25)
800	341(32)	15(17)	87(52)	72(55)
883	132(13)	63(19)	155(54)	92(58)
995	17(5)	0(8)	91(48)	91(48)
1416(24)	14(3)	15(14)	22(40)	8(42)
1706(28)	7(2)	0(9)	51(44)	51(51)

TABLE 4.18: Number of counts for $\gamma - \gamma$ coincidence for selection C (800 keV) for all m_γ events. Significant (such as $> 2\sigma$) coincidences are highlighted in blue. The photopeak of interest is highlighted in yellow.

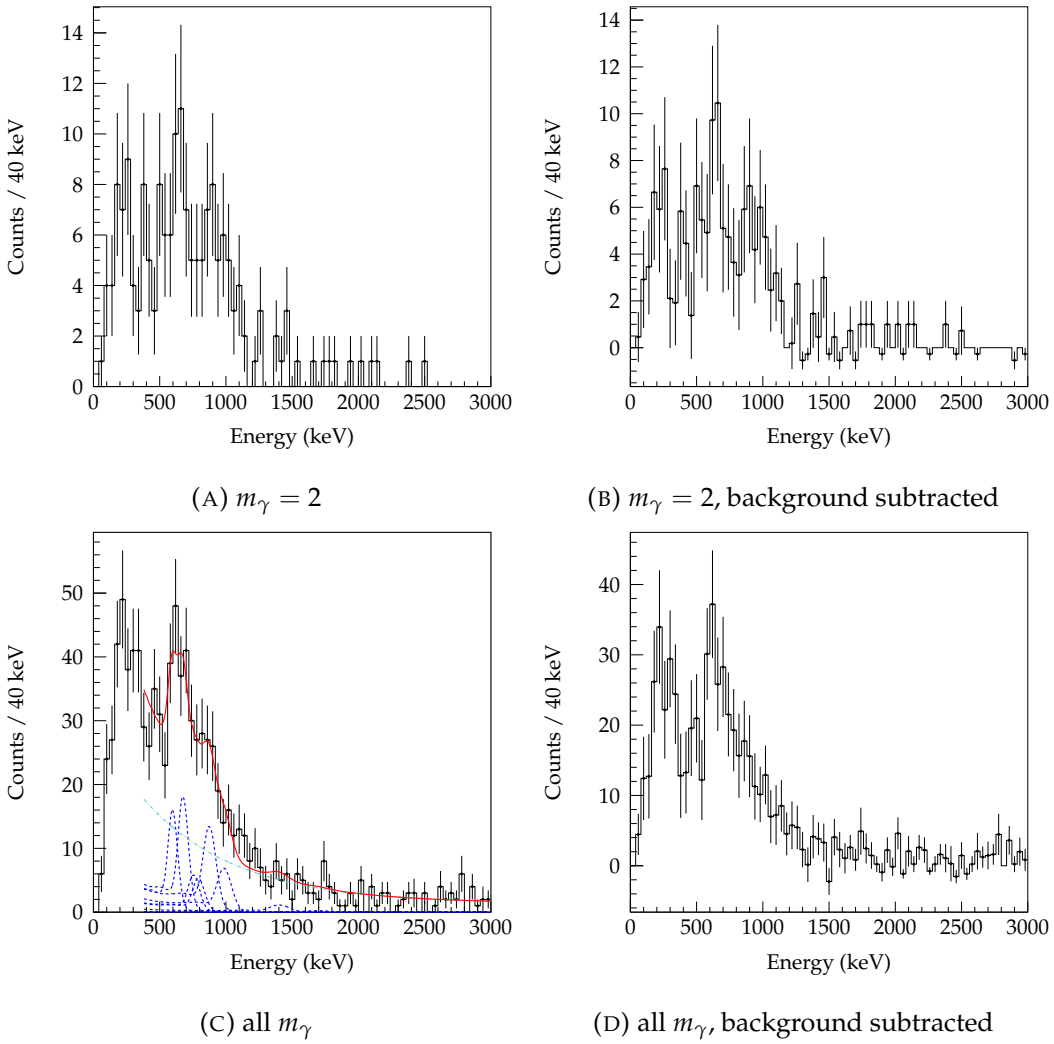

(A) $m_\gamma = 2$

(B) $m_\gamma = 2$, background subtracted

(C) all m_γ

(D) all m_γ, background subtracted

FIGURE 4.23: ^{40}Al(C/C_2H_4,X)^{39}Al selection D: 840 keV to 960 keV (for 883 keV peak)

E_γ (keV)	Selected	Background	Coincidence	Coinc.-Bkg.
415⋆	0	13(15)	0(11)	-13(19)
604(8)	0	0(10)	130(48)	130(50)
683(10)	0	37(16)	157(48)	121(57)
764	0(1)	0(10)	59(91)	60(92)
800	80(7)	16(18)	57(99)	41(101)
883	308(30)	67(20)	161(57)	94(60)
995	40(12)	0(9)	94(44)	95(45)
1416(24)	16(4)	16(16)	24(35)	8(39)
1706(28)	8(3)	0(10)	7(47)	7(48)

TABLE 4.19: Number of counts for $\gamma - \gamma$ coincidence for selection D (883 keV) for all m_γ events. Significant (such as $> 2\sigma$) coincidences are highlighted in blue. The photopeak of interest is highlighted in yellow.

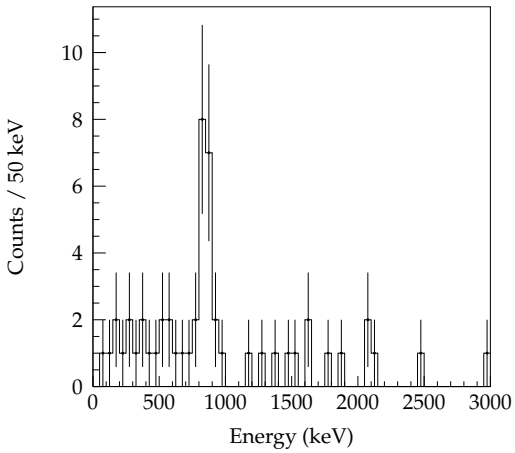

(A) $m_\gamma = 2$

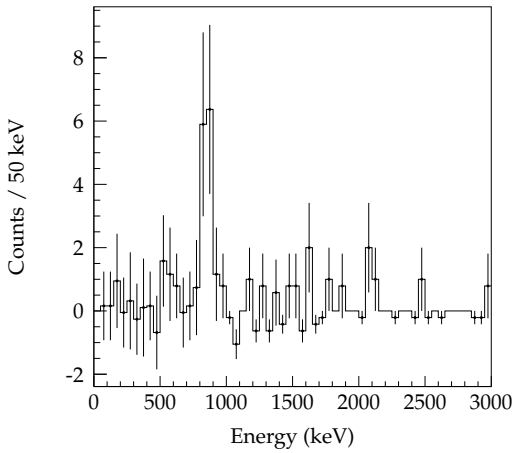

(B) $m_\gamma = 2$, background subtracted

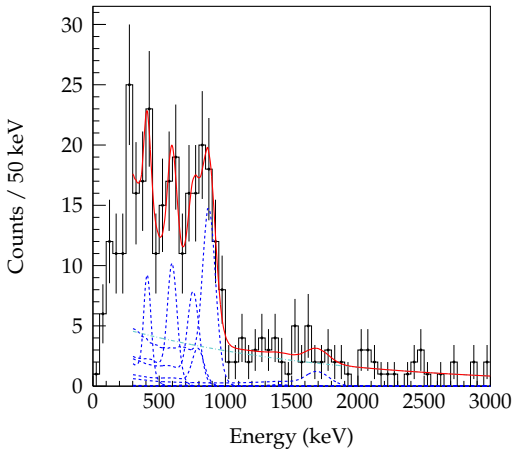

(C) all m_γ

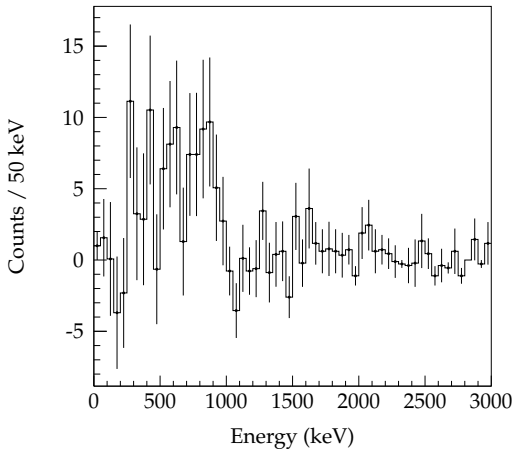

(D) all m_γ, background subtracted

FIGURE 4.24: ^{40}Al(C/C_2H_4,X)^{39}Al selection E: 1000 keV to 1100 keV (for 995 keV peak)

E_γ (keV)	Selected	Background	Coincidence	Coinc.-Bkg.
415⋆	0	9(11)	44(19)	34(22)
604(8)	0	0(7)	66(22)	66(23)
683(10)	0	26(12)	0(13)	-26(17)
764	0	0(7)	65(25)	65(26)
800	0	11(13)	26(26)	15(29)
883	6.0(6)	48(14)	142(29)	94(32)
995	44(11)	0(6)	0(20)	0(20)
1416(24)	16(4)	11(11)	2(73)	-9(74)
1706(28)	7(2)	0(7)	27(21)	27(22)

TABLE 4.20: Number of counts for $\gamma - \gamma$ coincidence for selection E (995 keV) for all m_γ events. Significant (such as $> 2\sigma$) coincidences are highlighted in blue. The photopeak of interest is highlighted in yellow.

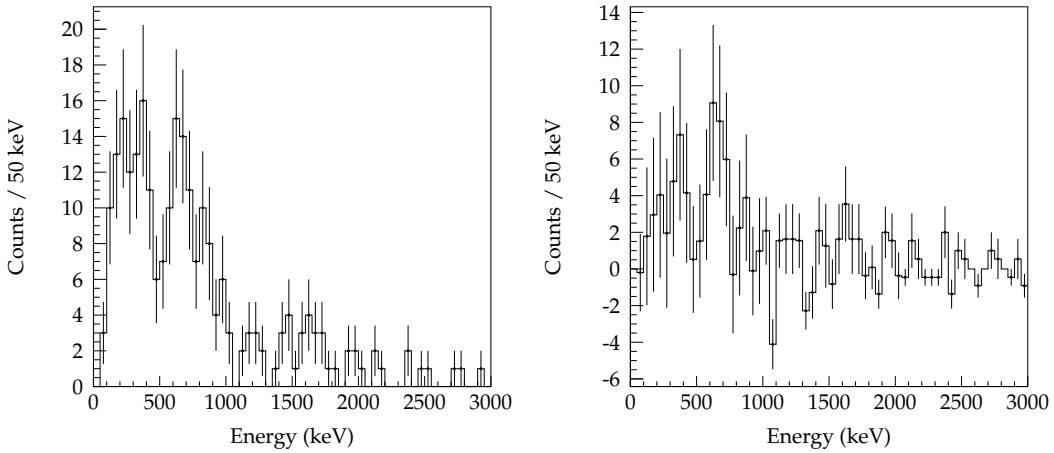

(A) $m_\gamma \leq 3$ (B) $m_\gamma \leq 3$, background subtracted

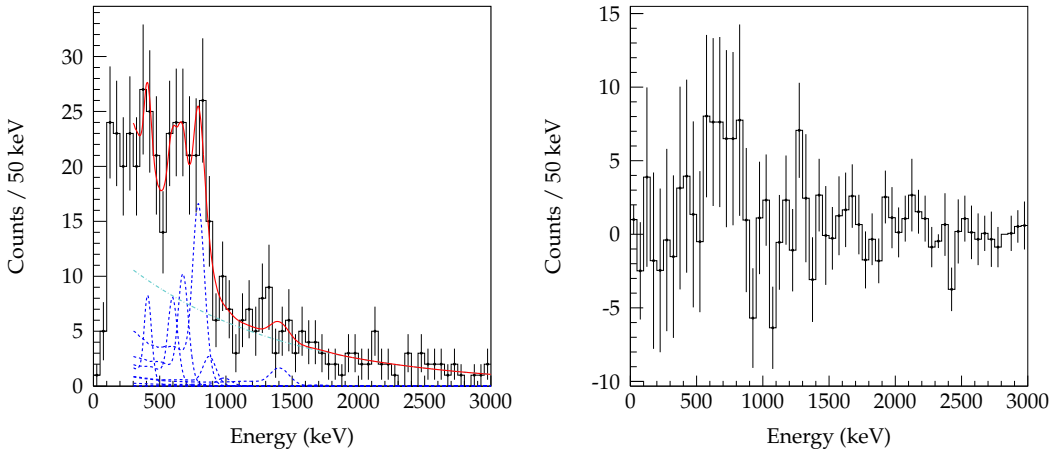

(C) all m_γ (D) all m_γ, background subtracted

FIGURE 4.25: ^{40}Al(C/C_2H_4,X)^{39}Al selection F: 1270 keV to 1500 keV (for 1416 keV peak)

E_γ (keV)	Selected	Background	Coincidence	Coinc.-Bkg.
415⋆	0	16(19)	39(26)	23(32)
604(8)	0	0(12)	52(32)	52(34)
683(10)	0	44(20)	71(30)	27(36)
764	0	0(11)	0(20)	0(23)
800	0	19(22)	143(40)	123(46)
883	0	82(24)	26(34)	-56(42)
995	0	0(11)	8(10)	8(15)
1416(24)	102(25)	19(19)	28(30)	9(36)
1706(28)	22(8)	0(12)	2(37)	2(39)

TABLE 4.21: Number of counts for $\gamma - \gamma$ coincidence for selection F (1416 keV) for all m_γ events. Significant (such as $> 2\sigma$) coincidences are highlighted in blue. The photopeak of interest is highlighted in yellow.

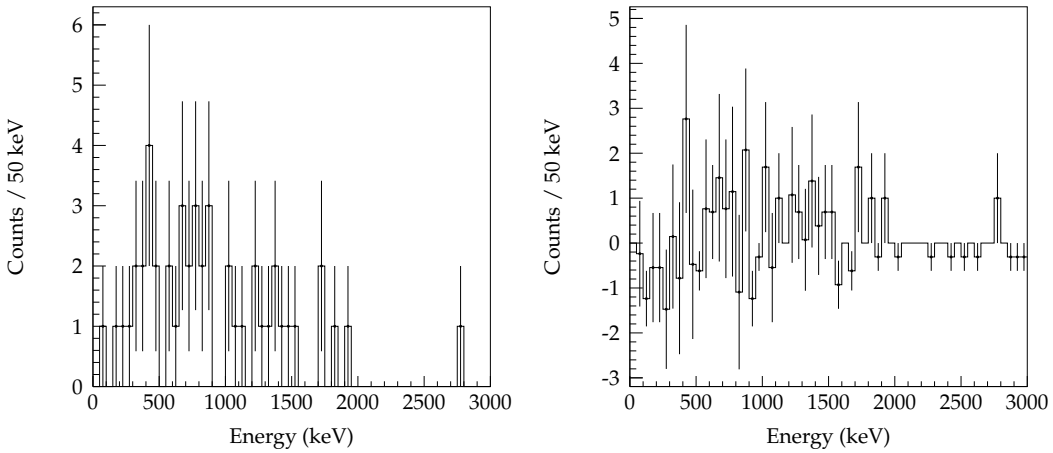

(A) $m_\gamma = 2$

(B) $m_\gamma = 2$, background subtracted

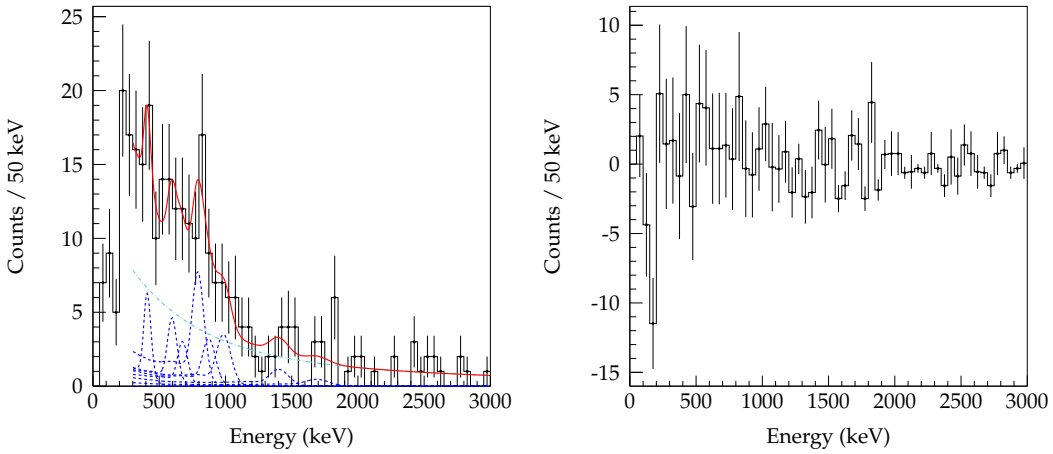

(C) all m_γ

(D) all m_γ, background subtracted

FIGURE 4.26: ^{40}Al(C/C_2H_4,X)^{39}Al selection G: 1600 keV to 1800 keV (for 1706 keV peak)

E_γ (keV)	Selected	Background	Coincidence	Coinc.-Bkg.
415⋆	0	11(12)	30(26)	19(28)
604(8)	0	0(8)	30(27)	30(28)
683(10)	0	29(13)	21(23)	-9(27)
764	0	0(8)	0(20)	0(21)
800	0	13(15)	66(33)	54(36)
883	0	54(16)	31(30)	-23(34)
995	0	0(7)	39(27)	39(28)
1416(24)	0	13(12)	19(23)	7(26)
1706(28)	50(17)	0(8)	20(32)	10(33)

TABLE 4.22: Number of counts for $\gamma - \gamma$ coincidence for selection G (1416 keV) for all m_γ events. Significant ($> 2\sigma$) coincidences are highlighted in blue. The photopeak of interest is highlighted in yellow.

Summary The multiplet around 800 keV can be attributed to transitions directly to the ground state by a few arguments. Firstly, these transitions are the only observed transitions in inelastic scattering and also observed strongly by the proton knockout reaction mechanism of Stroberg et al. (2014) [156]. The fitting of the inelastic spectrum with two photopeaks nearly reproduces the 764 keV and the 800 keV transitions within uncertainties. Secondly, these transitions have the strongest intensities. The lowest energy excited states decaying directly to the ground state can be fed by one or more higher energy states, thereby increasing this transition intensity. However, the strong overlap between potentially a 764 keV transition and the 800 keV transition would alter the calculated yields presented in table 4.14 and 4.15.

The interpretation of the coincidence results is not fully unambiguous. However, the strongest coincidences observed are those between 995 keV and 883 keV. In addition, the enhancement of the 995 keV and 883 keV coincidence at $m_\gamma = 2$ suggests a direct cascade with no intermediary transitions within the DALI γ-ray sensitivity range[5]. The 995 keV transition also appears to be coincident with lower transitions of around 600 keV and potentially weakly: 415 keV and around 300 keV.

The coincidence spectra of 883 keV shows indication of a 995 keV photopeak in $m_\gamma = 2$ spectra Fig. 4.23a 4.23b. Also in the coincidence spectra of 883 keV is a peak or peaks around 650 keV, it is not clear if this is the same photopeak observed in coincidence with the 995 keV transition as mentioned earlier.

In coincidence with the strong 800 keV transition is the 604 keV photopeak. There is an increased intensity for the 883 keV transition and 995 keV transitions, however it is difficult to draw a strong conclusion as the gate of 740 keV to 840 keV includes a portion of the Compton continuum of higher γ-rays, such as 883 keV and 995 keV which may be coincidence with each other.

For the coincidence spectra of 604 keV and 683 keV each appears coincident with a different 800 keV multiplet. The 604 keV and 800 keV are coincident with eachother, and the 683 keV and 883 keV are similarly coincident. It is interesting to note that under the reverse assignment, the sum would be the nearly equivalent.

The 1416 keV coincidence spectra possess a moderate photopeak around 650 keV for $m_\gamma = 2$ events. For all m_γ, the photopeak of 800 keV is pronounced, however, the background subtracted spectrum contains large uncertainties. Potentially the 1416 keV transitions sits above a 650 keV transition, which itself is above a 800 keV transition to the ground state. Or potentially the 1416 keV is directly to the ground state. Conversely, in the coincidence spectra gated on 800 keV, there is only a weak intensity in the area around 1416 keV.

The statistics in the case of 1706 keV coincidence spectra is poor, and therefore difficult to draw a conclusion. With greater statistics an assignment, such as directly feeding the ground state, may have been possible.

A large source of uncertainty is number of transitions within the multiplets of 600 keV and 800 keV. For example, the 604 keV photopeak may be degenerate as the transition appears in coincidences with both 995 keV and 800 keV, yet both do not show coincidence with each other. Also, the assumption of a triplet around 800 keV may not be correct, and one or more states may exist in this region.

Only the clearest coincidences are considered tentative, owing to the large statistical and systematic uncertainties. They are used to build the level scheme in Fig. 4.27. A table of all transitions is presented in table 4.23, with the suggested transitions and coincidences identified with star. Systematic uncertainty from beam velocity (section 3.4.4) and energy calibration (3.4.1.1) are shown.

[5]Very roughly, on the order of 150 keV to 3000 keV for practical efficiency

In many of the coincidence spectra, such as selections A though D, a large intensity appears around 250 keV and represents several transitions, given the larger than expected photo peak width. It is not possible to robustly fit due to the low statistics and the low energy shoulder of the background which cannot be reproduced rigorously. These transitions feeding the levels of 1404 keV and 1566 keV, as shown in Fig. 4.27, are shown as a possible scheme.

TABLE 4.23: ^{39}Al experimental transitions and coincidences. Systematic uncertainty from beam velocity and energy calibration. Values with stars are suggestive.

E_γ (keV)	Yield/100 ions[1]	Coincidence
250⋆[2]		
415⋆		
$604(8)_{stat.}(5)_{syst.}$	14(2)	800 & 250⋆
$683(10)_{stat.}(5)_{syst.}$	11(2)	883 & 250⋆
764(8)[3,4]	0(3)[3]	
800(8)[4]	27(3)	604 & 250⋆
883(8)[4]	25(2)	683 & 250⋆
995(8)[4]	7(2)	883
$1416(24)_{stat.}(5)_{syst.}$	9(2)	
$1706(28)_{stat.}(5)_{syst.}$	6(2)	

[1] Yield determined through fit of γ-ray energy spectrum with all m_γ and add-back.
[2] Several transitions at around this energy.
[3] Not directly observed.
[4] Observed but transition energy and uncertainty from literature [156].

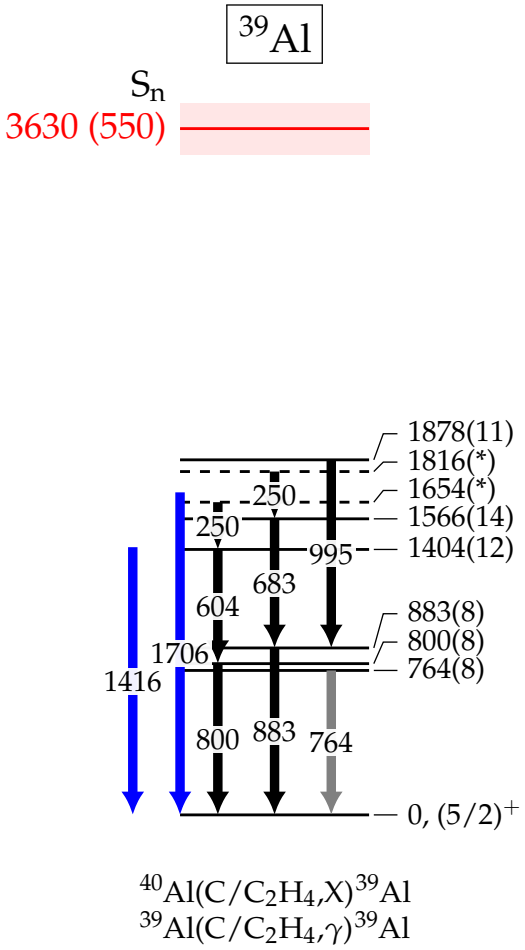

FIGURE 4.27: Experimental transitions and tentative level scheme of ^{39}Al. Black arrows represent transitions with tentative assignment based on coincidences. Blue arrow shows transition from singles spectra without coincidences. Grey arrow is an unobserved transition, but observed in a similar knockout reaction from [156] employing high resolution HPGe detectors. The neutron separation energy of 3630(550) keV [27] is shown in red. The uncertainty of the extrapolated neutron separation is shown as the level width.

4.3 ^{40}Al

4.3.1 ^{40}Al(C/C_2H_4,γ)^{40}Al

4.3.1.1 γ-ray analysis

TABLE 4.24: ^{40}Al(C/C_2H_4,X)^{40}Al γ-ray reconstruction settings

Setting		Velocity (MeV u^{-1} / β)		Beam at target (cm)			
Target	ZD $B\rho$	mid-point target	before target	X	fwmh	Y	fwhm
C	^{41}Al	224.5 / 0.5920	254.3 / 0.6188	-0.2	0.8	0	1.1
C_2H_4	^{41}Al	218.0 / 0.5463					
C	^{40}Mg	232.3 / 0.5993	261.5 / 0.6248				
C_2H_4	^{40}Mg	226.0 / 0.5564					

Average interaction points calculated from GEANT4 simulation of 800 keV γ-rays.

The Doppler reconstructed γ spectrum of inelastic scattered of ^{40}Al is presented in Fig. 4.28 for both targets separately. There is no strong evidence for a peak structures for the energy histogram including all detectors. The statistics are too low to observe $\gamma - \gamma$ coincidences.

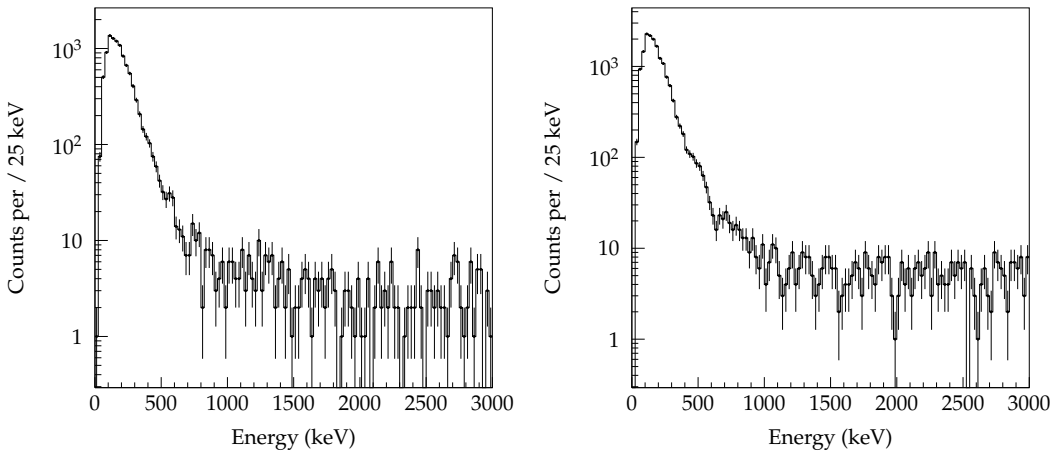

(A) C target, $m_\gamma \leq 4$ (B) C_2H_4 target, $m_\gamma \leq 4$

FIGURE 4.28: Inelastic scattering of ^{40}Al doppler reconstructed γ-ray energy spectrum, $m_\gamma \leq 4$, and with add-back

Through the selection of only forward detectors, which detect the most boosted in-flight emitted γ-rays, the low energy background from atomic processes can be suppressed. Shown in Fig. 4.29a is γ-ray energy as a function of detector number with add-back. The detector ID numbers roughly transition from backward angles to forward angles. The forward angle detectors above number 130 are chosen (42.5 to 20.5 degrees), displayed as a red line. The reconstructed γ-ray spectrum with this forward detector selection is presented in Fig. 4.29b. Two photopeaks can be fitted with the DALI response functions and double exponential background. The fitting region is 200 keV to 2000 keV, although not completely displayed.

The peak centroids correspond to 379(10) keV and 504(7) keV. For events $m_\gamma = 1$, the lower energy peak cannot be fit. The yield as a function of event maximum γ-ray multiplicity is presented in Fig. 4.30. The yield for the 504(7) keV transition

is close to flat, while the 379(10) keV transition increases with event maximum γ-ray multiplicity. The stable trend for the higher energy transition is significant, as a cascade of this transition to another excited state and then to the ground state would result in a drop towards events with $m_\gamma = 1$. Or, the reverse with this transition directly to the ground state as part of a cascade. Therefore, the 504(7) keV transition depopulates to the ground state with direct population in the reaction.

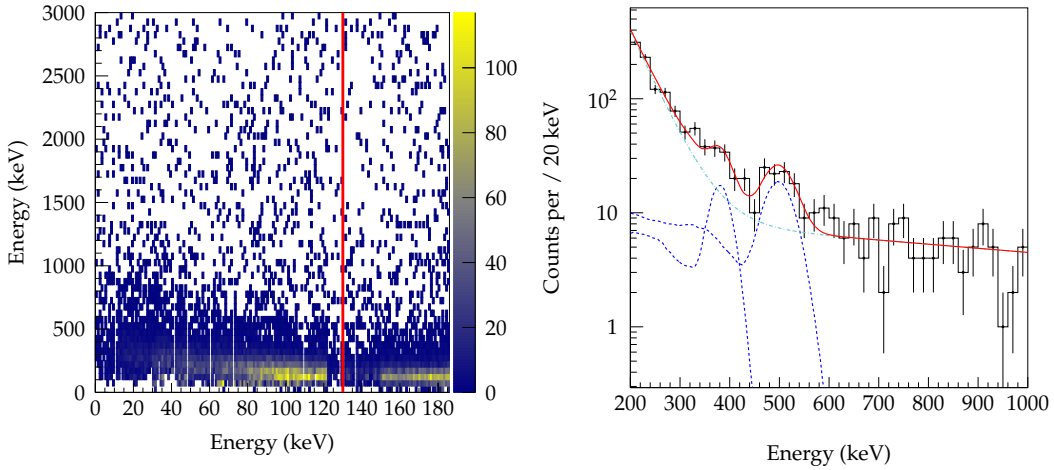

(A) all m_γ (B) all m_γ with forward detectors

FIGURE 4.29: Inelastic scattering of ^{40}Al with forward DALI detectors (detector ID number greater than 130) with add-back

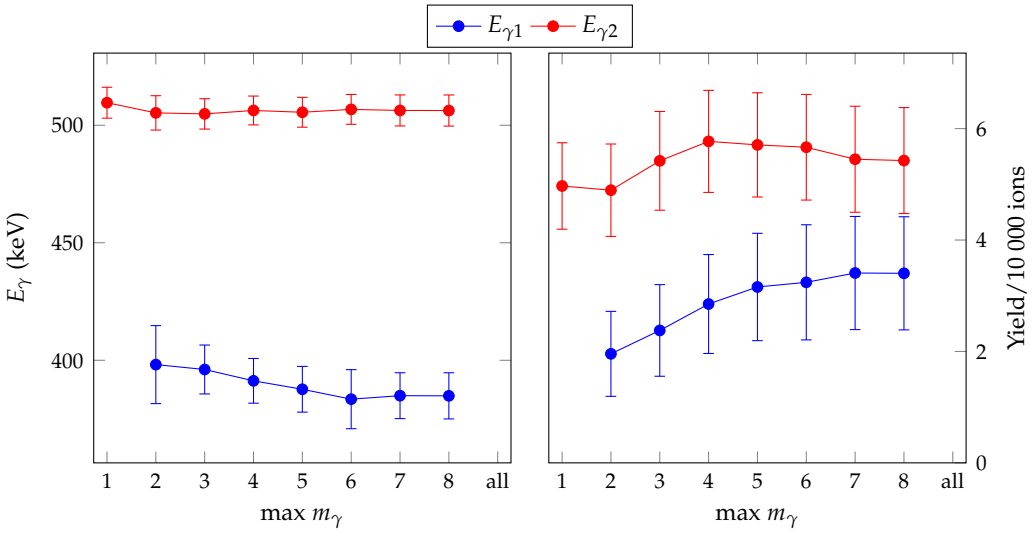

FIGURE 4.30: Summary of fit results of ^{40}Al inelastic scattering with forward DALI detectors (detector number > 130) with add-back

4.3.2 ^{41}Si(C/C_2H_4,X)^{40}Al and ^{41}Al(C/C_2H_4,X)^{40}Al

4.3.2.1 Reaction summary and inclusive cross section

TABLE 4.25: Summary of ^{41}Si(C/C_2H_4,X)^{40}Al and cross section

Setting			within ZeroDegree full momentum acceptance		
Target	ZD $B\rho$	Total reactions	Reactions	Projectiles	Inclusive cross section (mb)
C	^{41}Al	21	20	21678	5.5(1.8)
C_2H_4	^{41}Al	16	11	10665	11.5(2.8)
C	^{40}Mg	167	108	99662	3.2(5)
C_2H_4	^{40}Mg	496	182	202078	11.2(1.4)

TABLE 4.26: Summary of ^{41}Al(C/C_2H_4,X)^{40}Al and cross section

Setting			within ZeroDegree full momentum acceptance		
Target	ZD $B\rho$	Total reactions	Reactions	Projectiles	Inclusive cross section (mb)
C	^{41}Al	164	146	21395	36.7(4.8)
C_2H_4	^{41}Al	72	57	6439	110(18)
C	^{40}Mg	246	139	29330	25.5(3.4)
C_2H_4	^{40}Mg	1106	344	50093	85.7(9.8)

The inclusive cross sections for both targets and both ZeroDegree magnetic rigidity settings are in good agreement for the proton knockout reaction ^{41}Si(C/C_2H_4,X)^{40}Al. In the case of the neutron knockout ^{41}Al(C/C_2H_4,X)^{40}Al discrepancy between ZeroDegree magnetic rigidity settings is nearly out of uncertainties. This may be due to the underestimation of systematic uncertainties, which may contribute strongly at low statistics. Some cropping of the events by a $F5X$ and $F5A$ selection is necessary in all cases, as the reaction residue beam of ^{40}Al after the F8 reaction target is off-centred with respect to F9X and therefore a portion of the secondary beam falls over the edge of full ZeroDegree acceptance.

4.3.2.2 γ-ray analysis

TABLE 4.27: ^{41}Si(C/C_2H_4,X)^{40}Al γ-ray reconstruction settings

Setting		Velocity (MeV u^{-1} / β)		Beam at target (cm)			
Target	ZD $B\rho$	mid-point target	before target	X	fwmh	Y	fwhm
C	^{41}Al	227.1 / 0.5945	260.9 / 0.6243	-0.6	1.0	-0.1	0.9
C_2H_4	^{41}Al	219.7 / 0.5875					
C	^{40}Mg	227.5 / 0.5949	261.3 / 0.6246				
C_2H_4	^{40}Mg	220.2 / 0.5880					

Average interaction points calculated from GEANT4 simulation of 500 keV γ-rays.

TABLE 4.28: ^{41}Al(C/C_2H_4,X)^{40}Al γ-ray reconstruction settings

Setting		Velocity (MeV u^{-1} / β)		Beam at target (cm)			
Target	ZD $B\rho$	mid-point target	before target	X	fwmh	Y	fwhm
C	^{41}Al	215.1 / 0.5830	245.3 / 0.6111	-0.2	0.8	-0.2	1.3
C_2H_4	^{41}Al	208.5 / 0.5764					
C	^{40}Mg	224.8 / 0.5924	254.1 / 0.6187				
C_2H_4	^{40}Mg	218.5 / 0.5863					

Average interaction points calculated from GEANT4 simulation of 500 keV γ-rays.

The parameters for γ-ray reconstruction are presented in table 4.27 and 4.28. The results of one proton and neutron knockout are presented in 4.31. The close proximity of photopeaks to the effective DALI cut-off energy (product of Pb shield and CFD thresholds) poses difficulties for spectrum fitting. The previously used background function of a double exponential does not faithfully reproduce the background across the complete spectra.

The γ-ray spectrum from the inelastic channel, largely consisting of a background from atomic processes from within the target, would be used as a background for subsequent fits of knockout reaction γ-ray spectra. However, although the lowest energy region (cut-off) shape matches well, the inelastic spectrum falls offs at a higher rate with increasing energy. Fitting the proton and neutron knockout spectra with such a background function results in a poor fit. Convolution of the inelastic spectrum with an analytical function (such as an exponential with a transition or cut-off) is a possible solution to modify the higher energy slope of the background, but increases the background parameter space.

Alternatively, a double exponential function convoluted with a Gauss error function can duplicate the low energy shoulder. The functional form,

$$(1 - \mathrm{erf}(\frac{a-x}{b}))(\exp(c+dx) + \exp(e+fx)) \tag{4.4}$$

is employed as alternative to the inelastic reaction γ-ray spectrum or double exponential, for fitting the background for both knockout reactions to ^{40}Al γ-ray spectra. The applicability of this function is demonstrated through fitting the inelastic spectrum of ^{40}Al(C/C_2H_4,γ)^{40}Al, as shown in Fig. 4.31f. To reduce the number of background function parameters, the parameters of the cut-off (slope b and cut-off position a) are established with a fit with the inelastic reaction γ-ray spectrum (Fig. 4.31f)

In a similar fashion as the previous analysis, the number of photopeaks is evaluated in the fitting procedure. The proton and neutron knockout spectrum are furthermore fitted individually and the spectra from both targets combined. Confirmation of a transition in both spectra provides greater significance, and moreover, both reactions will preferentially populate different excited states. Fits with between two and seven DALI response functions for the neutron knockout reaction (^{41}Al(C/C_2H_4,X)^{40}Al) are presented in Fig. 4.32 and 4.33. Similarly, the proton knockout reaction (^{40}Al(C/C_2H_4,γ)^{40}Al) γ spectrum fits are presented in 4.34.

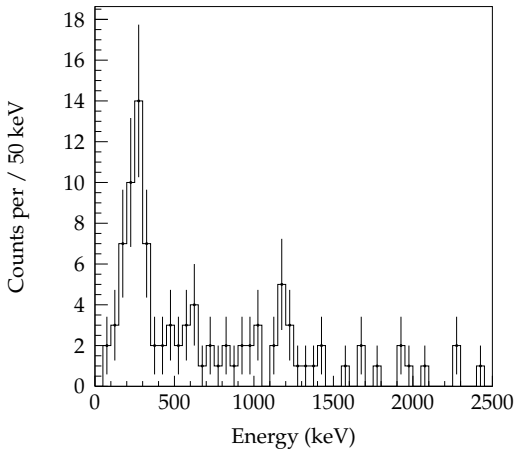

(A) ^{41}Si(C,X)^{40}Al

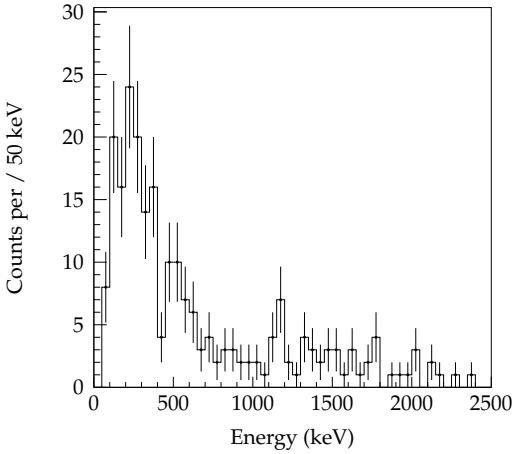

(B) ^{41}Si(C_2H_4,X)^{40}Al

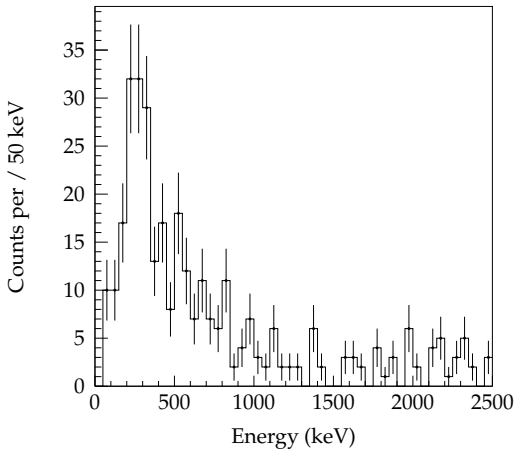

(C) ^{41}Al(C,X)^{40}Al

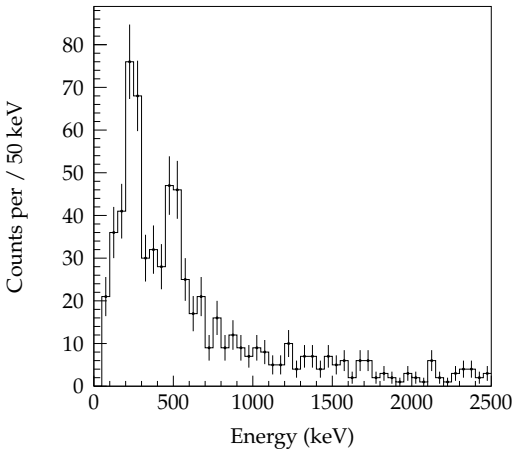

(D) ^{41}Al(C_2H_4,X)^{40}Al

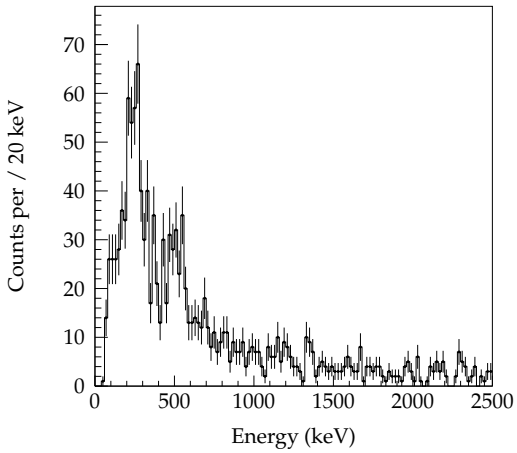

(E) ^{41}Si/^{41}Al(C/C_2H_4,X)^{40}Al combined

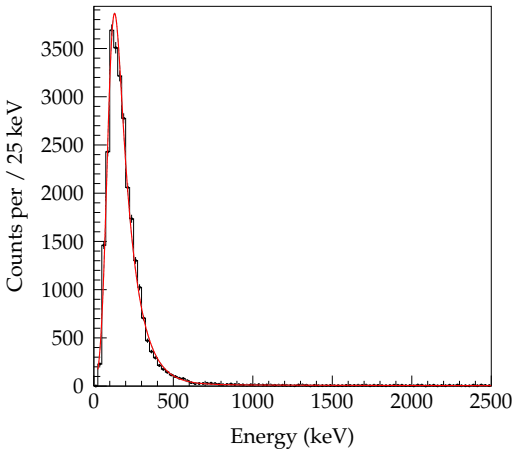

(F) ^{40}Al(C/C_2H_4,X)^{40}Al demonstration fit

FIGURE 4.31: ^{41}Si/^{41}Al(C/C_2H_4,X)^{40}Al Doppler reconstructed γ-ray energy spectra, all m_γ, and with add-back

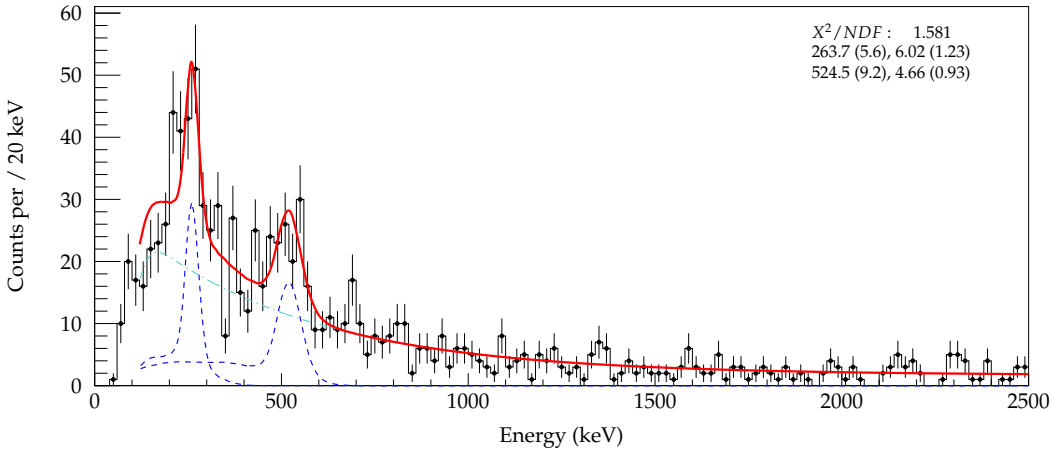

(A) Two peaks, all m_γ

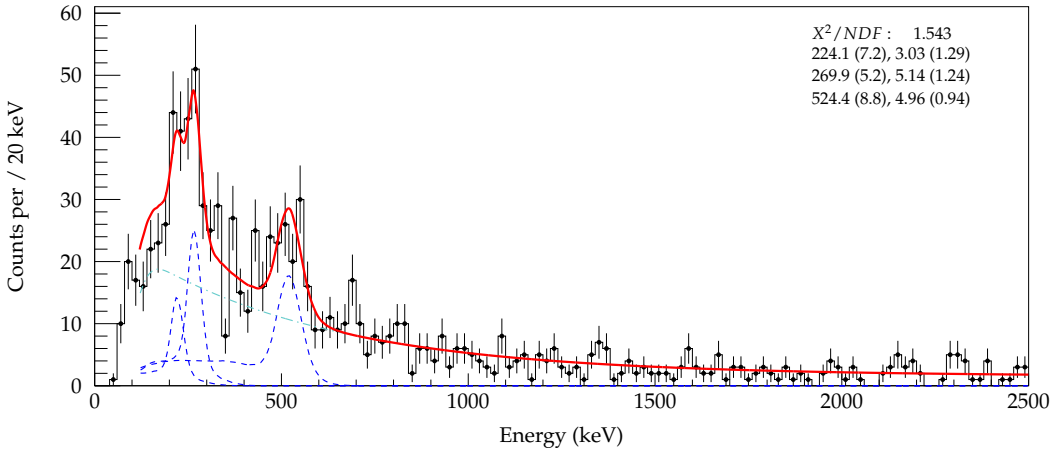

(B) Three peaks, all m_γ

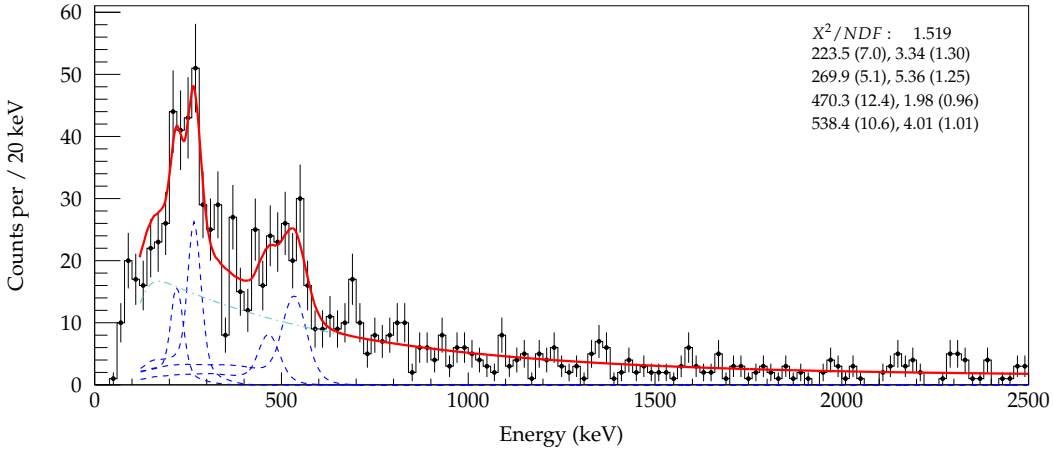

(C) Four peaks, all m_γ

FIGURE 4.32: Fitting 2, 3, 4 peaks of ^{41}Al(C/C_2H_4,X)^{40}Al doppler reconstructed γ-ray energy spectrum, all m_γ, and with add-back

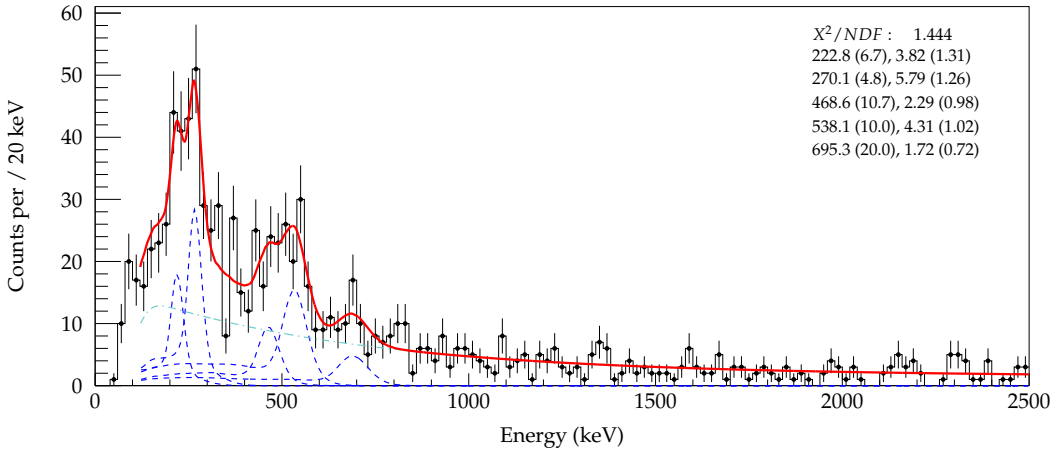

(A) Five peaks, all m_γ

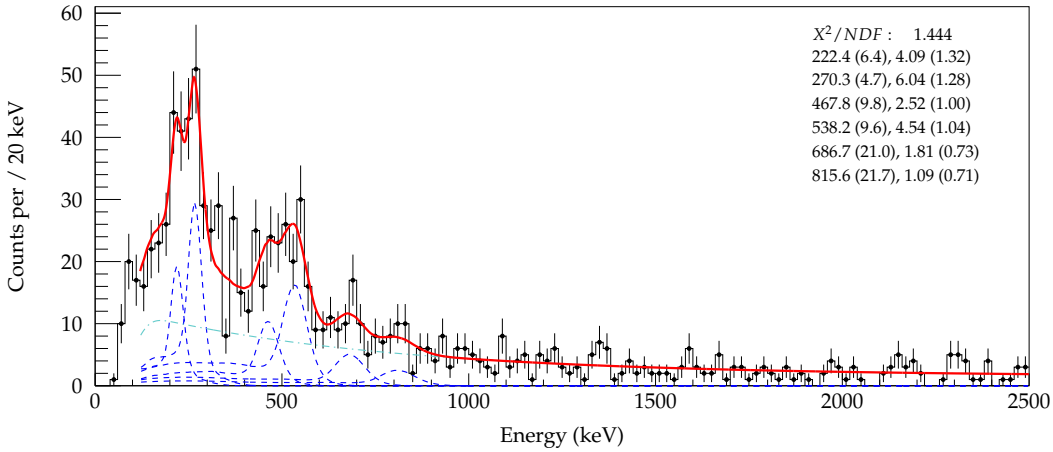

(B) Six peaks, all m_γ

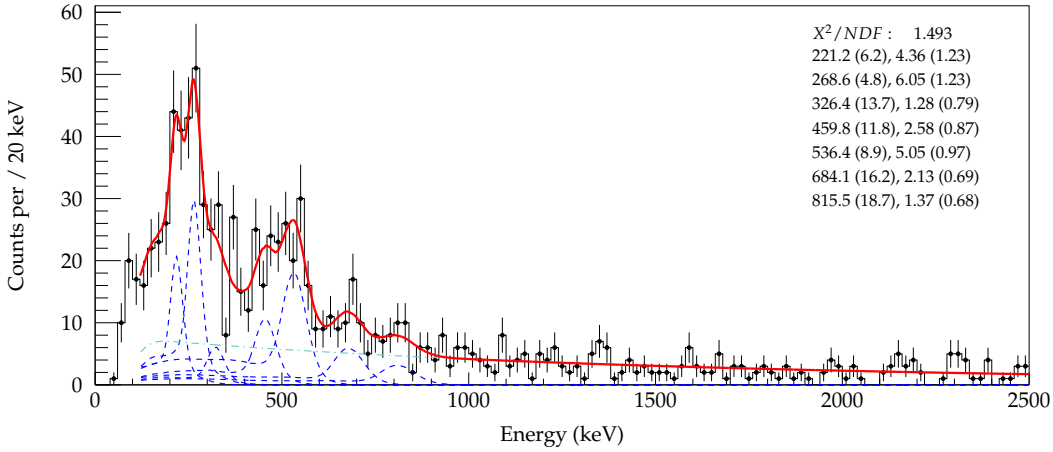

(C) Seven peaks, all m_γ

FIGURE 4.33: Fitting 4, 5, 6 peaks of ^{41}Al(C/C_2H_4,X)^{40}Al doppler reconstructed γ-ray energy spectrum, all m_γ, and with add-back

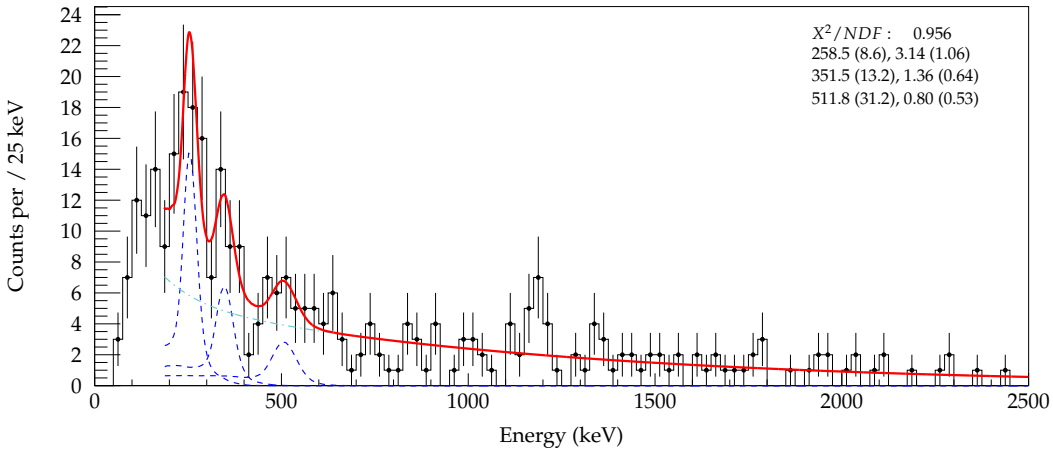

(A) Three peaks, all m_γ

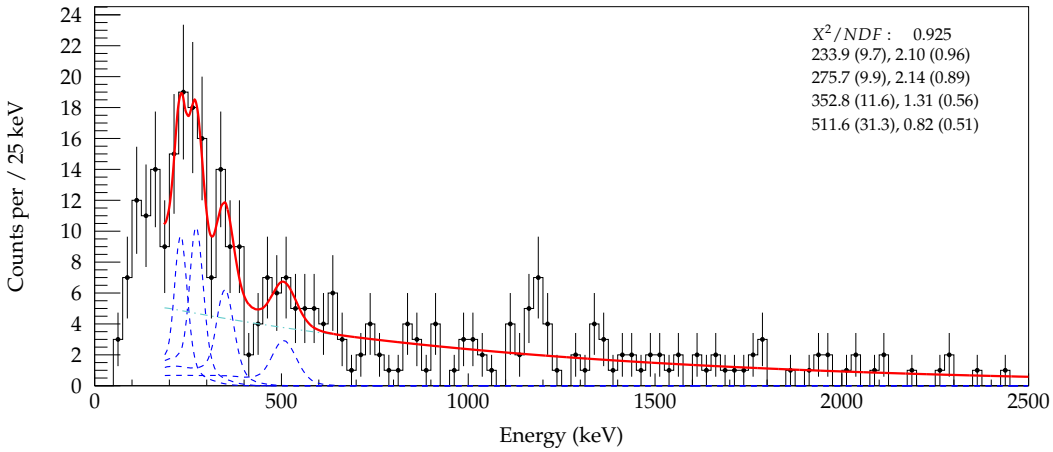

(B) Four peaks, all m_γ

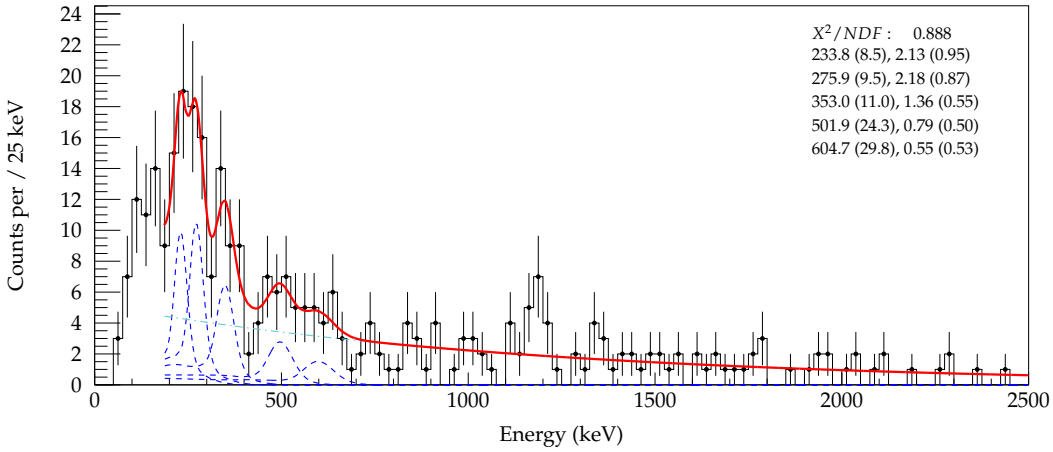

(C) Five peaks, all m_γ

FIGURE 4.34: Fitting 3, 4, 5 peaks of $^{41}Si(C/C_2H_4,X)^{40}Al$ doppler reconstructed γ-ray energy spectrum, all m_γ, and with add-back

Lastly, for the ^{41}Si(C/C_2H_4,X)^{40}Al reaction, an excess of counts can be fit at 1186(21) keV. Fitting convergence can only be achieved with five DALI response functions of the previous figure 4.34c. Alternatively, a partial fit of the experimental γ-ray spectrum can be accomplished with only one response function, as displayed in figure 4.35b. The scaling factor from the fit is 2σ, therefore this structure can be assigned as a tentative transition. Observing the alternative ^{41}Al(C/C_2H_4,X)^{40}Al reaction, no feature at this energy is clear.

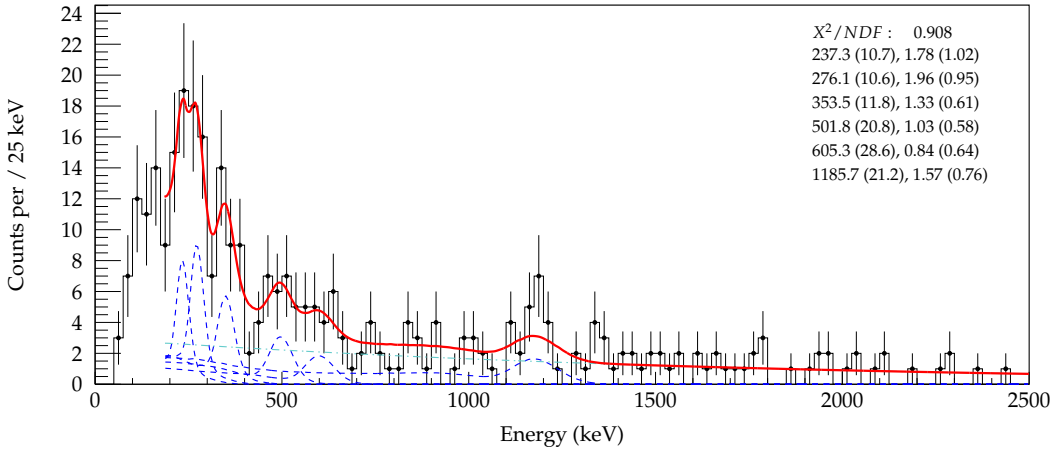

(A) Six peaks, all m_γ

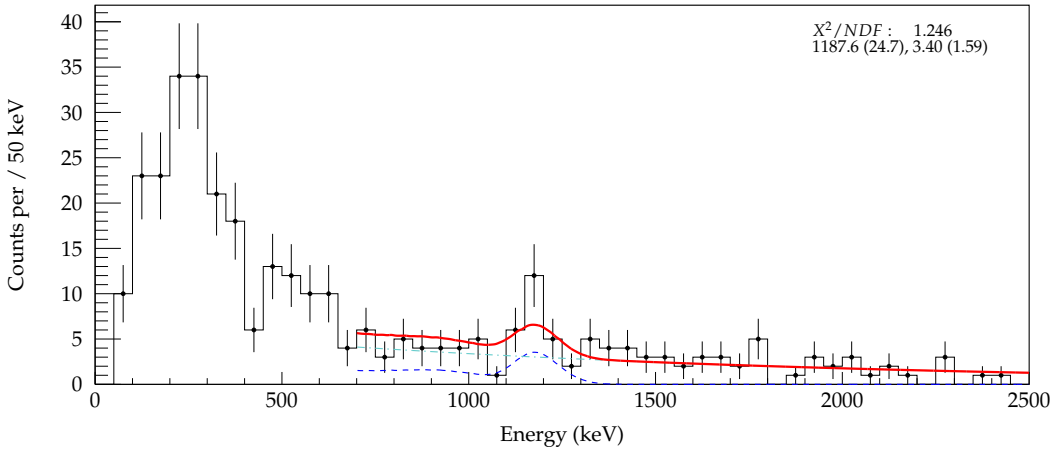

(B) 1200 keV, all m_γ

FIGURE 4.35: Fitting high energy peak of ^{41}Si(C/C_2H_4,X)^{40}Al doppler reconstructed γ-ray energy spectrum, all m_γ, and with add-back

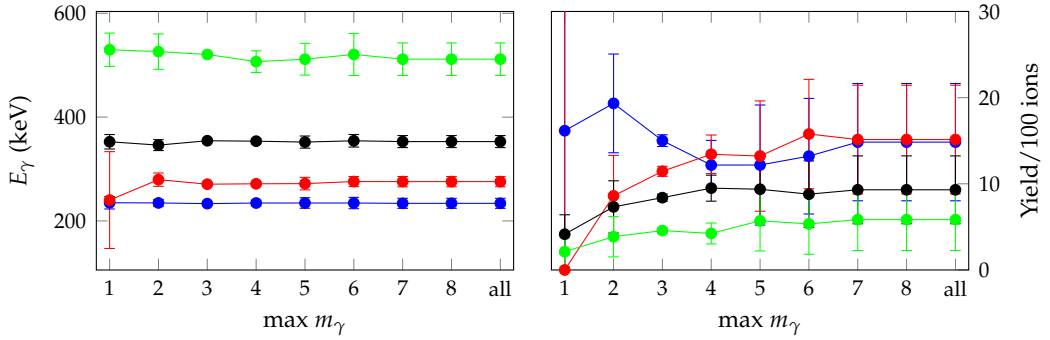

FIGURE 4.36: Summary of fit results of ^{41}Si(C/C_2H_4,X)^{40}Al with 4 DALI response functions

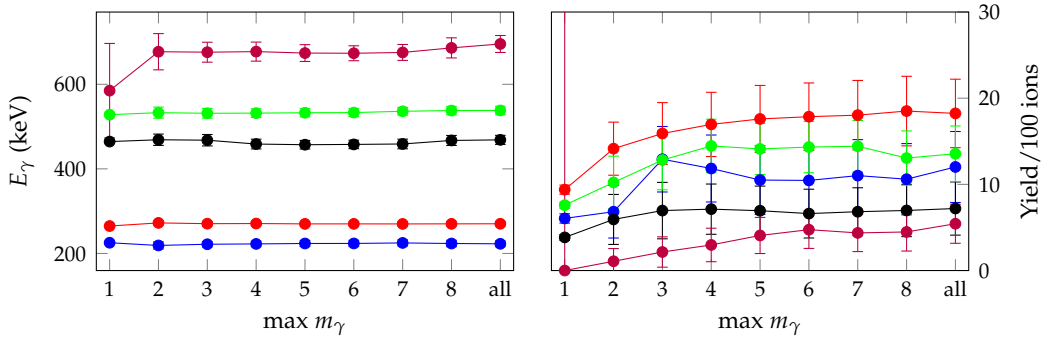

FIGURE 4.37: Summary of fit results of ^{41}Al(C/C_2H_4,X)^{40}Al with 5 DALI response functions

TABLE 4.29: ^{40}Al fit results

TABLE 4.30: ^{41}Al(C/C_2H_4,X)^{40}Al

E_γ (keV)	Yield/100 ions
223(8)	12(4)
270(5)	18(4)
465(10)	7(3)
532(10)	14(3)
685(23)	5(2)

TABLE 4.31: ^{41}Si(C/C_2H_4,X)^{40}Al

E_γ (keV)	Yield/100 ions
233(10)	12(5)
276(10)	12(5)
353(12)	7(3)
516(32)	5(3)
1186 (21)	9(4)

Fit summary Five and four response DALI functions fit to the γ-ray energy spectra of the neutron and proton knockout reactions, respectively, are found to be optimal (table 4.29) from the fitting criteria. Additional transitions beyond this number does not convincingly improve the fit and the scaling factor of the additional response functions does not achieve the requirement of greater than 2.5σ. The yield for each transition was determined through fits with all m_γ and add-back.

The response function centroid (energy) and yield for fitted transitions as a function of maximum event multiplicity m_γ are presented graphically in Fig. 4.36 and 4.37. Most fitted centroids are within fit uncertainties.

For both neutron and proton knockout reactions, similar low energy transitions are observed. The 223(8) keV and 233(10) keV transitions as well as the 270(5) keV and 276(10) keV transitions as part of observed doublets in both reactions, fall within

uncertainties. The motivation for the treatment of this large peak as a doublet is the greater than expected peak width and poor fitting with only one response function, such as Fig. 4.34a. However, the failure to clearly resolve the individual peaks leaves opens the possibility of a triplet and further transitions in this region.

Furthermore, the 532(10) keV and 516(32) keV transitions in both reaction spectra may additionally be the same transition. A lower energy transition of 465(10) keV can be fit in the neutron knockout reaction spectrum, due to the large peak width and is not required in the proton knockout reaction spectrum. A photopeak around 350 keV may exist in both reaction spectra, however the criteria of over 2.5σ is only nearly satisfied in the proton knockout reaction. In the combined γ spectrum of Fig. 4.39 this transition is more clearly observed. Lastly, a transition of 685 keV for one neutron knockout, is also identified and at edge of the 2.5σ criteria.

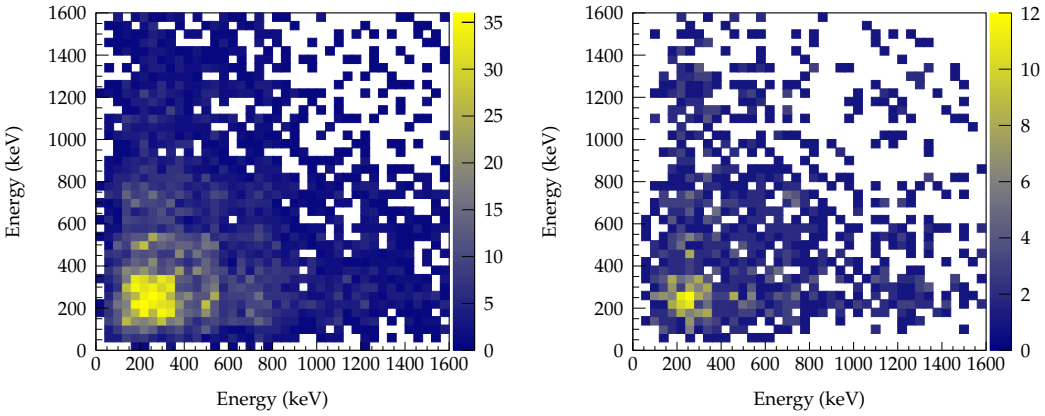

(A) all m_γ (B) all, m_γ, with add-back

FIGURE 4.38: ^{41}Si/^{41}Al(C/C_2H_4,X)^{40}Al γ-γ matrix with and without add-back

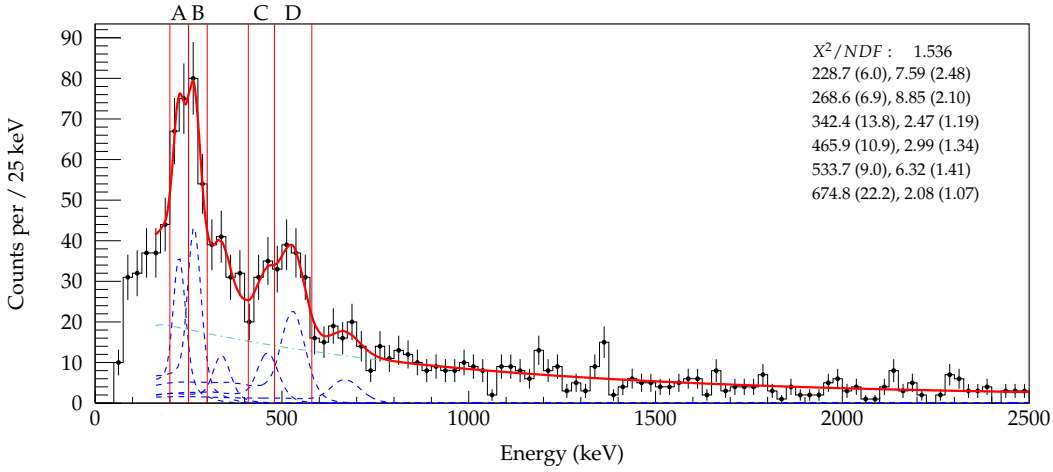

(A) Regions of selection for analysis of γ-γ coincidences, all m_γ

FIGURE 4.39: Selections for ^{41}Si/^{41}Al(C/C_2H_4,X)^{40}Al coincidence analysis, all m_γ, with add-back

γ-γ coincidence The combination of low statistics as well as a high density of states inhibits an in-depth γ-γ coincidence analysis. Another large difficulty is the identification of suitable region for background subtraction. The high density of γ-ray transitions in the energy spectrum, characteristic of odd-odd nuclei in this region, may not permit clean background subtraction.

The coincidence matrix is presented in Fig. 4.38 and shows a strong intensity around 250 keV. Four selections are identified for the highest amplitude photopeaks are shown in Fig. 4.39. The coincidence spectra for these region is presented in Fig. 4.41 and 4.40 without background subtraction. Most evident is the high intensity around 250 keV for both sections A and B. Tentatively, both 223 keV and 270 keV transitions are assigned as being in coincidence, however, as mentioned earlier other transitions cannot be ruled out. The coincidence spectra of sections C and D possess low statistics and are inconclusive.

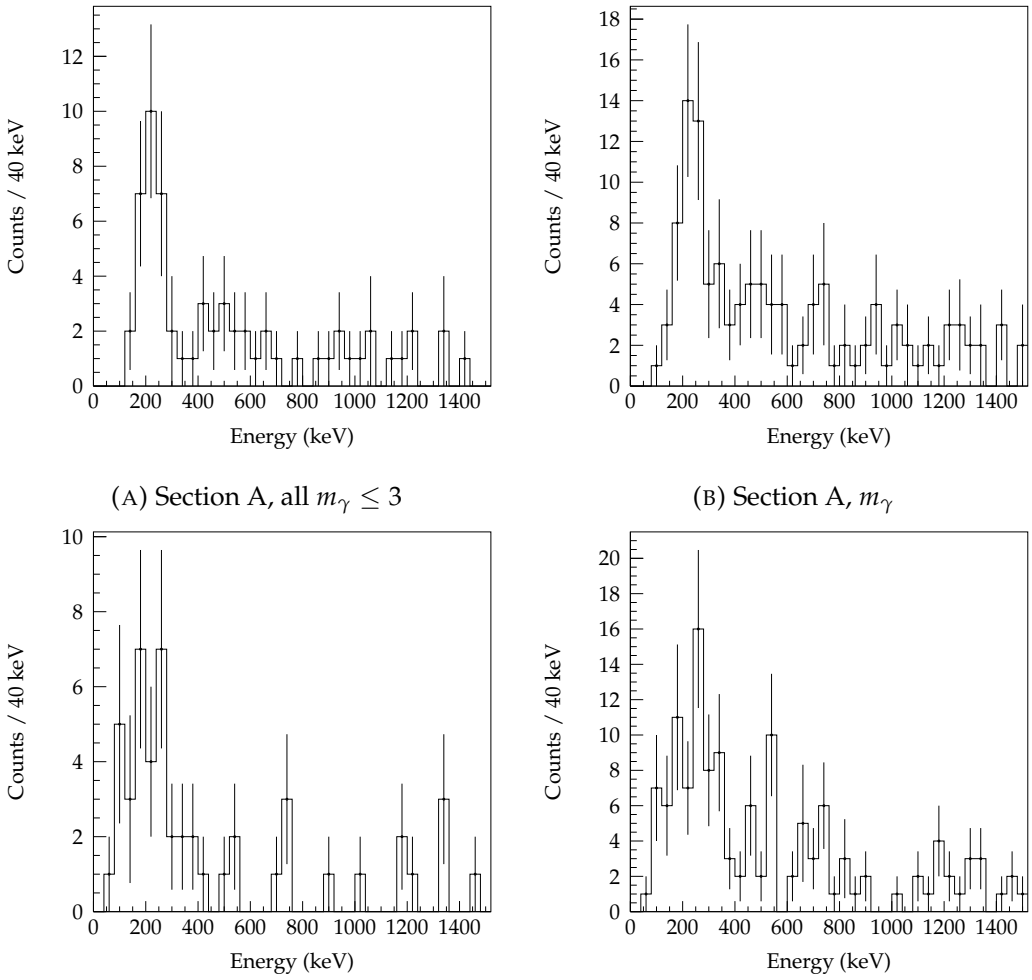

(A) Section A, all $m_\gamma \leq 3$

(B) Section A, m_γ

(C) Section B, $m_\gamma \leq 3$

(D) Section B, all m_γ

FIGURE 4.40: $^{41}Si/^{41}Al(C/C_2H_4,X)^{40}Al$ section A and B

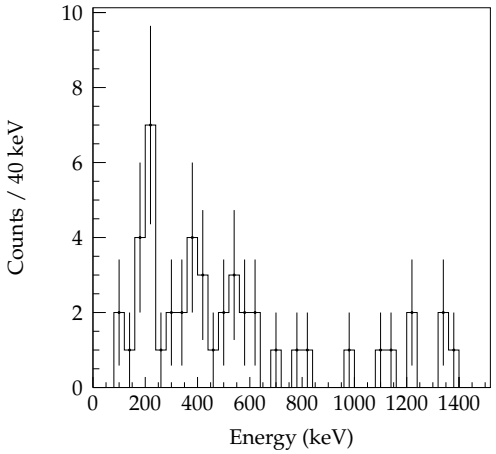

(A) Section C, $m_\gamma \leq 3$

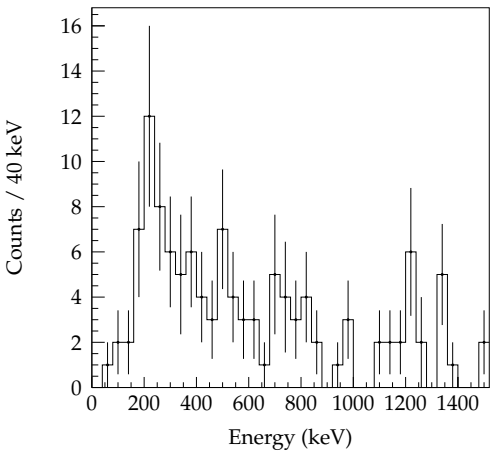

(B) Section C, all m_γ

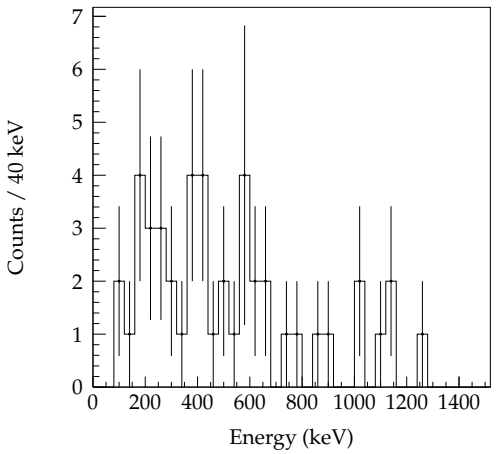

(C) Section D, all $m_\gamma \leq 3$

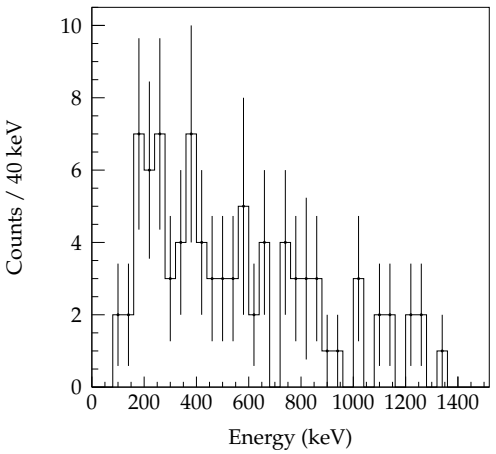

(D) Section D, all m_γ

FIGURE 4.41: ^{41}Si/^{41}Al(C/C_2H_4,X)^{40}Al section C and D

Summary In conclusion, the measured transitions from both knockout reactions can be combined through a weighted average or by a fit of the combined spectra (Fig. 4.39). The results of the summed fit are presented in table 4.32. Systematic uncertainty from beam velocity (section 3.4.4) and energy calibration (3.4.1.1) are shown. Given the poor peak to background of the lower energy 379(10) keV transition observed in inelastic scattering, it is not considered a new tentative transition. The inelastic scattering 504(7) keV transition is tentatively assigned as a new transition as it is outside of the uncertainty of the 533(9) keV transition.

The placement of all transitions within the level scheme of ^{40}Al is not possible under the current observations. The 504(7) keV γ-ray is placed as a transition directly to the ground state, by the argument of high yield for $m_\gamma = 1$. The coincident γ-rays 228(6) keV and 269(7) keV are tentatively placed in a cascade to the ground state given their high intensity. The suggested order of the two transitions is based on the higher intensity of the 269(7) keV transition, however the uncertainties are larger than the difference. Lastly, the deduced excited states energies of 497(9) keV and 504(7) keV fall within uncertainties, however a rejection of γ-ray coincidences cannot be established with the low statistics. The tentative transition at 1186(21) keV observed in the ^{41}Si(C/C_2H_4,X)^{40}Al reaction, likely depopulates directly to the ground state as the extrapolated neutron separation energy of ^{40}Al is 1130(570) keV. Occasionally, gamma decays will compete with proton emission due to hindrance from the Coulomb barrier. A notable example is the decay of the $7/2^+$ state in ^{23}Al [157]. The present case of gamma decay competing with neutron emission is not often observed, and may require a strong angular barrier. No barrier exists in ^{40}Al, as the low occupation of the high neutron $\nu 0g_{9/2}$ orbital is expected.

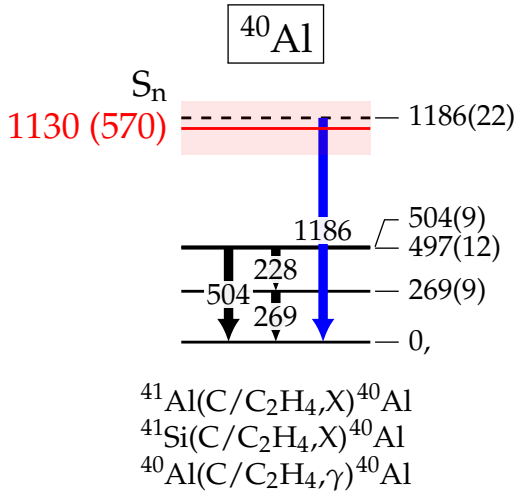

FIGURE 4.42: Experimental transitions and tentative level scheme of ^{40}Al. Blue arrow shows transition from singles spectra without coincidences. The neutron separation energy of 1130(570) keV [27] is shown in red. The uncertainty of the extrapolated neutron separation is shown as the level width.

TABLE 4.32: ^{40}Al experimental transitions and coincidences. All transitions execpt for 1186 keV from fit of the combined ^{41}Si/^{41}Al(C/C_2H_4,X)^{40}Al γ-ray energy spectrum. Systematic uncertainty from beam velocity and energy calibration.

E_γ (keV)	Coincidence
$228(6)_{stat.}(5)_{syst.}$	269
$269(7)_{stat.}(5)_{syst.}$	228
$342(13)_{stat.}(5)_{syst.}$	
$466(11)_{stat.}(5)_{syst.}$	
$504(7)_{stat.}(5)_{syst.}$	
$533(9)_{stat.}(5)_{syst.}$	
$675(22)_{stat.}(5)_{syst.}$	
$1186(21)_{stat.}(5)_{syst.}$	

4.4 ^{41}Al

4.4.1 ^{41}Al(C/C_2H_4,γ)^{41}Al

4.4.1.1 γ-ray analysis

TABLE 4.33: ^{41}Al(C/C_2H_4,X)^{41}Al γ-ray reconstruction settings

Setting		Velocity (MeV u^{-1} / β)		Beam at target (cm)			
Target	ZD $B\rho$	mid-point target	before target	X	fwmh	Y	fwhm
C	^{41}Al	211.3 / 0.5792	241.7 / 0.6078	-0.2	0.8	0	1.1
C_2H_4	^{41}Al	204.7/ 0.5724					
C	^{40}Mg	221.2 / 0.5889	250.8 / 0.6157				
C_2H_4	^{40}Mg	214.9 / 0.5435					

Average interaction points calculated from GEANT4 simulation of 700 keV γ-rays.

The Doppler reconstructed γ-ray spectrum of the inelastic scattering channel of ^{41}Al is presented in Fig. 4.43 for each target individually. There exists a clear intensity around 1000 keV for reactions on both targets. Fitting one or two peaks provides a good reproduction of the 1000 keV shape. Two DALI response functions produce the lowest χ^2/NDF goodness of fit for $m_\gamma > 2$ and with add-back.

The energy and statistical uncertainties for one fitted peak is 1002(7) keV, and two is 929(11) keV and 1021(8) keV for $m_\gamma \leq 3$ selected events for 15 cm add-back. Without add-back, the results are 1011(7) keV, and 945(21) keV and 1025(11) keV for $m_\gamma \leq 3$ selected events. The uncertainties are statistical and are provided by the ROOT minimizer. Varying the maximum γ-ray multiplicity produces no meaningful deviation in centroid position, owing to the unchanging distribution of counts as a function of maximum multiplicity. A plot showing the one and two fitted peaks is presented in Fig. 4.45. The corrected scaling factor, expressed as number of γ-rays ions per 10 000 ions is also plotted. No change is observed with maximum event multiplicity. This is consistent with transitions directly to the ground state.

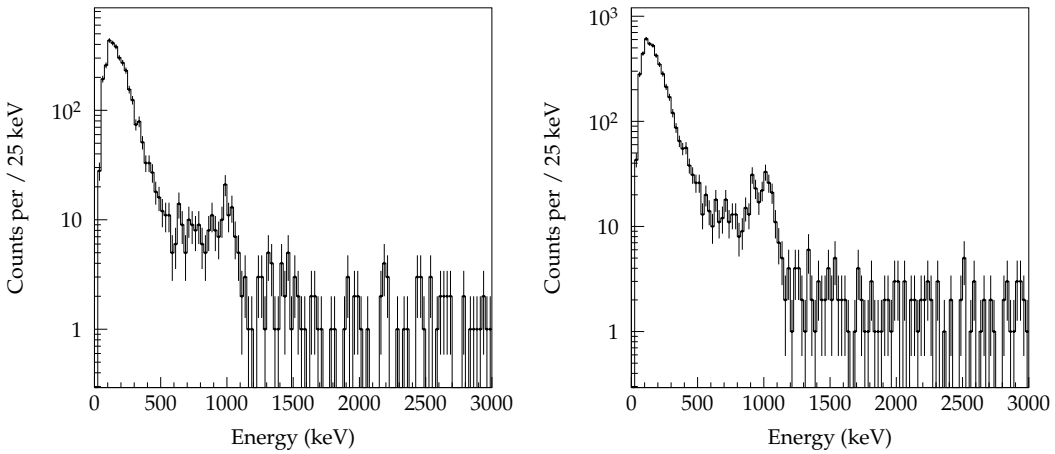

(A) C target, $m_\gamma \leq 3$ (B) C_2H_4 target, $m_\gamma \leq 3$

FIGURE 4.43: Inelastic scattering of ^{41}Al doppler reconstructed γ-ray energy spectrum with add-back

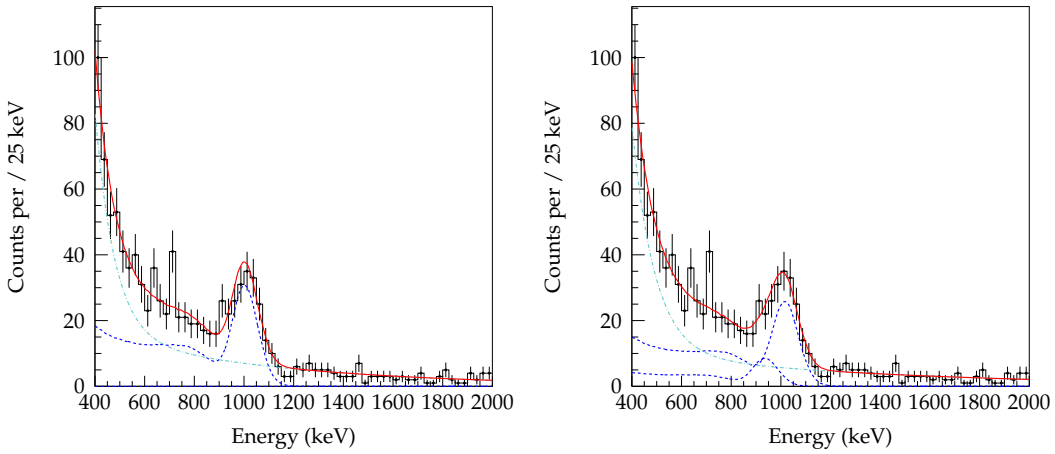

(A) $m_\gamma \leq 3$, one peak, $\chi^2/NDF = 0.881$

(B) $m_\gamma \leq 3$, two peaks, $\chi^2/NDF = 0.869$

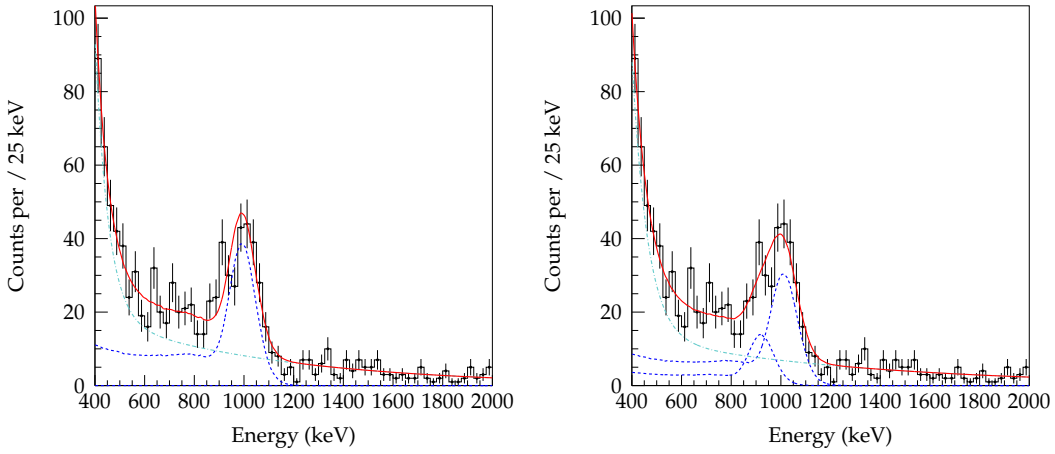

(C) $m_\gamma \leq 3$, add-back, one peak, $\chi^2/NDF = 1.703$

(D) $m_\gamma \leq 3$, add-back, two peaks, $\chi^2/NDF = 1.530$

FIGURE 4.44: Fit of doppler reconstructed ^{41}Al(C/C_2H_4,γ)^{41}Al with add-back procedure

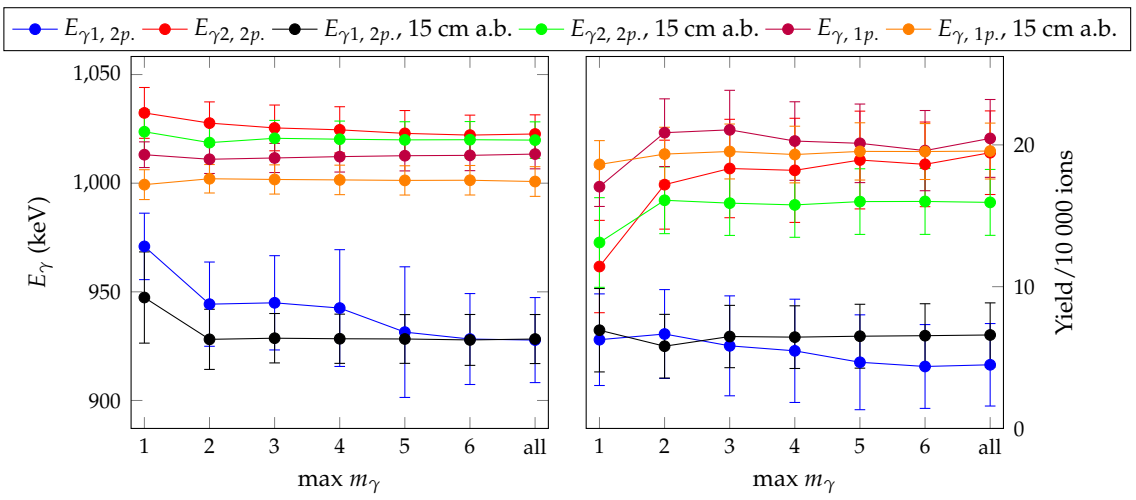

FIGURE 4.45: Summary of fit results of ^{41}Al inelastic scattering for one ($1p$) and two peak ($2p$) fitting.

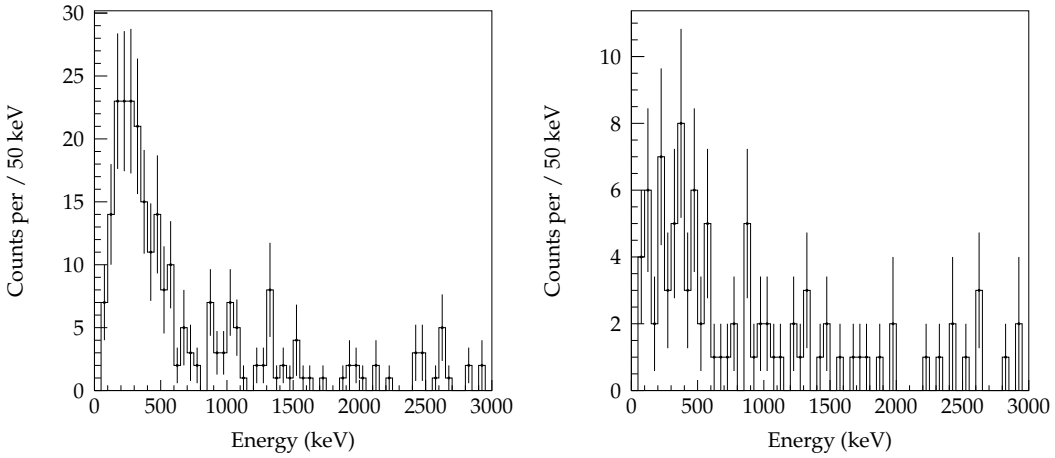

(A) without add-back (B) with 15 cm add-back

FIGURE 4.46: Inelastic ^{41}Al scattering $\gamma - \gamma$ coincidence spectrum, selection of 800 keV to 1200 keV, for all m_γ

The number of counts within the full energy peak, on the order of 300, should be sufficient to observe γ-ray coincidences. Assuming a direct feeding of a higher energy state, the number of coincidences should be on the order of magnitude of $300 \times 25\%$ efficiency $= 75$. In the coincidence spectra of Fig. 4.46, with add-back, there is no strong indication of a peak. The spectrum without add-back appears featureless. This additionally suggests a transition direct to the ground state and with direct population of this state or little fragmented feeding.

Lastly, the atomic background can be reduced by choosing only forward angle detectors from the DALI2 array (detectors with ID number greater than 130, or 42.5 to 20.5 degrees), in the same way as done for inelastic scattering of ^{40}Al. This is shown in Fig. 4.47b and 4.47a. If one photopeak is assumed for 1000 keV, an additional peak can be fit around 430 keV. The energies of the centroids are 434(13) keV and 982(10) keV. The uncertainties are estimated by the ROOT minimizer.

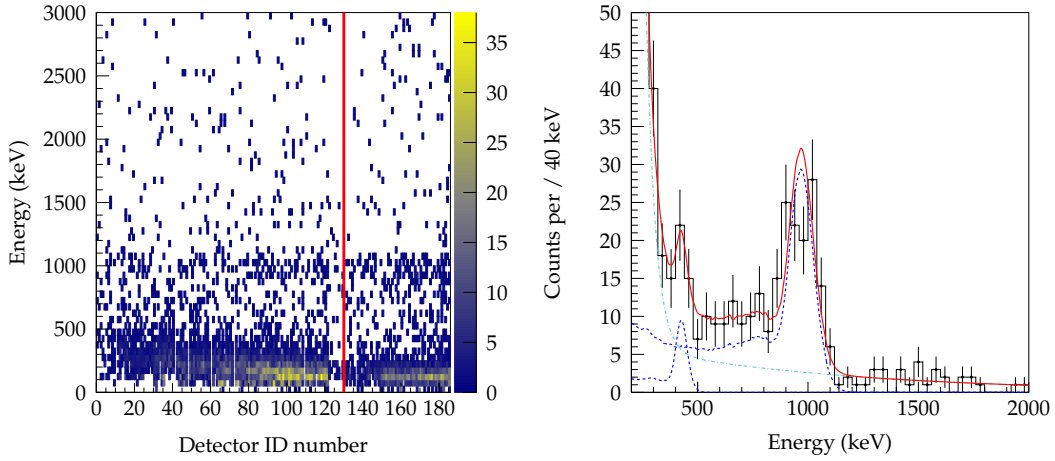

(A) $m_\gamma \leq 3$ (B) $m_\gamma \leq 3$ with forward detectors

FIGURE 4.47: Inelastic scattering of ^{41}Al with forward DALI detectors (detector ID number greater than 130) with add-back

As before, a plot of the yield as a function of event maximum multiplicity is presented in Fig. 4.48 and shows the same flat trend for both transitions. This suggests both are directly to the ground state with little feeding from higher excited states.

The difference between 982(10) keV and 1002(7) keV, with all detectors and the forward angle subset, are out of uncertainties. The uncertainties are likely underestimated. Another possibility is a missing systematic uncertainty from selecting only forward angle detectors. Anisotropic γ-ray emission may play a role in a altering the peak centroid and yield, and could be exaggerated for detecting only select emission angles.

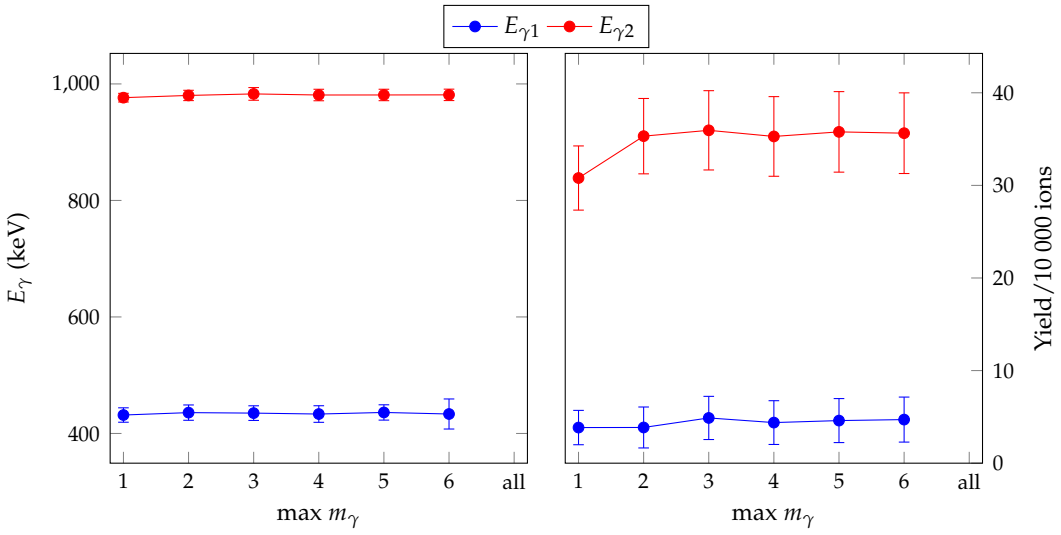

FIGURE 4.48: Summary of fit results of ^{41}Al inelastic scattering with forward DALI detectors (detector number $>$ 130)

4.4.2 ^{42}Si(C/C_2H_4,X)^{41}Al

4.4.2.1 Reaction summary and inclusive cross section

TABLE 4.34: Summary of ^{42}Si(C/C_2H_4,X)^{41}Al and cross section

Setting			within ZeroDegree full momentum acceptance		
Target	ZD $B\rho$	Total reactions	Reactions	Projectiles	Inclusive cross section (mb)
C	^{41}Al	410	218	100748	10.9(1.6)
C_2H_4	^{41}Al	189	108	52457	27.0(3.3)
C	^{40}Mg	4584	108	666169	8.3(1.0)
C_2H_4	^{40}Mg	11283	2267	1138227	24.9(2.5)

The inclusive cross sections for both targets and both ZeroDegree magnetic rigidity settings are in good agreement. Significant cropping of the events by a *F5X* and *F5A* selection is necessary for experimental runs with ZeroDegree magnetic rigidity set for ^{40}Mg acceptance, as evident by the difference between total reactions and reactions in the table. For these experimental runs, the reaction residue beam of ^{41}Al after the F8 reaction target is centred at the periphery of F9X and therefore at the edge of full ZeroDegree acceptance.

4.4.2.2 γ-ray analysis

TABLE 4.35: ^{42}Si(C/C_2H_4,X)^{41}Al γ-ray reconstruction settings

Setting		Velocity (MeV u^{-1} / β)		Beam at target (cm)			
Target	ZD $B\rho$	mid-point target	before target	X	fwmh	Y	fwhm
C	^{41}Al	214.3 / 0.5821	248.4 / 0.6138	-0.2	0.9	0.0	1.0
C_2H_4	^{41}Al	206.7 / 0.5745					
C	^{40}Mg	216.2 / 0.5840	250.1 / 0.6152				
C_2H_4	^{40}Mg	208.7 / 0.5765					

Average interaction points calculated from GEANT4 simulation of 800 keV γ-rays.

The parameters for γ-ray reconstruction are presented in table 4.35. The Average interaction poins for DALI detectors, for calculation of individual detector angle with respect to the reconstruction point, is simulated in GEANT4 with 800 keV γ-rays.

The reconstructed γ-ray spectrum of proton knockout to ^{41}Al is presented in Fig. 4.49 for both targets. The same procedure for fitting the spectrum is applied, namely, the sequential addition of peaks. Unlike for the fitting of ^{39}Al, the spectrum of events with $m_\gamma = 1$ is first fit. This spectrum shows the clearest high energy peak around 1430 keV.

Fitting with three, four and five peaks are presented in Fig. 4.50. Similarly, with the preconceived centroids, the same procedure is applied to events with maximum multiplicity $m_\gamma \leq 3$ (Fig. 4.51). The peak around 1000 keV appears most prominently for the spectrum of $m_\gamma = 1$. Furthermore, the addition of a second DALI response function around 500 keV appears to be necessary to represent the distorted

peak shape of the high intensity peak. This appears between figures 4.50a and 4.50b. Five DALI response functions faithfully reproduces the spectrum.

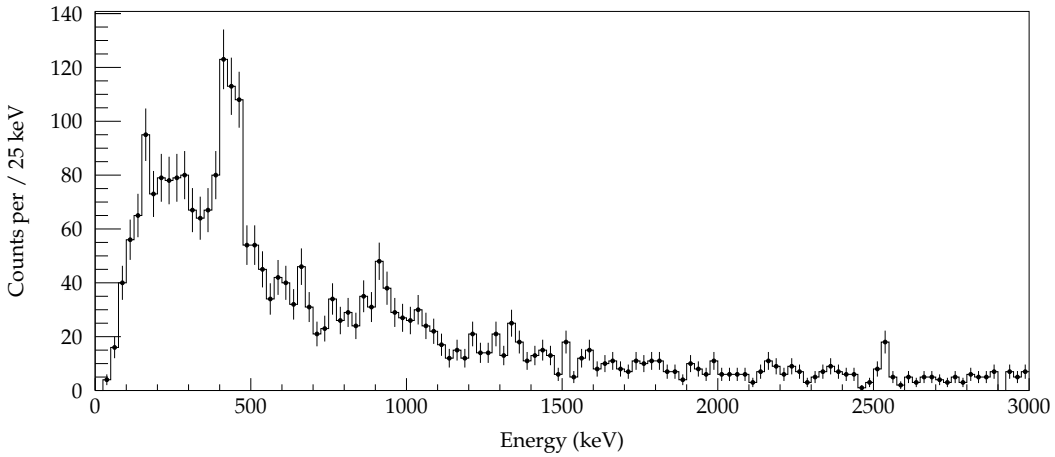

(A) C target, $m_\gamma \leq 5$

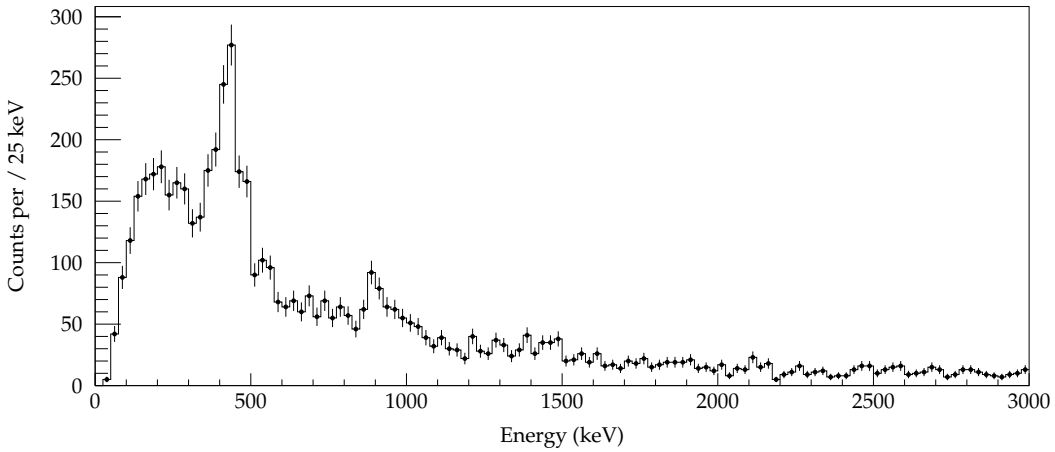

(B) C_2H_4 target, $m_\gamma \leq 5$

FIGURE 4.49: ^{42}Si(C/C_2H_4,X)^{41}Al Doppler reconstructed γ-ray energy spectrum with add-back

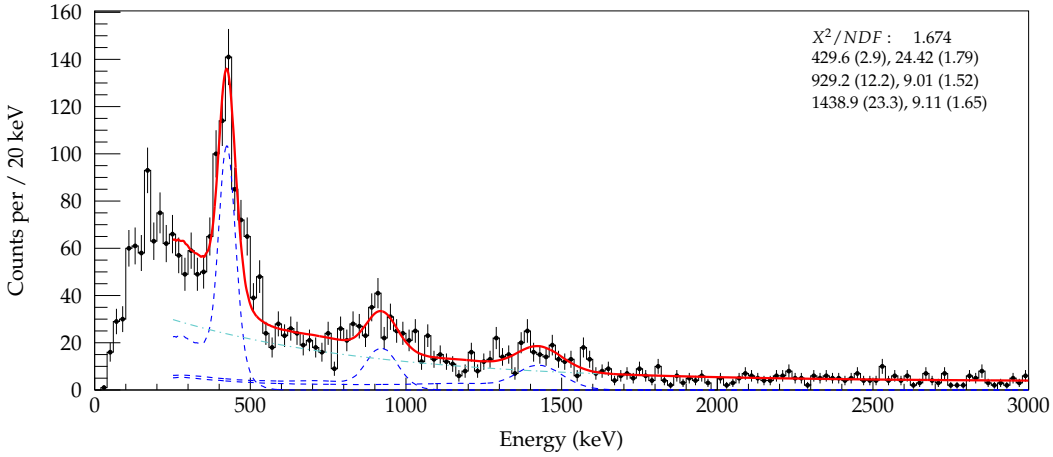

(A) 3 DALI functions, $m_\gamma = 1$

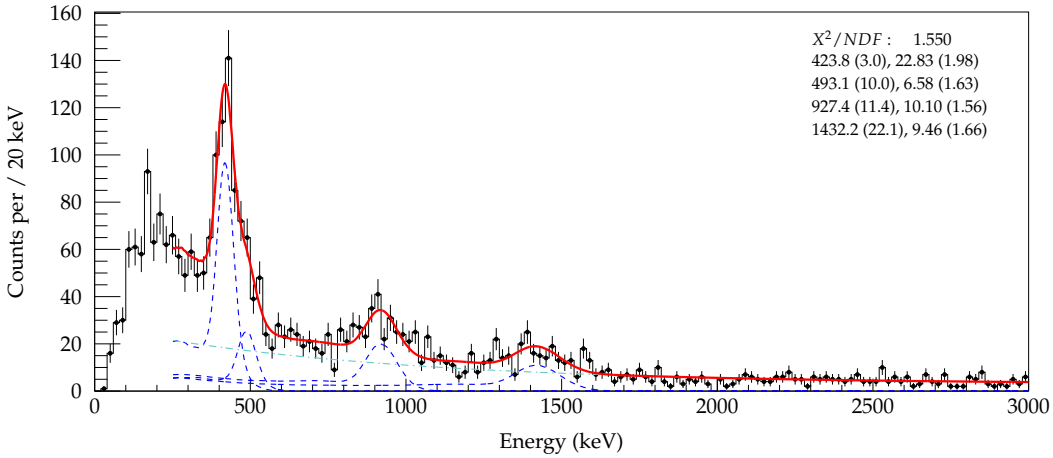

(B) 4 DALI functions, $m_\gamma = 1$

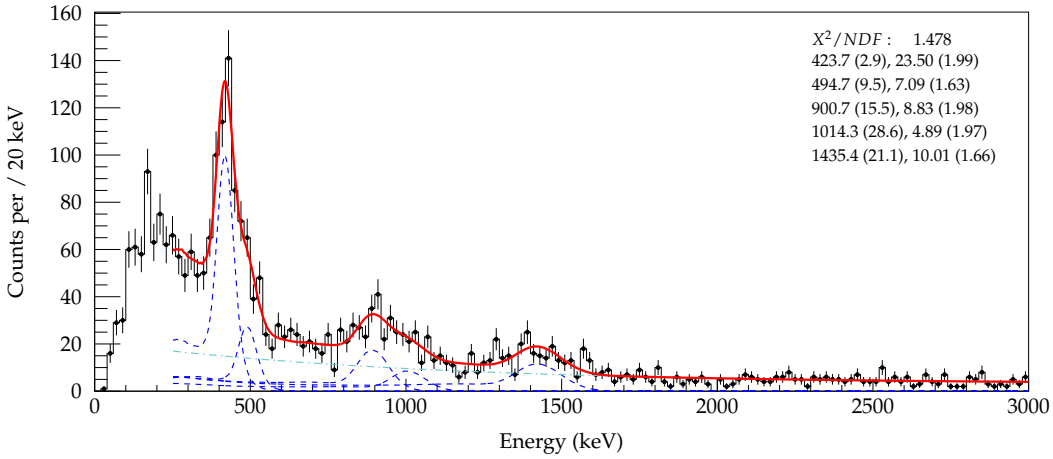

(C) 5 DALI functions, $m_\gamma = 1$

FIGURE 4.50: Fitting 3, 4, 5 peaks of $^{42}Si(C/C_2H_4,X)^{41}Al$ doppler reconstructed γ-ray energy spectrum, $m_\gamma = 1$, and with add-back

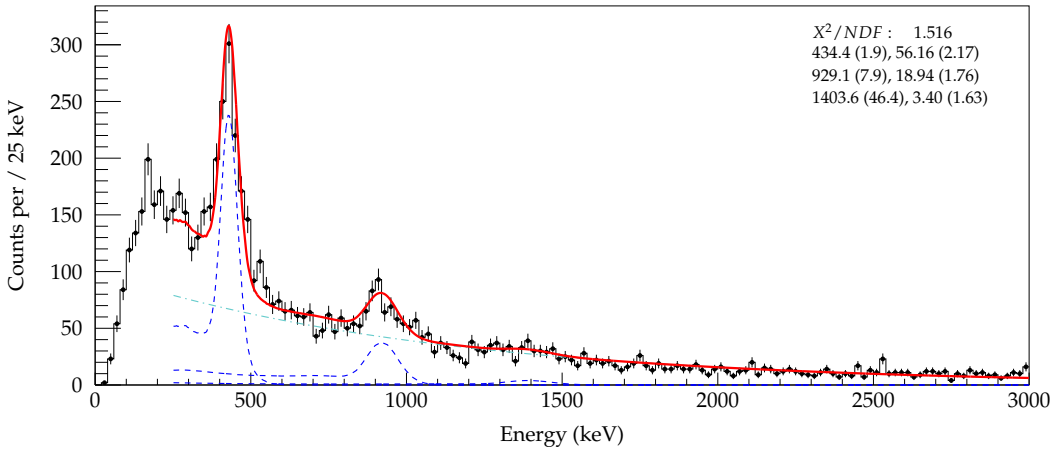

(A) 3 DALI functions, $m_\gamma \leq 3$

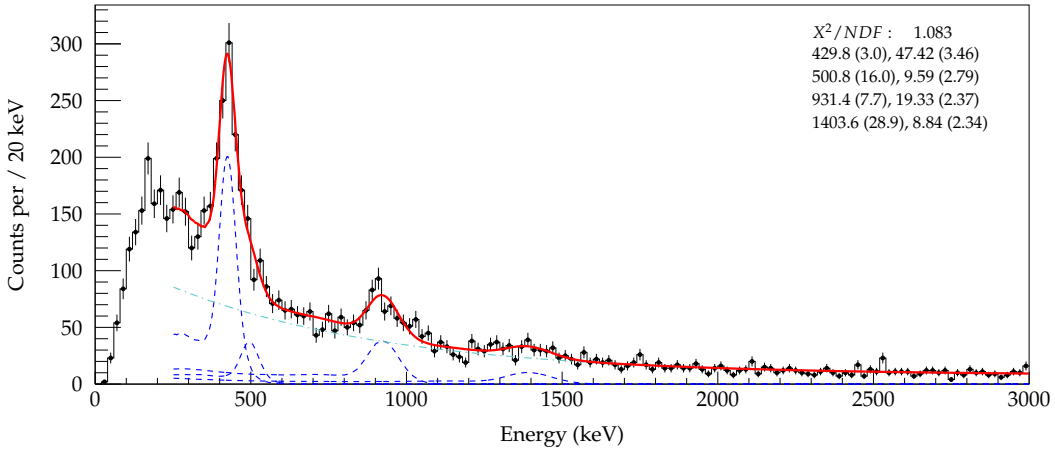

(B) 4 DALI functions, $m_\gamma \leq 3$

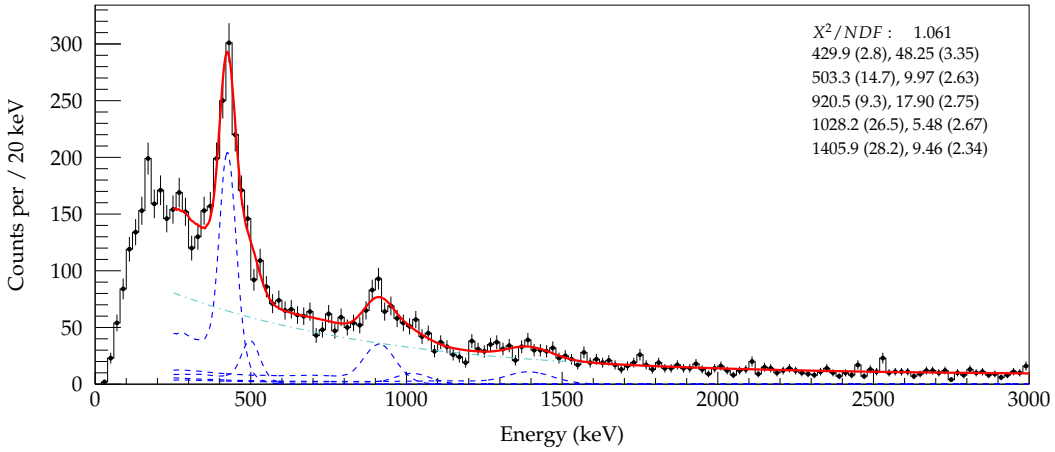

(C) 5 DALI functions, $m_\gamma \leq 3$

FIGURE 4.51: Fitting 3, 4, 5 peaks of ^{42}Si(C/C_2H_4,X)^{41}Al doppler reconstructed γ-ray energy spectrum, $m_\gamma \leq 3$, and with add-back

If only DALI forward angle detectors are selected (above ID number 130, 42.5 to 20.5 degrees), as displayed in Fig. 4.52a, the photopeak around 500 keV can be emphasized. The increased energy resolution for high energy γ-rays from the forward boost can be exploited. The 500 keV transition is most clear at $m_\gamma = 1$, with the lowest atomic background. Furthermore, as the atomic background is low with this condition, the fit can be extended to 80 keV. The cut-off double exponential function of ^{40}Al is utilized (equation 4.4), with the slope and cut-off energy fit with the atomic background spectra. An additional peak around 160 keV can be added to the total fit function.

If only the most extreme forward angle detectors are used, detector numbers above 178 (all set at an angle of 20.5 degrees), the lowest energy photopeak is pronounced. The GEANT4 generated DALI response function likely overestimates the energy resolution, as no γ source was available for energy resolution calibration around this energy regime.

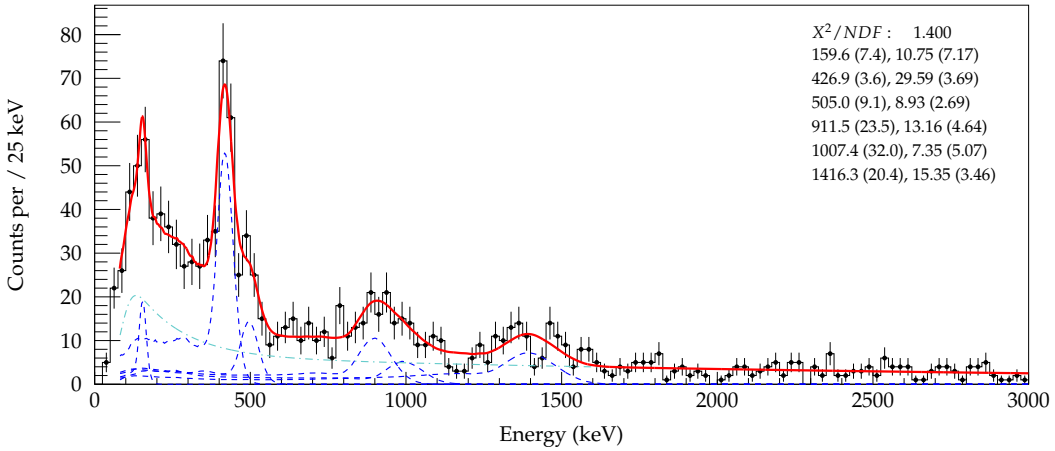

(A) 6 DALI functions, forward angle detectors, $m_\gamma = 1$

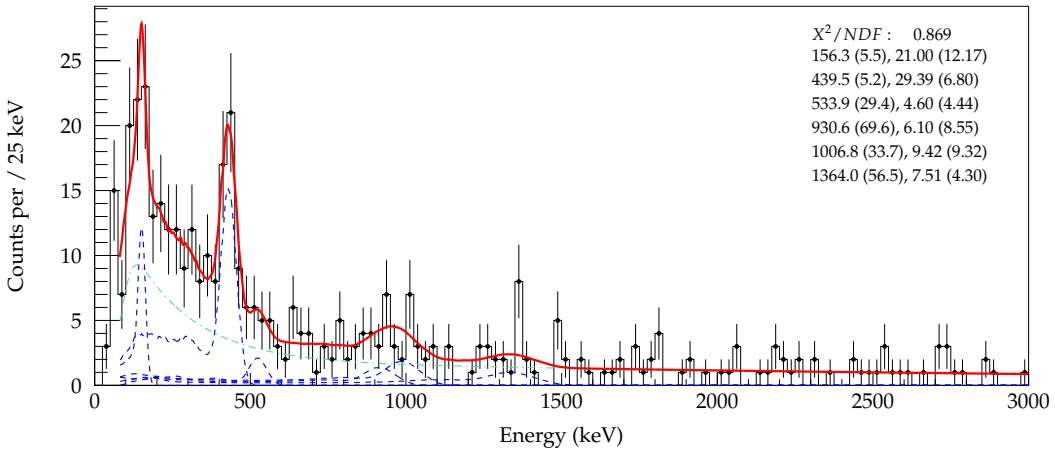

(B) 6 DALI functions, most forward angle detectors, $m_\gamma = 1$

FIGURE 4.52: ^{42}Si(C/C_2H_4,X)^{41}Al Doppler recontructed with forward angle detectors (detector ID number greater than 130) with add-back

Fit summary The five DALI response function fits are presented as a function of maximum event multiplicity in Fig. 4.53. The deviation in energy is considered in the final deduced uncertainties. The highest energy transitions show a flat trend of yield. All of the γ-rays are tabulated in 4.36.

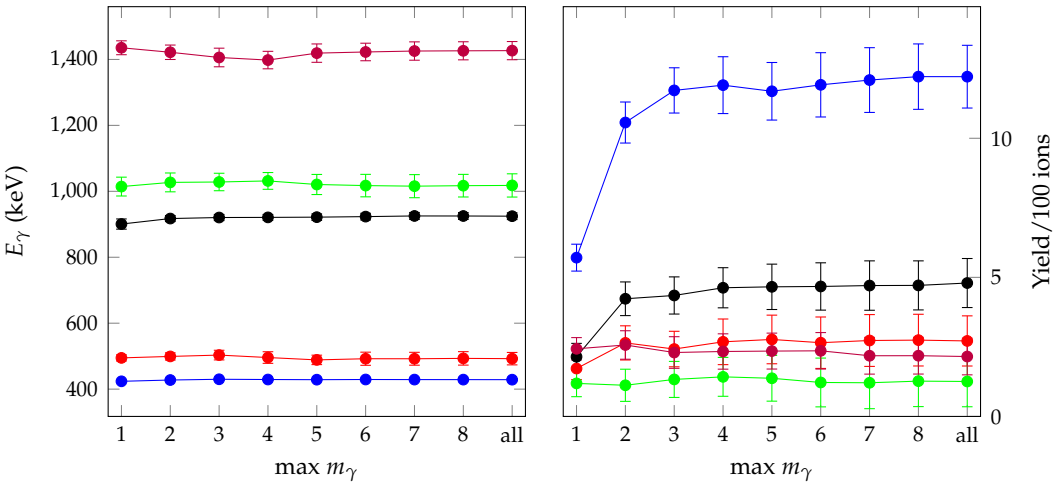

FIGURE 4.53: Summary of fit results of ^{42}Si(C/C_2H_4,X)^{41}Al with five DALI response functions

TABLE 4.36: ^{42}Si(C/C_2H_4,X)^{41}Al fit results

E_γ (keV)	Yield/100 ions
160⋆	
428(4)	12(1)
505(19)	2.7(9)
923(10)	4.8(9)
1017(35)	1.3(9)
1424(27)	2.2(7)

γ-γ coincidence The γ-γ matrix is presented in Fig. 4.54. For the application of γ-γ coincidence of ^{41}Al, the following sections were divided to isolate full energy photopeaks and a background regions. The background sections are employed for background subtraction. The sections are shown and labelled in Fig. 4.55. The following figures 4.57, 4.58, 4.59, and 4.60 show the coincidence spectra.

The γ-γ analysis is similar to the previous ^{39}Al analysis. The photopeak centroids are fixed from table 4.36 to reduce the parameter space.

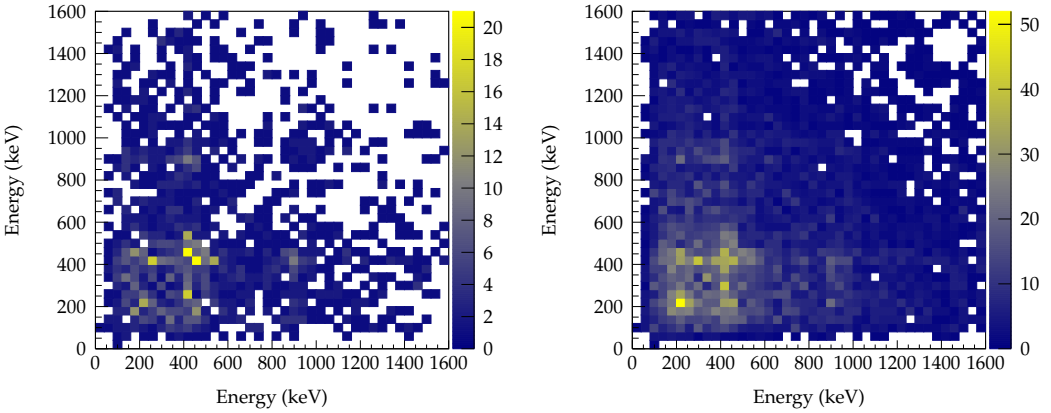

(A) $m_\gamma = 2$ (B) all m_γ

FIGURE 4.54: ^{42}Si(C/C_2H_4,X)^{41}Al γ-γ matrix with add-back

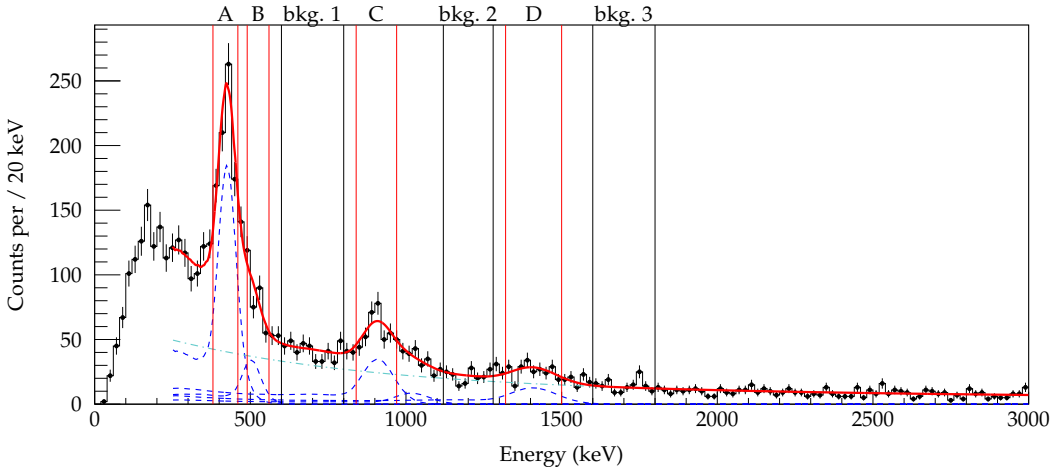

(A) 5 DALI functions, $m_\gamma \leq 2$

FIGURE 4.55: Selectons for ^{42}Si(C/C_2H_4,X)^{41}Al coincidence analysis, $m_\gamma \leq 2$, and with add-back

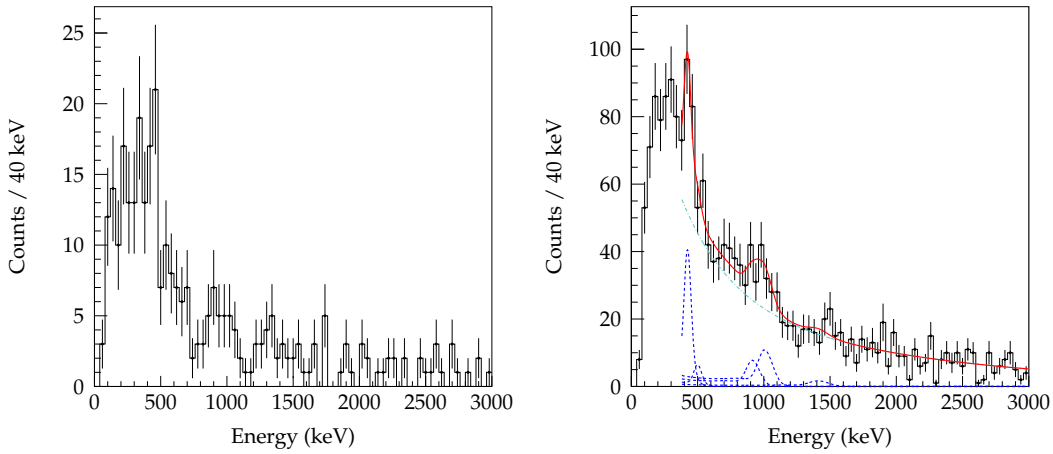

(A) $m_\gamma = 2$ (B) all m_γ and fit

FIGURE 4.56: ^{42}Si(C/C_2H_4,X)^{41}Al background coicidence γ-ray energy spectrum with add-back

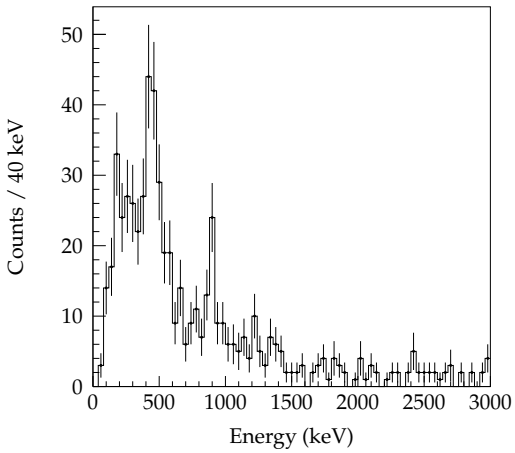

(A) $m_\gamma = 2$

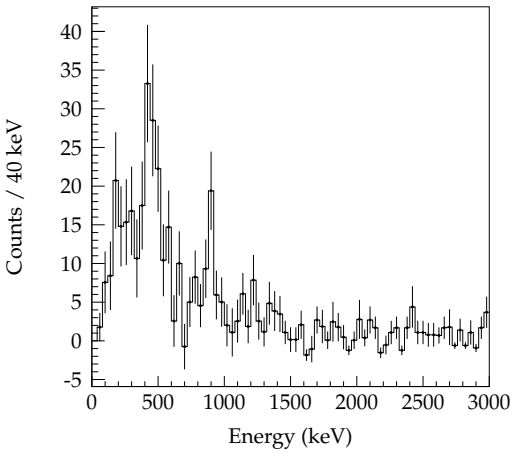

(B) $m_\gamma = 2$, background subtracted

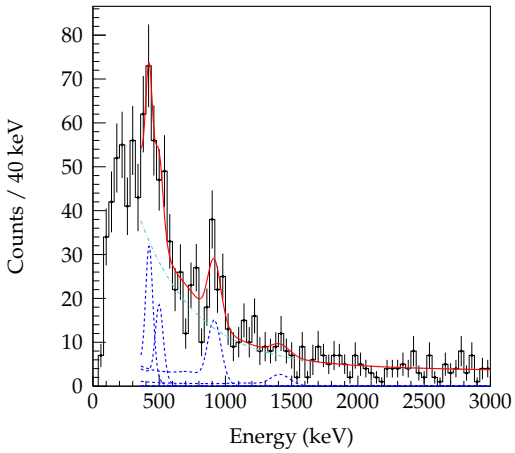

(C) all m_γ

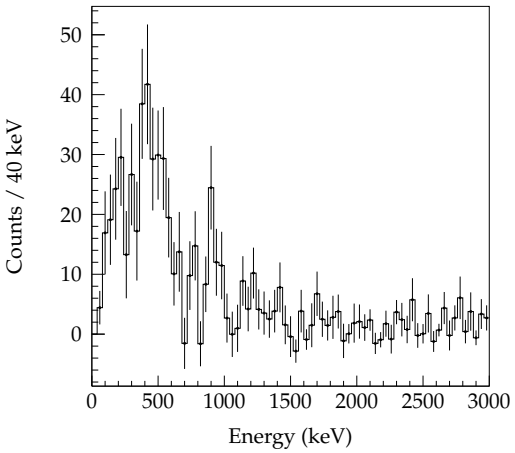

(D) all m_γ, background subtracted

FIGURE 4.57: ^{42}Si(C/C_2H_4,X)^{41}Al selection A: 380 keV to 460 keV (for 428 keV peak)

E_γ (keV)	Selected	Background	Coincidence	Coinc.-Bkg.
428	664(39)	77(24)	188(80)	111(83)
505	24(7)	7(10)	60(31)	53(32)
923	47(6)	32(21)	190(56)	159(60)
1017	11(5)	50(23)	0(80)	-50(83)
1424	15(4)	12(21)	58(51)	46(55)

TABLE 4.37: Number of counts for $\gamma - \gamma$ coincidence for selection A (428 keV) for all m_γ events. Significant (such as $> 2\sigma$) coincidences are highlighted in blue. The photopeak of interest is highlighted in yellow.

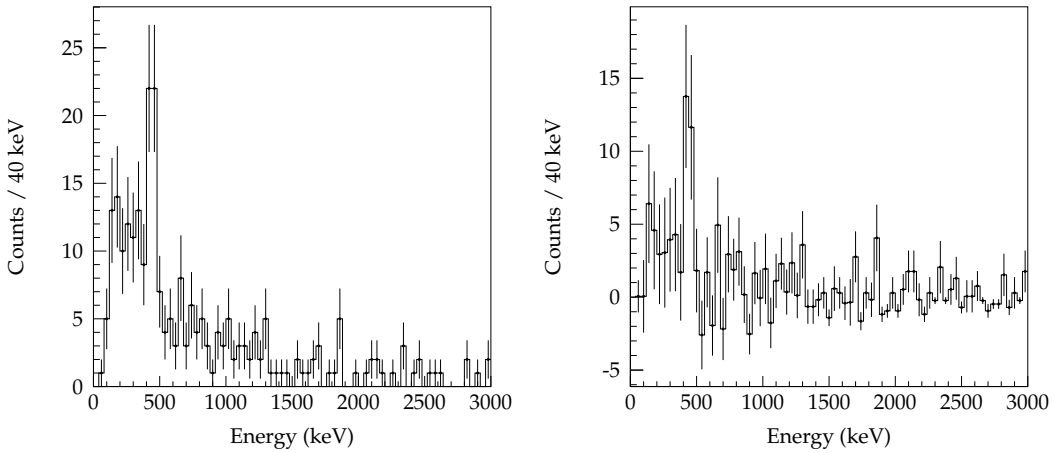

(A) $m_\gamma = 2$ (B) $m_\gamma = 2$, background subtracted

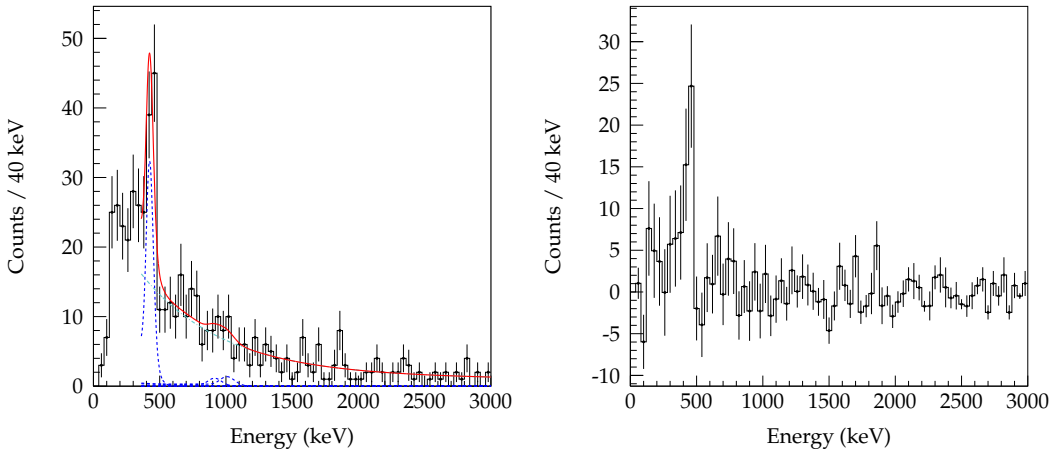

(C) all m_γ (D) all m_γ, background subtracted

FIGURE 4.58: ^{42}Si(C/C_2H_4,X)^{41}Al selection B: 490 keV to 560 keV (for 505 keV peak)

E_γ (keV)	Selected	Background	Coincidence	Coinc.-Bkg.
428	27(2)	59(18)	191(41)	132(46)
505	93(22)	5(7)	0(8)	-5(10)
923	30(4)	24(16)	14(32)	-10(36)
1017	8(4)	38(17)	20(33)	-18(37)
1424	10(3)	9(16)	0(14)	-9(21)

TABLE 4.38: Number of counts for $\gamma - \gamma$ coincidence for selection A (505 keV) for all m_γ events. Significant (such as $> 2\sigma$) coincidences are highlighted in blue. The photopeak of interest is highlighted in yellow.

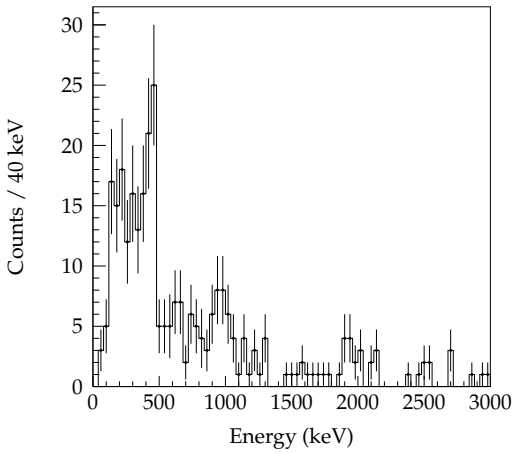

(A) $m_\gamma = 2$

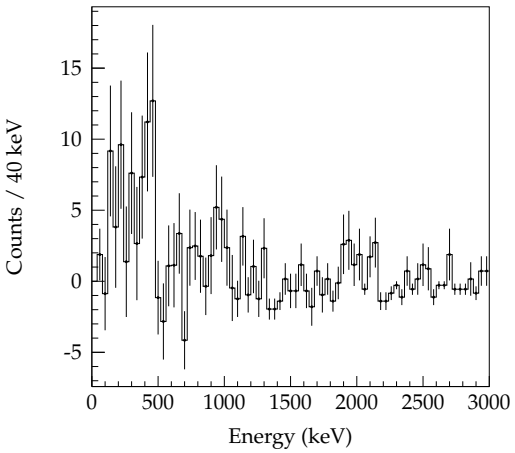

(B) $m_\gamma = 2$, background subtracted

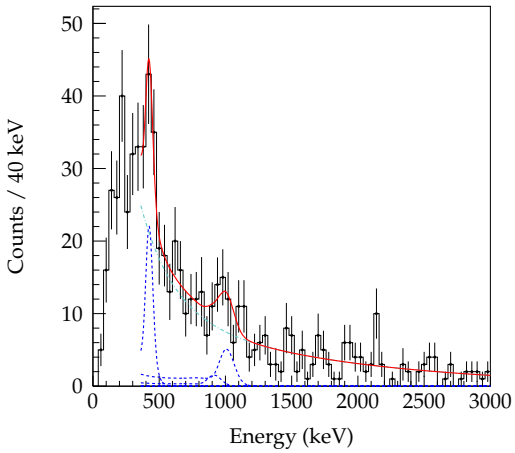

(C) all m_γ

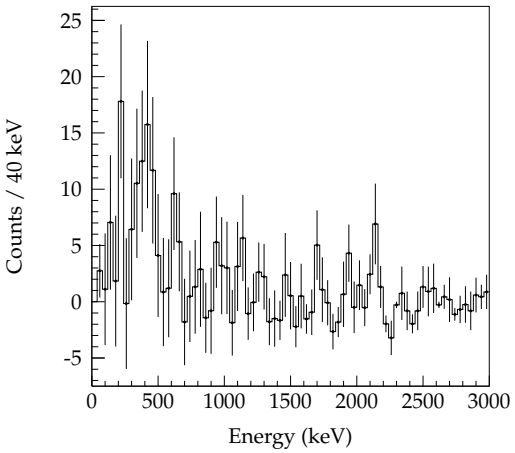

(D) all m_γ, background subtracted

FIGURE 4.59: ^{42}Si(C/C_2H_4,X)^{41}Al selection C: 840 keV to 970 keV (for 923 keV peak)

E_γ (keV)	Selected	Background	Coincidence	Coinc.-Bkg.
428	0	67(21)	130(52)	63(55)
505	0	6(8)	0(37)	-6(38)
923	200(29)	28(19)	19(38)	-8(42)
1017	24(11)	44(20)	73(42)	30(46)
1424	15(4)	10(18)	0(25)	-10(31)

TABLE 4.39: Number of counts for $\gamma - \gamma$ coincidence for selection B (923 keV) for all m_γ events. Significant (such as $> 2\sigma$) coincidences are highlighted in blue. The photopeak of interest is highlighted in yellow.

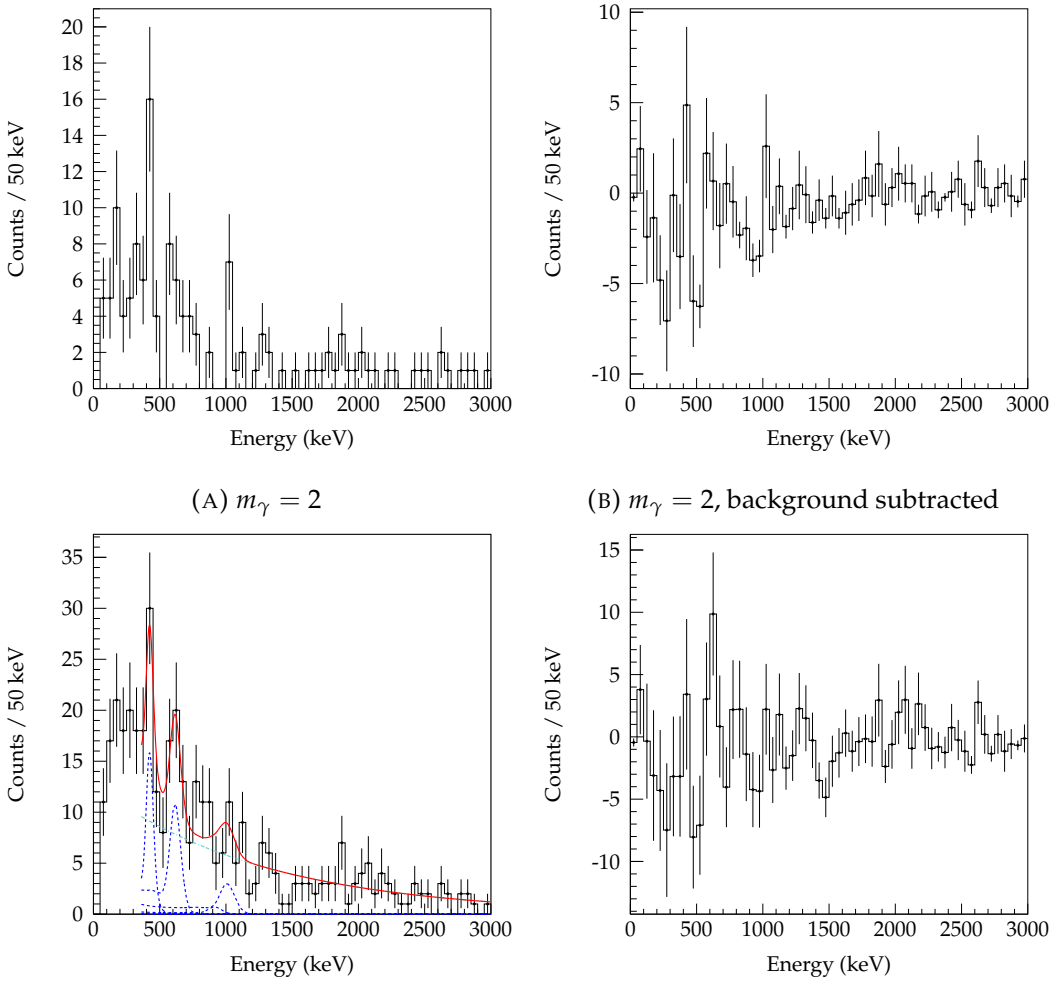

(A) $m_\gamma = 2$

(B) $m_\gamma = 2$, background subtracted

(C) all m_γ

(D) all m_γ, background subtracted

FIGURE 4.60: ^{42}Si(C/C_2H_4,X)^{41}Al selection D: 1320 keV to 1500 keV (for 1424 keV peak)

E_γ (keV)	Selected	Background	Coincidence	Coinc.-Bkg.
428	0	54(17)	93(30)	39(34)
505	0	5(7)	0(4)	-5(8)
623(15)	0	0(5)	100(34)	100(35)
923	0	22(15)	9(34)	-13(37)
1017	0	35(16)	43(37)	8(49)
1424	61(18)	8(15)	0(9)	-8(17)

TABLE 4.40: Number of counts for $\gamma - \gamma$ coincidence for selection C (1424 keV) for all m_γ events. Significant (such as $> 2\sigma$) coincidences are highlighted in blue. The photopeak of interest is highlighted in yellow.

Summary In selection A (highlighting 428 keV), coincidences between 505 keV (weakly) and 923 keV are seen. The 428 keV self coincidences are likely a consequence of the additional selection of Compton continuum of 505 keV and 923 keV and possibly other unobserved transitions which are coincident with 428 keV. Significant intensity around 150 keV to 350 keV in the background subtracted spectra may suggest other low energy transitions coincident with 428 keV. The statistics are too low for rigorous fitting the coincidence spectra and fitting the background subtracted spectra induces systematic uncertainties. Furthermore, the low energy features suggest several γ-rays at low energy, rather than a single photopeak.

In selection B (505 keV), the coincidence for 428 keV is significantly greater than uncertainties. The low energy intensity in found in selection A is no longer present.

In selection C (923 keV), coincidence for 428 keV is not clearly observed in the fit of spectra with all m_γ. However, in the unfit background subtracted spectra of both $m_\gamma = 2$ and all m_γ the coincidence is suggested by the peak around 430 keV. The likely cause of this discrepancy is the poor fit of the coincidence spectra. Specifically, the double exponential background may be overestimated under the DALI response function of 428 keV. There is some *noise* around 620 keV, which also appears in the background subtracted spectra. Adding a response function for this *bump* results in a scaling factor uncertainty of the same magnitude, and therefore is not included in the fit.

Lastly, selection D (1424 keV) does not show any strong coincidences with any of the previously identified transitions. What appears to be a photopeak around 620 keV is added to the fit of the coincidence spectra and may be assigned as a candidate transition. This transition is within the area of the backgrounds used in this analysis, however it's contribution to a perturbation of the results will be small. Such a transition is not clearly visible in any of previous spectra and therefore represents a small intensity. Also, removing background section one, which encompass this candidate, would result in poor statistics.

The poor statistics and large systematic uncertainties from the analysis does not permit quantification of branching ratios. The results of the knockout reaction and the inelastic scattering are presented in table 4.41 and used to build the proposed level scheme of ^{41}Al (Fig. 4.61). Systematic uncertainty from beam velocity (section 3.4.4) and energy calibration (3.4.1.1) are shown. In the case of the inelastic scattering, the 434(13) keV is likely to be the 428(4) keV transition observed in the knockout reaction. The two fits of the 1000 keV γ-ray, with one fit fit function, (982(10) keV and 1002(7) keV) can be averaged to 992(10) keV. The suggested assignment of one photopeak to the peak structure does not significantly result in a different χ^2/NDF relative to a fit with two DALI response functions.

Furthermore, this transition may have similarly been observed in the knockout reaction, as 1017(35) keV. The two γ-rays are within uncertainties. The inelastic 992(10) keV peak with superior peak-to-background is added to the tentative level scheme.

As the 428(4) keV transition can be suggested to be a transition directly to the ground state given it's large intensity, this infers that the 992(10) keV (averaged) γ-ray in the inelastic scattering spectra is also a transition directly to the ground state. The intensity of this γ-ray is significantly greater than the only other observed γ-ray in the same spectrum (434(13) keV), therefore cannot proceed through this de-excitation. Furthermore, the coincidence spectra of the inelastic scattering 992(10) keV photopeak does not suggest any strong coincidences.

The 505(19) keV and 923(10) keV can be added above 428(4) keV as they are not suggested to be coincident with each other.

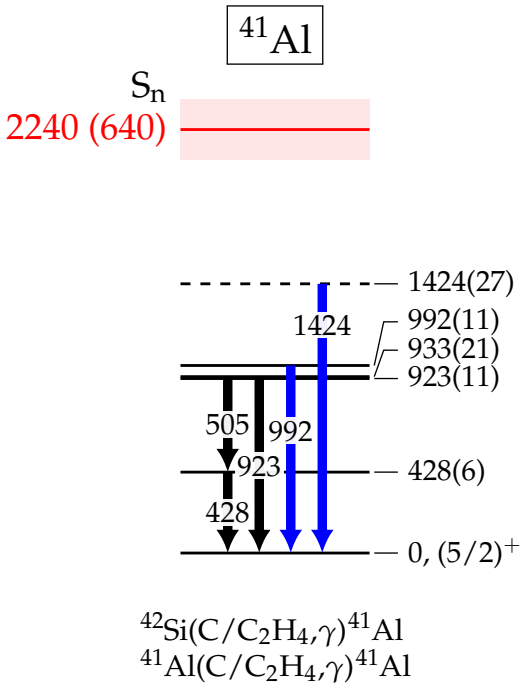

FIGURE 4.61: Experimental transitions and tentative level scheme of ^{41}Al. Blue arrow shows transition from singles spectra without coincidences. The neutron separation energy of 2240(640) keV [27] is shown in red. The uncertainty of the extrapolated neutron separation is shown as the level width.

TABLE 4.41: ^{41}Al experimental transitions and coincidences. Systematic uncertainty from beam velocity and energy calibration. Values with stars are suggestive.

E_γ (keV)	Yield/100 ions[1]	Coincidence
160⋆		428⋆
$428(4)_{stat.}(5)_{syst.}$	12(1)	505, 923
$505(19)_{stat.}(5)_{syst.}$	2.7(9)	428
623⋆		1424⋆
$923(10)_{stat.}(5)_{syst.}$	4.8(9)	428
$992(10)_{stat.}(5)_{syst.}$[2]		
$1017(35)_{stat.}(5)_{syst.}$[2]	1.3(9)	
$1424(27)_{stat.}(5)_{syst.}$	2.2(7)	623⋆

[1] Yield determined through fit of γ-ray energy spectrum with all m_γ and add-back.

[2] The 992 keV transition fit from inelastic scattering and 1017 keV transition fit from proton knockout fall within uncertainties.

4.5 Other cross sections

Two additional reaction channels are analyzed. Low statistics preclude γ-ray measurement, but nucleon knockout reaction cross sections are determined.

4.5.1 ^{42}Al(C/C_2H_4,X)^{41}Al

4.5.1.1 Reaction summary and inclusive cross section

TABLE 4.42: Summary of ^{42}Al(C/C_2H_4,X)^{42}Al and cross section

Setting		within ZeroDegree full momentum acceptance		
Target	ZD $B\rho$	Reactions	Projectiles	Inclusive cross section (mb)
C	^{40}Mg	2	359	29(21)
C_2H_4	^{40}Mg	14	667	262(76)

4.5.2 ^{43}Si(C/C_2H_4,X)^{42}Al

4.5.2.1 Reaction summary and inclusive cross section

TABLE 4.43: Summary of ^{43}Si(C/C_2H_4,X)^{42}Al and cross section

Setting		within ZeroDegree full momentum acceptance		
Target	ZD $B\rho$	Reactions	Projectiles	Inclusive cross section (mb)
C	^{40}Mg	15	66837	1.20(33)
C_2H_4	^{40}Mg	26	123487	2.63(58)

Chapter 5

Discussion and Interpretation

5.1 ^{32}Ne

5.1.1 Systematic trends around $N = 20$

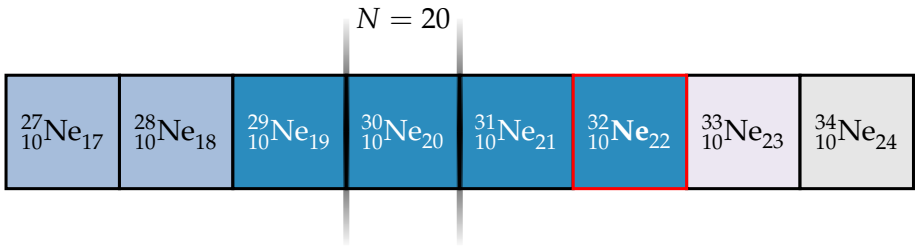

Significant experimental and theoretical efforts have revealed the nature of neon isotopes in the vicinity of the *island of inversion* (IoI) of $N = 20$. The evolution of nuclear properties leading up to the western side of the IoI has delineated both the border and it's softness.

In the case of the odd Ne isotopes, a soft transition to the IoI is suggested and the westward boundary can be defined as ^{29}Ne. At $N = 17$, ^{27}Ne, the first characteristics of the introduction of intruder states is suggested. The observation of a low-lying negative parity state $3/2^-$ [158, 159] indicates the presence of an excited intruder configuration. The next heavier odd isotope, ^{29}Ne ($N = 19$) is found to display the characteristic intruder ground state of IoI nuclei. The ^{29}Ne ground state largely consists of a $^{28}\text{Ne}(0^+_1) \otimes 2p_{3/2}$ neutron configuration. This deduction was accomplished through the neutron removal cross section and a narrow reaction parallel momentum distribution [160]. After transitioning past the border of ^{29}Ne, ^{31}Ne ($N = 21$) is additionally confirmed to be an intruder dominated nuclei. ^{31}Ne is shown to exhibit a p-wave halo structure of ground state spin parity $3/2^-$ by the observation of a large Coulomb breakup cross section [161] and one-nucleon removal reactions [91]. The next odd isotope ^{33}Ne ($N = 23$) is unbound and has yet to be investigated.

For even Ne isotopes a soft transition is likewise observed. Such a transition starts at ^{28}Ne. ^{28}Ne ($N = 18$) displays an enhancement in collectivity, with the significant lowering of the first 2^+_1 energy level ($E(2^+_1)$) [55]. The next nucleus, ^{30}Ne ($N = 20$), can be placed firmly within the island of inversion with a strong reduced $E2$ transition probability ($BE2$), an indicator of a large enhancement in collectivity [162]. In addition, the low excited first 2^+_1 state [163] is characteristic of loss of the $N = 20$ canonical magic number.

Lastly, ^{32}Ne ($N = 22$), the isotope of this study, has been previously investigated by in-beam gamma spectroscopy to reveal the first excited 2^+_1 state energy. This energy at $722(9)$ keV, in combination with predictions by shell model calculations of

Utsuno et al. [36] and Caurier et al. [164] reveals a continuing trend of strong deformation in this nucleus and a ground state dominated by intruder configurations [154]. The near drip-line ^{32}Ne is the most neutron-rich neon isotope known to belong to the island of inversion.

5.1.2 $4_1^+ \rightarrow 2_1^+$ transition

The strong transition at 709(12) keV, observed in both reactions (4.1.1 and 4.1.2), corresponds to the $2_1^+ \rightarrow 0_{g.s.}^+$ transition consistent with a previous measurement of 722(9) keV by both inelastic scattering and proton removal [154]. The previous experiment possessed lower statistics than the present work.

In addition, a new transition was observed in both one- and two-proton knockout reactions. This new transition at 1410(15) keV is assigned to the $4_1^+ \rightarrow 2_1^+$ decay. The reason for preliminary spin and parity assignment of the state is four fold. Firstly, the trend of experimental observation of $4_1^+ \rightarrow 2_1^+$ transitions in nucleon knockout reactions to ^{26,30}Ne with fast-beams [92, 165] is consistant in both the population of this state in direct reactions and the position of the 4_1^+ state above 2_1^+ state. Secondly, the predicted energy level from shell model calculations is reproduced in good agreement with the assignment. Third, reaction theory exclusive cross section ratios, as will be discussed later in the text, agree with experimental ratios. Lastly, the limited possibility of additional bound states due to a low extrapolated neutron separation energy (S_n) of 2250(570) keV [27] suggests few available other options.

The experimental energies of the first 2_1^+ and 4_1^+ states of Si, Mg and Ne are presented in Fig. 5.1. Included also in the figure are predicted level energies by shell model calculations with large valence spaces. The recent extended Kuo-Krenciglowa (EKK) derived effective interaction [43], henceforth called EEdf1, includes realistic multiparticle-multihole transition mixing across the $N = 20$ shell gap as predicted for IoI nuclei. Furthermore, the large model space spanning the complete *sdpf* orbitals permits contributions from many configurations. The EEdf1 effective interaction calculated excited states are presented as horizontal bars. The deduced levels of ^{32}Ne are presented as open red circles.

Additionally, the experimental and theoretical levels are shown in the level scheme of Fig. 5.2. Predicted levels are additionally included from shell model calculations with the SDPF-M interaction [36]. This interaction, unlike the previous EEdf1 interaction are restricted to the $sd - p_{3/2}f_{7/2}$ space, but also allows for mixing of *sd* and *pf* configurations. Both interactions provide a good description of the *island of inversion* and predict strongly deformed ground states dominated by intruder configurations for $N = 20$ neon and magnesium isotopes.

TABLE 5.1: ^{32,34}Mg and ^{30,32}Ne ground state neutron 0p-0h, 2p-2h and 4p-4h probabilties (%) calculated with the SDPF-M and EEDf1 interactions.

	SDPF-M			EEDf1		
	0p-0h	2p-2h	4p-4h	0p-0h	2p-2h	4p-4h
^{32}Mg	4.7	82.5	12.7	1.8	36.2	51.9
^{30}Ne	3.9	74.1	22.0	0.5	19.8	68.1
^{34}Mg	9.5	82.0	8.4	1.6	49.5	43.4
^{32}Ne	10.0	76.5	13.4	1.2	43.3	50.6

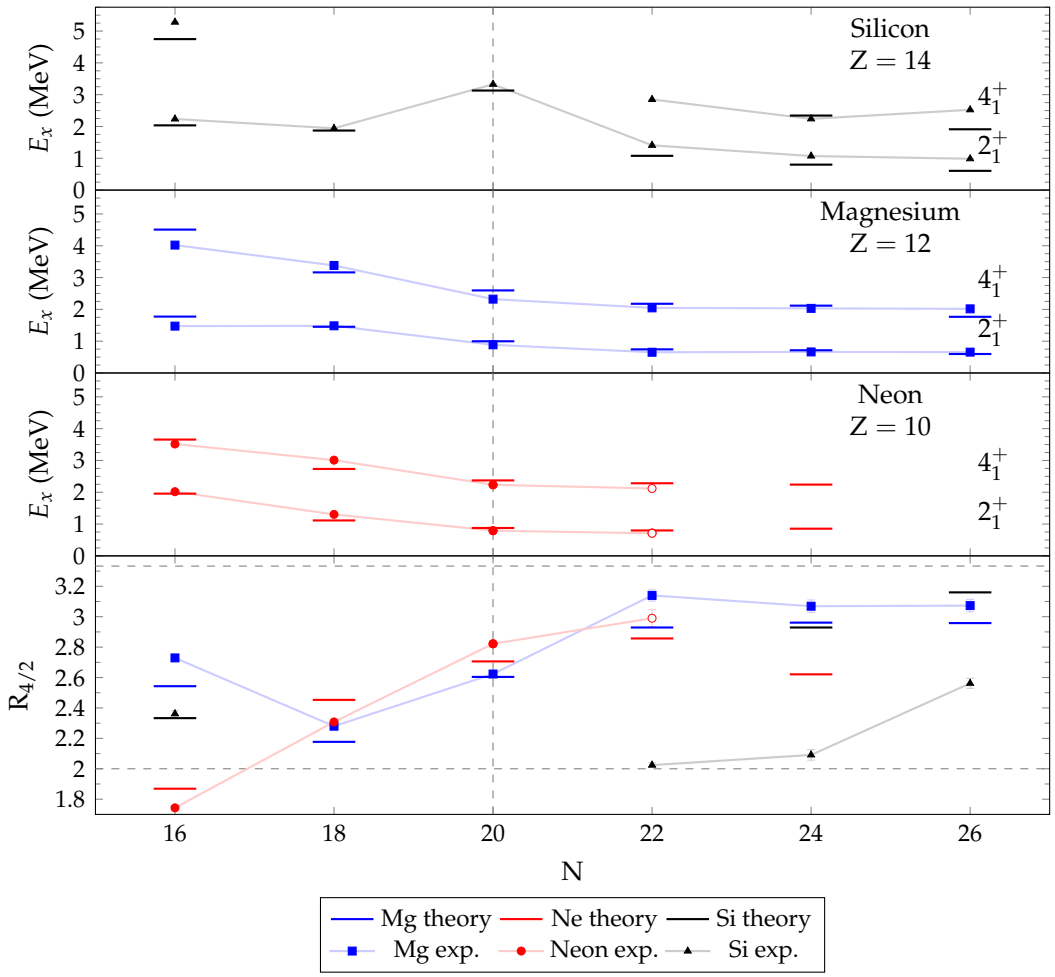

FIGURE 5.1: Systematics of experimental $R_{4/2}$ values, first excited 2_1^+ and 4_1^+ levels across $16 \leq N \leq 26$ for neon (circle), magnesium (square) and silicon (triangle). Open circles are measured in this work. Connecting lines are drawn to guide the eye. Horizontal bars are calculations with EKK developed *sdpf* effective interaction [43]. Dashed horizontal lines for vibrational and rotational limits are drawn at 2.0 and 3.33, respectively. A dashed vertical line at the traditional N=20 magic number. Experimental data were taken from [166, 167, 168, 169, 170, 171, 78].

The predicted excited state energies are in good agreement with the experimentally assigned levels in ^{32}Ne, with all predictions anticipating a less developed rotational band. The observed states and ground state are found to be almost pure intruder configurations with the EEdf1 interaction. They comprise mainly of two-particle two-hole (2p-2h) and four-particle four-hole (4p-4h) components, such as those introduced in section of 1.1.5 and Fig. 1.9. The fractional components of intruder configurations in each of the observed states shown as a percentage in table 5.1. In addition, the $R_{4/2}$ ratio of the 4_1^+ energy ($E(4_1^+)$) over the 2_1^+ energy ($E(2_1^+)$) is predicted to increase to a maximum at $N = 22$, as observed with the increased experimental $R_{4/2}$ of 2.99(6) in ^{32}Ne from 2.82(2) for ^{30}Ne. With the rigid rotor limit of 3.33, the present $R_{4/2}$ suggests a high degree of deformation. Also, with this confirmation of the $R_{4/2}$ ratio for the first time, ^{32}Ne marks the highest experimental $R_{4/2}$ ratio in the neutron-rich neon isotopic chain. These observations provide experimental evidence for the inclusion of ^{32}Ne inside the *island of inversion*.

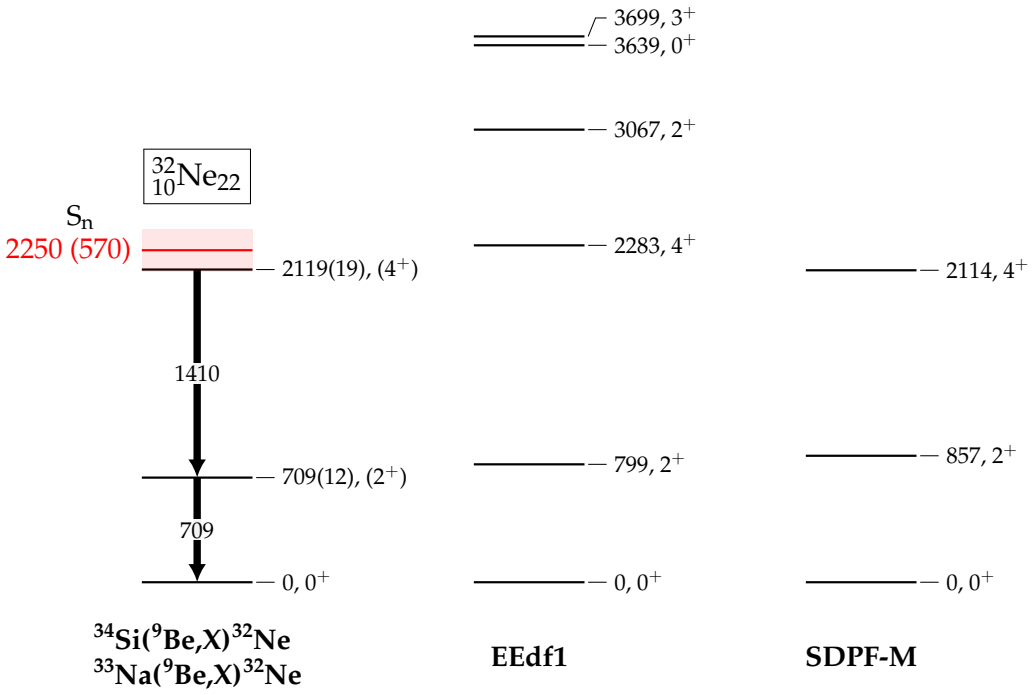

FIGURE 5.2: Tentative experimental and predicted level scheme of ^{32}Ne. Energy levels from the present experiment compared to *EEdf1* [43] and *SDPF-M* [36] effective interaction shell model calculations for ^{32}Ne. The neutron separation energy of 2250(570) keV [27] is shown in red. The uncertainty of the extrapolated neutron separation is shown as the level width.

The 2_1^+ and 4_1^+ energy levels ($E(2_1^+)$ and $E(4_1^+)$), and $R_{4/2}$ ratios of neutron-rich silicon, magnesium, and neon isotopes are shown in Fig. 5.1 and display signatures of shell evolution. The rapid increase in $E(2_1^+)$ for silicon at $N = 20$ is an indication of a good shell closure, in contrast to the lowering of $E(2_1^+)$ and $E(4_1^+)$ with increasing neutron filling for magnesium and neon. Conversely, the increasing $R_{4/2}$ ratio is emblematic of a developing quadrupole collectivity in magnesium, and this new measurement confirms the continuation of a similar trend in neon for $N > 20$.

5.1.3 Cross sections

The experimental one- and two-proton knockout cross sections can be compared to theoretical calculations. Direct reaction theory (as introduced in section 1.2) in combination with the shell model (nuclear structure) overlaps, given by the spectroscopic factors C^2S (equation 1.18), are used to calculate the exclusive and inclusive one-proton removal cross sections to ^{32}Ne. Similarly, for the theoretical calculation of the two-proton removal cross section, the two-nucleon amplitudes (TNA) are employed.

The sudden (fast collisions) and eikonal (forward scattering) approximations are used [172, 173, 89, 93] (section 1.2.2). Specific details to the inputs of these reaction calculations, and of the use of Hartee-Fock calculations to provide constraints to the projectile-target distorting interactions and the proton bound-state potential geometries are discussed in Ref. [94, 174] and [89, 93].

For the reaction of ^{34}Mg(^{9}Be,X)^{32}Ne, a similar reaction of one-proton removal in a direct step and the subsequent evaporation of a separate proton would be indistinguishable in the experimental setup. Such a reaction would have to be treated explicitly in the theoretical reaction cross section calculations due to the non-direct nature of the process. Fortunately, the direct nature of the two-proton removal mechanism is guaranteed by the energetics involved in the removal of the well-bound protons [92, 89]. The evaporation of a proton from ^{33}Na is highly suppressed as a consequence from the substantial asymmetry in the proton and neutron separation energies. For protons, 20.510(680) MeV of energy is required for removal. While for neutrons, the energy is only 2.930(450) MeV. Therefore, the loss of neutron over a proton is favoured for a high excitation of the intermediary nucleus ^{33}Na. Such an alternative reaction is clearly distinguishable, as the reaction residue would appear in the ZeroDegree PID as ^{32}Na.

In general, direct reactions using ^{9}Be targets will induce reactions proceeding by elastic (diffraction dissociation) and inelastic (stripping) processes (section 1.2.1 and equation 1.20). These mechanisms are calculated separately in reaction theory but are indistinguishable in the experimental setup. The relative contributions of elastic and inelastic processes were individually identified [175, 176] and shown to be in good agreement with eikonal model predictions in case of reactions involving both strongly and weakly-bound nucleons. For the strongly bound protons removed in the one- and two-proton knockout reactions to ^{32}Ne, the stripping mechanism is dominant.

The experimental inclusive cross sections to ^{32}Ne (section 4.1.1.1 and 4.1.2.1) are corrected to take into account tracking inefficiencies, indistinguishable reactions in the 1 mm plastic scintillator at F7 before the target, and acquisition deadtime. These corrections were previously detailed in section 3.3. Additionally, uncertainties in the target areal density, transmission, and reaction contaminants are included. The calculation of the exclusive cross sections requires the determination of the population fraction to each state. With the two transitions observed in ^{32}Ne (Fig. 5.2), it is straightforward to reconstruct the number of populated 4_1^+ states, 2_1^+ states and direct population of the ground state. A 6% uncertainty due to the difference between the simulated and measured DALI2 γ-source efficiency is additionally added.

5.1.3.1 Two-proton knockout cross section

The experimental inclusive cross section of the two-proton knockout reaction of 144(15) µb (section 4.1.1.1) is significantly smaller than the theoretical prediction of 530 µb with TNAs calculated by the EEDf1 interaction. With the SDPF-M interaction a similar large theoretical cross section is calculated to be 664 µb.

The inclusive cross sections are presented in Fig. 5.3 and table 5.2. The figure, showing two-proton knockout cross sections, additionally presents the systematic trend of reactions to ^{26,28,30}Ne. In the below figure, the reduction factor trend is shown. The inclusive reduction factor (section 1.2.3) is calculated as the ratio between theoretical to experimental cross sections. For the reaction to ^{32}Ne, this factor is 0.27(3) with the EEdf1 interaction TNA. A specific reduction factor for exclusive reaction channels (as explained later) can additionally be calculated, such as the population of the ground state ($0^+_{g.s.} \rightarrow 0^+_{g.s.}$) which is likewise shown in Fig. 5.3 for several reactions.

The drop in reduction factor, $R_s(2N)$, with increasing proton/neutron asymmetry, from values close to 0.5 deduced on less exotic nuclei [93, 177], may be understood as a missing structure difference between projectile and residue not present

in the shell model TNA. The 0.18(4) reduction factor in ^{30}Ne was interpreted as a missing neutron structure change between ^{32}Mg and ^{30}Ne [165]. It was proposed that SDPF-M calculations producing the TNA inputs did not incorporate a change in particle-hole excitation fraction in the ground state of ^{32}Mg and the excited and ground states of ^{30}Ne. It was suggested ^{30}Ne would contain a greater fraction of 4p-4h excitations. This interpretation of missing excitations was extended to binding of $^{(29,31)}$F. The SDPF-M interaction predicts ^{31}F to be particle unbound, contrary to experimental observations [178, 179].

The 4p-4h excitation fraction is higher in both ^{32}Mg and ^{30}Ne as predicted by recently available EEdf1 interaction (table 5.1). The same is true for ^{34}Mg and ^{32}Ne studied in this work, with a significant increase in 4p-4h between SDPF-M and EEdf1 interactions. For example in ^{32}Ne, 13.4% compared to 50.6%. Additionally, the relative difference between projectile and residue, Mg and Ne, particle-hole fraction is comparable in the predictions by SDPF-M and EEdf1 interactions. The relative difference is small and therefore not suggesting a substantial variation in nuclear structure.

With the available observations and theoretical predictions by the two shell model interactions, a conclusive interpretation of the large reduction factor for both ^{32}Mg to ^{30}Ne and ^{34}Mg to ^{32}Ne cannot be established. This is a consequence of the intertwined nature of a theoretical reaction calculation, where both input from shell model overlaps and reaction theory (and it's inputs) are required.

The result of similar theoretical inclusive cross sections, yet with different particle-hole fractions (table 5.1), can be understood as the result of similar TNA values by the SDPF-M and EEdf1 interactions. The TNA values are presented graphically in Fig. 5.4. The difference between the two interactions is the allocation of strength from the $0d_{5/2} \otimes 0d_{5/2}$ TNA to the *pf* shell orbital TNA values as seen in the figure.

5.1.3.2 One-proton knockout cross section interpretation

In the case of the one-proton knockout reaction the theoretically calculated inclusive cross section is 11.55 mb with TNA from the EEdf1 shell model interaction. This is higher than the experimental value of $4.3(5)$ mb. The corresponding reduction factor is 0.37(4). The systematic trend of nucleon reduction factor, as a function of separation-energy asymmetry, is shown in Fig. 5.5 from a wealth of experimental and theoretical results [94]. The value of one-proton knockout to ^{32}Ne is displayed in the figure and identified as the projectile ^{33}Na, and falls within the trend. The nucleon separation-energy asymmetry $\Delta S = S_p - S_n = +18.37$ MeV. A recent experiment, on one-proton removal from ^{30}Ne (for which $\Delta S = +21.0$ MeV), was analysed using similar theoretical methods [180] but with inputs that differ in detail from those used both here and in the systematic analyses of [94]. That analysis reported an R_s value of 0.30, also consistent with the published systematic trends.

The reason for deduced supression factor as a function of nucleon separation asymmetry has not been established. However, short and collective long range correlations unaccounted for in shell-model calculations have been suggested to contribute to the one-nucleon suppression factor for stable nuclei [181]. These nucleon-nucleon correlations extend the contributions from single-particle orbitals and shift strength from the particle to hole channel, resulting in a deviation from independent-particle-model occupancies. Measurements of electron-induced proton knockout reactions for nuclei close to stability have revealed quenching of the spectroscopic strengths on the order of $\approx$ 30% [88, 181]. As in the case with two-nucleon knockout, the intertwined nature of shell-model C^2S and reaction formalism (and inputs)

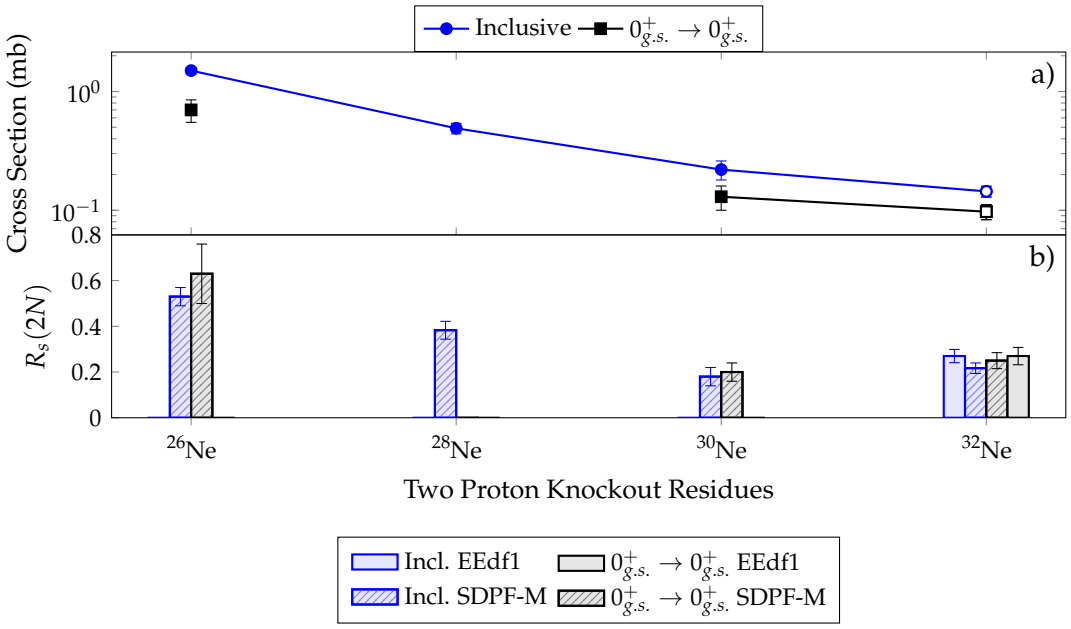

FIGURE 5.3: (a) Two-proton knockout experimental inclusive and $0^+_{g.s.} \rightarrow 0^+_{g.s.}$ cross sections. Data taken from [92, 93, 165]. (b) $R_s(2N)$ suppression factors utilizing EEdf1 and SDPF-M interactions. The theoretical inclusive cross sections to ^{26}Ne and ^{28}Ne are calculated with the eikonal reaction framework, described in this report, to be 2.82 mb and 1.28 mb. The associated 2N knockout inclusive $R_s(2N)$ are ^{26}Ne and ^{28}Ne are 0.53(4) and 0.38(4).

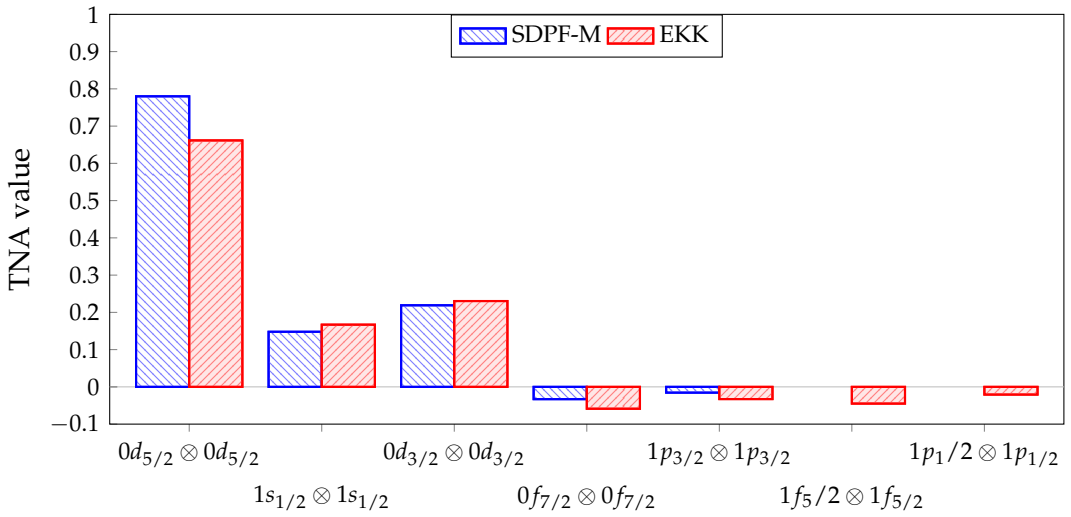

FIGURE 5.4: Visualization of the $^{34}_{12}$Mg ground state to $^{32}_{10}$Ne ground state TNA from shell model calculations with SDPF-M and EEdf1 interactions

to calculate a theoretical cross section, it is not possible to identify a direct contributor to the one-nucleon cross section deviation. However, recent transfer reaction experiments, as a spectroscopic probe, display a weak dependence of the reduction factors and correlations as a function of Fermi surface asymmetry [182, 183, 184].

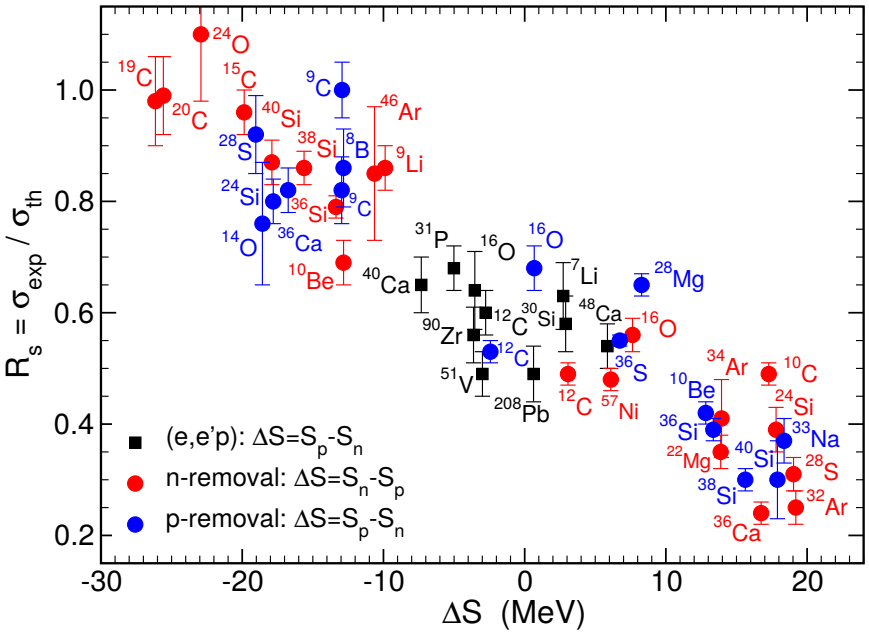

FIGURE 5.5: Systematic trend of reduction factors as a function of nucleon separation energy asymmetry. The mark of ^{33}Na is this work. Private communication by Jeff Tostevin.

5.1.3.3 Exclusive cross sections

The exclusive cross sections are presented in the chart of Fig. 5.6 and table 5.2. In the figure, the fractional population can be observed. A difference in this fraction appears between the two reaction mechanisms. For the one-proton knockout reaction, the population of the 2_1^+ is favoured, while for the two-proton knockout reaction the ground state is populated strongly. The results for a similar two-proton knockout reaction to ^{30}Ne, observed at lower beam energy but also employing an ^{9}Be target, is also presented in the figure. In the reaction to ^{30}Ne, similarly, the direct population of the ground state is favoured. The theoretical predictions of the exclusive cross sections included infigure (5.6) and table (5.2). For visualization in the plot, the exclusive cross sections are scaled by the reaction inclusive reduction factors. The theoretical scaled exclusive cross sections show the same general features as the experimental results. In the one-proton knockout exclusive cross sections, both experimental and theoretical cross section to the 2_1^+ is strongly favoured over the population of the 4_1^+ state. This adds to the tentative spin and parity assignment of the two excited states, as a reverse assignment of the experimentally observed transitions would not agree with this theoretical result.

The small theoretical exclusive cross section for directly populating the ground state of ^{32}Ne is a consequence of the small occupancy of the $0d_{3/2}$ orbital in the ^{33}Na ground state.

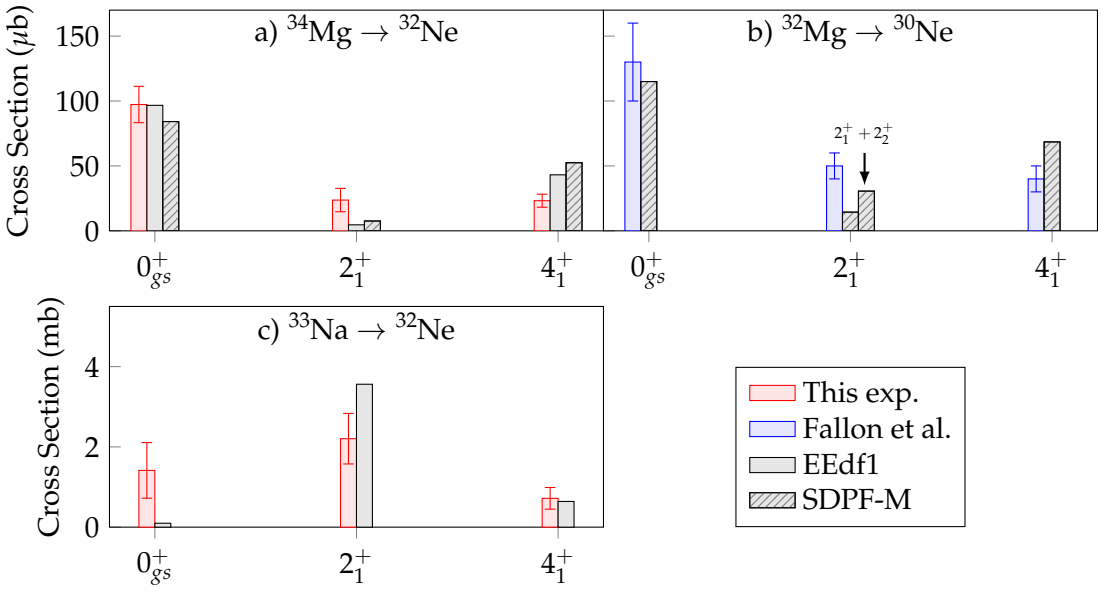

FIGURE 5.6: Experimental exclusive cross sections and theoretical predictions from shell model calculations. Exclusive theoretical cross sections are scaled by the inclusive R_s value for the visualization of the populated ratio. (a) Two-proton knockout reactions to $^{32}_{10}$Ne. (b) Two-proton knockout reactions to $^{30}_{10}$Ne [165]. The cross section to 2^+_1 was conjectured to be unobserved feeding from a 2^+_2 state. The combined cross section is also plotted. (c) One-proton knockout reactions to $^{32}_{10}$Ne.

TABLE 5.2: One- and two-proton knockout cross sections for ^{9}Be(^{33}Na,^{32}Ne)X and ^{9}Be(^{34}Mg,^{32}Ne)X reactions. Spin and parity assignment J^{π}, excitation energy E_x, transition energy E_γ, calculated single-particle cross section σ_{sp} and shell-model spectroscopic factor C^2S for the one-proton knockout reaction, and theoretical and experimental individual cross section, σ^{th} and σ^{exp}, respectively. The inclusive suppression factors are 0.37(4) for the ^{9}Be(^{33}Na,^{32}Ne)X reaction ($\Delta S = +18.37$) and 0.27(3) for the ^{9}Be(^{34}Mg,^{32}Ne)X reaction calculated with the EKK-SDPF interaction.

(A) One-proton knockout

			^{9}Be(^{33}Na,^{32}Ne)X					
						EEdf1		
J^{π}	E_x (kev)	E_γ (kev)	$n\ell_j$	C^2S	σ_{sp} (mb)	σ^{th}_{-1p} (mb)	σ^{th}_{-1p} (mb)	σ^{exp}_{-1p} (mb)
0			$0d_{3/2}$	0.026	9.53	0.262	0.262	1.4(7)
2	709(12)	709(12)	$1s_{1/2}$	0.010	9.91	0.101	9.563	2.2(6)
			$0d_{3/2}$	0.037	9.37	0.367		
			$0d_{5/2}$	0.864	9.89	9.095		
4	2119(19)	1410(15)	$0d_{5/2}$	0.169	9.58	1.721	1.721	0.72(3)
			Inclusive:				11.55	4.3(5)

(B) Two-proton knockout

			^{9}Be(^{34}Mg,^{32}Ne)X		
			EEdf1	SDPF-M	
J^{π}	E_x (kev)	E_γ (kev)	σ^{th}_{-2p} (μb)	σ^{th}_{-2p} (μb)	σ^{exp}_{-2p} (μb)
0			355	387	97(14)
2	709(12)	709(12)	17	34.8	24(9)
4	2119(19)	1410(15)	158	241	23(5)
		Inclusive:	530	664	144(15)

5.2 $^{(39-41)}_{13}$Al

5.2.1 Systematic trends around $N = 28$

The evolution of proton and neutron orbits while moving from stability to the last known neutron-rich $N = 28$ isotone ($^{40}_{12}$Mg), either along isotones or isotopes, is strongly influenced by the dynamic nature of the proton-neutron interaction with respect to orbital occupancy (section 1.1.6). A imprint of these transformations is found in the excited state structure of neutron-rich isotopes.

A compilation of excited level energies spin and parity of odd-even $_{17}$Cl, $_{15}$P and $_{13}$Al is presented in Fig. 5.7. Superimposed over these levels are the $E(2^+_1)$ excited energies of the even-even nuclei $^{(A-1)}_{(Z-1)}$X. Even-even nuclei provide a clean indication of the erosion of the *magic numbers*. The disappearance of the $N = 20$ and $N = 28$ spherical shells are seen in the lowering of the $E(2^+_1)$ energies. Neutron number $N = 20$ was previously discussed within the context of the *island of inversion* and shown in Fig. 5.1. The dotted line for $^{40}_{12}$Mg is the predicted energy levels by state-of-the-art shell model calculations with the SDPF-MU interaction (733 keV) and SDPFU-SI interaction (546 keV) [79]. Additional predictions by mean field calculations (1DAMP+GCM and 3DAMP+GCM) are additionally plotted as 556 keV and 533 keV [185]. The low predicted energy suggest a lack of a spherical $N = 28$ shell.

The evolution of single-particle excitated states has been investigated and discussed for isotopic chains of $_{19}$K, $_{17}$Cl and $_{15}$P [69]. Excited states of $1/2^+$ and $3/2^+$ of single-proton nature provide an understanding on the dramatic evolution of the proton $\pi 0d^+_{3/2}$ and $\pi 1s^+_{1/2}$ orbits, the collapse of the $Z = 16$ subshell also provides a benchmark for central, spin-orbit and tensor components of the nucleon-nucleon interaction [69]. The extracted energy difference between these states can be observed in the overview of experimental level schemes of Fig. 5.7, and is isolated in Fig. 5.8. In $_{17}$Cl isotopes the lowering of $1/2^+$ eventually replaces the $3/2^+$ ground state.

Along neutron-rich aluminium isotopes, as shown in Fig. 5.7, no spin or parity assignment is provided in literature above ^{31}Al. Therefore, the assignment of excited state spin and parity based on systematic trends of experimental excited state spin and parity is not possible for the odd-even $^{(39,41)}_{13}$Al isotopes studied. Instead, shell model calculations produced with SDPF-M and SDPF-MU interactions can provide guidance on tentative assignments.

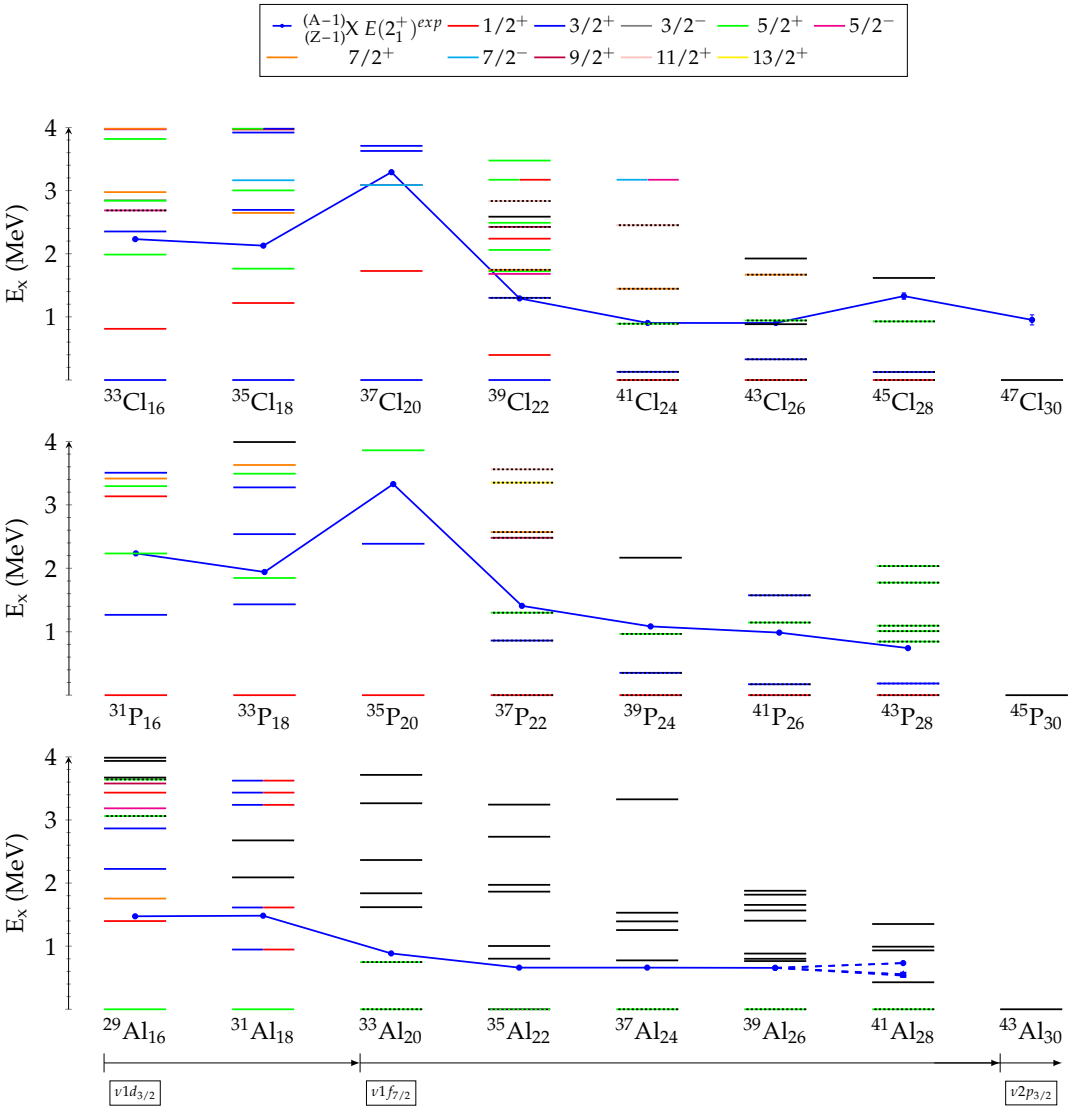

FIGURE 5.7: Systematic trends of level schemes of $_{17}$Cl, $_{15}$P, $_{13}$Al and core nucleus $E(2^+_1)$ energies. The $^{40}_{12}$Mg $E(2^+_1)$ predicted by shell model calculations are drawn at 732 keV (SDPF-MU interaction), 546 keV (SDPFU-SI interaction) [79]. Additional mean-field results are drawn at 556 keV and 533 keV [185].

5.2.2 $^{39}_{13}$Al

The tentative experimental level scheme of $^{39}_{13}$Al is compared to shell model predictions in Fig. 5.9. The assignment of 764, 800 and 883 keV transitions directly to the ground state closely resembles the level configuration predicted by the SDPF-MU interaction, with a triplet of states well separated from a higher density of states. The

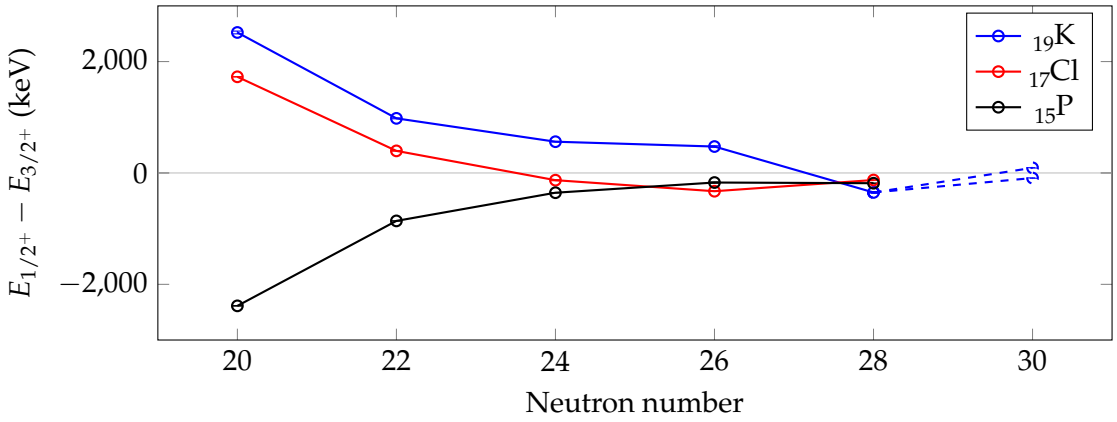

FIGURE 5.8: Evolution of the $E(1/2^+_1) - E(3/2^+_1)$ energy differences for odd-mass $_{19}$K, $_{17}$Cl and $_{15}$P. Dashed lines show two possible spin assignments for $^{49}_{19}$K. The inversion of $_{15}$P energy differences is a consequence of the opposite proton-hole nature of the states. Data from [69] and citations within.

experimental energy levels of this triplet closely matches the predicted energy levels within approximately 100 keV. This assignment has previously been suggested in the first spectroscopy of $^{39}_{13}$Al produced by proton knockout reactions [156], although only the highest intensity 800 keV γ-ray was placed in the level scheme.

The SDPF-MU interaction reduced transition probabilities ($B(E2)$ and $B(M1)$) are calculated to corroborate decay patterns, spin assignment and to study the collectivity. Effective charges for protons and neutrons of 1.25e and 0.45e are used. The g factors in calculations of $B(M1)$ are the free nucleon g factors. The predicted branching ratios (greater than 10%) are displayed in Fig. 5.9 by the width of the arrows. The states 863 keV and 855 keV are not predicted to appreciatively feed the first excited 836 keV state and instead transition directly to the ground state. The predicted branching ratios (greater than 10%) from higher energy states (between 1448 keV to 1868 keV) reveals only the state at 863 keV is populated by more than one state. The states 1448 keV and 1803 keV decay to 863 keV with transitions of 585 keV and 940 keV. This provides a weak suggestion that the experimental level at 883 keV, with two observed coincidences, may match the predicted 863 keV state with spin parity of $7/2^+$. The process of inelastic scattering favours collective vibrational or rotational excitations. The reduced transition probabilities $B(E2; 5/2_{g.s.} \rightarrow 7/2^+_1)$, $B(E2; 5/2_{g.s.} \rightarrow 3/2^+_1)$, and $B(E2; 5/2_{g.s.} \rightarrow 1/2^+_1)$ are calculated by SDPF-MU to be 178, 15.1, 21.3 $e^4(\text{fm})^2$ or 21.2, 1.80, 2.50 Weisskopf units (W.u.), respectively. Therefore, the highly collective excitations to this triplet are favoured. A two DALI response function fit to the low statistics inelastic scattering γ-ray energy spectrum results in centroid energies of 879(19) keV and 783(14) keV, as described in section 4.2.1. This suggests a $7/2^+$ assignment to one of these tentative levels.

Furthermore, the experimental and SDPF-MU predicted level scheme is similar in the separation between lower energy and higher energy level groupings on the order of 600 keV to 900 keV. However, the predicted branching ratios do not reproduce the experimental low energy transitions of 250 keV and their suggested placement. The two experimental transitions observed in the singles γ-ray energy spectrum (coloured in blue), suggested as direct ground state transitions, depopulation from several excited states within the higher energy group. The similar energy and overlap in uncertainty between the 1416(25) keV transition and the tentative

1404(12) keV excited state may suggest the same excited state.

For additional comparison, the predicted level scheme produced by shell model calculations with the SDPF-M interaction is presented on the right in Fig. 5.9. The SDPF-M interaction does not encompass the complete *pf* valence space for neutrons and is limited to $1f_{7/2}2p_{3/2}$ orbits, unlike the SDPF-MU interaction. This truncation may contribute to the predicted higher first excited states and lowered first $9/2^+$ state through limiting neutron occupancies above the $2p_{3/2}$ orbit.

Lastly, the state lifetimes can be predicted from the calculated M1 and E2 transition rates from the SDPF-MU shell model calculations. The levels at 836 keV, 855 keV have relatively long predicted lifetimes of 44 ps and 11 ps compared to the 863 keV (0.1 ps) and all other shell model levels. The experimental γ-ray energy spectra are fit with DALI response functions for prompt decays and do take into consideration the potential lifetime related shift in energy, as previously considered for ^{32}Ne (section 4.1.1). Such a shift would be expected to be on the order of 10 keV.

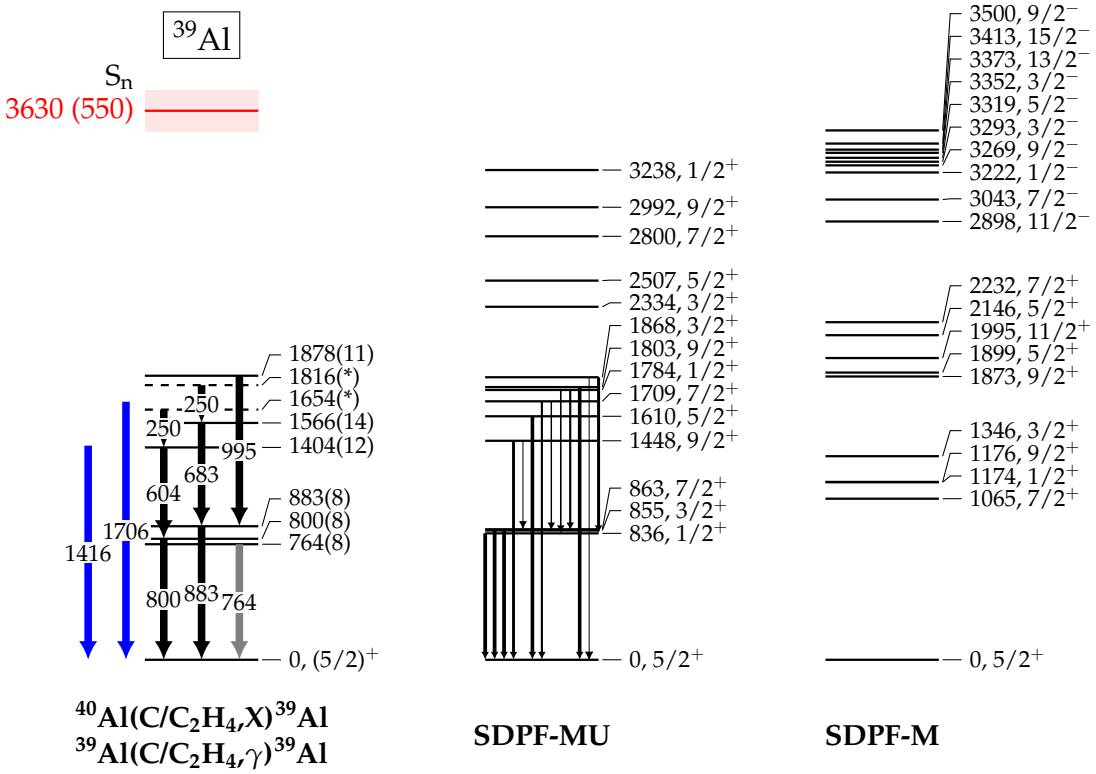

FIGURE 5.9: Experimental transitions, tentative and predicted levels of $^{39}_{13}$Al. Black arrows represent transitions with tentative assignment based on coincidences. Blue arrow shows transition from singles spectra without coincidences. Grey arrow is an unobserved transition, but observed in a similar knockout reaction from [156] employing high resolution HPGe detectors. Predicted branching ratios greater than 10% are drawn for SDPF-MU. The neutron separation energy of 3630(550) keV [27] is shown in red.

5.2.3 $^{40}_{13}$Al

The odd-odd $^{40}_{13}$Al proposed experimental level scheme is difficult to interpret with guidance from the shell model calculations. The high density of predicted states restricts assignment based on calculated level energy. If the experimental suggested levels at 497 keV and 504 keV are the same state, the competition between two $E2$ and $M1$ transitions may manifest in the branching between a direct ground state transition and the population of the tentative 269 keV state.

Future detailed investigation of the level structure of $^{40}_{13}$Al may necessitate employing higher energy resolution detectors, such as solid state high purity germanium (HPGe) detectors or next generation single-crystal scintillators as investigated in appendix C. Odd-odd nuclei with highly asymmetric neutron to proton ratios, such as $^{40}_{13}$Al may contribute to future benchmarks of nucleon-nucleon interactions.

The SDPF-M interaction prediction anticipates an inversion of parities between low energy and high energy levels, a possible consequence from the missing full pf valence space.

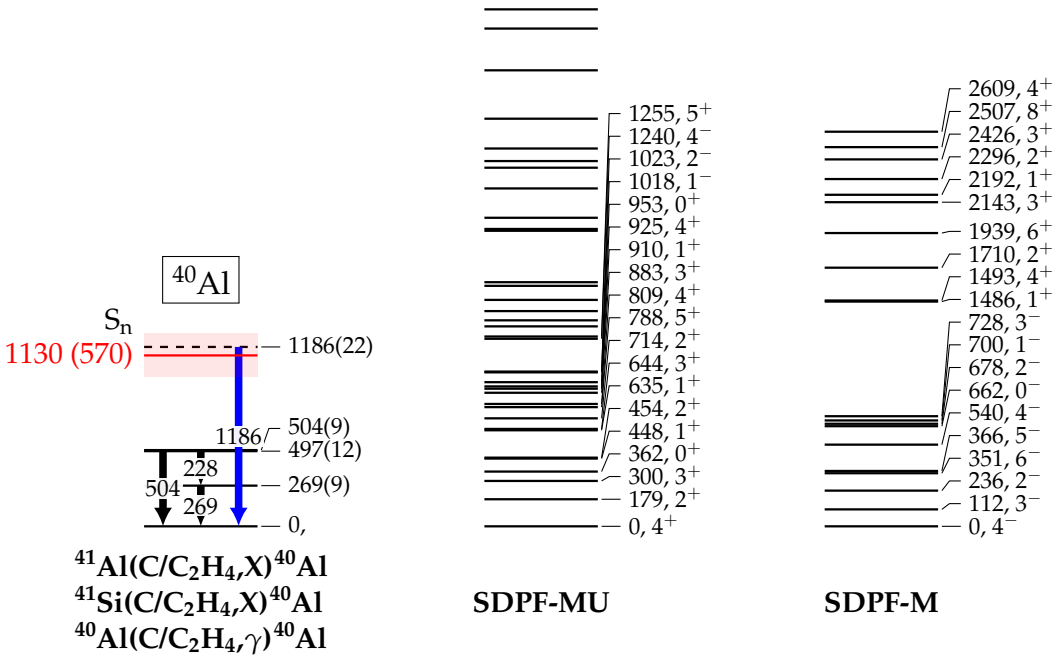

FIGURE 5.10: Experimental transitions, tentative and predicted levels of $^{40}_{13}$Al. Blue arrow shows transition from singles spectra without coincidences. Predicted branching ratios greater than 10% are drawn for SDPF-MU. The neutron separation energy of 1130(570) keV [27] is shown in red.

5.2.4 $^{41}_{13}$Al

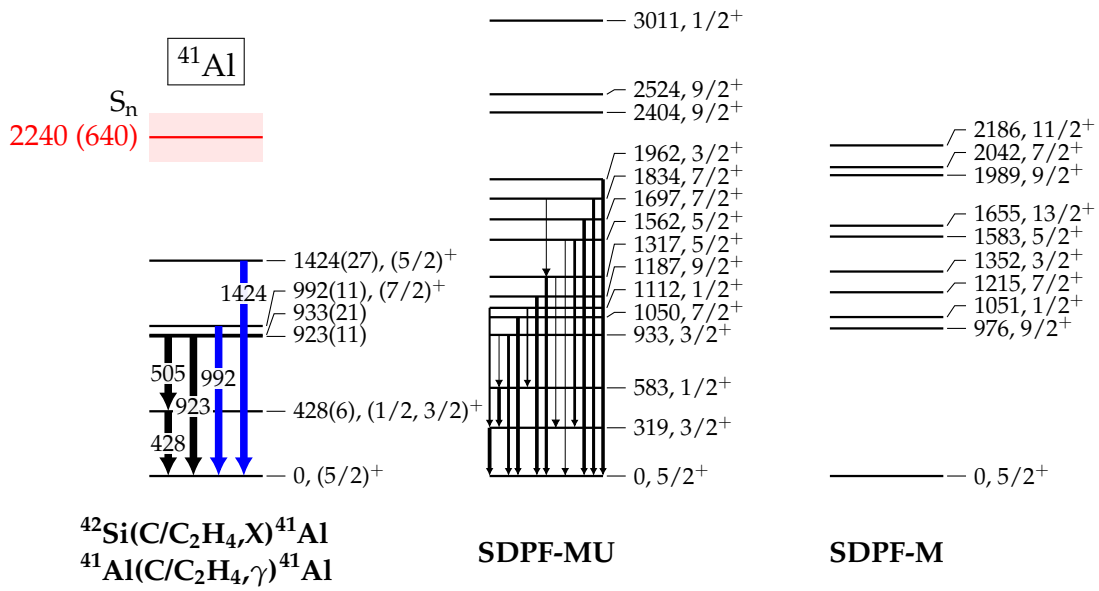

FIGURE 5.11: Experimental transitions, tentative and predicted levels of $^{41}_{13}$Al. Blue arrow shows transition from singles spectra without coincidences. Predicted branching ratios greater than 10% are drawn for SDPF-MU. The neutron separation energy of 2240(640) keV [27] is shown in red.

The experimental and predicted level schemes from shell model calculations of $^{41}_{13}$Al are shown in Fig. 5.11 and show good agreement. The tentative assignment of the low energy excited state at 428 keV matches with predictions of low energy states with the SDPF-MU interaction. Across odd-even neutron-rich isotopes of aluminium, this represents the lowest excited state by nearly a factor of two (shown in Fig. 5.7).

Calculations with the SDPF-MU interaction predict two low excited states at 319 keV and 583 keV. As such, assignment of the experimental low energy state cannot be made only by level energy. Spectroscopic factors describing the parentage between the $0^+_{g.s.}$ ground state of the $^{42}_{14}$Si projectile and $^{41}_{13}$Al are presented in table A.1 in appendix A and suggest a strong overlap to both low energy states. The C^2S value of 0.266 and 0.481 suggest a greater populated fraction of the 583 keV state for a one-proton knockout reaction. However, the theoretical branching ratios calculated by reduced transition rates ($B(M1)$ and $B(E2)$) predict the 583 keV state decaying predominately to the 319 keV state (95%). Therefore, the γ-ray transition from the depopulation of the first excited state would be expected to have the greatest intensity. With this prediction the experimental 428 keV excited state is tentatively assigned spin and parity of $3/2^+$.

The low energy strength in the coincidence γ-ray energy spectrum of Fig. 4.57 and the singles spectrum with only forward angle DALI detectors Fig. 4.52 showing an unplaced 160 keV γ-ray (predominately for events of low m_γ) may suggest a low energy transition in coincidence with 428 keV. If placed above the 428 keV first excited state, the structure would match the predicted SDPF-MU level of $1/2^+$. However, the limited statistics does not provide strong enough evidence for this level assignment.

The one-proton knockout reaction from deeply bound *spsd* protons favours population of excited states in $^{41}_{13}$Al of $5/2^+$ given the high occupancy of the $\pi 1d^+_{5/2}$ orbit. This is seen in the spectroscopic values of table A.1. The largest value corresponds to the $^{41}_{13}\mathrm{Al}\ 5/2^+_{g.s.}$ and is compatible to the observed low γ-ray yield per ion. The second $5/2^+_2$ state additionally has a large spectroscopic value, with a predicted level energy of 1317 keV and decays mainly (85%) directly to the ground state. Both the high predicted intensity and γ-ray energy may weakly suggest assignment to the observed 1424 keV γ-ray with large experimental intensity at low m_γ (Fig. 4.53).

The large $B(E2; 5/2_{g.s.} \rightarrow 7/2^+_1)$ value calculated by the SDPF-MU interaction of 169.1 $e^4(\mathrm{fm})^2$ (20.1 W.u.) for the predicted $7/2^+$ state at 1050 keV, in combination with the absence of a nuclear overlap with the $0^+_{g.s.}$ ground state of $^{42}_{14}$Si (table A.1) (due to angular momentum coupling), suggests a strong population of the $7/2^+$ state in inelastic scattering and absence in the one-proton knockout reaction. The experimental tentative level at 992 keV (observed as 1017 keV in the one-proton knockout reaction) fits this description with strong intensity for inelastic scattering and near absence in the knockout reaction γ-ray energy spectrum. A highly collective excitation to $7/2^+_1$ is also predicted by SDPF-MU calculations for $^{39}_{13}$Al.

The observation of the population of this state in the one-proton knockout γ-ray energy spectrum (Fig. 4.51 and 4.52) can be understood as the consequence of the three-step nature of projectile fragmentation. With friction from kinetic energy loss, exchange of nucleons, and transformation into internal degrees of freedom [186]. In the removal of deeply bound nucleons (such as protons from neutron-rich nuclei), forbidden states can arise from these dissipative processes during the core-target collusion time. The reaction occurs at the projectile surface increasing the chance for nucleon rearrangement.

Lastly, the two tentative experimental states at 923(11) keV and 933(21) keV are within uncertainties and may represent the same excited state. The SDPF-MU excited state at 933 keV, with spin of $3/2^+$, is a candidate for the experimental combined 923 keV and 933 keV state because of similar energies and decay pattern. The predicted 933 keV $3/2^+$ state decays to the ground state and the first $1/2^+$ state. The branching ratio (calculated by $B(M1)/B(E2)$ values) to the ground state is 76% and to the$1/2^+$ (583 keV) state is 24%. This is similar to the ratio betwen the experimental 505 keV and 923 keV γ-rays, with 2.7(9) γ-rays per 100 ions and 4.8(9) γ-rays per 100 ions, respectively. This requires the experimental 428 keV state to be labeled as $1/2^+$ instead of $3/2^+$. However, as mentioned previously, the complete depopulation of the first $1/2^+$ to first $3/2^+$ is predicted by SDPF-MU.

An alternative scenario of placing the 505 keV transition feeding a missing $1/2^+$ state above the 428 keV $3/2^+$ state by less than 50 keV may be possible. A large difference in energy between a missing $1/2^+$ and $3/2^+$ state at 428 keV would not allow for the energy sum to match the 933 keV direct ground state transition. The inversion of first $1/2^+$ and $3/2^+$ states may also be a scenario, but must be separated by a small energy difference.

In a similar manner to $^{(39,40)}$Al, the predicted level scheme of SDPF-M is presented on the right of Fig. 5.11. The previous comparisons show large deviation between SDPF-M and SDPF-MU and with the increased neutron filling of $^{41}_{13}$Al, the SDPF-M interaction is not anticipated to be accurate. Nonetheless, the deficiency of low-lying excited states in the predicted levels of SDPF-M suggest the necessity of neutron excitations above $\nu 2p_{3/2^+}$ playing a role in their formation.

Like $^{39}_{13}$Al, state lifetimes are calculated from SDPF-MU transition probabilities. Similarly, the lowest shell model levels at 319 keV and 583 keV have relatively long

predicted lifetimes of 46 ps and 10 ps compared to most other levels. This may induce a lifetime effect, shifting the transition energy on the order of 10 keV.

5.2.5 Odd-even Al systematic trends and discussion

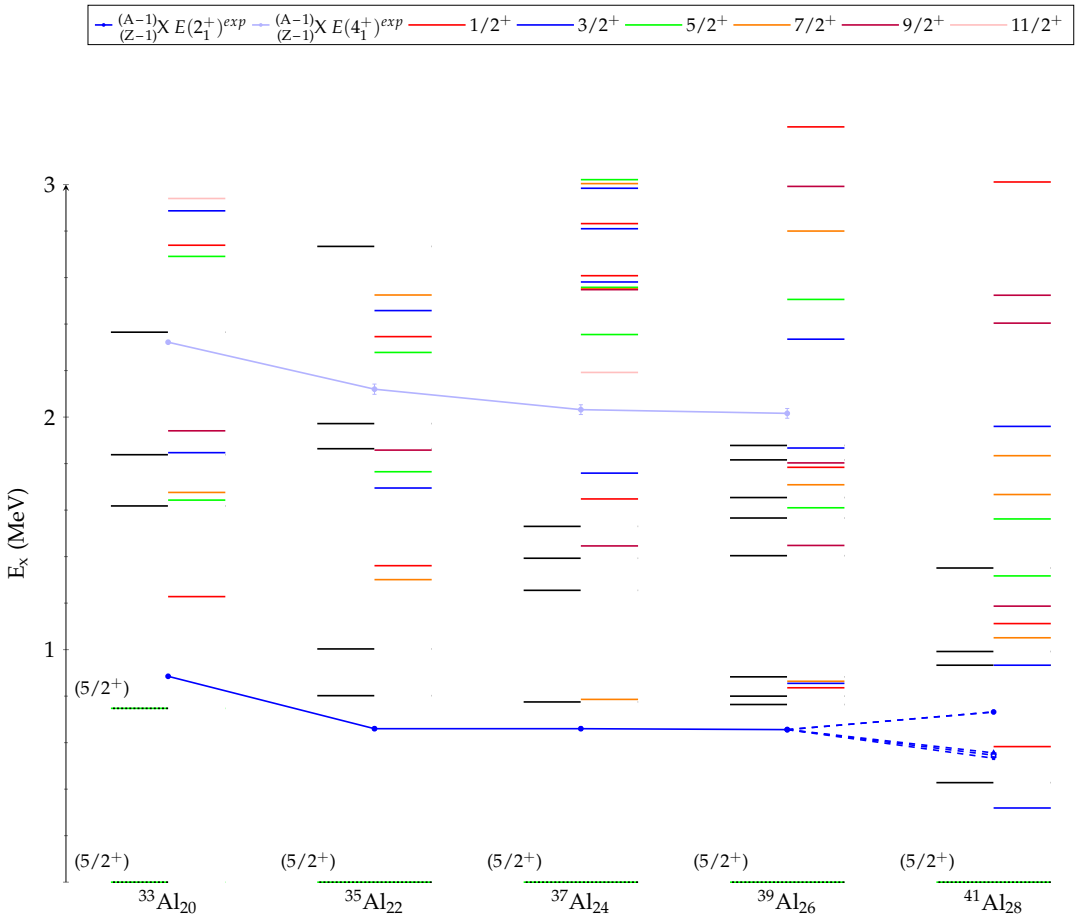

FIGURE 5.12: Experimental (left side of each isotope) and predicted (right side of each isotope) level scheme of odd-even neutron-rich aluminium. Predicted level energies, spins and parities from shell model calculations with the SDPF-M ($^{(33,35,37)}_{13}$Al) and SDPF-MU interactions ($^{(39,41)}_{13}$Al). The $^{40}_{12}$Mg $E(2_1^+)$ predicted by shell model calculations are drawn at 732 keV (SDPF-MU interaction), 546 keV (SDPFU-SI interaction) [79]. Additional mean-field results are drawn at 556 keV and 533 keV [185].

The systematic trend of excited states in odd-even aluminium isotopes and $E(2_1^+)$ and $E(4_1^+)$ energies of magnesium are presented in Fig. 5.12. In addition, predicted levels by shell model calculations employing SDPF-M ($^{(33,35)}_{13}$Al) and SDPF-MU interactions ($^{(37,39,41)}_{13}$Al) are displayed for each isotope on the right side. The shell model calculations show agreement with the suggested experimental level schemes. The first excited state energies as well as the formation of higher energy excited state groupings is reproduced.

The significant drop in the first excited state energy, observed in the first spectroscopy of $^{41}_{13}$Al, is also inline with shell model predictions. The trend of first excited state energies of odd-even aluminium remains flat in Fig. 5.12 and appears to follow the general trend of experimental $E(2_1^+)$ of the magnesium (Fig. 5.7).

The fate of shell closures far from stability can be studied through odd-even nuclei, which may be described by a valence particle or hole coupled to an even-even neighbouring core. An example of this investigation is the recent study of ^{79}Cu to study the shell closures in $^{78}_{28}$Ni [187], with the lack of knockout feeding to low energy excited states suggesting the existence of spherical shell gaps. For odd-A nuclei with low deformation, such as those with magic numbers, the so-called weak-coupling model [188] can be applied. The odd-A basis states are constructed from the particle or hole coupled the $0^+_{g.s}$ ground state and also the collective vibrations of the adjacent even-even nucleus. The latter results in the emergence of a multiplet of states from $l + j_p ... |l + j_p|$, where l is the angular moment of the vibration and j_p is the angular moment of the particle or hole. The identification of this multiplet, predicting the a high E_{2^+} of the even-even neighbouring nuclei therefore can suggest a spherical shell closure.

Aluminium isotopes may likewise be described as a valence proton outside a core of magnesium. The sudden change in $^{41}_{13}$Al at $N = 28$ may suggest a transformation in the $^{40}_{12}$Mg core with the addition of only two neutrons.

The nucleus $^{40}_{12}$Mg sits along the rapid shape changing $N = 28$ isotones and is predicted to be a well-deformed prolate rotor [189]. The neighbouring even-even isotope $^{42}_{14}$Si is suggested to be characterized with an oblate ground state [26, 78]. Shape-coexistence is also expected for both of these isotopes by shell model calculations, with low-lying 0^+_2 prolate and 0^+_2 oblate excited state predicted for $^{42}_{14}$Si and $^{40}_{12}$Mg, respectively [189, 190]. This is additionally predicted by relativistic and nonrelativistic mean-field calculations [191, 76, 185, 192]. Calculated values of the quadrupole deformation parameter (β_2) for $^{42}_{14}$Si and $^{40}_{12}$Mg are introduced later in figure 5.17. The angular momentum projected generator coordinate method (AMP-GCM) with the Gogny force calculates yrast states and a second band existing within opposite wells (prolate and oblate) of AMP potential energy surfaces, for $^{40}_{12}$Mg and $^{42}_{14}$Si [76]. Potential energy surfaces calculated by Hartree-Fock-Bogoliubov (HFB) D1S Gogny [193] effective interaction from the AMEDEE database [194] are shown in Fig. 5.13. The evolution of the oblate deformation is calculated in $_{14}$Si isotopes, with a deepening of an oblate minima. Conversely in $_{12}$Mg isotopes, the prolate well grows, with a secondary minima with oblate deformation with a similar potential energy depth.

Shape-coexistence has been previously reported in $^{44}_{16}$S, with the observation of a low energy 0^+_2 [65], interpreted as spherical state with a prolate ground state [1]. A two-level mixing model is used to understand the mixing of the two shape configurations [198]. This mixing model was similarly adopted to $^{40}_{12}$Mg to interpret the two-proton knockout cross section [79], the only structural evidence of this isotope. The calculations suggest opposite dominate components of oblate and prolate in the ground states of $^{42}_{14}$Si and $^{40}_{12}$Mg, respectively.

Under the normal filling scheme of $^{41}_{13}$Al and a spherical core, the unpaired valence proton would occupy spherical $\pi d_{5/2^+}$ orbit. The core-coupled state spins and parities available for coupling an even-even core, ground state and first 2^+ state, to a valence $\pi d^+_{5/2}$ are,

$$\left|0^+_{g.s} \otimes \pi d^+_{5/2}\right\rangle \rightarrow \frac{5}{2}^+ \qquad \left|2^+_1 \otimes \pi d^+_{5/2}\right\rangle \rightarrow \frac{1}{2}^+, \frac{3}{2}^+, \frac{5}{2}^+, \frac{7}{2}^+, \frac{9}{2}^+ \tag{5.1}$$

As a means to decompose the predicted level wave functions as core-coupled or single-proton-particle states, the spectroscopic factors are calculated between $^{41}_{13}$Al

[1] Interpretations of $^{44}_{16}$S have continued development, such as [195, 196, 197]

and $^{40}_{12}$Mg coupled to *sd* proton orbits and presented in appendix A (table A.2). Table A.3 additionally shows the spectroscopic factors for $^{39}_{13}$Al and $^{38}_{12}$Mg. A similar procedure was adopted for investigating the wavefunctions of the levels in $N = 28$ isotones of $^{47}_{19}$K, $^{45}_{17}$Cl and $^{43}_{15}$P for quantifying the contribution of the $(\pi 0d_{5/2^+})^{-1}$ and the $Z = 14$ subshell gap [70].

The tabulated values show large fragmentation of calculated excited states in both $^{39}_{13}$Al and $^{41}_{13}$Al from pure single-particle character. In both ground states of $^{(39,41)}_{13}$Al, the spectroscopic factors calculate dominate components of $\pi 0d_{5/2}$ valence proton coupled to ground and excited cores of $^{(38,40)}_{12}$Mg. And similarly, the $1/2^+_1$ and $3/2^+_2$ excited states as mainly $\pi 1s_{1/2}$ $\pi 0d_{3/2}$ protons coupled to magnesium ground states. Unique to $^{41}_{13}$Al, is the contribution of the excited 0^+_2 magnesium core contributing to the $1/2_2$ and $5/2_2$ excited states. The 0^+_2 magnesium core does not contribute strongly to the states of $^{39}_{13}$Al. This is likely a consequence of the significantly lower predicted energy level of 0^+_2 in $^{40}_{12}$Mg (1683 keV) as opposed to $^{38}_{12}$Mg (2672 keV).

The structure of odd-A neutron-rich aluminium may be clarified by switching to a deformed basis: the Nilsson model (section: 1.1.4).

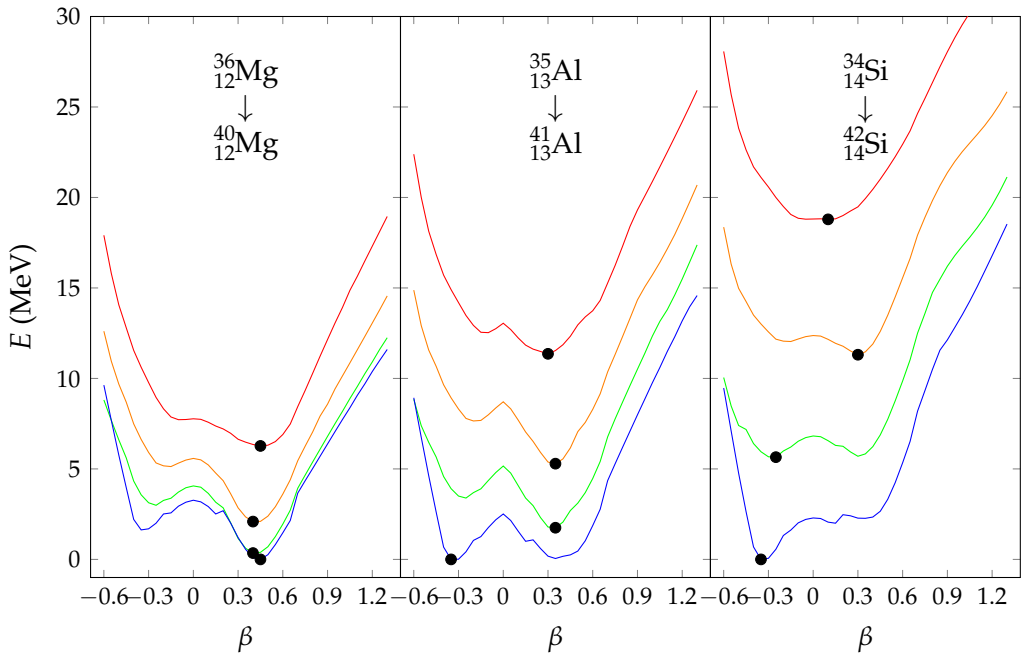

FIGURE 5.13: Hartree-Fock-Bogoliubov calculated energy surfaces of $^{(34,36,38,40)}_{12}$Mg, $^{(35,37,39,41)}_{13}$Al, $^{(36,38,40,42)}_{14}$Si with the D1S Gogny effective interaction [193] from the AMEDEE database [194]. The surfaces of Mg, Al, SI are offset by 259.1 MeV, 281.8 MeV, and 307.7 MeV, respectively. The minima of the energy surfaces are marked for visualization.

5.2.5.1 Deformed basis

The description of deformed nuclei as a valence particle (or hole) coupled to a deformed core may successfully reproduce electromagnetic observables, such as rotational bands. This framework, as described in section 1.1.4 as the Nilsson model, has been successfully applied to proton-rich *sd* nuclei exhibiting significant prolate deformation to interpret experimental observations. For example, the exited states

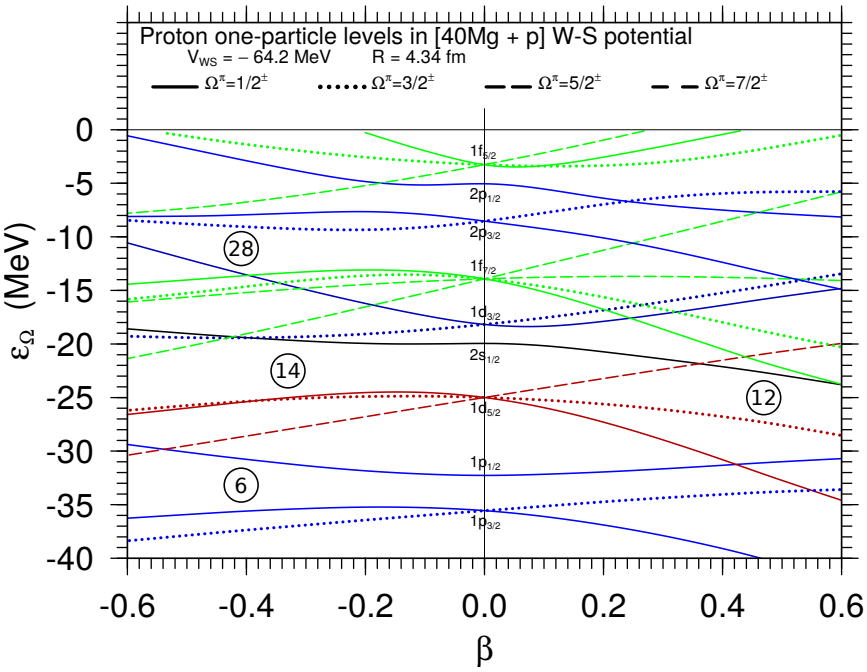

FIGURE 5.14: One-particle energies for protons of the $^{40}_{12}$Mg $\otimes$ π system as a function of axially symmetric quadrupole deformation with the Woods-Saxon potential and standard parametrization of [199] (page 239). Colours are added to the orbits to guide the eye. I. Hamamoto private communication.

of odd-A prolate deformed mirror nuclei $^{25}_{12}$Mg and $^{25}_{13}$Al [200, 47, 201] (Fig. 5-1 5 Bohr, A. & Mottelson, B., Nuclear Structure Vol II) and prolate deformed $^{29}_{13}$Al [202] can be well reproduced.

It should be illustrated that for the intermediate nucleus between these examples, $^{27}_{13}$Al, a simple collective rotational model [7] does not well reproduce experimental observations. The isotope $^{27}_{13}$Al is positioned in the transition region between prolate ($A = 23 - 25$) and oblate deformation ($A = 28$). Although the spin sequence of excited states is consistent with $K^\pi = 5/2^+$ and $K^\pi = 1/2^+$ rotational bands, fitting the observed low-lying level energies leads to significant discrepancies of the calculated momentum of inertia [203, 204, 205, 206]. In addition, observed transition strengths are inconsistent with simple rotational behaviour. Forbidden transitions, as defined by the K-selection rule [7], such as those between $K = 1/2$ and $K = 5/2$ ($\Delta K = 2$) of M1 nature were observed greater than expected [207]. Other inconsistencies include expected intraband and cross-band E2 enhancements [206]. Alternative models for this nucleus include, the weak coupling model, coupling the $0^+_{g.s}$ and excited states (2^+_1) of $^{28}_{14}$Si to a $0d_{5/2}$ hole state [208], rotation-vibration coupling models [209] and Coriolis band-mixing models [210]. This emphasizes application of a simple collective model is not always assured, and detailed spectroscopic information provides clarity for model agreement.

Therefore, a rotational model in the strong-coupling limit can be suggested for $^{(39,41)}_{13}$Al, but cannot be rigorously verified with the limited observation of low-lying experimental level energies. The strong-coupling limit can be justified on the basis of the predicted strong deformation around $N = 28$ in both magnesium and silicon (Fig. 5.17 and references inside). Accordingly, similar rotational bands (e.g. $K^\pi = 5/2^+$, $K^\pi = 1/2^+$) identified for $^{(25-29)}_{13}$Al may be found in $^{(39,41)}_{13}$Al.

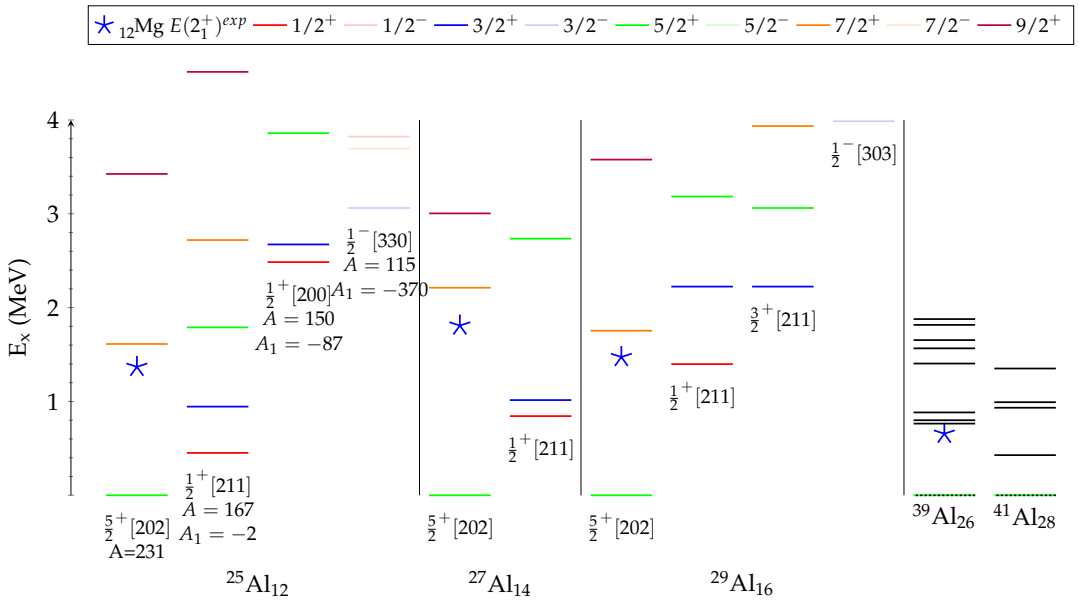

FIGURE 5.15: Rotational bands of $(25,27,29)_{13}$Al [47] and experimental tentative levels of $^{(39,41)}_{13}$Al

The rotational bands of $^{(25-29)}_{13}$Al and the experimental levels of $^{(39,41)}_{13}$Al are compared in Fig. 5.15. The ground state bands of $^{(25,29)}_{13}$Al have been identified as belonging to Nilsson orbitals $5/2^+[202]$, with a spin sequence of excited levels $5/2^+, 7/2^+, 9/2^+$.... The next observed lowest rotational band head is built on the $1/2^+[211]$ Nilsson orbit. Higher energy band heads have been identified as $1/2^+[200]$ and $1/2^-[303]$.

The level energies and the predicted spin and parity of three lowest levels ($1/2^+$, $3/2^+$, $7/2^+$) and ground state ($5/2^+$) in $^{(39,41)}_{13}$Al appear in the assigned levels of $^{(25-29)}_{13}$Al. The lowering of $1/2^+_1, 3/2^+_1$ predicted levels by SDPF-MU calculationd may be understood as the lowering of a $K^\pi = 1/2^+$ band. The close spacing $^{39}_{13}$Al in and reversal in $^{41}_{13}$Al between $1/2^+_1$ and $3/2^+_1$ SDPF-MU levels might be understood in this framework as the manifestation of strong Coriolis coupling. The level energy equation 1.13 for $K^\pi = 1/2$ would suggest the decoupling parameter (a) with a value near -1 for the degenerate levels in $^{39}_{13}$Al and < -1 for a reversal in $^{41}_{13}$Al.

The tentative experimental $7/2^+_1$ assigned in $^{(39,41)}_{13}$Al can be interpreted as part of a rotational band built on the $5/2^+[202]$ Nilsson orbit. The predicted decay pattern from the $9/2^+_2$ states in $^{(39,41)}_{13}$Al and strong M1 nature, as calculated by the SDPF-MU interaction, are consistent with this interpretation. The experimental $7/2^+_1$ assigned level can provide access to the moment of inertia. The relationships of,

$$E(J) = E_k + AJ(J+1) \tag{5.2}$$

$$E(J) = E_k + AJ(J+1) + BJ^2(J+1)^2 \tag{5.3}$$

can be used to extract moment of inertia parameters A and B. As moments of inertia of odd-A nuclei are generally similar to neighbouring even-even nuclei, the $E(7/2^+_1)$ level energies can provide predictions for the $E(2^+_1)$ energies in magnesium. To first order (equation 5.2) $A \approx \frac{\hbar}{2\mathcal{I}}$.

Firstly for $^{39}_{13}$Al, the linear fit is presented in Fig. 5.16 overlaid with experimental

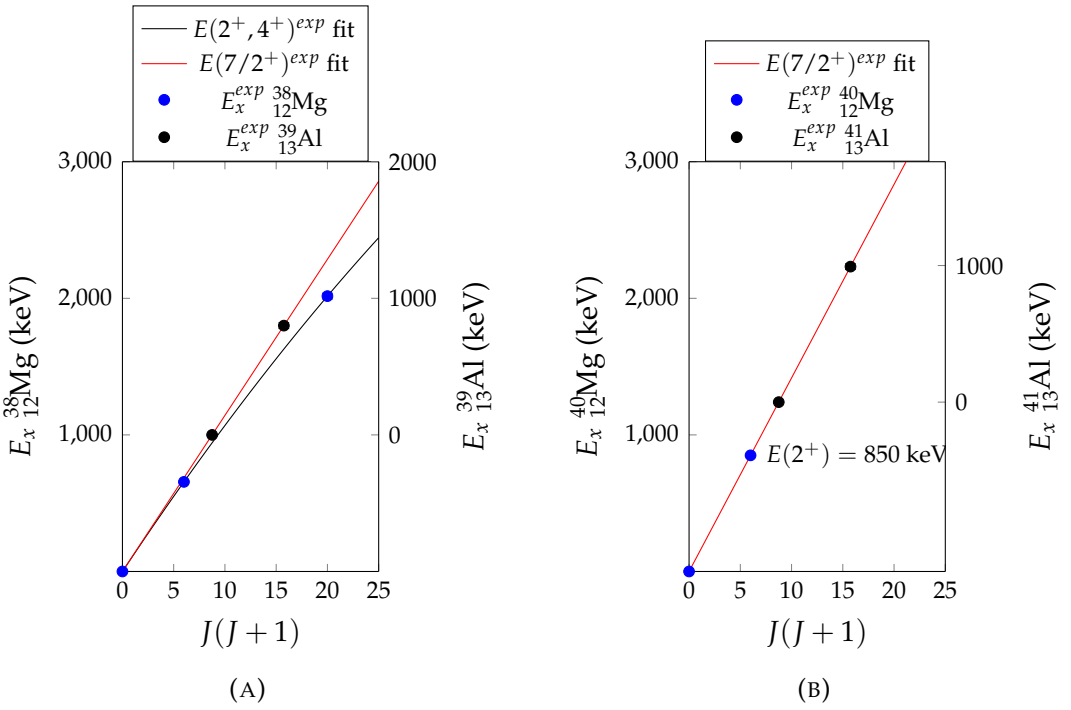

FIGURE 5.16: Level energies of ground state rotational bands of $^{38}_{12}$Mg ($K^\pi = 0^+$) and $^{(39,41)}_{13}$Al ($K^\pi = 5/2^+$) and fit. The predicted $^{40}_{12}$Mg $E(2^+)$ intercept is 850 keV by the parameter fit of the $^{41}_{13}$Al ground state rotational band moment of inertia.

level energies of $^{39}_{13}$Al and $^{38}_{12}$Mg. With the first order equation 5.2, $A = 114$ and the predicted $E(2^+_1)$ energy of ^{38}Mg is 686 keV. This is near the experimental value of 656(6) keV. Conversely, it is possible to derive $E(7/2^+_1)$ from $E(2^+_1)$. With this procedure to first order (equation 5.2), the relationship reduces to a factor of 6/7 between $E(7/2^+_1)$ and $E(2^+_1)$ energies.

This procedure can be extended across the aluminium and magnesium isotopic chains. For $^{37}_{13}$Al, the predicted $E(7/2^+)$ is calculated at 768 keV. Spin and parity assignment of the excited states in ^{37}Al is not assigned, but the first experimental excited state energy at 775(4) keV provides good agreement. Shell model calculations with both SDPF-U and SDPF-MU interactions assign the first excited state of $^{37}_{13}$Al as $7/2^+[156]$. And the reverse calculates $E(2^+_1)$ as 664 keV compared to the experimental value of 662(6) keV for $^{36}_{12}$Mg. Similarly for $^{35}_{13}$Al, the experimental level of 802(4) keV provides agreement with the calculated value of 770 keV.

The results are tabulated and plotted in Fig. 5.17, with experimental observations presented as marks and predicted values drawn as lines. The greatest deviation is found for $^{27}_{13}$Al, but is expected by the previous description of this isotope as not completely fitting the particle-rotor model. The $R_{4/2}$ ratios are additionally plotted below in Fig. 5.17 to illustrate collectivity in magnesium isotopes and predicted adherence to an ideal rotor or vibrational model. It may be expected that at $^{31}_{13}$Al the strong-coupling limit may not hold with the lowering of the $R_{4/2}$ ratio in $^{30}_{12}$Mg. Additionally shown in Fig. 5.17 are predictions of the quadrupole deformation parameter β_2 from various models. The dimensionless parameter β_2 is not directly experimentally observable[2], but is often employed to meaningfully describe

[2]It can be derived from experimental observables, such as $B(E2)$ values, but requires the root mean square (rms) matter radius, which is often empirically specified. (equation 4.3)

configurations for experimental interpretation.

The predicted $R_{4/2}$ approaching the rotational limit and the predicted large deformation for $^{40}_{12}$Mg by some models can provide justification for strong-coupling in $^{41}_{13}$Al. The $E(2^+_1)$ for $^{40}_{12}$Mg would be expected by this interpretation at 850 keV. Such a low energy is consistent with the disappearance of $N = 28$ and a relatively low energy predicted by some models already introduced. Several assumptions are required for such an interpretation. For example, the invariably of the moment-of-inertial between even-even and even-odd nuclei is postulated. Pair-blocking by the odd-proton in aluminium may could be understood to modify or reduce pairing correlations in the core, increasing the moment-of-inertia for aluminium. Secondly, conversely, $^{41}_{13}$Al could be described as a hole state coupled to a $^{42}_{14}$Si, which may reproduce experimental observables. In addition, the influence of low-lying shape coexistence and band-mixing, for example between $|\Delta K = 1|$ bands, may contribute to the structural interpretation of excited states of $^{41}_{13}$Al.

Moreover, the construction of the ground state band from the intrinsic state of $5/2^+[202]$ would not be expected for an oblate ground state of $^{41}_{13}$Al, which could favour a $1/2^+[220]$ (or $3/2^+[211]$) state. HFB calculations [194] suggest such a configuration.

Returning to the Nilsson diagram of Fig. 5.14, deformation around $N = 28$ ($^{41}_{13}$Al) can be understood from the features of one-particle levels as a function of quadrupole deformation and has been discussed by I. Hamamoto [211, 212, 213, 214] and noted by other authors [196]. Several common rules, from observations of trends of deformation in nuclei, can be applied. Namely, deformation is often biased to a minimal local density of one-particle levels for a select particle number. In addition, the formation of a large gap between levels can lead to deformation stability. Lastly, downward sloping orbits are energetically favoured.

The appearance of ground state oblate deformation in $^{42}_{14}$Si can be motivated by the opening of the large energy gap on the oblate side of the Nilsson diagram (between orbits $1/2^-[330]$ and $3/2^-[312]$) as shown[3] in Fig. 5.14 [196, 213] ($\beta_2 \approx -0.35$). Likewise, $Z = 14$ also favours oblate deformation with an gap between $1/2^+[220]$ (or $3/2^+[211]$) and $1/2^+[211]$ levels. It has also been noted that the magic numbers emerging from the deformed harmonic oscillator at frequency ratios $\omega_{x,y} : \omega_z$ of 1 : 2 and 2 : 3 on the oblate side ($Z, N = 2, 6, 14, 26, 44...$ and $Z, N = 2, 8, 14, 18, 28, 34...$, respectively), includes $Z = 14$ (1 : 2 and 2 : 3) and $N = 28$ (2 : 3). As mentioned, large gaps (magic numbers) may lead to increased stability in deformation [47, 213].

For $^{40}_{12}$Mg the prolate configuration arises out of the gap formed by neutrons between $1/2^-[321]$ and $7/2^-[303]$ levels and strongly by protons between $3/2^+[211]$ and $5/2^+[202]$ [196] for which $\beta_2 \approx 0.35$. The oblate neutron gap has been suggested to contribute to the secondary saddle point in relativistic Hartee-Bogoliubov triaxial quadrupole energy surfaces (Fig. 1) [196]. This saddle point is additionally observed in separate calculations of Hartree-Fock-Bogoliubov energy surfaces [194] previously displayed in Fig. 5.13.

The aluminium isotope $^{41}_{13}$Al, sits between configures of $^{42}_{14}$Si and $^{40}_{12}$Mg and the HFB energy surfaces [194] of Fig. 5.13 show two pronounced minima. The arguments for the ground state oblate configuration for $^{42}_{14}$Si by means of the Nilsson one-particle levels can be applied to $^{41}_{13}$Al, with a similarly positioned Fermi surface. The unpaired proton would be predicted to reside on the $1/2^+[220]$ (or $3/2^+[211]$)

[3] Although the Nilsson diagram of Fig. 5.14 is produced for proton one-particle levels, Nilsson diagrams for protons and neutrons do not significantly diverge in shape for light nuclei [213].

level for oblate deformation, resulting in a $1/2^+$ or $3/2^+$ ground state configuration, contrary to SDPF-MU and SDPF-M shell model predictions.

The intrinsic quadrupole moment can be calculated from the shell model spectroscopic quadrupole moment in the strong-coupling limit by,

$$Q_S = \frac{3K^2 - I(I+1)}{(I+1)(2I+3)} Q_0 \tag{5.4}$$

and then to the quadruple deformation parameter to the first order,

$$Q_0 = \frac{3}{\sqrt{5\pi}} ZeR_0^2\beta_2 \tag{5.5}$$

where R_0 is often specified as the liquid drop radius[4]. The calculated deformation in $^{41}_{13}$Al as predicted by SDPF-MU is prolate and $\beta_2 = 0.33$. A prolate ground state configuration is also calculated in $^{39}_{13}$Al, with $\beta_2 = 0.37$.

5.2.5.2 Observation of $^{42}_{13}$Al

In addition to the spectroscopic information provided by neutron-rich odd-even Al, the location of the neutron drip-line is an important result for the interpretation of the $N = 28$ spherical shell. It has been previously shown the drip-line extents at least to ^{44}Si [217] and $^{42}_{13}$Al and $^{43}_{13}$Al [80] with one observed ion. The observation of $^{42}_{13}$Al in the present experiment is the second published observation of this nucleus. No counts belonging to $^{43}_{13}$Al are clearly observed in the particle identification plot, however the BigRIPS magnetic rigidity was not optimized for transmission for this ion.

It has been suggested that the gain in binding energy due to correlations in deformed nuclei can be the cause of this extension of the neutron-drip line. And the reduction of the $N = 28$ shell gap may be interpreted as the cause of this feature, although not a direct observable [218]. In contrast, the existence of double magic numbers in the neutron-rich isotope $^{24}_{8}$O results in a large neutron separation energy and the close presence of the neutron drip-line. The spherical shell gaps $Z = 8$ and $N = 16$ in $^{24}_{8}$O resists the onset of quadrupole correlations.

5.2.6 Cross sections

5.2.6.1 Proton-induced quasi-free knockout reactions

Proton-induced *quasi-free* knockout reactions (p, pN), or generally *quasi-free* scattering (QFS), offer an alternative to knockout reactions with heavier targets, such as ^{9}Be, for interrogating nuclear structure. The *quasi-free* description refers to lack of violent interactions of the incident proton with spectator nucleons in the process for sufficiently high beam energy. Proton-induced QFS and knockout reactions with heavier targets are both hadronic probes, and as such are mostly peripheral. They do not have the same sensitivity to the interior volume of the nucleus as electron-induced proton knockout reactions $(e, e'p)$ [219]. However, unlike electron-induced reactions, they can be used for neutron removal. The surface domination for spectroscopic information is a consequence of strong absorption in the nucleus [88]. The smaller proton target relative to standard ^{9}Be target provides higher relative sensitivity to deeply bound orbitals.

[4] $R_0 = 1.2A^{1/3}$

N	10	12	14	16	18	20	22	24	26	28
$_{12}$Mg $E(2^+)^{exp}$	1247(3)	1369(5)	1809(4)	1474(10)	1483(3)	885(1)	660(7)	660(6)	656(6)	
$_{12}$Mg $E(2^+)^{th\ rotor}$		1382	1896	1504			687	664	686	850
$_{13}$Al $E(7/2^+)^{exp}$		1613(5)	2212(10)	1754(16)			802(4)	775(4)	800(8)	992(11)
$_{13}$Al $E(7/2^+)^{th\ rotor}$	1455	1597	2110	1719	1730	1033	770	770	765	

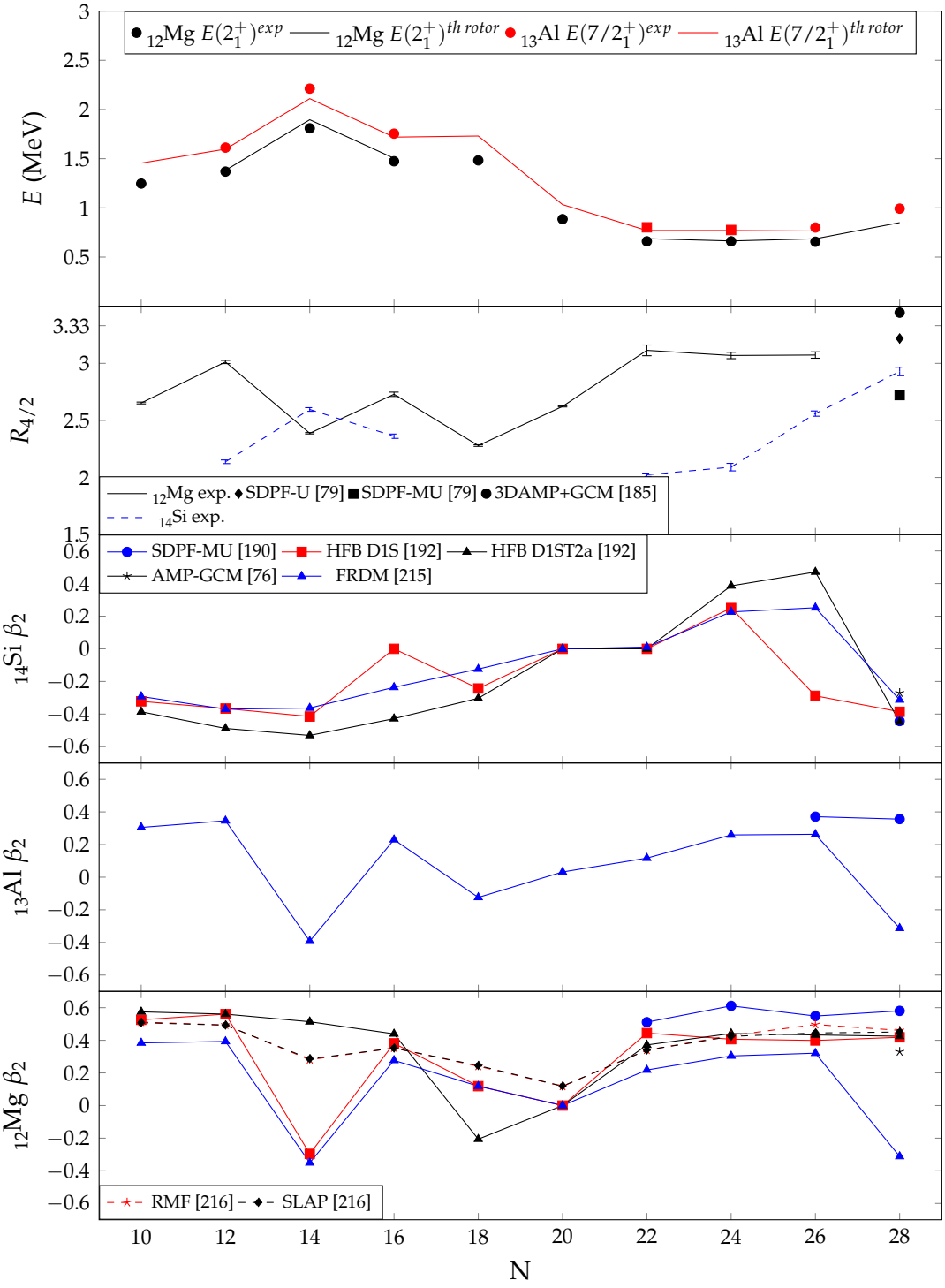

FIGURE 5.17: (Top) Experimental and predicted $E(2_1^+)$ and $E(7/2_1^+)$ energies of $_{12}$Mg and $_{13}$Al. Predicted energies of $E(2_1^+)^{th\ rotor}$ and $E(7/2_1^+)^{th\ rotor}$ from a simple rotor model from neighboring nuclei $E(7/2_1^+)^{exp}$ and $E(2_1^+)^{exp}$, respectively. The experimental levels 802(4) keV ($^{35}_{13}$Al) and 775(4) keV ($^{37}_{13}$Al) are not assigned spin and parity, but fit with the $E(7/2_1^+)$ systematic trend. (Middle) $R_{4/2}$ experimental and predicted ratios. (Bottom) Quadrupole deformation parameter.

The use of a C_2H_4 target during the NP1312-RIBF03 experiment permits the extraction of the inclusive (p, pN) cross section reactions on H. This requires the subtraction of the carbon-induced knockout fraction, and the employment of the pure C target permits an estimation of this fraction. The hydrogen cross section can be calculated with the previously determined C and C_2H_4 reactions, areal densities and molar masses,

$$N^{H}_{residues} = \frac{1}{2}(N^{C_2H_4}_{residues} - \frac{L^{C_2H_4}}{L^{C}} N^{C}_{residues}) \tag{5.6}$$

where L is the luminosity of the C_2H_4 and C target runs,

$$L^{C_2H_4} = \frac{N_A d_t^{C_2H_4}}{M^{C_2H_4}} N^{C_2H_4}_{projectiles} \tag{5.7}$$

$$L^{C} = \frac{N_A d_t^{C}}{M^{C}} N^{C}_{projectiles} \tag{5.8}$$

By the definition of the cross section, introduced in chapter 3 as equation 3.2, equation 5.6 can be reduced to the simple form,

$$\sigma_H = \frac{1}{2}(\sigma_{C_2H_4} - \sigma_C) \tag{5.9}$$

5.2.6.2 Summary of nucleon knockout cross section results

A summary plot of all the knockout reactions studied from the NP1312-RIBF03 experiment to $^{(39-41)}_{13}Al$ are presented in graphical form in Fig. 5.18. Notability, the neutron knockout cross sections from $^{(40-42)}_{13}Al$ are larger for all targets (C, C_2H_4 and H) than similar proton knockout cross sections.

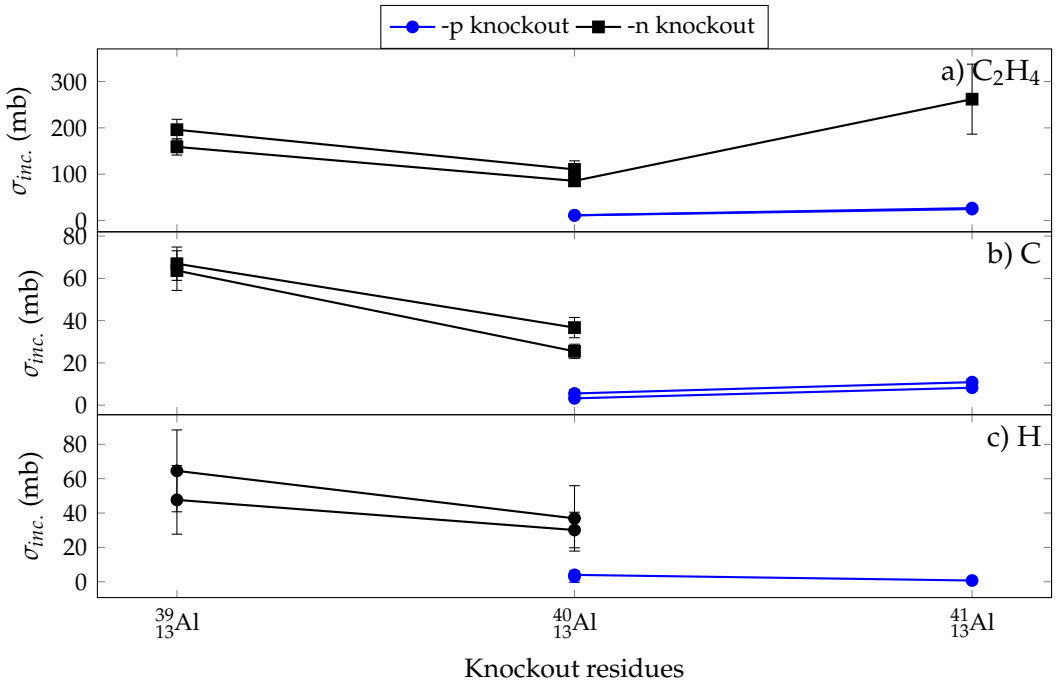

FIGURE 5.18: Inclusive cross sections for (a) on C_2H_4 and (b) C targets. (c) Calculated inclusive cross sections on H.

This can be generally understood as the projectiles are all neutron-rich species, thereby containing more neutrons than protons which may react. In addition the large $1\nu f_{7/2}$ orbit is full or nearly full and the binding energy of protons is much greater than neutrons.

5.2.7 Nuclear halos

At the very edge of nuclear stability, with nuclear systems with highly asymmetric numbers of neutrons to protons, particular conditions can allow for the formation of neutron halos: a dilute neutron cloud with large radius [220, 221, 222, 223]. A low neutron separation energy and valence neutron low angular momenta $\ell = 0, 1$ are favourable for neutron halo generation. Nuclei with neutron halos can display soft E1 excitations and narrow momentum distribution after nucleon knockout. In addition, the large spatial radii leads to substantial reaction cross sections [221]. The heaviest halo nuclei are ^{31}Ne and the candidate $^{37}_{12}$Mg [91]. The later deduced from cross sections of one-neutron removal reactions, in addition to parallel momentum distributions, suggests the existence of low-ℓ p-wave halo structure in $^{37}_{12}$Mg [90]. This is consistent with calculations which predict the increase in occupancies of p shell orbits (beyond standard filling) moving towards $N = 28$ in the Magnesium isotopes and the potential formation of a neutron halos, such as in $^{40}_{12}$Mg [8].

The large observed neutron knockout cross sections from the aluminium isotopes $^{(40-42)}_{13}$Al possess large uncertainties in their extrapolated neutron separation energies ($1130(570)$ keV, $3370(640)$ keV and $1390(780)$ keV, respectively) [27]. Reduction in atomic mass uncertainties, in combination with direct radii measurement or the momentum distributions in neutron removal reactions will allow future investigation of neutron halo structures around $N = 28$.

Chapter 6

Conclusion

Employing the DALI2 detector array and BigRIPS separator and ZeroDegree spectrometer at the RI-beam facility at the RIKEN Nishina Center Radioactive Isotope Beam Factory (RIBF), two investigations were completed in two close regions of the neutron-rich landscape.

Near, and at $N = 28$, the first spectroscopy of $^{(40,41)}_{13}$Al and spectroscopy of $^{39}_{13}$Al by means of proton and neutron knockout reactions. And east of $N = 20$, spectroscopy of $^{32}_{12}$Ne and inclusive and exclusive knockout cross sections. These areas have been observed to exhibit properties distinct from stable nuclei, with *emergence* of collectively and deformation and the erosion of spherical shell gaps known as *magic numbers*. Contributing to understanding of these regions provides benchmarks for the development and extension of theoretical of present and future theoretical work.

The spectroscopy of $^{32}_{12}$Ne revealed the $E(4^+)$ energy from the first observation of a 1410(15) keV transition, and the first measurement of the $R_{4/2}$ ratio, confirms the placement of this isotope into the *island of inversion* almost 20 years after the highlighting of this isotope as shown in Fig. 1.7 [49]. In addition, the extension of systematic trend of one- and two-nucleon inclusive and exclusive reduction factors, calculated shell model and eikonal reaction dynamical calculations, can contribute to the development of predictions for nuclei with large asymmetry in nucleon separation energy. Future extension to potential drip-line nucleus $^{34}_{12}$Ne [224, 225] may confirm the merging of the $N = 20$ and $N = 28$ islands of deformation in neon [8].

The study of $^{(39,40,41)}$Al by spectroscopic means permitted the extension of the level scheme in $^{39}_{13}$Al and the first development of tentative level schemes in $^{(40,41)}_{13}$Al. The experimental observations are inline with predictions from shell model calculations with the SDPF-MU effective interaction and with the minimal electromagnetic observables, spins and parities could be suggested for several levels. The sudden drop in the first excited state of ^{41}Al was confirmed and predicted by SDPF-MU calculations, which contributes to verifying the robustness of this interaction for predicting the exotic nuclei near $N \approx 28$. The application of a simple particle-rotor model to suggest a rotational band built on the intrinsic $5/2^+[202]$ Nilsson orbit fits with shell model calculations and was applied to predict the $E(2_1^+)$ energies in neighbouring magnesium isotopes. Good reproducibility with the available observations was found across the magnesium and aluminium isotopic chains. In addition, the experimental levels 802(4) keV ($^{35}_{13}$Al) and 775(4) keV ($^{37}_{13}$Al) are not assigned spin and parity but fit with the systematic trend. Extending to $^{40}_{12}$Mg, the predicted low $E(2_1^+)$ energy around 850 keV suggests the continued disappearance of magicity for neutron-rich $N = 28$ isotones. In addition, the tentative ground state assignment of $^{41}_{13}$Al based on the agreement with shell model calculations and the application of the particle-rotor model, suggests prolate deformation in the ground state of $^{41)}_{13}$Al. The competition of prolate and oblate shapes of similar configuration energy gives rise to disagreement with theoretical predictions of the ground state. Continued study

of this isotope is warranted to expose possible shape coexistence at low energy. The placement of $^{41}_{13}$Al between oblate and prolate even-even silicon and magnesium may manifest as excited phenomena. Future theoretical work may focus on identification of additional low-lying rotational bands (such as $K = 1/2^+$ or $K = 3/2^+$) which may be expected to appear in $^{(39,41)}_{13}$Al. Additional observables resulting from increased statistics, for example, observation new transitions, deduced M1/E2 mixing ratios, exclusive cross sections, and spin and parity assignment (such as through nucleon knockout momentum distributions), will be necessary future directions.

To reach these new frontiers requires the development and application of new technologies. At the same time while new facilities are upgraded and constructed, the enhancement of detector sensitivities must be accomplished. To this end, the novel single inorganic crystal scintillator GAGG(Ce) was studied and an important improvement in energy resolution observed. The simulation of GAGG(Ce) scintillators as part of a new-generation detector array, potentially a future DALI3, showed good promise. A brief report is presented in appendix C.

Appendix A

Spectroscopic factors

TABLE A.1: $^{42}_{14}$Si/$^{41}_{13}$Al C^2S calculated with the SDPF-MU interaction

Level (keV)	J	C^2S
0	$5/2^+_{g.s.}$	2.837
319	$3/2^+_1$	0.266
583	$1/2^+_1$	0.481
933	$3/2^+_2$	0.077
1051	$7/2^+_1$	
1112	$1/2^+_2$	0.163
1187	$9/2^+_1$	
1317	$5/2^+_2$	0.305
1562	$5/2^+_3$	0.011
1697	$7/2^+_2$	
1834	$7/2^+_3$	
1961	$3/2^+_3$	0.185
2403	$9/2^+_2$	
2523	$9/2^+_3$	
3011	$1/2^+_3$	0.000

TABLE A.2: Spectroscopic factor C^2S between $^{40}_{12}$Mg $\otimes$ sd proton and $^{41}_{13}$Al calculated with the SDPF-MU interaction

		$^{40}_{12}$Mg $\otimes$ $\pi 1d_{5/2}$ orbit						$^{40}_{12}$Mg $\otimes$ $\pi 2s_{1/2}$ orbit						$^{40}_{12}$Mg $\otimes$ $\pi 1d_{3/2}$ orbit					
^{40}Mg (keV)		0	733	1995	1683	2079	2724	0	733	1995	1683	2079	2724	0	733	1995	1683	2079	2724
	J	$0^+_{g.s.}$	2^+_1	4^+_1	0^+_2	2^+_2	2^+_3	$0^+_{g.s.}$	2^+_1	4^+_1	0^+_2	2^+_2	2^+_3	$0^+_{g.s.}$	2^+_1	4^+_1	0^+_2	2^+_2	2^+_3
^{41}Al (keV)	J																		
0	$5/2^+_{g.s.}$	0.187	0.296	0.042	0.083	0.019	0.310		0.001			0.033	0.001		0.000	0.000		0.015	0.000
319	$3/2^+_1$		0.013	0.015		0.463	0.047		0.061			0.000	0.183	0.000	0.004		0.040	0.044	0.001
583	$1/2^+_1$		0.062			0.081	0.094	0.249			0.044				0.095			0.012	0.063
933	$3/2^+_2$		0.016	0.108		0.001	0.001		0.122			0.002	0.018	0.318	0.217		0.015	0.002	0.002
1051	$7/2^+_1$		0.178	0.153		0.087	0.040			0.008					0.000	0.001		0.019	0.001
1112	$1/2^+_2$		0.079			0.086	0.043	0.056			0.122				0.385			0.018	0.010
1187	$9/2^+_1$		0.012	0.019		0.303	0.024			0.000						0.000			
1317	$5/2^+_2$	0.074	0.328	0.048	0.150	0.032	0.052		0.010			0.002	0.003		0.005	0.003		0.034	0.008
1562	$5/2^+_3$	0.071	0.005	0.045	0.019	0.013	0.077		0.163			0.066	0.009		0.006	0.060		0.026	0.023
1697	$7/2^+_2$		0.105	0.008		0.021	0.002			0.096					0.389	0.093		0.012	0.004
1834	$7/2^+_3$		0.220	0.338		0.051	0.071			0.014					0.061	0.033		0.003	0.008
1961	$3/2^+_3$		0.000	0.001		0.000	0.009		0.002			0.215	0.005	0.005	0.024		0.051	0.002	0.021
2403	$9/2^+_2$		0.092	0.586		0.019	0.012			0.000						0.005			
2523	$9/2^+_3$		0.002	0.012		0.008	0.091			0.001						0.000			
3011	$1/2^+_3$		0.005			0.035	0.030	0.003			0.018				0.005			0.003	0.002

TABLE A.3: Spectroscopic factor C^2S between $^{38}_{12}$Mg $\otimes$ sd proton and $^{39}_{13}$Al calculated with the SDPF-MU interaction

		$^{38}_{12}$Mg $\otimes$ $\pi 1d_{5/2}$ orbit						$^{38}_{12}$Mg $\otimes$ $\pi 2s_{1/2}$ orbit						$^{38}_{12}$Mg $\otimes$ $\pi 1d_{3/2}$ orbit					
^{38}Mg (keV)		0	766	2223	2672	1512	3050	0	766	2223	2672	1512	3050	0	766	2223	2672	1512	3050
	J	$0^+_{g.s.}$	2^+_1	4^+_1	0^+_2	2^+_2	2^+_3	$0^+_{g.s.}$	2^+_1	4^+_1	0^+_2	2^+_2	2^+_3	$0^+_{g.s.}$	2^+_1	4^+_1	0^+_2	2^+_2	2^+_3
^{39}Al (keV)	J																		
0	$5/2^+_{g.s.}$	0.307	0.639	0.098	0.002	0.014	0.008		0.001			0.031	0.000		0.001	0.000		0.000	0.000
835	$1/2^+_1$		0.128			0.236	0.000	0.293			0.002				0.035			0.033	0.013
854	$3/2^+_1$		0.041	0.116		0.478	0.001		0.200			0.009	0.002	0.040	0.030		0.008	0.005	0.013
863	$7/2^+_1$		0.495	0.449		0.001	0.002			0.004					0.001	0.001		0.000	0.000
1447	$9/2^+_1$		0.010	0.062		0.430	0.000			0.000						0.001			
1610	$5/2^+_2$	0.033	0.050	0.003	0.001	0.014	0.001		0.256			0.001	0.001		0.000	0.006		0.000	0.001
1708	$7/2^+_2$		0.005	0.083		0.075	0.005			0.112					0.068	0.013		0.003	0.006
1784	$1/2^+_2$		0.056			0.428	0.004	0.019			0.017				0.390			0.000	0.027
1803	$9/2^+_2$		0.088	0.560		0.024	0.000			0.007						0.006			
1867	$3/2^+_2$		0.006	0.065		0.028	0.000		0.001			0.000	0.017	0.261	0.135		0.027	0.000	0.027
2333	$3/2^+_3$		0.069	0.032		0.010	0.001		0.003			0.248	0.001	0.020	0.044		0.001	0.140	0.068
2506	$5/2^+_3$	0.035	0.019	0.002	0.000	0.184	0.000		0.068			0.005	0.005		0.078	0.280		0.013	0.006
2800	$7/2^+_3$		0.006	0.008		0.002	0.001			0.001					0.265	0.049		0.008	0.026
2991	$9/2^+_3$		0.033	0.029		0.000	0.006			0.177						0.000			
3238	$1/2^+_3$		0.001			0.000	0.012	0.016			0.028				0.041			0.024	0.068

Appendix B

The upgrade of DALI2 to DALI2+

As a precursor to the spring 2017 SEASTAR campaign, the DALI2 detector array, comprised of 186 detectors, was upgraded to a new configuration and with the inclusion of more than 50 new detectors to a total of 226. Over their two decades of use, a fraction of the DALI detectors show signs of ageing, with a degradation of resolution and gain stability. The addition of replacement detectors to remove the lowest performance detectors was a large motivation for the upgrade. Furthermore, through the increase in the number of detectors and a new configuration, the detector array radius can be increased. An increase in detector radius reduces the average opening angle as observed from the reaction target, thereby reducing angular uncertainty. In addition, the placement of the detectors in *log cabin* arrangement increases the average detector array thickness, resulting in a boost in efficiency at high γ-ray energy. Lastly, the 2017 SEASTAR campaign at the SAMURAI spectrometer, in combination with the MINOS liquid hydrogen target, induces several physical constraints which necessitates a configuration change.

A few of the technical drawings of new components which were fabrication to realize the DALI2 upgrade, known as DALI2+, are presented. In addition, a 3D rendering of the array geometry is shown.

A RIKEN Accelerator Report is included describing the effort.

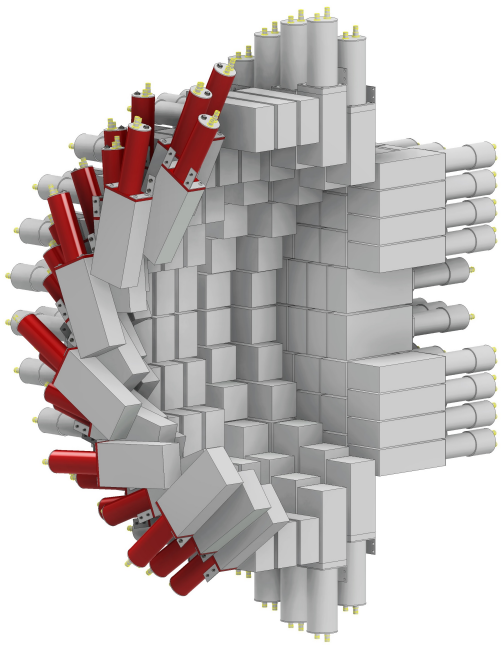

FIGURE B.1: Render of DALI2+ half section.

DALI2+ at the RIKEN Nishina Center RIBF

I. Murray,[*1*2] F. Browne,[*2] S. Chen,[*3*2] M. L. Cortés,[*2] P. Doornenbal,[*2] H. Sakurai,[*2*7] J. Lee,[*4] M. MacCormick,[*1] W. Rodriguez,[*5] V. Vaquero,[*6] D. Steppenback,[*2] and K. Wimmer[*7]

The utilization of large arrays of γ-ray sensitive detectors in combination with fast beams and a reaction target, is a powerful approach to interrogate nuclear structure[1]. This technique, known as in-beam γ ray spectroscopy, often in association with additional particle detectors, permits access to observables such as excited state energies, transition probabilities, exclusive and differential cross-sections, deformation lengths and parameters, state lifetimes and exclusive parallel momentum distributions. Highlights of results can be found in the references[2–4].

The Detector Array for Low Intensity Radiation (DALI) was constructed in 1995 for observing nuclear reactions with low yield[5]. DALI originally consisted of 60 6 x 6 x 12 cm^3 thallium-doped sodium iodide (NaI(Tl)) scintillators arranged around a reaction target to cover a large solid angle. The granularity of the detector array permitted a correction to the Doppler shifted γ-rays produced in-flight at RI beam velocities of $v/c \sim 0.3$.

DALI was supplemented with additional NaI(Tl) detectors up to a total of 186 in 2002[6] and named DALI2. With the opening of the RIBF facility, where the RI beam velocities are $v/c \sim 0.6$, DALI2's greater angular resolution and detection efficiency was integral to its continuing success.

In the spring of 2017, DALI2 was further upgraded to DALI2+ by the inclusion of additional new detectors to the array, bringing the total to 226. Poorly performing older detectors were substituted. A rendering of the new arrangement is shown in Fig. 1. Additional support structures were fabricated to accommodate the new detectors. The simulated full-energy-peak efficiency (FEP) and inherent energy resolution of the DALI2 and DALI2+ configurations for various photon energies (in a centre-of-mass (CM) frame) are shown in Table 1. The beam pipe, shield, target thickness, beam velocity distribution and individual detector resolutions are not included in the simulations. The γ-rays are emitted isotropically in the CM frame and Doppler corrected. The small reduction in FEP efficiency of the DALI2+ configuration is a consequence of the reduced angular coverage. The smaller opening angles of the detectors leads to an increase in inherent energy resolution because of Doppler correction.

*1 IPNO, CNRS, Univ. Paris-Sud, Univ. Paris-Saclay
*2 RIKEN Nishina Center
*3 Peking University
*4 Department of Physics, The University of Hong Kong
*5 Universidad Nacional de Colombia
*6 Instituto de Estructura de la Materia, CSIC
*7 Department of Physics, University of Tokyo

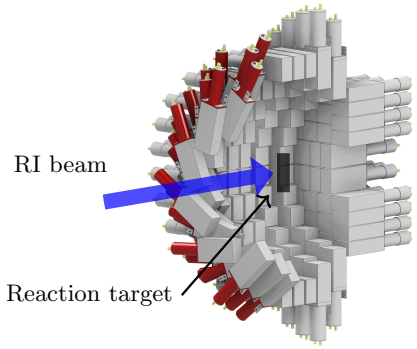

Fig. 1. A 3D rendering of the half sector of DALI2+.

Table 1. GEANT4 simulated FEP efficiencies and inherent energy resolution of the DALI2 and DALI2+ arrays. (without addback / with 15 cm radius addback)

	v/c = 0	**v/c = 0.6**	
E_γ (MeV)	eff. (%)	eff. (%)	FWHM (keV)
DALI2 & standard target position			
0.5	41/48	42/51	38/43
1.0	25/33	25/36	76/85
2.0	14/20	15/25	150/161
DALI2+ & standard target position			
0.5	37/43	40/48	38/43
1.0	22/29	24/34	76/85
2.0	13/19	15/23	139/155
DALI2+ & MINOS target position			
0.5	36/42	39/48	36/41
1.0	22/29	24/34	72/80
2.0	12/18	14/23	138/146

DALI2+ was employed for the first time for the third SEASTAR campaign[7–9]. It surrounded the liquid hydrogen target of MINOS[10] which was situated between BigRIPS[11] and SAMURAI[12] spectrometers.

References

1) P. Doornenbal: Prog. Theor. Exp. Phys **2012**, 1, (2012).
2) D. Steppenbeck, et al.: Nature **502**, 7470, (2013).
3) T. Nakamura, et al.: Phys. Rev. Lett. **96**, 25, (2006).
4) T. Motobayashi, et al.: Phys. Lett. B **346**, 1, (1995).
5) T. Nishio, et al.: RIKEN APR **29**, 184 (1996).
6) S. Takeuchi, et al.: NIM. A **763**, (2014).
7) S. Chen, et al, In this report.
8) M. L. Cortés, et al, In this report.
9) H. N. Liu, et al, In this report.
10) A. Obertelli, et al.: Eur. Phys. J. A **50**, 8, (2014).
11) T. Kubo, et al.: PTEP **2012**, 1, (2012).
12) T. Kobayashi, et al.: NIM. B **317B**, (2013).

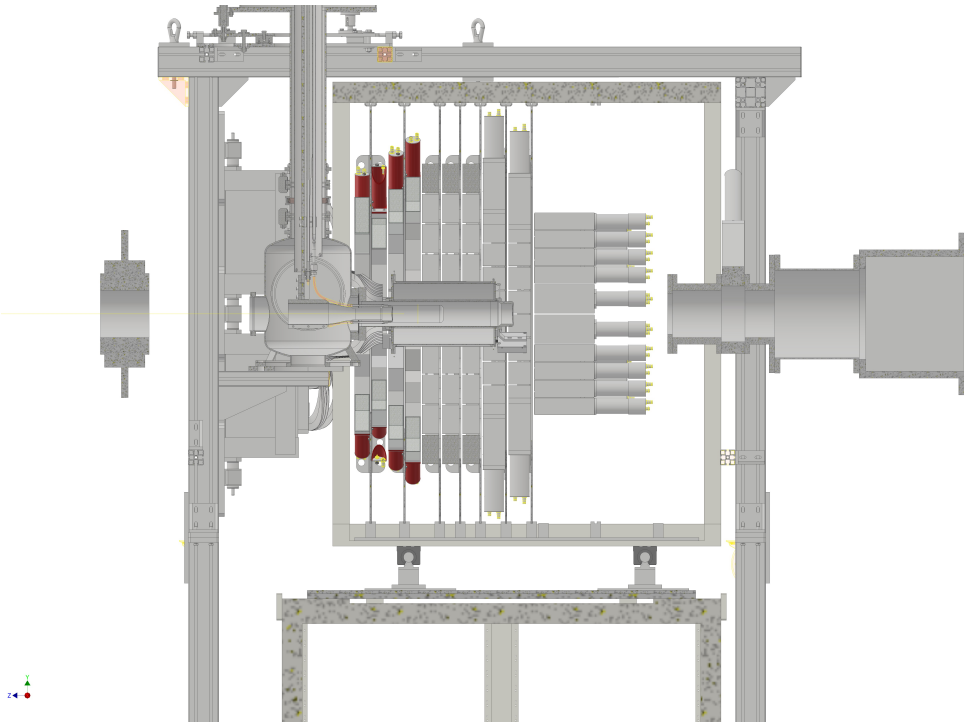

(A) Side view

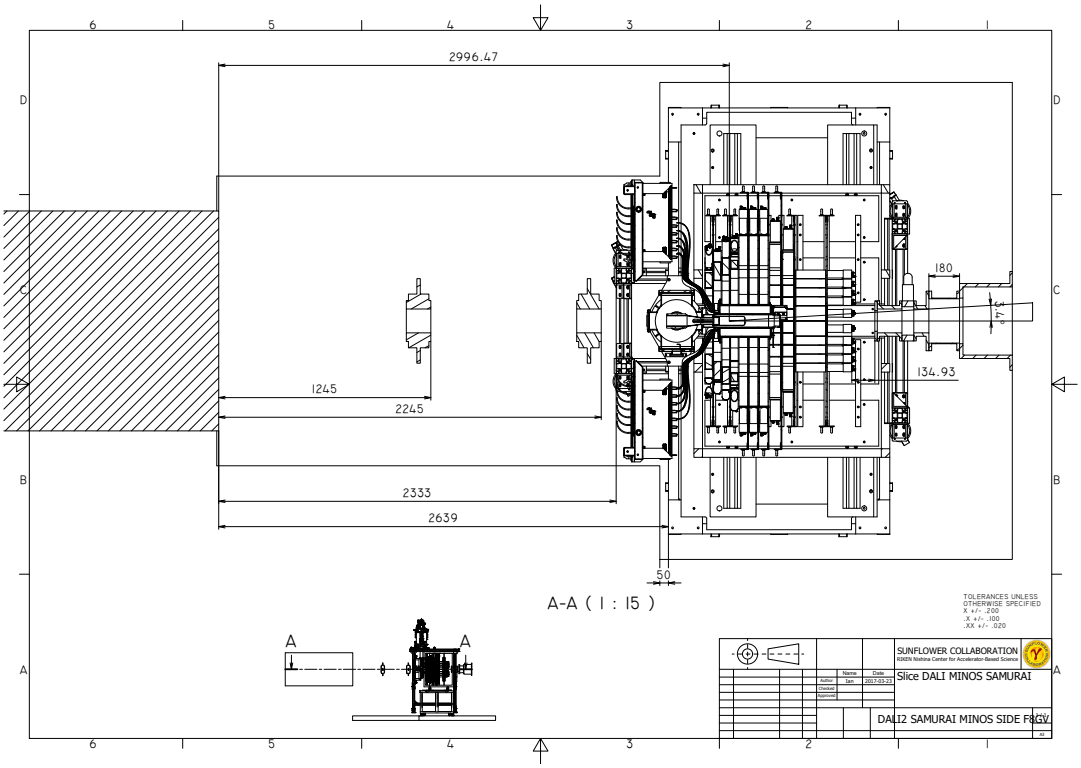

(B) Top view

FIGURE B.2: Render of DALI2+ and the MINOS liquid target. Half slice view.

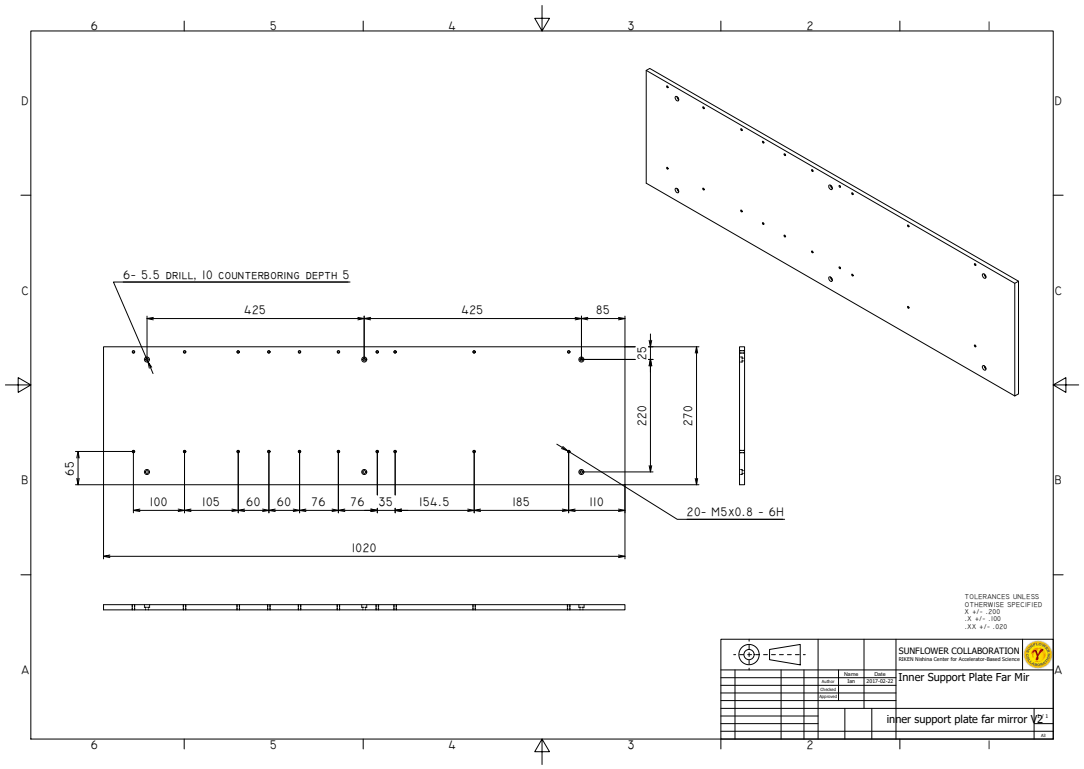

(A)

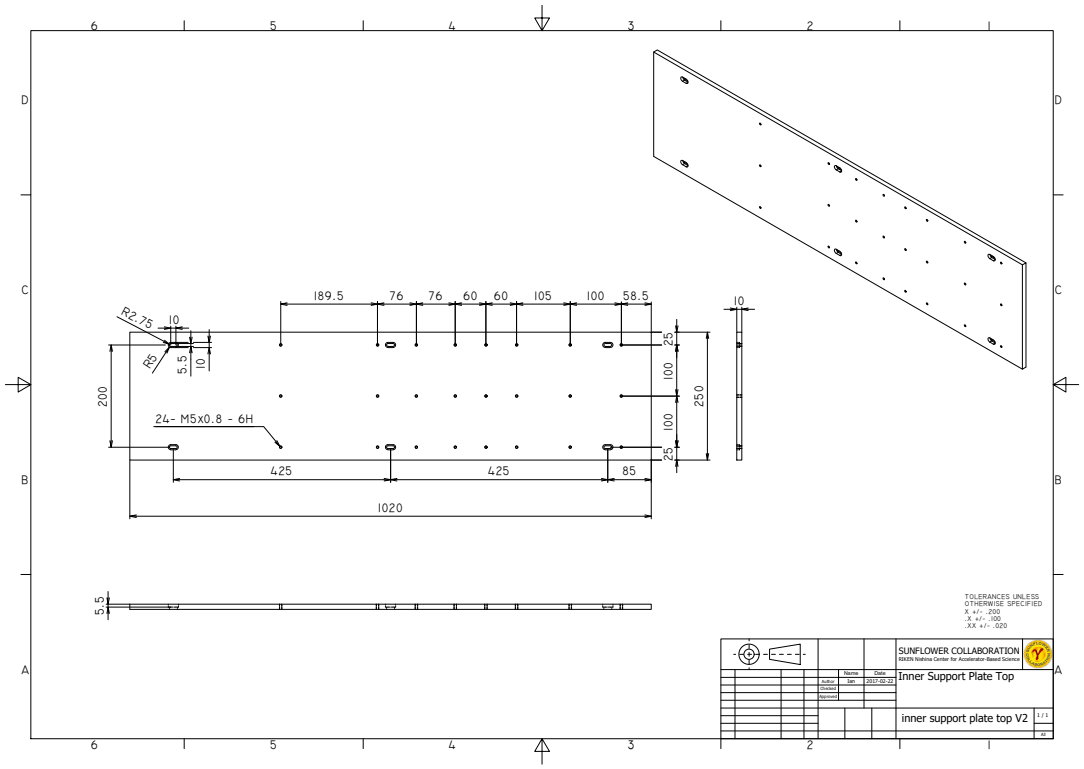

(B)

FIGURE B.3: Two of eight new different positioning plates.

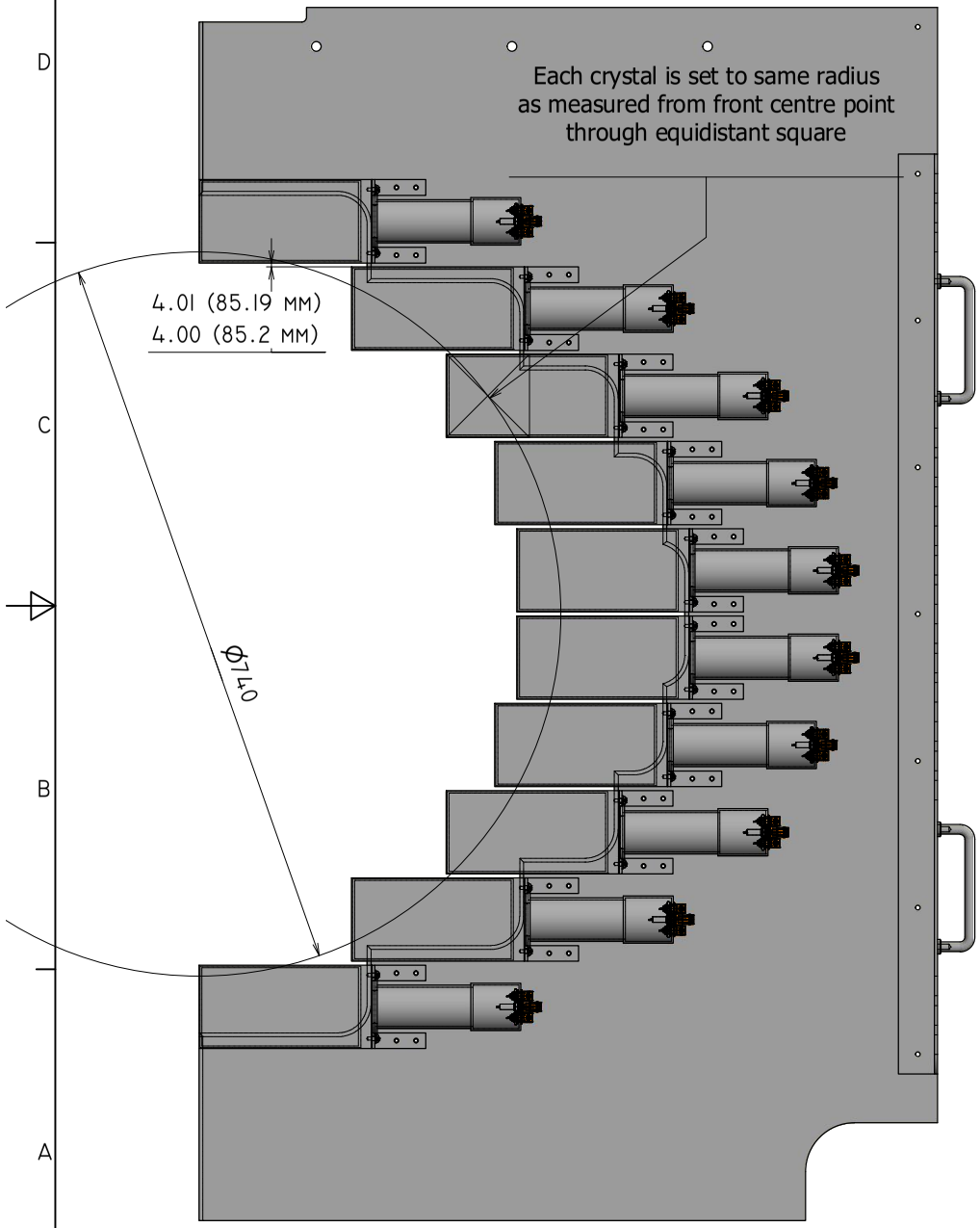

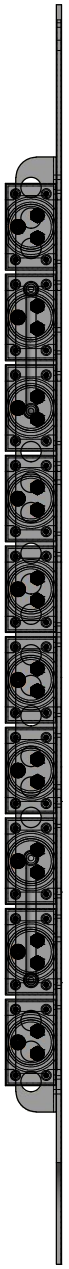

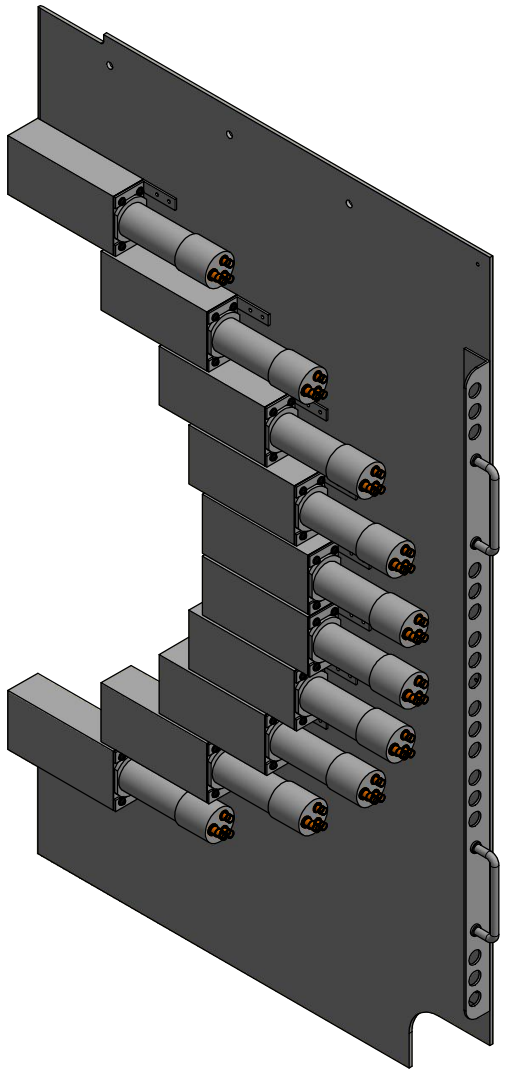

TOLERANCES UNLESS
OTHERWISE SPECIFIED
X +/- .200
.X +/- .100
.XX +/- .020

	Name	Date
Author	Ian	2017-02-22
Checked		
Approved		

SUNFLOWER COLLABORATION
RIKEN Nishina Center for Accelerator-Based Science

Layer 8 Right Assembly

layer 8 new V4 r outline

1 / 1

A3

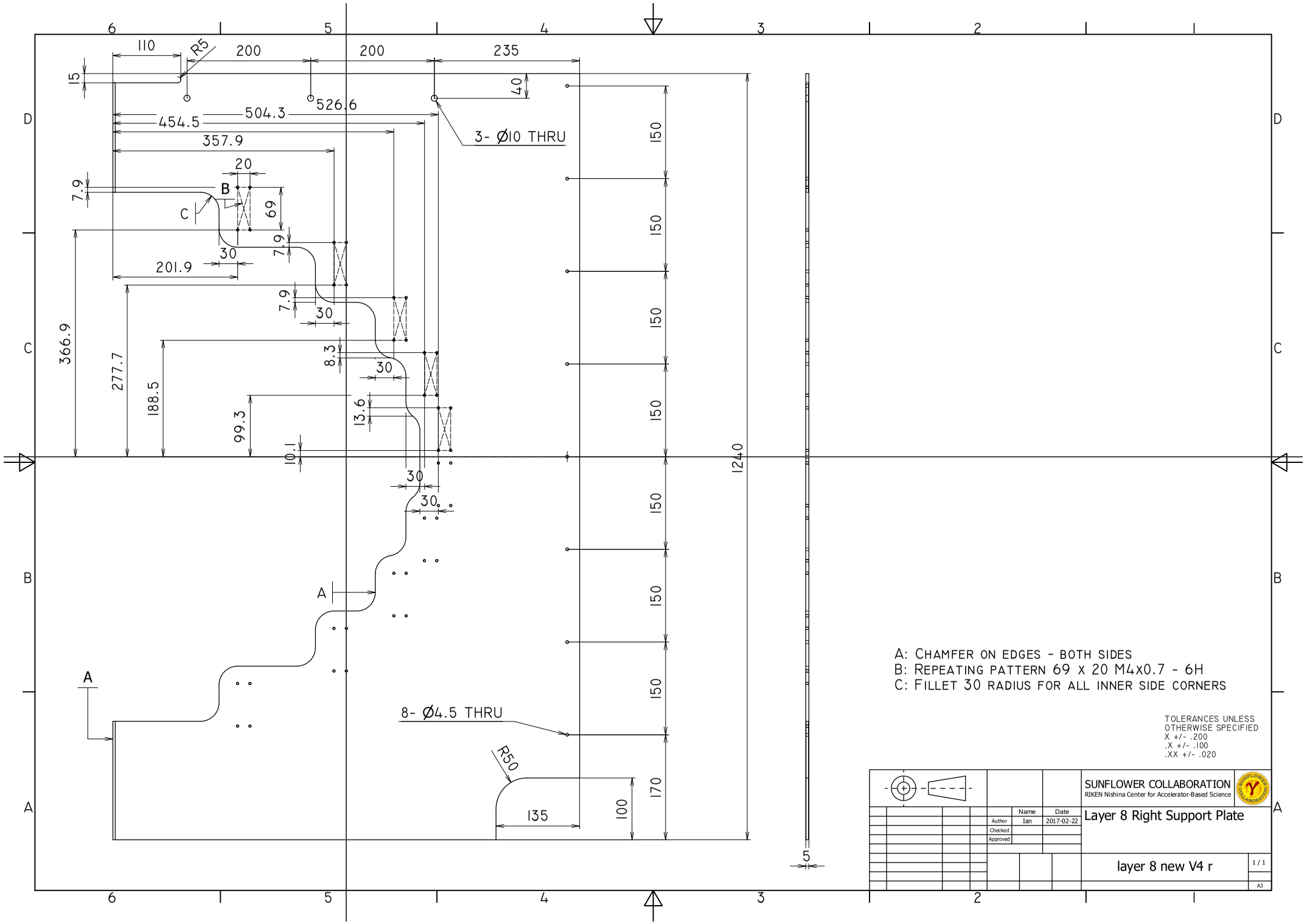
110
R5
200
200
235
15
40
526.6
504.3
454.5
357.9
3- Ø10 THRU
20
7.9
B
C
69
7.9
30
201.9
7.9
30
8.3
30
13.6
99.3
10.1
30
30
366.9
277.7
188.5
1240
150
150
150
150
150
150
150
150
A
A
8- Ø4.5 THRU
R50
135
100
170
5
A: CHAMFER ON EDGES - BOTH SIDES
B: REPEATING PATTERN 69 X 20 M4X0.7 - 6H
C: FILLET 30 RADIUS FOR ALL INNER SIDE CORNERS
TOLERANCES UNLESS
OTHERWISE SPECIFIED
X +/- .200
.X +/- .100
.XX +/- .020
SUNFLOWER COLLABORATION
RIKEN Nishina Center for Accelerator-Based Science
Name
Date
Author
Ian
2017-02-22
Checked
Approved
Layer 8 Right Support Plate
layer 8 new V4 r
1 / 1
A3

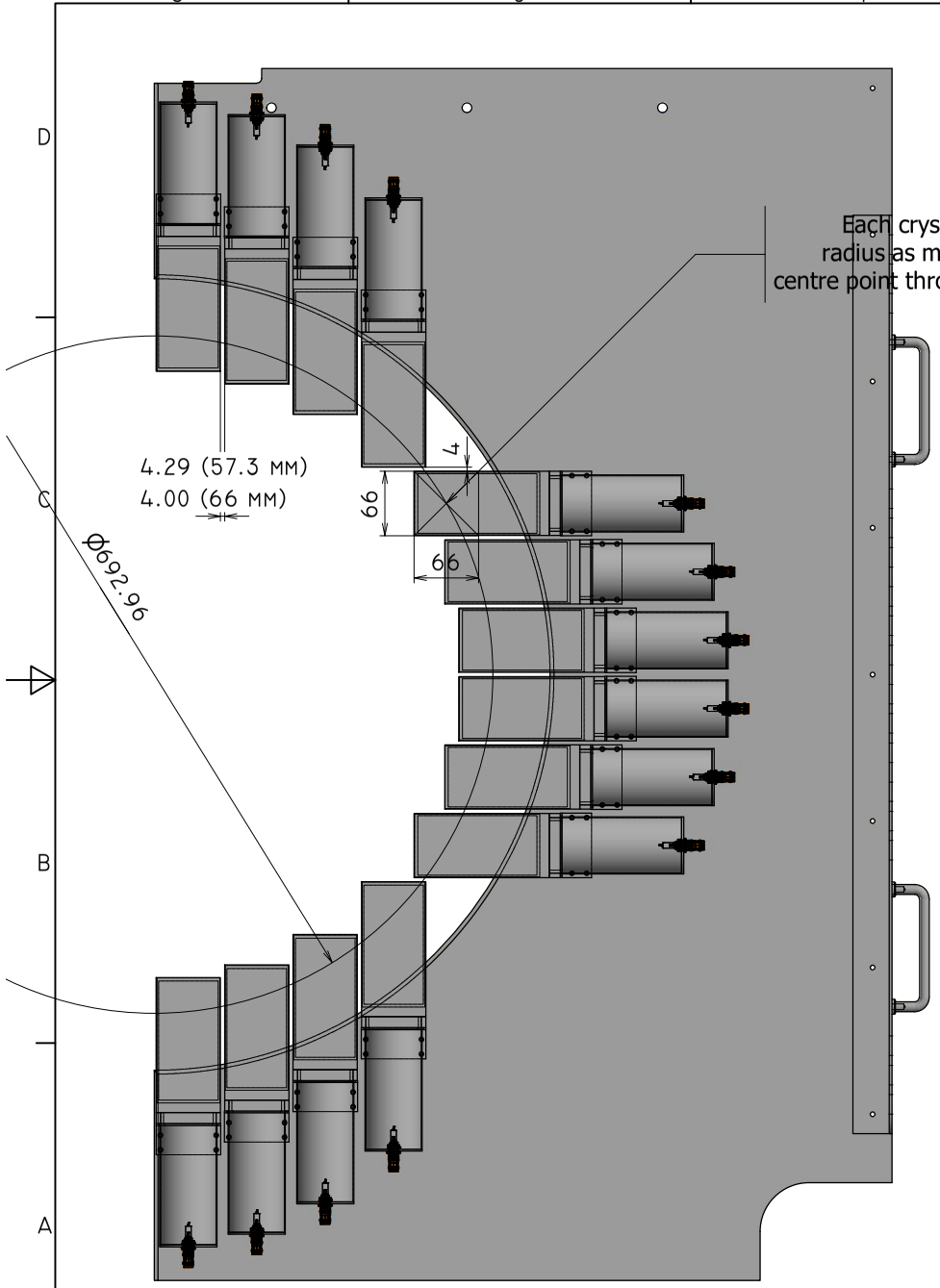

Each crystal is set to same
radius as measured from front
centre point through equidistant square

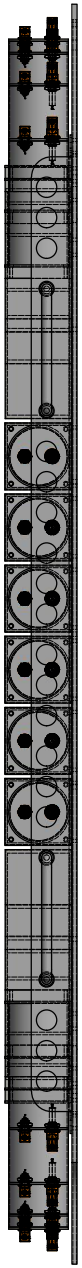

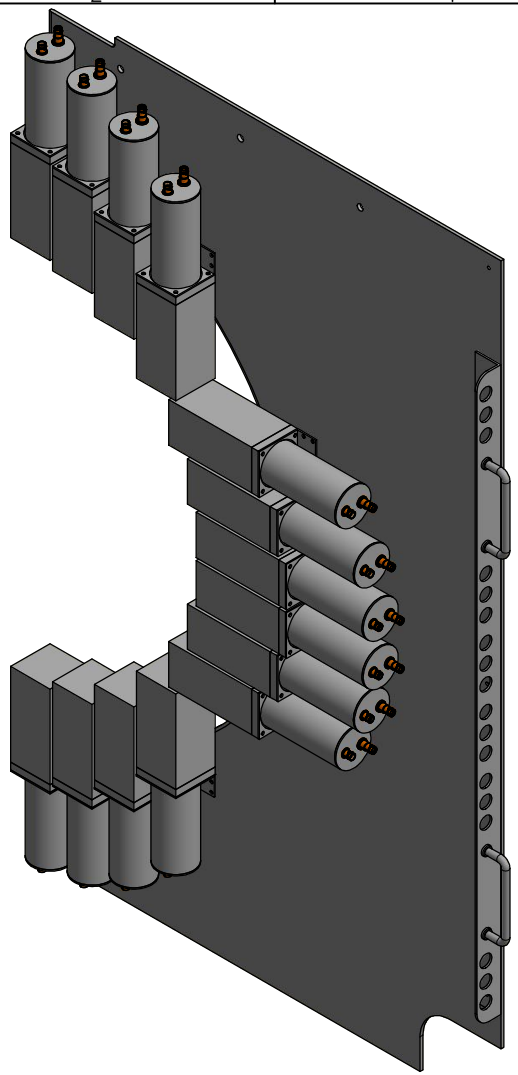

TOLERANCES UNLESS
OTHERWISE SPECIFIED
X +/- .200
.X +/- .100
.XX +/- .020

	Name	Date
Author	Ian	2017-02-21
Checked		
Approved		

SUNFLOWER COLLABORATION
RIKEN Nishina Center for Accelerator-Based Science

Layer 10 Right Assembly

layer 10 new V4 r outline

1 / 1

A3

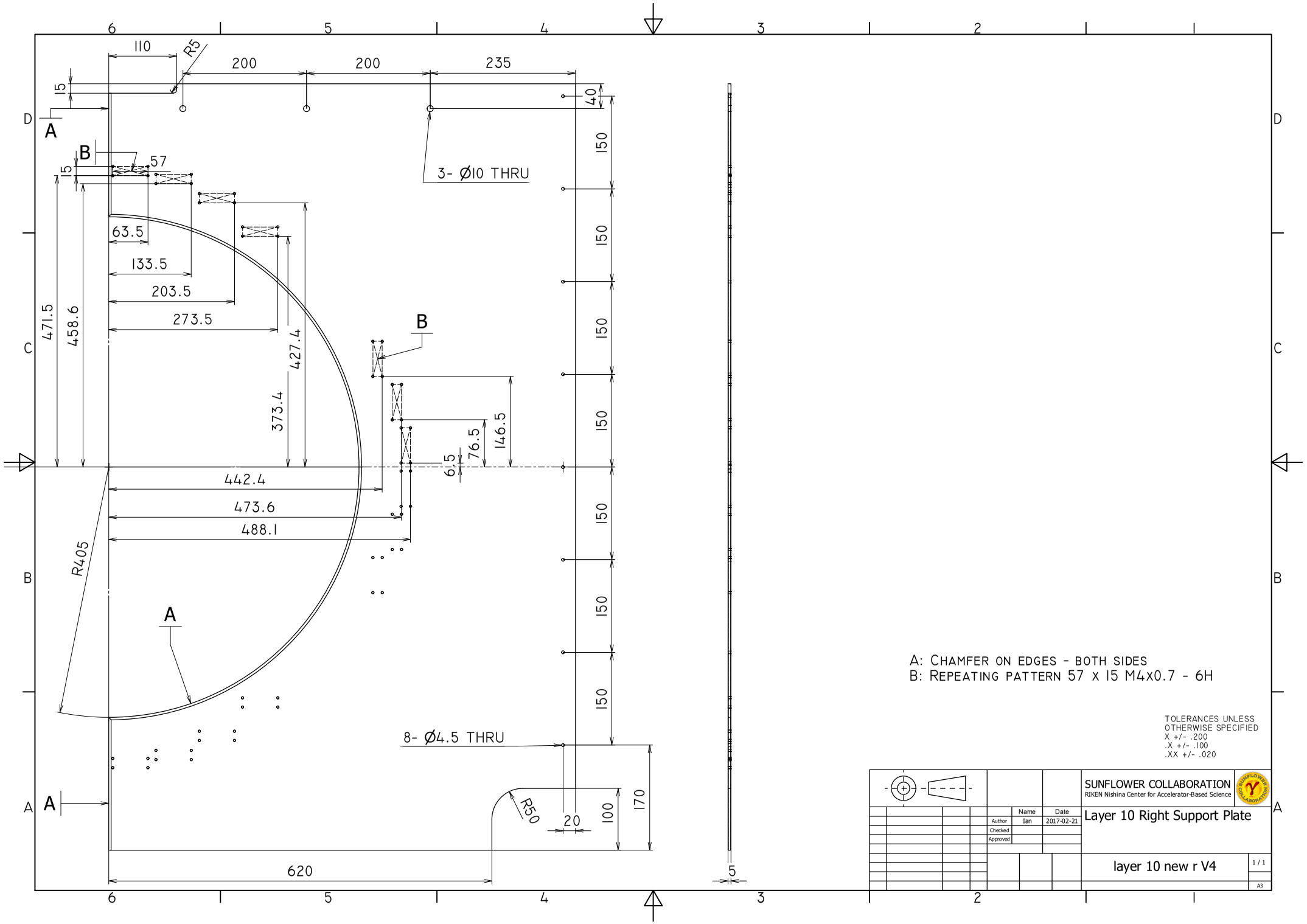
110
R5
200
200
235
15
4.0
A
B
57
15
3- Ø10 THRU
150
63.5
133.5
203.5
273.5
471.5
458.6
427.4
373.4
B
146.5
76.5
6.5
442.4
473.6
488.1
R405
A
8- Ø4.5 THRU
R50
20
100
170
620
5
A: CHAMFER ON EDGES - BOTH SIDES
B: REPEATING PATTERN 57 x 15 M4x0.7 - 6H
TOLERANCES UNLESS OTHERWISE SPECIFIED
X +/- .200
.X +/- .100
.XX +/- .020
SUNFLOWER COLLABORATION
RIKEN Nishina Center for Accelerator-Based Science
Name
Date
Author
Ian
2017-02-21
Checked
Approved
Layer 10 Right Support Plate
layer 10 new r V4
1 / 1
A3

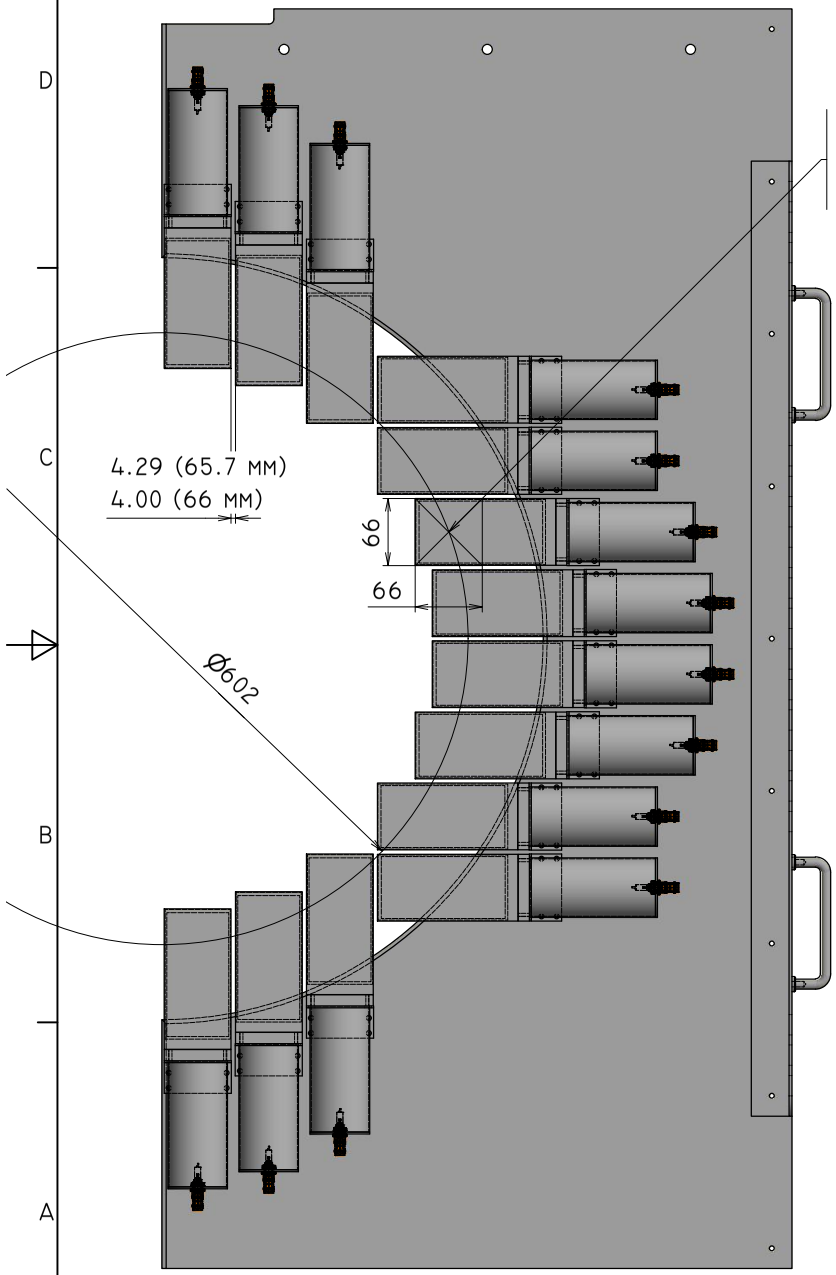

Each crystal is set to same radius as measured from front centre point through equidistant square

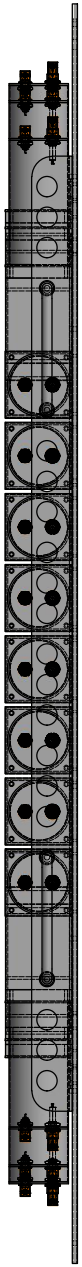

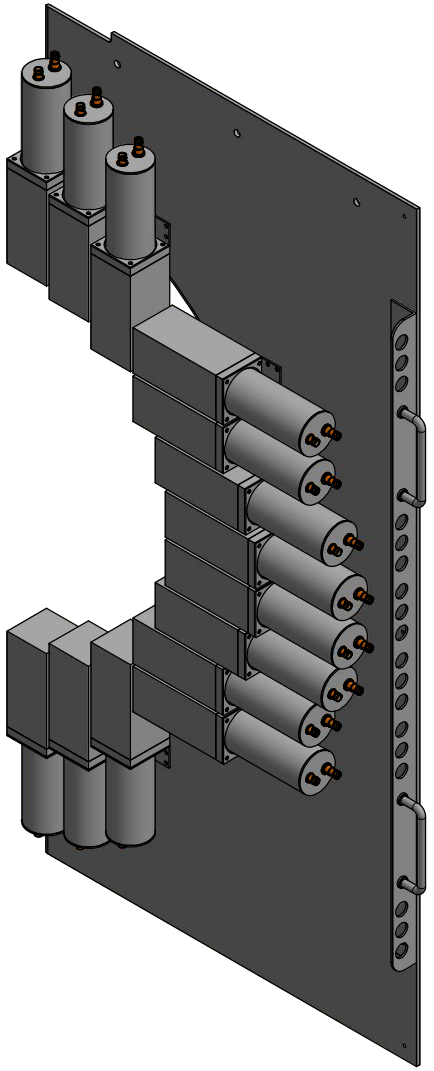

TOLERANCES UNLESS OTHERWISE SPECIFIED
X +/- .200
.X +/- .100
.XX +/- .020

SUNFLOWER COLLABORATION
RIKEN Nishina Center for Accelerator-Based Science

	Name	Date
Author	Ian	2017-02-21
Checked		
Approved		

Layer 11 Right Assembly

layer 11 new V4 r outline

1 / 1

A3

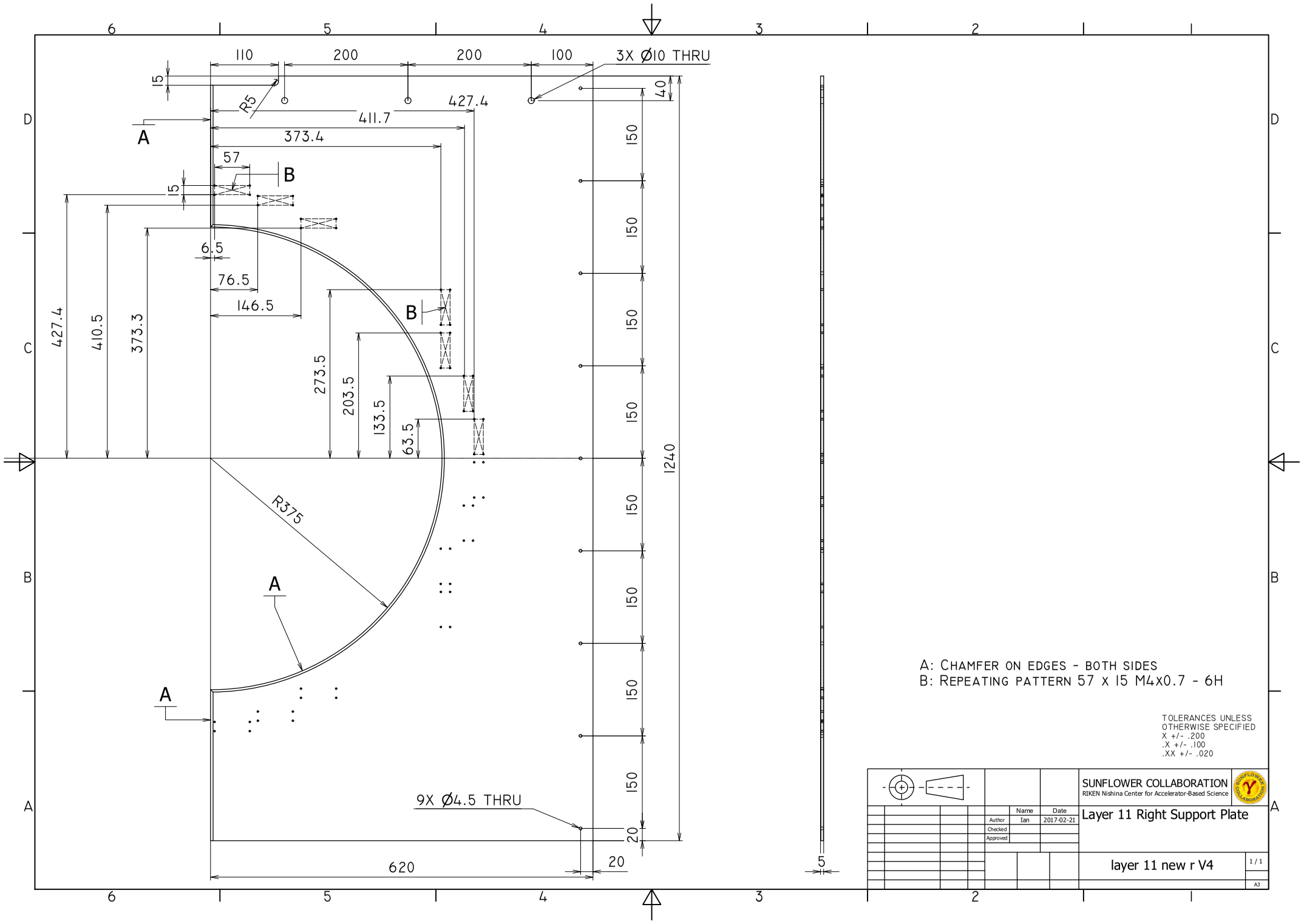
110
200
200
100
3X Ø10 THRU
15
R5
427.4
411.7
373.4
57
B
15
40
150
6.5
76.5
146.5
427.4
410.5
373.3
273.5
203.5
133.5
63.5
R375
A
1240
9X Ø4.5 THRU
20
620
20
5
A: CHAMFER ON EDGES - BOTH SIDES
B: REPEATING PATTERN 57 X 15 M4x0.7 - 6H
TOLERANCES UNLESS OTHERWISE SPECIFIED
X +/- .200
.X +/- .100
.XX +/- .020
SUNFLOWER COLLABORATION
RIKEN Nishina Center for Accelerator-Based Science
Name
Date
Author
Ian
2017-02-21
Checked
Approved
Layer 11 Right Support Plate
layer 11 new r V4
1 / 1
A3

Appendix C

Single crystal GAGG(Ce) scintillator study

One of the main engines for growth of understanding nuclear structure and exploring the limits of nuclear existence is the increase in detection sensitivity and resolution in the last century. An example of a paradigm shifting technology in nuclear physics research has been the evolution of the γ-ray sensitive detectors, which have been used since the start of modern nuclear physics. The use of these detectors for in-beam γ-ray spectroscopy as a tool is a relatively modern innovation. To expand the performance of in-beam γ-ray spectroscopy requires a further evolution of γ-ray sensitive detectors.

This *pre-print* manuscript summarizes the research into a novel γ-ray detector for application to in-beam spectroscopy. The new γ-ray detector is fabricated by single crystal Gadolinium Aluminium Gallium Garnet GAGG(Ce) scintillator, which has become recently commercially available. GAGG(Ce) in combination with a photosensitive detector, offers several performance advantages over the presently used Sodium Iodine NaI(Tl) scintillator based detectors of the DALI2 array. The performance is characterized through lab measurements on a custom test setup. The increase in detection performance can be translated through GEANT4 simulation to evaluate the impact on potential in-beam detection. A future DALI3 detector array may comprise of this novel scintillator.

Investigation of large-volume GAGG:Ce Crystals for Applicability to In-beam gamma-ray Spectroscopy

I. Murray[a,*], P. Doornenbal[b], F. Browne[b], M. L. Cortés[b], W. Rodriguez[d], R. Taniuchi[c], K. Wimmer[c]

[a]*Institut de Physique Nucléaire, IN2P3-CNRS, Université Paris-Sud, Université Paris-Saclay, 91406 Orsay Cedex, France*
[b]*RIKEN Nishina Center, Wako, Saitama 351-0198, Japan*
[c]*Department of Physics, University of Tokyo, Tokyo, Japan*
[d]*Universidad Nacional de Colombia, Bogotá, Colombia*

Abstract

Large-volume single crystal cerium-doped gadolinium aluminium gallium garnet (GAGG:Ce) scintillators are evaluated for new applications in next-generation detector arrays for fundamental nuclear physics research, such as in-beam γ-ray spectroscopy. Samples of GAGG:Ce scintillators, in combination with photomultiplier and avalanche photodiode light detector modalities, are characterized by light yield and energy resolution. Monte Carlo simulations of a GAGG:Ce detector array are performed to evaluate potential performance enhancements over presently employed scintillator-based detectors. This study shows that GAGG:Ce scintillators provide advantages in full-energy-peak efficiency, peak-to-total ratio, energy resolution and resolving power for scintillator-based detector arrays for in-beam γ-ray spectroscopy.

Keywords:
GAGG:Ce, in-beam γ-ray spectroscopy

1. Introduction

Scintillator detectors are currently employed in diverse experimental setups in fundamental particle and nuclear physics research, as well as industry. The development of new scintillating materials can expand the sensitivities, such as efficiency and energy resolution, to radiation detection and spawn new applications.

A powerful approach to interrogate nuclear structure is the utilization of fast ion beams and large granular arrays of γ-ray sensitive detectors surrounding a reaction target [5]. This technique, often in association with additional particle detectors, permits access to a multitude of nuclear properties. These can include: excited state energies, transition probabilities, exclusive and differential cross-sections, deformation lengths and parameters, state lifetimes and exclusive parallel momentum distributions.

The present available beam rates from accelerator facilities and practical experimental durations place upper limits on reaction luminosities for in-beam gamma spectroscopic experiments. To have the furthermost reach to map the *terra incognita* (unknown land) of exotic isotopes, the most efficient use of each reaction is necessary. This can be accomplished through increasing the detection efficiency, or the resolving power, of detector arrays through advances in detector technologies. This has been illustrated through the evolution of high-purity germanium (HPGe) detector arrays, with advances in Compton suppression, energy add-back in clover and cluster detectors, position-sensitivity and γ-ray tracking over course of the past several decades [15, 16]. Scintillator-based detector arrays are currenly undergoing a similar transformation, with the development and utilization of new scintilaltors. Presently active detector arrays commonly utilize established NaI scintillators [8, 24, 25], CsI [28, 27], and BaF_2 [6] with photomultiplier tube light readout. Recent applications include LaBr [1, 3], motived by high light yield, timing properties, and excellent energy resolution [26].

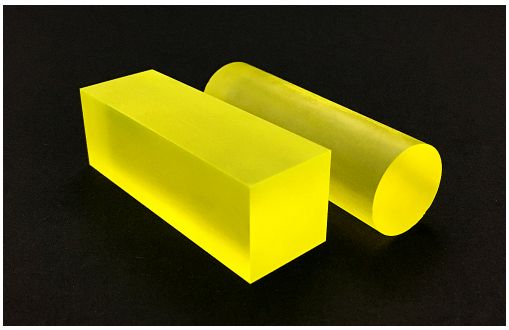

Figure 1: Photo of square cuboid ($25.4 \times 25.4 \times 76.2$ mm) and cylindrical (25.4 mm diameter x 76.2 mm) GAGG:Ce single crystal geometries.

In the family of non-hygroscopic ceramic gadolinium garnet based scintillators, cerium-doped $Gd_3Al_2Ga_3O_{12}$ (GAGG:Ce) grown by the Czochraski method [9, 30], has been shown to exhibit high light yield and moderately fast scintillation response [11, 10], making this garnet crystal attractive for gamma-ray spectroscopy. A high density (6.3-6.6 g/cm^3), large average atomic number (Z_{eff} = 52), short radiation length, high

*Corresponding author

light output (40-60,000 photon/MeV) and no internal radioactivity are characteristics attractive to many applications. A recent review article on the progress of gadolinium aluminate garnet developments can be found in ref. [17]. Most notably, the advent of the successful growth of large crystals, 2 inch in 2012 [11] and 3 inch in 2016 [10] may permit commercial adoption in sensitive high energy γ-ray detectors. Scintillators with large interaction volumes are necessity to reach favourable efficiencies for high-energy gamma-rays.

To evaluate the potential application of large-volume GAGG:Ce scintillators in detector arrays for in-beam gamma spectroscopy, we present an investigation of the properties of three samples of GAGG:Ce scintillators with two cerium doping concentrations. A performance characterization of the scintillators, including detected light yield and energy resolution is presented. Two light detection modalities of avalanche photodiode (APD) and photomultipliers tube (PMT) are evaluated. Furthermore, the influence of wrapping material is investigated. A proof-of-principle measurement of position dependant responses is discussed.

The performance of a GAGG:Ce-based in-beam γ-ray detector array is evaluated by a GEANT4 Monte Carlo simulation. A relative performance difference between the 226 thallium-doped sodium iodine (NaI:Tl) scintillator detector array DALI2+ [25] and a GAGG:Ce-based substitute is assessed.

2. Characterization measurements of GAGG:Ce crystals

Three GAGG:Ce samples, of two geometries (Fig. 1), are evaluated in this study and are amongst the largest available at the present time. A square cuboid crystal doped with 2.5 % cerium, henceforth referred as HR-GAGG type, measuring $25.4 \times 25.4 \times 76.2$ mm. Two cylindrical crystals of 25.4 mm-diameter by 76.2 mm-length of HR-GAGG type and a doping of 3 % cerium, hereafter distinguished as GAGG. The crystals were fabricated by Furukawa Scintitech. Surfaces were etched by the manufacturer.

2.1. Setup

To achieve high reproducibility for scintillator measurements, a custom test bench constrains the scintillator, coupled detector and radiative sources in defined positions, as illustrated in Fig. 2. A light-tight stainless steel EMI/RFI-shielded box encompasses the setup. The radioactive source is set at a fixed central axial position, or lateral position relative to the scintillator. In the lateral position, γ-rays are collimated to produce a well-defined beam of 6 mm in diameter over the lateral scintillator face. The collimator is fabricated of tungsten with a size of 100 mm diameter by 100 mm length with a bored hole of 5 mm. Auxiliary NaI:Tl scintillator detectors are positioned behind the γ-sources to permit γ-ray coincidence gating.

Three light detectors are tested with the GAGG:Ce scintillator samples, including a Hamamatsu S8664-1010 reverse-type APD with a photosensitive area of 10×10 mm, Hamamatsu wide spectral response photomultiplier R374 with a25 mm diameter photosensitive area and Hamamatsu green-extended

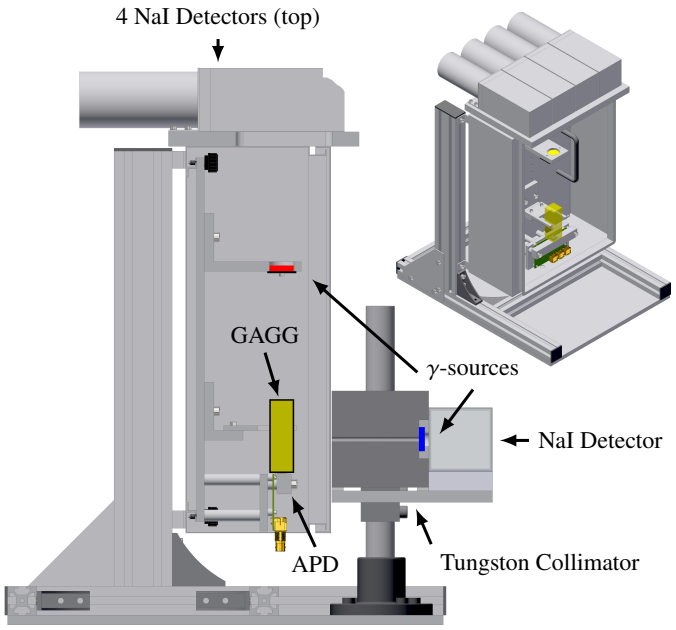

Figure 2: Sliced view of scintillator measurement setup, including custom test bench configured for APD measurements. (Top right) 3D view with enclosure lid and collimator removed for illustration.

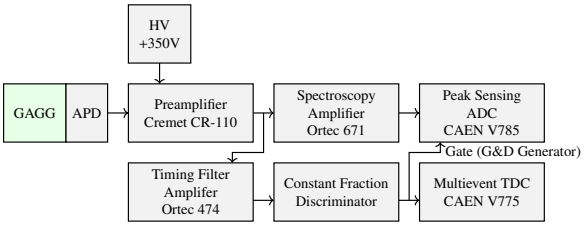

(a) Avalanche photodiode detector circuit schematic

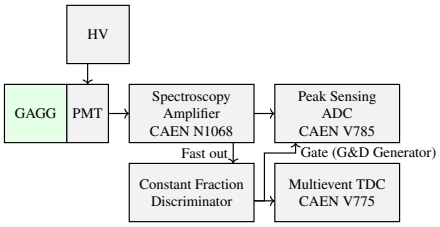

(b) Photomultiplier detector circuit schematic

Figure 3: Schematics of measurement setups for APD and PMT detectors.

photomultiplier R11265U-300 with effective photosensitive area 23×23 mm. The two photomultipliers can be distinguished by the photocathodes of extended green bialkali (EGBA) and multialkali, for the R11265U and R374 models, respectively. The quantum efficiency provided by manufacturer near the peak of GAGG:Ce emission (520 nm [11]), is reported as 21 % for model R11265U and 11 % for model R374. The quantum efficiency for the S8664-1010 APD is reported as near 80 % by the manufacturer.

The circuit schematics for APD and PMT measurements are show in Fig. 3. Signals from the Hamamatsu S8664-1010 APD are fed to a charge sensitive preamplifier, Cremat model CR-110. The charge integrated signal is supplied to a spectroscopic amplifier and timing filter amplifier for the energy and timing branches, respectively. The PMT measurements utiziled a CAEN spectroscopic amplifier (model N1068) for both of these functions. Both APD and PMT measurements are provided to a CAEN V785 peak sensing ADC and CAEN V775 TDC for energy and timing recording, respectively. In all GAGG:Ce measurements, the bias voltage and shaping times are optimized to provide the highest energy resolution with the available γ-sources.

2.2. Light Output

The utilization of an APD provides a straightforward method for evaluation of scintillator light yield [13, 23, 19]. Firstly, the number of charge carriers liberated by scintillation photons is determined by a reference measurement of direct x-ray interaction, at an energy with appreciable efficiency for complete absorption. The energy to produce a charge carrier in silicon is 3.62 eV [14]. The charge carrier yield is,

$$Y_{e-hAPD} = \frac{Channel_{\gamma}}{Channel_{x-ray}} \frac{E_{x-ray}}{E_{\gamma}} \frac{1}{3.62\,\mathrm{eV}} \tag{1}$$

where $Channel_{\gamma}$ and $Channel_{x-ray}$ are the ADC channel numbers and E_{x-ray}, and E_{γ} are accompanying energies for scintillator full-energy-peak and direct x-ray peak, respectively. The APD is calibrated with 5.9 keV x-rays from an ^{55}Fe source, and an example energy spectrum is shown in Fig. 4b. The number of intrinsic scintillation photons can then be determined by the APD quantum efficiency and collection efficiency,

$$Y_{ph} = \frac{Y_{e-hAPD}}{F} \frac{1}{Q.E.} \tag{2}$$

where $Q.E.$ is the quantum efficiency and F is the collection efficiency, encompassing losses due to scintillator self-absorption, reflectivity of wrapping material and transport efficiency. Small scintillators often are assumed to present bulk properties and the collection efficiency is unity. The large size of the crystal samples of this work relative to the active area of the APD, and their elongated aspect ratios, likely result in a non-negligible loss of scintillation photons. Determination of this loss fraction is beyond the scope of this work, therefore, the reported light yields are distinguished as detected light yields.

X-ray and photon interactions within the APD differ in the effect of space charges, and the point-like nature of the primary electron cloud produced by the x-ray interaction, resulting in a non-linear response [2, 20, 18]. For the APD model S8664-101, with a gain of 50, a 32(5) % quenching in x-ray gain at 5.9 keV for 525 nm LED has been reported [7]. This quenching factor and a quantum efficiency of 80 % is used for determining the scintillator detected light yields. The relative γ-source positions are standardized between all measurements at a position 13.5(1) cm from the front face of the scintillator, as illustrated in Fig. 2 by the red γ-source.

Table 1: Summary of results of various wrappings and square/cylindrical geometries with avalance photodiode (Hamamatsu 8664-1010, 350 V bias, gain of 50), multialkali photomultiplier (Hamamatsu R374, 1000 V bias) and extended green bialkali photomultiplier (Hamamatsu R11265U-300, 900 V bias). ⋆Energy resolution determined with ^{137}Co source at 661 keV and uncertainties are statistical. †Detected light yield shared systematic uncertainties are beyond the scope of this report and are assumed to be larger than statistical uncertainties.

Detector	**Wrapping**	**Energy res.⋆** (%)	**Det. light yield†** (Photon MeV^{-1})
Cylindrical HR-GAGG, 2.5 % cerium doping			
S8664 APD	Al.	10.64(6)	15,000
S8664 APD	Al. Mylar	9.90(5)	17,000
S8664 APD	Teflon	6.03(3)	38,000
S8664 APD	ESR	5.57(6)	46,000
R374 PMT	ESR	12.50(5)	-
Square cuboid GAGG, 3 % cerium doping			
S8664 APD	ESR	7.49(4)	26,000
R11265U PMT	ESR	15.1(1)	-
Square cuboid HR-GAGG, 2.5 % cerium doping			
S8664 APD	ESR	5.98(2)	36,000
R11265U PMT	ESR	7.78(6)	-

The detected light yields are tabulated in Table 1 to directly compare crystal samples and wrapping materials. Four commonly utilized wrapping materials are evaluated for the cylindrical HR-GAGG sample: aluminum foil, aluminized mylar foil, triple layered teflon tape and 65 μm thick Vikuiti™ Enhanced Specular Reflector (ESR) film, of which, the ESR foil displays the highest yield of 46 000 Photon MeV^{-1}. Triple layered teflon provides a similarly high yield.

A comparison between scintillator sample crystals with ESR wrapping suggests an influence of scintillator geometry on detected light yield. The HR-GAGG sample of cylindrical geometry displays a higher detected light yield over the square cuboid sample. Several studies [21, 22] have previously demonstrated the importance of scintillator geometry on light transport and performance characteristics.

2.3. Energy resolution

The energy resolution was measured for variously wrapped sample crystals. The cylindrical HR-GAGG type sample with ESR foil wrapping provides the highest energy resolution of 5.57(6)% for 661 keV γ-rays as presented in Table 1. This represents an improvement relative to typical energy resolutions of NaI:Tl detectors on the order of 7 − 8%. The 30 highest energy resolution large-volume NaI:Tl detectors of the DALI2+ detector array yield an average resolution of 7.3% at 661 keV. An example of cylindrical HR-GAGG $\gamma - ray$ energy spectra is plotted in Fig. 4a with a ^{60}Co source. Additionally, a coincidence requirement with the NaI detector directly behind the source is used to isolate the 1173 keV peak for improved fitting, as illustrated in Fig. 4a.

The cylindrical and square cuboid HR-GAGG and DALI2+ NaI:Tl energy resolution as a function of γ-ray energy are fitted with a two parameter function

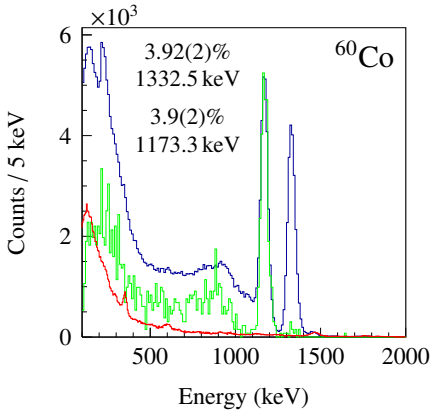

Figure 4(a): ESR foil wrapped cylindrical HR-GAGG with Hamamatsu S8664-1010 APD. Self triggered (blue), gated with top NaI detectors on 1332 keV peak (green, scaled), background (red, scaled).

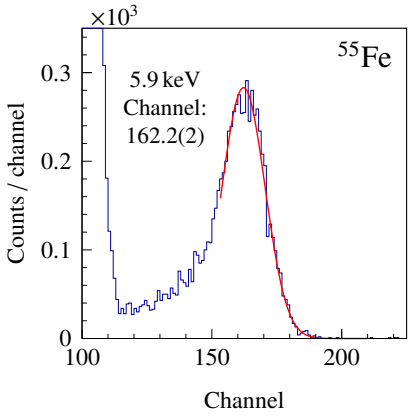

Figure 4(b): Hamamatsu S8664-1010 APD with ^{55}Fe source for charge carrier calibration.

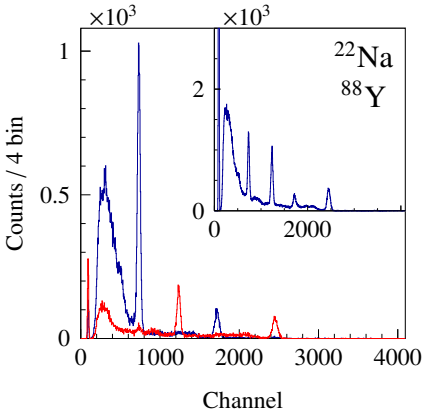

Figure 4(c): Example spectrum for position dependant measurements. Coincidence with top NaI detectors to isolate ^{22}Na peaks (blue) and coincidence with NaI behind collimated ^{88}Y source (red). (Insert) No coincidence.

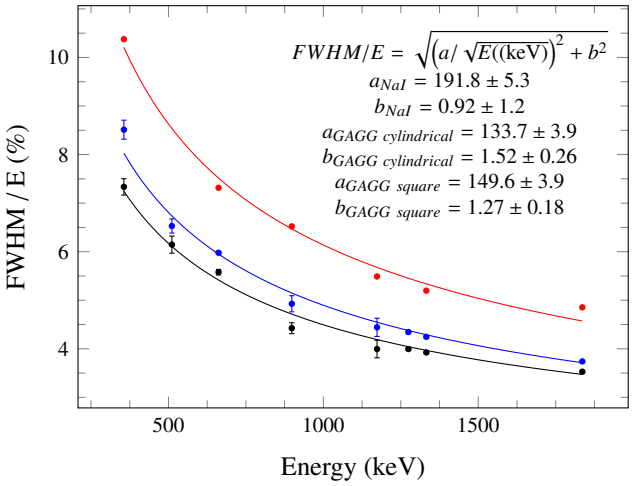

Figure 5: Energy resolution of GAGG:Ce scintillators of HR-GAGG type and cylindrical (black) and square geometry (blue). GAGG:Ce samples measured with Hamamatsu S8664-1010 APD. Energy resolution of average of 30 highest resolution NaI:Tl detectors as part of the DALI2+ array additionally shown for comparison.

$FWHM/E = \sqrt{\left(a/\sqrt{E((\mathrm{keV})}\right)^2 + b^2}$, as presented in Fig. 5.

2.4. *Proof-of-principle position dependence measurement*

Owing to the stochastic nature of γ-ray interactions, the complete volume of a scintillator is effectively sampled by high energy γ-rays. Inhomogeneous light yield and light collection result in a degradation of energy resolution, contributing to the observed intrinsic energy resolution [19]. For single crystal scintillators, segregation of the dopant during the formation process can result in gradients of dopant and therefore light yield. For GAGG:Ce single crystals, the mismatch of ionic radii of dopant Ce^{3+} (103 pm) and the Gd^{3+} (94 pm) substitutional sites results in a segregation coefficient less than unity. The segregation coefficient has been previously been measured to be 0.36 for Ce^{3+} in GAGG:Ce [12].

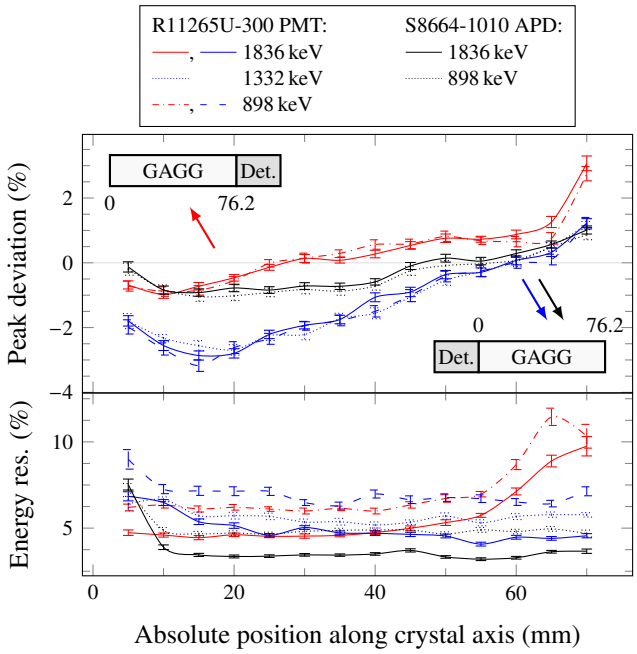

Figure 6: Position dependant full-energy-peak deviation of square cuboid HR-GAGG wrapped with ESR foil measured with Hamamatsu R11265-300 PMT and S8664-1010 APD detectors. Inversion of the sample, with respect to the light detector (as illustrated), results in a similar deviation gradient. The energy resolution worsens near the light detector face and is constant through the remaining volume.

For the detector arrays, Compton scattering between closely packed detectors results in an additional source of distributed γ-ray interaction depth. Therefore, it is important large-volume scintillators for γ-ray energy spectroscopy possess high uniformity of light production. The light yield as a function of position along the longest axis of the GAGG:Ce scintillators was investigated for the HR-GAGG sample of square cuboid geometry. Sources of ^{88}Y/^{60}Co, placed at the lateral position and collimated (Fig. 2), are scanned along the long face of the scintil-

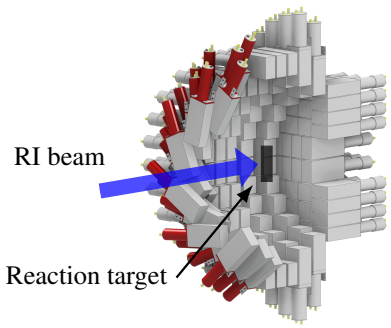

Figure 7: A 3D rendering of the half sector of the DALI2+ detector array

lator at 5 mm intervals. Environmental influences, such as temperature, over the measurement cycle are mitigated by the simultaneous measurement of a secondary ^{22}Na source at a fixed axial position above the top face of the crystal. Coincidence between 4 top auxiliary NaI:Tl detectors near the ^{22}Na source isolates peaks in the γ-ray energy spectrum of the GAGG samples. In a similar way, coincidence between the auxiliary NaI:Tl detector behind the collimated γ-source isolates the ^{88}Y/^{60}Co GAGG response, as shown in Fig. 4c. The employment of γ-ray coincidence additionally improves the peak-to-background ratio, resulting in a reduction of the influence of the background shape in peak fitting.

The relative change in full-energy-peak deviation along the long axis of the sample is calculated compared to the fixed ^{22}Na source response and displayed in Fig. 6. Peaks are fitted with a Gaussian function and linear polynomial background. The peak deviation is approximately linear with both the R11265-300 PMT and S8664-1010 APD detectors and independent of γ-ray energy (898 keV, 1332 keV and 1836 keV). Furthermore, an additional measurement of the sample in a reversed orientation displays a similar gradient. The slope is less pronounced with APD detector which may suggest a relationship to the size of the detector active area. In addition, the energy resolution is approximately constant over the axis of the sample. Reduction in energy resolution near light detector face is observed in all measurements, as shown in Fig. 6.

The slope of the position dependant response, on the order of 0.2 % cm^{-1} to 0.4 % cm^{-1}, may be admissible for some applications, such as large-volume crystals as part of detector arrays. Studies with additional scintillator samples are necessary to understand sample variance as a result of the manufacturing process. The optimization of growth parameters to limit inhomogeneity in GAGG:Ce has been investigated [29], and may be improved in future manufacturing of this new scintillator.

3. Simulation of a GAGG-based detector array

The performance of an in-beam γ-ray spectroscopy detector array can be characterized by three central attributes. These are the Doppler-reconstructed energy resolution, full-energy-peak (FEP) efficiency and peak-to-total ratio (P/T), full-energy events to total events. To compare detector arrays by a singular benchmark, the concept of a resolving power has been applied

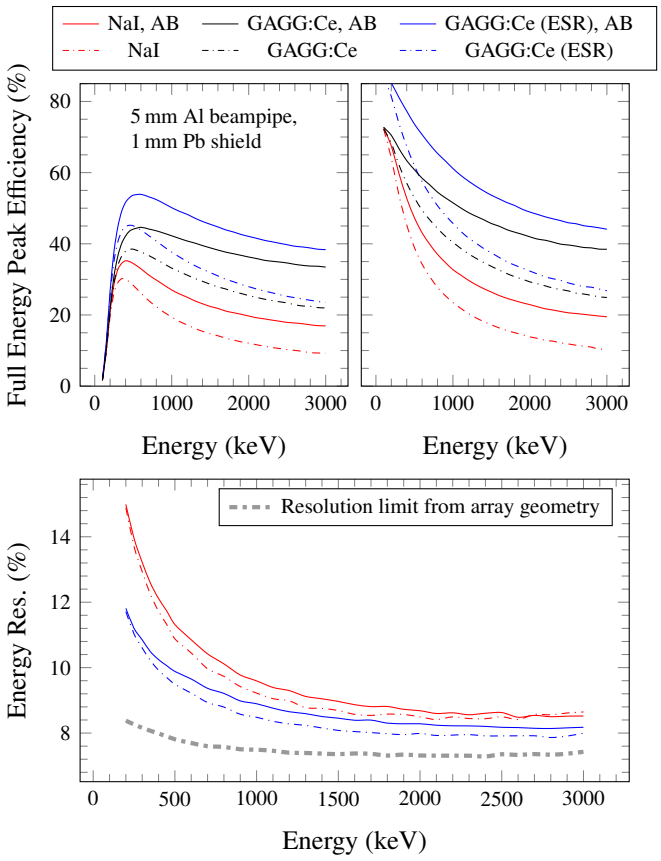

Figure 8: (Top) Monte Carlo simulated in-flight (β = 0.6) Doppler-reconstructed FEP efficiency for DALI2+ with NaI:Tl detectors with exterior MgO coating and Al casing (red), NaI:Tl substituted with GAGG:Ce (black) and substituted GAGG:Ce scintillators with 65 µm ESR wrapping material (blue). Solid lines include energy add-back procedure between adjacent detectors within a 15 cm radius for increased FEP efficiency. (Bottom) Simulated in-flight (β = 0.6) energy resolution of the three detector arrays. Grey dashed lines indicates simulated energy resolution limit from the DALI2+ array geometry.

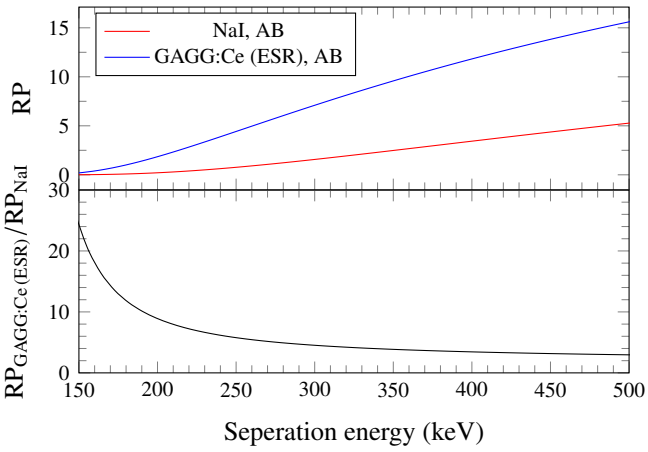

Figure 9: (Top) Simulated DALI2+ detector array resolving power (RP) for NaI detectors with MgO coating and Al casing (red) and GAGG detectors with 65 µm ESR wrapping (blue) scintillators, with 15 cm energy add-back procedure. (Bottom) Ratio of resolving powers. β = 0.6, E_γ= 1 MeV, N_0 = 10^4, N = 100. 5 mm Al beampipe and 1 mm Pb sheild included around target. See text for details.

by Deleplanque et al. [4] to describe γ-ray energy spectra with several transitions as part of a cascade. This is defined as,

$$\text{Resolving power} = \exp\left[\log\left(N_0/N\right)/(1 - \log\left(\epsilon\right)/\log\left(R\right))\right] \tag{3}$$

where N_0 and N are the total number of events and number of events within the full-energy peak, respectively, ϵ is the total full-energy-peak efficiency and R is a background reduction factor. The background reduction factor describes the enhancement of the peak-to-background by energy-gating on a peak as part of cascade. The background reduction factor is often defined as $R = 0.76(SE/\delta E)(P/T)$ by choice of an energy gate of FWHM width (δE) over a Gaussian peak, where SE is average energy spacing per cascade transition.

To evaluate the relative difference in these performance characteristics, including resolving power, for a potential GAGG:Ce-based array over conventional NaI:Tl-based detector arrays, GEANT4 Monte Carlo simulations were performed with a fixed detector array geometry. A common simulated geometry isolates the influence by the scintillator material. The geometry of the DALI2+ array is utilized and comprises of 226 detectors of three detector sizes and surrounding a reaction target, as shown in Fig. 7. Each NaI:Tl scintillator is coated by by approximately 2 mm MgO and encapsulated by a 1 mm thick Al enclosure. A typical experimental in-flight γ-ray emission velocity for the RIKEN RIBF of $\beta = 0.6$ is used in the simulations and for Doppler reconstruction of the γ-ray energy spectra.

The GAGG:Ce energy resolution from the HR-GAGG cylindrical sample and the average of 30 highest resolution NaI:Tl detectors (Fig. 5) are used for Monte Carlo GEANT4 simulations to compare performance for experimental conditions. The non-hygroscopic property of GAGG:Ce scintillators furthermore permits the elimination of Al airtight detector enclosures. Additional simulations are performed with 65 µm ESR wrapping as a substitute of Al casings and MgO coatings. ESR foil is simulated as polyethylene terephthalate (PET) $(C_{10}H_8O_4)_n$ at a density of 1.29 g cm^{-1}.

The FEP efficiency and energy resolution determined by GEANT4 simulation is shown in Fig. 8 as a function of energy for both GAGG:Ce and NaI:Tl-based DALI2+ array geometries, and with and without a vacuum beampipe and Pb shield typically employed for experiments with DALI2+. The direct substitution of GAGG:Ce drastically improves the FEP efficiency due to the decreased radiation length. The utilization of thin 65 µm ESR wrappings additionally contributes to a significant increase in FEP efficiency. At 1 MeV and with the typical vacuum beampipe and Pb shield around the reaction target, the FEP efficiency is 33 % for the present NaI:Tl-based DALI2+ array and 50 % for a GAGG:Ce-based DALI2+ array with 65 µm ESR wrapping material. The peak-to-total ratio is similary improved, from 0.47 to 0.65.

The simulated Doppler-reconstructed energy resolution (Fig. 8) is enhanced with GAGG:Ce scintillators. A large component of the Doppler-reconstructed energy resolution is dictated by the detector array geometry: the opening angle of the detectors as observed by Doppler reconstruction position. This

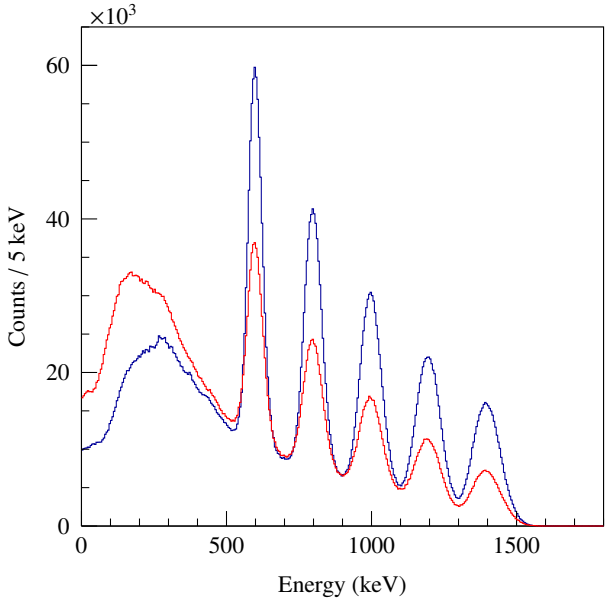

Figure 10(a): Without energy add-back procedure

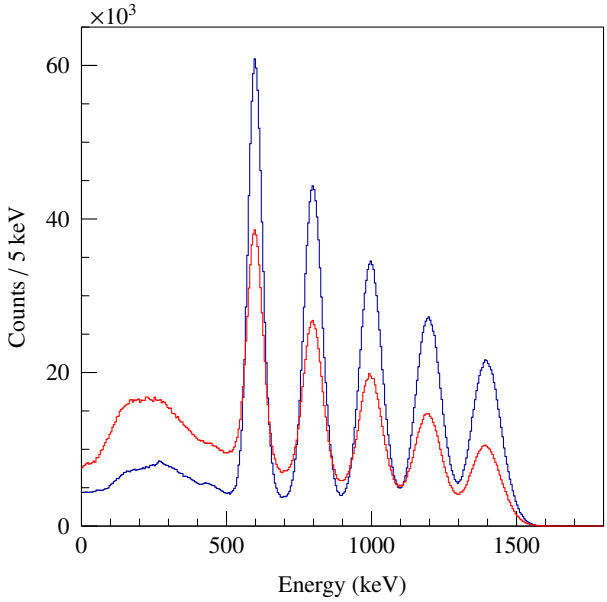

Figure 10(b): With 15 cm energy add-back procedure

Figure 10: Monte Carlo simulated in-flight ($\beta = 0.6$) γ-ray energy spectrum of DALI2+ detector array and 10^6 events of 600 keV, 800 keV, 1000 keV, 1200 keV and 1400 keV γ-rays. (Blue) GAGG:Ce with 65 µm ESR foil. (Red) NaI:Tl with 2 mm MgO coating and 1 mm Al casing.

induces a lower limit of attainable Doppler-reconstructed energy resolution and is displayed as the grey dash-dotted line in the Figure. Additional contributions to the energy resolution due to Doppler broadening generated by in-flight velocity distribution and target energy losses is expected in typical experiments, but is not included in these simulations.

The resolving power at 1 MeV for the condition of $N_0 = 10^4$ and $N = 100$ is shown in Fig. 9 for both GAGG:Ce (with

ESR wrapping) and NaI:Tl (MgO and Al) scintillators. The resolving power is enhanced for separation energies between 150 keV to 500 keV by a factor of 4 – 20 with an add-back procedure applied. The simulated Doppler-reconstructed γ-ray energy spectra for an artificial cascade of 600 keV, 800 keV, 1000 keV, 1200 keV and 1400 keV γ-rays of equal intensity is shown in Fig. 10, exemplifying the improved FEP efficiency, peak-to-total ratio and resolution of a GAGG:Ce-based detector array. An experiment-specific beam-induced background component is expected for typical of experimental conditions but is not simulated.

4. Summary

Large-volume single crystal cerium-doped gadolinium aluminium gallium garnet scintillators are demonstrated to achieve high light yield and energy resolution, surpassing NaI:Tl scintillators of similar size. The application of GAGG:Ce scintillators is shown to be advantageous for in-beam γ-ray spectroscopy by GEANT4 simulations, providing enhanced full-energy-peak efficiency, peak-to-total ratio, Doppler-reconstructed energy resolution and resolving power relative to NaI:Tl-based detector arrays, such as the RIKEN RIBF DALI2+ array. Future studies will investigate larger GAGG:Ce scintillator samples, optimized detector geometries and detector array configurations.

[1] A. Maj, e. a., 2009. The paris project. Acta physica polonica b 40 (3), 565–575.

[2] Allier, C., Valk, H., Huizenga, J., Bom, V., Hollander, R., Van Eijk, C., 1998. Comparative study of silicon detectors. IEEE Transactions on Nuclear Science 45 (3), 576–580.

[3] Camera, F., Giaz, A., Pellegri, L., Riboldi, S., Blasi, N., Boiano, C., Bracco, A., Brambilla, S., Ceruti, S., Coelli, S., Crespi, F., Csatlòs, M., Krasznahorkay, A., Gulyàs, J., Lodetti, S., Frega, S., Miani, A., Million, B., Stuhl, L., Wieland, O., 2014. Characterization of large volume 3.5" × 8" LaBr3:ce detectors for the HECTOR+array. EPJ Web of Conferences 66, 11008.

[4] Deleplanque, M., Lee, I., Vetter, K., Schmid, G., Stephens, F., Clark, R., Diamond, R., Fallon, P., Macchiavelli, A., 1999. Greta: utilizing new concepts in γ-ray detection. Nuclear Instruments and Methods in Physics Research Section A: Accelerators, Spectrometers, Detectors and Associated Equipment 430 (2), 292–310.

[5] Doornenbal, P., 2012. In-beam gamma-ray spectroscopy at the ribf. Progress of Theoretical and Experimental Physics 2012 (1).

[6] Guillemaud-Mueller, D., 1997. In: Tours Symposium on Nuclear Physics III. Vol. 425. AIP Conf, p. 290.

[7] Ikagawa, T., Kataoka, J., Yatsu, Y., Saito, T., Kuramoto, Y., Kawai, N., Kokubun, M., Kamae, T., Ishikawa, Y., Kawabata, N., 2005. Study of large area hamamatsu avalanche photodiode in a γ-ray scintillation detector. Nuclear Instruments and Methods in Physics Research Section A: Accelerators, Spectrometers, Detectors and Associated Equipment 538 (1), 640–650.

[8] Jääskeläinen, M., Sarantites, D., Woodward, R., Dilmanian, F., Hood, J., Jääskeläinen, R., Hensley, D., Halbert, M., Barker, J., 1983. The spin spectrometer: Design, instrumentation and response characteristics of $4\pi\gamma$-ray multidetector system. Nuclear instruments and methods in physics research 204 (2-3), 385–405.

[9] Kamada, K., Endo, T., Tsutumi, K., Yanagida, T., Fujimoto, Y., Fukabori, A., Yoshikawa, A., Pejchal, J., Nikl, M., 2011. Composition engineering in cerium-doped (lu, gd) 3 (ga, al) 5o12 single-crystal scintillators. Crystal Growth & Design 11 (10), 4484–4490.

[10] Kamada, K., Shoji, Y., Kochurikhin, V. V., Okumura, S., Yamamoto, S., Nagura, A., Yeom, J. Y., Kurosawa, S., Yokota, Y., Ohashi, Y., et al., 2016. Growth and scintillation properties of 3in. diameter ce doped gd 3 ga 3 al 2 o 12 scintillation single crystal. Journal of Crystal Growth 452, 81–84.

[11] Kamada, K., Yanagida, T., Endo, T., Tsutumi, K., Usuki, Y., Nikl, M., Fujimoto, Y., Fukabori, A., Yoshikawa, A., 2012. 2inch diameter single crystal growth and scintillation properties of ce: Gd 3 al 2 ga 3 o 12. Journal of Crystal Growth 352 (1), 88–90.

[12] Kamada, K., Yanagida, T., Pejchal, J., Nikl, M., Endo, T., Tsutsumi, K., Fujimoto, Y., Fukabori, A., Yoshikawa, A., 2012. Crystal growth and scintillation properties of ce doped gd3gaal5o12 single crystals. IEEE Transactions on Nuclear Science 59 (5), 2112–2115.

[13] Kim, M., Kang, H., Kim, H., Kim, W., Park, H., Kim, S., 2008. A study of csi (tl) scintillator with optimized conditions of large area avalanche photodiode. Journal of Nuclear Science and Technology 45 (sup5), 586–589.

[14] Knoll, G. F., 2010. Radiation detection and measurement. John Wiley & Sons.

[15] Lee, I., Deleplanque, M., Vetter, K., 2003. Developments in large gamma-ray detector arrays. Reports on Progress in Physics 66 (7), 1095.

[16] Lee, I.-Y., 2013. Large gamma-ray detector arrays and electromagnetic separators. Nuclear Instruments and Methods in Physics Research Section B: Beam Interactions with Materials and Atoms 317, 644–648.

[17] Li, J.-G., Sakka, Y., 2015. Recent progress in advanced optical materials based on gadolinium aluminate garnet (gd3al5o12). Science and technology of advanced materials 16 (1), 014902.

[18] Moszynski, M., Kapusta, M., Balcerzyk, M., Szawlowski, M., Wolski, D., Wegrzecka, I., Wegrzecki, M., 2001. Comparative study of avalanche photodiodes with different structures in scintillation detection. IEEE Transactions on Nuclear Science 48 (4), 1205–1210.

[19] Moszyński, M., Szawlowski, M., Kapusta, M., Balcerzyk, M., 2002. Large area avalanche photodiodes in scintillation and x-rays detection. Nuclear Instruments and Methods in Physics Research Section A: Accelerators, Spectrometers, Detectors and Associated Equipment 485 (3), 504–521.

[20] Pansart, J., 1997. Avalanche photodiodes for particle detection. Nuclear Instruments and Methods in Physics Research Section A: Accelerators, Spectrometers, Detectors and Associated Equipment 387 (1-2), 186–193.

[21] Pauwels, K., Auffray, E., Gundacker, S., Knapitsch, A., Lecoq, P., oct 2012. Effect of aspect ratio on the light output of scintillators. IEEE Transactions on Nuclear Science 59 (5), 2340–2345.

[22] Sasano, M., Nishioka, H., Okuyama, S., Nakazawa, K., Makishima, K., Yamada, S., Yuasa, T., Okumura, A., Kataoka, J., Fukazawa, Y., Hanabata, Y., Hayashi, K., jul 2013. Geometry dependence of the light collection efficiency of BGO crystal scintillators read out by avalanche photo diodes. Nuclear Instruments and Methods in Physics Research Section A: Accelerators, Spectrometers, Detectors and Associated Equipment 715, 105–111.

[23] Shagin, P., Gomez, R., Oberlack, U., Cushman, P., Sherwood, B., McClish, M., Farrell, R., 2009. Avalanche photodiode for liquid xenon scintillation: quantum efficiency and gain. Journal of Instrumentation 4 (01), P01005.

[24] Simon, R. S., 1980. The darmstadt-heidelberg crystal ball. Le Journal de Physique Colloques 41 (C10), C10–281.

[25] Takeuchi, S., Motobayashi, T., Togano, Y., Matsushita, M., Aoi, N., Demichi, K., Hasegawa, H., Murakami, H., 2014. Dali2: A nai (tl) detector array for measurements of γ rays from fast nuclei. Nuclear Instruments and Methods in Physics Research Section A: Accelerators, Spectrometers, Detectors and Associated Equipment 763, 596–603.

[26] van Loef, E. V. D., Dorenbos, P., van Eijk, C. W. E., Krmer, K., Gdel, H. U., sep 2001. High-energy-resolution scintillator: Ce3+ activated LaBr3. Applied Physics Letters 79 (10), 1573–1575.

[27] Weisshaar, D., Gade, A., Glasmacher, T., Grinyer, G., Bazin, D., Adrich, P., Baugher, T., Cook, J., Diget, C. A., McDaniel, S., et al., 2010. Caesara high-efficiency csi (na) scintillator array for in-beam γ-ray spectroscopy with fast rare-isotope beams. Nuclear Instruments and Methods in Physics Research Section A: Accelerators, Spectrometers, Detectors and Associated Equipment 624 (3), 615–623.

[28] Y. Togano, M. Shikata, K. K. T. N., 2014. Development of a gamma-ray calorimeter for the measurement of highly excited states. Tech. rep., RIKEN Accelerator Progress Report 47.

[29] Yokota, Y., Kudo, T., Ohashi, Y., Kurosawa, S., Kamada, K., Zeng, Z., Kawazoe, Y., Yoshikawa, A., 2017. Effects of dopant distribution im-

provement on optical and scintillation properties for ce-doped garnet-type single crystals. Journal of Materials Science: Materials in Electronics 28 (10), 7151–7156.

[30] Yoshikawa, A., Chani, V., Nikl, M., 2014. Czochralski growth and properties of scintillating crystals. Zeszyty Historyczne Politechniki Warszawskiej (16), 135–149.

Appendix D

Article

Preprint article on spectroscopy and crossections of ^{32}Ne produced by knockout reactions.

Spectroscopy of Strongly Deformed ^{32}Ne by Proton Knockout Reactions

I. Murray,[1] M. MacCormick,[1] D. Bazin,[2] P. Doornenbal,[3] N. Aoi,[4] H. Baba,[3] H. Crawford,[5] P. Fallon,[5] K. Li,[3] J. Lee,[6] M. Matsushita,[3] T. Motobayashi,[3] T. Otsuka,[7,3,2,8] H. Sakurai,[3,9] H. Scheit,[10,3] D. Steppenbeck,[3] S. Takeuchi,[3] J. A. Tostevin,[11] N. Tsunoda,[7] Y. Utsuno,[12] H. Wang,[3] and K. Yoneda[3]

[1]*Institut de Physique Nucléaire, IN2P3-CNRS, Université Paris-Sud, Université Paris-Saclay, Orsay Cedex 91406, France*
[2]*National Superconducting Cyclotron Laboratory, Michigan State University, East Lansing, Michigan 48824, USA*
[3]*RIKEN Nishina Center, Wako, Saitama 351-0198, Japan*
[4]*Research Center for Nuclear Physics (RCNP), Osaka University, Ibaraki, Osaka 567-0047, Japan*
[5]*Nuclear Science Division, Lawrence Berkeley National Laboratory, Berkeley, United States*
[6]*The University of Hong Kong, Hong Kong*
[7]*Center for Nuclear Study (CNS), University of Tokyo, Wako-shi, Saitama 351-0198, Japan*
[8]*Instituut voor Kern- en Stralingsfysica, Katholieke Universiteit Leuven, Leuven B-3001, Belgium*
[9]*Department of Physics, University of Tokyo, 7-3-1 Hongo, Bunkyo, Tokyo 113-0033, Japan*
[10]*Technische Universität Darmstadt, Darmstadt 64289, Germany*
[11]*Department of Physics, University of Surrey, Guildford, Surrey GU2 7XH, United Kingdom*
[12]*Japan Atomic Energy Agency, Tokai, Ibaraki 319-1195, Japan*

(Dated: September 3, 2018)

Low lying states of neutron-rich ^{32}Ne were populated by means of one- and two-proton knockout reactions at the RIKEN Radioactive Isotope Beam Factory. A new transition is observed at 1410(15) keV and assigned to the $4_1^+ \rightarrow 2_1^+$ decay. With this energy the $R_{4/2}$ ratio is calculated to be 2.99(6), lying close to the rigid rotor limit and suggests a high degree of collectivity and strongest deformation among neutron-rich Neon isotopes. Comparisons of experimental inclusive and exclusive reaction cross sections with shell model and eikonal reaction dynamical calculations reveals considerable quenching for this highly asymmetric system and contributes to systematic trends.

Canonical magic numbers [1, 2], found near the β-stability line on the Segré chart, have wide applicability to the understanding of many facets of nuclear properties. Their existence is a consequence of nuclear shell structure and large energy gaps between packets of orbitals. In nuclear systems with unbalanced neutron and proton numbers, these magic numbers can disappear (N=8, 20, 28...) and new ones precipitate in neutron-rich nuclei (N=16, 32, 34...) [3]. Atomic mass trends [4] and 2_1^+ excitation energies [5–8] have provided the first clues to this phenomenon and contribute to improving our understanding of shell structure.

The first signature of the breakdown of the N = 20 major shell effect was the observation of excessive binding energy for sodium isotopes, with $^{31-32}$Na more bound than predicted [9]. This was later extended to $^{31-32}$Mg [10]. A low lying first excited 2^+ state [11, 12] and the Coulomb excitation of ^{32}Mg [13, 14] provided additional evidence.

This dramatic and sudden change in structure for Z $\leq$ 12 and N $\geq$ 20 was termed the *island of inversion* (IOI) [15] and interpreted as due to the introduction of intruder configurations, neutron multiparticle-multihole excitations, in the ground state. The neutrons are promoted across the N = 20 gap from *sd* to *pf* orbitals [16] as a consequence of an increase in correlations and reduction of the spherical shell gap.

As protons are removed from the $\pi d_{5/2}$ orbital, the neutron $\nu d_{3/2}$ orbital is less bound and approaches the $\nu f_{7/2}$ and $\nu p_{3/2}$ levels, quenching the shperical N = 20 shell gap. The driving force of the evolution of orbitals is understood as being due to the spin-isospin components of the monopole interaction [17], the tensor force. This component of the nucleon-nucleon interaction is highlighted in increasing proton/neutron asymmetry isotopes [18].

Originally, the IOI was predicted to exist between $10 \leq Z \leq 12$ and $20 \leq N \leq 22$ [15]. However, through great experimental effort the transition to the IOI has been revealed to be soft. However, the borders of the IOI are not entirely delineated on the exotic south-east side, driving theoretical and experimental progress. With many studies focused on magnesium and sodium isotopes, the latter known up to N=24 [19], the IOI has been barely reached for Ne (Z=10) isotopes.

For odd Ne isotopes, the ground state spin-parity reveals a soft transition from ^{27}Ne, to a westward boundary of the IOI for ^{29}Ne, and full inclusion into the IOI for ^{31}Ne.

Intruder configurations were suggested for ^{27}Ne (N = 17) through the observation of a low-lying negative parity state $3/2^-$ [20, 21]. The ground state of ^{29}Ne (N = 19) was established through the neutron removal cross section and a narrow parallel momentum distribution [22], thus supporting the ground state as largely consisting of a $^{28}\mathrm{Ne}(0_1^+) \otimes 2p_{3/2}$ neutron intruder configuration. ^{31}Ne (N = 21) is suggested to exhibit a p-wave halo structure of ground state spin parity $3/2^-$ by observation of a large Coulomb breakup cross section [23] and one-nucleon removal reactions [24].

For even Ne isotopes a soft transition is also reported from ^{28}Ne and admittance of ^{30}Ne and ^{32}Ne within the

IOI. ^{28}Ne (N = 18) is observed to have a significantly lowered 2_1^+ energy level ($E2_1^+$) [14], a characteristic signature of increasing collectivity. The reduced E2 transition probability of ^{30}Ne (N = 20), indicates a large enhancement in collectivity [25]. In addition, the low excited first 2_1^+ state [26] firmly place it within the IOI. The first excited 2_1^+ state at 722(9) keV [27] by in-beam spectroscopy of the near drip line nucleus ^{32}Ne (N = 22) has been identified. The low level energy and predictions by shell model calculations of Utsuno et al. [28] and Caurier et al. [29] reveal a continuing trend of strong deformation and a ground state dominated by intruder configurations [27]. ^{32}Ne is the most neutron-rich neon isotope known to belong to the IOI and understanding the role of intruder configurations to the yet unknown drip line commands further study.

Here, we present an in-beam spectroscopic study of ^{32}Ne (N = 22) to extend its limited level scheme and to determine inclusive and exclusive cross sections by one- and two-proton knockout reactions. These reactions directly probe the active orbitals near the Fermi surface via the one- and two-particle overlaps of the wave functions of the projectiles (^{33}Na and ^{34}Mg) and the final states of the reaction product (^{32}Ne). They also add information on the nucleon removal cross section trends for highly asymmetric systems.

For one-nucleon removal experiments, the growing data set for the ratio of the measured inclusive cross section to the calculated one ($R_s = \sigma_{ex}/\sigma_{th}$), shows greater suppression when removing a nucleon from the minority species in more asymmetric systems [30, 31]. In two-nucleon (2N) removal reactions the requirement that the reaction is direct [32, 33], and not contaminated by sequential processes, has restricted the analogous comparisons to involve well-bound minority species, as for the ^{9}Be(^{34}Mg,^{32}Ne)X reaction here. No asymmetry dependence in the 2N removal cross section ratio R_s has been established. This ratio has been shown to be close to 0.5 for several *sd*-shell systems [34], but with greater suppression observed when there are large structural and/or deformation changes between the initial and final states [35, 36], situations which challenge truncated basis shell model calculations.

It is emphasized that due to the unbound nature of ^{32}F, in-beam spectroscopy employing proton removal reactions is one of the only techniques capable of interrogating the excited states and structure of ^{32}Ne.

The present experiment was performed at the BigRIPS fragment separator and ZeroDegree spectrometer [37] at the Radioactive Isotope Beam Factory (RIBF), operated by the RIKEN Nishina Center and the Center for Nuclear Study, University of Tokyo. Secondary radioactive cocktail beams of ^{33}Na (2%) and ^{34}Mg (21%) were produced by projectile fragmentation of a 345 MeV u^{-1} primary beam of ^{48}Ca on a 15 mm thick rotating Be target. The average beam intensity was 90 pnA. Secondary beams were purified via the $B\rho - \Delta E - B\rho$ method using dipoles and 5 mm thick aluminium degraders at the

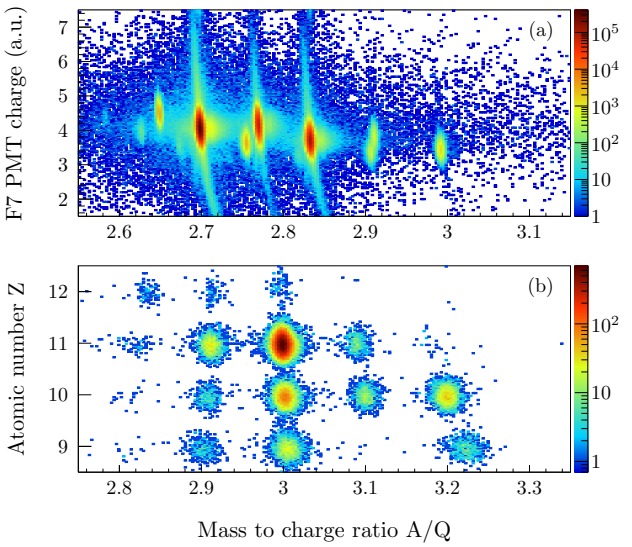

FIG. 1. (a) BigRIPS separator and (b) ZeroDegree spectrometer particle identification, before and after the ^{9}Be secondary reaction target, respectively.

BigRIPS dispersive focal planes F1 and F5. Event-by-event identification of the secondary beam particles in BigRIPS was accomplished by the $TOF-B\rho-\Delta E$ method, wherein the time-of-flight (TOF), magnetic rigidity, and energy loss were used to determine the mass-to-charge ratios (A/Q) and atomic numbers (Z) [38]. The time-of-flight was measured with plastic scintillators at achromatic focal planes F3 and F7. The two-stage structure of BigRIPS and the twofold $B\rho$ determination through trajectory determination at focal planes F3, F5, and F8 removed any dependence upon energy losses in the F5 aluminium degrader. The energy loss (ΔE), determined through the geometric mean of left and right photomultiplier charges of the F7 plastic scintillator, provided separation in atomic number. The rates of secondary beams of ^{33}Na and ^{34}Mg were 85 and 8000 particles per second (pps), respectively.

A 1032 mg cm^{-2} thick Be solid target at focal plane F8 induced secondary reactions the products of which were transmitted to the ZeroDegree spectrometer. The magnetic rigidity of BigRIPS and ZeroDegree spectrometers were set to maximize transmission of ^{34}Mg at F8 and 2-proton knockout reaction residues, ^{32}Ne, beyond the F8 secondary target. The large momentum acceptance of the ZeroDegree spectrometer (8%) permitted simultaneous acceptance of 1-proton knockout residues from ^{33}Na secondary beam particles. The mid-target beam energies were 235 MeV u^{-1} and 221 MeV u^{-1} for ^{34}Mg and ^{33}Na, respectively.

The $TOF - B\rho - \Delta E$ method was likewise implemented for the identification of reaction residues in the ZeroDegree spectrometer. A particle identification diagram (PID) is presented in Fig. 1 and shows a clear separation of ^{32}Ne.

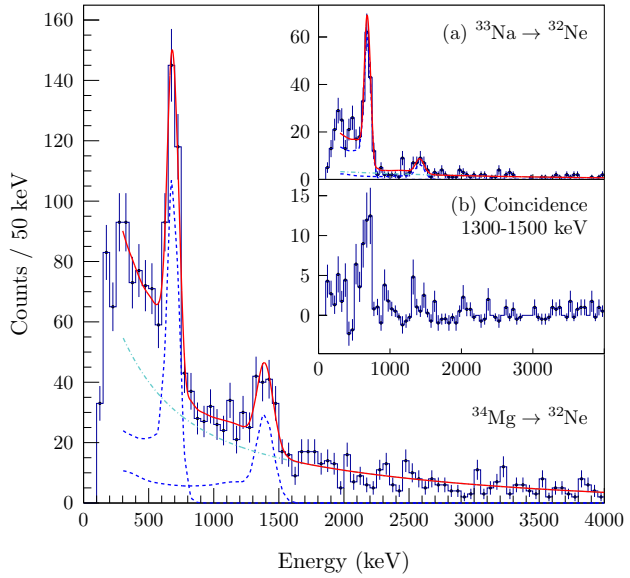

FIG. 2. Doppler reconstructed γ spectrum of two-proton and (a) one-proton knockout reactions leading to ^{32}Ne. A least square fit (red solid line) of a global function comprised of simulated responses of DALI2 (dotted blue) and a two-component exponential background (dotted cyan) is applied. (b) Coincidence of combined one- and two-proton knockout reactions for 1410 keV transition (1300 to 1500 keV). Add-back and a maximum γ-ray multiplicity threshold of 3 are applied.

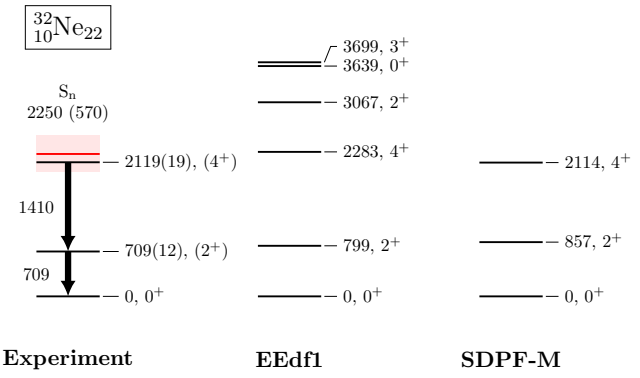

FIG. 3. Energy levels from the present experiment compared to *EEdf1* [42] and *SDPF-M* [28] effective interaction shell model calculations for ^{32}Ne. The extrapolated neutron separation energy (S_n) of 2250(570) keV [43] is shown in red. The uncertainty is shown as the width.

To observe the decay of short lived populated states the DALI2 gamma spectrometer [39], comprised of 186 NaI(Tl) crystals, encompassed the secondary target with an angular coverage of 18-148 degrees. Calibration for individual crystals was completed using ^{88}Y, ^{60}Co, and ^{137}Cs sources to provide gamma energies near the range of experimentally observed transitions. The Doppler corrected in-flight energy resolution ($\beta = 0.6$) for 1 MeV gamma-rays is 10% (FWHM) with an efficiency of 20% [39]. In the offline γ-ray reconstruction, an energy add-back procedure was applied within a radius of 15 cm between hit detectors to increase photopeak efficiency. A multiplicity threshold of 5 and 3 was selected for the recontruction of one- and two-proton knockout spectra used for energy determination. A GEANT4-based [40] simulation of the DALI2 array was utilized to produce full response functions based on individual detector energy resolutions and thresholds (200 keV), mean beam velocity, energy loss in the target [41], and lifetime of a given state.

The Doppler reconstructed spectra of both one- and two-proton knockout reactions to ^{32}Ne are presented in Fig. 2. A strong transition at 709(12) keV, observed in both reactions, corresponds to the $2^+_1 \rightarrow 0^+_{g.s.}$ transition and is consistent with a previous measurement of 722(9) keV by both inelastic scattering and proton removal with lower statistics [27]. A new transition at 1410(15) keV was observed in one- and two-proton knockout reactions. The γ-ray spectrum of Fig. 2(b), obtained with the condition of a prompt coincidence with this transition, indicates a decay sequence with the 722(9) keV transition with a relative intensity of 108(20) %.

The 1410(15) keV transition is tentatively assigned to the $4^+_1 \rightarrow 2^+_1$ decay. Spin and parity assignment is based on (i) prompt coincidence with the $2^+_1 \rightarrow 0^+_{g.s.}$ transition (ii) population of 4^+_1 states in nucleon knockout reactions to ^{28,30}Ne with fast-beams [32, 35], (iii) the reproduction of energy levels with shell model calculations, (iv) reaction theory exclusive cross section ratios as will be discussed later in the text, (v) the limited possibility of additional bound states due to a low extrapolated neutron separation energy (S_n) of 2250(570) keV [43].

A global parametric function, comprised of a DALI2 response function and a two-component exponential background, fit to the reconstructed experimenal spectra was used to extract the energies and intensities of the transitions. Doppler reconstructions of both experimental and simulated data were performed at the target center. The uncertainty in the deduced transition energies include a statistical contribution, detector calibration errors, uncertainty in beam energy (translating to an uncertainty in reconstruction), uncertainty from the unmeasured lifetime of the 2^+_1 state, and an uncertainty for a chosen maximum multiplicity threshold. The lifetime of the 2^+_1 state was chosen to be 60 ps, as predicted by global trends [44]. Variation of this lifetime by a factor of two produces a shift of the $2^+_1 \rightarrow 0^+_{g.s.}$ transition by 10 keV and is the largest contribution to the systematic uncertainty. The 2^+_1 lifetime is a small uncertainty component (1 keV) in the $4^+_1 \rightarrow 2^+_1$ transition uncertainty, due to the large difference in energy. In addition, systematic errors in transition energies are shared between one- and two-proton knockout reactions.

In addition to the experimentally determined states, shell model calculations with large valence spaces have

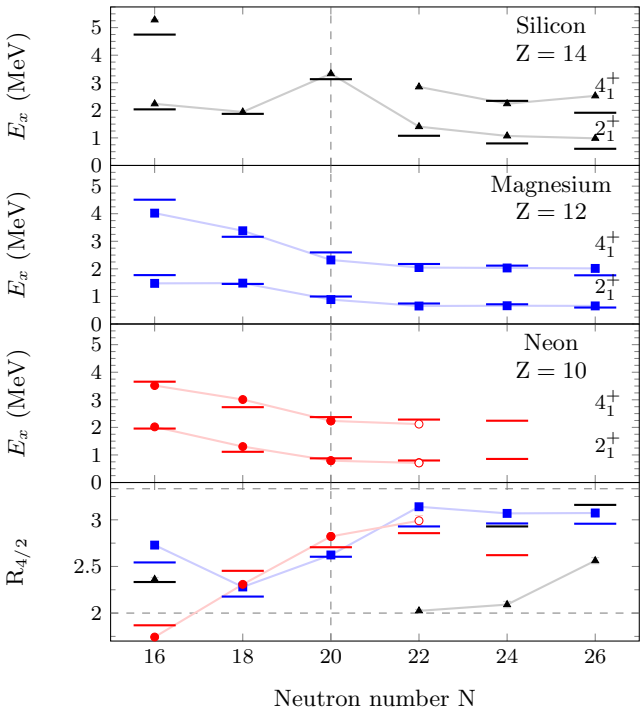

FIG. 4. Systematics of experimental $R_{4/2}$ values, first excited 2_1^+ and 4_1^+ levels across $16 \leq N \leq 26$ for neon (circle), magnesium (square) and silicon (triangle). Open circles are measured in this work. Connecting lines are drawn to guide the eye. Horizontal bars are calculations with EKK developed *sdpf* effective interaction [42]. Dashed horizontal lines for vibrational and rotational limits are drawn at 2.0 and 3.33, respectively. A dashed vertical line at the traditional N = 20 magic number. Experimental data were taken from [45–51].

been performed. The recently available extended Kuo-Krenciglowa (EKK) derived effective interaction [42], henceforth called EEdf1, includes multiparticle-multihole transition mixing across the N = 20 shell gap in a complete *sdpf* model space. This is compared to the SDPF-M interaction [28], restricted to the $sd - p_{3/2}f_{7/2}$ space, but which allows for mixing of *sd* and *pf* configurations. Both interactions have been shown to provide a good description of the IOI and predict strongly deformed ground states dominated by intruder configurations for N = 20 neon and magnesium isotopes. Figure 4 shows the predicted lowest excited states in the even silicon, magnesium, and neon isotopes calculated with the EEdf1 effective interaction.

The predicted states are in agreement with the experimentally assigned levels in ^{32}Ne, as shown in Fig. 3. The lowered 2_1^+ and 4_1^+ states are reproduced, with both shell model calculations anticipating a less developed rotational band. The observed states and ground state are found to be almost pure intruder configurations with the EEdf1 interaction. They comprise mainly of 2p-2h ($\approx 40\%$) and 4p-4h ($\approx 50\%$) components. In addition, the $R_{4/2}$ ratio, defined as the ratio of $E4_1^+$ and $E2_1^+$ energies, is predicted to increase to a maximum at N = 22. Confirmation of this increase is established from the newly deduced 4_1^+ state energy and is thus the highest experimental $R_{4/2}$ ratio in the neutron-rich neon isotopic chain. These observations provide additional experimental evidence for the inclusion of ^{32}Ne inside the *island of inversion*.

The 2_1^+ and 4_1^+ energy levels ($E2_1^+$ and $E4_1^+$), and $R_{4/2}$ ratios of neutron-rich silicon, magnesium, and neon isotopes are shown in Fig. 4 and display signatures of shell evolution. The peak in $E2_1^+$ for silicon at N = 20 is an indication of a good shell closure, in contrast to the lowering of $E2_1^+$ and $E4_1^+$ with increasing neutron filling for magnesium and neon. Conversely, the increasing $R_{4/2}$ ratio is emblematic of a developing quadrupole collectivity in magnesium, and this new measurement confirms the continuation of a similar trend in neon for $N > 20$.

Direct reaction theory is combined with the shell model overlaps, given by the spectroscopic factors (C^2S) and two-nucleon amplitudes (TNA), respectively, to calculate the exclusive and inclusive one- and two-proton removal cross sections to ^{32}Ne. The sudden (fast collisions) and eikonal (forward scattering) approximations are applied [33, 34, 52, 53]. Details of the inputs to the reaction calculations, and of the use of Hartee-Fock calculations to constrain the projectile-target distorting interactions and the proton bound-state potential geometries are discussed in Ref. [30, 31] and [33, 34]. The direct nature of the two-proton removal mechanism is guaranteed by the energetics involved in the removal of the well-bound protons [32, 33]. The asymmetry in the ^{33}Na separation energies for protons (20.510(680) MeV) and neutrons (2.930(450) MeV) will suppresses the competing proton evaporation channel following the population of highly excited ^{33}Na nuclei via one-proton removals from ^{34}Mg.

The ^{9}Be target induces reactions proceeding by elastic (diffraction dissociation) and inelastic (stripping) processes. These mechanisms are calculated separately by reaction theory and are indistinguishable in the experiment. Their relative contributions have been studied previously [54, 55] and were shown to be in good agreement with eikonal model predictions for reactions involving both strongly and weakly-bound nucleons. Given the strong binding of the protons in the present cases, the stripping mechanism is dominant.

The experimental cross sections were determined by the number of projectiles and fragments in BigRIPS and ZeroDegree spectrometers, respectively. Corrections for the tracking efficiency of parallel plate avalanche counters (PPAC), indistinguishable reactions in the 1 mm plastic scintillator at F7 before the target, and acquisition deadtime were applied. Uncertainties in the target areal density, transmission, and reaction contaminants are included. The determination of exclusive cross sections requires the observation of transitions with the DALI2 spectrometer and a fit to the GEANT4 simulated response functions. To account for a difference between the simulated and measured DALI2 γ-source efficiency, a

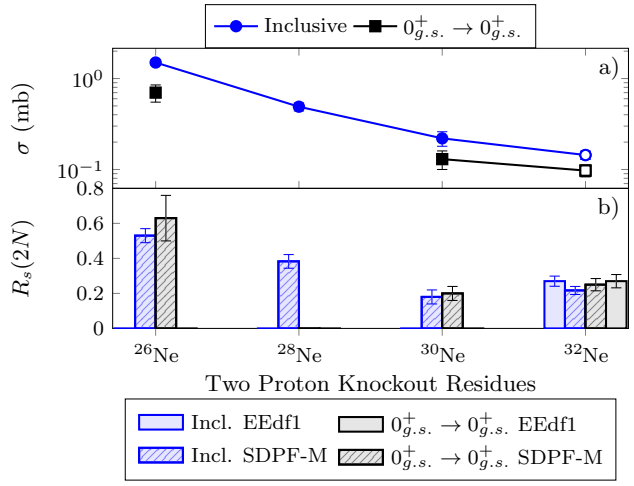

FIG. 5. (a) Two-proton knockout experimental inclusive and $0^+_{g.s.} \rightarrow 0^+_{g.s.}$ cross sections (σ). Data taken from [32, 34, 35]. (b) $R_s(2N)$ suppression factors utilizing EEdf1 and SDPF-M interactions. The theoretical inclusive cross sections to ^{26}Ne and ^{28}Ne are calculated with the eikonal reaction framework, described in this report, to be 2.82 mb and 1.28 mb. The associated 2N knockout inclusive $R_s(2N)$ are ^{26}Ne and ^{28}Ne are 0.53(4) and 0.38(4).

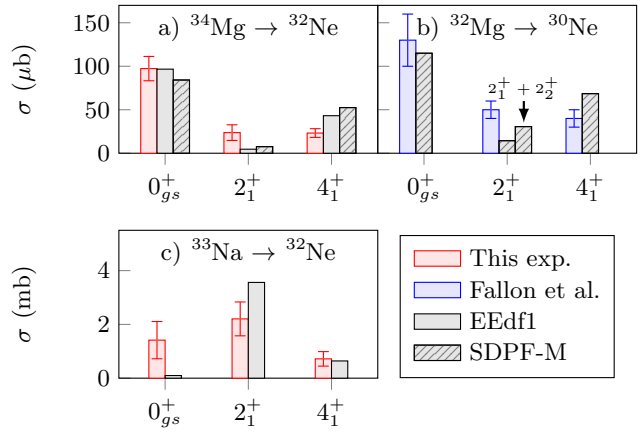

FIG. 6. Experimental exclusive cross sections and theoretical predictions from shell model calculations. Exclusive theoretical cross sections are scaled by the inclusive R_s value for the visualization of the populated ratio. (a) Two-proton knockout reactions to $^{32}_{10}$Ne. (b) Two-proton knockout reactions to $^{30}_{10}$Ne [35]. The cross section to 2^+_1 was conjectured to be unobserved feeding from a 2^+_2 state. The combined cross section is also plotted. (c) One-proton knockout reactions to $^{32}_{10}$Ne.

6% uncertainty was included.

The calculated inclusive two-proton removal reaction cross section (to the two shell model states below the neutron separation threshold) is 530 µb based on the TNA of the EEdf1 shell model interaction. This is significantly greater than the measured inclusive cross section of 144(15) µb. The accompanying inclusive suppression factor $R_s(2N)$ is 0.27(3) with the EEdf1 interaction shell model TNAs. Detailed results are presented in table II.

TABLE I. ^{32,34}Mg and ^{30,32}Ne ground state neutron 0p-0h, 2p-2h and 4p-4h probabilties (%) calculated with the SDPF-M and EEDf1 interactions.

	SDPF-M			EEDf1		
	0p-0h	2p-2h	4p-4h	0p-0h	2p-2h	4p-4h
^{32}Mg	4.7	82.5	12.7	1.8	36.2	51.9
^{30}Ne	3.9	74.1	22.0	0.5	19.8	68.1
^{34}Mg	9.5	82.0	8.4	1.6	49.5	43.4
^{32}Ne	10.0	76.5	13.4	1.2	43.3	50.6

The suppression factor $R_s(2N)$ is consistant with the trend from previous experiments and analysis for neon isotopes, as shown in Fig. 5b, and may signal a saturation of $R_s(2N)$ values. In the case of the two-proton removal reaction to ^{30}Ne [35], the small $R_s(2N)$ value was interpreted as due to a change in neutron configuration between ^{32}Mg and ^{30}Ne ground states, absent from the SDPF-M interaction shell-model calculations. Assuming a dominant 2p-2h neutron configuration in ^{32}Mg, consistent with SDPF-M, this interpretation implied a significant ($\approx$ 50%) 4p-4h component in ^{30}Ne. Shell model calculations with the newly developed EEdf1 interaction predict higher 4p-4h components in both ^{30}Ne and ^{32}Mg as well as ^{32}Ne and ^{34}Mg ground states, as shown in table I. However, the TNA from the two interactions are not drastically different, and this is reflected by the similar calculated suppression factors $R_s(2N)$ shown in Fig. 5b. As a result, it is not possible to firmly establish the $R_s(2N)$ value as a missing structural difference present in the TNAs or a consequence of the reaction theory framework. No general trend of $R_s(2N)$ has been established, unlike for one nucleon knockout reactions.

The exclusive measurement, made possible with the DALI2 gamma spectrometer, requires determination of the population to different states in ^{32}Ne. The following assumptions were made: (i) 4^+ feeds directly to the 2^+ state in a cascade, (ii) and no feeding from higher unobserved states is present. To compare the ratio to each state to theoretical predictions, the theoretical cross sections are scaled by the inclusive suppression factor and are shown in Fig. 6. The trend of populating the excited states is reproduced by the theoretical calculations and and follows a similar sequence as the 2p-knockout reaction to ^{30}Ne [35], with both displaying a greater 4^+ and smaller 2^+ fraction, while the largest strength feeds directly to the ground state.

In the case of the one-proton knockout reaction ^{9}Be(^{33}Na,^{32}Ne)X, the calculated inclusive cross section, based on the EEdf1 interaction shell model spectroscopic factors, is 11 mb. The experimental inclusive cross section is 4.3(5) mb. Thus, the suppression factor is 0.37(4) and the associated separation-energy asymmetry $\Delta S = S_p - S_n = +18.37$ MeV. This value falls en-

TABLE II. One- and two-proton knockout cross sections (σ) for ^{9}Be(^{33}Na,^{32}Ne)X and ^{9}Be(^{34}Mg,^{32}Ne)X reactions. Spin and parity assignment J^{π}, excitation energy E_x, transition energy E_γ, calculated single-particle cross section σ_{sp} and shell-model spectroscopic factor C^2S for the one-proton knockout reaction, and theoretical and experimental individual cross section, σ^{th} and σ^{exp}, respectively. The inclusive suppression factors are 0.37(4) for the ^{9}Be(^{33}Na,^{32}Ne)X reaction ($\Delta S = +18.37$) and 0.27(3) for the ^{9}Be(^{34}Mg,^{32}Ne)X reaction calculated with the EKK-SDPF interaction.

			^{9}Be(^{33}Na,^{32}Ne)X						^{9}Be(^{34}Mg,^{32}Ne)X		
						EEdf1			EEdf1	SDPF-M	
J^{π}	E_x (kev)	E_γ (kev)	$n\ell_j$	C^2S	σ_{sp} (mb)	σ^{th}_{-1p} (mb)	σ^{th}_{-1p} (mb)	σ^{exp}_{-1p} (mb)	σ^{th}_{-2p} (μb)	σ^{th}_{-2p} (μb)	σ^{exp}_{-2p} (μb)
0			$0d_{3/2}$	0.026	9.53	0.262	0.262	1.4(7)	355	387	97(14)
2	709(12)	709(12)	$1s_{1/2}$	0.010	9.91	0.101	9.563	2.2(6)	17	34.8	24(9)
			$0d_{3/2}$	0.037	9.37	0.367					
			$0d_{5/2}$	0.864	9.89	9.095					
4	2119(19)	1410(15)	$0d_{5/2}$	0.169	9.58	1.721	1.721	0.72(3)	158	241	23(5)
			Inclusive:				11.55	4.3(5)	530	664	144(15)

tirely within, and adds to, the one-nucleon removal trend shown in Fig. 1 of Ref [30]. A further recent experiment, on one-proton removal from ^{30}Ne (for which $\Delta S = +21.0$ MeV), was analysed using similar theoretical methods [56] but with inputs that differ in detail from those used both here and in the systematic analyses of [30]. That analysis reported an R_s value of 0.30, also consistent with the published systematics. The fractional populations of each final state are reasonably well reproduced by the EEdf1 interaction shell model C^{2}S and reaction calculations, as shown in Fig. 6. These support the spin assignments made, with the largest fraction to the 2^+ level. The small theoretical cross section to the $0^+_{g.s.}$ reflects the small occupancy of the proton $0d_{3/2}$ orbital in the ^{33}Na ground state.

Short and collective long range correlations unaccounted for in shell-model calculations have been suggested to contribute to the one-nucleon suppression factor for stable nuclei [57]. Measurements of electron-induced proton knockout reactions for nuclei close to stability have revealed quenching of the spectroscopic strengths on the order of $\approx 30\%$ [57, 58]. Given the intertwined nature of shell-model C^{2}S and reaction formalism (and inputs) to calculate a theoretical cross section, it is not possible to identify a direct contributor to the one-nucleon cross section deviation. However, recent transfer reaction experiments, as a spectroscopic probe, display a weak dependence of the reduction factors and correlations as a function of Fermi surface asymmetry [59–61].

In summary, a new transition of 1410(15) keV was identified in one- and two-proton knockout reactions to ^{32}Ne at 221 MeV u^{-1} and 235 MeV u^{-1} using the DALI2 gamma spectrometer and BigRIPS and ZeroDegree spectrometers. This transition was assigned to the $4^+_1 \rightarrow 2^+_1$ transition based on systematics, excellent agreement with shell model calculations and reaction theory, and the limited expectation of additional bound states. This first $R_{4/2}$ ratio of 2.99(6) indicates a continuation of the trend of increasing collectivity above N > 20 for neon, as well as further evidence to the incorporation of this nuclide within the *island of inversion*. A measurement of inclusive and exclusive cross sections in the two-proton knockout reaction revealed a significant suppression factor R_s, as seen with ^{30}Ne [35]. A similarly reduced suppression factor was measured for the one-proton knockout reaction. Extending spectroscopic investigations to the potential drip line nucleus ^{34}Ne [62, 63], to confirm the merging of the N = 20 and N=28 islands of inversion in neon [64], will be a challenge for future experimental facilities and demands further development in both RI production and gamma detection sensitivity.

ACKNOWLEDGMENTS

The authors wish to express their gratitude to the RIKEN Nishina RIBF accelerator staff and the BigRIPS team for providing the high intensity beams which made this experiment possible. IM acknowledges the support of the RIKEN IPA program and enlightening discussions with Freddy Flavigny. J.A.T. acknowledges the support of Science and Technology Facilities Council (UK) grant ST/L005743/1.

[1] M. G. Mayer, Physical Review **74**, 235 (1948).
[2] O. Haxel, J. H. D. Jensen, and H. E. Suess, Physical Review **75**, 1766 (1949).
[3] O. Sorlin and M.-G. Porquet, Progress in Particle and Nuclear Physics **61**, 602 (2008).
[4] F. Wienholtz, D. Beck, K. Blaum, C. Borgmann, M. Breitenfeldt, R. B. Cakirli, S. George, F. Herfurth, J. Holt, M. Kowalska, *et al.*, Nature **498**, 346 (2013).
[5] C. Hoffman, T. Baumann, D. Bazin, J. Brown, G. Christian, D. H. Denby, P. DeYoung, J. Finck, N. Frank, J. Hinnefeld, *et al.*, Physics Letters B **672**, 17 (2009).
[6] K. Tshoo, Y. Satou, H. Bhang, S. Choi, T. Naka-

mura, Y. Kondo, S. Deguchi, Y. Kawada, N. Kobayashi, Y. Nakayama, *et al.*, Physical review letters **109**, 022501 (2012).

[7] D. Steppenbeck, S. Takeuchi, N. Aoi, P. Doornenbal, M. Matsushita, H. Wang, H. Baba, N. Fukuda, S. Go, M. Honma, *et al.*, Nature **502**, 207 (2013).

[8] B. Bastin, S. Grévy, D. Sohler, O. Sorlin, Z. Dombrádi, N. Achouri, J. Angélique, F. Azaiez, D. Baiborodin, R. Borcea, *et al.*, Physical Review Letters **99**, 022503 (2007).

[9] C. Thibault, R. Klapisch, C. Rigaud, A. Poskanzer, R. Prieels, L. Lessard, and W. Reisdorf, Physical Review C **12**, 644 (1975).

[10] D. Vieira, J. Wouters, K. Vaziri, R. Kraus Jr, H. Wollnik, G. Butler, F. Wohn, and A. Wapstra, Physical review letters **57**, 3253 (1986).

[11] C. Détraz, D. Guillemaud, G. Huber, R. Klapisch, M. Langevin, F. Naulin, C. Thibault, L. Carraz, and F. Touchard, Physical Review C **19**, 164 (1979).

[12] D. Guillemaud-Mueller, C. Detraz, M. Langevin, F. Naulin, M. de Saint-Simon, C. Thibault, F. Touchard, and M. Epherre, Nuclear Physics A **426**, 37 (1984).

[13] T. Motobayashi, Y. Ikeda, K. Ieki, M. Inoue, N. Iwasa, T. Kikuchi, M. Kurokawa, S. Moriya, S. Ogawa, H. Murakami, *et al.*, Physics Letters B **346**, 9 (1995).

[14] B. Pritychenko, T. Glasmacher, P. Cottle, M. Fauerbach, R. Ibbotson, K. Kemper, V. Maddalena, A. Navin, R. Ronningen, A. Sakharuk, *et al.*, Physics Letters B **461**, 322 (1999).

[15] E. Warburton, J. Becker, and B. Brown, Physical Review C **41**, 1147 (1990).

[16] A. Poves and J. Retamosa, Physics Letters B **184**, 311 (1987).

[17] T. Otsuka, R. Fujimoto, Y. Utsuno, B. A. Brown, M. Honma, and T. Mizusaki, Physical Review Letters **87**, 082502 (2001).

[18] T. Otsuka, T. Suzuki, R. Fujimoto, H. Grawe, and Y. Akaishi, Physical Review Letters **95** (2005), 10.1103/physrevlett.95.232502.

[19] P. Doornenbal, H. Scheit, S. Takeuchi, Y. Utsuno, N. Aoi, K. Li, M. Matsushita, D. Steppenbeck, H. Wang, H. Baba, *et al.*, Progress of Theoretical and Experimental Physics **2014**, 053D01 (2014).

[20] A. Obertelli, A. Gillibert, N. Alamanos, M. Alvarez, F. Auger, R. Dayras, A. Drouart, G. De France, B. Jurado, N. Keeley, *et al.*, Physics Letters B **633**, 33 (2006).

[21] J. Terry, D. Bazin, B. Brown, C. Campbell, J. Church, J. Cook, A. Davies, D.-C. Dinca, J. Enders, A. Gade, T. Glasmacher, P. Hansen, J. Lecouey, T. Otsuka, B. Pritychenko, B. Sherrill, J. Tostevin, Y. Utsuno, K. Yoneda, and H. Zwahlen, Physics Letters B **640**, 86 (2006).

[22] N. Kobayashi, T. Nakamura, Y. Kondo, J. Tostevin, N. Aoi, H. Baba, R. Barthelemy, M. Famiano, N. Fukuda, N. Inabe, *et al.*, Physical Review C **93**, 014613 (2016).

[23] T. Nakamura, N. Kobayashi, Y. Kondo, Y. Satou, N. Aoi, H. Baba, S. Deguchi, N. Fukuda, J. Gibelin, N. Inabe, *et al.*, Physical review letters **103**, 262501 (2009).

[24] T. Nakamura, N. Kobayashi, Y. Kondo, Y. Satou, J. Tostevin, Y. Utsuno, N. Aoi, H. Baba, N. Fukuda, J. Gibelin, *et al.*, Physical review letters **112**, 142501 (2014).

[25] P. Doornenbal, H. Scheit, S. Takeuchi, N. Aoi, K. Li, M. Matsushita, D. Steppenbeck, H. Wang, H. Baba, E. Ideguchi, N. Kobayashi, Y. Kondo, J. Lee, S. Michimasa, T. Motobayashi, A. Poves, H. Sakurai, M. Takechi, Y. Togano, and K. Yoneda, Physical Review C **93** (2016), 10.1103/physrevc.93.044306.

[26] Y. Yanagisawa, M. Notani, H. Sakurai, M. Kunibu, H. Akiyoshi, N. Aoi, H. Baba, K. Demichi, N. Fukuda, H. Hasegawa, *et al.*, Physics Letters B **566**, 84 (2003).

[27] P. Doornenbal, H. Scheit, N. Aoi, S. Takeuchi, K. Li, E. Takeshita, H. Wang, H. Baba, S. Deguchi, N. Fukuda, H. Geissel, R. Gernhuser, J. Gibelin, I. Hachiuma, Y. Hara, C. Hinke, N. Inabe, K. Itahashi, S. Itoh, D. Kameda, S. Kanno, Y. Kawada, N. Kobayashi, Y. Kondo, R. Krcken, T. Kubo, T. Kuboki, K. Kusaka, M. Lantz, S. Michimasa, T. Motobayashi, T. Nakamura, T. Nakao, K. Namihira, S. Nishimura, T. Ohnishi, M. Ohtake, N. A. Orr, H. Otsu, K. Ozeki, Y. Satou, S. Shimoura, T. Sumikama, M. Takechi, H. Takeda, K. N. Tanaka, K. Tanaka, Y. Togano, M. Winkler, Y. Yanagisawa, K. Yoneda, A. Yoshida, K. Yoshida, and H. Sakurai, Physical Review Letters **103** (2009), 10.1103/physrevlett.103.032501.

[28] Y. Utsuno, T. Otsuka, T. Mizusaki, and M. Honma, Physical Review C **60** (1999), 10.1103/physrevc.60.054315.

[29] E. Caurier, F. Nowacki, and A. Poves, Nucl. Phys. **A693**, 374 (2001), arXiv:nucl-th/0011010 [nucl-th].

[30] J. Tostevin and A. Gade, Physical Review C **90**, 057602 (2014).

[31] A. Gade, P. Adrich, D. Bazin, M. Bowen, B. Brown, C. Campbell, J. Cook, T. Glasmacher, P. Hansen, K. Hosier, *et al.*, Physical Review C **77**, 044306 (2008).

[32] D. Bazin, B. A. Brown, C. M. Campbell, J. A. Church, D. C. Dinca, J. Enders, A. Gade, T. Glasmacher, P. G. Hansen, W. F. Mueller, H. Olliver, B. C. Perry, B. M. Sherrill, J. R. Terry, and J. A. Tostevin, Physical Review Letters **91** (2003), 10.1103/physrevlett.91.012501.

[33] J. A. Tostevin, G. Podolyák, B. A. Brown, and P. G. Hansen, Physical Review C **70** (2004), 10.1103/physrevc.70.064602.

[34] J. A. Tostevin and B. A. Brown, Physical Review C **74** (2006), 10.1103/physrevc.74.064604.

[35] P. Fallon, E. Rodriguez-Vieitez, A. Macchiavelli, A. Gade, J. Tostevin, P. Adrich, D. Bazin, M. Bowen, C. Campbell, R. Clark, *et al.*, Physical Review C **81**, 041302 (2010).

[36] A. Gade, P. Adrich, D. Bazin, M. D. Bowen, B. A. Brown, C. M. Campbell, J. M. Cook, S. Ettenauer, T. Glasmacher, K. W. Kemper, S. McDaniel, A. Obertelli, T. Otsuka, A. Ratkiewicz, K. Siwek, J. R. Terry, J. A. Tostevin, Y. Utsuno, and D. Weisshaar, Physical Review Letters **99** (2007), 10.1103/physrevlett.99.072502.

[37] T. Kubo, D. Kameda, H. Suzuki, N. Fukuda, H. Takeda, Y. Yanagisawa, M. Ohtake, K. Kusaka, K. Yoshida, N. Inabe, T. Ohnishi, A. Yoshida, K. Tanaka, and Y. Mizoi, Progress of Theoretical and Experimental Physics **2012**, 3C003 (2012).

[38] N. Fukuda, T. Kubo, T. Ohnishi, N. Inabe, H. Takeda, D. Kameda, and H. Suzuki, Nuclear Instruments and Methods in Physics Research Section B: Beam Interactions with Materials and Atoms **317**, 323 (2013).

[39] S. Takeuchi, T. Motobayashi, Y. Togano, M. Matsushita, N. Aoi, K. Demichi, H. Hasegawa, and H. Murakami, Nuclear Instruments and Methods in Physics Research Section A: Accelerators, Spectrometers, Detectors and Associated Equipment **763**, 596 (2014).

[40] S. Agostinelli, J. Allison, K. a. Amako, J. Apostolakis, H. Araujo, P. Arce, M. Asai, D. Axen, S. Banerjee, G. Barrand, *et al.*, Nuclear instruments and methods in physics research section A: Accelerators, Spectrometers, Detectors and Associated Equipment **506**, 250 (2003).
[41] P. M. J. K. Hans Geissel, Christoph Scheidenberger and H. Weick, "Atima - gsi,".
[42] N. Tsunoda, T. Otsuka, N. Shimizu, M. Hjorth-Jensen, K. Takayanagi, and T. Suzuki, Physical Review C **95** (2017), 10.1103/physrevc.95.021304.
[43] W. Huang, G. Audi, M. Wang, F. Kondev, S. Naimi, and X. Xu, Chinese Physics C **41**, 139 (2017).
[44] S. Raman, C. Nestor, and P. Tikkanen, Atomic Data and Nuclear Data Tables **78**, 1 (2001).
[45] M. Basunia and A. Hurst, Nuclear Data Sheets **134**, 1 (2016).
[46] M. Shamsuzzoha Basunia, Nuclear Data Sheets **114** (2013).
[47] M. S. Basunia, Nuclear Data Sheets **111**, 2331 (2010).
[48] N. Nica and B. Singh, Nuclear Data Sheets **113**, 1563 (2012).
[49] P. Doornenbal, H. Scheit, S. Takeuchi, N. Aoi, K. Li, M. Matsushita, D. Steppenbeck, H. Wang, H. Baba, H. Crawford, C. R. Hoffman, R. Hughes, E. Ideguchi, N. Kobayashi, Y. Kondo, J. Lee, S. Michimasa, T. Motobayashi, H. Sakurai, M. Takechi, Y. Togano, R. Winkler, and K. Yoneda, Physical Review Letters **111** (2013), 10.1103/physrevlett.111.212502.
[50] N. Nica, J. Cameron, and B. Singh, Nuclear Data Sheets **113**, 1 (2012).
[51] S. Takeuchi, M. Matsushita, N. Aoi, P. Doornenbal, K. Li, T. Motobayashi, H. Scheit, D. Steppenbeck, H. Wang, H. Baba, *et al.*, Physical review letters **109**, 182501 (2012).
[52] J. Tostevin, Nuclear Physics A **682**, 320 (2001).
[53] P. Hansen and J. Tostevin, Annual Review of Nuclear and Particle Science **53**, 219 (2003).
[54] D. Bazin, R. J. Charity, R. De Souza, M. A. Famiano, A. Gade, V. Henzl, D. Henzlová, S. Hudan, J. Lee, S. Lukyanov, *et al.*, Physical review letters **102**, 232501 (2009).
[55] K. Wimmer, D. Bazin, A. Gade, J. Tostevin, T. Baugher, Z. Chajecki, D. Coupland, M. Famiano, T. Ghosh, G. Grinyer, *et al.*, Physical Review C **90**, 064615 (2014).
[56] J. Lee, H. Liu, P. Doornenbal, M. Kimura, K. Minomo, K. Ogata, Y. Utsuno, N. Aoi, K. Li, M. Matsushita, *et al.*, Progress of Theoretical and Experimental Physics **2016** (2016).
[57] W. Dickhoff and C. Barbieri, Progress in Particle and Nuclear Physics **52**, 377 (2004).
[58] V. R. Pandharipande, I. Sick, and P. K. deWitt Huberts, Reviews of Modern Physics **69**, 981 (1997).
[59] J. Lee, M. Tsang, D. Bazin, D. Coupland, V. Henzl, D. Henzlová, M. Kilburn, W. G. Lynch, A. M. Rogers, A. Sanetullaev, *et al.*, Physical review letters **104**, 112701 (2010).
[60] J. Lee, M. Tsang, D. Bazin, D. Coupland, V. Henzl, D. Henzlová, M. Kilburn, W. G. Lynch, A. M. Rogers, A. Sanetullaev, *et al.*, Physical Review C **83**, 014606 (2011).
[61] F. Flavigny, A. Gillibert, L. Nalpas, A. Obertelli, N. Keeley, C. Barbieri, D. Beaumel, S. Boissinot, G. Burgunder, A. Cipollone, *et al.*, Physical review letters **110**, 122503 (2013).
[62] M. Notani, H. Sakurai, N. a. Aoi, Y. Yanagisawa, A. Saito, N. Imai, T. Gomi, M. Miura, S. Michimasa, H. Iwasaki, *et al.*, Physics Letters B **542**, 49 (2002).
[63] S. Lukyanov, Y. E. Penionzhkevich, R. Astabatyan, S. Lobastov, Y. Sobolev, D. Guillemaud-Mueller, G. Faivre, F. Ibrahim, A. Mueller, F. Pougheon, *et al.*, Journal of Physics G: Nuclear and Particle Physics **28**, L41 (2002).
[64] E. Caurier, F. Nowacki, and A. Poves, Physical Review C **90**, 014302 (2014).

Appendix E

Résumé en français

E.1 Introduction

La nature du noyau atomique en tant que système quantique à corps multiples conduit à *lémergence* de propriétés microscopiques. Une de ces propriétés, lobservation des *nombres dits magiques* (8, 20, 28, 50...) des nucléons (section X) a permis le développement du modèle de coquille de particules indépendantes du noyau. Cette thèse sintéresse à lévolution de cette compréhension du système nucléaire, à travers létude des isotopes du rapport neutron/proton asymétrique. La modification du remplissage des orbites de protons ou de neutrons a été réalisée afin de mettre laccent sur les composantes des forces entre les nucléons, se manifestant par la dissolution des *nombres magiques* canoniques et la précipitation de nouveaux nombres (section 1.1.3).

Les isotopes exotiques riches en neutrons du néon ($^{32}_{10}$Ne) et de laluminium ($^{(39-41)}_{13}$Al) ont été étudiés dans deux expérimentations différentes pour mieux comprendre cette évolution autour de deux régions du paysage nucléaire avec des changements drastiques des nombres magiques aux nombres de neutrons $N = 20, 28$. Cez zones correspondent à ce quon appelle *lîlot dinversion* (section 1.1.5) et les isotones riches en neutrons aux alentours de $N = 28$ près de la ligne dégouttement des neutrons, et les deux zones peuvent être décrites ensemble comme une grande zone de déformation [8]. On a observé que ces zones présentent des propriétés distinctes des noyaux stables, avec *lémergence* de déformations collectives et l'érosion des interstices sphériques de la coquille, connus sous le nom de *nombres magiques*. Contribuer à la compréhension de ces régions fournit des points de repère pour le développement et l'extension des travaux théoriques actuels et futurs.

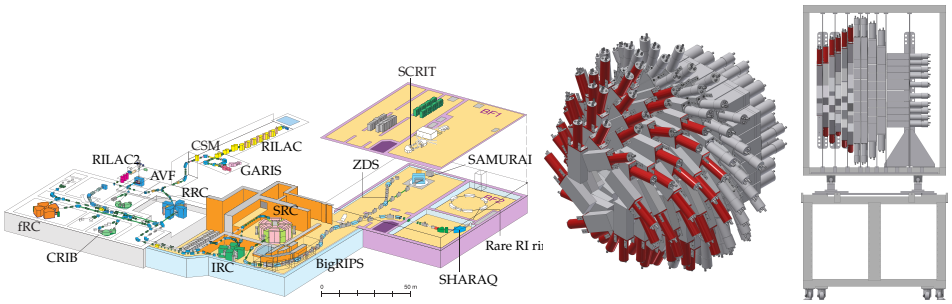

(A) RIKEN RIBF center overview [121] (B) DALI2 (C) DALI2

FIGURE E.1: Dispositif expérimental

E.2 Dispositif expérimental

La technique expérimentale de spectroscopie gamma dans le faisceau (section 1.3) est utilisée pour interroger les structures nucléaires excitées de $^{32}_{10}$Ne et de $^{(39-41)}_{13}$Al produites par des réactions directes de nucléon (section 1.2) à des vitesses relativistes (environ 60% de la vitesse de la lumière). Les réactions ont éliminé un ou deux protons ou un neutron d'ions projectiles pour peupler les états excités des isotopes d'intérêt. Les faisceaux d'ions radioactifs (section 1.4) ont été produits dans l'établissement de classe mondiale, RIKEN (section XXX) pour la réalisation des expérimentations, voir Fig. E.1. Le séparateur BigRIPS et le spectromètre ZeroDegree du Nishina Center Radioactive Isotope Beam Factory (RIBF) ont permis d'isoler le type de réaction.

Le dépeuplement des états excités par l'émission de rayons gamma a permis de mesurer l'énergie des rayons gamma émis, par des détecteurs entourant la cible de réaction. Le réseau de détecteurs de RIKEN, DALI2 (section 2.5), a été utilisé pour observer ces signatures caractéristiques inconnues, comme le montre la Fig. E.1. DALI2 est composé de 186 détecteurs de NaI.

De plus, le comptage du nombre de réactions et d'ions incidents fournit les sections transversales de réaction inclusives et, combinées avec DALI2, les sections transversales de réaction knockout exclusives.

E.3 Résultats et interprétation

E.4 $^{32}_{12}$Ne

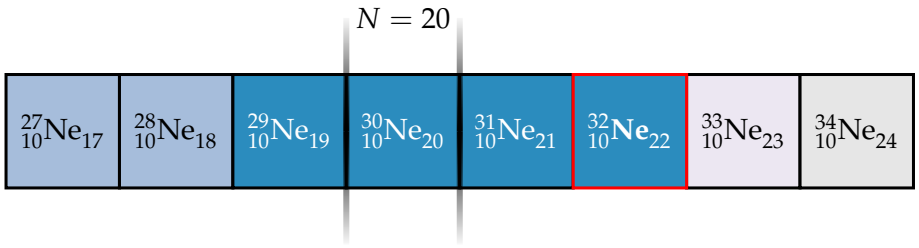

Le spectre d'énergie gamma reconstruit pour les réactions d'élimination d'un et de deux protons à $^{32}_{12}$Ne a révélé une nouvelle transition à 1410(15) keV. Cette transition a été provisoirement assignée à $4^+_1 \rightarrow 2^+_1$. L'énergie de transition est en bon accord avec les calculs du modèle d'enveloppe avec deux interactions SDPF-M et EEdf1. L'énergie de la transition précédemment identifiée $2^+_1 \rightarrow 0^+_{g.s.}$ permet le calcul du rapport $R_{4/2}$ des deux énergies. La valeur élevée de 2,99(6) près de la limite rigide du rotor de 3,33 suggère un degré élevé de déformation et donc le placement de cet isotope dans *l'îlot d'inversion*. Ce résultat est presque 20 ans après la mise en évidence de cet isotope comme faisant partie de *l'îlot d'inversion* comme le montre la Fig. 1.7 [49].

En outre, l'extension de la tendance systématique des facteurs de réduction inclusifs et exclusifs à un et deux nucléons a été rendue possible par le calcul du rapport entre les sections transversales expérimentales et théoriques de la réaction. Les coupes transversales théoriques ont été produites par un modèle de coque et des calculs dynamiques de réaction eikonale. L'extension des facteurs de réduction contribue au développement de prédictions pour les noyaux avec une grande asymétrie dans l'énergie de séparation des nucléons. De plus, une bonne concordance des sections transversales théoriques et expérimentales exclusives à 4^+_1 and 2^+_1 états excités fournit des preuves supplémentaires pour la rotation et l'assignation de parité de la nouvelle transition.

E.5 $^{(39-41)}_{13}$Al

L'étude des isotopes de l'aluminium $^{(39,40,41)}$Al par spectroscopie gamma en faisceau a permis l'extension du schéma de niveau $^{39}_{13}$Al et le premier développement de schémas de niveau provisoire en $^{(40,41)}_{13}$Al. Ceci a été accompli par l'observation des transitions dans les spectres d'énergie gamma reconstruits. De plus, les coïncidences entre les rayons gamma observés fournissent des preuves pour les cascades provisoirement assignées dans les schémas de niveaux.

Les observations expérimentales sont en ligne avec les prédictions des calculs du modèle de coque avec l'interaction efficace SDPF-MU et avec les observables électromagnétiques minimaux, les spins et les parités pourraient être suggérés pour plusieurs niveaux. La chute soudaine dans le premier état excité de ^{41}Al a été confirmée et prédit par les calculs SDPF-MU, ce qui contribue à vérifier la robustesse de cette interaction pour prévoir les noyaux exotiques près de $N \approx 28$. L'application d'un simple modèle de rotor de particules pour suggérer une bande de rotation construite sur l'orbite intrinsèque de $5/2^+[202]$ Nilsson correspond aux calculs du modèle de coque et a été appliquée pour prédire l'énergie $E(2_1^+)$ dans les isotopes de magnésium voisins. Une bonne reproductibilité avec les observations disponibles a été trouvée à travers les chaînes isotopiques du magnésium et de l'aluminium. De plus, les niveaux expérimentaux 802(4) keV ($^{35}_{13}$Al) et 775(4) keV ($^{37}_{13}$Al) ne sont pas

assignés à la rotation et à la parité mais s'inscrivent dans la tendance systématique. En s'étendant jusqu'à $^{40}_{12}$Mg, le faible niveau d'énergie $E(2_1^+)$ autour de 850 keV suggère la disparition continue de la magie pour les isotones riches en neutrons $N = 28$. De plus, l'assignation provisoire de l'état du sol de $^{41}_{13}$Al, basée sur l'accord avec les calculs du modèle d'enveloppe et l'application du modèle du rotor de particules, suggère de prolonger la déformation dans l'état du sol de $^{41}_{13}$Al. La compétition de formes prolates et oblates d'énergie de configuration similaire donne lieu à un désaccord avec les prédictions théoriques de l'état de base.

E.6 Conclusion

Dans le cas de l'expérience de $^{32}_{12}$Ne, l'extension future du noyau potentiel de $^{34}_{12}$Ne [224, 225] peut confirmer la fusion des îlots de déformation du néon $N = 20$ et $N = 28$, comme prévu par les calculs du modèle de coque [8]. La délimitation de la ligne d'égouttement des neutrons dans le néon n'est pas connue expérimentalement.

Une étude plus poussée du $^{(39,41)}_{13}$Al, riche en neutrons, est justifiée pour exposer la coexistence possible de formes à faible énergie. Le placement de $^{41}_{13}$Al entre l'oblate et le prolate, même le silicium et le magnésium peuvent se manifester sous forme de phénomènes d'excitation. Les travaux théoriques futurs pourraient se concentrer sur l'identification d'autres bandes de rotation de faible élévation (comme $K = 1/2^+$ ou $K = 3/2^+$) qui devraient apparaître dans $^{(39,41)}_{13}$Al. D'autres éléments observables résultant de statistiques accrues, par exemple, les nouvelles transitions d'observation, les rapports de mélange M1/E2 déduits, les sections transversales exclusives et l'assignation de rotation et de parité (par exemple, par le biais de distributions de momentum de nucléon knockout), seront des orientations futures nécessaires pour révéler une structure nucléaire plus détaillée.

Pour atteindre ces nouvelles frontières, il faudrait développer et appliquer de nouvelles technologies. En même temps, pendant que de nouvelles installations sont mises à niveau et construites, il faudrait améliorer aussi la sensibilité des détecteurs. A cette fin, le nouveau scintillateur monocristallin inorganique GAGG(Ce) a été étudié et une amélioration importante de la résolution énergétique a été observée. La simulation des scintillateurs GAGG(Ce) dans le cadre d'un réseau de détecteurs de nouvelle génération, potentiellement un futur DALI3, s'est révélée prometteuse. Un bref rapport est présenté à l'annexe C.

Bibliography

[1] Steven Weinberg. *Dreams of a Final Theory*. Vintage, 1994. ISBN: 978-0679744085.

[2] R. B. Laughlin and D. Pines. "The Theory of Everything". In: *Proceedings of the National Academy of Sciences* 97.1 (2000), pp. 28–31. DOI: 10.1073/pnas.97.1.28.

[3] P. W. Anderson. "More Is Different". In: *Science* 177.4047 (1972), pp. 393–396. DOI: 10.1126/science.177.4047.393.

[4] Mark A. Bedau and Paul Humphreys, eds. *Emergence*. The MIT Press, 2008. DOI: 10.7551/mitpress/9780262026215.001.0001.

[5] Ernest Rutherford. "The scattering of α and β particles by matter and the structure of the atom". In: *The London, Edinburgh, and Dublin Philosophical Magazine and Journal of Science* 21.125 (1911), pp. 669–688.

[6] L. P. Gaffney et al. "Studies of pear-shaped nuclei using accelerated radioactive beams". In: *Nature* 497.7448 (2013), pp. 199–204. DOI: 10.1038/nature12073.

[7] Aage Niels Bohr and Benjamin Roy Mottelson. "Collective and individual-particle aspects of nuclear structure". In: *Dan. mat. fys. Medd.* 27.CERN-57-38 (1953), pp. 1–174.

[8] Etienne Caurier, Frederic Nowacki, and Alfredo Poves. "Merging of the islands of inversion at N= 20 and N= 28". In: *Physical Review C* 90.1 (2014), p. 014302.

[9] C. F. v. Weizsäcker. "Zur Theorie der Kernmassen". In: *Zeitschrift für Physik* 96.7-8 (1935), pp. 431–458. DOI: 10.1007/bf01337700.

[10] Hans Albrecht Bethe and Robert Fox Bacher. "Nuclear physics A. Stationary states of nuclei". In: *Reviews of Modern Physics* 8.2 (1936), p. 82.

[11] William D. Myers and Wladyslaw J. Swiatecki. "Nuclear masses and deformations". In: *Nuclear Physics* 81.1 (1966), pp. 1–60. DOI: 10.1016/0029-5582(66)90639-0.

[12] P. Möller et al. “Nuclear mass formula with a finite-range droplet model and a folded-Yukawa single-particle potential”. In: *Atomic Data and Nuclear Data Tables* 39.2 (1988), pp. 225–233. DOI: 10.1016/0092-640x(88)90023-x.

[13] C. Samanta and S. Adhikari. “Extension of the Bethe-Weizsäcker mass formula to light nuclei and some new shell closures”. In: *Physical Review C* 65.3 (2002). DOI: 10.1103/physrevc.65.037301.

[14] Michael W. Kirson. “Mutual influence of terms in a semi-empirical mass formula”. In: *Nuclear Physics A* 798.1-2 (2008), pp. 29–60. DOI: 10.1016/j.nuclphysa.2007.10.011.

[15] G. Royer. “On the coefficients of the liquid drop model mass formulae and nuclear radii”. In: *Nuclear Physics A* 807.3-4 (2008), pp. 105–118. DOI: 10.1016/j.nuclphysa.2008.04.002.

[16] Byeongnoh Kim and Dongwoo Cha. “On the Mass Number Dependence of the Semi-empirical Mass Formula”. In: *Journal of the Korean Physical Society* 56.5 (2010), pp. 1546–1549.

[17] W. Elsasser. In: *J. de Phys. et le Rad.* 5.625 (1934).

[18] Maria G Mayer. “On closed shells in nuclei”. In: *Physical Review* 74.3 (1948), p. 235.

[19] Otto Haxel, J Hans D Jensen, and Hans E Suess. “On the" magic numbers" in nuclear structure”. In: *Physical Review* 75.11 (1949), p. 1766.

[20] Jouni Suhonen. *From Nucleons to Nucleus: Concepts of Microscopic Nuclear Theory*. Springer Science & Business Media, 2007.

[21] O Sorlin and M-G Porquet. “Nuclear magic numbers: New features far from stability”. In: *Progress in Particle and Nuclear Physics* 61.2 (2008), pp. 602–673.

[22] F Wienholtz et al. “Masses of exotic calcium isotopes pin down nuclear forces”. In: *Nature* 498.7454 (2013), pp. 346–349.

[23] CR Hoffman et al. “Evidence for a doubly magic 24 O”. In: *Physics Letters B* 672.1 (2009), pp. 17–21.

[24] K Tshoo et al. “N= 16 Spherical Shell Closure in O 24”. In: *Physical review letters* 109.2 (2012), p. 022501.

[25] David Steppenbeck et al. “Evidence for a new nuclear magic number from the level structure of 54Ca”. In: *Nature* 502.7470 (2013), pp. 207–210.

[26] B Bastin et al. "Collapse of the N= 28 Shell Closure in Si 42". In: *Physical Review Letters* 99.2 (2007), p. 022503.

[27] W.J. Huang et al. "The AME2016 atomic mass evaluation". In: *Chinese Physics C* 41.3 (2017), pp. 139–480.

[28] J. P. Elliott and A. M. Lane. "Evidence for Two-Body Spin-Orbit Forces in Nuclei". In: *Physical Review* 96.4 (1954), pp. 1160–1162. DOI: 10.1103/physrev.96.1160.

[29] I Talmi and I Unna. "Order of Levels in the Shell Model and Spin of Be 11". In: *Physical Review Letters* 4.9 (1960), p. 469.

[30] Steven C. Pieper and V. R. Pandharipande. "Origins of spin-orbit splitting inN15". In: *Physical Review Letters* 70.17 (1993), pp. 2541–2544. DOI: 10.1103/physrevlett.70.2541.

[31] Jason D Holt et al. "Three-body forces and shell structure in calcium isotopes". In: *Journal of Physics G: Nuclear and Particle Physics* 39.8 (2012), p. 085111. DOI: 10.1088/0954-3899/39/8/085111.

[32] K. Sieja and F. Nowacki. "Three-body forces and persistence of spin-orbit shell gaps in medium-mass nuclei: Toward the doubly magic78Ni". In: *Physical Review C* 85.5 (2012). DOI: 10.1103/physrevc.85.051301.

[33] Marianne Dufour and Andrés P. Zuker. "Realistic collective nuclear Hamiltonian". In: *Physical Review C* 54.4 (1996), pp. 1641–1660. DOI: 10.1103/physrevc.54.1641.

[34] E. Caurier et al. "The shell model as a unified view of nuclear structure". In: *Reviews of Modern Physics* 77.2 (2005), pp. 427–488. DOI: 10.1103/revmodphys.77.427.

[35] A. Poves and A. Zuker. "Theoretical spectroscopy and the fp shell". In: *Physics Reports* 70.4 (1981), pp. 235–314. DOI: 10.1016/0370-1573(81)90153-8.

[36] Yutaka Utsuno et al. "Varying shell gap and deformation inN∼20unstable nuclei studied by the Monte Carlo shell model". In: *Physical Review C* 60.5 (1999). DOI: 10.1103/physrevc.60.054315.

[37] N. A. Smirnova et al. "Nuclear shell evolution and in-mediumNNinteraction". In: *Physical Review C* 86.3 (2012). DOI: 10.1103/physrevc.86.034314.

[38] Takaharu Otsuka et al. “Magic numbers in exotic nuclei and spin-isospin properties of the NN interaction”. In: *Physical Review Letters* 87.8 (2001), p. 082502.

[39] Takaharu Otsuka et al. “Evolution of Nuclear Shells due to the Tensor Force”. In: *Physical Review Letters* 95.23 (2005). DOI: 10.1103/physrevlett.95.232502.

[40] Takaharu Otsuka, Toshiaki Matsuo, and Daisuke Abe. “Mean Field with Tensor Force and Shell Structure of Exotic Nuclei”. In: *Physical Review Letters* 97.16 (2006). DOI: 10.1103/physrevlett.97.162501.

[41] Takaharu Otsuka et al. “Novel Features of Nuclear Forces and Shell Evolution in Exotic Nuclei”. In: *Physical Review Letters* 104.1 (2010). DOI: 10.1103/physrevlett.104.012501.

[42] T. Duguet and G. Hagen. “Ab initioapproach to effective single-particle energies in doubly closed shell nuclei”. In: *Physical Review C* 85.3 (2012). DOI: 10.1103/physrevc.85.034330.

[43] Naofumi Tsunoda et al. “Exotic neutron-rich medium-mass nuclei with realistic nuclear forces”. In: *Physical Review C* 95.2 (2017). DOI: 10.1103/physrevc.95.021304.

[44] K. Heyde et al. “A shell-model description of 0+ intruder states in even-even nuclei”. In: *Nuclear Physics A* 466.2 (1987), pp. 189–226. DOI: 10.1016/0375-9474(87)90439-8.

[45] James Rainwater. “Nuclear energy level argument for a spheroidal nuclear model”. In: *Physical Review* 79.3 (1950), p. 432.

[46] A Bohr. “A. Bohr, Mat. Fys. Medd. K. Dan. Vidensk. Selsk. 26, 14 (1952).” In: *Mat. Fys. Medd. K. Dan. Vidensk. Selsk.* 26 (1952), p. 14.

[47] Aage Bohr and Ben R Mottelson. *Nuclear structure, vol. II*. 1975.

[48] Sven G Nilsson. “SG Nilsson, Mat. Fys. Medd. K. Dan. Vidensk. Selsk. 29, 16 (1955).” In: *Mat. Fys. Medd. K. Dan. Vidensk. Selsk.* 29 (1955), p. 16.

[49] EK Warburton, JA Becker, and BA Brown. “Mass systematics for A=29-44 nuclei: The deformed A=32 region”. In: *Physical Review C* 41.3 (1990), p. 1147.

[50] C Thibault et al. “Direct measurement of the masses of Li 11 and Na 2 6- 3 2 with an on-line mass spectrometer”. In: *Physical Review C* 12.2 (1975), p. 644.

[51] DJ Vieira et al. "Direct mass measurements of neutron-rich light nuclei near N= 20". In: *Physical review letters* 57.26 (1986), p. 3253.

[52] C Détraz et al. "Beta decay of Na27-32 and their descendants". In: *Physical Review C* 19.1 (1979), p. 164.

[53] D Guillemaud-Mueller et al. "β-decay schemes of very neutron-rich sodium isotopes and their descendants". In: *Nuclear Physics A* 426.1 (1984), pp. 37–76.

[54] T Motobayashi et al. "Large deformation of the very neutron-rich nucleus 32 Mg from intermediate-energy Coulomb excitation". In: *Physics Letters B* 346.1 (1995), pp. 9–14.

[55] BV Pritychenko et al. "Role of intruder configurations in 26, 28Ne and 30, 32Mg". In: *Physics Letters B* 461.4 (1999), pp. 322–328.

[56] A Poves and J Retamosa. "The onset of deformation at the N= 20 neutron shell closure far from stability". In: *Physics Letters B* 184.4 (1987), pp. 311–315.

[57] M. Stanoiu et al. "N=14and 16 shell gaps in neutron-rich oxygen isotopes". In: *Physical Review C* 69.3 (2004). DOI: 10.1103/physrevc.69.034312.

[58] R. Kanungo et al. "One-Neutron Removal Measurement RevealsO24as a New Doubly Magic Nucleus". In: *Physical Review Letters* 102.15 (2009). DOI: 10.1103/physrevlett.102.152501.

[59] C. R. Hoffman et al. "Determination of the N=16 Shell Closure at the Oxygen Drip Line". In: *Physical Review Letters* 100.15 (2008). DOI: 10.1103/physrevlett.100.152502.

[60] P Doornenbal et al. "Rotational level structure of sodium isotopes inside the island of inversion". In: *Progress of Theoretical and Experimental Physics* 2014.5 (2014), p. 053D01.

[61] Y. Uozumi et al. "Shell-model study ofCa40with the 56-MeV (d→,p) reaction". In: *Physical Review C* 50.1 (1994), pp. 263–274. DOI: 10.1103/physrevc.50.263.

[62] Y. Uozumi et al. "Single-particle strengths measured with 48Ca(, p)49Ca reaction at 56 MeV". In: *Nuclear Physics A* 576.1 (1994), pp. 123–137. DOI: 10.1016/0375-9474(94)90740-4.

[63] L. Gaudefroy et al. "Reduction of the Spin-Orbit Splittings at the N=28 Shell Closure". In: *Physical Review Letters* 97.9 (2006). DOI: 10.1103/physrevlett.97.092501.

[64] T. Glasmacher et al. "Collectivity in 44S". In: *Physics Letters B* 395.3-4 (1997), pp. 163–168. DOI: 10.1016/s0370-2693(97)00077-4.

[65] S. Grévy et al. "Observation of the 02+ state in 44S". In: *The 4th International Conference on Exotic Nuclei and Atomic Masses*. Springer Berlin Heidelberg, 2005, pp. 111–113. DOI: 10.1007/3-540-37642-9_32.

[66] R. W. Ibbotson et al. "Quadrupole Collectivity in 32,34,36,38Si and the N=20 Shell Closure". In: *Physical Review Letters* 80.10 (1998), pp. 2081–2084. DOI: 10.1103/physrevlett.80.2081.

[67] P. Doll et al. "The quasihole aspect of hole strength distributions in odd potassium and calcium isotopes". In: *Nuclear Physics A* 263.2 (1976), pp. 210–236. DOI: 10.1016/0375-9474(76)90169-x.

[68] C. E. Thorn et al. "S36(d,p)S37 and S34,36(d,He3)P33,35 reactions". In: *Physical Review C* 30.5 (1984), pp. 1442–1453. DOI: 10.1103/physrevc.30.1442.

[69] A. Gade et al. "Evolution of the $E(1/2)$-$E(3/2)$ energy spacing in odd-mass K, Cl, and P isotopes for N=20-28". In: *Physical Review C* 74.3 (2006). DOI: 10.1103/physrevc.74.034322.

[70] L. Gaudefroy. "Shell model study of N=28 neutron-rich nuclei". In: *Physical Review C* 81.6 (2010). DOI: 10.1103/physrevc.81.064329.

[71] J. P. Elliott. "Collective Motion in the Nuclear Shell Model. I. Classification Schemes for States of Mixed Configurations". In: *Proceedings of the Royal Society A: Mathematical, Physical and Engineering Sciences* 245.1240 (1958), pp. 128–145. DOI: 10.1098/rspa.1958.0072.

[72] A. P. Zuker et al. "Spherical shell model description of rotational motion". In: *Physical Review C* 52.4 (1995), R1741–R1745. DOI: 10.1103/physrevc.52.r1741.

[73] P.-G. Reinhard and E.W. Otten. "Transition to deformed shapes as a nuclear Jahn-Teller effect". In: *Nuclear Physics A* 420.2 (1984), pp. 173–192. DOI: 10.1016/0375-9474(84)90437-8.

[74] G. A. Lalazissis et al. "Relativistic Hartree + Bogoliubov description of the deformedN=28region". In: *Physical Review C* 60.1 (1999). DOI: 10.1103/physrevc.60.014310.

[75] S Péru, M Girod, and JF Berger. "Evolution of the N= 20 and N= 28 shell closures in neutron-rich nuclei". In: *The European Physical Journal A-Hadrons and Nuclei* 9.1 (2000), pp. 35–47.

[76] R. Rodríguez-Guzmán, J. Egido, and L. Robledo. "Quadrupole collectivity in N≈28 nuclei with the angular momentum projected generator coordinate method". In: *Physical Review C* 65.2 (2002). DOI: 10.1103/physrevc.65.024304.

[77] J. Fridmann et al. "'Magic' nucleus 42Si". In: *Nature* 435.7044 (2005), pp. 922–924. DOI: 10.1038/nature03619.

[78] Satoshi Takeuchi et al. "Well Developed Deformation in Si 42". In: *Physical review letters* 109.18 (2012), p. 182501.

[79] H. L. Crawford et al. "Shell and shape evolution at N=28: The Mg40 ground state". In: *Physical Review C* 89.4 (2014). DOI: 10.1103/physrevc.89.041303.

[80] T. Baumann et al. "Discovery of 40Mg and 42Al suggests neutron drip-line slant towards heavier isotopes". In: *Nature* 449.7165 (2007), pp. 1022–1024. DOI: 10.1038/nature06213.

[81] Alexandra Gade and Jeffrey Tostevin. "Knockout Reactions". In: *Nuclear Physics News* 20.1 (2010), pp. 11–16. DOI: 10.1080/10506890903178889.

[82] Carlos A. Bertulani. *Nuclear Reactions*. Ed. by WileyVCH Verlag GmbH & Co. KGaA. 2014. DOI: https://doi.org/10.1002/9783527600434.eap277.pub3.

[83] K Wimmer. "Nucleon transfer reactions with radioactive beams". In: *Journal of Physics G: Nuclear and Particle Physics* 45.3 (2018), p. 033002. DOI: 10.1088/1361-6471/aaa2bf.

[84] P.G. Hansen and J.A. Tostevin. "Direct Reactions with Exotic Nuclei". In: *Annual Review of Nuclear and Particle Science* 53.1 (2003), pp. 219–261. DOI: 10.1146/annurev.nucl.53.041002.110406.

[85] Max Born. "Quantenmechanik der Stossvorgange". In: *Zeitschrift fur Physik* 38.11-12 (1926), pp. 803–827. DOI: 10.1007/bf01397184.

[86] Robert Hofstadter. "Electron Scattering and Nuclear Structure". In: *Reviews of Modern Physics* 28.3 (1956), pp. 214–254. DOI: 10.1103/revmodphys.28.214.

[87] T W Donnelly and J D Walecka. "Electron Scattering and Nuclear Structure". In: *Annual Review of Nuclear Science* 25.1 (1975), pp. 329–405. DOI: 10.1146/annurev.ns.25.120175.001553.

[88] Vijay R Pandharipande, Ingo Sick, and Peter KA deWitt Huberts. "Independent particle motion and correlations in fermion systems". In: *Reviews of Modern Physics* 69.3 (1997), p. 981.

[89] J. A. Tostevin et al. "Correlated two-nucleon stripping reactions". In: *Physical Review C* 70.6 (2004). DOI: 10.1103/physrevc.70.064602.

[90] N Kobayashi et al. "Observation of a p-Wave One-Neutron Halo Configuration in Mg 37". In: *Physical review letters* 112.24 (2014), p. 242501.

[91] Takashi Nakamura et al. "Deformation-Driven p-Wave Halos at the Drip Line: Ne 31". In: *Physical review letters* 112.14 (2014), p. 142501.

[92] D. Bazin et al. "New Direct Reaction: Two-Proton Knockout from Neutron-Rich Nuclei". In: *Physical Review Letters* 91.1 (2003). DOI: 10.1103/physrevlett.91.012501.

[93] J. A. Tostevin and B. A. Brown. "Diffraction dissociation contributions to two-nucleon knockout reactions and the suppression of shell-model strength". In: *Physical Review C* 74.6 (2006). DOI: 10.1103/physrevc.74.064604.

[94] JA Tostevin and A Gade. "Systematics of intermediate-energy single-nucleon removal cross sections". In: *Physical Review C* 90.5 (2014), p. 057602.

[95] Pieter Doornenbal. "In-beam gamma-ray spectroscopy at the RIBF". In: *Progress of Theoretical and Experimental Physics* 2012.1 (2012).

[96] Gordon Gilmore. *Practical gamma-ray spectroscopy*. John Wiley & Sons, 2011.

[97] Carl Eugene Crouthamel, Freddy Adams, and Richard Dams. *Applied gamma-ray spectrometry*. Vol. 41. Elsevier, 2013.

[98] H Geissel, G Munzenberg, and K Riisager. "Secondary exotic nuclear beams". In: *Annual Review of Nuclear and Particle Science* 45.1 (1995), pp. 163–203.

[99] T. Nakamura, H. Sakurai, and H. Watanabe. "Exotic nuclei explored at in-flight separators". In: *Progress in Particle and Nuclear Physics* 97 (2017), pp. 53–122. DOI: 10.1016/j.ppnp.2017.05.001.

[100] David Gareth Jenkins. "Recent advances in nuclear physics through on-line isotope separation". In: *Nature Physics* 10.12 (2014), pp. 909–913. DOI: 10.1038/nphys3165.

[101] T. Kubo et al. "The RIKEN radioactive beam facility". In: *Nuclear Instruments and Methods in Physics Research Section B: Beam Interactions with Materials and Atoms* 70.1-4 (1992), pp. 309–319. DOI: 10.1016/0168-583x(92)95947-p.

[102] M. Buenerd et al. "Similarity of Cross Sections for Peripheral Collisions at 20 MeV/Aand 2.1 GeV/A". In: *Physical Review Letters* 37.18 (1976), pp. 1191–1194. DOI: 10.1103/physrevlett.37.1191.

[103] Y. P. Viyogi et al. "Fragmentations of 40Ar at 213 MeV/Nucleon". In: *Physical Review Letters* 42.1 (1979), pp. 33–36. DOI: 10.1103/physrevlett.42.33.

[104] G. D. Westfall et al. "Production of Neutron-Rich Nuclides by Fragmentation of 212-MeV/amuCa48". In: *Physical Review Letters* 43.25 (1979), pp. 1859–1862. DOI: 10.1103/physrevlett.43.1859.

[105] DJ Morrissey et al. "Microscopic and macroscopic model calculations of relativistic heavy-ion fragmentation reactions". In: *Physical Review Letters* 43.16 (1979), p. 1139.

[106] BM Young et al. "Strong isomer production in fragmentation reactions". In: *Physics Letters B* 311.1-4 (1993), pp. 22–26.

[107] A.S. Goldhaber. "Statistical models of fragmentation processes". In: *Physics Letters B* 53.4 (1974), pp. 306–308. DOI: 10.1016/0370-2693(74)90388-8.

[108] H Geissel et al. "Ions penetrating through ion-optical systems and matter-Non-liouvillian phase-space modelling". In: *Nuclear Instruments and Methods in Physics Research Section A: Accelerators, Spectrometers, Detectors and Associated Equipment* 282.1 (1989), pp. 247–260.

[109] Klaus Sümmerer. "Improved empirical parametrization of fragmentation cross sections". In: *Physical Review C* 86.1 (2012), p. 014601.

[110] B Mei. "Improved empirical parameterization for projectile fragmentation cross sections". In: *Physical Review C* 95.3 (2017), p. 034608.

[111] N. Metropolis et al. "Monte Carlo Calculations on Intranuclear Cascades. II. High-Energy Studies and Pion Processes". In: *Physical Review* 110.1 (1958), pp. 204–219. DOI: 10.1103/physrev.110.204.

[112] Y. Yariv and Z. Fraenkel. "Intranuclear cascade calculation of high-energy heavy-ion interactions". In: *Physical Review C* 20.6 (1979), pp. 2227–2243. DOI: 10.1103/physrevc.20.2227.

[113] K. Sümmerer et al. "Charge-pickup processes in relativistic heavy-ion reactions". In: *Physical Review C* 52.2 (1995), pp. 1106–1109. DOI: 10.1103/physrevc.52.1106.

[114] B. K. Srivastava et al. "Comparison of the 1AGeV 197Au+C interaction with first-stage transport codes". In: *Physical Review C* 60.6 (1999). DOI: 10.1103/physrevc.60.064606.

[115] A. Stolz et al. "Projectile fragmentation of112SnatElab=1A GeV". In: *Physical Review C* 65.6 (2002). DOI: 10.1103/physrevc.65.064603.

[116] W.J. Swiatecki J.D. Bowman and C.E. Tsang. *Lawrence Berkeley Laboratory report LBL-2908*. Tech. rep. Lawrence Berkeley Laboratory, 1973.

[117] J. Gosset et al. "Central collisions of relativistic heavy ions". In: *Physical Review C* 16.2 (1977), pp. 629–657. DOI: 10.1103/physrevc.16.629.

[118] J-J Gaimard and K-H Schmidt. "A reexamination of the abrasion-ablation model for the description of the nuclear fragmentation reaction". In: *Nuclear Physics A* 531.3-4 (1991), pp. 709–745.

[119] M. de Jong, A.V. Ignatyuk, and K.-H. Schmidt. "Angular momentum in peripheral fragmentation reactions". In: *Nuclear Physics A* 613.4 (1997), pp. 435–444. DOI: 10.1016/s0375-9474(96)00460-5.

[120] K. Sümmerer and B. Blank. "Modified empirical parametrization of fragmentation cross sections". In: *Physical Review C* 61.3 (2000). DOI: 10.1103/physrevc.61.034607.

[121] H Okuno, N Fukunishi, and O Kamigaito. "Progress of RIBF accelerators". In: *Progress of Theoretical and Experimental Physics* 2012.1 (2012).

[122] Toshiyuki Kubo. "In-flight RI beam separator BigRIPS at RIKEN and elsewhere in Japan". In: *Nuclear Instruments and Methods in Physics Research Section B: Beam Interactions with Materials and Atoms* 204 (2003), pp. 97–113. DOI: 10.1016/s0168-583x(02)01896-7.

[123] JP Dufour et al. "Projectile fragments isotopic separation: Application to the lise spectrometer at GANIL". In: *Nuclear Instruments and Methods in Physics Research Section A: Accelerators, Spectrometers, Detectors and Associated Equipment* 248.2-3 (1986), pp. 267–281.

[124] K-H Schmidt et al. "The momentum-loss achromata new method for the isotopical separation of relativistic heavy ions". In: *Nuclear Instruments and Methods in Physics Research Section A: Accelerators, Spectrometers, Detectors and Associated Equipment* 260.2-3 (1987), pp. 287–303.

[125] T. Kubo et al. "BigRIPS separator and ZeroDegree spectrometer at RIKEN RI Beam Factory". In: *Progress of Theoretical and Experimental Physics* 2012.1 (2012), pp. 3C003–0. DOI: 10.1093/ptep/pts064.

[126] H. Geissel et al. "The GSI projectile fragment separator (FRS): a versatile magnetic system for relativistic heavy ions". In: *Nuclear Instruments and Methods in Physics Research Section B: Beam Interactions with Materials and Atoms* 70.1-4 (1992), pp. 286–297. DOI: 10.1016/0168-583x(92)95944-m.

[127] David J Morrissey and Brad M Sherrill. "In-flight separation of projectile fragments". In: *The Euroschool Lectures on Physics with Exotic Beams, Vol. I*. Springer, 2004, pp. 113–135.

[128] T. Kobayashi et al. "SAMURAI spectrometer for RI beam experiments". In: *Nuclear Instruments and Methods in Physics Research Section B: Beam Interactions with Materials and Atoms* 317 (2013), pp. 294–304. DOI: 10.1016/j.nimb.2013.05.089.

[129] Hermann Wollnik. *Optics of charged particles*. Elsevier, 2012.

[130] Kyoko Makino and Martin Berz. "Cosy infinity version 9". In: *Nuclear Instruments and Methods in Physics Research Section A: Accelerators, Spectrometers, Detectors and Associated Equipment* 558.1 (2006), pp. 346–350.

[131] R. Grzywacz et al. "Identification of μs-isomers produced in the fragmentation of a 112Sn beam". In: *Physics Letters B* 355.3-4 (1995), pp. 439–446. DOI: 10.1016/0370-2693(95)00501-b.

[132] K. Yoshida H. Kumagai. *PPAC for Beam Profile Monitor at the RIPS*. RIKEN Accel. Prog. Rep. 28. RIKEN, 1995.

[133] I. Tanihata H. Kumagai. *Development of Fast Two-Dimensional PPAC*. RIKEN Accel. Prog. Rep. 3. RIKEN, 1998.

[134] H. Kumagai et al. "Delay-line PPAC for high-energy light ions". In: *Nuclear Instruments and Methods in Physics Research Section A: Accelerators, Spectrometers, Detectors and Associated Equipment* 470.3 (2001), pp. 562–570. DOI: 10.1016/s0168-9002(01)00804-x.

[135] H. Kumagai et al. "Development of Parallel Plate Avalanche Counter (PPAC) for BigRIPS fragment separator". In: *Nuclear Instruments and Methods in Physics Research Section B: Beam Interactions with Materials and Atoms* 317 (2013), pp. 717–727. DOI: 10.1016/j.nimb.2013.08.050.

[136] Eljen Technology. *Organic Scintillators Datasheet*.

[137] K. Kimura et al. "High-rate particle identification of high-energy heavy ions using a tilted electrode gas ionization chamber". In: *Nuclear Instruments and Methods in Physics Research Section A: Accelerators, Spectrometers, Detectors and Associated Equipment* 538.1-3 (2005), pp. 608–614. DOI: 10.1016/j.nima.2004.08.100.

[138] H. Baba et al. "New data acquisition system for the RIKEN Radioactive Isotope Beam Factory". In: *Nuclear Instruments and Methods in Physics Research Section A: Accelerators, Spectrometers, Detectors and Associated Equipment* 616.1 (2010), pp. 65–68. DOI: 10.1016/j.nima.2010.02.120.

[139] S Takeuchi et al. "DALI2: A NaI (Tl) detector array for measurements of γ rays from fast nuclei". In: *Nuclear Instruments and Methods in Physics Research Section A: Accelerators, Spectrometers, Detectors and Associated Equipment* 763 (2014), pp. 596–603.

[140] Peter Rudolph. *Handbook of crystal growth: Bulk crystal growth*. Elsevier, 2014.

[141] Inc Saint-Gobain Ceramics & Plastics. "NaI(Tl) and Polyscin NaI(Tl) Sodium Iodide Scintillation Material Datasheet". 2016.

[142] RC Murty. "Effective atomic numbers of heterogeneous materials". In: *Nature* 207.4995 (1965), p. 398.

[143] R Anholt et al. "Observation of Radiative Capture in Relativistic Heavy-IonAtom Collisions". In: *Physical review letters* 53.3 (1984), p. 234.

[144] R Anholt et al. "Atomic collisions with relativistic heavy ions: Target inner-shell ionization". In: *Physical Review A* 30.5 (1984), p. 2234.

[145] R Anholt et al. "Atomic collisions with relativistic heavy ions. VI. Radiative processes". In: *Physical Review A* 33.4 (1986), p. 2270.

[146] JH Hubbell. "Tables of X-Ray Mass Attenuation Coefficients and Mass Energy-Absorption Coefficients. National Institute of Standards and Technology HP, Radiation interactions and dosimetry group". In: *http://physics. nist. gov/PhysRefData/XrayMassCoef/cover. html* (1996).

[147] M. O. Krause. "Atomic radiative and radiationless yields for K and L shells". In: *Journal of Physical and Chemical Reference Data* 8.2 (1979), pp. 307–327. DOI: 10.1063/1.555594.

[148] H. Scheit R. Holzmann. "ABKG code (GSI)". 1998.

[149] F. Biggs, L.B. Mendelsohn, and J.B. Mann. "Hartree-Fock Compton profiles for the elements". In: *Atomic Data and Nuclear Data Tables* 16.3 (1975), pp. 201–309. DOI: 10.1016/0092-640x(75)90030-3.

[150] James P. Rodman and Harlan J. Smith. "Tests of Photomultipliers for Astronomical Pulse-Counting Applications". In: *Applied Optics* 2.2 (1963), p. 181. DOI: 10.1364/ao.2.000181.

[151] M. Gadsden. "Some Statistical Properties of Pulses from Photomultipliers". In: *Applied Optics* 4.11 (1965), p. 1446. DOI: 10.1364/ao.4.001446.

[152] V. Borrel et al. "Peripheral Ar induced reactions at 44 MeV/u - similarities and deviations with respect to a high energy fragmentation process". In: *Zeitschrift für Physik A Atoms and Nuclei* 314.2 (1983), pp. 191–197. DOI: 10.1007/bf01879877.

[153] Anthony A. Tovar and Lee W. Casperson. "Generalized beam matrices: Gaussian beam propagation in misaligned complex optical systems". In: *Journal of the Optical Society of America A* 12.7 (1995), p. 1522. DOI: 10.1364/josaa.12.001522.

[154] P. Doornenbal et al. "Spectroscopy of Ne 32 and the "Island of Inversion"". In: *Physical Review Letters* 103.3 (2009). DOI: 10.1103/physrevlett.103.032501.

[155] S. Raman, C.W. Nestor, and P. Tikkanen. "Transition probability from the ground to the first excited 2+ state of even even nuclides". In: *Atomic Data and Nuclear Data Tables* 78.1 (2001), pp. 1–128. DOI: 10.1006/adnd.2001.0858.

[156] SR Stroberg et al. "Single-particle structure of silicon isotopes approaching Si 42". In: *Physical Review C* 90.3 (2014), p. 034301.

[157] A Gade and T Glasmacher. "In-beam nuclear spectroscopy of bound states with fast exotic ion beams". In: *Progress in Particle and Nuclear Physics* 60.1 (2008), pp. 161–224. DOI: 10.1016/j.ppnp.2007.08.001.

[158] A Obertelli et al. "Shell gap reduction in neutron-rich N= 17 nuclei". In: *Physics Letters B* 633.1 (2006), pp. 33–37.

[159] J.R. Terry et al. "Direct evidence for the onset of intruder configurations in neutron-rich Ne isotopes". In: *Physics Letters B* 640.3 (2006), pp. 86–90. DOI: 10.1016/j.physletb.2006.06.061.

[160] Nobuyuki Kobayashi et al. "One-neutron removal from Ne 29: Defining the lower limits of the island of inversion". In: *Physical Review C* 93.1 (2016), p. 014613.

[161] T Nakamura et al. "Halo Structure of the Island of Inversion Nucleus Ne 31". In: *Physical review letters* 103.26 (2009), p. 262501.

[162] P. Doornenbal et al. "Mapping the deformation in the "island of inversion": Inelastic scattering of Ne30 and Mg36 at intermediate energies". In: *Physical Review C* 93.4 (2016). DOI: 10.1103/physrevc.93.044306.

[163] Y Yanagisawa et al. "The first excited state of 30 Ne studied by proton inelastic scattering in reversed kinematics". In: *Physics Letters B* 566.1 (2003), pp. 84–89.

[164] E. Caurier, F. Nowacki, and A. Poves. "Shell model studies of neutron rich nuclei". In: *Nucl. Phys.* A693 (2001), pp. 374–382. DOI: 10.1016/S0375-9474(00)00579-0. arXiv: nucl-th/0011010 [nucl-th].

[165] P Fallon et al. "Two-proton knockout from Mg 32: Intruder amplitudes in Ne 30 and implications for the binding of F 29, 31". In: *Physical Review C* 81.4 (2010), p. 041302.

[166] MS Basunia and AM Hurst. "Nuclear Data Sheets for A= 26". In: *Nuclear Data Sheets* 134 (2016), pp. 1–148.

[167] M Shamsuzzoha Basunia. "Nuclear Data Sheets for A= 28". In: *Nuclear Data Sheets* 114.10 (2013).

[168] M. Shamsuzzoha Basunia. "Nuclear Data Sheets for A = 30". In: *Nuclear Data Sheets* 111.9 (2010), pp. 2331–2424. DOI: 10.1016/j.nds.2010.09.001.

[169] Ninel Nica and Balraj Singh. "Nuclear Data Sheets for A= 34". In: *Nuclear Data Sheets* 113.6-7 (2012), pp. 1563–1733.

[170] P. Doornenbal et al. "In-Beam gamma-ray Spectroscopy of Mg 34,36,38: Merging of the N=20 and N=28 Shell Quenching". In: *Physical Review Letters* 111.21 (2013). DOI: 10.1103/physrevlett.111.212502.

[171] Ninel Nica, John Cameron, and Balraj Singh. "Nuclear data sheets for A= 36". In: *Nuclear Data Sheets* 113.1 (2012), pp. 1–155.

[172] JA Tostevin. "Single-nucleon knockout reactions at fragmentation beam energies". In: *Nuclear Physics A* 682.1-4 (2001), pp. 320–331.

[173] P.G. Hansen and J.A. Tostevin. "Direct Reactions with Exotic Nuclei". In: *Annual Review of Nuclear and Particle Science* 53.1 (2003), pp. 219–261. DOI: 10.1146/annurev.nucl.53.041002.110406.

[174] A Gade et al. "Reduction of spectroscopic strength: Weakly-bound and strongly-bound single-particle states studied using one-nucleon knockout reactions". In: *Physical Review C* 77.4 (2008), p. 044306.

[175] D Bazin et al. "Mechanisms in knockout reactions". In: *Physical review letters* 102.23 (2009), p. 232501.

[176] K Wimmer et al. "Elastic breakup cross sections of well-bound nucleons". In: *Physical Review C* 90.6 (2014), p. 064615.

[177] K. Yoneda et al. "Two-neutron knockout from neutron-deficientAr34,S30, andSi26". In: *Physical Review C* 74.2 (2006). DOI: 10.1103/physrevc.74.021303.

[178] H. Sakurai et al. "Evidence for particle stability of F and particle instability of N and O". In: *Physics Letters B* 448.3-4 (1999), pp. 180–184. DOI: 10.1016/s0370-2693(99)00015-5.

[179] Yutaka Utsuno et al. "Extreme location of F drip line and disappearance of the N=20 magic structure". In: *Physical Review C* 64.1 (2001). DOI: 10.1103/physrevc.64.011301.

[180] J Lee et al. "Asymmetry dependence of reduction factors from single-nucleon knockout of 30Ne at 230 MeV/nucleon". In: *Progress of Theoretical and Experimental Physics* 2016.8 (2016).

[181] WH Dickhoff and C Barbieri. "Self-consistent Green's function method for nuclei and nuclear matter". In: *Progress in Particle and Nuclear Physics* 52.2 (2004), pp. 377–496.

[182] Jenny Lee et al. "Neutron-proton asymmetry dependence of spectroscopic factors in Ar isotopes". In: *Physical review letters* 104.11 (2010), p. 112701.

[183] Jenny Lee et al. "Neutron spectroscopic factors of Ar 34 and Ar 46 from (p, d) transfer reactions". In: *Physical Review C* 83.1 (2011), p. 014606.

[184] Freddy Flavigny et al. "Limited asymmetry dependence of correlations from single nucleon transfer". In: *Physical review letters* 110.12 (2013), p. 122503.

[185] J. M. Yao et al. "Configuration mixing of angular-momentum-projected triaxial relativistic mean-field wave functions. II. Microscopic analysis of low-lying states in magnesium isotopes". In: *Physical Review C* 83.1 (2011). DOI: 10.1103/physrevc.83.014308.

[186] O. Tarasov. "Analysis of momentum distributions of projectile fragmentation products". In: *Nuclear Physics A* 734 (2004), pp. 536–540. DOI: 10.1016/j.nuclphysa.2004.01.099.

[187] L. Olivier et al. "Persistence of the Z=28 Shell Gap Around Ni78 : First Spectroscopy of Cu79". In: *Physical Review Letters* 119.19 (2017). DOI: 10.1103/physrevlett.119.192501.

[188] A. de Shalit. "Core Excitations in Nondeformed, Odd-A, Nuclei". In: *Physical Review* 122.5 (1961), pp. 1530–1536. DOI: 10.1103/physrev.122.1530.

[189] F. Nowacki and A. Poves. "New effective interaction for 0hw shell-model calculations in the sd-pfvalence space". In: *Physical Review C* 79.1 (2009). DOI: 10.1103/physrevc.79.014310.

[190] Yutaka Utsuno et al. "Shape transitions in exotic Si and S isotopes and tensor-force-driven Jahn-Teller effect". In: *Physical Review C* 86.5 (2012), p. 051301.

[191] MV Stoitsov et al. "Quadrupole deformations of neutron-drip-line nuclei studied within the Skyrme Hartree-Fock-Bogoliubov approach". In: *Physical Review C* 61.3 (2000), p. 034311.

[192] Rémi N Bernard and Marta Anguiano. "Interplay between tensor force and deformation in even–even nuclei". In: *Nuclear Physics A* 953 (2016), pp. 32–64.

[193] J.F. Berger, M. Girod, and D. Gogny. "Time-dependent quantum collective dynamics applied to nuclear fission". In: *Computer Physics Communications* 63.1-3 (1991), pp. 365–374. DOI: 10.1016/0010-4655(91)90263-k.

[194] S. Hilaire and M. Girod. "Large-scale mean-field calculations from proton to neutron drip lines using the D1S Gogny force". In: *The European Physical Journal A* 33.2 (2007), pp. 237–241. DOI: 10.1140/epja/i2007-10450-2.

[195] Tomás R. Rodríguez and J. Luis Egido. "Configuration mixing description of the nucleus44S". In: *Physical Review C* 84.5 (2011). DOI: 10.1103/physrevc.84.051307.

[196] Z. P. Li et al. "Energy density functional analysis of shape evolution in N=28 isotones". In: *Physical Review C* 84.5 (2011). DOI: 10.1103/physrevc.84.054304.

[197] R. Chevrier and L. Gaudefroy. "Shell model structure of 43S and 44S re-examined". In: *Physical Review C* 89.5 (2014). DOI: 10.1103/physrevc.89.051301.

[198] C. Force et al. "Prolate-Spherical Shape Coexistence at N=28 in S44". In: *Physical Review Letters* 105.10 (2010). DOI: 10.1103/physrevlett.105.102501.

[199] Aage Bohr and B Mottelson. *Nuclear Structures, Vol. 1*. 1969.

[200] A. E. Litherland et al. "AN INTERPRETATION OF THE LOW-LYING EXCITED STATES OF Mg25 AND Al25". In: *Canadian Journal of Physics* 36.3 (1958), pp. 378–404. DOI: 10.1139/p58-039.

[201] Y. Fujita et al. "Evidence for the Existence of the [202]3/2 Deformed Band in Mirror Nuclei Mg25 and Al25". In: *Physical Review Letters* 92.6 (2004). DOI: 10.1103/physrevlett.92.062502.

[202] R. G. Hirko. "Structure of the sd shell nuclei". Yale University, 1969.

[203] E. Almqvist et al. "Low levels of Al27". In: *Nuclear Physics* 19 (1960), pp. 1–17. DOI: 10.1016/0029-5582(60)90214-5.

[204] J.H. Towle and W.B. Gilboy. "Spin assignments in Al27 from neutron scattering studies". In: *Nuclear Physics* 39 (1962), pp. 300–317. DOI: 10.1016/0029-5582(62)90394-2.

[205] T.R. Ophel and B.T. Lawergren. "The low-lying levels of Al27 (I)". In: *Nuclear Physics* 52 (1964), pp. 417–436. DOI: 10.1016/0029-5582(64)90704-7.

[206] P. R. Gardner. "Nuclear Spectroscopy in the 2s-1d shell". The Australian National University, 1973.

[207] P. J. M. Smulders, C. Broude, and J. F. Sharpey-Schafer. "Lifetime measurements in 27Al". In: *Canadian Journal of Physics* 46.4 (1968), pp. 261–267. DOI: 10.1139/p68-036.

[208] G. M. Crawley and G. T. Garvey. "Inelastic Scattering in the2s-1dShell. II. Odd-ANuclei". In: *Physical Review* 167.4 (1968), pp. 1070–1090. DOI: 10.1103/physrev.167.1070.

[209] H. Röpke, V. Glattes, and G. Hammel. "Rotation-vibration interaction in 27Al". In: *Nuclear Physics A* 156.3 (1970), pp. 477–488. DOI: 10.1016/0375-9474(70)90245-9.

[210] Ching-Liang Lin. "Band-Mixing Effects in Low-Lying States of 27Al". In: *Chinese Journal of Physics* 14.4 (1977), pp. 95–99.

[211] Ikuko Hamamoto. "One-particle properties of deformed N $\approx$ 28 odd-N nuclei with weakly bound or resonant neutrons". In: *Physical Review C* 79.1 (2009). DOI: 10.1103/physrevc.79.014307.

[212] Ikuko Hamamoto. "Neutron shell structure and deformation in neutron-dripline nuclei". In: *Physical Review C* 85.6 (2012). DOI: 10.1103/physrevc.85.064329.

[213] Ikuko Hamamoto. "Oblate deformation of light neutron-rich even-even nuclei". In: *Physical Review C* 89.5 (2014). DOI: 10.1103/physrevc.89.057301.

[214] Ikuko Hamamoto. "Shell structure of one-particle resonances in deformed potentials". In: *Physical Review C* 93.5 (2016). DOI: 10.1103/physrevc.93.054328.

[215] P. Möller et al. "Nuclear ground-state masses and deformations: FRDM(2012)". In: *Atomic Data and Nuclear Data Tables* 109-110 (2016), pp. 1–204. DOI: 10.1016/j.adt.2015.10.002.

[216] Hong-Bo Bai, Zhen-Hua Zhang, and Xiao-Wei Li. "Investigation of the Mg isotopes using the shell-model-like approach in relativistic mean field theory". In: *Chinese Physics C* 40.11 (2016), p. 114101. DOI: 10.1088/1674-1137/40/11/114101.

[217] OB Tarasov et al. "New isotope Si 44 and systematics of the production cross sections of the most neutron-rich nuclei". In: *Physical Review C* 75.6 (2007), p. 064613.

[218] O Sorlin and M-G Porquet. "Evolution of the N = 28 shell closure: a test bench for nuclear forces". In: *Physica Scripta* T152 (2013), p. 014003. DOI: 10.1088/0031-8949/2013/t152/014003.

[219] R. Palit et al. "Exclusive measurement of breakup reactions with the one-neutron halo nucleus 11Be". In: *Physical Review C* 68.3 (2003). DOI: 10.1103/physrevc.68.034318.

[220] I. Tanihata. "Nuclear structure studies from reaction induced by radioactive nuclear beams". In: *Progress in Particle and Nuclear Physics* 35 (1995), pp. 505–573. DOI: 10.1016/0146-6410(95)00046-l.

[221] A. S. Jensen et al. "Structure and reactions of quantum halos". In: *Reviews of Modern Physics* 76.1 (2004), pp. 215–261. DOI: 10.1103/revmodphys.76.215.

[222] T. Frederico. "Universal Aspects of Neutron Halos in Light Exotic Nuclei". In: *Few-Body Systems* 55.8-10 (2014), pp. 651–657. DOI: 10.1007/s00601-014-0874-7.

[223] Isao Tanihata, Herve Savajols, and Rituparna Kanungo. "Recent experimental progress in nuclear halo structure studies". In: *Progress in Particle and Nuclear Physics* 68 (2013), pp. 215–313. DOI: 10.1016/j.ppnp.2012.07.001.

[224] M Notani et al. "New neutron-rich isotopes, 34 Ne, 37 Na and 43 Si, produced by fragmentation of a 64 A MeV 48 Ca beam". In: *Physics Letters B* 542.1 (2002), pp. 49–54.

[225] SM Lukyanov et al. "Experimental evidence for the particle stability of 34Ne and 37Na". In: *Journal of Physics G: Nuclear and Particle Physics* 28.9 (2002), p. L41.

université PARIS-SACLAY | ÉCOLE DOCTORALE PHENIICS

Titre : Cartographie du grand îlot de déformation autour de N = 20 et 28

Mots clés : Structure nucléaire, Spectrométrie gamma, Noyaux exotiques

Résumé : Les nombres magiques de nucléons, qui se manifestent par de grandes écarts en énergie dans le modèle en couches sphériques, s'érodent dans les systèmes nucléaires asymétriques. L'évolution de ce comportement est étudiée dans deux régions sur, et près, des nombres magiques de neutrons N=20 et N=28 dans les isotopes de néon et d'aluminium riches en neutrons. La collectivité et la structure des états excités est étudiée par la spectroscopie gamma en-ligne des réactions de knock-out d'un et deux nucléons, et la diffusion inélastique.

Les expériences ont eu lieu au RIKEN Nishina Center à Tokyo, Japon. Les rayons gamma prompts ont étés observées dans le détecteur DALI2 et la structure nucléaire des isotopes de néon et d'aluminium riches en neutrons ont étés déduites.

Entre outre, les sections-efficaces inclusives et exclusives des états liés induites par le knockout d'un ou deux protons, en combinaison avec les calculs du modèle en couche et la théorie réactionnelle, élargissent les tendances systématiques de la région.

Les deux régions riches en neutrons à N = 20 et N = 28 ont été discutés dans les contexte d'un grand îlot de déformation réuni par la chaîne isotopique du magnésium. Ces observations élargissent la cartographie de cette région et contribue à la compréhension des forces motrices derrière sa formation.

Title : Mapping the Extended Island of Deformation around N=20 and 28

Keywords : Nuclear structure, Gamma spectroscopy, First observations

Abstract : Magic numbers of nucleons, which appear as large energy gaps in the spherical nuclear shell model, have been known to erode in asymmetric nuclear systems. The evolution of this behaviour is studied in two regions at, and near, magic neutron numbers N=20 and N=28 in neutron-rich neon and aluminium nuclei. Collectivity and excited state structure is studied through in-beam gamma-ray spectroscopy of one- and two-nucleon knockout reactions, and inelastic scattering.

Experiments were carried out at the RIKEN Nishina Center in Tokyo, Japan. Prompt gamma-rays were observed in the DALI2 detector and the nuclear structure of neutron-rich neon and aluminium isotopes were deduced.

In addition, inclusive and exclusive cross sections to bound states from one- and two-proton knockout reactions, in combination with shell model calculations and reaction theory, extends systematic trends in the region.

The two neutron-rich territories of N=20 and N=28 have been discussed as an extended island of deformation, joined-up through the magnesium isotopic chain. These observations enhance the mapping of this region and contribute to understanding the driving forces behind its formation.